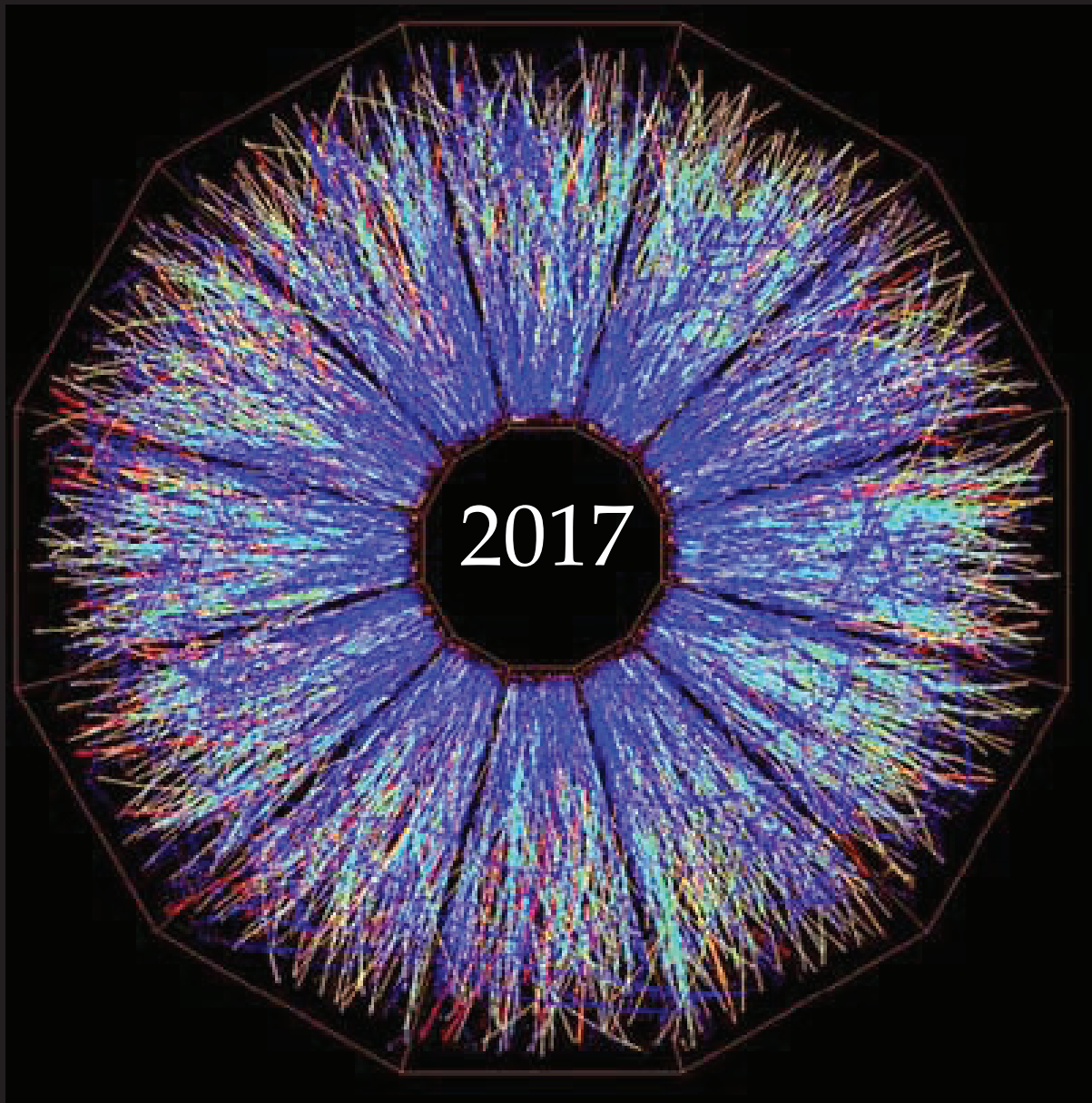


# A Compilation of Internship Reports



Prepared for The Office of Educational Programs  
Brookhaven National Laboratory  
Office of Educational Programs

### **DISCLAIMER**

This work was prepared as an account of work sponsored by an agency of the United States Government. Neither the United States Government nor any agency thereof, nor any of their employees, nor any of their contractors, subcontractors or their employees, makes any warranty, express or implied, or assumes any legal liability or responsibility for the accuracy, completeness, or any third party's use or the results of such use of any information, apparatus, product, or process disclosed, or represents that its use would not infringe privately owned rights. Reference herein to any specific commercial product, process, or service by trade name, trademark, manufacturer, or otherwise, does not necessarily constitute or imply its endorsement, recommendation, or favoring by the United States Government or any agency thereof or its contractors or subcontractors. The views and opinions of authors expressed herein do not necessarily state or reflect those of the United States Government or any agency thereof.



**BROOKHAVEN**  
NATIONAL LABORATORY

# Table of Contents

Ecological studies: Variations in habitat and clutch sizes of eastern box turtles in the northeastern United States. . . . .	7
<i>Octavia Allen</i>	
Mark and recapture analysis of mammal density and its impact on tick prevalence and the spread of Lyme disease. . . . .	11
<i>Scarlett Alvarez and Sofia Vaca</i>	
Testing materials for 10 ps timing resolution MCP-PMT detectors. . . . .	16
<i>Jaime E. Avilés Acosta</i>	
Support for the Collider Accelerator Department for the assembly of a Halbach dipole, design and construction of an improved diagnostic box, and design of a mechanical punch to improve the processing of radioisotope targets . . . . .	20
<i>Brian Brenton</i>	
Analyzing astrometric residuals and ellipticity of stars with MonoCam . . . . .	22
<i>Jason Brooks</i>	
Self-assembly of gold nanoparticles guided by tile-based DNA cubes . . . . .	27
<i>Dana Capitano</i>	
Using cosmic microwave background lensing to measure the bias of damped Lyman-alpha systems . . . . .	32
<i>Joseph Colosimo</i>	
Preparing the Baryon Mass Experiment (BMX) telescope for data acquisition . . . . .	35
<i>Chandler Conn</i>	
Performance simulation of electron multiplying charge coupled devices . . . . .	40
<i>Jenna DeCordova</i>	
An analysis of charge transparency in a LArTPC . . . . .	45
<i>Michael Dolce</i>	
Implementation of a graphics card based radio frequency spectrometer for the Baryon Mapping Experiment. . . . .	51
<i>Hindy Drillick</i>	
Development of cooling systems for sPHENIX components. . . . .	55
<i>Timothy Dvorak and Olivia Holmes</i>	
Concentration effect of LiNO <sub>3</sub> electrolyte in lithium-sulfur batteries . . . . .	60
<i>Ruby Epler</i>	
Pattern recognition in generalized continued fraction encodings of the Riemann Zeta zeros . . . . .	65
<i>Danielle Fieseler and Janelle Walker</i>	

Support structure design for the sPHENIX inner hadronic calorimeter . . . . .	69
<i>Howard Graham Giese</i>	
Examining transgenic poplar trees as a route towards improving cellulosic biofuel yields . .	74
<i>Timothy Grace</i>	
Low charge state ion beam production using a sub-nanosecond neodymium-doped yttrium aluminium garnet laser . . . . .	77
<i>Colin Guilbault</i>	
Study of the nonlinearity response for Large Synoptic Survey Telescope sensors. . . . .	81
<i>Thomas Hagan</i>	
ZSM-5 supported molybdenum carbide and oxide catalysts for methane dehydroaromatization: elucidation of active sites and deactivation pathways . . . . .	85
<i>Leah Harper and Sheima Khatib</i>	
Calibration interval of truck scales within waste management . . . . .	88
<i>Matthew Harris</i>	
Analyzing meteorological measurements and determining the operational comparability . .	91
<i>Brooke Hildebrand</i>	
Vast challenge mystery at the wildlife preserve . . . . .	95
<i>Rumeel</i>	
Implementing a Wire-Stretch test to locate the position of the electrical center of radio frequency cavities in operation in the RHIC . . . . .	98
<i>Wayne Johnson</i>	
The importance of bees: an interdisciplinary unit for fifth grade students . . . . .	100
<i>Michelle Joseph</i>	
Assessing preference by white-footed mice ( <i>Peromyscus leucopus</i> ) for coarse woody debris . . . . .	102
<i>Eric Juers</i>	
An assessment of bee diversity at “No-Mow” sites and the Long Island Solar Farm at Brookhaven National Laboratory . . . . .	106
<i>Julie Kapuvári, Claire Y. O’Kane, Trevor McIntosh, and Alexander Whittle</i>	
Dose assessment of radiation fields inside 8-ID-A first optical enclosure at the National Synchrotron Light Source-II. . . . .	110
<i>Kalifa O. Kelly, Jessie R. Zapata, and Mark C. Harvey</i>	
Microhabitat and vegetation selection of eastern box turtles ( <i>Terrapene carolina carolina</i> )	114
<i>Katherine Kennedy</i>	



Electromagnetic calorimeter quality control and mechanical design for the sPHENIX Project . . . . .	117
<i>Spencer Laddy-Locks</i>	
Improving machine-learning classification accuracy of x-ray scattering images . . . . .	120
<i>Ronald Lashley, Nicole Meister, Ziqiao Guan, and Bo Sun</i>	
Morphological effects of the nanostructured ceria support on the activity of Cu/CeO <sub>2</sub> catalysts for the reverse water-gas shift reaction. . . . .	123
<i>JinYing Lin</i>	
Characterization of <i>Arabidopsis thaliana</i> mutants defective in starch synthesis and lipid turnover. . . . .	128
<i>Tiffany Lin</i>	
Exploring $\Delta^{12}$ fatty acid desaturase (FAD) family protein interaction specificity . . . . .	131
<i>Katherine Lo</i>	
Evaluating the radiation dose around a hot cell after the bombardment of a Thorium target	135
<i>Juliana Mendes</i>	
Electron multiplying charge coupled device calibration for the NSLS-II soft inelastic x-ray scattering beam line . . . . .	141
<i>Lorena Mezini</i>	
A study of digital signal processing algorithms for time extraction from digitized multi-Gap Resistive Plate Chamber waveforms. . . . .	147
<i>Abioye Mohammed and Brendyn Van Demark</i>	
Designing a high-temperature superconducting magnet compression fixture . . . . .	149
<i>Patrick O'Donnell</i>	
Laser energy absorption efficiency as a function of laser intensity . . . . .	153
<i>Haejun Oh</i>	
An assessment of butterfly diversity at the Long Island Solar Farm . . . . .	157
<i>Claire Y. O'Kane, Julie Kapuvvari, Trevor McIntosh, and Alexander Whittle</i>	
Mass and mobility diameter classification of emissions from a wood-burning boiler . . . . .	160
<i>Kristen Okorn</i>	
Analysis of micrometeorites at the National Synchrotron Light Source II; introducing secondary education teachers to beamline science . . . . .	165
<i>Lauren Osojnak</i>	
Optimization of geometry and a radiation damage study of acrylic lightguides. . . . .	169
<i>Zackary S. Parsons</i>	

3-D printed multi-gap resistive plate chamber development . . . . .	172
<i>Abigail Paysinger, Marcus Alfred and Gaylon Robinson</i>	
Efficient full-stack web development for multidimensional scientific data visualization . . .	175
<i>Miguel Rodriguez</i>	
Characterization of Co-CeO <sub>2</sub> powder catalysts for the dry reforming of methane into synthesis gas . . . . .	179
<i>David Salazar</i>	
Using Advanced Metering Infrastructure for improved grid phase balancing . . . . .	183
<i>Hayden Sierra</i>	
Automated data verification and validation using zero-power nuclear reactors . . . . .	189
<i>Sukhjinder Singh</i>	
Value engineering: defining a beamline’s basic control system . . . . .	195
<i>Aliyah Smith</i>	
Assessing the cryptographic strength of RSA moduli using algorithmic entropy reduction in sequenced binary quadratic forms . . . . .	200
<i>Nicole Soder and Danielle Fieseler</i>	
Combining microscope images on a common coordinate system . . . . .	204
<i>Tunisia Solomon</i>	
Synthesis, activity, and characterization of Cu loaded ZSM-5 catalysts for the water-gas shift reaction . . . . .	207
<i>James Tata</i>	
The effects of human-made disturbances on small mammal populations . . . . .	211
<i>Leanna Thalmann</i>	
Modeling of superconducting magnet for ALPHA G experiment . . . . .	214
<i>Justin Tufaro</i>	
Optimizing the Large Synoptic Survey Telescope camera’s thermal mechanical performance . . . . .	217
<i>Julianna Volpe</i>	
Using Fourier analysis of web server logs to defeat low observable cybersecurity threats . .	221
Impact of Pine Barrens forest vegetation on population density of mice (small mammals) at Brookhaven National Laboratory . . . . .	224
<i>Tre’ Wise and Russell Burke</i>	
The process of aligning the carbon dioxide laser final amplifier in the Accelerator Test Facility II . . . . .	227
<i>Rick Zirkel</i>	

# Ecological studies: Variations in habitat and clutch sizes of eastern box turtles in the northeastern United States

Octavia Allen, Department of Natural Sciences, Southern University at New Orleans, New Orleans, LA 70126

Murty Kambhampati, Department of Natural Sciences, Southern University at New Orleans, New Orleans, LA 70126

Russell L. Burke, Department of Biology, Hofstra University, Hempstead, NY 11549

Timothy Green, Department of Environmental Protection Division, Brookhaven National Laboratory, Upton, NY 11973

## Abstract

**The Eastern Box Turtle (*Terrapene carolina carolina*) (EBT) is a popular charismatic species that has been the subject of multiple previous experiments. Clutch size (number of eggs per clutch) is a critical characteristic of reproductive fitness easily measured in EBT. Despite considerable research on EBT reproduction, it is unclear what factors cause variation in clutch size. Previous studies have shown a trend in an increase in clutch such in relation to higher latitudes. I also compared the Brookhaven National Laboratory (BNL) gravid turtles' carapace length to its average clutch size. From 2013-2017, EBTs were tracked at BNL using radio telemetry and data were collected using a digital infrared temperature gun, Kestrel weather station, and handheld Garmin GPS. Eight female *T. carolina carolina* were tracked twice/day, while another 11 EBT, male and female, were tracked twice/week. Adult female EBTs were radiographed to determine their gravidity status and clutch size. Out of 104 radiographs taken over 4 years, 32 EBT were gravid. Clutch size ranged from 3-7, annual average clutch size varied from 4.3 (2017) to 6.5 (2015), the overall average was  $5.4 \pm 0.78$  eggs/clutch. There is no significant evidence to suggest that precipitation, humidity, or temperature and the microhabitat directly affect the gravidity status and clutch size of EBT. The microhabitats of the EBT tracked via radio telemetry in the 2017 summer were observed, recorded, and analyzed in relation to the temperature and humidity taken. This work helped me better understand our environment and its effects on wildlife. I've learned various types of vegetation and how to identify them, the intricacies of radio telemetry, and can now implement techniques to record location, temperature, and humidity from doing research this summer.**

## I. Introduction and Objectives

The Eastern Box Turtle (*Terrapene carolina carolina*) is a popular charismatic terrestrial reptilian of the Testudines order, Emydidae family, and *Terrapene* genus. EBT are omnivores and have been known to be a good source of seed dispersal. They will eat earthworms, mushrooms, berries, insects, amphibians and carrion. They are active about early May to October, but they may be active earlier and later. They overwinter buried in leaves and soil. They seek damp mud or pools when temperatures get too high. They are found in most open forested habitats with lots of cover. EBT are prevalent in U.S. eastern deciduous forests, however many populations are experiencing different environmental factors that could be contributing to various outcomes in clutch sizes in diverse geographical regions. There are Pine Barren forests at BNL that they frequently inhabit. Environmental factors such as temperature, precipitation, and microhabitat play roles in

the quality of a turtle's existence.

North American box turtles (*Terrapene* spp.) typically demonstrate localized activity patterns that are highly dependent on temperature and precipitation.<sup>1</sup> Atypical activity patterns are frequently influenced by unusual weather conditions such as high temperatures, variable precipitation, and long droughts.<sup>1</sup> Ordinarily, *Terrapene* species prefer warm, humid, rainy conditions suggesting that box turtle populations are restricted to such micro-climatic ranges.<sup>1</sup> In east Texas, no documented reports were found of activity patterns, clutch sizes, sex ratios, or ratios of gravid to non-gravid females in *T. carolina triunguis* in relation to those conditions, which are in the same family and genus of EBT.<sup>1</sup>

Iverson et al. (1993) demonstrated a significant positive relationship between latitude and clutch size in many turtle species.<sup>2</sup> They noted that this pattern also occurred in other vertebrates as well as turtles. After adjusting for the possible effects of body size, they predicted larger clutches of smaller eggs in species at high latitudes. However, EBT were not included in the Iverson et al. (1993) analysis because insufficient clutch size data were available at that time.<sup>2</sup>

Usually, populations of northern *T. carolina* females deposit four or more eggs per clutch, whereas clutch sizes in the south tend to be one to three eggs per clutch.<sup>3</sup> However, there are exceptions. Currently, there are only vague clues as to what may account for the variation in clutch size in box turtles. I found the pattern of clutch sizes increasing at higher latitudes intriguing to see where Brookhaven National Laboratory would be on that trend line. Also, I wanted to see if there was a correlation between the EBT carapace length and average clutch size from 2013-2017 at BNL. I hypothesized that the larger the turtle is, the more eggs the turtle can carry.

## II. Methods and Materials

Radio telemetry has become a popular research instrument for studying the mobility of animals, because it permits scientists to find radio tagged wildlife on a regular basis that otherwise would be difficult to locate.<sup>4</sup> EBTs were tracked five times/week via radio telemetry. Eight were tracked twice/day and another 11 were tracked twice a week. Once found, GPS points were taken using a handheld Garmin 64s GPS that records the location in Universal Transverse Mercator (UTM). Other data were collected using an EXTECH Mini Infrared Thermometer 42500 gun to record the EBT carapace temperature and the ground temperature directly beside the EBT. A Kestrel 4000 pocket weather tracker was used to collect the temperature and humidity at ground level right beside the EBT and at standing height level, approximately 1.5m above ground. Also, the EBT micro and macro habitats were observed and the data were recorded based on dominate type

of vegetation. The mean annual temperature and precipitation at BNL from 2012-2017 was recorded and analyzed in comparison to the mean annual clutch size here at BNL (<https://www.bnl.gov/weather/>). Those data were analyzed since 2012 because the prior year has effect on the following year's production of nutrition. A SPI Dial Caliper (0.1mm) was used to measure the carapace length of all the turtles that were gravid.

In late May to early July, female EBTs were taken to get radiographed with a digital x-ray machine to determine their gravidity status. There were 24 female EBTs radiographed over the course of this study. Of the 24 females radiographed in 2017, 16 of them were gravid. The female would no longer be radiographed in the calendar year again once it was determined to be gravid. The remainders of the non-gravid EBT were radiographed until early July to analyze if they became gravid in later weeks. The carapace length was also measured on all the EBT found at any time on

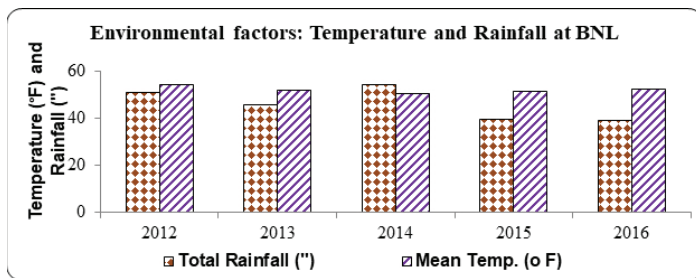


Figure 1: The total rainfall and mean temperature at BNL annually

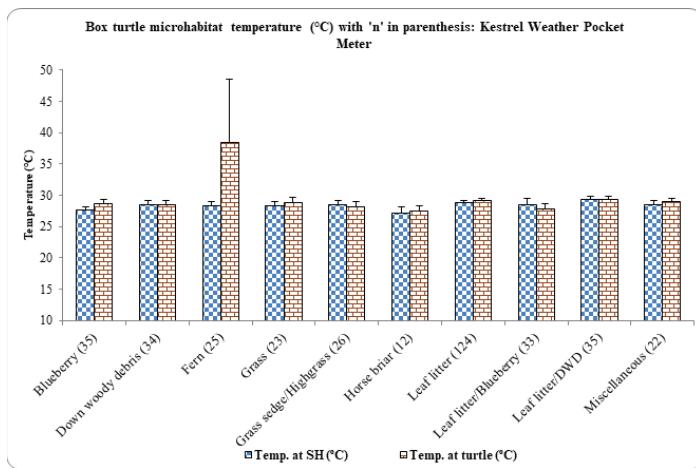


Figure 2: BNL EBT microhabitat in relation to temperature in 2017

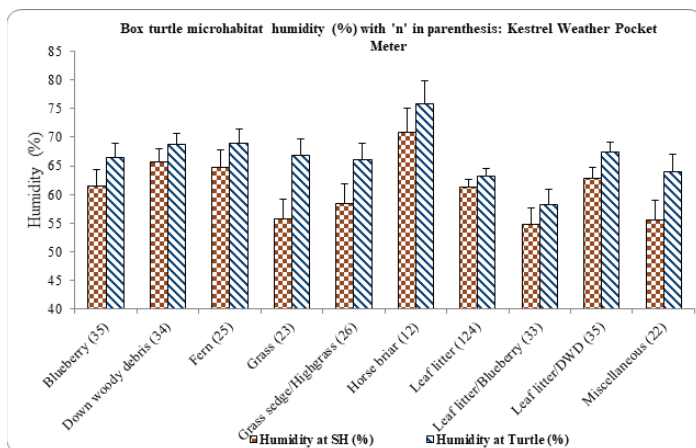


Figure 3: BNL EBT microhabitat in relation to humidity in 2017

the BNL site, including the gravid turtles. The carapace length to its clutch size average from 2013-2017 were compared to find if there is any significant correlation between these two variables.

### III. Results

The correlation coefficients were: Temp vs gravids (0.2611); Temp vs Clutch size (-0.0797); Gravids vs clutch size (-0.1751); Gravids vs rainfall (0.3471); Clutch size vs Rainfall (0.8764). Environmental factors of the previous year and the gravids and clutch size of the following year were analyzed to see any relationship.

The temperature of the turtle's microhabitat recorded using the Kestrel at standing height ranged from about 27-29°C. The temperature at the turtle was most often only approximately ± 1°C from the standing height temperature, except for fern which was about 10°C warmer at the turtle's height.

The humidity of the EBT microhabitat at standing height using the Kestrel varied from about 55-71%. However, the humidity at the turtle's height consistently surpassed the humidity at standing height in various microhabitats, ranging from about 58-76%. Suggesting the preference of higher humidity for EBT thermoregulation.

The dominant macrohabitat vegetation at Brookhaven National Laboratory consisted of maple, oak, and pine trees. Also, the temperature at the turtle's height was higher than the macrohabitat standing height temperature.

The humidity at the turtle's height was a greater percentage than at standing height, suggesting the optimal conditions for the EBT are warm and humid habitats.

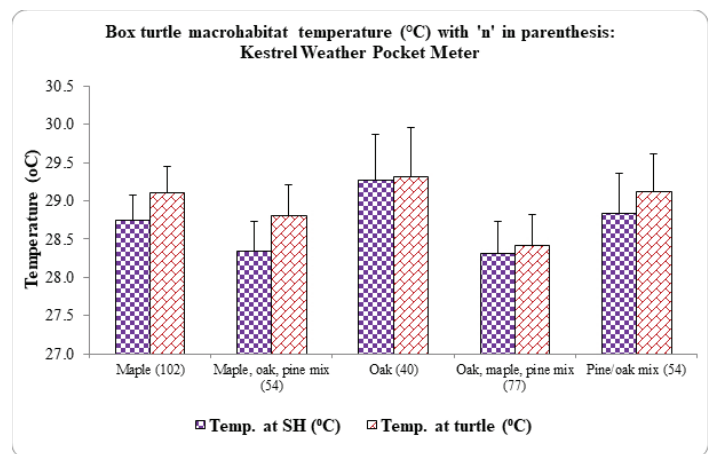


Figure 4: BNL EBT macrohabitat in relation to temperature in 2017

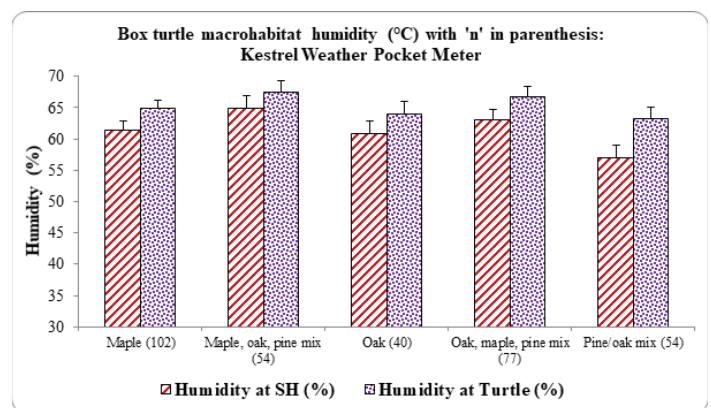


Figure 5: BNL EBT macrohabitat in relation to humidity in 2017



There wasn't any gradual decline or increase in the number of gravid EBT that were captured and radiographed over the course of this study.

There also wasn't a continuous gradual decline or increase in the mean clutch sizes of the BNL gravid EBT.

There is a slight positive correlation in EBT carapace length and average clutch size at BNL ( $r^2 = 0.1197$ ,  $t = 1.38$ ,  $p = 0.189227$ ).

Although there are differences in clutch sizes in different northeast regions in the United States, there seems to be a correlation with the clutch size and location relative to northern and southern locations with Brookhaven being the reference point. In Shirley, NY, which is south of Upton, NY, the average clutch size is lower than what was recorded at Brookhaven. North of Upton in Connecticut, the average clutch size was calculated to be higher than Brookhaven's. I compiled several studies on their latitude in which the study was conducted and compared the mean clutch sizes to see if there is indeed a positive, negative, or no correlation. There is a positive correlation (0.5339) in higher latitudes relative to bigger clutch sizes ( $r^2 = 0.53$ ,  $t = 2.87$ ,  $p = 0.009166$ ). However, it is not true in all cases.

#### IV. Conclusion

At higher latitudes, there tends to be larger clutch sizes in box turtles resulting in a slight positive correlation. Also, larger or longer turtles have the ability to hold more eggs. Temperature and clutch size have a negative correlation suggesting that there isn't much of an impact on the clutch sizes due to temperature. We found no relationship between environmental factors and the gravidity, carapace length, and clutch size of box turtles and accepted our null hypotheses.

#### V. Discussion

The 5.4 average at BNL is higher than the average clutch size of 4.1 at Wertheim National Wildlife Refuge in Shirley, NY approximately 11 km south, and lower than the average clutch size in Connecticut approximately 109 km north with 6.7 eggs/clutch.<sup>5,6</sup> Although they're relatively close, clutch sizes still vary in those different regions with Connecticut having the highest lat-

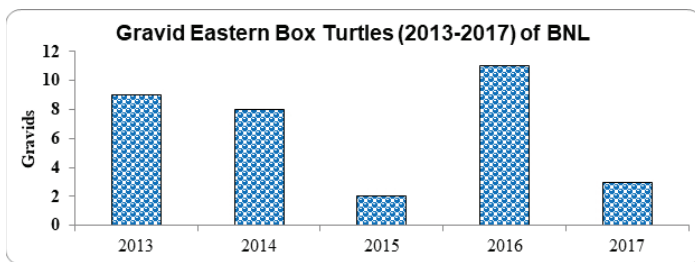


Figure 6: The number of gravid EBT at BNL annually

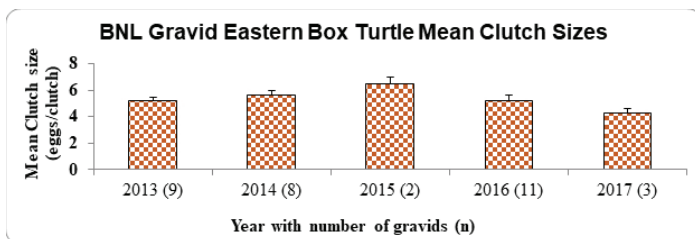


Figure 7: Number of gravids annually and its annual mean clutch size

itude, followed by BNL, then WNWR in Shirley. Although there are differences in clutch sizes in different northeast regions in the United States, there seems to be a correlation with the clutch size and location relative to northern and southern locations with Brookhaven being the reference point. In Shirley, NY, which is south of Upton, NY, the average clutch size is lower than what was recorded at Brookhaven. North of Upton in Connecticut, the average clutch size was calculated to be higher than Brookhaven's. I compiled several studies on their latitude in which the study was conducted and compared the mean clutch sizes to see if there is indeed a positive, negative, or no correlation. There is a positive correlation (0.5339) in higher latitudes relative to bigger clutch sizes ( $r^2 = 0.53$ ,  $t = 2.87$ ,  $p = 0.009166$ ). However, it is not true in all cases. The null hypothesis for the current study was that the variables (carapace length and clutch size) are unrelated. Since the table value is greater than the observed value, we cannot reject the null hypothesis ( $r = 0.3459$ ;  $df = 14$ ; table value 0.497) and the relationship was significant at  $p > 0.05$ .

#### VI. Acknowledgements

I'd like to thank Dr. Timothy Green for this wonderful opportunity and mentoring me throughout this process. Also, Dr. Kam who has been such an influential mentor since I've met him at SUNO and introduced me to this program. Thank you to Dr. Burke and Miranda for your guidance and teachings. I appreciate The Moriches Hospital for Animals for their hospitality and letting us use their facility. I am so grateful for James and Patricia Allen, my parents, for their encouragement and always supporting me. We also express our gratitude to the US Department of Education for partial financial support through SUNO-MSEIP grant. This project was supported in part by the U.S. Department of Energy, Office of Science, and Office of Workforce Development for Teachers and Scientists (WDTS) under the Science Undergraduate Laboratory Internships (SULI) program.

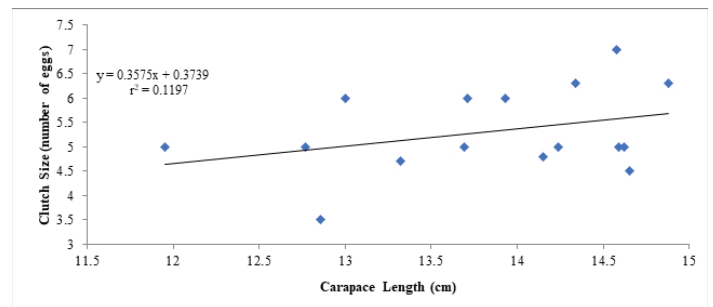


Figure 8: The carapace length of the 16 gravids versus its mean clutch size

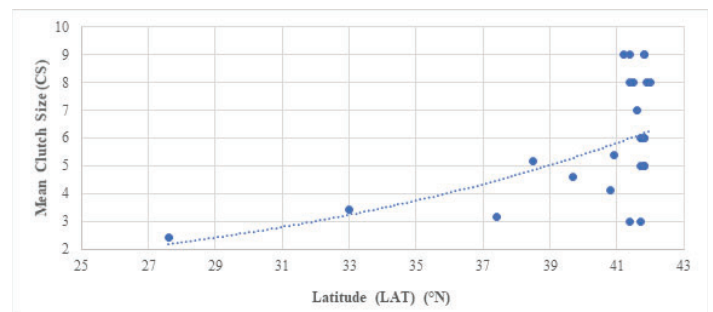


Figure 9: The latitude of *Terrapene carolina carolina* analyzed versus its mean clutch size<sup>2,5,6,7,8,9</sup>

## VII. References

- <sup>1</sup>A.B. Buchman, J.C. Cureton, W.I. Lutterschmidt, and E.D. Wilson, *Bios* 81: 84-90 (2010).
- <sup>2</sup>J.B. Iverson, C.P. Balgooyen, K.K. Byrd, and K.K. Lyddan, *Can. J Zool.* 71: 2448-2461 (1993).
- <sup>3</sup>C.K. Dodd, *North American box turtles: a natural history* (University of Oklahoma Press, Norman, 2002).
- <sup>4</sup>R.B. Iglay, J.L. Bowman, and N.H. Nazdrowicz, *Wildlife Society Bulletin* 34: 208-210 (2006).
- <sup>5</sup>R.L. Burke and W. Capitano, *The American Midland Naturalist* 165: 137-142 (2011).
- <sup>6</sup>M.W. Klemens, *Amphibians and reptiles of Connecticut and adjacent regions* (State Geological and Natural History Survey of Connecticut, Hartford, 1993).
- <sup>7</sup>T.M. Farrell, C.K. Dodd, and P.G. May, *Chelonian Research Monographs* 3: 235-248 *Biology and Conservation of Florida Turtles* (2006).
- <sup>8</sup>G.L. Wilson and C.H. Ernst, *Southeastern Naturalist* 4: 689-702 (2005).
- <sup>9</sup>R.L. Kipp, University of Delaware (2003).
- <sup>10</sup>S. Jones, W. Jordan, S. Meiners, A. Miller, and A. Methven, *The American Midland Naturalist* 157: 121-126 (2007).
- <sup>11</sup>A.F. Currylow, P.A. Zollner, B.J. Macgowan, and R.N. Williams, *The American Midland Naturalist* 165: 143-149 (2011).
- <sup>12</sup>R. Kiester and L. Willey, *Chelonian Research Monographs Conservation Biology of Freshwater Turtles and Tortoises* (2015).
- <sup>13</sup>L.L. Willey and P.R. Sievert, *Northeastern Naturalist* 19: 361-372 (2012).
- <sup>14</sup>P.M. Nieuwolt-Dacanay, *Copeia* 1997, 4: 819-826 (1997).
- <sup>15</sup>Virginia Herpetological Society, *Woodland Box Turtles: Terrapene carolina carolina* (2017).
- <sup>16</sup>Green, Timothy, Institutional Animal Care and Use Committee (IACUC) ANIMAL USE PROTOCOL # 436 (Eastern Box Turtles), Brookhaven National Laboratory, Upton, NY 11973 (2017).

# Mark and recapture analysis of mammal density and its impact on tick prevalence and the spread of Lyme disease

Scarlett Alvarez and Sofia Vaca, Department of Biology, Hofstra University, Hempstead, NY, 11549

Russell Burke, Department of Biology, Hofstra University, Hempstead, NY 11549

Timothy Green, Environmental Protection Division, BNL, Upton, NY, 11973

## Abstract

Lyme disease (LD) is the most common vector borne disease in North America; it is transmitted to humans primarily by the nymphal stage of blacklegged ticks (*Ixodes scapularis*). In most of the northeastern and Midwestern U.S., persistence of Lyme disease depends mostly on white-footed mice (*Peromyscus leucopus*) as they are common hosts for larval and nymphal blacklegged ticks and are highly competent reservoirs of the LD agent, *Borrelia burgdorferi*. Levi et al. (2012) linked the spread of coyotes into the eastern U.S. with increases in Lyme disease. We attempted to test 3 hypotheses that follow from Levi et al. (2012): 1) that white-footed mouse densities are positively associated with *Ixodes* tick densities, 2) that white-tailed deer densities are only correlated with *Ixodes* tick population densities when deer densities are low and 3) that red fox densities are negatively associated with small mammal densities. We collected relevant data in the Long Island Pine Barrens ecosystem. Sherman live traps were set up in sixteen sites for a total of 8,192 trap nights for mark-recapture analyses. We also collected ticks by flagging at each site. Ticks collected were categorized by species and life stage. We previously conducted research using the same methods in only four sites and found that there was a significant positive linear relationship between the density of mice and amount of nymphal *Ixodes* at each site.

## I. Introduction

Lyme disease (LD) is the most common tick-borne disease in the United States; the number of LD cases in eastern U.S. has been increasing constantly since 1995 (CDC, 2015). LD is caused by the spirochete bacteria *Borrelia burgdorferi* and, in the eastern U.S., is transmitted by blacklegged ticks *Ixodes scapularis* (Maloney, 2015). LD is a serious public health problem because if patients are left untreated, the infection can spread to other parts of the body such as the heart or nervous system and symptoms can continue for several months, ultimately becoming fatal (CDC, 2015). It is important to understand the dynamics of ecological systems that affect tick populations so that risk of Lyme disease can be properly assessed and reduced.

Host competence is a major factor in the spread of Lyme disease. Competent hosts are likely to maintain the bacteria and infect other ticks that subsequently feed on them (Hersh et al., 2012). *Borrelia burgdorferi* is found in a wide variety of mammals such as chipmunks, squirrels, and shrews, as well as birds, being that they are suitable hosts for the completion of the bacterium's enzootic life cycle (Wood and Lafferty, 2013). In the eastern U.S., *I. scapularis* ticks typically acquire *Borrelia* from

infected rodents while the larval ticks are feeding (Lane et al., 1991). During June and July, infected nymphs feed on other vertebrates prior to the larval feeding of the next generation in August (Frank et al. 1998). LD is transmitted to humans primarily by the nymphal stage of *I. scapularis* ticks which otherwise feed mostly on small mammals and birds in northeastern United States (Anderson and Magnarelli, 1984). Small mammals have no response to *B. burgdorferi* and can become competent reservoir hosts for adult ticks (Tilly et al. 2008).

Since *P. leucopus* are common, widespread, and a major keystone species among the ecological factors affecting Lyme disease, it is important to understand all the relationships that influence their population and density. Recently, coyotes (*Canis latrans*) have spread into eastern and northeastern United States (Kays et al, 2008). *C. latrans* may reduce the numbers of red foxes (*Vulpes vulpes*) through predation or competition, which can indirectly cause an increase in *P. leucopus* populations. Levi et al. (2012) suggested that without *V. vulpes* abundance and their regulation of the numbers of small-mammals, especially white-footed mice, more infected *I. scapularis* would be expected where there are high small mammal densities. Thus, Lyme disease may be increased indirectly due to the spread of coyotes.

The relationship between white-tailed deer (*Odocoileus virginianus*) and *I. scapularis* has been studied because they are important reproductive hosts for adult ticks (Barbour and Fish, 1993). However, Levi et al. also concluded that *O. virginianus* populations contributed to the prevalence of Lyme disease when populations were non-existent or low (2012). As the deer population grows, the probability of an adult tick finding a *O. virginianus* host becomes saturated. Thus, other factors such as suitable hosts and climate may become more important limiting factors. This is contrary to what many scientists believe, specifically in relation to the density of *O. virginianus* affecting the prevalence of *I. scapularis*, thus influencing the prevalence of Lyme disease.

In 2016 we conducted a pilot study testing Levi et al. (2012)'s hypotheses by measuring the abundance of *P. leucopus* populations, *I. scapularis* ticks, *O. virginianus*, and *V. vulpes* at four plots in the Long Island Pine Barrens ecosystem. However, this year we modified our investigation by adding twelve more plots. Particularly, we focused on examining only the relationships between the distributions of *I. scapularis* ticks at different life cycle stages found on *P. leucopus* populations. The data previously collected allowed us to infer about the types of effects that coyotes could have on hosts' susceptibility to this disease prior to their arrival. However, with the additional data collected this year we hope to gather vital information that would be useful when devising a plan to effectively control the spread of Lyme disease.

This research project involves testing some of Levi et al.

(2012)'s hypotheses. We accomplished this by measuring the abundance of *P. leucopus* populations, *I. scapularis* ticks, *O. virginianus*, and *V. vulpes* at four plots in the Long Island Pine Barrens ecosystem. In particular, we examined the relationships between the distributions of *I. scapularis* ticks at different life cycle stages found on *P. leucopus* populations.

We hypothesized that:

$H_1$ : *P. leucopus* population sizes are positively associated with *I. scapularis* population densities.

$H_2$ : *O. virginianus* densities are only correlated with *I. scapularis* population densities when *O. virginianus* densities are low.

$H_3$ : *V. vulpes* densities are negatively associated with small mammal densities.

## II. Methods

We conducted small mammal surveys beginning in June and lasting until the first week of August 2017 at Brookhaven National Laboratory in Upton, NY. Sixteen study plots were selected within BNL's campus (Figure 1, Leanna E. Thalmann). At each of the sixteen sites we established an 8x8 grid of Sherman traps spaced 5 meters apart, 64 traps per grid. Traps were baited with a peanut butter/oat mixture. Animals were trapped at each site over four consecutive nights during alternate weeks for a total of 8 days (or 512 trap nights/site, 8,192 total trap nights).

Traps were checked each morning, captured animals were weighed, sexed, and marked with individual ear tags. Recaptured individuals were noted. All attached ticks were removed and preserved. We collected ticks directly by flagging twice at each corner of the four sites for one minute intervals, ticks collected from flagging were also preserved. The number and life stage of each tick species were later determined in the lab. Four camera traps per week were set up at each site to monitor the abundance of other mammals such as *Vulpes vulpes* and *Odocoileus virginianus* at those sites. To attract mammals to the camera traps a scented disc was placed under the vegetation surrounding each camera.

Program MARK Version 8.1, robust design model was used for a parameter estimate of white-footed mice abundance at each site. The robust design model considers the time interval between trapping sessions as "open" and the time interval during trapping



Figure 1. Map of Brookhaven Laboratory of the sixteen sites used in the study. GPS coordinates (Universal Traverse Mercator units) were used to locate the sites on this map.

as "closed" (Cooch and White 2006). Although Program MARK is useful in comparing site to one another, it does not present a parameter for the population size. Therefore, Program DENSITY Version 5.0 was used to predict the size of *P. leucopus* population within 100m using the spatially explicit capture-recapture data collected (Efford, 2012). Program DENSITY was important so that the number of mice per hectare could be calculated. Program MARK and Program DENSITY were both important to conduct due to the different parameters. Tick prevalence was assessed calculating the proportion of mice with at least one attached tick during the experimental period. Average number of ticks per mouse was also calculated. Lastly, a basic linear regression was conducted to test for relationship of density of mice with prevalence of nymphal *Ixodes scapularis*.

## III. Results

A total of 1040 ticks (*Amblyomma americanum* and *Ixodes scapularis*) were collected from small mammals; the majority (N= 558) were *I. scapularis*. Four hundred forty-five small mammals were captured, of which 439 were *Peromyscus leucopus*, 5 were *M. pennsylvanicus*, and 1 was *T. striatus*.

Table 1 Prevalence of ticks on *Peromyscus leucopus* from all sites.

Site	Number of mice	Mice with > 1	Total ticks on mice	Mean # ticks/ mouse
1	41	16	150	3.7
2	40	12	139	3.5
3	6	0	0	0
4	18	2	3	0.2
5	10	3	8	0.8
6	47	19	248	5.3
7	25	12	78	3.1
8	24	11	152	6.3
9	18	3	20	1.1
10	13	2	14	1.1
11	20	5	21	1
12	35	17	82	2.3
13	42	3	0	0
14	36	1	0	0
15	25	14	76	3.04
16	39	15	49	1.3
Total	439	131	1040	32.7
Mean	27	8.2	65	2

Tick flagging obtained more *A. americanum* than *I. scapularis* in every site where ticks were found (Table 2). Furthermore, flagging at site 10 obtained the most ticks, despite sites 1 and 6 having the highest densities of *P. leucopus* as calculated by MARK recapture analysis and program Density (Table 3). The highest percentage of encounters that obtained *I. scapularis* were from site 8.

The DENSITY analysis gave larger populations for *P. leucopus* per hectare when compared to MARK recapture analysis.



**Table 2 Number of *Amblyomma* and *Ixodes* obtained from flagging at each site.**

Site	<i>Amblyomma</i> 1st dragging (L/N/A)	<i>Ixodes</i> 1st dragging (L/N/A)	<i>Amblyomma</i> 2nd dragging (L/N/A)	<i>Ixodes</i> 2nd dragging (L/N/A)	Total <i>Amblyomma</i> dragging (L/N/A)	Total <i>Ixodes</i> dragging (L/N/A)
1	0/4/0	0/0/0	0/1/2	0/0/0	0/5/2	0/0/0
2	0/3/0	0/0/1	0/4/1	0/0/1	0/7/1	0/0/2
3	0/2/2	0/0/0	0/3/0	0/0/0	0/5/2	0/0/0
4	0/0/3	0/0/1	0/0/2	0/0/0	0/0/5	0/0/2
5	0/0/0	0/0/0	0/0/0	0/0/0	0/0/0	0/0/0
6	0/2/2	0/0/0	0/0/0	0/0/0	0/2/2	0/0/0
7	0/1/2	0/0/0	0/20/0	0/0/0	0/21/2	0/0/0
8	0/7/2	0/0/2	0/9/3	0/0/2	0/16/5	0/0/4
9	0/4/0	0/0/0	0/5/0	0/0/0	0/9/0	0/0/0
10	0/7/1	0/0/0	0/17/0	0/0/0	0/24/1	0/0/0
11	0/4/0	0/0/0	0/6/0	0/0/0	0/0/0	0/10/0
12	0/2/1	0/0/0	0/1/2	0/0/0	0/0/0	0/3/3
13	0/0/0	0/0/0	0/0/0	0/0/0	0/0/0	0/0/0
14	0/2/0	0/0/0	0/0/0	0/0/0	0/2/0	0/0/0
15	0/0/0	0/0/0	0/0/0	0/0/0	0/0/0	0/0/0
16	0/1/0	0/0/0	0/2/0	0/0/0	0/3/0	0/0/0

**Table 3 Abundance of *P. leucopus* calculated from MARK recapture analysis, Program Density and percentage of *P. leucopus* that had at least one tick on them from each encounter at each site.**

Site	Abundance of mice from MARK analysis	Densities of mice calculated from program DENSITY	Percentage of encounters where mice had least 1 tick
1	35.4	27	39
2	31.1	30.5	30
3	3.3	6	0
4	35.4	35	11
5	8.6	9	30
6	35.6	18.5	40
7	12.6	18.5	48
8	19	19	46
9	11.1	13.5	17
10	8.5	12.5	15
11	13	12.5	25
12	24.8	27	49
13	26.9	31.5	7
14	20.5	26.5	3
15	14.3	13.5	56
16	22.3	24	38

However, the same trend in number *P. leucopus* per site was observed (Table 3). The basic linear regression showed there was no significant relationship between the density of mice calculated from program DENSITY with the prevalence of *I. scapularis* at each site (Fig 2A;  $R^2=0.05$ ,  $t(14) = 0.87$ ,  $p = 0.4$ ,  $n=16$ ). However, there was a significant and positive relationship between the sizes of the populations of mice calculated from program MARK and the prevalence of *I. scapularis* at each site (Fig 2B;  $R^2=0.25$ ,  $t(14) = 2.16$ ,  $p = 0.05$ ,  $n=16$ ).

The camera traps were mostly unsuccessful; they only recorded 16 *O. virginianus* (one in each of sites not including the two prescribed burn sites). There were no other mammals captured on footage, thus I was unable to test the relationship between the density of *O. virginianus* and *V. vulpes* in respect to the population of larval and nymphal *I. scapularis*.

#### IV. Discussion

*Peromyscus leucopus* is a keystone species in relation to *Ixodes scapularis* and *Borrelia burgdorferi* bacteria in major Lyme disease infection regions (Tsao et al., 2004). Therefore, understanding the ecological relationships that affect their populations are crucial to assessing LD disease risks. It's common to suggest a link between *Odocoileus virginianus* densities and LD prevalence (Barbour and Fish, 1993). However, there may also be less obvious relationships that increase the disease's prevalence. *Canis latrans* populations are increasing in eastern U.S. (Kays et al, 2008), which could lead to the reduction of meso-predator populations, perhaps increasing *P. leucopus* populations (Ostfeld and Holt, 2004). Levi et al. (2012) suggested that *Vulpes vulpes* abundance would be lowered due to the spread of *C. latrans*, then small mammal populations, which include *P. leucopus*, would be expected to increase. However, Way and White (2013) suggested that the Levi et al. model may be logically flawed, therefore unrepresentative of the real world.

Since my camera traps were unsuccessful, we could not evaluate possible relationship of *O. virginianus* densities to other species. However, in areas where ticks were found on mice, at least 15% of *P. leucopus* had ticks on them. Therefore, the density of *P. leucopus* is significantly and positively related to the density of *I. scapularis*. This is a critical foundation of Levi et al.,'s model that further indicated that LD rates may be increased indirectly due to the spread of *C. latrans* in the northeast. Furthermore, *I. scapularis* prevalence had a significant positive relationship with *P. leucopus* populations calculated by MARK recapture analysis.

However, there was no relationship found between *P. leucopus* populations calculated by program DENSITY and *I. scapularis* prevalence. Since nymphs are the primary transmission of Lyme disease to humans, an increase in *P. leucopus* density may lead to an increase in the transmission of LD to humans (Anderson and Magnarelli, 1984).

We attempted to test three hypotheses: (1) *P. leucopus* populations are positively

associated with *I. scapularis* densities, (2) *O. virginianus* densities are only correlated with *I. scapularis* densities when *O. virginianus* densities are low, and (3) *V. Vulpes* densities are negatively associated with small mammal densities. The results only allowed us to test the first hypothesis. Due to the discrepancies between results, it is difficult to conclude whether our hypothesis was supported. A significant positive relationship may yet be found between

*P. leucopus* populations and *I. scapularis* densities on each mouse if more sites were tested and for a longer period.

Other experiments may replicate this study using more sites to obtain a better understanding of the relationship between the ecological relationships that affect Lyme disease. Additionally, being able to obtain substantial data on the *O. virginianus* and *V. vulpes* populations would be important to further knowledge of this relationship. Some potential modifications to this experiment's replication may include sites located in other areas besides BNL and testing the ticks for the presence of *B. burgdorferi*. However, if *C. latrans* spreads into eastern Long Island, including BNL, then this experiment may be repeated to further evaluate the Levi et al., (2012) model.

#### V. Citations

- Anderson, J. F. & Magnarelli, L. A. (1984) Avian and mammalian hosts for spirochete-infected ticks and insects in a Lyme disease focus in Connecticut. *Yale J Biol Med*, 57(4), 627–641.
- Cooch, E., & White, G. (2006). Program MARK: a gentle introduction. Available in pdf format for free download at <http://www.phidot.org/software/mark/docs/book>.
- Efford, M. G. (2012). DENSITY 5.0: software for spatially explicit capture–recapture. *Department of Mathematics and Statistics, University of Otago, Dunedin, New Zealand* <http://www.otago.ac.nz/density>.
- Barbour, A. G. & Fish, D. (1993). The Biological and Social Phenomenon of Lyme Disease. *Science*, 260(5114), 1610–1616.

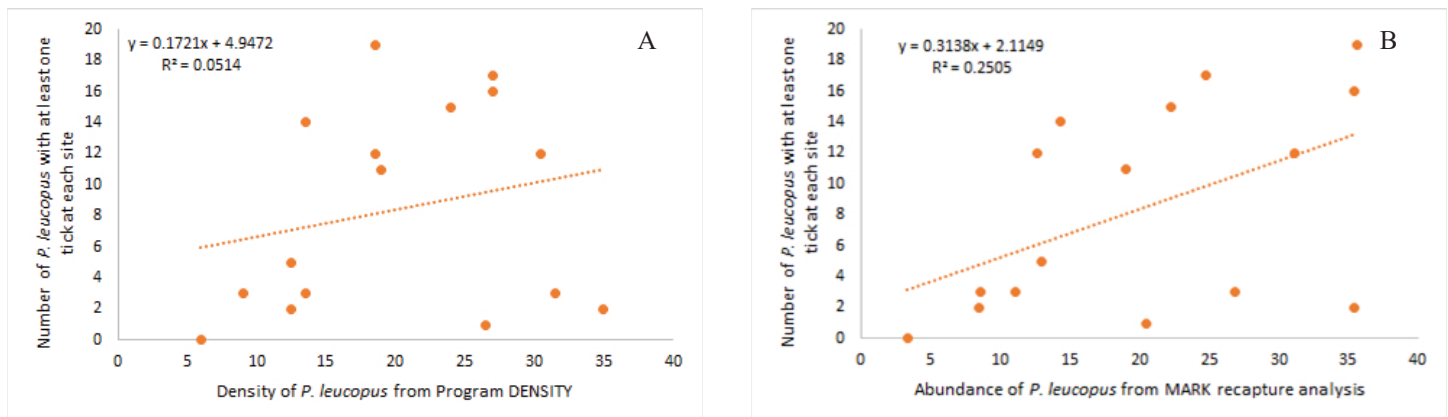


Figure 1 A- Prevalence of *I. scapularis* in relation to the density of mice calculated from Program DENSITY at each site. B- Prevalence of *I. scapularis* in relation to the abundance of mice from MARK recapture analysis at each site.

- Frank, D. H., Fish, D. & Moy, F. H. (1998). Landscape features associated with lyme disease risk in a suburban residential environment. *Landscape Ecology*, 13(1), 27–36.
- Hersh, M., Tibbetts, M., Strauss, M., & Ostfeld, R.S. (2012). Reservoir Competence of Wildlife Host Species for *Babesia microti*. *Emerging Infectious Disease journal – CDC*, 18(12), 1951–1957.
- Johnson, K.A., and Crabtree, R.L. (1999). Small prey of carnivores in the Greater Yellowstone Ecosystem. *Carnivores in Ecosystems: the Yellowstone Experience*. Yale University Press 239-263.
- Kays, R. W., Gompper, M. E. & Ray, J. C. (2008). Landscape Ecology of Eastern Coyotes Based on Large-Scale Estimates of Abundance. *Ecological Applications*, 18(4), 1014–1027.
- Lane, R. S., Piesman, J. & Burgdorfer, W. (1991). Lyme borreliosis: relation of its causative agent to its vectors and hosts in North America and Europe. *Annu. Rev. Entomol*, 36(1), 587–609.
- Levi, T., Kilpatrick, A. M., Mangel, M. & Wilmers, C. C. (2012). Deer, predators, and the emergence of Lyme disease. *PNAS*, 109(27), 10942–10947.
- Maloney, E. (2015). What Every Primary Care Clinician Should Know About the Diagnosis of Lyme Disease. *The Taproot*, 24(2), 4.
- Ostfeld, R. S., Jones, C. G. & Wolff, J. O. (1996). Of Mice and Mast. *BioScience*, 46(5), 323–330.
- Ostfeld, R. S. (1997). The Ecology of Lyme-Disease Risk: Complex interactions between seemingly unconnected phenomena determine risk of exposure to this expanding disease. *American Scientist*, 85(4), 338–346.
- Tilly, K., Rosa, P. A. & Stewart, P. E. (2008). Biology of infection with *Borrelia burgdorferi*. *Infect. Dis. Clin. North Am*, 22(2), 217–234.
- Tsao, J. I., Wootton, J.T., Bunikis, J., Luna, M.G., Fish, D., & Barbour, A.G. (2004). An ecological approach to preventing human infection: vaccinating wild mouse reservoirs intervenes in the Lyme disease cycle. *Proc. Natl. Acad. Sci. U.S.A.*, 101(52), 18159–18164.
- Way, J. G. & White, B. N. (2013). Coyotes, Red Foxes, and the Prevalence of Lyme Disease. *Northeastern Naturalist*, 20(4), 655–665.
- Wood, C. L. & Lafferty, K. D. (2013). Biodiversity and disease: A synthesis of ecological perspectives on Lyme disease transmission. *Trends in Ecology & Evolution*, *Trends in Ecology & Evolution*, *Trends in ecology & evolution (Personal edition)*, *Trends in Ecology and Evolution*, 28(4), 239–247.

# Testing materials for 10 ps timing resolution MCP-PMT detectors

Jaime E. Avilés Acosta, Physics Department, Indiana University, Bloomington, IN 47401

Mickey Chiu, Physics Department, Brookhaven National Laboratory, Upton, NY 11973

Alfred Marcus, Department of Physics & Astronomy, Howard University, Washington, D.C. 20059

## Abstract

A proposed upgrade to the sPHENIX experiment, at the Relativistic Heavy Ion Collider (RHIC) at Brookhaven National Laboratory, aims to improve its particle identification (PID) capabilities by developing detectors with a 10 ps timing resolution for time-of-flight (TOF) measurements. Over the summer, I worked on two projects to help achieve this: Characterizing the deep ultraviolet (UV) transmissivity of UV fused synthetic silica as a candidate Cherenkov radiating window material for microchannel plate photomultiplier tube (MCP-PMT) detectors, and measuring the deep UV quantum efficiency (QE) of a large area picosecond photon detector (LAPPD) MCP-PMT prototype, with a bialkali K<sub>2</sub>CsSb photocathode, developed in collaboration with the Argonne National Laboratory (ANL) and University of Chicago. The timing resolution of MCP-PMTs depends on the light yield of the detector's materials; the Cherenkov spectrum peaks in the deep UV, hence Cherenkov radiating materials with high UV transmissivity will improve the timing resolution of MCP-PMT detectors. K<sub>2</sub>CsSb photocathodes are expected to have a higher QE in the deep UV range; similarly, this would improve timing resolution. Advances by the LAPPD collaboration can be spun-off to industry, driving down the cost of large area high performance photodetectors detectors. The transmissivity of a 7.92 mm thick UV fused silica window (Alkor) stays above 40% even at 170 nm; we compare this the transmissivity of other materials in the same range. As of this writing, preliminary QE measurements have been done for the LAPPD MCP-PMT, with more underway. With these measurements, we will have made progress towards affordable 10 ps timing detectors that can yield new physics from RHIC. This project has developed my versatility with LabView programming and lab instrumentation; it has deepened my understanding of detector physics, and how advances in detector technology can push the boundaries of our knowledge.

## I. METHODOLOGY

### A. Deep UV Transmissivity measurements of UV fused silica

We use a McPherson UV spectrometer to measure the transmissivity of a UV fused quartz window, a UV fused silica window, two UV fused silica windows with a gas gap, and two UV fused silica windows with the gap filled with DC200 optical grease (Dow Corning). The windows were purchased from Alkor Technologies. A diffraction grating and a double slit edge are used to control the wavelength range of the beam and its bandwidth, respectively. We sampled wavelengths between 155 nm and 195 nm at an interval of 2 nm, with a UV collimated beam with bandwidth of 4 nm. For measurements at this wavelength range, we needed to purge the spectrometer with argon gas (99.9995% pu-

rity) beforehand, achieving O<sub>2</sub> concentrations below 5 ppm and H<sub>2</sub>O concentrations below 17 ppm for all our measurements. To measure the windows' transmissivities, we illuminate a PMT with a collimated beam from a deuterium lamp: Once with the window in the beam, and twice without the window in the beam before and after the former measurement. These are referred to as the sample and the pre- and post-reference scans, respectively. The reference scans are averaged to take any drift in intensity into account.

The PMT operates in single photoelectron mode, at a voltage of 190V to achieve saturation of its photocathode. The ratio of the sample scan current,  $I_{smp,i}$ , to the reference scan current,  $I_{ref}$ , taken at a wavelength setting, after taking dark current  $I_{dark}$  into account, yields the transmissivity of the window(s) at that wavelength (eq. 1) for that measurement  $i$ .

$$T_i(\lambda) = \frac{I_{smp,i}(\lambda) - I_{dark,i}}{I_{ref,i}(\lambda) - I_{dark,i}} \quad (\text{eq. 1})$$

### B. Deep UV quantum efficiency measurement of MCP-PMT with K<sub>2</sub>CsSb photocathode

The quantum efficiency (QE) measurement of the LAPPD MCP-PMT is conducted with the same spectrometer under similar conditions; the wavelength range we sample will be between 155 nm and 195 nm at an interval of 2 nm, and a bandwidth of 4 nm. We apply a voltage of 3.1kV to the MCP-PMT's photocathode, and use a voltage divider to apply a 2.7kV bias to the first MCP just below the photocathode (Fig. 2).

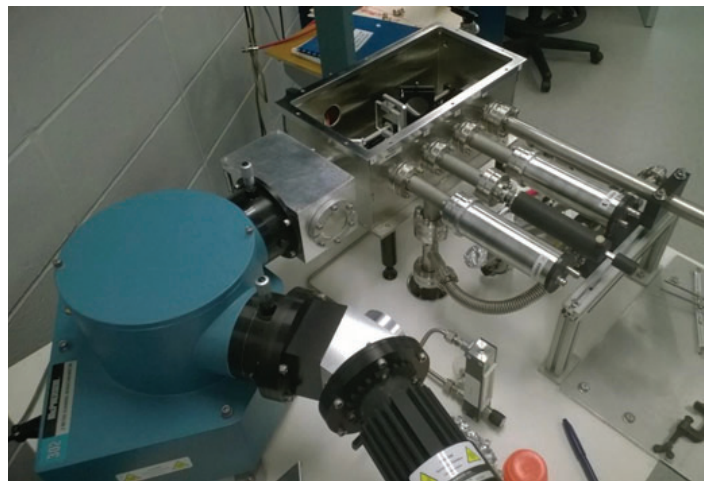


Figure 1. The McPherson UV spectrometer. Equipped with a deuterium lamp (bottom), a diffraction grating and beam collimator (left) is used to shine UV light through the window samples (top) and then reflected into a PMT (top right).



As before, the chamber is filled with nitrogen gas (99.90% purity), to reduce O<sub>2</sub> and H<sub>2</sub>O concentrations below 5 ppm and 17 ppm, respectively. Like the transmissivity measurements, two reference scans will be done before and after doing a sample scan, where a sample scan is done when the UV beam is shining on the LAPPD. The reference scans are done with the same PMT as before (Hamamatsu 6835), since it has a known QE for the sampled wavelength range; we read the photocurrent of the PMT without gain, such that we can calculate the number of photons impinging the PMT. The absolute photon flux,  $\Phi_{\gamma}(\lambda)$ , is calculated by dividing the PMT's photocurrent measured at a certain wavelength by the PMT's corresponding QE at that wavelength,  $QE_{PMT}(\lambda)$

$$\Phi_{\gamma,i}(\lambda) = \frac{I_{ref,i}(\lambda) - I_{dark,i}}{QE_{PMT}(\lambda)} \quad (\text{eq. 2}).$$

Knowing the number of incident photons impinging on the LAPPD MCP-PMT at a certain wavelength, we calculate the relative QE of the MCP-PMT,  $QE_{MCP}(\lambda) * Gain$ , by taking the ratio of the measured current at a wavelength setting to the absolute flux of photons at that wavelength (eq. 3).

$$QE_{MCP,i}(\lambda) * Gain = \frac{I_{MCP,i} - I_{ark,MCP,i}}{\Phi_{\gamma,i}(\lambda)} \quad (\text{eq. 3})$$

### C. Statistical analysis of data and measurement considerations

Since the PMTs used during these measurements do not have gain, at some wavelengths we are reading small currents in the picoamp scale with a significant dark current component in our

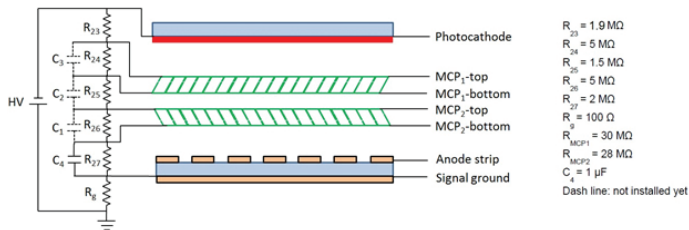


Figure 2. LAPPD MCP-PMT electronic circuit diagram.

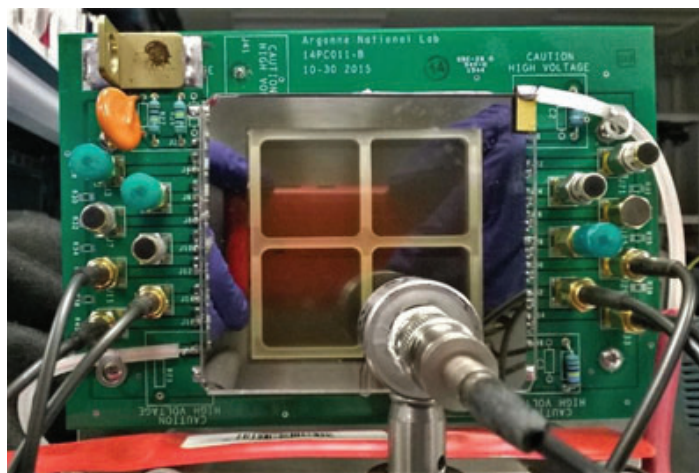


Figure 3. LAPPD MCP-PMT on a PCB. The dark areas on the front are the photocathode.

readings. The dark current depends on the voltage applied to the photocathode; in our case we apply enough voltage until the photocathode reaches saturation (Fig. 5). To eliminate this current offset, we measure the dark current before a pre-reference scan and after a post-reference scan and then subtract the averaged dark current from our current readings. In the case of our QE measurements, the dark current in the PMT and the LAPPD are both measured before and after the pre- and post-reference scans.

All measurements are partly or fully automated with Lab-View virtual instruments (VI) modified or written by myself; individual current readings taken by VI are the mean of several readings from picoammeters (Keithley 6487), with  $N = 5$  for LAPPD scans, and  $N = 20$  for PMT scans, with an accompanying standard deviation. Individual sets of data, which consist of reference scans, sample scans, and dark current measurements, are used to calculate the transmissivity of the window samples or the relative QE of the LAPPD MCP-PMT. Several sets of data are used to calculate the transmissivities of each sample and the MCP-PMT's QE at corresponding wavelengths, with accompanying propagated uncertainties for each of those transmissivity values and relative QE values. Naturally, transmissivity and QE values for one wavelength will deviate from each other; to obtain our final values, we took the weighted means of the calculated transmissivities and QE for a corresponding wavelength from each data set (eq. 4).

$$\bar{x}_{weighted} = \frac{\sum_{i=1}^N \frac{x_i}{\sigma_i^2}}{\sum_{i=1}^N \frac{1}{\sigma_i^2}} \quad (\text{eq. 4})$$

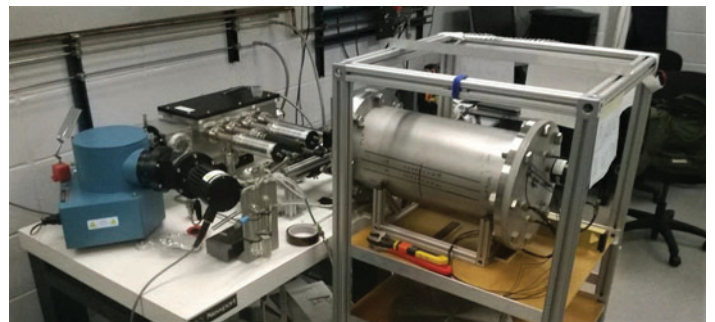


Figure 4. The set-up used to measure the QE of the LAPPD MCP-PMT.

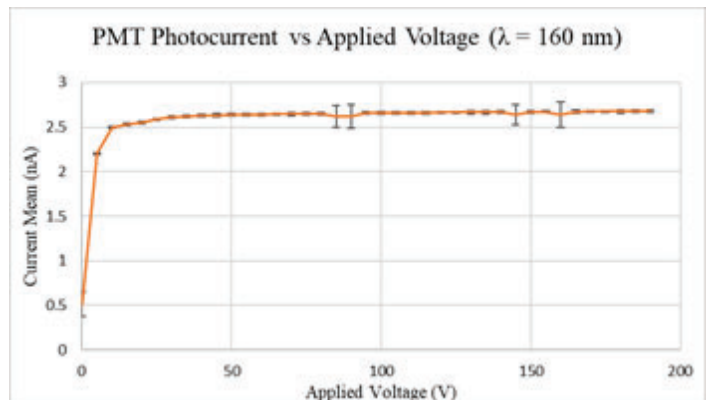


Figure 5. IV curve for PMT when shone with the deuterium UV lamp ( $\lambda=160nm$ ).

## II. RESULTS

### A. Transmissivity of UV fused silica

We compare our transmissivity measurements to those of a colleague<sup>3</sup> performed at wavelengths ranging from 190 nm to 800 nm, allowing one to interpolate the materials' transmissivities between the two ranges. Several data sets were taken for determining the transmissivity of each of our window(s) samples; final values displayed here are obtained by taking the weighted mean for the transmissivity at each point from all available data sets, and we determined their corresponding errors through propagation of uncertainty (Fig. 6).

### B. Relative QE of LAPPD MCP-PMT with K<sub>2</sub>CsSb photocathode and UV fused silica window

The relative QE measurements for the ANL-developed LAPPD are displayed below (Fig. 7). We expected a bump around 170 nm<sup>5</sup>, indicating the emission of two or more photoelectrons by energetic photons, although it might be obscured by the anomalously large QE above 170 nm.

Note that the calculated relative QE above is adjusted for transmissivity and the result of taking weighted averages over several data sets.

### C. Issues with QE Measurement and Suggestions

We noticed that our collaborators at ANL built the MCP-PMT with a UV fused silica window from GM Associates; the quality of UV fused silica windows varies depending on the manufacturing process, which can introduce contaminants. To test for this, we requested a UV fused silica window from our collaborators at ANL from GM Associates to test its transmissivity in the wavelength range of interest, from 149 nm to 199 nm. Yet, there are other potential issues:

The CsI PMT we use for our reference scan is operating already at the upper edge of its range of sensitivity to UV light—non-linear effects dominate too much in this range, or the PMT has expended its usability in this range. Comparing the measured UV lamp's intensity spectrum to that expected from McPherson's data sheets indicates this may be the case. A reference scan with another PMT of known QE, with an overlapping wavelength range with those of our measurements, would be prudent.

The beam spot position from the UV lamp is not the same for all wavelengths—the spot position could begin to change for wavelengths > 170 nm, drifting it away above or below the middle strip of the bottom-right side of the MCP-PMT (which is

where we originally aimed the UV beam). Since the strips were not all being measured at once, it would be better to connect them in series to account for this.

## III. FURTHER DISCUSSION

We demonstrate higher deep UV transmittance in UV fused silica compared to UV fused quartz and even DC200 optical grease; to our knowledge, there is no optical grease with comparable transmittance to UV fused silica. The LAPPD we tested features a bialkali K<sub>2</sub>CsSb photocathode expected to have a higher QE in the deep UV range due to double photoelectron emission<sup>2,5</sup>. Our measurements do not conclusively demonstrate this double photoelectron emission, but the hump of relative QE around 170 nm looks promising. The higher transmissivity of UV fused silica, and higher QE of K<sub>2</sub>CsSb at the deep UV range, will increase the number of photoelectrons released by charged particles, and thus increase the timing resolution of the detector. The time it takes for electrons to travel through the detector has an uncertainty, the transit time spread (TTS), measured to be 50 ps for this MCP-PMT design<sup>2</sup>. We can average the amount of time it takes for electrons to travel through the detector and achieve a time resolution of  $50 \text{ ps}/\sqrt{N_{PE}}$ , where  $N_{PE}$  is number of photoelectrons. The differential spectrum of the Cherenkov photons (eq. 5) can be used to estimate the number of generated photoelectrons by integrating over wavelength and window width (eq. 6).

$$\frac{d^2 N_\gamma}{dz d\lambda} = \frac{2\pi Z^2 \alpha_{EM}}{\lambda^2} \left[ 1 - \frac{1}{n^2 \beta^2} \right] \quad (\text{eq. 5})$$

$$N_{pe} = \int dz \int d\lambda \frac{d^2 N_\gamma}{dz d\lambda} QE(\lambda) T(\lambda) \quad (\text{eq. 6})$$

$Z$  is the charge of the particle in elementary charge units of  $e$ , and  $\alpha_{EM}$  is the fine structure constant.  $T(\lambda)$ ,  $n$ , and  $QE(\lambda)$  are the transmittance, index of refraction, and quantum efficiency of the window, respectively. With the currently known QE of LAPPD MCP-PMT with a borosilicate window down to 330 nm, calculations show that  $N_{PE} = 127 \text{ ps}$ , and with a TTS of 50 ps, the absolute best timing resolution of this detector should be  $50 \text{ ps}/\sqrt{127} = 4.4 \text{ ps}$ .

However, with a UV fused silica window, light can be transmitted down 170 nm, where the QE of K<sub>2</sub>CsSb is expected to increase; with this combination, the number of photoelectrons

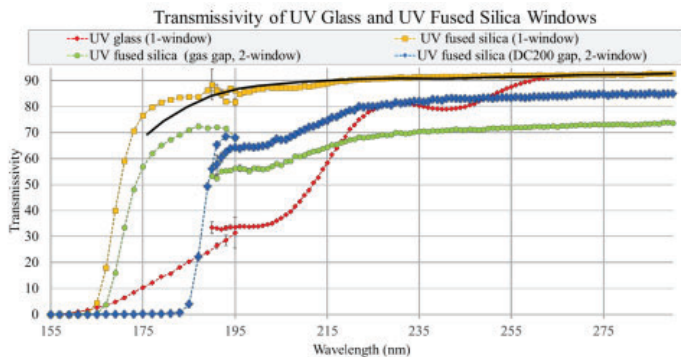


Figure 6. A plot of our calculated transmissivities, along with those found by another intern, Taylor Shimek<sup>3</sup>, in the range 190 – 800 nm. The solid black line is the transmissivity quoted by Alkor<sup>4</sup> for their UV fused silica window.

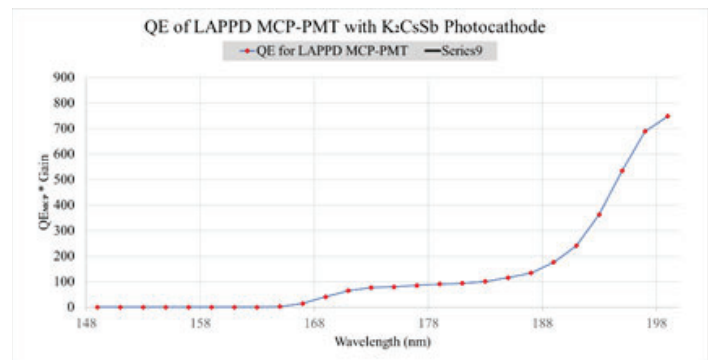


Figure 7. The calculated relative QE for the LAPPD MCP-PMT, based on our data. We believe that this curve is erroneous, and that the high relative QE at wavelengths above 170 nm is due to some systematic error.

is expected to double, yielding a best possible timing resolution of 3.1 ps. Our study will be followed up with tests with pico-lasers, which will directly test the timing resolution of the LAPPD MCP-PMT. We have also established procedures for measuring the LAPPD MCP- PMT's gain, which can also be done with the pico-laser.

Another criteria for candidate detectors for the sPHENIX upgrade, besides performance, is affordability. The LAPPD collaboration made their MCPs by extruding glass ingots with capillaries until the channels were shrunk to a diameter of 10  $\mu\text{m}$ ; the collaboration's advances in manufacturing the MCPs can be spun-off to industry, driving down the cost of large area high performance photodetectors detectors. With this study, we have shown progress towards cheaper, yet better performing, prospective detectors for the sPHENIX upgrade.

#### IV. REFERENCES

- <sup>1</sup>Woody, Craig. (October 2010). Photodetector Applications, NSS/MIC ShortCourse
- <sup>2</sup>Chiu, Mickey. (July 2017). Calculation of Photoelectron Yield for a MCP-PMT TOF with Radiator. Private communication.
- <sup>3</sup>Shimek, Taylor. (July 2017). Privatecommunication.
- <sup>4</sup>Alkor Technologies. (N.d). Graph of UV fused silica transmissivity. Retrieved July31, 2017 from:[http://www.alkor.net/FusedSilica\\_windows\\_and\\_lenses.html](http://www.alkor.net/FusedSilica_windows_and_lenses.html),
- <sup>5</sup>Araujo, et al. (June 1998). IEEE Transactions on Nuclear Science, vol. 4.5, no.3.

#### V. ACKNOWLEDGEMENTS

I am very grateful for the oversight and guidance provided by my mentors Dr. Mickey Chiu and Professor Marcus Alfred. Dr. Babak "Bob" Azmoun also deserves special acknowledgement for helping me build on the UV spectrometer and program new LabView virtual instruments, as well as for his technical insight, all of which was indispensable for this project. This project was made possible in part by the support of the U.S. Department of Energy's Office of Science, and the Supplemental Undergraduate Research Program (SURP).

I would also like to thank my fellow interns working under the guidance of Dr. Chiu and Professor Alfred, Gaylon Robinson, Brendyn Van Demark, Abioye Mohammed, and Abby Paysinger, for their support and willingness to teach me new skills that helped develop this project.



# Support for the Collider Accelerator Department for the assembly of a Halbach dipole, design and construction of an improved diagnostic box, and design of a mechanical punch to improve the processing of radioisotope targets

Brian Brenton, Division of Engineering Programs, SUNY New Paltz, New Paltz, NY 12561  
George Mahler, Collider Accelerator Department, Brookhaven National Laboratory, Upton, NY 11973

## Abstract

The Collider Accelerator Department (CAD) at Brookhaven National Lab (BNL) works on a multitude of projects with particle accelerators. Currently, the CAD is working with Cornell University on the Cornell-BNL Energy Recovery Linac (ERL) Test Accelerator (C-BETA), a step in the right direction coinciding with BNL's plans to build the electron Relativistic Heavy Ion Collider (eRHIC) based on the effectiveness of technology used in C-BETA. Such an accelerator uses Halbach dipole magnets. We successfully developed an assembly process for constructing a prototype of the dipole that is to be replicated in the construction of dipoles for C-BETA. Additionally, the CAD works with facilities such as the Tandem Van de Graaff and Brookhaven Linac Isotope Producer (BLIP). At Tandem, an improvement to the diagnostic box, specifically the length the capacitors can move is desired. Consequently, we have designed new support plates for both the bearings and motors, and an attachment to the current carriage which drives the plates. The new design was successful in increasing the distance the capacitors can move allowing Tandem to pursue further research. Lastly, BLIP conducts research in nuclear medicine specifically radioisotopes which have shown promising results in cancer treatment. Radioisotopes are created by shooting beam at specific targets. We have been working on a design to mechanically remove the targets from their holders. The prototypes so far have yet to be tested, but our intentions are that once tested they will improve the processing of the radioisotopes by making it more efficient and secure. As a result of my time at BNL I have become exposed with the design process and the fabrication of both particle accelerators and its compliments. I have also added Creo Parametric and Cura to my repertoire of familiar computer software.

## I. Background

### A. C-BETA Dipole magnets

The dipole magnet that is to be used in C-BETA uses Fixed Field Alternating Gradient (FFAG) technology, meaning force vectors of the magnets are of different directions and magnitudes. The forces among the magnets must be taken into consideration when assembling the dipole and should be kept at a minimum. The dipole is assembled in halves and then the two blocks are brought together mechanically.

### B. Diagnostic Box

In order to allow the rails to extend the full length of the track in the diagnostic box at Tandem, a lead screw must go the full length of the track, therefore a longer rod is needed and the motor must be moved. We decided the best placement given the other components in the box and the ability to reuse existing parts were to offset the drive to the carriage.

### C. BLIP

The processing of the radioisotope targets at BLIP takes place behind thick concrete walls. A mechanical arm is operated from outside the walls which controls manipulator tips on the inside. The target punch and catcher were designed in accordance to be a feasible method of removing the targets from their holders.

## II. Methods

### A. Assembly of C-BETA Dipole

The rare earth magnets used to construct the dipole are neodymium iron boron magnets. These magnets are purposely manufactured stronger than necessary on purpose as copper shims can be inserted between the magnets to create the necessary spacing to decrease the magnetic field as desired. When placing the magnets in their proper positions, 3D printed plastic parts are used to serve as placeholders. Once all magnets have been assembled, a pump is used to create a vacuum in addition to using fixtures and plumbers putty to seal any leaks. Next, epoxy is poured on the top fixture and drawn by vacuum to fill in any spaces between the magnets. Once settled the hardened epoxy holds the magnets in place. The two halves are brought together using clamps and screws, constructing a dipole.

### B. Linear Motion Design

To extend the length of the rails, the parts for the new design were plotted using an Ultimaker 3+, a 3-D printer, which provided quick and testable prototypes. These parts consisted of new support plates for the motor and bearing, and an attachment to the current carriage. A longer lead screw was machined to provide drive to the entire length of the track.

### C. Design of the Target Removal Mechanism

The target punch was designed to be for handled by the manipulator tips from multiple angles. The catcher allows for easy and safe removal of the target. These were modeled in Creo Parametric, A computer aided design 3D modeling software. They were then plotted using Cura software and 3d printed using an Ultimaker.





Figure 1. Completion of a working prototype of the Halbach dipole.



Figure 2. Epoxy is being poured into the vacuum fixture and being drawn

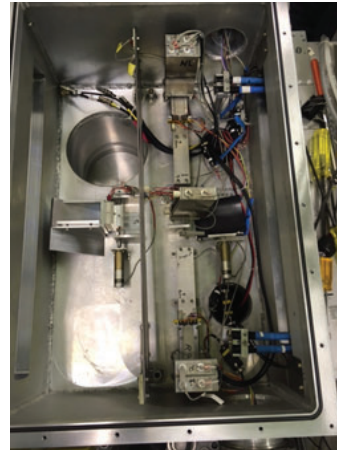


Figure 3. Old design of the diagnostic box. Rails only have the capability to extend half the length of the track.



Figure 4. Diagnostic box with rails extended, note white and yellow 3D printed parts.

### III. Results

#### A. Halbach Dipole Construction

By following the methods of assembly, we were able to construct a working prototype of the Halbach dipole as shown in Figure 1. The use of plastic place holders and vacuum fixtures used made for a feasible method of constructing the dipole. The epoxy was strong enough to hold the magnets in place and the blocks provided for a sturdy structural set up. A similar assembly process as shown in Figure 2 is to be replicated by companies when constructing these Halbach dipoles.

#### B. Implementation of Extended Rails

The new design which consisted of the extended rails, new support plates for the bearings, motors and carriages allowed for further linear motion of the cups. Looking at the old design in Figure 3, you can see the cups only have the ability to move half the length of the plate. Compared to the new design shown in Figure 4, which has offset motors and drives to the carriages allows for full mobility of the cups along the rails allowing further tests to be performed.

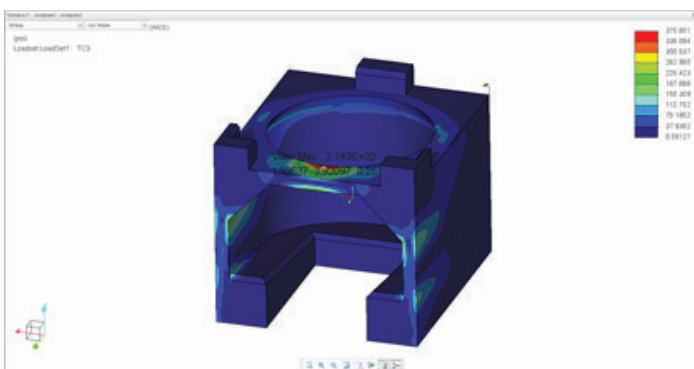


Figure 5. Stress Analysis shows a maximum stress under 50lbs of force of 374 psi. PLA has a yield strength of about 8,000 psi giving us a high safety factor.

#### C. Design and analysis of Mechanical Punch and Catcher

The mechanical catcher underwent a stress analysis test to make sure it can withstand the amount of force applied when being used. This was performed using a structural simulation using Creo Parametric as seen in Figure 5. The maximum stress under 50lbs of force as expected was where the least amount of support was. This stress was well under the Von Mises stress of polylactic acid (PLA), allowing for this material to be used. Therefore we could easily produce these parts using a 3D printer. Hopefully these parts can easily be handled by the manipulator tips at BLIP allowing for the quick and efficient processing of the radioisotope targets.

### IV. Conclusion

The Halbach dipole upon completion was then tested using a sophisticated rotating coil measuring device at the Magnet Division. The magnet passed inspection and now the process of making CAD drawings has begun in order to allow companies to bid on the cost of the manufacturing of the magnets. The new design for the diagnostic box was successful as the cups now have the ability to move the entire length of the track. However, some adjustments needed to be made to the switches as there was a timing mechanism on the code that would tell the user where the cups were. We were able to trick the switches by tying them down with zip ties. The target punch and catcher have yet to be tested at BLIP. Furthermore, we are working on a new design which will allow for an easier and more efficient way to remove the targets.

### V. Acknowledgements

This project was supported in part by the U.S. Department of Energy, Office of Science, Office of Workforce Development for Teachers and Scientists (WDTS) under the Science Undergraduate Laboratory Internships Program (SULI).

# Analyzing astrometric residuals and ellipticity of stars with MonoCam

Jason Brooks, Physics, The University of Texas at Austin, Austin, TX 78705

Andrei Nomerotski, Department of Physics, Brookhaven National Laboratory, Upton, NY 11973

## Abstract

We compare the positions of well-known stars with measurements taken by MonoCam, a camera that consists of a single prototype Large Synoptic Survey Telescope (LSST) charge-coupled device (CCD) sensor. Images were taken at the U.S. Naval Observatory in Flagstaff, Arizona (NOFS) employing its 61-inch telescope and the LSST G, R, I, and Z filters. Differences in star position measurements can reveal defects in the sensor that could warrant correction in LSST software. Using two different catalogs of known star positions, we found through an autocorrelation procedure that residuals (differences between MonoCam measured positions and well-known catalog star positions) are not entirely random and show the strongest correlation up to about 300 arcseconds; though correlations decrease when we remove stars with very low flux and high flux. We also found that astrometric residuals with the Gaia catalog are relatively small, confirming that MonoCam holds fairly well to its specifications, despite being in a different location and different telescope than LSST. However, we have not found any clear indication that sensor defects are apparent. It was also suspected that residuals around the edge of the sensor would be most prominent, and we found that residuals close to the sensor edge grew larger the closer to the edge they were, after removing low and high flux stars from our analysis. Lastly, we found that removing low flux stars significantly improved ellipticity measurements and astrometric residual results.

## I. Introduction

The Large Synoptic Survey Telescope (LSST) aims to explore the night sky in six optical bands ranging from 320nm to 1100nm.<sup>1</sup> LSST will have unprecedented precision to probe the nature of dark energy and dark matter, to take an inventory of the Solar System, to map the Milky Way, and to explore transient phenomena in the optical sky.<sup>1,2</sup> The LSST focal-plane array will have 21 Science Rafts each composed of nine 4K×4K CCDs with a pixel size of 10×10μm.<sup>3</sup> The large field of view, 9.6 square degrees, and ability to read out all CCDs in only 2 seconds with a total exposure time of 15 sec, will allow LSST to image the entire accessible sky in only two to three days.

The fully depleted sensors are 100 μm thick to improve their IR sensitivity. Figure 1 shows the total LSST throughput in the six bands. The specifications of LSST sensors is given in<sup>4</sup> and require that median error in absolute astrometric positions do not exceed 50 milliarcseconds (mas). Astrometric residuals can also reveal sensor defects such as tree rings,<sup>5</sup> and can be useful in identifying defects like this.

This experiment utilizes "MonoCam," a camera with a single LSST CCD read out by a commercial controller and equipped with an LSST y4 filter. MonoCam collected data at the 61 inch

telescope at NOFS in Flagstaff, AZ in May 2016 (more on this below).

## II. MonoCam

MonoCam employs a single LSST prototype sensor, CCD-250 113-03, produced by e2v.<sup>7</sup> The sensor is divided up into two rows of eight 512×2002 amplifier regions stacked side-by-side for a total size of 4096×4004 pixels, and is read out by a commercial Reflex controller<sup>8</sup> using RTS-2 software.<sup>9</sup> MonoCam was placed in a cryostat cooled with liquid nitrogen to keep the CCD back biased to -70V at a temperature of 120 C under vacuum of about 10<sup>-6</sup> torr. A Keithley source meter 2410 was used to provide the back side bias for the sensor. All equipment including the CCD cryostat was used for LSST CCD R&D at BNL between 2008-2015, and is described in more detail elsewhere.<sup>10</sup>

### A. Telescope

All data analyzed in this paper was taken at the U.S. Naval Observatory located at Flagstaff, Arizona on the night of May 3 and the night of May 4, 2016 using its 61 inch telescope. In addition, these images came from the two star fields at RA 13 16 30.05 and DEC +29 06 02.09 and RA 15 32 09.69 and DEC +13 56 15.9. In this paper we will refer to these two fields as lsst1316+3 and lsst1532+1, respectively.

The telescope used was a reflector with a focal plane scale of 13.5 arcsec/mm and an overall focal ratio of f/9.8. The diameter of the primary mirror is 1.55m (61 inches) with a focal ratio of f/9.8 and has a paraboloid figure. The secondary mirror has a diameter of 0.89m and a flat figure. The MonoCam field of view at this telescope is 0.15×0.15 square degrees.<sup>11</sup>

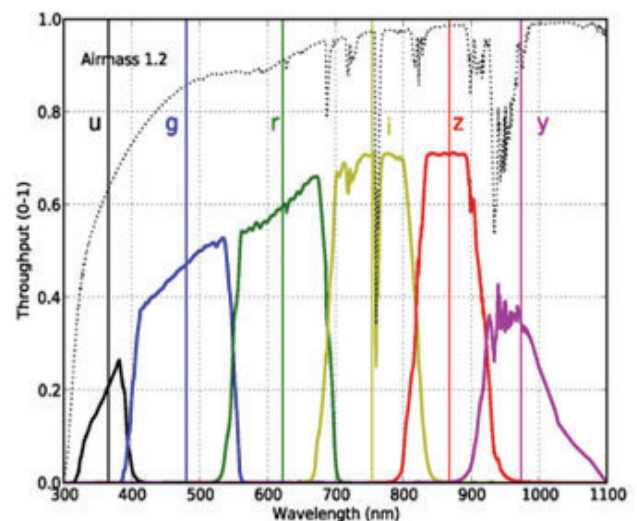


Figure 1: LSST filter bands.<sup>6</sup> All images analyzed in this paper were taken with the G, R, I and Z filters. The dotted line represents the throughput or transmission of the atmosphere at a given wavelength.

## B. Data Acquisition

Data at the 61inch telescope was taken two nights. On both nights, images were taken of both lsst1316+3 and lsst1532+1 fields using the G,R,I, and Z filters with 5 dithers per filter for a total of eighty exposures. Twilight sky flats and bias exposures were also taken, but no dark exposures.

## C. Data Reduction

Images that were analyzed in this paper were first run through LSST Data Management software.<sup>12,13</sup> This software was used to generate calibrated exposure ("calexp") images and source catalog files that utilized flat field correction and bias subtraction. Flat field correction helps to account for unwanted static features on the images, as well as differences in amplifier gain. Bias subtraction aids in removing amplifier offsets on a pixel-by-pixel basis. Flat fielding seems to have added some unwanted smudges in the processed data, but apart from this, it does appear to "flatten" out the image. The gaia catalog was used to match with stars measured by MonoCam. Gaia is a space telescope that can measure stars positions to a precision of about 0.1mas to 1mas.<sup>14</sup>

## III. Astrometry and Ellipticity Measurements

### A. Gaia Catalog residuals

The scatter and histogram plot in Figure 2 shows residuals (distance between MonoCam measured stars and their associated stars in the gaia catalog) as a function of integrated point spread function (psf) flux. We find the median residual to be 23.5mas and mean residual to be 45.4mas. The center of the bin in Figure 2 with the most counts is 6.8mas. For dim stars and very bright stars, we find that the scatter of residuals is fairly large compared to the residual for medium-brightness stars. This implies that there were issues matching stars in these regions; for low flux stars it is possible that the noise level was roughly comparable to the star's flux, making it difficult to find the center of each star's psf, and for high flux stars over-saturation of pixels could have also warped the star's psf so much that finding the true star center was also difficult to accurately determine.

The patterns shown in Figure 3 show the residual vectors, which point from source star to reference star. From this image, it is not immediately apparent that meaningful patterns exist, but in the we will show that there exists some correlation between the residuals.

### B. Ellipticity Measurements

Ellipticity measurements can reveal information about the atmosphere the night data was taken (wind and atmospheric distur-

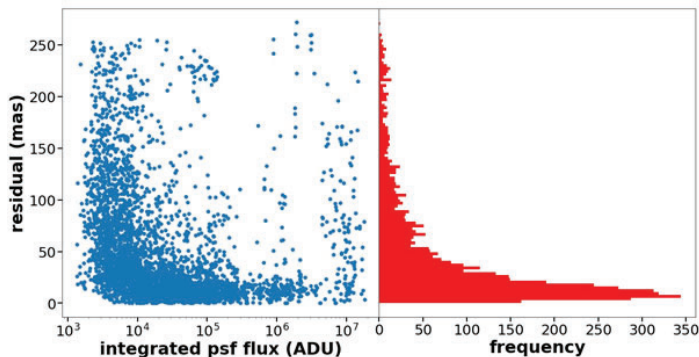


Figure 2: residual scatter plot as a function of integrated psf flux (left) and histogram of residuals (left).

tions can also distort star measurements), and can give insight into the quality of images taken. We measured the ellipticity of source stars, shown in Figure 4, as a function of integrated psf flux. We define ellipticity,  $e$ , for each star to be:

$$e = \frac{a^2 - b^2}{a^2 + b^2}$$

where  $a$  is the star's semimajor axis (in arcseconds) and  $b$  is the star's semiminor axis (also in units of arcseconds). Note that, just like with the astrometric residuals shown in Figure 2, high flux stars have a fairly uniform distribution of ellipticity values compared to lower flux stars. There also appears to be two extra rows of ellipticity values for lower flux stars. We will show later that these rows largely come about due to some visits with bad measurements of stars.

Figure 5 shows the whisker plot for all ellipticities from all stars in all visits combined into one plot. The length of each whisker is proportional to the ellipticity of the measured star rotated to point in the same direction as the star's semimajor axis.

Figure 6 shows the average ellipticity and average orientation of the semi major axis as a function of visit number. From this plot we can see that there are about six visits that appear to stand out from the rest. Otherwise, ellipticity values appear to cluster around a nominal value of 10%, and has a relatively random orientation going from visit to visit.

### C. Edge Residuals

It is expected that residuals will grow larger as stars get closer to the edge of the device due to sensor edge effects. We calculate the average residual in 10 pixel-sized bins starting from 100 pixels from the left, right, top, and bottom sensor edge and going to their respective edge, and then combine them into two plots that show how residuals change as a function of distance from the top or bottom sensor edge (left plot in Figure 7) or as a function of distance from the left or right sensor edge (right plot in Figure 7). We can see that there could be some downward trend as residuals move further away from the sensor edge, but the plots as they are now are possibly distorted due to bad visits, bad residuals from high flux stars, and bad residuals from low flux stars. In the next section we will remove these possible issues and see how the results change in response.

### D. Removal of Bad Visits, Low Flux Stars, and High Flux Stars

The results shown in Figures 2 and 4 seem to imply that we could improve our results if we remove high flux stars and low flux stars from our analysis, as well as a handful of what appears to be bad visits from the average ellipticity plot shown in Figure 6.

When we remove stars lower than the 30th percentile flux and greater than the 90th percentile flux, as well as the six worst visits from Figure 6, we find the new median and mean residual to be 15.5mas and 29.4mas, respectively. The plots in Figure 8 show significant improvement over their respective plots without all of the cutoffs applied. The downward trend in the value of the residuals as a function of distance from the sensor edge also becomes more apparent, but more study is needed to accurately quantify this trend in the MonoCam data.



#### IV. Autocorrelation Procedure and Results

Next, we will quantify the relationship between astrometric residuals (refer to Figure 3) as a function of distance from any source star using an autocorrelation procedure. For this procedure, we start with a single star (which we will call the origin star) and its associated residual vector. Next, we find all the stars and their associated residual vectors that fall within a certain distance range from the origin star. We then take the dot product of the origin star residual vector with all residual vectors that fall within this distance and sum them all together. If the orientation of the stars was truly random, then we would expect this dot product sum to go to zero. We then increment the lower and upper bounds of the distance range from the star and repeat this procedure until all stars in the visit are accounted for. After this, we move on to another star (i.e. we change the origin star) and repeat the procedure for all stars in every visit. After this, we take the average value of the dot product sum for each distance range and plotted them in Figure 10. We can see that removing bad visits, low flux and high flux stars reduces the correlation between residuals.

Next, we performed the same process, but with the ellipticity vectors shown in Figure 5. After this, we performed another autocorrelation procedure, this time between the ellipticity vectors and their associated residual vectors. Results are shown below in Figure 11. From this Figure, we can again see that cutting off bad visits, low flux and high flux stars generally lowers the correlation values. However, it appears that there is still some correlation apparent between ellipticities around 200arcsec to 400arcsec. We also see some correlation between ellipticities and residuals at a distance of about 300arcsec to 400arcsec.

#### V. Conclusions

We find that MonoCam, situated in a different telescope in a different part of the world from LSST, satisfies the absolute astrometry specification, with a median residual of 23.5mas. Also, it appears that high flux and low flux stars have the worst astromet-

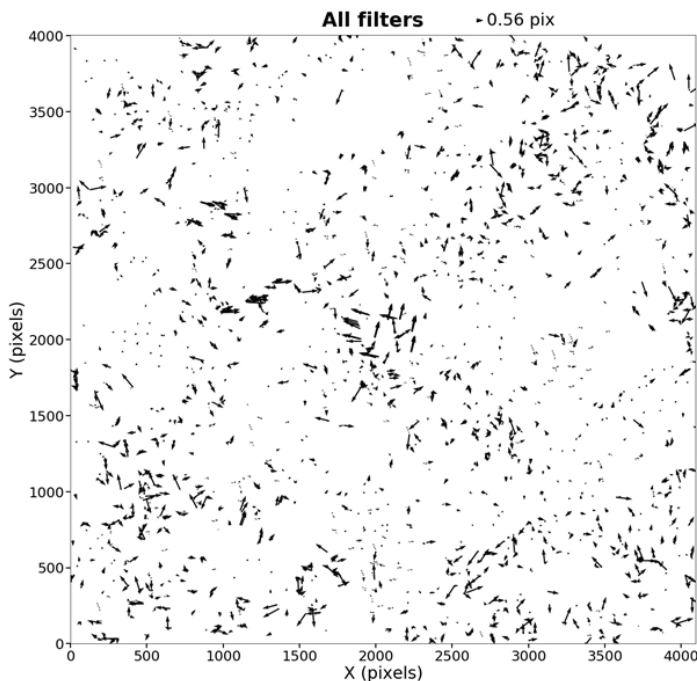


Figure 3: vector plot of astrometric residuals; vectors point from source star (measured by MonoCam) towards reference star (measured by Gaia). Keep in mind that the plate scale is 135mas/pixel.

ric residuals. Removing these stars, along with a few other bad visits, improves the results shown in all of our plots, and pushes back the median astrometric residual to 15.5mas.

A slight trend in edge residuals is found; residuals gradually decrease as residual locations move further away from the sensor edge. Correlations between residuals, ellipticities, and ellipticities combined with residuals are also apparent, and it is noticed that up to distances of about 300arcseconds correlations appear to be the strongest, but this correlation is reduced or eliminated when high flux, low flux, and bad visits are removed from the calculation. More study is needed to verify the behavior of the edge residuals and the correlations discussed in this paper.

#### VI. Acknowledgment

We would like to thank Kirk Gilmore for providing the filter throughput plot shown in Figure 1, in addition to his assistance throughout this project. Lastly, we thank Petr Kubanek, Woodrow Gilbertson, David Monet and the Naval Observatory telescope personnel for their help with the camera setup and operation, and data taking. This project was supported in part by the U.S. Department of Energy, Office of Science, Office of Workforce De-

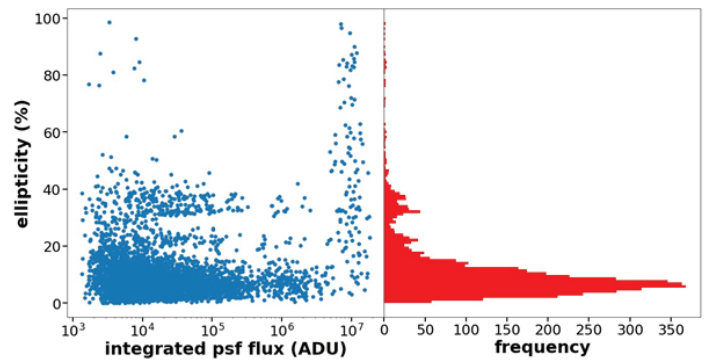


Figure 4: ellipticity scatter plot as a function of integrated psf (left) and histogram of residuals (left).

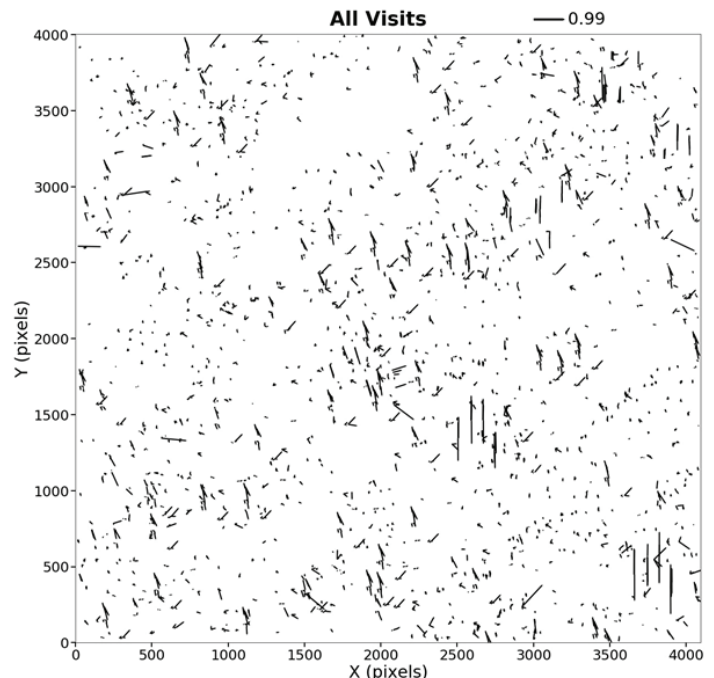


Figure 5: ellipticity “whisker” plot. Whiskers point along each star’s respective semi major axis.

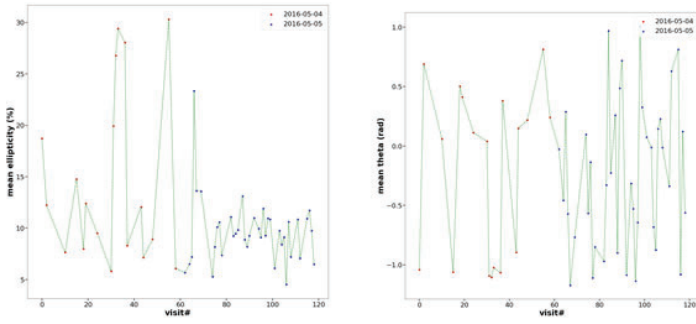


Figure 6: Left plot: plot of the mean ellipticity value per visit. Bottom plot: plot of mean orientation of ellipticity “whiskers” shown in Figure 5 or mean angle of semi major axis as a function of visit number.

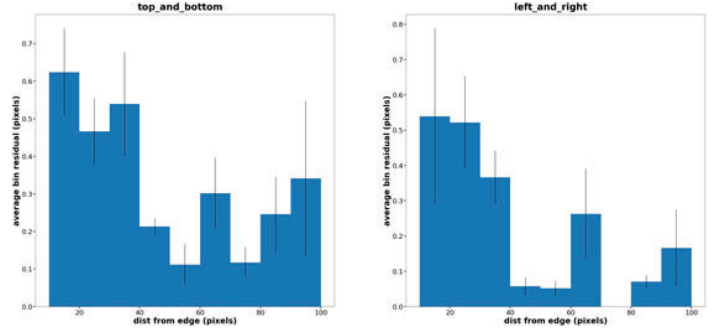


Figure 9: same plots as in Figure 7, but with the flux cutoff conditions used to make the plots in Figure 8.

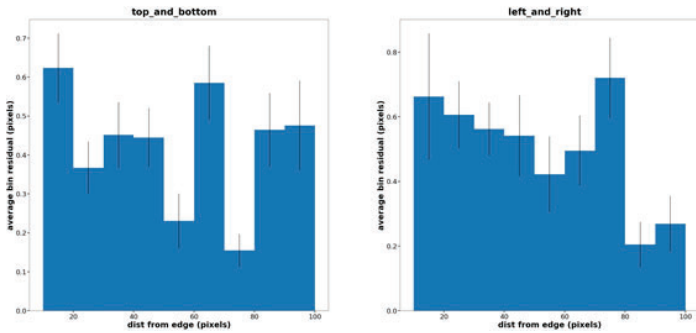


Figure 7: Left plot: mean residuals per 10 pixel bin (with of each blue rectangle is 10 pixels) plotted with its standard deviation shown by the vertical black line for stars within 100 pixels of the top or bottom sensor edge. Bottom plot: same as left plot, but looking at residuals at both the left and right edge of the sensor.

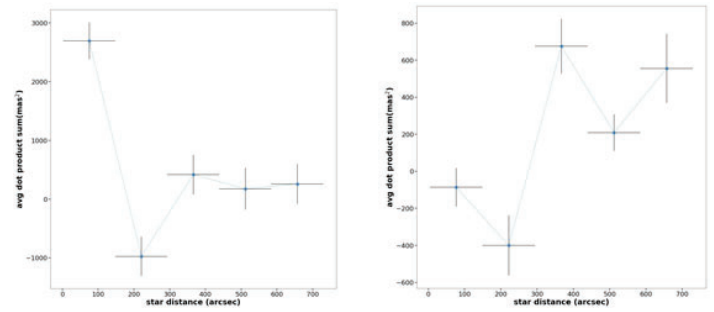


Figure 10: autocorrelation of residual vectors. We can see in the left plot that not cutting off high flux and low flux stars reveals a stronger correlation than the right plot, which only used stars without any extreme flux values or bad visits.

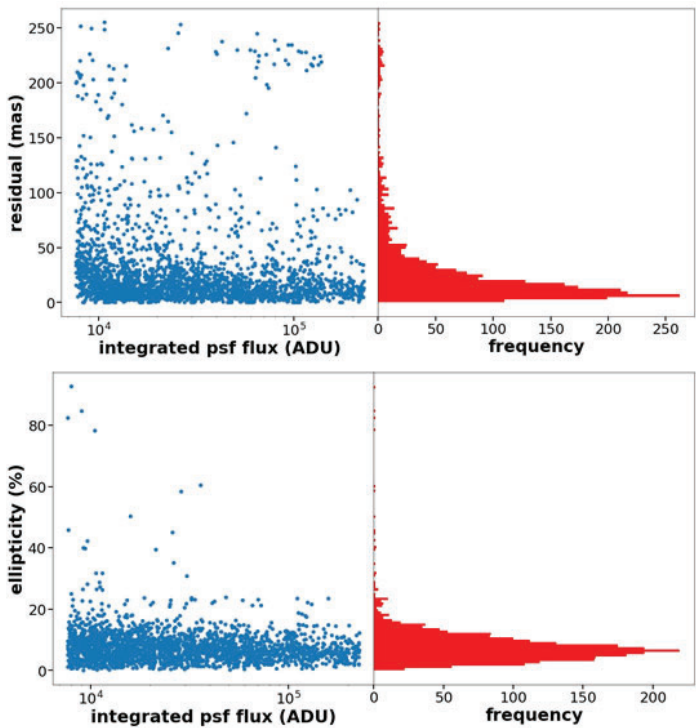


Figure 8: Left plot: residual flux scatter plot removing stars with a flux greater than the 90th percentile or stars lower than the 30th percentile, along with the six visits with the highest average ellipticity shown in Figure 6 Right plot: ellipticity flux scatter plot and histogram, with the same flux cutoff conditions as applied to the left plot.

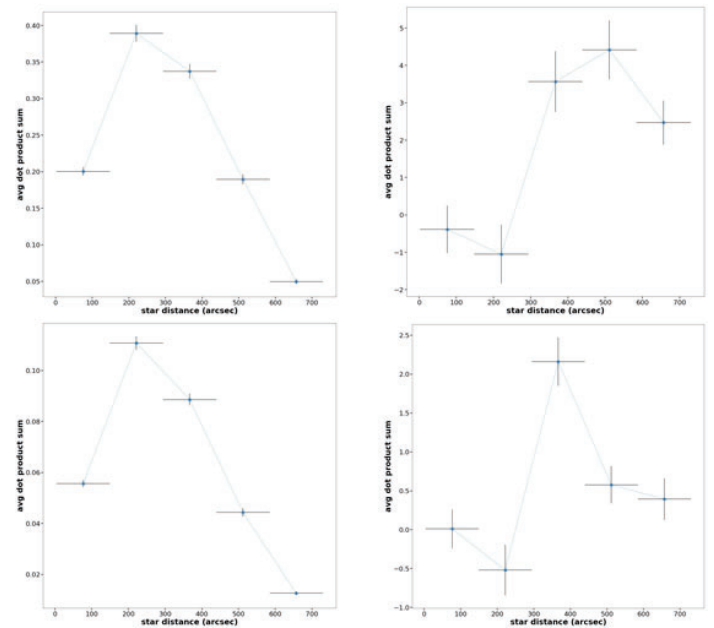


Figure 11: Top plots: autocorrelation plots for the ellipticity (top left) and autocorrelation plot showing the correlation between ellipticity and astrometric residual (top right) Bottom plots: same as the above plots, but with the stars whose flux lies below the 30th percentile or above the 90th percentile removed, and with the six visits with the worst ellipticity removed.

velopment for Teachers and Scientists (WDTS) under the Science Undergraduate Laboratory Internships Program (SULI). This paper makes use of software developed for the Large Synoptic Survey Telescope. We thank the LSST Project for making their code available as free software at <http://dm.lsst.org>.

## VII. References

- <sup>1</sup>LSST Science Collaboration 2009, “LSST Science Book, Version 2.0.” arXiv:0912.0201.
- <sup>2</sup>M. Jurić *et al.*, “LSST: from Science Drivers to Reference Design and Anticipated Data Products,” May 2008, arXiv:0805.2366.
- <sup>3</sup>“LSST technical details.” <https://www.lsst.org/about/camera/features>.
- <sup>4</sup>Zeljko Ivezić and the LSST Science Council, “The lsst system science requirements document, v5.1.3,” Tech. Rep. 6, LSST Corporation, 7 2011. An optional note.
- <sup>5</sup>M. J. Jee and J. A. Tyson, “Toward Precision LSST Weak-Lensing Measurement. I. Impacts of Atmospheric Turbulence and Optical Aberration,” *pas*, vol. 123, p. 596, May 2011, arXiv: 1011.1913.
- <sup>6</sup>K. Gilmore. Personal Communication, November 2016.
- <sup>7</sup>P. R. Jorden, D. Jordan, P. A. Jerram, J. Pratlong, and I. Swindells, “e2v new ccd and cmos technology developments for astronomical sensors,” in *SPIE Astronomical Telescopes+ Instrumentation*, pp. 91540M–91540M, International Society for Optics and Photonics, 2014.
- <sup>8</sup>Semiconductor Technology Associates, Inc., 27122 Paseo Espada, Ste 1004, San Juan Capistrano, CA 92675, *Reflex: a high performance modular CCD controller*, 2011. <http://www.sta-inc.net/wp-content/uploads/2011/04/Reflex.pdf>.
- <sup>9</sup>P. Kubánek, M. Jelínek, M. Nekola, M. Topinka, J. Strobl, R. Hudec, T. de J. Mañeo Sanguino, A. de Ugarte Postigo, and A. J. Castro-Tirado, “RTS2 - remote telescope system, 2nd version,” *AIP Conference Proceedings*, vol. 727, no. 1, pp. 753–756, 2004. <http://aip.scitation.org/doi/abs/10.1063/1.1810951>.
- <sup>10</sup>P. O’Connor, J. Frank, J. C. Geary, D. K. Gilmore, I. Kotov, V. Radeka, P. Takacs, and J. A. Tyson, “Characterization of prototype lsst ccds,” *Proc. SPIE*, vol. 7021, pp. 702106–702106–12, 2008.
- <sup>11</sup>“The 1.55-m Kaj Strand Astrometric Reflector.” <http://www.nofs.navy.mil/>.
- <sup>12</sup>M. Jurić *et al.*, “The LSST data management system,” 2015, arXiv:1512.07914.
- <sup>13</sup>T. Axelrod, J. Kantor, R. H. Lupton, and F. Pierfederici, “An open source application framework for astronomical imaging pipelines,” *Proc. SPIE*, vol. 7740, pp. 774015–774015–10, 2010.
- <sup>14</sup>R. Lupton. Personal Communication, May 2017.

# Self-assembly of gold nanoparticles guided by tile-based DNA cubes

Dana Capitano, Chemical & Molecular Engineering, Stony Brook University, Stony Brook, NY 11794  
Oleg Gang, Center for Functional Nanomaterials, Brookhaven National Laboratory, Upton, NY 11973

## ABSTRACT

In recent years, deoxyribonucleic acid (DNA) has garnered much interest from the nanotechnology community for its ability to self-assemble into pre-programmed structures. Much of this interest lies in using DNA to generate tailored architectures containing other functional components. Predictable fabrication of different architectures using the same functional component allows us to tailor materials to specific optical and structural needs. Our study involved the synthesis of nanolattices composed of alternating DNA cubes and spherical gold nanoparticles. The DNA cubes were fabricated by combining eight complementary Y-shaped tiles and then linking spherical gold nanoparticles to the cubes via Watson-Crick hybridization. Throughout this process, characterization techniques such as dynamic light scattering and ultraviolet-visible spectroscopy are used to confirm proper DNA adherence to the nanoparticles and observe the structures generated. DNA cubes have previously been used to create ordered lattices of spherical nanoparticles, but our study used a novel tile-based technique to simplify the cube formation process. This moves the field one step closer to a predictable fabrication technique for tailored nanolattices.

## I. INTRODUCTION

Self-assembly techniques for the manufacture of nanocomposites have gained attention in recent decades<sup>1,2</sup>, particularly DNA mediated self-assembly<sup>3-6</sup>. These techniques allow for precision in the formation of nanomaterial composites not possible in more conventional synthesis methods<sup>7,8</sup>. The synthesis of architectures composed of multiple varieties of nanoparticles has been researched much of late due to the ability of these materials to exhibit optical and structural properties not seen in natural materials<sup>9</sup>. However, the ability to combine nanoparticles of one kind into different lattice formations in a predictable manner has remained elusive until recent years<sup>10</sup>. This is mostly due to the tendency for the nanoparticle shape to be the determining factor for lattice architecture<sup>11,12</sup>.

Spherical particles especially tend to condense in a formations based on spherical packing, rather than into structured arrays desirable for nanocomposites<sup>12</sup>. The ability to arrange these nanoparticles in designed architectures is sought after because it enables the engineering of materials with enhanced collective and emergent properties<sup>12</sup>. Since the characteristics of the nanoparticles themselves leave little room for strategic design in nanocomposites, the solution is to use other nanoparticles to create a framework to direct the functional particles, rather than let them determine the framework<sup>12</sup>.

One method of lattice assembly using frame-shaping particles involves mixing the functional spheres with a polyhedral (cubic or octagonal) shaped frame particles, where the spheres

and polyhedra bind to each other in alternatingly to create long-range order. This approach has been done previously using both DNA-functionalized gold nanocubes<sup>12</sup> and DNA origami polyhedra frames<sup>13-15</sup>. In both studies, gold nanospheres were functionalized with DNA complementary to that of the polyhedra, and the two heterogeneously shaped objects bound together due to Watson-Crick base pairing.

In both cases, long-range ordered lattices of spherical gold nanoparticles were experimentally created. The directional interactions of the spherical nanoparticles were controlled locally by the shape of the polyhedra<sup>14</sup>, and long-range order was formed due to the reduced ways the spherical particles could interact<sup>12-15</sup>. Tuning the flexibility of the DNA was necessary to prevent the particles from forming amorphous clusters, but when the flexibility and length of DNA linkages were correctly tuned, these polyhedra facilitated the creation of different lattices using the same spherical particles. This technique marks a step closer to the creation of a predictable manufacturing technique for tailored lattices in metamaterials.

Our group sought to simplify the previously discussed technique of using polyhedral framework nanoparticles to tailor arrays of spherical nanoparticles. While functionalized gold nanocubes create the long-range lattice order desired, the metallic nature of the gold nanocubes could interfere with the desired optical properties of the nanocomposites, so using a low electron density organic material like DNA to structure the functional particles is sensible. DNA origami cubes were also used in previous experiments, but the complex nature of DNA origami fabrication leaves room for improvement in the form of a simpler polyhedra fabrication method. The goal of this project is to use a tile-based method<sup>16</sup> to synthesize DNA cubes used to create ordered assemblies of gold nanoparticle (Figure 1), and take another step on the way to simplifying the process of creating nanostructures tailored to exhibit specific properties.

## II. METHODS

### A. Functionalization of gold nanoparticles with DNA

Gold nanoparticles (AuNPs) with a nominal size of 10 nm in aqueous solution were purchased unconjugated from Ted Pella Inc. Three varieties of thiol modified DNA oligonucleotides (See Table 1 for oligonucleotide sequences) of varying lengths were purchased from Integrated DNA Technologies, Inc. as disulfides. The DNA disulfides were reduced to monothiol by tris(2-carboxyethyl) phosphine (TCEP) with a molar ratio of TCEP:DNA = 100:1 at room temperature for 1.5 hours, and then purified by size exclusion columns (G-25, GE Healthcare). The fresh monothiol-modified DNA oligonucleotides were mixed with AuNP aqueous solution in a ratio of 300:1 between DNA and AuNPs. The solution was then incubated on an orbital shaker for 1.5 hours at room temperature before using a phosphate adjustment buffer



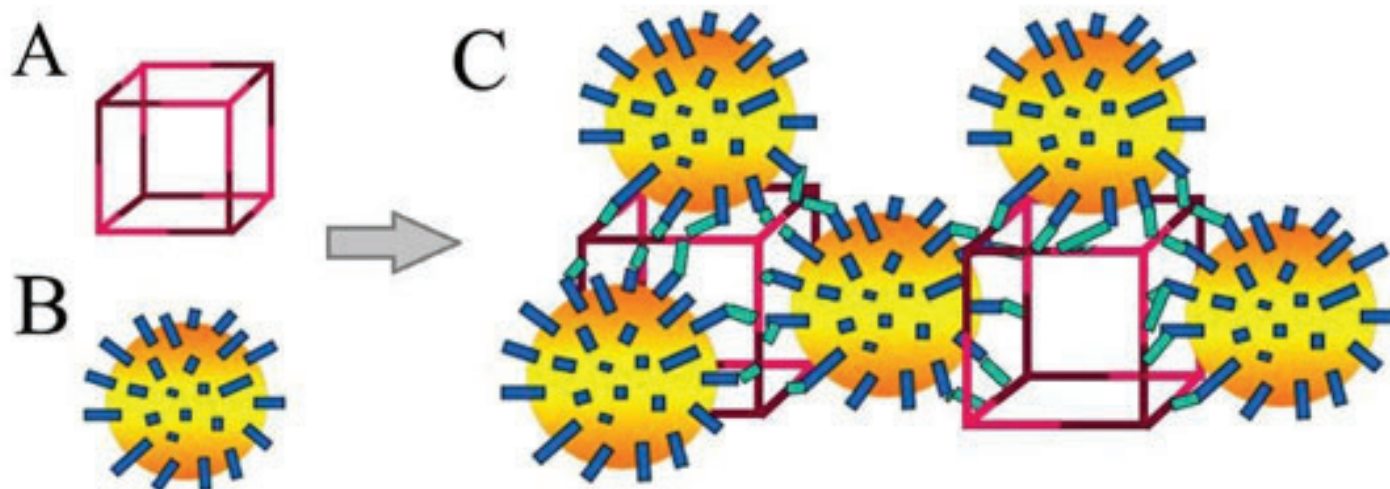


**Figure 1.**(A) A Tile-based DNA cube model with color differentiating Y1 and Y2 tiles. (B) Individual gold nanoparticle functionalized with DNA strands. (C) Model of gold nanoparticle and DNA cube nanocluster. The functionalized gold nanoparticles bond to the S1 strands (green) of the DNA cube via complementary strands loaded on them (blue).

(100 mM phosphate, pH 7.4) to obtain a concentration of 10mM of phosphate. After another 2 hours of incubation, salting buffer (10 mM phosphate, 2 M NaCl, pH 7.4) was added in a stepwise process until the solution's final concentration of NaCl was 0.3 M. During each addition step, the solution was sonicated for 20 s and incubated for 1 hour. After the last addition, the solution was left to equilibrate overnight. To purify the DNA-functionalized AuNPs, the nanoparticle solution was centrifuged at 20,000 rcf for 1 hour to remove the supernatant fluid. After centrifugation, the sample pellets were resuspended in 10mM phosphate buffer with 100 mM NaCl and a pH of 7.4. The centrifugation was repeated 4 times and the final DNA-AuNPs were stored at 4°C. The DNA-AuNPs were characterized using dynamic light scattering (DLS), ultraviolet-visible (UV-Vis) spectroscopy methods, as well as transmission electron microscopy (TEM) and small angle x-ray scattering(SAXS).

**Table 1.** Sequences of thiol-modified DNA used to functionalize AuNPs.

Name	Sequence
5-8	TCTCTCTCTTTTT-(CH <sub>2</sub> ) <sub>3</sub> -SH
10-8	TCTCTCTCTTTTTTTTT-(CH <sub>2</sub> ) <sub>3</sub> -SH
22-8	TCTCTCTCTTTTTTTTTTTTTTTTTTTTT-(CH <sub>2</sub> ) <sub>3</sub> -SH

**Table 2** The DNA sequences used to form tile-based nanocubes.

Name	Sequence
Y1-L1	AGGCACCATCGTAGGTTTAACTTGCCAGGCACCATCGTA GGTTTAACTTGCCAGGCACCATCGTAGGTTTAACTTGCC
Y1-M1	TAGCGCCTGCCTGGCAAGCCTACGATGGACGAACACTGT CAC
Y1-S1	GAGAGAGATTTTGTTTCGTGGCGCTAAGTCGTT
Y2-L1	GGAGCTTTTTTCGATCCTAGCACCTCTGGAGCTTTTTTCGAT CCTAGCACCTCTGGAGCTTTTTTCGATCCTAGCACCTCT
Y2-M1	TGAGCCCTGCTAGGATCGGCTCCAGAGGACTGCTCAACG ACT
Y2-S1	GAGAGAGATTTGAGCAGTGGGCTCAGTGACAG

### B. Assembly of tile-based DNA nanocubes

The tile-based DNA nanocubes were prepared using a procedure reported earlier<sup>16</sup>. Each nanocube is composed of 8 Y-shaped DNA tiles (Figure 1A). There are 2 tile varieties used, Y1 and Y2, composed of 3 different types of oligonucleotide strands: L1, M1, and S1. The nucleotide sequences for each strand are described in Table 2. All strands are used for structural purposes, and the 5'-end of S1 strand has 8 nucleotides that remain unpaired after the assembly of the nanocubes. This sequence is used during the conjugation of the AuNPs and nanocubes, and hybridizes with the sequences of the functionalized AuNPs. Each variety of oligonucleotide was purchased from Integrated DNA technologies Inc. The oligonucleotides are mixed in a molar ratio of L1:M1:S1 = 1:3.1:3.1 in a TAE buffer (12.5 mM Mg<sup>2+</sup>). The mixture is then heated to 90 °C and slowly cooled down to 22°C to form the two varieties of Y-shaped tile (Y1 and Y2), separately. The final step in nanocube formation is to mix the two groups of tiles in a 1:1 ratio before heating to 40 °C. Cooling slowly to 4 °C allows the cubes to anneal to the energetically favored cubes. The cubes were then characterized using TEM.

### C. Conjugation of DNA-AuNPs with DNA cubes

To conjugate the AuNPs with the cubic DNA frames, the functionalized AuNPs were added into solution with the cubes in a ratio of 3:1 in the TAE/Mg buffer. The concentration of Mg<sup>2+</sup> in



the TAE buffer was increased to 16 mM. The mixture is then heated to 35°C and slowly cooled to 22°C over the course of 3 days. Post-annealing, black precipitate was observed. The precipitate was then characterized using SAXS.

### III. RESULTS & DISCUSSION

#### A. Functionalization of AuNPs

Data to confirm the grafting of DNA to the AuNPs was gathered using dynamic light scattering technology and ultraviolet-visible spectroscopy. Using the Malvern Zetasizer Nano ZS, the hydrodynamic size was measured for bare AuNPs stabilized by citrate and each of the three functionalized AuNPs, as shown in Figure 2. The bare gold nanoparticles had an average diameter of 9.24 nm with a standard deviation of 2.4 nm. This was expected for the gold nanoparticles (with nominal size of 10 nm from the company) prior to functionalization. The hydrodynamic sizes of the AuNPs functionalized with 5-8, 10-8, and 22-8 DNA were  $14.26 \pm 3.6$  nm,  $16.9 \pm 4.0$  nm, and  $21.9 \pm 5.0$  nm, respectively. This data is in line with our expectations, with the diameter increasing by amounts consistent with the increasing lengths of the DNA strands. As a result, the peaks of the functionalized particles shift right as the amount of nucleotides in functionalizing strands increases, confirming that the DNA is attaching to the nanoparticles as predicted.

Ultraviolet-visible spectroscopy was used to characterize the bare and functionalized particles as well. The absorbances of each sample were gathered by using UV-Vis Lambda-35 at wavelengths from 220 to 800 nm. Both the bare and functionalized gold nanoparticles exhibit surface plasmon resonance (SPR) peaks near 520 nm, characteristic of ~10 nm AuNPs. These peaks can be used to calculate the nanoparticle concentration using the Beer-Lambert law. The SPR peak is located at 520 nm for the bare gold nanoparticles, but shifted right to the large wavelengths for the functionalized AuNPs by 2-3 nm. This “red shift” phenomenon is due to DNA functionalization on the surfaces of AuNPs. On the other hand, the slight peaks seen at ~260 nm for the functionalized gold particles is also caused by the attachment of DNA chains, as the DNA has typical absorption at 260 nm wavelength.

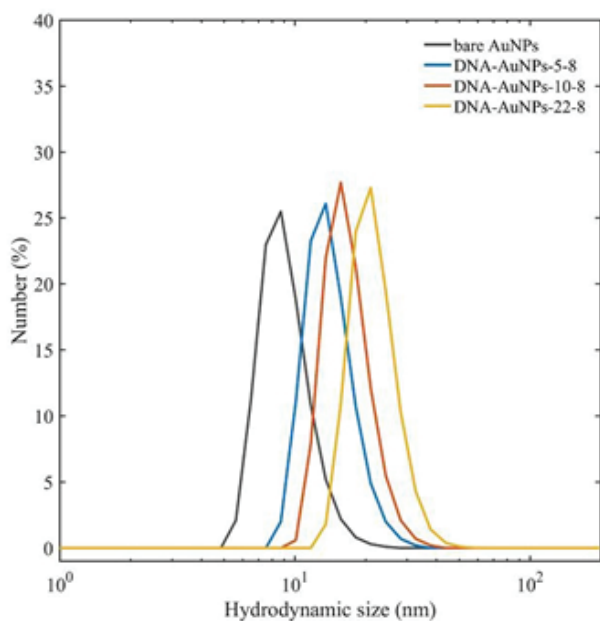


**Figure 2.** Hydrodynamic sizes of bare gold nanoparticles and DNA-coated nanoparticles.

It is estimated that each gold nanoparticle has between 40–60 DNA strands attached to it. As the length of the DNA chains used to functionalize the AuNPs increases, so does peak intensity, as can be seen in Figure 3. The red shift and increase in peak height confirm the successful functionalization of the AuNPs.

Combined results from dynamic light scattering and ultraviolet-visible spectroscopy confirm that the AuNP functionalization procedure was successful.

#### B. Conjugation of DNA-functionalized AuNPs with DNACubes

DNA-functionalized AuNPs and DNA nanocubes were imaged by transmission electron microscopy prior to conjugation. As shown in Figure 4, based on the imaging of DNA-22-8 functionalized nanoparticles, the diameter of the bare gold nanoparticles is approximately 9 nm. Any DNA attached to the nanoparticles is difficult to see due to the low electron density of DNA compared to high electron density of the gold nanoparticles. However, in the images of the DNA nanocubes, the structure of the cube is visible after the negative staining using uranyl acetate, and can be shown to have a length of 15 nm. These images show that the tile-based synthesis method for DNA framework particles succeeded in creating the desired structures.

#### C. Conjugation of DNA-AuNPs with DNACubes

Small angle X-ray scattering (SAXS) at the NSLS-II beamline CMS was used to characterize the DNA-AuNPs. A typical scattering profile of AuNPs can be seen in Figure 5A. These AuNPs are freely dispersed in buffer, so they are expected to have little to no correlation between each other. The form factor, displayed in Figure 5A, is a model that depicts the expected scattering behavior of spherical particles the same size as the AuNPs. The best fit of form factor gives us information about the size and size distribution of the AuNP core, as the electron density of DNA chain is similar to the buffer surrounding them. Our data follows the curve of the form factor, showing that the nanoparticles are freely dispersed hard spheres and have a diameter of  $9.0 \pm 1.0$  nm, which is consistent with the DLS and TEM results.

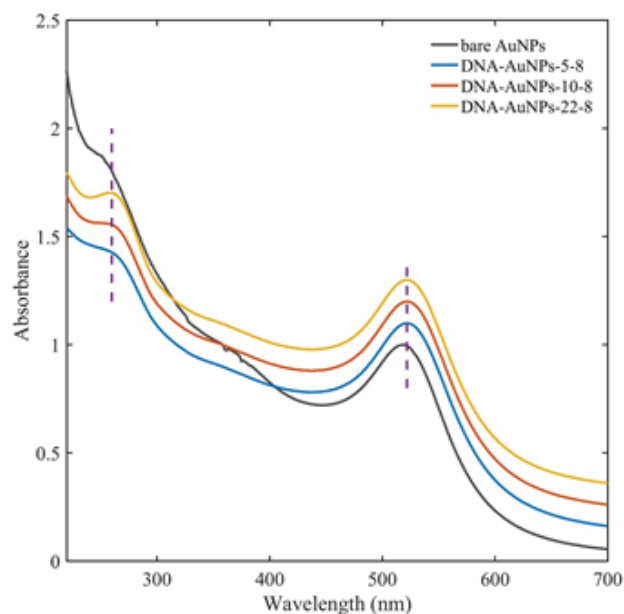


**Figure 3.** UV-Vis spectra of bare AuNPs and DNA-AuNPs. The plot is shifted vertically for display purpose.

SAXS was also used to characterize assemblies of gold nanoparticles and DNA cubes (visible black precipitates). The peaks seen in Figure 5B give us information about the structural order of the assemblies. All samples show short-range order: assemblies made using the 5-8 DNA sequences exhibit one broad peak, 10-8 has a single sharper peak, and 22-8 exhibits one sharp peak and one broad peak. The increasing sharpness and number of peaks in the scattering graph is the result of an increase in the order of the structures produced by each sample. The bars along the x-axis of the graph are the standard diffraction pattern of a face-centered cubic (FCC) lattice, and as the length of the DNA used to functionalize the AuNPs increases, the more the scattering peaks conform to the FCC structure. Thus, it can be inferred that as the length of the DNA linkages increases, the order of the assemblies created increases as well. This is compatible with earlier findings that flexibility of the linkages is required to create ordered structures.

The positions of the peaks also give us information about the nearest-neighbor distance of the assemblies,  $d_n$ . For the assemblies with the shortest DNA chains (DNA-5-8), we estimated that  $d_n$  is  $2\pi/q_1 \approx 9$  nm ( $q_1$  being the primary peak) as they are weakly ordered. For other two assemblies using longer DNA chains, the  $d_n$  is assumed to be  $\sqrt{6}\pi/q_1$  as they are closed to FCC ordering. Thus,  $d_n$  is  $\sim 23$  nm for DNA-10-8 and  $\sim 28$  nm for DNA-22-8. With the increase of the DNA length on AuNPs, the nearest-neighbor distance becomes larger. For the longest DNA chain tested (22-8), the lattice constant of FCC structure is  $\sim 40$  nm. Since the radius of the bare AuNPs is  $\sim 4.5$  nm and the length of the DNA cubes is  $\sim 15$  nm, that means the DNA linkages holding them together are approximately 8 nm in length. Considering that there are  $\sim 30$  bases between the cubes and AuNPs, this shows that the cubes and spheres are packed loosely rather than tightly, resulting in short-range order close to an FCC lattice.

#### IV. CONCLUSIONS

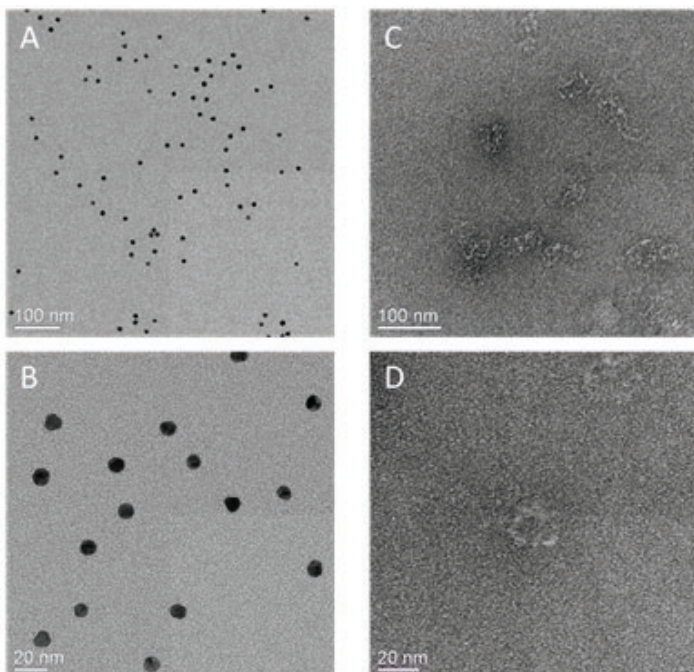


**Figure 4.** Representative TEM images of DNA-AuNPs of 22-8 strands (A, B) and tile-based DNA nanocubes under negative staining using uranyl acetate (C, D).

In conclusion, our study has shown that tile-based synthesis methods can create DNA framework cubes used for ordering spherical gold nanoparticles. The UV spectroscopy and DLS confirmed the conjugation of the spherical nanoparticles with the 3 types of DNA. The TEM imaging confirmed the diameter of the bare AuNPs as 9 nm, and the length of the DNA cube to be  $\sim 15$  nm. SAXS determined that the scattering results of the bare AuNPs were in line with those expected from nanoparticles with a diameter  $\sim 9$  nm, and that the DNA-AuNPs and DNA-cubes self-assembled into structures with short-range order. The structural order increases as the length of the functionalizing DNA of the AuNPs grows, and for the longest DNA tested in this study with 30 bases, the assembled structure is comparable to an FCC lattice. This is likely caused by the increased flexibility of the linkages, which compensates for the difference in shape between the spherical AuNPs and cubic DNA. Although this study resulted only in short-range ordered AuNPs, the tile-based synthesis technique for creating DNA polyhedra shows much promise for simplifying the path to tailored architectures of nanocomposites. Future studies will focus on optimizing the self-assembly conditions to increase the crystallinity.

#### V. ACKNOWLEDGEMENTS

This project was supported in part by the U.S. Department of Energy, Office of Science, Office of Workforce Development for Teachers and Scientists (WDTS) under the Science Undergraduate Laboratory Internships (SULI) Program. This research used resources of the Center for Functional Nanomaterials, and the National Synchrotron Light Source II, which are US DOE Office of Science Facilities, operated at Brookhaven National Laboratory under Contract No. DE-SC0012704. Additionally, I would like to thank Honghu Zhang and Don DiMarzio for their guidance and support throughout this project.

#### VI. REFERENCES

- Whitesides, G.; Mathias, J.; Seto, C. Molecular self-assembly and nanochemistry: a chemical strategy for the synthesis of nanostructures. *Science* 1991, 254, 1312-1319.
- Whitesides, G. M.; Boncheva, M. Beyond molecules: Self-assembly of mesoscopic and macroscopic components. *Proc. Natl. Acad. Sci. USA* 2002, 99, 4769-4774.

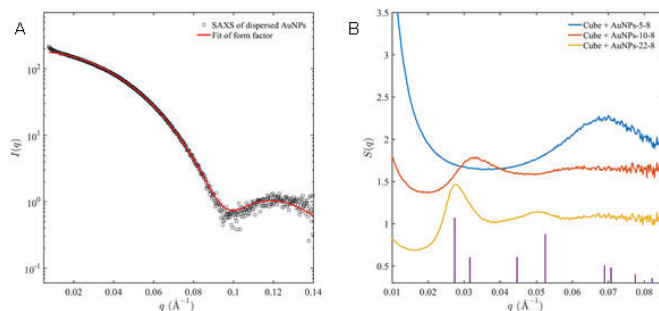


**Figure 5.** (A) A SAXS profile of dispersed AuNPs and a fit of form factor. (B) Structure factor  $S(q)$  of assemblies of AuNPs and DNA nanocubes. The purple bars along the x-axis are a standard diffraction pattern for a face-centered cubic (FCC) lattice.

3. Mirkin, C. A.; Letsinger, R. L.; Mucic, R. C.; Storhoff, J. J. A DNA-based method for rationally assembling nanoparticles into macroscopic materials. *Nature* 1996, 382, 607-609.
4. Alivisatos, A. P.; Johnsson, K. P.; Peng, X.; Wilson, T. E.; Loweth, C. J.; Bruchez, M. P.; Schultz, P. G. Organization of 'nanocrystal molecules' using DNA. *Nature* 1996, 382, 609-611.
5. Nykypanchuk, D.; Maye, M. M.; van der Lelie, D.; Gang, O. DNA-guided crystallization of colloidal nanoparticles. *Nature* 2008, 451, 549-552.
6. Park, S. Y.; Lytton-Jean, A. K. R.; Lee, B.; Weigand, S.; Schatz, G. C.; Mirkin, C. A. DNA-programmable nanoparticle crystallization. *Nature* 2008, 451, 553-556.
7. Soukoulis, C. M.; Wegener, M. Past achievements and future challenges in the development of three-dimensional photonic metamaterials. *Nat. Photon.* 2011, 5, 523-530.
8. Liu, Y.; Zhang, X. Metamaterials: a new frontier of science and technology. *Chem. Soc. Rev.* 2011, 40, 2494-2507.
9. Young, K. L.; Ross, M. B.; Blaber, M. G.; Rycenga, M.; Jones, M. R.; Zhang, C.; Senesi, A. J.; Lee, B.; Schatz, G. C.; Mirkin, C. A. Using DNA to Design Plasmonic Metamaterials with Tunable Optical Properties. *Adv. Mater.* 2014, 26, 653-659.
10. Macfarlane, R. J.; Lee, B.; Jones, M. R.; Harris, N.; Schatz, G. C.; Mirkin, C. A. Nanoparticle Superlattice Engineering with DNA. *Science* 2011, 334, 204-208.
11. Jones, M. R.; Macfarlane, R. J.; Lee, B.; Zhang, J.; Young, K. L.; Senesi, A. J.; Mirkin, C. A. DNA-nanoparticle superlattices formed from anisotropic building blocks. *Nat. Mater.* 2010, 9, 913-917.
12. Lu, F.; Yager, K. G.; Zhang, Y.; Xin, H.; Gang, O. Superlattices assembled through shape-induced directional binding. *Nat. Commun.* 2015, 6, 6912
13. Tian, Y.; Wang, T.; Liu, W.; Xin, H. L.; Li, H.; Ke, Y.; Shih, W. M.; Gang, O. Prescribed nanoparticle cluster architectures and low-dimensional arrays built using octahedral DNA origami frames. *Nat. Nanotechnol.* 2015, 10, 637-644.
14. Tian, Y.; Zhang, Y.; Wang, T.; Xin, H. L.; Li, H.; Gang, O. Lattice engineering through nanoparticle-DNA frameworks. *Nat. Mater.* 2016, 15, 654-661.
15. Liu, W.; Halverson, J.; Tian, Y.; Tkachenko, A. V.; Gang, O. Self-organized architectures from assorted DNA-framed nanoparticles. *Nat. Chem.* 2016, 8, 867-873.
16. Zhang, C.; Ko, S. H.; Su, M.; Leng, Y.; Ribbe, A. E.; Jiang, W.; Mao, C. Symmetry Controls the Face Geometry of DNA Polyhedra. *J. Am. Chem. Soc.* 2009, 131, 1413-1415.



# Using cosmic microwave background lensing to measure the bias of damped Lyman-alpha systems

Joseph Colosimo, Physics, Georgia Institute of Technology, Atlanta, Georgia 30332  
Añze Slosar, Physics, Brookhaven National Laboratory, Upton, NY 11973

## Abstract

Gravitational lensing occurs when light passes nearby a massive object, bending its path toward the object. This effect can be observed in the Cosmic Microwave Background (CMB), the farthest source of radiation we can detect. This makes CMB Lensing a good indicator of the mass and dark matter distribution in the visible universe. Bias measures the relationship between fluctuations in the number density of objects and the density of dark matter. The objective of my project was to measure the bias of Damped Lyman- $\alpha$  systems (DLA), clouds of hydrogen which completely absorb part of the spectrum of a quasi-stellar object (QSO or quasar). I measured the bias by fitting data from the Planck satellite and the Baryonic Oscillation Spectroscopic Survey (BOSS) to theoretical predictions dependent on the QSO and DLA biases. The QSO bias has been measured multiple times; however, until now, the DLA bias has only been measured relative to other uncertain parameters. I have measured the DLA bias to be around 2.4; however, the error is still uncertain as different members of the collaboration have different results. While the project is not yet completed, we are much closer to reaching results due to my contributions to the code. Knowing the DLA bias will help cosmologists put constraints on current models of DLAs and dark matter halos.

## I. INTRODUCTION

### A. CMB Lensing

The Cosmic Microwave Background (CMB) is the radiation from 400,000 years after the big bang, when the matter was dispersed enough for light to escape. Massive objects curve the path of the light traveling from the CMB, causing it to be lensed. The CMB is incredibly isotropic, with fluctuations on the order of one part in a million. The most recent measurement of the fluctuations was done by the European Space Agency's Planck space telescope. From their measurement of the fluctuations in Temperature and Polarization, they were able to find the lensing convergence, the weighted integral of gravitating mass density along the line of sight.

### B. QSOs and DLAs

Quasi Stellar Objects (QSOs) are the farthest detectable objects that constantly emit light. QSOs are galactic cores (super-massive black holes) which are accreting matter, creating an enormous amount of light. These objects have spectra have prominent hydrogen emission lines, including a prominent Lyman-alpha ( $\text{Ly-}\alpha$ ) line. Due to the expansion of the universe, these objects are moving away from us at rates proportional to their distance. This causes their emission lines to be redshifted. Objects in our line of sight absorb light from the QSO, where the light is also

redshifted by an amount dependent on their distance. Damped Lyman-alpha systems (DLAs) are observed in the spectra of QSOs as a large  $\text{Ly-}\alpha$  absorption line at their redshift. They are thought to be large clouds of hydrogen in the dark matter halos of galaxy clusters with no galaxies luminous to be observed on Earth. Together, these objects provide a good indicator of the distribution of matter at distances too far to be probed by other techniques.

### C. Bias

Dark matter is thought to make up 85% of the mass of the universe.<sup>1</sup> It is known that large clouds of dark matter called dark matter halos surround galaxy clusters. Because of this, we expect there to be some correlation between the distribution of dark matter and galaxies. The bias measures the relationship between fluctuations in the number density of objects and the density of dark matter.

$$\delta_{obj} = b_{obj} \delta_{dm} \quad (1)$$

Equation 1 shows that the bias of an object is the ratio of expected fluctuations in the object with fluctuations in dark matter. Because DLAs and QSOs are both found in galaxy clusters with dark matter halos, we expect these objects to be in denser regions of the universe, so we expect the mean lensing convergence to be positive.

### D. Objectives

My objectives were to calculate the mean lensing convergence and the biases. I wanted to calculate the mean lensing convergence for the entire sky, points with QSOs and points with DLAs. I wanted to calculate the biases by finding the actual cross power spectra and fitting predicted cross power spectra to find the QSO and DLA biases. I wanted to find biases with probability from  $\chi^2$  in between 0.05 and 0.95 indicating an appropriate

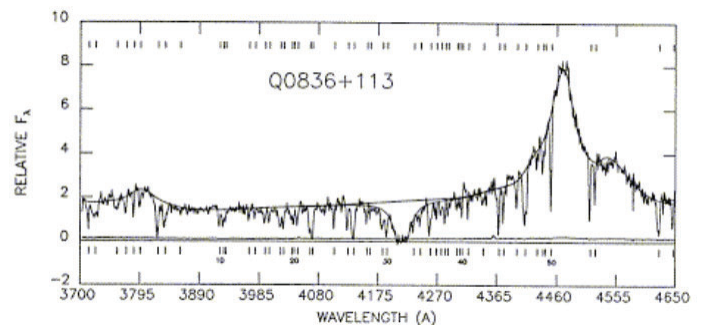
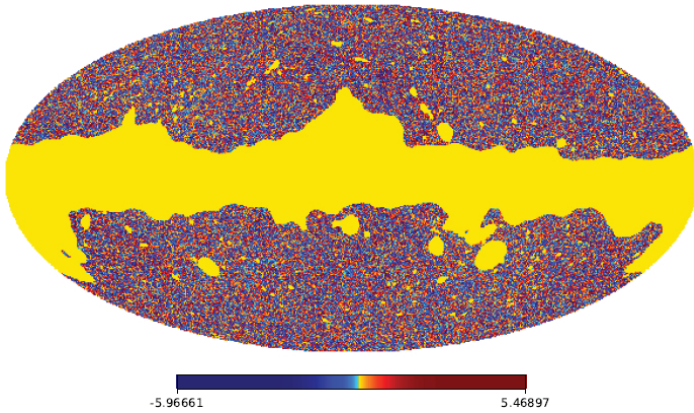


Figure 1: Spectrum of a quasar with a DLA, the large dip in the middle. The  $\text{Ly-}\alpha$  emission line is the large peak to the right. At rest, the  $\text{Ly-}\alpha$  line is around 1200  $\text{\AA}$ , as we can see in the spectrum, it has been redshifted by almost a factor of four, meaning that both the QSO and DLA lie between redshifts 3 and 4. (adapted from *Turnshek et al, 1989*)



**Figure 2: Planck's map of the lensing convergence.** The blue regions correspond to lensing divergence and underdense regions of the sky, while the red regions correspond to lensing convergence and overdense regions of the sky. The yellow is the area that is unusable due to it being obscured by the Milky Way.

amount of error in the measurements. I also wanted to find biases and errors close to values found by others in my collaboration using different methods.

## II. METHODS

### A. Mean Lensing Convergence

I measured the mean value of the lensing convergence for the QSOs and DLAs in the Barionic Oscillation Spectroscopy Survey (BOSS) using the Planck lensing convergence map (Fig 2). I weighted the QSOs so that their redshift distribution matches that of the DLAs.

This ensures that the redshift would not have an effect on the mean lensing convergence, but just the type of object. The error was calculated using bootstrap resampling, a method using random sampling to find statistical data about the whole.

### B. Bias

My primary tool for calculating the bias is using the cross power spectrum. The cross power spectrum is a measure of the correlation at different angular frequencies.

In order to calculate the error, I used 100 simulations in which Planck had the same characteristics as the original, but had differ-

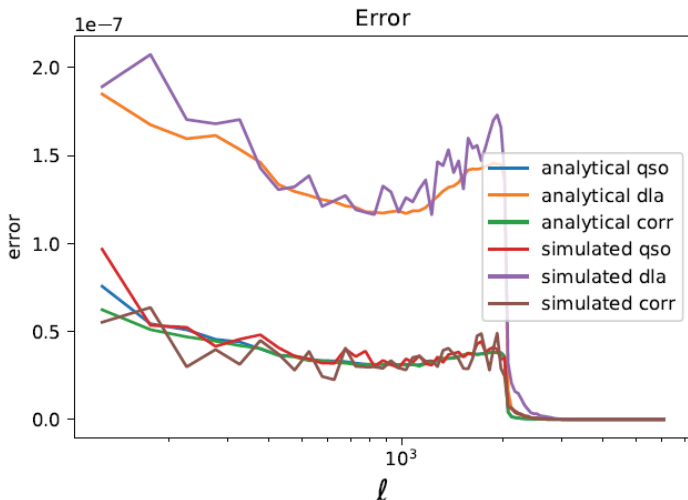


**Figure 3: The error for the QSO and DLA cross power spectra as well as the correlation of the two calculated analytically (from equation 2) and from using the simulations.**

ent arrangements, so that we would expect no correlation between lensing convergence and DLAs or QSOs. From variations in these simulations I was able to compute the covariance matrix, which measures the error of the DLA and QSO cross power spectra and the covariance between DLAs and QSOs and different  $\ell$  bins.

$$\sqrt{\frac{C_{\kappa} C_{obj} + C_{\kappa,obj}^2}{\sum (2\ell + 10 f_{mask})}} \quad (2)$$

Equation 2 is the formula for calculating the error of the cross power spectrum analytically, where  $C_{\kappa}$  is the power spectrum of the kappa,  $C_{obj}$  is the power spectrum of DLAs or QSOs,  $C_{\kappa,obj}$  is the cross power spectrum, and  $f_{obj}$  is the fraction of the sky used. I then confirmed that the error matched what was expected (seen in figure 3).

I used the core cosmology library (CCL) in python to predict the shape of the cross power spectra based on the redshift distribution of DLAs and the the QSOs associated with DLAs. The cross power spectrum scales linearly with the bias,<sup>2</sup> making the likelihood (or fit) a function of the bias. I then maximized the log likelihood to find the corresponding values of DLA and QSO bias. I calculated the log likelihood by measuring the square of the theory minus data multiplied by the inverse of the covariance matrix. The error is given the second derivative with respect to the biases, because the likelihood function is a gaussian.

## III. RESULTS

### A. Mean Lensing Convergence

I measured the mean lensing convergence for the entire sky (the background) to be very close to zero:  $\langle k_{background} \rangle = -2 \times 10^{-4} \pm 8 \times 10^{-5}$ . This makes sense, as light lensed towards some points on the sky must be lensed away from others. The mean lensing convergence for QSOs is  $\langle k_{qso} \rangle = 0.0044 \pm 0.0016$ . I measured the mean lensing convergence for DLAs to be  $\langle k_{dla} \rangle = 0.0167 \pm 0.0046$ . The error is higher due to the fewer points measured. Both of these values are over two standard deviations above the mean, showing that there is statistical significance to these objects being in overdense regions of the sky.

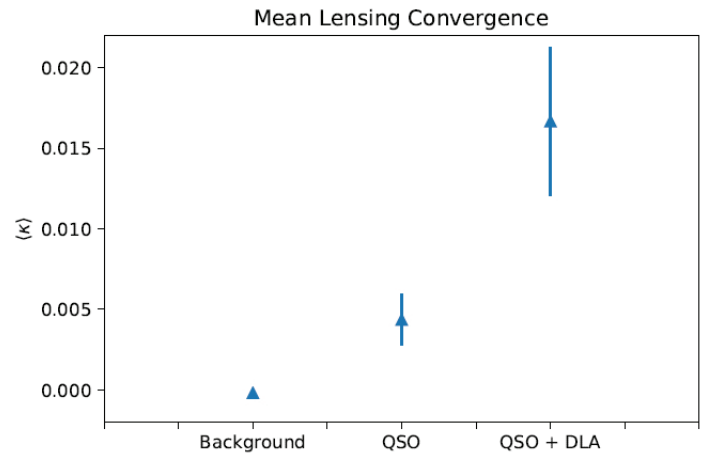


**Figure 4: Average values of lensing convergence ( $\kappa$ ) for the entire sky, points with QSOs and points with DLAs.**

## B. Bias

Many measurements have been done of the QSO bias. My results seem to indicate that the QSO bias is  $2.7 \pm 0.5$ . This is significantly smaller than previous measurements done in Laurent et al which put its value around  $4.0 \pm 0.20$  for quasars near redshift 2.<sup>4</sup>

The DLA I calculated is  $2.4 \pm 1.2$ , similar to the value previously measured in Font et al.,  $b_{\text{DLA}} = (2.17 \pm 0.2)\beta_F^{0.22}$  where  $\beta_F$  is the unit-less distortion factor.<sup>3</sup> This measurement had not yet been done independently, making us more confident in this previous value.

These values are fairly consistent for different  $\ell$  bin sizes (for the cross power spectra) and for different maximum  $\ell$ 's used to find the log likelihood. The error of these biases is still uncertain because I have calculated the error to be over twice as large as a colleague who made these measurements with the same data using different techniques, however the values seem consistent across both methods.

## IV. CONCLUSION

While this project is not yet concluded because of the differing errors, we are much closer to results. I have found methods for creating maps, finding the power spectra, and calculating the bias. My code and results will be able to be used to find the issues with the error and find the correct results for the QSO and DLA biases.

The value of the QSO bias that I calculated should challenge others to do more independent studies to find the accurate value of the QSO bias. More studies of the DLA bias will also help increase confidence of challenge these results. An accurate value for the DLA bias is important because it will help place constraints on our current models of DLAs. The DLA bias will allow us to have a better idea of the DLA cross-section, or the portion of the sky in which we can find DLAs. It will also help us to have better es-

timates of the mass of dark matter halos in the host galaxy clusters in which DLAs are found. These parameters will help give us a better idea of the physics inside DLAs and galaxy clusters.<sup>3</sup>

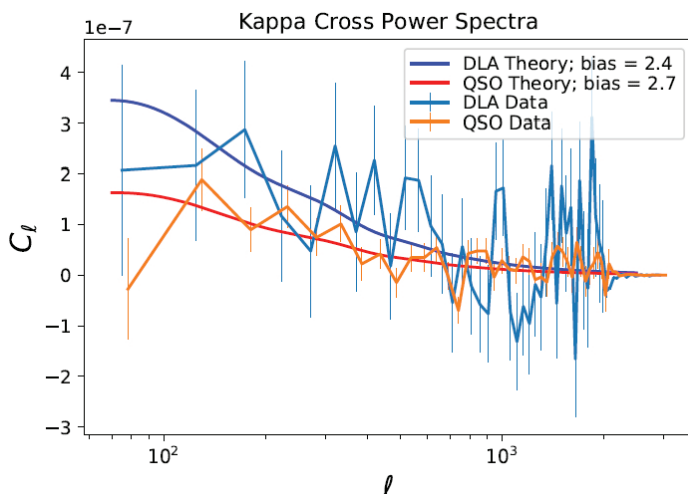


Figure 5: The calculated cross power spectrum with the predicted power spectrum using the best fit values of the bias.

## V. ACKNOWLEDGEMENTS

I would like to thank my mentor, Ane Slosar, for all of his guidance and all of the Cosmology Department at Brookhaven National Laboratory for their encouragement and support. I would also like to express my appreciation for the Office of Educational programs for all their work put into this program. This project was supported in part by the U.S. Department of Energy, Office of Science, Office of Workforce Development for Teachers and Scientists (WDTS) under the Science Undergraduate Laboratory Internships Program (SULI).

## VI. References

- <sup>1</sup>Ade, P. A. R.; Aghanim, N.; Armitage-Caplan, C.; (Planck Collaboration); et al. (22 March 2013). Planck 2013 results. I. Overview of products and scientific results Table 9. Astronomy and Astrophysics.
- <sup>2</sup>Fan, Zuhui. Measuring the Deviation from the Linear and Deterministic Bias through Cosmic Gravitational Lensing Effects. The Astrophysical Journal 594.1 (2003).
- <sup>3</sup>Font-Ribera, Andreu et al. The large-scale cross-correlation of Damped Lyman alpha systems with the Lyman alpha forest: first measurements from BOSS. Journal of Cosmology and Astroparticle Physics 2012.11 (2012)
- <sup>4</sup>Laurent, P., Goff, J. L., Burtin, E., Hamilton, J., Hogg, D. W., Myers, A., et al. A 14h?3Gpc3 study of cosmic homogeneity using BOSS DR12 quasar sample. Journal of Cosmology and Astroparticle Physics (2016).



# Preparing the Baryon Mass Experiment (BMX) telescope for data acquisition

Chandler Conn, Physics and Astronomy, Northwestern University, Evanston, IL 60201  
Paul O'Connor, Instrumentation, Brookhaven National Laboratory, Upton, NY 11973

Recent developments in cosmology have demonstrated the need for a better understanding of the far distances of the universe. Measurements of the cosmic microwave background (CMB) radiation have become immensely popular and widely-studied ways to map the early universe, providing insight into the physics of this time period. Keeping in the spirit of paving new scientific paths, we seek to extend much of this information by taking a novel measurement of the universe's early distribution of matter, using the 21cm hydrogen emission line as our reference. This differs from the majority of contemporary experiments, as we are not measuring the CMB, but the physical matter (hydrogen) in the universe. The Baryon Mass Experiment (BMX) telescope is a relatively small-scale prototype, intended to demonstrate success in measuring this hydrogen distribution, and to serve as a launching point for a much larger-scale experiment. Recent and ongoing preliminary tests show that it has physical properties in agreement with the pre-production theories. In particular, it exhibits a low enough level of information loss to successfully pick up a faint space radio signal and has successfully detected signals in the lab environment. The telescope mounting tower and reflector dish have already been installed in an on-site basin, supposedly shielded as well as possible from outside radio signals, and we are just awaiting the installation of the orthomode transducer (OMT) to allow for data collection.

## I. BACKGROUND

### A. Relevant timeline of the early universe

While the exact details are not known yet, it is widely accepted that the universe “began” around 13.8 billion years ago, in an event known as the Big Bang.<sup>1</sup> The moments after this were marked by physical phenomena wildly different from those we know and witness today, as the background temperatures were on the order of  $10^5$  to  $10^{20}$  K, hot enough to prevent the formation of atoms.<sup>2</sup> As such, until around 378,000 years after the Big Bang, the universe was opaque – Thomson scattering of free electrons with hadrons meant that the mean free path of photons (average distance that light could travel before being reflected) was very short. However, when temperatures dropped to  $\sim 4000$ K, electrons became bound to hadrons and formed the first neutral hydrogen atoms, leaving few free electrons for light scattering purposes. Thus, the universe became largely transparent following this time period, known as “recombination.” The last photons of the opaque era are visible at extremely large distances, and are known as the Cosmic Microwave Background (CMB) due to their prevalence across the entirety of the sky and the frequencies at which they are observed.<sup>3</sup> This CMB map is shown in Figure 1 below.

### B. Redshift and its use in cosmology

In wave physics, the change in the observed wavelength of an incoming wave due to the relative motion of the source and

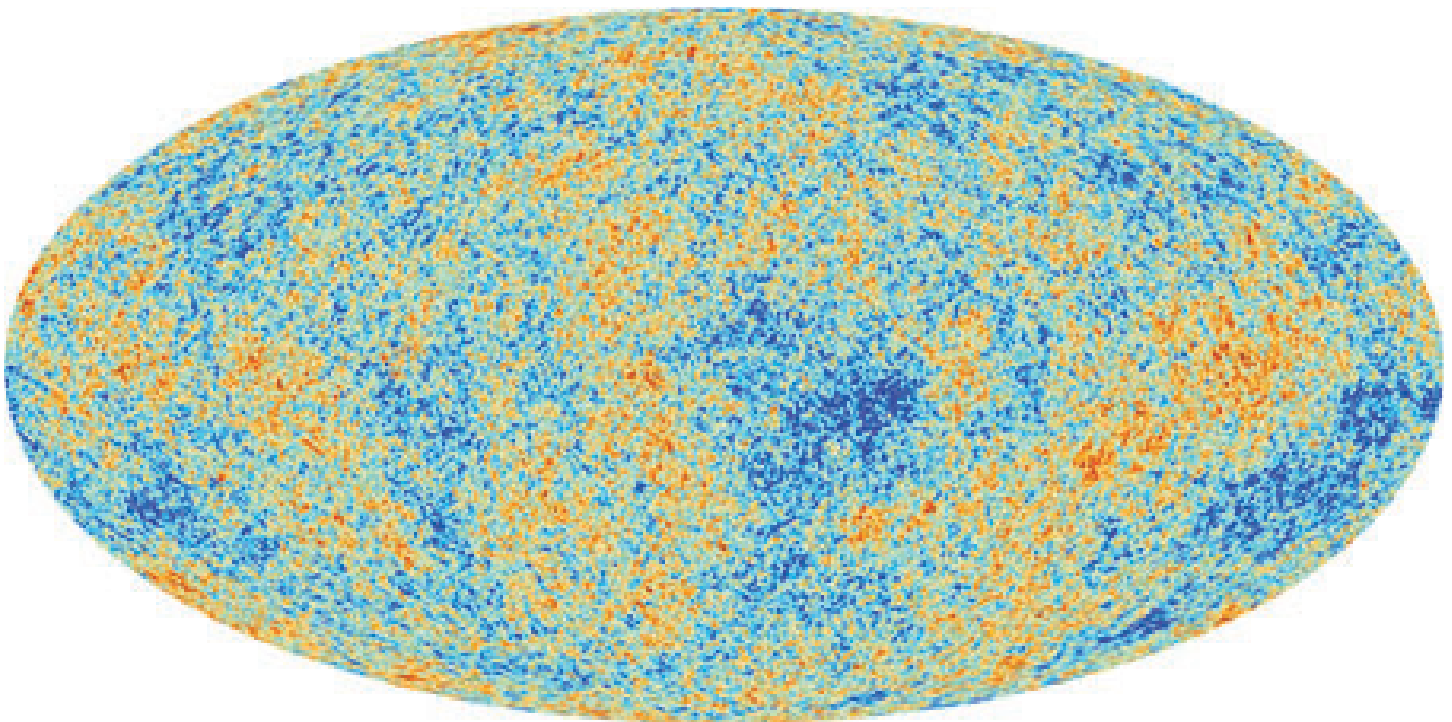


Figure 1 – The cosmic microwave background  
*Planck Collaboration*

the observer is known as a Doppler shift. When the source that is producing the wave is traveling towards the observer, or if the observer is traveling towards the source, then the wavelength of the wave as measured by the observer appears to be lower, and the inverse is true as well. The common example of this with sound is an ambulance’s siren sounding higher-pitched when it is driving towards you, and lower when it is driving away. Doppler shift with light is usually referred to as redshift and blueshift, due to the incoming light’s wavelength either being increased (redshifted, as if moved towards the red end of the visible spectrum) or decreased (blueshifted). Due to the expansion of the universe all astronomical objects appear to be moving away from us, with more distant objects appearing to travel at a faster rate.<sup>4</sup> Thus, by observing an object with a known wavelength or wavelength emission spectrum, such as hydrogen, and comparing the measured results with known results on earth, the distance of the emitting object can be inferred. It becomes common then to equate redshift with distance, using the degree that an object’s wavelength has been redshifted as a metric of its distance from us.

### C. The orthomode transducer

In general, an orthomode transducer (OMT) is a component that splits incoming microwave radiation into two polarization components, allowing for independent measurement of the amplitudes of two orthogonal polarizations.<sup>5</sup> The general shape and size of an OMT changes depending on the frequencies to be measured. Images of the OMT constructed specifically for BMX are given below in Figures 2a-2f. Crucial properties of an OMT are conveyed by its scattering parameters, typically given in an *S*-matrix.<sup>6</sup> The *S*-matrix,

$$S = \begin{bmatrix} S_{11} & S_{21} \\ S_{12} & S_{22} \end{bmatrix}$$

has four relevant parameters:  $S_{11}$ ,  $S_{21}$ ,  $S_{12}$ , and  $S_{22}$ , ranging

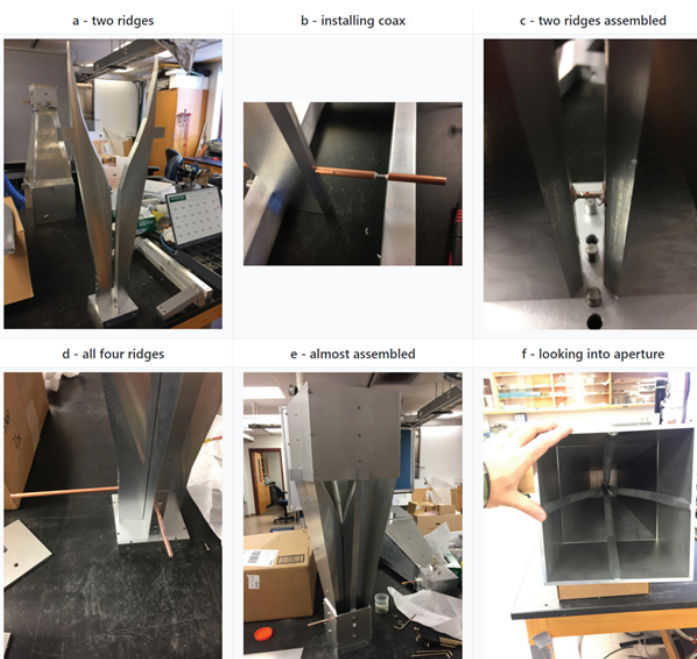


**Figure 2 – Stages of OMT construction**  
Chris Sheehy, BNL

from 0 to 1. Each parameter refers to the amount of signal that is either being transmitted or reflected. More specifically, the value of  $S_{ij}$  is the proportion of a signal that originates from side *i* of the OMT and terminates in side *j*. If the OMT had no internal reflections,  $S_{11}$  and  $S_{22}$  should be 0, and  $S_{12}$  and  $S_{21}$  would be 1, meaning that a signal is fully transmitted through the OMT.

## II. METHODS

### A. Basis of data

Because light in space travels at a constant, non-infinite speed, radiation that reaches Earth from a large distance away is also light that was emitted a long time ago. Thus, by measuring this far distant light, we are able to get a glimpse of the universe from a long time ago – this is the rationale behind CMB measurements. However, in order to better understand the dynamics of this early system, it becomes important to measure (and subsequently map) the times before and after. As discussed above, it is difficult to measure pre-recombination era physics using astronomical methods due to the radiative opacity of the universe during this time; thus, the next logical step is to examine the era following recombination, to understand how this matter distribution changes from one era to another. This is the ultimate goal of BMX: to map the matter distribution of hydrogen in the early universe. By sweeping the sky and measuring the amplitude of the incoming radiation from a redshifted 21cm hydrogen emission line, it is possible to map the spatial distribution of hydrogen, providing a “mass map” of the universe that would complement similar maps of the CMB. By understanding the relation between redshift and distance, it is possible to only consider the distant hydrogen distribution, ignoring local features.

### B. The telescope site

BMX is currently being constructed on-site at Brookhaven National Laboratory (BNL), in an emergency water overflow basin. Photos of the site as well as construction progress are included in Figure 3 below. The site was chosen due to its distance from BNL buildings and also for its relative openness with regards to trees and other flora. Radio frequency interference (RFI) from local weather stations and airplanes provides a challenge in the basin as it can be interpreted as data if not calibrated out correctly; thankfully, work has been done to document the RFI in the basin so as to better understand when an actual signal has been reported. Progress is almost complete on one of the telescope dishes, with three additional dishes planned after initial data has been taken from the first.

### C. OMT tests

Many tests were required to ensure that the OMT specifications were in agreement with pre-production theories, mainly  $S_{11}$  and  $S_{21}$  parameter determination, from which we calculate the signal loss through the OMT. *S*-parameter measurements were taken with a vector network analyzer (VNA), a device which sweeps across many frequencies and measures the signal being reflected and transmitted at those frequencies. For the  $S_{11}$  measurement, the OMT was pointed into an absorbing cube (Figure 4) so as to prevent any signal from entering that did not originate from the VNA (which would result in a value for  $S_{11}$  that is greater than 1). For  $S_{21}$ , two OMTs were pointed into each other and the signal was measured from one OMT to the other (Figure 5). *S*-parameter values were recorded in decibels, a common convention, which



is simply a logarithmic conversion of the normal 0-1 values described earlier.

In addition to these tests ran above were tests of shielding materials – materials to be placed in front of the OMT in order to block out potential air-based creatures, but to still allow transmission of the desired signal. Two materials have been tested so far: acrylic at 1/8", 1/16", and 2"; and Delrin® acetal resin at 1/8" and 1/16". Similar tests to the S-parameter ones described above were run but with these various materials placed in front of the OMT aperture, in order to measure the change in reflectivity, absorption, or loss when these materials were used.

Finally, a test was run where the OMT was pointed straight up in the basin, with the correct frontend data collecting chain (Figure 6). This was a multifold test, partially performed to test whether or not everything functioned as desired, and partially to measure the background RFI levels with the OMT, which had never been done before.

### III. DATA AND RESULTS

#### A. Initial S-parameter and loss measurements

$S_{11}$  and  $S_{21}$  measurements were largely in agreement with pre-production theories, as well as with previously collected data from an earlier edition of the OMTs (before they had to be rebuilt due to damage suffered in transit). This information is displayed

in Figures 7a,b in the Appendix. In many cases these plots appear cluttered and layered on top of each other, which is good in the sense that it indicates repeatability of the S-parameter measurements.

The loss calculations performed on the earlier version of the OMTs, as well as those for this edition performed by myself, are plotted as well in Figures 8a,b. Despite being performed on separate VNAs with different connecting cables and on a different assembly of the OMTs, the loss magnitudes are on the same order and indicate a sufficient level of confidence in the loss levels that are to be expected when the OMT is in the full experimental setup.

#### B. Shielding material

Unfortunately, results from the various shielding materials were not as fruitful. Figure 9 shows the reflectivity measurements, which were very good and indicated low reflection with the material. Despite altering both the material thickness and the angle at which it rests on the OMT, the reflected power was essentially zero. Absorption and loss measurements, however, were of a magnitude too great to simply be ignored, as seen in Figure 10. What is strange about these results is how the magnitude of the signal actually *increases* when the shielding material is placed in front of the OMT, a phenomena that we in the group have still not fully come to understand. Another worrying fact is the degree to

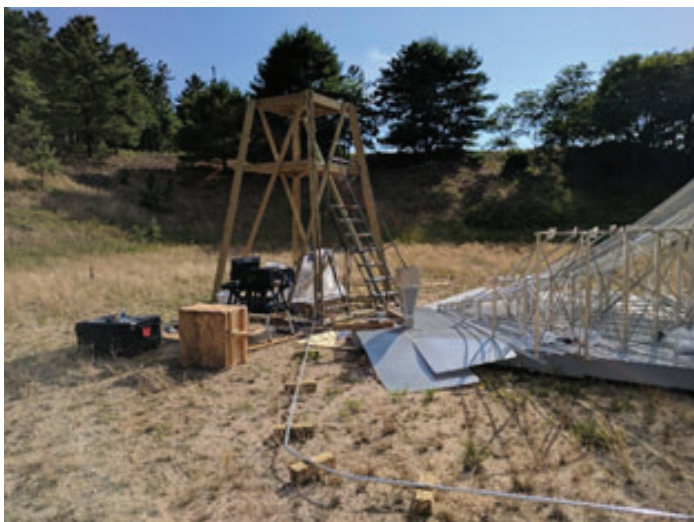


Figure 3 – Basin photos

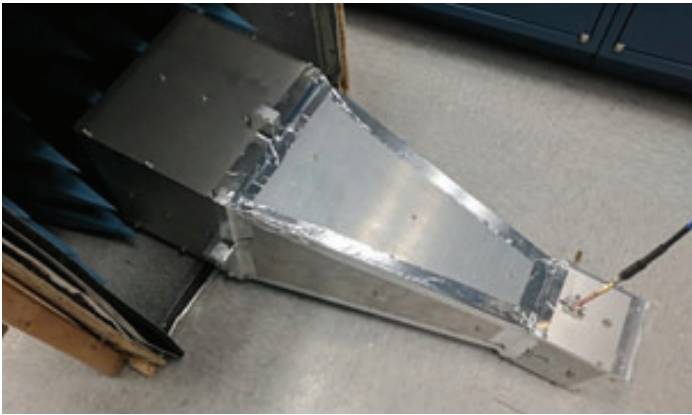


Figure 4 –  $S_{11}$  measurements, OMT pointed into absorber

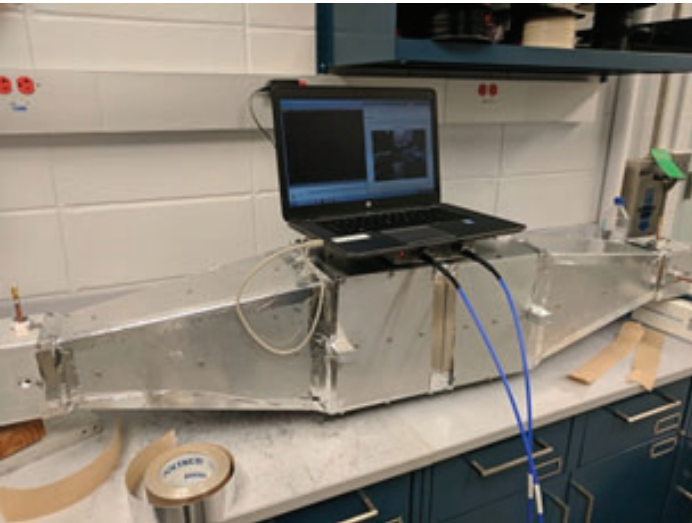


Figure 5 –  $S_{21}$  measurements, two shorted OMTs



Figure 6 – OMT pointed straight up in the basin

which this measurement changes depending on the experimental setup, which was not present in the reflectivity measurements. All of these features are ongoing problems regarding the BMX telescope, and no conclusion has been reached at the moment.

### C. Basin tests

With the OMT in the basin, the interesting measurement in question is the background RFI levels. Figures 11a,b show the magnitude of the OMT signal when pointed at the sky under different conditions. Figure 11a, the waterfall plot, has nine sections, which are from top to bottom: junk data, absorber in front of OMT, nothing in front of OMT, 1/8" Delrin®, 1/16" Delrin®, 1/8" acrylic, 1/16" acrylic, 2" acrylic, and nothing again. Figure 11b shows slices of this data for the absorber section and for the first open section, demonstrating the difference in amplitude of the data. While a difference is to be expected, the magnitude and scope of this difference is not, as the signal with no absorber is so extremely high compared to the predicted background levels. Some RFI still creeps in with the absorber covering the OMT, but the majority of the signal is the stochastic noise. We were expecting to receive a measurement of the noise when pointing straight into the sky, but the background RFI levels prevented this. As such, we are hoping that the results from the full experimental setup will be better than this and shed more light on the desired information.

### IV. CONCLUSIONS

At its current stage, the BMX telescope seems promising. Internal measurements of the system indicate full agreement with theorized specifications, which was one of the main goals of this telescope. While the telescope has not yet been employed in the complete setup, these preliminary results imply that no strange behavior inherent to the OMT is to be expected.

The shielding material results are not as promising and definitely require further testing and understanding before they can be used in the experiment. It is possible to get a better understanding of the behavior of these materials and then calibrate their effects out in post-analysis, but this is something that would require more examination before being implemented.

Preliminary basin tests are somewhat unusual as well. Results indicate high RFI levels and a very noisy environment. While these results are not to be taken to heart quite yet, as the full experimental setup was not used, they are still worrying. However, no strong conclusions can be reached about the effectiveness of the telescope in the basin without completion of the full telescope.

### V. ACKNOWLEDGEMENTS

This project was supported in part by the U.S. Department of Energy, Office of Science, Office of Workforce Development for Teachers and Scientists (WDTS) under the Science Undergraduate Laboratory Internships Program (SULI). I would also like to personally thank my mentor, Paul O'Connor, for accepting me for this position and his mentorship, as well as Anže Slosar and Chris Sheehy for their guidance and assistance with the entire internship process.



## VI. REFERENCES

<sup>1</sup>Wollack, Edward J. (10 December 2010). “Cosmology: The Study of the Universe”. Universe 101: Big Bang Theory. NASA.

<sup>2</sup>Peebles, P. J. E. (1968). “Recombination of the Primeval Plasma”. Astrophysical Journal. 153: 1.

<sup>3</sup>Fixsen, D. J. (2009). “The Temperature of the Cosmic Microwave Background”. The Astrophysical Journal. 707 (2): 916–920.

<sup>4</sup>Yu N Parijskij (2001). “The High Redshift Radio Universe”. In Norma Sanchez. Current Topics in Astrofundamental Physics. Springer. p. 223.

<sup>5</sup>everini, O.; Tascone, R.; Olivieri, A.; Baralis, M.; Orta, R.; Virone, G. (2003). “A microwave measurement procedure for a full characterization of ortho-mode transducers”. IEEE Transactions on Microwave Theory and Techniques. 51: 1207–1213.

<sup>6</sup>Gonzalez, Guillermo (1997); Microwave Transistor Amplifiers Analysis and Design, Second Edition; Prentice Hall NJ; pp 212-216.

## VII. APPENDIX

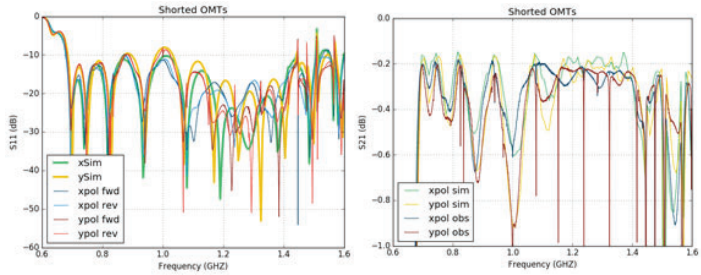


Figure 7a –  $S_{11}$  measurement on VNA

Figure 7b –  $S_{21}$  measurement on VNA

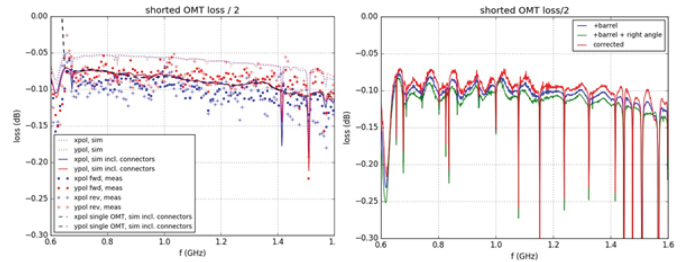


Figure 8a – Previous loss measurement

Figure 8b – Current loss measurement

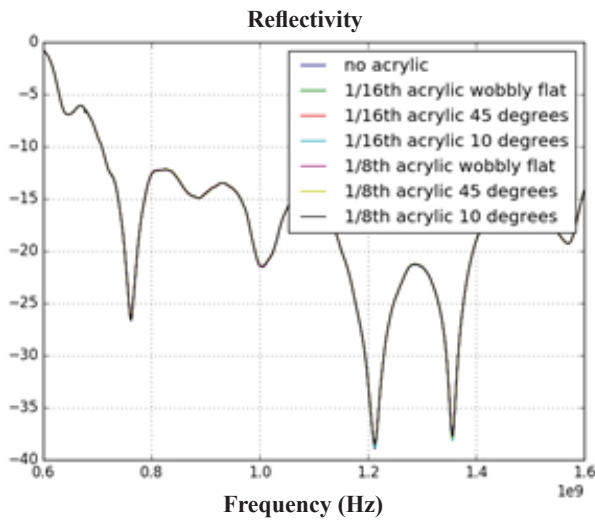


Figure 9 – Acrylic reflectivity measurements with VNA (all of the plots are layered on top of each other)

# Performance simulation of electron multiplying charge coupled devices

Jenna DeCordova, Computer Programming and Information Systems, Farmingdale State College, Farmingdale, NY 11735  
Ivan Kotov, Physics, Brookhaven National Laboratory, Upton, NY 11793

## ABSTRACT

The National Synchrotron Light Source (NSLS-II) at Brookhaven National Laboratory provides the brightest x-rays for a variety of research areas. In particular, the 2ID beamline, Soft Inelastic X-ray Scattering (SIX), will use the light source for electronic excitation studies using soft x-ray detectors. The x-ray energies for these studies are in the 200 eV – 2000 eV range. The detectors are Electron Multiplying Charge Coupled Devices (EMCCD). Currently an Iron-55 ( $^{55}\text{Fe}$ ) calibration source is used for sensor calibration.  $^{55}\text{Fe}$  has a higher energy, 5.9 keV than what will be used when the RIXSCam2 is attached to the light source. This puts some limitations on what can be learned in device characterization. Nevertheless, the device performance simulation is important for choosing optimal operational settings. The device parameters—for example gain dependence on applied bias—can be measured with  $^{55}\text{Fe}$  and used for device simulations. In writing code in C++ and Python within the ROOT Framework, we can study the x-ray hit shape to better understand where the center of the energy is. In analyzing the EMCCD images, we can find the highest energy spots, which will help us once we switch to the NSLS-II. One approach to this is to use the ideal pixel matrix that will best capture the signal against the noise. We successfully developed a subroutine that selects the pixels in an isolated event and presents them graphically so that they may be better interpreted.

## I. INTRODUCTION

Soft x-ray range is important for the study of materials containing rare earth atoms or transition metals.<sup>1</sup> The x-ray energy range for these studies is from 200 eV – 2000 eV. The detectors that are being used are Electron Multiplying Charge Coupled Devices, EMCCD. The x-ray source being used for sensor calibration is  $^{55}\text{Fe}$ . The  $^{55}\text{Fe}$  sits inside the camera in front of the detectors and emits x-rays. These photons then strike the detectors generating electrons in the silicon. This charge can then be collected and converted to voltages to produce an image. EMCCDs were the detectors of choice for this area of study because of their ability to amplify low signals without amplifying the noise. The gain is produced in the serial register extension designed for multiplication. Code written in C++ within ROOT Framework was used to locate x-ray hits and make multiple histograms to better understand the shape and spread of charge across the pixels.

## II. SETUP

### A. RIXSCam2 EMCCD

The detectors are full-frame architecture, back-illuminated EMCCDs. Three-phase clocks are used to shift charges row by row in a parallel fashion. Each row of electrons is then transferred into the serial register and converted into an electrical signal with

an on-chip charge to voltage converter.<sup>2</sup> The full-frame architecture has 100% fill factor, this means that all pixels are used to detect photon activity. The RIXSCam2 consists of two sensors as seen in Figure 1. They are mounted on a tilt-able table enabling the user to reduce the effective size of the pixels. Each sensor has a 1632 by 1608 pixel area. These particular EMCCDs have two different registers as shown in Figure 2.<sup>3</sup> These registers are used depending on the type of signal which can be observed.

### 1. Multiplication

With traditional charged coupled devices, CCDs, low signal levels get lost in the readout noise of the sensor. With an electron multiplying CCD, there is on chip multiplication gain. This gain is produced in the serial register extension designed for multiplication. For the RIXSCam2 EMCCD this extension is 536 pixels long. This multiplication register increases the signal without amplifying the noise using a process called impact ionization. Multiplication works with a series of four gates that are held at differ-

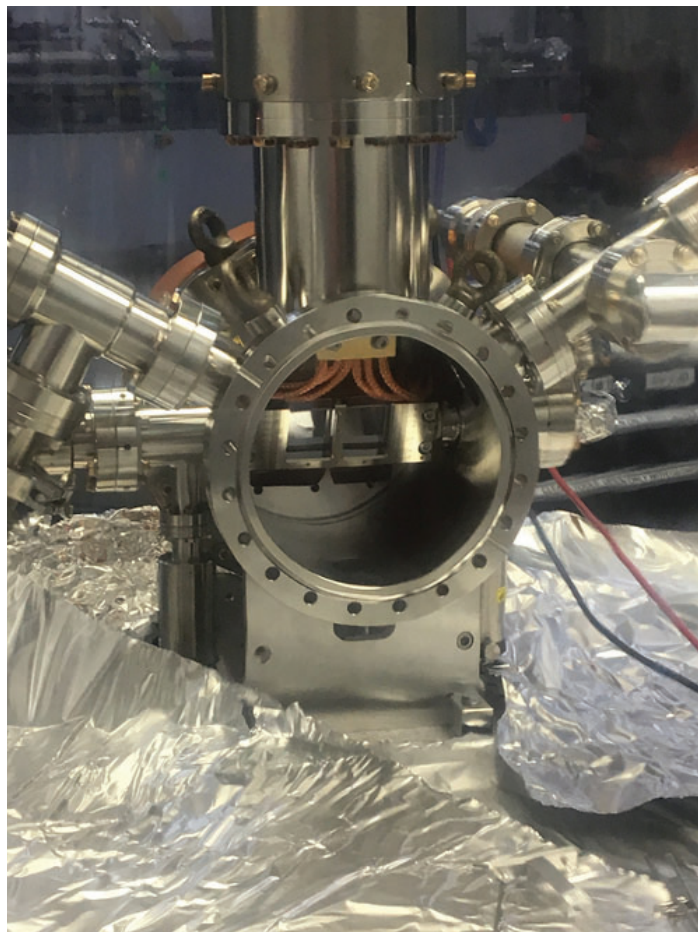


Figure 1. Two EMCCDs sitting inside of the RIXSCam2. Photo taken during detector preparation.



ent voltages. Two are held at a relatively normal voltage between 5-15 volts. This is followed by a low DC gate and a gate clocked at a much higher voltage between 35-50 volts. The potential difference between the DC gate and the high voltage clocked gate causes the impact ionization process. This multiplication process is illustrated in Figure 3 from Robbins and Hadwen, where the Phi2 clock is held at a much higher voltage than Phi1 and Phi3 clocks which causes impact ionization to occur.<sup>4</sup> The greater the potential difference, the greater the probability that electrons transferred from the first two gates can knock off additional electrons in the Silicon.<sup>5</sup> In RIXSCam2 sensors, there are two options for readout. There is the serial register readout for normal to large signals and then there is also the multiplication readout for low signals.

## 2. Noise in EMCCD

The pixel values that are read out contain the noise produced in the readout process.

There are two main types of noise in the EMCCD. One source of noise is dark current. The dark current is electrons thermally generated in EMCCD Silicon. To fix this, the sensor is thoroughly cooled to about -110°C. It is especially important that EMCCDs are kept cold because any dark current that may be produced will be multiplied along with the signal.<sup>6</sup> Another major contributor of noise is the excess signal noise caused by the multiplication process. This is due to the uncertainty in the gain because of the stochastic nature of the impact ionization process.<sup>5</sup> Excess noise factor, E defined in Robbins and Hadwen as:

$$\sigma_{out}^2 = \sigma_{input}^2 \cdot E \cdot M^2, \quad (1)$$

where M is the mean multiplication gain and  $\sigma_{input}^2$  and  $\sigma_{out}^2$  are the variances of the signal on the input and the output. The analytical expression for the excess noise factor obtained in Robbins and Hadwen is:

$$E = \frac{1}{M} \left( \frac{2M + \alpha - 1}{\alpha + 1} \right) = 2(M-1)M^{-((N+1)/N)} + \frac{1}{M}, \quad (2)$$

where N is the number of identical elements of the multiplication register and is the probability of a multiplication event.<sup>4</sup> This is derived treating the gain as a Bernoulli process and using Binomial distribution. In our case N=536 is large and this expression

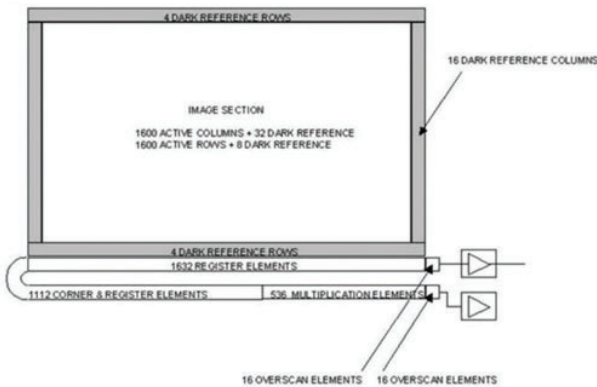


Figure 2 (above). EMCCD schematic displaying dual readout registers.

Figure 3 (right). EMCCD schematic displaying the multiplication process.

can be simplified further:

$$E = 2 - \frac{1}{M} \quad (3)$$

In our case, the variance of the input signal for x-rays registered in Si is  $\sigma_{input}^2 = N_e F$  where F is the Fano factor and  $N_e$  is the number of electrons created by the x-ray. After multiplication the signal variance becomes  $\sigma_{out}^2 = N_e F \cdot E \cdot M^2$ . The system resolution (the ratio of signal rms, to average signal amplitude,  $A_{signal}$ ) can be expressed as

$$R = \frac{\sigma_{signal}}{A_{signal}} = \frac{\sqrt{N_e F \cdot E \cdot M^2 + \sigma_{readout}^w}}{N_e \cdot M}, \quad (4)$$

where is the noise associated with converting the charge from each pixel into a digitalized unit. Inserting the excess noise, E from (3) into (4) and simplifying, the signal resolution can be written as follows:

$$R = \frac{\sqrt{2N_e F - \frac{N_e F}{M} + \frac{\sigma_{readout}^2}{M^2}}}{N_e}. \quad (5)$$

This expression can be rewritten as

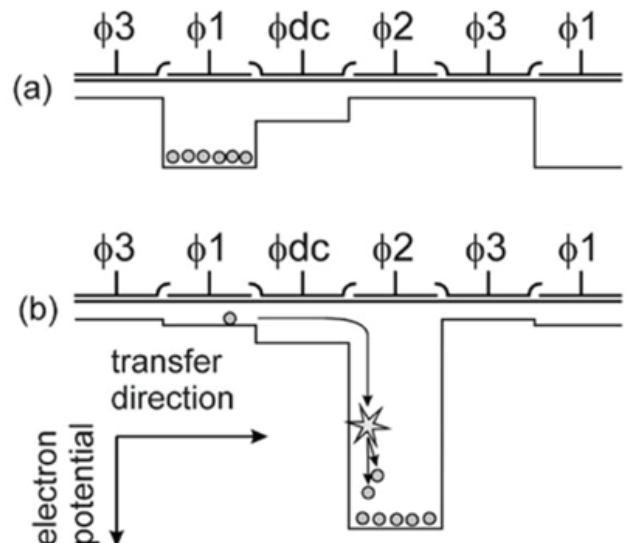
$$R = \frac{\sqrt{N_e F}}{N_e} \sqrt{2 - \frac{1}{M} + \frac{B}{M^2}}, \quad (6)$$

where the first factor is the ultimate resolution achievable with the given source and the second factor depends only on multiplication

M and readout noise to signal variance ratio  $B = \frac{\sigma_{readout}^2}{N_e F}$ .

Dark current has not been taken into account in this formula because this contribution was found negligible for our sensors. The Fano factor reduces fluctuations that exist in the stochastic nature of  $N_e$ .<sup>4</sup> When creating a large potential difference between the DC gate and the high voltage gate, the multiplication factor will greatly increase. As follows from (5 and 6) with a sufficiently high multiplication factor, M, the readout noise can be diminished.

## B. <sup>56</sup>Fe calibration source



The source used for beam line SIX detectors calibration is  $^{55}\text{Fe}$ . The  $^{55}\text{Fe}$  atoms naturally decay into Manganese-55 ( $^{55}\text{Mn}$ ) by electron capture. The  $^{55}\text{Mn}$  atoms are borne with a vacancy in the K shell. In the process of filling this vacancy Mn K-alpha, K-beta x-rays are emitted with probabilities 24.4% for K-alpha and 2.85% for K-beta. The corresponding energies are 5.8988 keV for K-alpha and 6.49045 keV for K-beta.<sup>7</sup> These x-rays are detected by EMCCD sensors and used for calibration purposes.

Interactions of Mn K-alpha and K-beta x-rays with Si and the mechanism of the energy loss is discussed by Fraser. The most probable process for these x-rays is photoelectric absorption by Si K-shell electrons. This creates a photoelectron with the energy  $E_e = E_x - E_k$ ,  $E_k = 1839$  eV and Si K-shell vacancy. The subsequent Si atom relaxation tree is provided in Fraser, Figure 2.<sup>8</sup> These processes result in the creation of 1613 electron-hole pairs by Mn K-alpha x-ray and 1774 electron-hole pairs by the Mn K-beta x-ray.<sup>8</sup>

### III. CLUSTER ANALYSIS

#### A. Compact and diffuse events

There are two main type of clusters that are observed in the EMCCD images, compact and diffuse events. Compact events can be described as a bright pixel sometimes with a trailing tail of three or four pixels behind it, Figure 4 (a). A diffuse event will have the brightest pixels in the center and less bright pixels spread around it, Figure 4 (b). Tails occur in compact events during the multiplication phase when lower signals need to be picked up. Sometimes in this process too many electrons are produced in the impact ionization process that they will spill into the pixels next to them as they are being read out causing the tail effect. A diffuse event happens when the charges in an electron cloud disperse into adjacent pixels. At very high voltages diffuse events can also be observed with tails. Specific voltage and threshold settings need to be found where lower signals can be picked up, but not produce tails. Figure 4 (c) shows the compact (pink) and diffuse (green) clusters that appear in the images obtained from the EMCCD.

#### B. Using code to find compact and diffuse clusters

After images from both sensors have been digitalized, they are analyzed by finding compact and diffuse clusters. Code written in C++ within ROOT CERN Framework, first logs all of the amplitudes in each pixel. Pixels with both signal and noise are included. Then a baseline is established through subtracting enough

amplitude to bring the “no signal” pixels to zero. The values are then fitted using a Gaussian distribution to find sigma. In order to have 1% of the signal to the right of the distribution, a threshold of 3 sigma of the width is created.

Once baseline subtraction and a threshold is handled, the program can begin to identify clusters. The dimensions of the cluster zone are entered into the program before runtime. The program will locate the brightest pixel, put it in the center of the cluster zone and analyze pixels in this zone. Due to the matrix being created around a center pixel, the dimensions selected always need to be odd. It will then add additional columns or rows depending on if a vertical or horizontal tail was specified. The pixels in this cluster then get flagged and the program locates the next brightest cluster. This continues until all the clusters in that image have been accounted for. If pixels in two clusters overlap the program will discard both clusters.

To make two dimensional bar graphs and histograms of only compact clusters, specific pixels have to be selected and tested. This is done testing rows of pixels above and below the central pixel in the presence of a spread out signal. If there is no signal detected in these rows the cluster is compact. The corresponding amplitudes will be plotted. The histogram of the sum of all the pixel amplitudes in the compact event shows K-alpha and K-beta peaks as seen in Figure 5. In this image, p1 is the mean of the K-alpha peak and p4 is the mean of the K-beta peak.

### IV. GAIN MEASUREMENTS

#### A. Total gain

The total gain of the sensor at a specified voltage can be obtained using a Gaussian fit on a histogram of isolated x-ray hits amplitudes. Through the fit, we get the mean of the K-alpha peak which is related to a mean gain in analog-to-digital units (adu). Figure 6 shows how the K-alpha amplitude increases with increasing voltage. These amplitudes were obtained from running our code on EMCCD images taken at 36 different voltages ranging from 20 to 45.3 volts. From the graph, it can be seen that K-alpha amplitude stays relatively constant until about 40 volts where it increases almost exponentially. The reason for this is that the multiplication gain does not occur at lower voltage settings. Once the voltage is increased enough, multiplication through the process of impact ionization can be observed.

#### B. Electronics gain

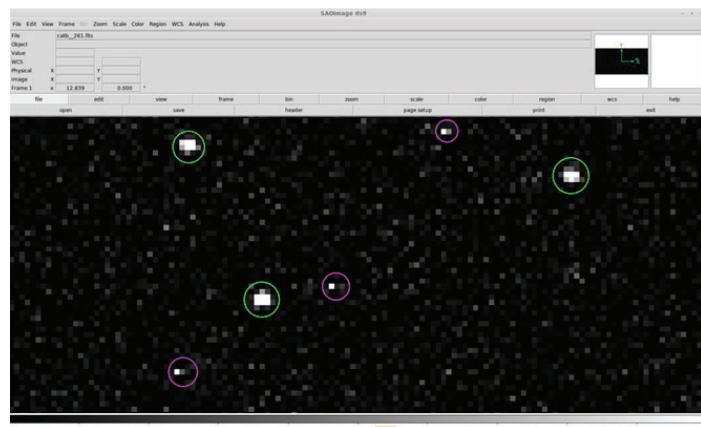
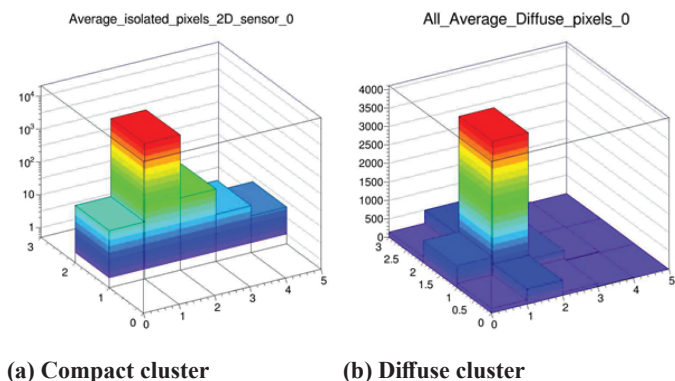


Figure 4. Figures (a) and (b) show the average compact and diffuse clusters graphed with ROOT Cern. (c) Shows the compact (pink) and diffuse (green) clusters as they appear in the images from the EMCCD using DS9, an imaging application.

The electronics gain expressed in electrons/adu provides a conversion factor from a signal measured in adu to the number of electrons generated by this signal. The electronics gain is obtained from the data where the multiplication gain,  $M$ , equals 1. Mean values from Gaussian fitting were averaged for low voltage images (20, 25 and 30V). The amplitude for K-alpha was found to be around 92 adu for sensor 1 and about 87 adu for sensor 2. It is known that interactions between Mn K-alpha x-rays and the Silicon sensor result in the creation of 1613 electron-hole pairs. In knowing these two things, the electronics gain can be calculated by dividing the number of electrons created by the amount of adu measured for the K-alpha peak with no multiplication. This results in an electronics gain of 17.53 electrons/adu for sensor 1 and 18.54 electrons/adu for sensor 2.

### C. Multiplication factor

The multiplication factor can be calculated at different voltages by using the electronics gain when the voltage value is very low and no multiplication exists; i. e.,  $M = 1$ . A Gaussian fit on the isolated hit histograms was used to get the mean value of K-alpha. This value could then be divided by the amplitude of K-alpha under low voltage settings which will give the multiplication gain for the high voltage image files.

The optimal multiplication factor for the best resolution can be found by taking the derivative of the resolution with respect to multiplication,  $M$ . In setting the derivative equal to zero, we can get the value of  $M$  that makes the resolution a minimum. This can be written as follows:

$$M_{opt} = \frac{2 \cdot \sigma^2}{N_e \cdot F} \quad (7)$$

For 5.9 keV x-rays, we have found the ideal multiplication factor to be between 175 and 320 depending on the sensor that is used. We were not able to observe this because such a large multiplication gain is out of the range of our EMCCDs.

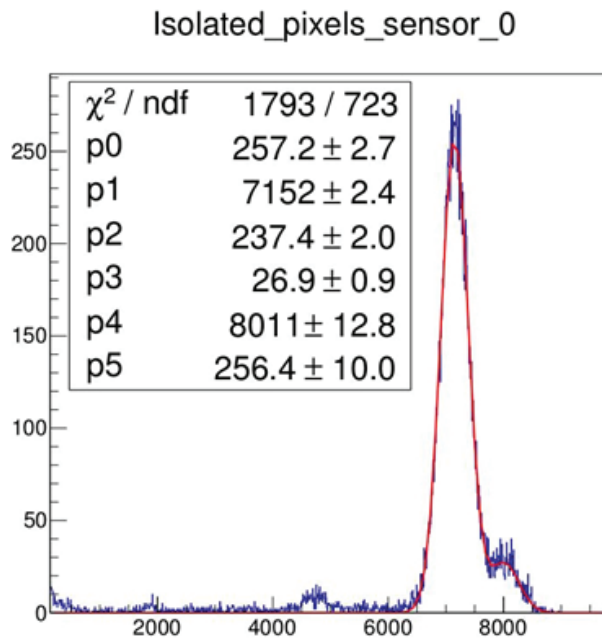


Figure 5. A Gaussian fit of K-alpha and K-beta peaks for isolated hits on a sensor.

### V. OPTIMAL MULTIPLICATION FACTOR PREDICTIONS FOR LOW SIGNAL

For the varying energy levels that can be used, there exist different multiplication factors for optimum resolution. These can be found by either setting the derivative of the resolution to zero or it can be seen by graphing the resolution for varying multiplication factors and observing where the graph is at a minimum. From equation (7), we can gather that when a very large energy source is used, it will create more electrons causing the optimal multiplication factor to be lower for the best resolution. This can also be observed in Figure 8 where resolution was graphed against varying multiplication factors for different energies. In this graph,  $B$  represents readout noise to signal variance ratio (see equation 6). From Figure 8 we can see that for  $B=0.1$  (better readout noise or higher energy), the best resolution is obtained at a much lower multiplication factor. We can conclude that depending on what energy source is used, the applied voltages that cause impact ionization may need to be adjusted accordingly in order to reach optimal multiplication for the best resolution. In addition, if readout noise is minimized, this would allow for lower signals to have better resolution with multiplication.

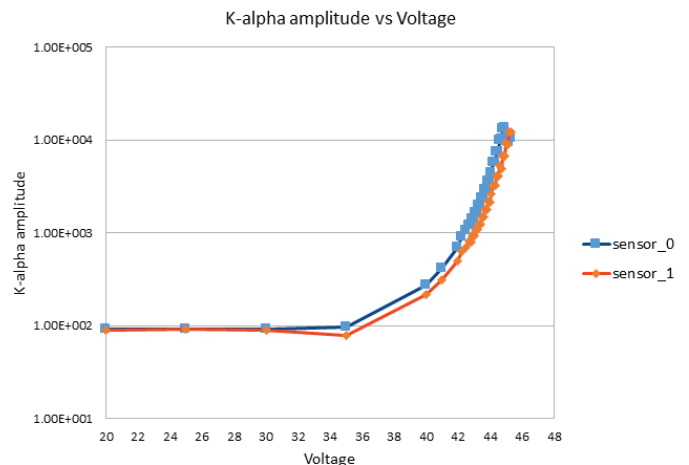


Figure 6. K-alpha amplitude graphed against voltage for 36 voltage settings

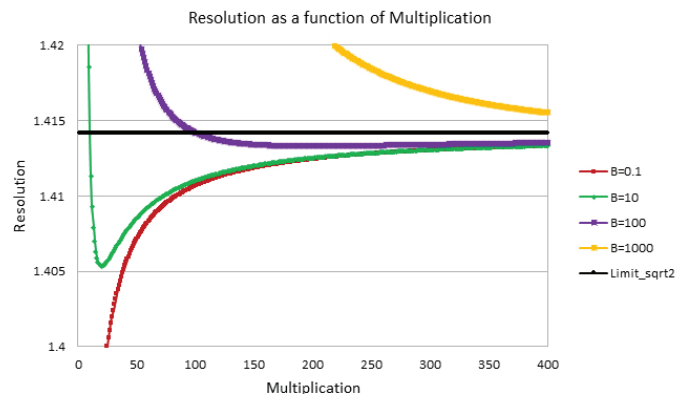


Figure 8. Resolution depending on multiplication and energy levels.

## VI. ACKNOWLEDGEMENTS

This project was supported in part by the U.S. Department of Energy, Office of Science, Office of Workforce Development for Teachers and Scientists (WDTS) under the Science Undergraduate Laboratory Internships Program (SULI).

## VII. REFERENCES

- <sup>1</sup> M.R. Soman, D.J. Hall, J.H. Tutt, N.J. Murray, A.D. Holland, T. Schmitt, J. Raabe, and B. Schmitt, *Journal of Instrumentation* 6, 1 (2011).
- <sup>2</sup> J.R. Janesick, *Scientific charge-Coupled devices* (SPIE-The International Society for optical engineering, Bellingham, WA, 2001).
- <sup>3</sup> D. Colebrook, *System Operating Manual for RIXSCam2 System 2014-00003* (2017).
- <sup>4</sup> M. Robbins and B. Hadwen, *IEEE Transactions on Electron Devices* 50, 1227 (2003).
- <sup>5</sup> T.J. Fellers and M.W. Davidson, *Hamamatsu Learning Center: Electron Multiplying Charge-Coupled Devices (EMCCDs)*.
- <sup>6</sup> D. Dussault and P. Hoess, Noise performance comparison of ICCD with CCD and EMCCD cameras. *Proc. SPIE 5563, Infrared Systems and Photoelectronic Technology*, 195 (October 21, 2004); doi:10.1117/12.561839
- <sup>7</sup> E.M.A. Hussein, *Handbook on radiation probing, gauging imaging and analysis* (Springer, 2003).
- <sup>8</sup> G. Fraser, A. Abbey, A. Holland, K. Mccarthy, A. Owens, and A. Wells, *Nuclear Instruments and Methods in Physics Research Section A: Accelerators, Spectrometers, Detectors and Associated Equipment* 350, 368 (1994).



# An analysis of charge transparency in a LArTPC

Michael Dolce, Department of Physics, University at Albany, Albany NY 12222  
Mary Bishai, Department of Physics, Brookhaven National Laboratory, Upton NY 11973

## Abstract

The MicroBooNE experiment, located at the Fermi National Accelerator Laboratory, uses a 170-ton liquid argon time projection chamber (LArTPC) to detect neutrinos. Three layered anode wire planes and a cathode plane sit on opposing sides of the LArTPC. Interacting neutrinos ionize electrons from the argon atoms in the detector that then drift towards the anode wire planes due to the voltage at the cathode. The ionized electrons travel through the U and V induction wire planes and then deposit their charge on the Y collection wire plane at 230 V. At Brookhaven National Laboratory, a newer design has been pioneered. Referred to as the transparency design, our study investigates the data of reduced Y plane voltages from 210 V to 30 V. This lower Y plane voltage allows the V plane to become a partial collection plane, which increases the signal strength of the V plane. This would reduce the performance of the Y plane, but increase the performance of the V plane. The goal of our study is to better understand the effects of these different voltages on the signals of the V and Y planes by analyzing their waveforms as a function of the track angle and the transparency voltage. We have found a clear, unipolar signal on the V plane for 30 V for the track angles investigated. The ultimate objective is to identify an ideal Y plane voltage to improve the shape and amplitude of the signal on the V while preserving the performance on the Y plane.

## I. Introduction

### A. Experiment Overview

The subfield of neutrino physics has become incredibly popular and actively studied. Experiments seeking to learn more about these elusive quantum mechanical particles exist across the

world. The Micro Booster Neutrino Experiment (MicroBooNE) is one of these leading experiments in neutrino physics that utilizes a liquid argon time projection chamber (LArTPC). The primary physics goal of MicroBooNE is to further understand short baseline neutrino oscillations; it will analyze the excess of electron-like events at low energy from the Booster Neutrino Experiment. In addition, MicroBooNE is capable of detecting supernova neutrinos and will begin to look for proton decay signatures. It will also perform a series of measurements, but the continued development and understanding of the operational physics of a LArTPC is considered one of the primary goals of the MicroBooNE experiment [1]. The physics from cosmic rays and atmospheric particles and the signal processing methods from these events will be critical for future LArTPC experiments such as the Deep Underground Neutrino Experiment (DUNE), which will be a massive experiment that will employ a fiducial mass of approximately 40,000 kT of liquid argon [2].

MicroBooNE is located within Fermilab; the Booster Neutrino Beam (BNB) delivers a 0.5-2 GeV muon beam in discrete pulses towards the LArTPC 470 m downstream. A layout of the experiment can be seen in Figure 1. In that distance, the muons decay into muon neutrinos and various secondary particles. The muon neutrinos oscillate into electron neutrinos where they interact with the liquid argon atoms in the detector resulting in ionized electrons. In addition, due to its placement above ground, other particles will interact with the detector such as cosmic rays and atmospheric muons.

### B. The MicroBooNE LArTPC

MicroBooNE is a leading force in the deployment of LArTPCs for high precision neutrino physics measurements. It utilizes



Figure 1: An aerial view of the MicroBooNE experiment. The beam travels from right to left along the dashed orange line. The MicroBooNE beam (BNB) is 470 m from the detector (LArTPC).

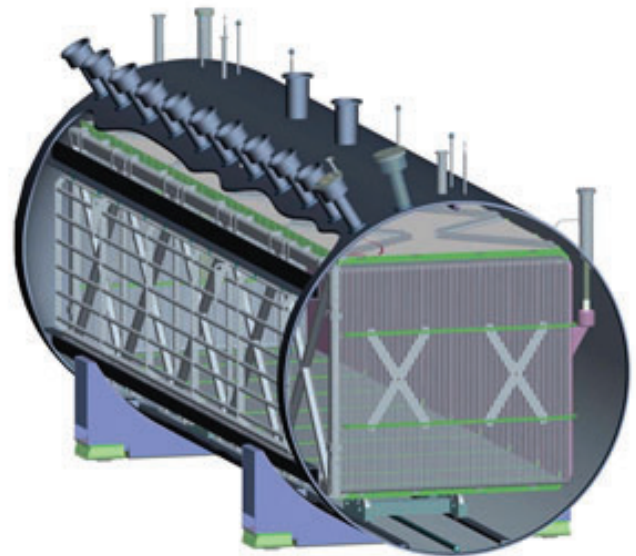
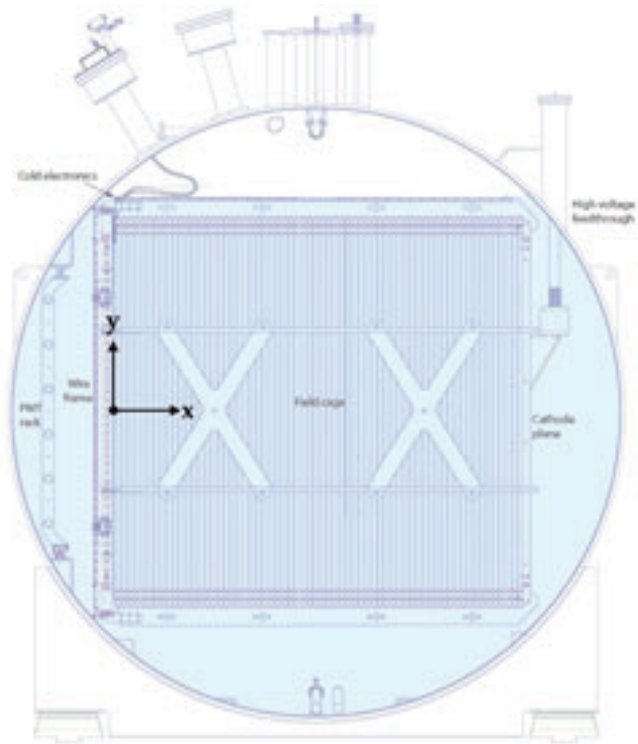


**Figure 2:** In (a), a cross-sectional view of the MicroBooNE LArTPC with the beam directed along the longitudinal direction 10.4 m out of the page. In (b), the schematic of the full volume of the LArTPC inside the cryostat kept at 87 K.

its advantages of high spatial resolution and calorimetry to identify particle tracks. In the detector, 170 tonnes of liquid argon are cooled to its operational temperature of 87 K. The volume of the LArTPC is 2.56 m x 2.3 m x 10.4 m, where on opposite sides of the 2.56 m are a cathode and three layered anode wire planes, parallel to the beam direction. A cross-sectional view can be seen in Figure 2. The three anode wire planes are referred to as the U, V, and Y wire planes, all of which are held at certain voltages. The U and V wire planes each contain 2400 wires angled at  $\pm 60^\circ$ , but with voltages held at -110 V and 0 V respectively, while the Y plane possesses 3456 vertically oriented wires held at 230 V. The U, V, and Y wire planes are spaced 3 mm apart with a wire pitch also of 3 mm. Meanwhile, the cathode is held at a voltage of -70 kV, and due to this voltage creates a drift field of 273 V/cm causing the ionized electrons, or tracks, to drift along the 2.56 m direction with a velocity of 1.105 mm/ $\mu$ s towards the anode wire planes [3]. As they drift, the electrons induce currents on the U and V wires, which are measured as bipolar waveform signals, and then terminate and are collected on the Y wires as unipolar waveform signals, which can be seen in Figure 3.

### C. Signal Processing

In MicroBooNE, the ultimate goal is to work backwards from the waveforms to quantify the total charge from a signal to identify the energy and type of particle to classify the original interaction. The method for this signal processing is long and sophisticated, so only processes relevant to the transparency study are explained.

The bipolar waveforms on the U and V planes and the unipolar waveforms on the Y plane are the result of elementary electrostatics. As an ionized charge travels, it induces current on nearby U, V, and Y wires. The principle of current induction on the wire planes is described by the Shockley-Ramo theorem

$$i = q \cdot E_w \cdot v_q \quad (1)$$

where the instantaneous induced current  $i$ , is proportional to an element of ionized charge,  $q$ , multiplied by the dot product of the weighting field  $E_w$  at the location of the charge and drift velocity  $v_q$  [4,5]. The weighting field is calculated by using a 2D simulation based on Garfield [6].

Next, the signal on a wire is described by the signal response function, where the induced current from the wire is received, amplified, and shaped by a pre-amplifier all of which operate in the front-end, cold application specific integrated circuits (ASICs). The shaped and amplified signal is then sent to the warm analog-to-digital converters (ADCs) where the signal is converted into counts. It is these counts that are used in this study to quantify the strength of the waveform from a specific wire, known

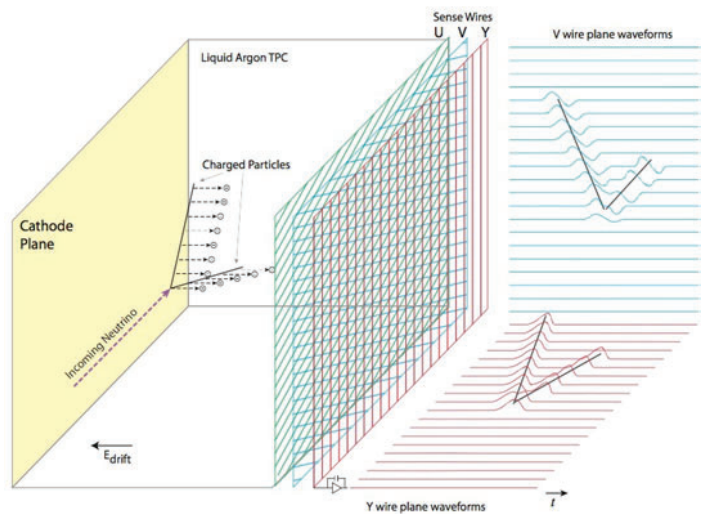


**Figure 3:** A design of the operational principle of the LArTPC. The U plane waveform is omitted for simplicity. An ionized electron is released due to an interacting neutrino and, due to the drift field caused by the cathode voltage, drifts towards the anode wire planes inducing current on all three planes and terminating on the Y plane.

as a channel, in the wire planes. A schematic of the entire signal processing layout can be seen in Figure 4.

The shape of the waveform signal is also a well understood process. The effect of the bipolar waveform for the U and V wire planes is due to the voltages set preventing charge to be collected on them. As a result, an equal and opposite current is induced on the wires as they enter and exit the U and V plane wires without any charge from the drifting electrons deposited, hence they are transparent to the Y plane. However, on the Y wire plane all of the charge is collected on the wires; the effect of this is also due to voltages set because the electric field lines terminate along the Y wires. Therefore, the ionized electrons must deposit their charge on the Y plane resulting in a unipolar waveform that is read by the ASICs and converted into counts from the ADC as shown in the schematic in Figure 4. The waveform from the readout electronics indicates the amount of charge passing through the wires, which is why they are crucial to this study. Understanding the waveform, and thus the amount of charge, can reveal what voltage may be best for the transparency design as the goal is to find the Y voltage that produces the best signal to noise on the V and Y wire planes.

## II. Experimental Design

### A. Transparency Design

In the presently used nominal design the U and V planes are entirely transparent [7]. This is ensured because of the specific voltages applied to the wire planes (-110 V on the U plane and 0 V on the V plane), which cause the drift field lines to terminate on the Y plane. Therefore, due to the Shockley-Ramo theorem (1), the drifting electrons induce current on the U and V wires

and continue to pass through where they are ultimately collected on the Y plane resulting in a single collection plane. This design yields an optimal signal strength on the Y plane; however, due to the induction plane's performance, it is difficult to measure the signal on the Y plane for large angle tracks. For example, tracks that are perpendicular to the anode wire planes have a smaller signal amplitude and can be misidentified as background or noise. This effect is seen in Figure 5, where the charge reconstruction efficiency is plotted against the incoming angle.

That is why this transparency design has been proposed, the voltage on the Y plane is reduced from its nominal 230 V down to 30 V in steps of 20 V thus altering the transparency of the U and V planes. The result is the transformation of the V plane from an induction plane to a collection plane where drifting electrons are collected resulting in unipolar waveforms instead of bipolar waveforms. The result is a tradeoff; an increased signal strength on the V plane for a reduced signal strength on the Y plane. This compromise between the two to find the optimal signal to background ratio for the V and Y planes is the long-term objective of this study. Before this goal can be achieved, the impact of these reduced Y plane voltages on the signals of the V and Y planes must be understood, which is done in this study by analyzing their waveforms as a function of the track angle and the transparency voltage. Understanding how the waveforms from the V and Y planes are impacted by the reduced Y plane voltages will allow us to learn more about the effect of the unipolar signals on the V plane. The result of this would enhance the signal of all tracks regardless of the incoming angle due to the presence of a second collection plane.

Meanwhile, the range of track angles will provide insight into

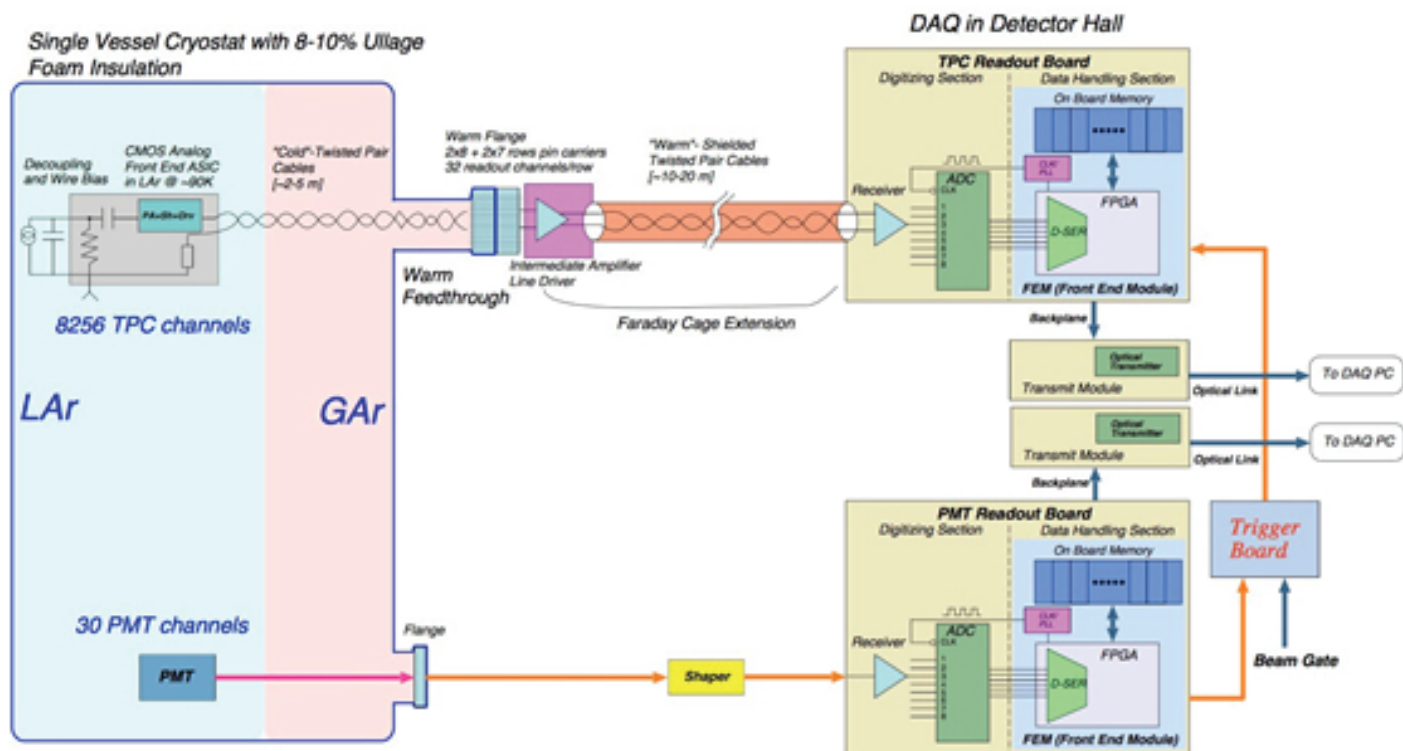


Figure 4: An overview of the entire electronic readout process. It is this schematic that displays how a measured waveform on the wire planes results in a measure of the ADC counts for this study, and the complexity of the signal processing.



how perpendicularly angled tracks are impacted by two collection planes; this might improve identifying these types of tracks from background compared to the nominal design of one collection plane. It is important to note that this study does not include an analysis on the U plane; the possibility of charge terminating, and thus observing unipolar signals on the U plane was not investigated. We also note that the data used for this study was of cosmic muon events and not data from neutrino interactions from the BNB.

A brief description of the significance of perpendicular tracks is required. In the Micro-BooNE LArTPC, the incoming tracks approach the anode wire planes in any direction. However, this study focuses only on perpendicularly oriented tracks. For example, a perpendicular track would be any track drifting towards the wire planes that is approaching normal to the Y-axis (see Figure 2). Therefore, a drifting  $0^\circ$ , perpendicularly oriented track is normal to the anode wire planes. A  $30^\circ$  track is still approaching the anode wire planes in the same XZ-plane, but at a  $30^\circ$  angle. Recall also that the U and V wire planes are angled at  $60^\circ$  and the Y is vertical, therefore a  $30^\circ$  track in the V plane is not the same angle as a  $30^\circ$  track in the Y plane; all track angles are labeled with respect to their *own* wire plane. It is also crucial to note that for this study *all* track angles mentioned are perpendicularly oriented as described.

### III. Results

#### A. Nominal Data

Before analyzing the transparency data, the first investigation was to understand the effect the track angle has on the signal shape and amplitude in the nominal data. To do this, an individual

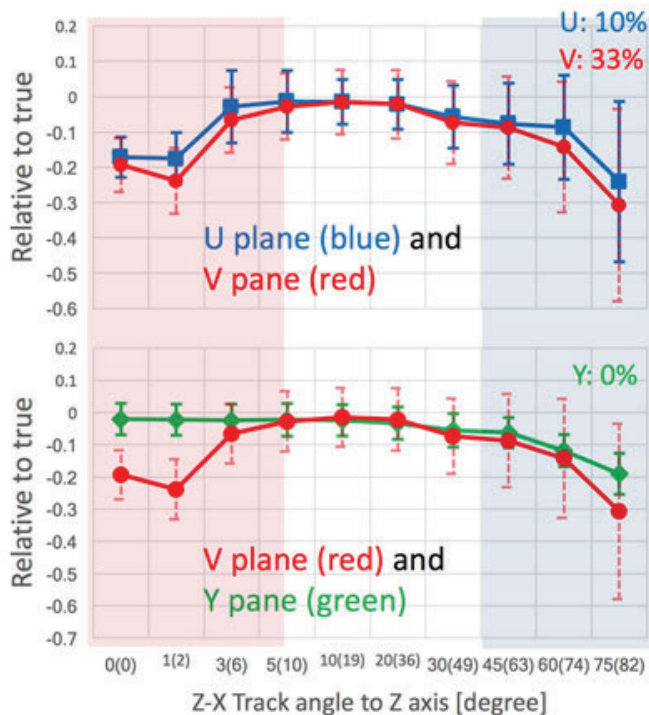


Figure 5: A plot of the inefficiency of the charge reconstruction as a function of the incoming angle. The regions of small and large angles indicate the largest inefficiency from the true charge. It is due to this inefficiency that the transparency design is investigated. A second collection plane could improve the charge reconstruction for these inefficient angles. Courtesy of Hanyu Wei.

channel was selected manually of approximately  $0^\circ$ ,  $30^\circ$ , and  $60^\circ$  angled tracks and their ADC counts and the full waveforms were analyzed for the V and Y planes. After normalizing each angled V waveform to their respective Y plane waveform, it was concluded the larger angled tracks yield smaller waveform amplitudes. This effect can be seen in Figure 6 from the smaller amplitudes of the  $60^\circ$  tracks in both the V and Y planes, particularly compared to the  $0^\circ$ . A sample of these angled waveforms from the nominal data can be seen in Figure 6. While the un-normalized waveforms are in units of ADC counts, after normalizing, the waveforms are measured in arbitrary units, or A.U.

This result from the data was then compared to the simulation waveforms of the nominal design produced by tracks at varying angles. The purpose was to confirm our understanding of the relationship between track angle and waveform shape for the nominal data in addition to validating the accuracy and correctness of the simulation. This was done by taking an average of the V plane waveform for each of the three angles studied ( $0^\circ$ ,  $30^\circ$ , and  $60^\circ$ ). The purpose for averaging together multiple waveforms further improves the shape of the waveform and helps to reduce excess background; this study only averaged over five for  $0^\circ$  and ten channels for  $30^\circ$  and  $60^\circ$  because each of the waveforms were selected manually from the data, which was a time consuming process to select appropriate waveforms. However, increasing the number of channels would, in principle, improve the shape of the waveform even further. In the future, we hope to be able to automate this process of selecting waveforms now that we understand the method of doing so. The average waveform was also properly aligned in time by shifting it by several bins. In this comparison, the simulation and data were both normalized to their respective minimum points. The comparison is displayed in Figure 7.

Again, in Figure 7, the V plane waveform  $0^\circ$  plot was averaged over five channels and the  $30^\circ$  and  $60^\circ$  plots were averaged over ten channels. The Y plane waveforms were not averaged since the noise in the nominal design of the collection plane is negligible because of the large signal strength from a single collection plane; therefore, averaging is not required. However, the V plane waveforms were averaged because of the smaller amplitudes particularly for large incoming angles, as seen in Figure 5. For the  $60^\circ$  plots specifically, the comparison could be improved further by selecting more channels than the ten used and then averaging their waveforms together as described. Averaging the

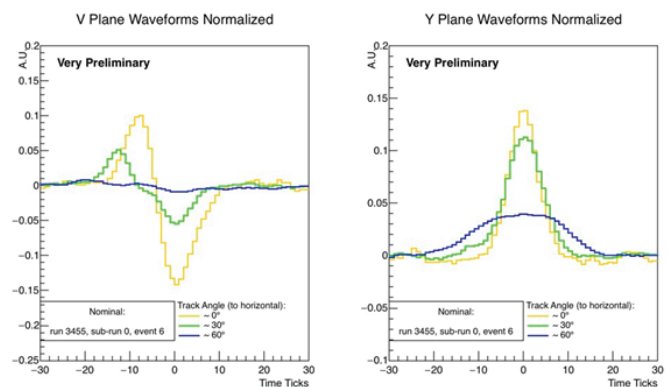


Figure 6: Plot of the nominal data looking at track angles of  $0^\circ$ ,  $30^\circ$ , and  $60^\circ$  normalized to the corresponding angle's Y plane waveform. As the angle increases the strength of the signal decreases. One time tick corresponds to  $0.5 \mu\text{s}$ .



Y plane waveforms for all angles would improve the comparison too. Ultimately, the next logical step is to automate the process of selecting wires so that we can maximize the number of channels, which would improve the average, and save substantial amounts of time compared to selecting the channels manually.

The  $0^\circ$  and  $30^\circ$  plot of data and simulation comparisons unsurprisingly provide a robust comparison because they are not at near-perpendicular angles. However, they are not exactly identical. This can be seen from the slightly larger width of the simulation compared to the data for the Y planes of the  $0^\circ$  and  $30^\circ$  plots and the larger widths at the beginning and end of the waveforms on the V planes for is understood. The simulation contains a shielding effect due to the U and V planes where the drifting electrons will bend around the approaching U and V wires. This results in a longer travel time and thus a larger width of the V and Y waveforms for the  $0^\circ$  and  $30^\circ$  plots. This effect is not as prominent in the  $60^\circ$  plots where in the Y plane plot the time spread of the data dominates over the shielding effect, and con-

versely for the V plane waveform, the width of the simulation is markedly wider than the data, particularly in the negative end of the waveform. The cause of both of these effects in the  $60^\circ$  waveforms is unclear. An investigation into this discrepancy between the data and simulation at these large angles will be carried out in the future. Despite this, the comparison of the nominal design simulation to the nominal data demonstrated that they are acceptable and more importantly provided a necessary reference to the transparency data which was analyzed next.

## B. Transparency Data

Once the simulation and data were in agreement, the next step was to take the data of the nominal design and compare it to the data taken from the scan of the transparency volt-ages. With this accurate understanding of the nominal waveforms, it provided a valuable reference to analyze the various features of the transparency data. For the transparency data, the scan of lower voltages began at 210 V and was reduced by 20 V down to 30 V,

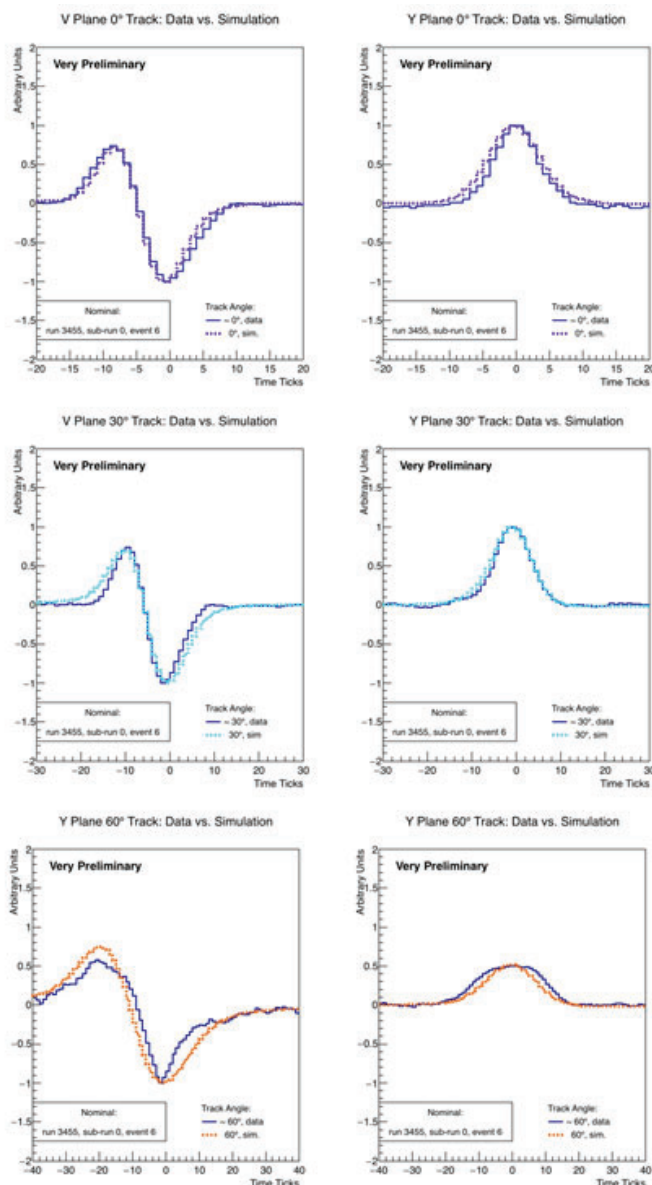


Figure 7:  $0^\circ$ ,  $30^\circ$ , and  $60^\circ$  plots of the waveform from the data compared with the simulation. Simulation provided courtesy of Brooke Russell.

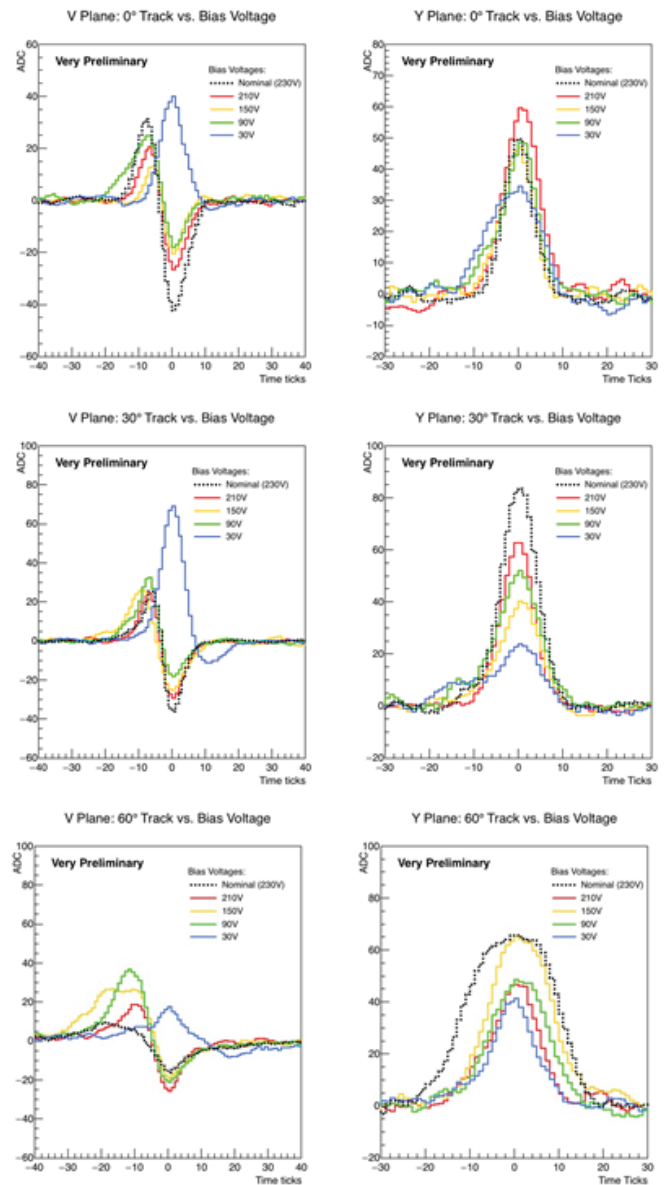


Figure 8:  $0^\circ$ ,  $30^\circ$ , and  $60^\circ$  plots of the waveform from the scan of transparency data (colored) compared to the nominal data (dotted).

resulting in ten different runs of voltages. Due to time constraints, only the 210 V, 150 V, 90 V, and 30 V data were analyzed for this study. These voltages provided a wide enough range that any effects of the transparency would be discernible. Similar to the nominal data, the transparency waveforms were averaged over five channels for all three of the angles. Figure 8 displays the results from the transparency scan; the dotted black waveforms represent the data waveform from their respective track angles from Figure 7. The waveforms are centered at their respective maximum/minimum points.

There are many interesting conclusions to be made from this comparison of transparency voltages. The first, and most prominent, is the transformation from a bipolar signal to a unipolar signal on the V plane, particularly with the 30 V data. This can be explained by the decreased voltage on the Y plane; the Y plane voltage is closer to 0 V, which is also the V plane voltage, and thus weakening the drift field around the Y plane. As a result, the field lines are terminating on the V plane and the charge is collected on its wires instead of the Y plane; this can also be seen in the reduced amplitude of the Y plane waveform. We have the ability to transform the second induction plane into a collection plane with a sizable amplitude. One setback is the amplitude on larger angles, such as the 60° V plane plot, may not be large enough to distinguish a signal from the noise, but this would need to be confirmed with a charge reconstruction analysis. This second collection plane comes at the price of a reduced amplitude in the Y plane, but having two collection planes is a significant breakthrough.

#### IV. Summary and Conclusion

This study focuses only on perpendicularly oriented tracks. For example, a perpendicular track would be any track drifting towards the wire planes that is approaching normal to the Y-axis. Therefore, a drifting 0°, perpendicularly oriented track is normal to the anode wire planes. A 30° track is still approaching the anode wire planes in the same XZ-plane, but at a 30° angle. Also, the V and Y wire planes are angled at -60° and 0° respectively; therefore a 30° track in the V plane is not the same angle as a 30° track in the Y plane. Lastly, all track angles in this study are perpendicularly oriented.

From the nominal data analysis, we have developed an understanding of the waveform shape in the simulation and the data. Different effects dominate the width of the waveform at different angles. The shielding effect from the simulation dominates at smaller angles and it is unclear why the shielding effect does not do so at larger angles. While agreement between data and simulation is acceptable, this question is something that will be investigated further to improve our understanding and the accuracy of the simulation.

The primary discovery of the transparency data analysis is the confirmation of the transformation from induction to collection on the V plane. Specifically, we see at 30 V a clear, unipolar signal on the V plane for all three of the angles investigated, which signifies charge is being collected on it. It is important to note that there is still charge being collected on the Y plane too; therefore, there are two wire planes that can confirm the presence of a signal on the detector compared to the original one from the nominal design. This demonstrates we utilize two collection planes that can improve the signal to noise for perpendicular tracks.

There are multiple next steps to proceed from this study. Re-

lating to the nominal design, the first step would be to improve the current simulation with the understanding of the shielding effect and the longer travel time of the ionized electrons on tracks from varying angles. In the transparency design, the next step would be to investigate the charge reconstruction efficiency of the varying track angles and determine quantitatively how well the V plane is collecting charge, from all angles of incoming tracks. If this analysis proves that the V plane is collecting charge well, a possible next step would be to investigate the U plane and survey the transparency the data for any collection, whether partial or whole, on the U plane. The last, and most important, step would be to automate this study. For example, now that we know and understand the types of channels that should be selected for analysis, automating the process of selecting channels, ideally more than five or ten, would allow the analysis to be done significantly faster and by selecting more channels would improve the shape of the waveform, from the averaging technique. Lastly, further into the future, all of this work learning about the operational physics of the MicroBooNE LArTPC, a 170 ton detector, will prove valuable as it will be employed in DUNE where it will make use of a fiducial mass of 40,000 kT of liquid argon.

#### V. Acknowledgements

I would like to thank Mary Bishai for her instruction and guidance as a mentor on this work. I would also like to thank Xin Qian, Brooke Russell, and Hanyu Wei for their assistance throughout the project. This project was supported in part by the U.S. Department of Energy, Office of Science, Office of Workforce Development for Teachers and Scientists (WDTS) under the Science Undergraduate Laboratory Internships Program (SULI).

#### VI. References

- <sup>1</sup>MiniBooNE Collaboration: A. A. Aguilar-Arevalo et al. *Unexplained Excess of Electron- Like Events From a 1-GeV Neutrino Beam* Phys. Rev. Lett. 102 (2009) 101802, [arXiv:0812.2243].
- <sup>2</sup>The LBNF/DUNE Collaboration *CDR Volume 3: The Long-Baseline Neutrino Facility for DUNE* (2015).
- <sup>3</sup>The MicroBooNE Collaboration: R. Acciarri et al. *Design and Construction of the MicroBooNE Detector* JINST (2017) P02017, [arXiv:1612.05824v2].
- <sup>4</sup>W. Shockley. *Currents to conductors induced by a moving point charge.* Journal of Applied Physics, 9:635, 1938.
- <sup>5</sup>S. Ramo. *Currents induced by electron motion.* Proceedings of the ORE, 27:584, 1939.
- <sup>6</sup><http://garfield.web.cern.ch/garfield/>.
- <sup>7</sup>The MicroBooNE Collaboration, *A Method to Extract the Charge Distribution Arriving at the TPC Wire Planes in MicroBooNE* (2016).

# Implementation of a graphics card based radio frequency spectrometer for the Baryon Mapping Experiment

Hindy Drillick, Department of Mathematics, Stony Brook University, Stony Brook, 11794  
Anže Slosar, Department of Physics, Brookhaven National Laboratory, Upton, NY, 11973

## Abstract

The Baryon Mapping Experiment is building a prototype radio telescope at Brookhaven National Lab for 21-cm intensity mapping. This technique maps the 21-cm hydrogen emission line, and allows us to study the distribution of mass in the universe at extremely large scales. The BMX telescope will be composed of four dishes, and four corresponding orthomode transducers that split the incoming radio signal into orthogonal X and Y polarizations. Each OMT will have two channels feeding into an analog to digital converter, one for each polarization. Radio spectrometer software reads in packets of this digitized data, and computes its power spectra, using the Nvidia GeForce GTX 1080 Graphics Processing Unit (GPU), and CUDA, a platform for parallel programming on GPUs. Currently, only one dish and two channels are operational. This project expands the features of the current spectrometer to include real time detection, and the rejection of radio frequency interference (RFI), and also optimizes the code so that consecutive data packets are handled concurrently. We split each packet into smaller chunks and flag chunks with outlying variances as RFI. Flagged chunks are zeroed out before we take the Fast Fourier Transform of the entire packet, and calculate its power spectrum. A CUDA stream is a set of operations that are carried out in serial order, and operations in different streams can execute concurrently. By sending consecutive data packets to different streams, we free up GPU cycles and allow for more computation per packet. Since computation time will increase in the future with more channels, this will help the code scale up to more than two channels

## I. Background

### A. 21-cm Intensity mapping

Neutral hydrogen emits a 21-cm line that can pass through cosmic dust clouds, unlike visible light, and is therefore well suited to map matter density in the universe. A program to measure the Baryon Acoustic Oscillations using a 21 cm mapping telescope has been proposed by Peterson et al.<sup>1</sup> The Baryon Mapping Experiment (BMX) at Brookhaven National Laboratory is building a prototype radio telescope to detect these 21-cm hydrogen emissions with the goal of perfecting data acquisition and mapping techniques needed for further, large-scale 21-cm surveys.

### B. BMX Telescope Design

The BMX telescope will be composed of four parabolic dishes as shown in Figure 1. Each dish will have a corresponding Orthomode Transducer (OMT). The OMT's function is to split incoming radio waves into polarized X and Y channels, which allows for separate analysis of the polarized channels. Each OMT is attached to two amplifier and filter chains, one for each polarization. These chains feed into analog digital converter (ADC)

and the digitized signal is then sent to a GPU based radio spectrometer. Currently, only one dish and its corresponding X and Y channels are completed.

### C. Data Acquisition and GPU processing

Graphics Processing Units are circuits that are designed to rapidly and efficiently manipulate large amounts of data on numerous parallel threads. The Spectrum ADC is sampling data at 1.1 Ghz and 8-bit resolution, which amounts to 1.1 Gb of data per second. In order to process all this data, we implemented a radio frequency spectrometer on a GPU with CUDA so that we can compute and reduce power spectra in real time. CUDA is an application programming interface (API) for parallel programming on a GPU, which allows for code to run on multiple GPU threads concurrently.

A CUDA kernel is a function that executes on the GPU. Multiple instance of the kernel are launched concurrently on a requested number of threads. Each instance of the kernel knows which thread it's on, so this allows for each thread to perform the same operation on a different segment of data. A CUDA stream is a set of CUDA operations that get executed in serial order. These operations include memory transfers from CPU to GPU, memory transfers from GPU to CPU, and kernel calls.

### D. Radio Frequency Interference

One of the difficulties in radio astronomy is dealing with radio signals emitted from terrestrial sources. Such signals are known as RFI and can heavily corrupt the data, making it difficult to detect the astronomical signals we are looking to examine. Certain terrestrial signals such those emitted by a nearby weather station are periodic at well-determined frequencies, and can simply be excised from the data in Fourier space. Other more transient signals, such as cell phone signals or Wi-Fi, can be detected as outliers in the time domain. By examining the signal timeseries coming in from the telescope, we can perform real time transient RFI detection, which simplifies the amount of RFI detection needed later on in Fourier space. We implemented an RFI detection and rejection unit in our GPU spectrometer to be able to efficiently find and cut out these transients before they could corrupt the power spectra.

## II. Methods

### A. Data Pipeline

21 cm signals have a frequency of 1.42 Ghz at redshift  $z = 0$ , and 1.11 Ghz at redshift  $z = 0.3$ . We are therefore interested in signals within the range 1.1 – 1.65 Ghz. Signals of any frequency are split by the OMT into X and Y polarizations and are then amplified and filtered so that only signals within the desired range remain. The filtered signal is sampled by a Spectrum M4i2223 8-bit digitizer card at a sampling rate of 1.1 Ghz. Although the Nyquist frequency for our range of 1.1 – 1.65 Ghz would be 3.3 Ghz, this



is beyond the sampling capability of the digitizer. Instead, we undersample the signal at 1.1 Ghz and rely on aliasing to map the desired range to the range 0 - .55 GHz, which is the range that we are actually measuring.

Digitized data is then copied over to the Nvidia GeForce GTX 1080 GPU in packets containing  $2^{27}$  bytes per polarization channel. This amounts to  $2^{27}/(1.1e9) = 122.016$  ms of data per packet. The data arrives in a single array, with the two channels interleaved. A CUDA kernel separates the data into two separate arrays, and simultaneously converts the data from bytes to floats in order to allow for floating point calculations later on. If RFI rejection is turned on then the data packet is split into smaller chunks of a user-selected size. User specified statistics such as mean, variance, and absolute maximum are calculated for each chunk using CUDA parallel reduction algorithms. If a chunk's statistics are more than a user specified number of standard deviations from the mean of that statistic across all chunks, then that chunk is flagged as RFI.

Flagged chunks are zeroed out, but extreme outliers are first written to a file for further study in case they are actually astronomical transients that are of interest. Extreme outliers are chunks that are a higher number (user selected) of standard deviations away from the mean, than the other outliers.

The Fast Fourier Transform (FFT) is taken for the entire packet using the Nvidia CUDA Fast Fourier Transform library (cuFFT). The power spectrum is then computed for each channel. We use a parallel reduction algorithm to bin multiple frequencies along the power spectrum to ensure that the data is of manageable size. We also compute the cross-spectrum for the two polarization channels. We correct for the chunks that are zeroed out by the following corrections:

1. For each channel the power spectrum  $P(f)$  is corrected based on the number of chunks nulled in that channel:

$$P(f) = P(f) * \frac{\text{number of chunks in channel}}{\text{number of chunks in channel} - \text{number of nulled chunks in channel}} \quad (1)$$

2. The cross-spectrum  $C(f)$  of the two channels is similarly corrected. However, instead of using the total number of chunks nulled in the two channels, we take a bit array for each channel containing ones in the indices of the nulled chunks. We take the

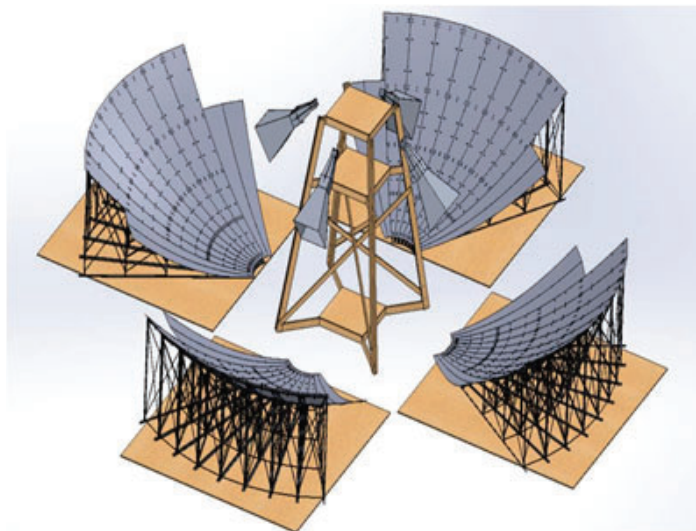


Figure 1. BMX telescope design

logical OR of the two arrays, and the total number of ones in that array is the number we use in our correction:

$$C(f) = C(f) * \frac{\text{number of chunks per channel}}{\text{number of chunks per channel} - \text{number of nulled chunks in channel 1 OR 2}} \quad (2)$$

The spectra are then copied back to the CPU and written to binary files.

## B. CUDA streams

We created multiple CUDA streams in the spectrometer so that consecutive data packets can be handled concurrently. It currently takes  $\sim 100$  ms to handle a data packet with RFI rejection turned on, but that is only for two channels. We will eventually have to deal with more channels from the other three telescope dishes, which will increase our processing time proportionally to the number of new channels. If it takes more than 122 ms to process a packet then incoming packets will be backed up in the digitizer's buffer in RAM and the program will quickly run out of memory. With multiple streams, consecutive data packets can go to different streams, which allows for some concurrency, and gives us more time to process each packet without fear of a memory overflow.

The bulk of processing time for each packet is split between CPU-GPU memory transfers and kernel calls. The GPU is able to handle memory copy in one stream simultaneously with kernel execution in another stream. Theoretically, it can also handle concurrent kernel execution among multiple streams, however each of our kernel calls uses up all the available GPU resources, so there aren't enough threads to allocate to two separate kernels at once. Therefore, using streams gives us only concurrent memory copy and kernel execution, not multiple concurrent kernels.

Since each stream requires separate memory to be allocated on the GPU in order to hold a data packet, we can currently only implement up until three streams. Our GPU model has 4GB of RAM, so it runs out of available memory with four streams.

## III. Data and Results

### A. CUDA Optimization

The following table shows the times for the CUDA operations performed on each packet. The data was collected with two channels (packet size of  $2 * 2^{27}$ ), and RFI chunk sizes of  $2^{20}$ . Times are approximate, as they change slightly with each packet.

As seen in table 1, the most time intensive operations are the CPU to GPU memory transfers and FFTs.

RFI Detection	Memory Copy: CPU to GPU 268.435 MB ( $2^{28}$ bytes)	22.3 ms
	Convert bytes to floats and split the two channels	5.7 ms
	Calculate mean for all chunks	4.3 ms
	Calculate variance for all chunks	4.3 ms
	Calculate absolute mean for all chunks	4.3 ms
	Write outlier chunk to file	1.5 ms per chunk
	FFT	48.3 ms
	Calculate and reduce power spectra	4.5 ms
	Calculate and reduce cross-spectrum	4.5 ms
	Memory copy: GPU to CPU 85.072 kB	7.6 $\mu$ s

Table 1.



## B. RFI Detection and Rejection

We ran the spectrometer at the telescope site between July 18 and July 20, 2017 with the purpose of examining the quantity and characteristics of RFI at the site. Each data packet was broken into chunks of  $2^{20}$  numbers. Chunks were flagged as RFI if their variance was more than 5 sigma away from the mean variance. We plotted the RFI density over the day in Figure 2, and as expected, most of the transients appear during the daytime hours when people are awake.

We wrote all flagged RFI to a file, and selected some random RFI chunks to examine their waveforms and power spectra. Figure 4 is the waveform of one of those random chunks, and Figure 5 is its power spectrum.

## IV. Conclusions

Real time RFI rejection can be implemented in the time domain to eliminate transient signals. As a lot of RFI still appears in the cleaned power spectra, further RFI rejection still needs to

be done. There is significant structure to the RFI density, as it the events seem to heavily cluster, so further examination is needed to help us understand the primary sources of RFI and how to best correct for them.

Use of CUDA streams allows more computation time per packet due to concurrent memory copy and kernel execution across streams. However, there is still not enough time to process four or eight channels. Further optimization or more GPU cores will be needed to scale up to more than two channels.

## V. Acknowledgements

This project was supported in part by the U.S. Department of Energy, Office of Science, Office of Workforce Development for Teachers and Scientists (WDTS) under the Science Undergraduate Laboratory Internships Program (SULI).

I would like to thank Anže Slosar, Chris Sheehy, Paul Stankus, Paul O'Connor and the other members of the Brookhaven Cosmology group for all of their help with this project.

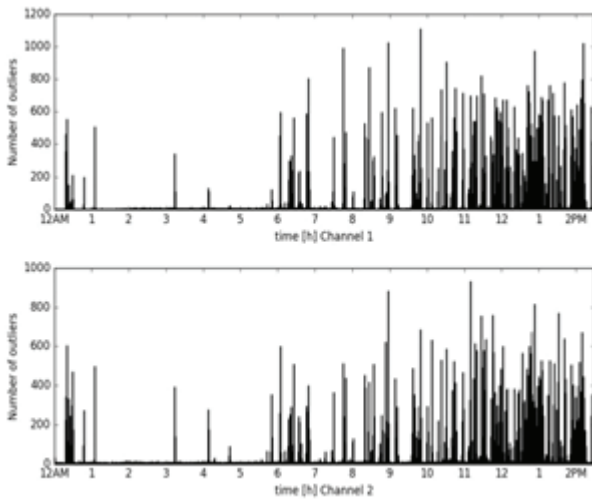


Figure 2. RFI density plots showing the number of chunks flagged as RFI per minute between 12 AM and 3 PM, July 20. Notice the decrease in RFI during the nighttime hours.

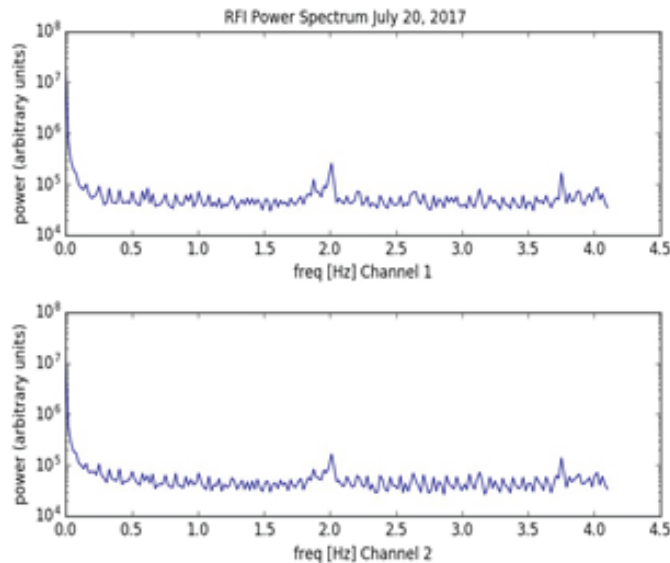


Figure 3. Power spectrum of time distribution of RFI events in Figure 2. The y-axis is plotted on log scale.

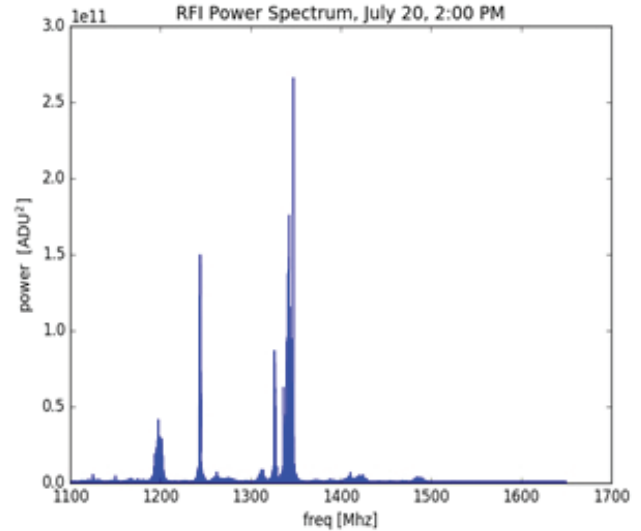


Figure 4. Waveform of randomly selected RFI chunk

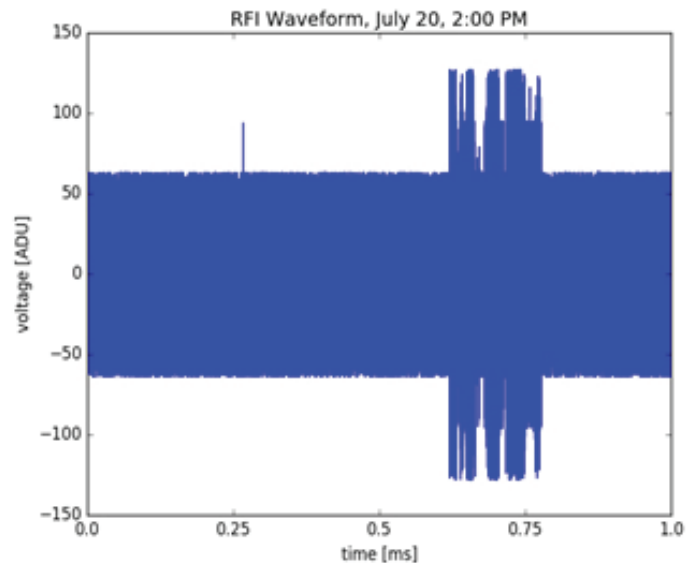


Figure 5. Power spectrum of chunk in Figure 4

## VI. References

- <sup>1</sup>J. B. Peterson, R. Aleksan, R. Ansari, K. Bandura, D. Bond, J. Bunton, K. Carlson, T.- C. Chang, F. DeJongh, M. Dobbs, S. Dodelson, H. Darhmaoui, N. Gnedin, M. Halpern, C. Hogan, J.-M. Le Goff, T. T. Liu, A. Legrouri, A. Loeb, K. Loudiyi, C. Magneville, J. Marriner, D. P. McGinnis, B. McWilliams, M. Moniez, N. Palanque-Delabruille, R. J. Pasquinelli, U.-L. Pen, J. Rich, V. Scarpine, H.-J. Seo, K. Sigurdson, U. Seljak, A. Stebbins, J. H. Steffen, C. Stoughton, P. T. Timbie, A. Vallinotto, and C. Teche. “21-cm Intensity Mapping.” *astro2010: The Astronomy and Astrophysics Decadal Survey*, volume 2010 of *ArXiv Astro- physics e-prints*, 2009.

# Development of cooling systems for sPHENIX components

Timothy Dvorak, Chemical Engineering, University of Notre Dame, Notre Dame, IN 46556

Olivia Holmes, Chemical Engineering, Stony Brook University, Stony Brook, NY 11794

Donald Lynch and Robert Pisani, Physics Department, Brookhaven National Laboratory, Upton, NY 11973

## Abstract

The PHENIX detector of the Relativistic Heavy Ion Collider (RHIC) is in the process of being upgraded to the sPHENIX detector at Brookhaven National Laboratory. New detector components such as the Electromagnetic Calorimeter (EMCal) and Intermediate Tracker (INTT) generate heat. Our studies will focus on removing this heat. sPHENIX is on the cutting-edge of exploring high energy collisions and by maintaining a cool, constant temperature, noise from electronics will be minimized. This will aid scientists in the further understanding of the Quark-Gluon plasma discovered by PHENIX. Cooling for the inner detectors requires a novel approach. Thinner, non-ferromagnetic materials must be used in order to decrease interactions inside the superconducting magnet leading to the exploration of carbon composite versus carbon fiber and pyrolytic graphite sheets thermal capabilities for use in the INTT. Through experimental analysis we have concluded that the optimal choice of material is carbon composite with an epoxied pyrolytic graphite sheet (PGS) bonded on top. The EMCal produces a significantly larger amount of heat than the INTT (11 kW vs. 300 W) and must use a system of cooling pipes to keep the electronics inside this detector at a cool, constant temperature. Based on experimental testing of an EMCal prototype, we have concluded that between parallel and series, running this system in series provides slightly better uniformity, but a combination of both will most likely be used when scaled up to an entire sector in order to combine advantages.

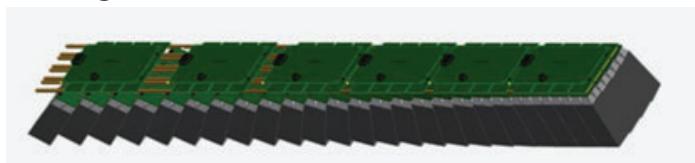


Figure 1. EMCal Sector

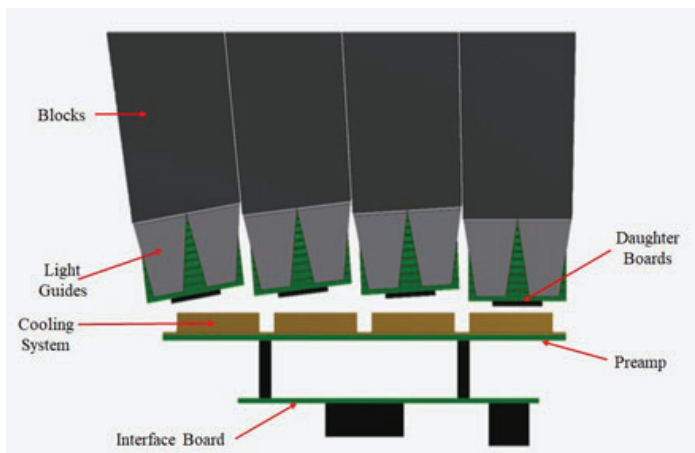


Figure 2. EMCal module with cooling

## I. Introduction

The PHENIX detector of the Relativistic Heavy Ion Collider (RHIC) is in the process of being upgraded to the sPHENIX detector at Brookhaven National Laboratory. sPHENIX is the attempt to further understand the properties of the quark-gluon plasma discovered by PHENIX. Improvements to PHENIX include updates to the Electromagnetic Calorimeter (EMCal), Time Projection Chamber (TPC), Intermediate Tracker (INTT), and Monolithic Active Pixel (MAPS) Vertex Detector (MVTX). The TPC, INTT, and MVTX form the tracking system of the sPHENIX while the EMCal is central to the direct photon and upilon measurements. (CDR) All of these detectors will create a specific amount of heat determined by the electronics being used. Due to the effect of heat on the output of the electronics, each of these detectors needs to be kept at a constant temperature, below a given threshold. Our studies will focus on the INTT and EMCal. Calculations will be done for each of these detectors in order to determine their individual cooling requirements.

The EMCal contains 64 sectors split into North and South halves. Four towers make a block, four blocks make a module, and 24 modules form a complete sector. Towers are made up of tungsten powder, epoxy, and scintillating fibers. Each block is attached to four light guides which are connected to 16 silicon photomultipliers (SiPM) on a daughter board. Each module contains four daughter boards attached to a preamp board, and four preamp boards then connect to an interface board. The EMCal in total generates approximately 11 kW of heat.

The INTT consists of 116 total ladders over four separate barrel layers. Each ladder has two silicon modules, which break

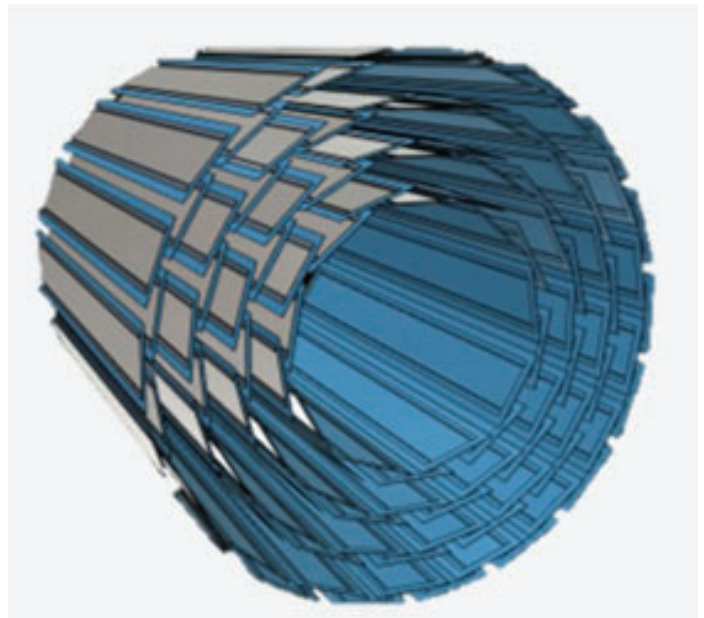


Figure 3. INTT Ladder Layout



each ladder into half-ladders. Using bus extenders, half-ladders are connected to the ROC boards located on either side of the TPC endcaps. The total heat load expected from each half-ladder is approximately 1.3 W, which totals to about 300 W over the entire INTT.

## II. Methods

### A. Electromagnetic Calorimeter (EMCal)

The EMCal consists of 64 sectors each with 96 SiPM daughter boards and 24 preamps, which have expected heat loads of 0.075 Watts and 6.25 Watts, respectively. In order to remove this heat from the detector, a system of cooling pipes is designed to transfer the heat to chillers located outside of the detector. The two setups being tested can be seen in Figure 1 and Figure 2. In order to determine the best cooling setup, the theoretical temperature of the electronics is calculated in a scaled down prototype of the EMCal. Simplifying assumptions made include each region representing 4 preamps, all SiPM and preamp temperatures are

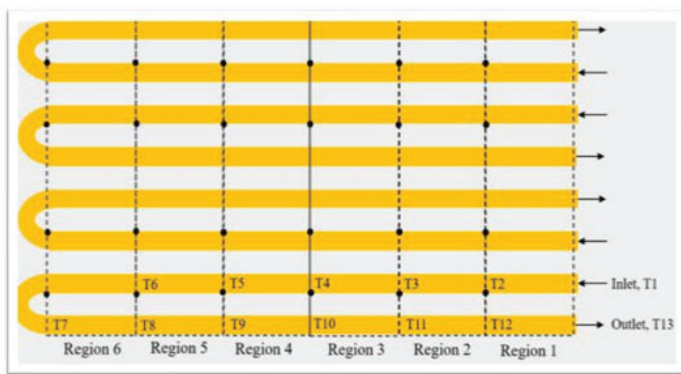


Figure 4. Parallel setup of the cooling system

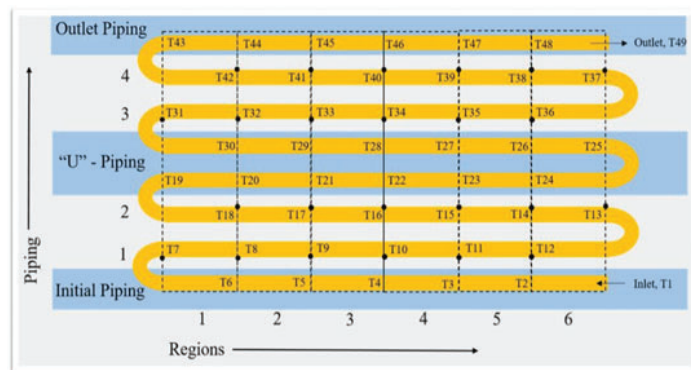


Figure 5. Series setup of the cooling system

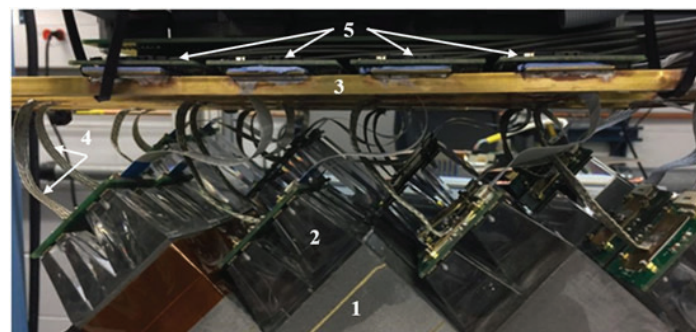


Figure 6. Thermal Straps attached to the daughter boards (1-Tungsten block, 2- Light guide, 3- Cooling system, 4- Thermal strap, 5-Preamp)

calculated at the hottest possible temperature value in each region for each pass of the piping, all four loops of the parallel setup are identical, and natural convection from air to the electronics is insignificant.

Once we confirm these calculations by testing the cooling system in the prototype, we will scale up the theoretical calculations to simulate an entire sector of the EMCal. The experimental setup of the prototype can be seen in Figure 4 and Figure 5.

### B. Intermediate Tracker (INTT)

The INTT consists of 232 half ladders with silicon detectors each with an expected heat load of approximately 2 Watts. In order to remove this heat from the detector, the stave must be constructed from thermally conductive materials. We will determine the best possible material by testing carbon fiber high gloss woven sheets and carbon composite with and without pyrolytic graphite sheets (PGS). These sheets have been engineered to be thermally conductive and are bonded to the carbon fiber and composite using Omega 101 Epoxy Adhesive, a thermally conductive epoxy. After curing, the strips are tested using a 10 W heater and thermocouples placed on top and on bottom of the strip seen in Figure 5. This setup was insulated with Buna-N/PVC foam insulation sheets in order to minimize the amount of heat lost to the environment.

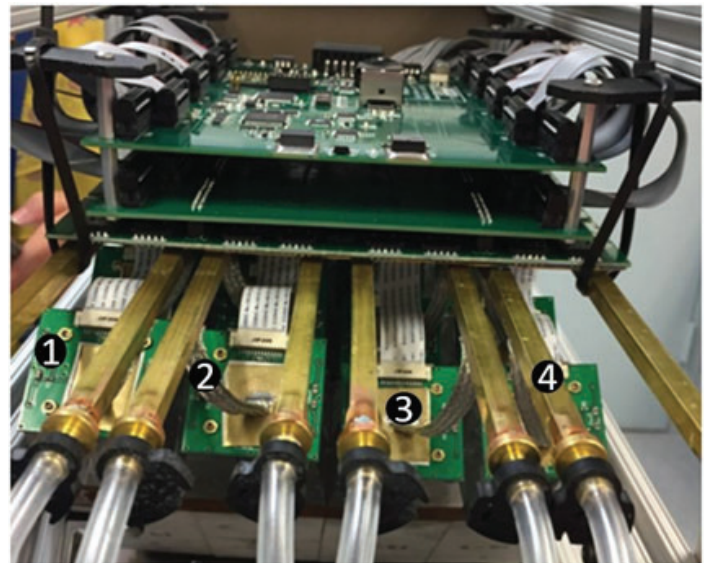


Figure 7. Cooling system clamped to the preamp boards (1- Daughter board, 2- Thermal strap, 3- Brass Plate, 4- Cooling system)

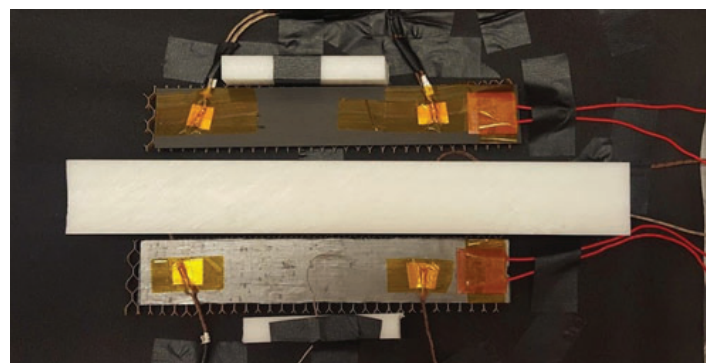


Figure 8. Testing setup, specifically carbon composite tested with and without PGS



### III. Results

#### A. Electromagnetic Calorimeter (EMCal)

Results from the theoretical calculations and experimental setup of parallel for the prototype are shown in Table 1.

Figure 9 displays the SiPM temperatures while running the prototype in parallel. The prototype runs without cooling for approximately 30 minutes, during which the temperature values reach their peak of 33 °C. Cooling begins with a water flow rate of about 4 gph, and the SiPMs cool to approximately 26.2 °C after 30 minutes. At this point the cooling flow rate is increased to 8 gph, and the temperature of the SiPMs decreases to 25.6 °C.

Figure 10 displays the preamp temperatures while running the prototype in parallel. The prototype runs without cooling for 30 minutes, which allows temperature values to reach their peak of 53 °C. Cooling begins with a water flow rate of 4 gph and then increases to 8 gph, the preamps cool to 32.5 °C and then 30.5 °C respectively.

Results from the theoretical calculations and experimental setup of series for the prototype are shown in Table 2.

Figure 11 displays the SiPM temperatures while running the prototype in series. The prototype runs first without cooling for approximately 30 minutes. Cooling begins with a water flow rate of 4 gph and then increases to 8 gph. The SiPMs cool to 26.1 °C and then 25.5 °C respectively.

Figure 12 displays the preamp temperatures while running

the prototype in series. The prototype runs first without cooling for approximately 30 minutes. Cooling begins with a water flow rate of 4 gph and then increases to 8 gph. The preamps cool to 30.1 °C and then 30 °C respectively.

Results from the theoretical calculations for series and parallel for an entire sector of the EMCal are shown below.

Figure 13 displays maximum SiPM temperatures throughout a sector resulting from varying inlet cooling temperatures. The parallel setup reaches a local max of about 22 °C at an inlet temperature of 16 °C. After the 16 °C inlet temperature, the series and parallel setups are essentially equal and increase linearly with inlet temperature.

Figure 14 displays maximum preamp temperatures throughout a sector resulting from varying inlet cooling temperatures. The parallel setup reaches a local max of about 18 °C at an inlet temperature of 16 °C. After the 16 °C inlet temperature, the series and parallel setups are approximately equal and increase linearly with inlet temperature.

Figure 15 displays the difference between overall inlet and outlet temperatures of the coolant throughout a sector resulting from varying inlet cooling temperatures. Series setup results in a fairly constant difference while the parallel setup decreases linearly until the inlet temperature reaches 17 °C. After an inlet temperature of 17 °C the difference becomes fairly constant for both setups.

Table 1. Comparison of parallel cooling system temperatures

	Calculated	Observed
Inlet Temperature (°C)	23.8	23.8
Outlet Temperature (°C)	24.1	24.8
Average SiPM Temperature (°C)	24.7	25.3
Average Preamp Temperature (°C)	28.7	28.4

Table 2. Comparison of series cooling system temperatures

	Calculated	Observed
Inlet Temperature (°C)	23.7	23.7
Outlet Temperature (°C)	26.2	24.3
Average SiPM Temperature (°C)	25.6	25.3
Average Preamp Temperature (°C)	28.0	28.0

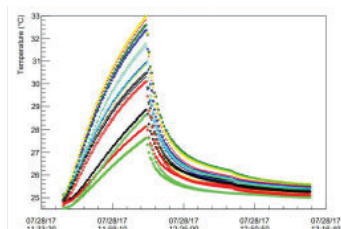


Figure 9. SiPM temperatures resulting from parallel prototype setup

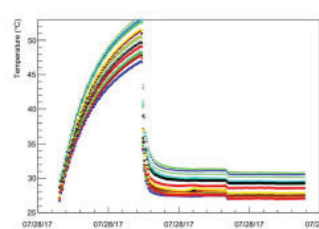


Figure 10. Preamp temperatures resulting from parallel prototype setup.

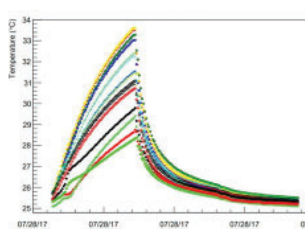


Figure 11. SiPM temperatures resulting from series prototype setup

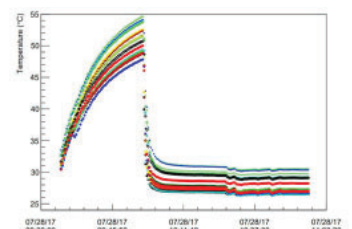


Figure 12. Preamp temperatures resulting from series prototype setup

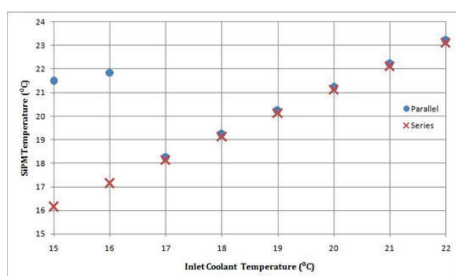


Figure 13. Max SiPM temperature for varying inlet coolant temperatures.

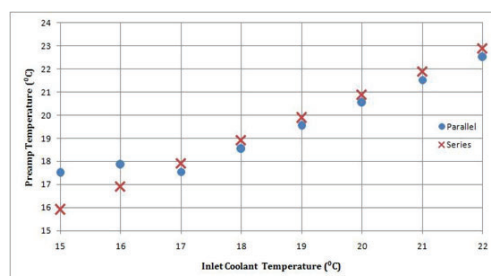


Figure 14. Max Preamp temperature for varying inlet coolant temperatures

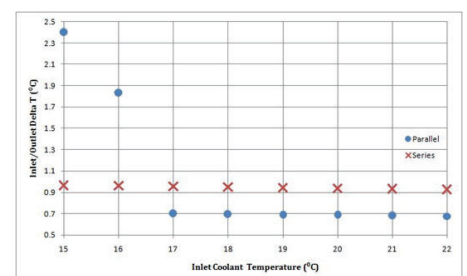


Figure 15. Difference between the overall inlet and outlet temperatures of the coolant.

## B. Intermediate Tracker (INTT)

Carbon fiber and composite are both heated by 2 Watts. Thermocouples are placed according to the diagram shown in Figure 16, and the temperatures are recorded until an equilibrium is reached.

Figure 17 shows the carbon fiber strip without PGS tested using 2 W. All five thermocouples begin at approximately 20 °C. The thermocouple placed closest to the heater, thermocouple 5, reaches a max temperature of about 24.75 °C. Thermocouples placed slightly

further away from the heater on top and bottom reach a maximum temperature of about 22.5 and 22.1 °C, respectively. Finally, the thermocouples placed furthest from the heater near the end of the strip on top and bottom reach a maximum temperature of 20.7 and 20.4 °C, respectively. For this trial the heater is run for approximately 22 minutes.

Figure 18 shows the carbon composite material without PGS tested using 2 W. The four thermocouples begin at approximately 21 °C. Close to the heater, thermocouple 1 on top and thermocouple 3 on bottom both reach approximately 26.75 °C. On the opposite end of the strip, further from the heater, thermocouple 2 on top and thermocouple 4 on bottom reach a maximum temperature of approximately 21.6 °C and 21.4 °C, respectively. For this trial the heater is run for approximately 18 minutes.

Figure 19 shows the carbon composite strip with PGS tested using 2 W. All four thermocouples begin between 21 and 22 °C. The thermocouples placed closest to the heater on top and bottom reach maximum temperatures of about 27.5 and 27 °C, respectively.

Thermocouples placed near the end of the strip on top and bottom reach maximum temperatures of about 23 and 23.5 °C, respectively. For this trial the heater is run for approximately 18 minutes.

## IV. Discussion

### A. Electromagnetic Calorimeter (EMCaI)

Table 1 and Table 2 show the calculated and observed values of inlet, outlet, average SiPM, and average preamp tempera-



Figure 16. Thermocouple placement on experimental setup.

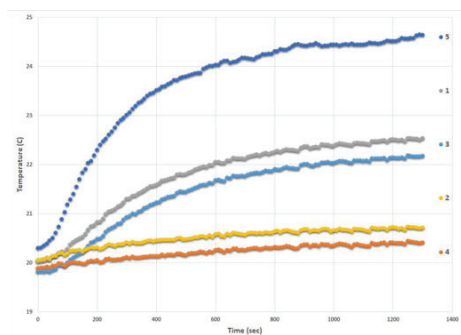


Figure 17 . Carbon fiber heated by 2W with an extra thermocouple for most illuminating results.

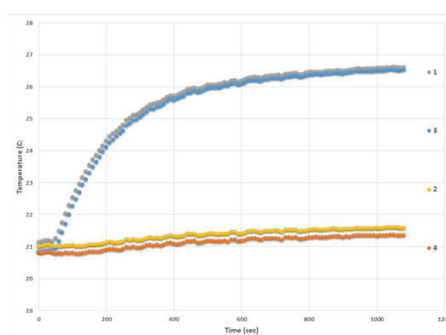


Figure 18. Carbon composite heated by 2W.

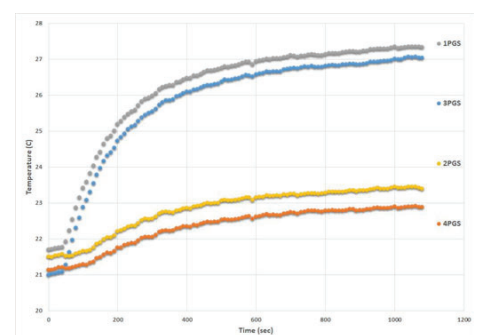


Figure 19. Carbon composite with PGS heated by 2W.

tures for the parallel and series setups. All four observed values lie within 1 °C for both setups with the exception of outlet temperature for series. Seven of the eight temperatures are also overestimated due to conservative assumptions. This is an important feature to the calculations because if conservative estimates can be within given specifications, then what actually occurs will certainly be within specifications. These tables show that both setups are almost identical when it comes to the most important parameter, SiPM temperature. While the SiPM temperature needs to be low, it also needs to be constant. Figure 9 and Figure 11 show the SiPM temperatures for both setups over time. After the cooling is turned on and the temperatures are allowed to equilibrate, the spread of temperatures for both setups are approximately equal. In fact, the thermocouples used are accurate to about 1 °C, so the spread might be even smaller than seen in these graphs. Although the preamps do need to be cooled, they are less sensitive to the heat than the SiPMs and are not a main concern when choosing the cooling setup for the EMCaI.

Seeing that our calculations for the prototype closely match what is observed, we will use the same method in order to predict the behavior of each system in an entire sector of the EMCaI. Figure 13 displays maximum SiPM temperature for varying inlet coolant temperature. Below a 17 °C inlet temperature, the parallel setup experiences a spike in SiPM temperature while the series setup continues to decrease. This can be explained by the efficiency of heat transfer with turbulent flow. Heat is transferred through the boundary layer of flow, and as the flow becomes more turbulent, the boundary layer decreases in size as does the resistance to heat transfer. In the parallel setup, the flow must be divided into four pipes, which combined with the lower inlet temperature leads to laminar flow and less efficient heat transfer. As the inlet temperature increases the density of the coolant decreases resulting in turbulent flow. After this critical temperature is reached, both the parallel and series setups are approximately equal.

Figure 14 shows similar results for the maximum preamp temperatures due to varying coolant temperature. Below 17 °C inlet temperature, heat is transferred by laminar fluid flow in the parallel setup. This results in higher preamp temperatures than the series setup until the critical temperature is reached at which point the preamp temperatures are similar in value for both setups.

Similarly, Figure 15 represents the difference between the overall inlet and outlet temperatures. Below 17 °C the laminar flow in the parallel setup affects the difference in temperature in the same way it does the maximum temperatures of the SiPMs and preamps. Once in the turbulent regime, the change in temperature from the inlet temperature is smaller for the parallel system. The

shorter path of the parallel system encounters less heat than the series system, which winds back and forth through the entire sector. Since less heat is transferred, and both experience turbulent flow, the parallel system has a smaller change in temperature.

## B. Intermediate Tracker (INTT)

As seen in Figure 17, the thermocouple closest to the heater reaches a maximum temperature of almost 25 °C while the thermocouple furthest from the heater only reaches a maximum temperature of about 20.5 °C. All of the thermocouples begin at approximately 20 °C, so the furthest thermocouples receive almost no heat from thermal conduction. This negative correlation between distance and temperature shows that the carbon fiber material has a low thermal conductivity and is unable to conduct heat well over distance. Figure 18, however, shows the same test run but with carbon composite. The difference between the composite and fiber is that the composite is specifically designed to be more thermally conductive and the fiber is designed for structural rigidity. Starting at approximately 21 °C, the temperature of the far thermocouples again only changes by about 0.5 °C, but the mid-range thermocouples at positions 1 and 3, seen in Figure 18, increases significantly from fiber to composite. On the carbon composite, these temperatures reach almost 27 °C while the same position on the carbon fiber only reaches 22.5 °C. This shows that carbon composite is more thermally conductive than carbon fiber over a short distance, but still lacks the ability to conduct heat over longer distances in a reasonable amount of time.

The next phase of testing was adding a pyrolytic graphite sheet (PGS) on top of the carbon composite. PGS is a graphite sheet designed with excellent thermal conductivity. Figure 19 shows the results of a 2 W heat load on a carbon composite strip with PGS epoxied on top.

The temperatures of the thermocouples placed furthest from the heater start at 21 and 21.5 °C and rise to 23 and 23.5 °C. This is a temperature gradient four times larger than the carbon composite alone. PGS adds the ability to conduct heat over longer distances, which is important because the cooling system will most likely not run near the electronics that are creating this heat. These tests were run with similar results at 1.5 and 2.5 Watts as well and can be seen in the appendix.

## V. Conclusions & Recommendations

### A. Electromagnetic Calorimeter (EMCal)

The importance of the EMCAL cooling system results from the 11 kW of heat produced while the detector is running. The heat originates from the SiPMs and preamps. A system of piping runs directly above the preamps and is connected to the SiPMs by thermal straps. Cooling liquid runs through the pipes in order to conduct the heat away from these electronics. A cooling system run in parallel and series was tested in an EMCAL prototype. Experimental results show both methods are able to decrease the temperatures and, importantly, keep them constant. The series system of cooling slightly surpasses that of parallel. However, once scaled up to an entire sector of the detector, a series system will experience a larger rise in temperature. As a result the optimal cooling method would be by two series systems in parallel down the length of each sector.

### B. Intermediate Tracker (INTT)

Overall, the INTT produces 300 W of heat, which needs to be

removed from the detector. The current plan is to transfer the heat to the outside of the detector using materials with optimal thermal conductivity. Through our testing we have concluded that carbon composite has better thermal conductivity than carbon fiber and should be the preferred material. Carbon composite conducts heat more efficiently over longer distances and through its thickness. We have also found that the thermal conductivity of carbon composite can be enhanced by adding a layer of PGS epoxied on top. At the current state of research, we would recommend that carbon composite with PGS be used in the INTT; however, more research into different thermally conductive materials should be conducted. We would also recommend that the use of individual cooling loops built into each half-ladder be researched in order to determine if that would be a more efficient method of cooling.

## VI. Acknowledgments

This project was supported in part by the U.S. Department of Energy, Office of Science, Office of Workforce Development for Teachers and Scientists (WDTS) under the Science Undergraduate Laboratory Internships Program (SULI) at Brookhaven National Laboratory. Also, a special thank you to our mentors Don Lynch (sPHENIX chief engineer), Rob Pisani (Physics associate), and all of the sPHENIX scientists and engineers for their help and guidance. We would also like to thank our fellow interns, Dan Cacace, Graham Giese, and Spencer Laddy-Locks for being a pleasure to work with and for making this a great summer learning experience.

## VII. References

- <sup>1</sup> sPHENIX, comp. *sPHENIX Conceptual Design Report*. Vol. 1.51. Upton: sPHENIX, 2017. Print.

## VIII. Appendix

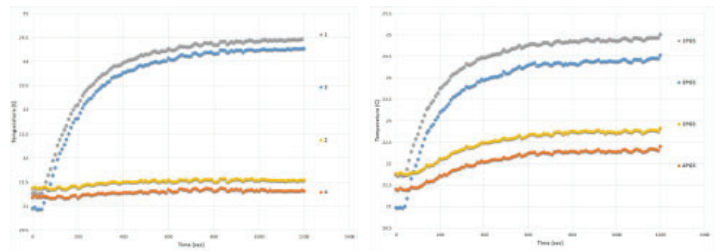


Figure 20. Carbon composite heated by 1.5W. Figure 21. Carbon composite with PGS heated by 1.5W.

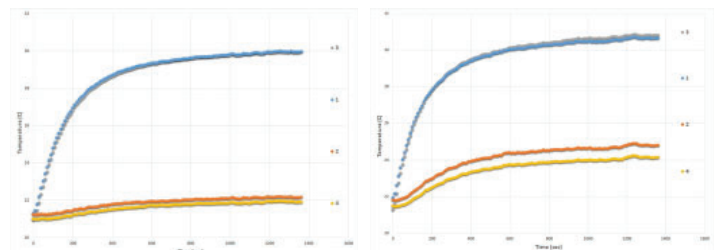


Figure 22. Carbon composite heated by 2.5W. Figure 23. Carbon composite with PGS heated by 2.5W.



# Concentration effect of $\text{LiNO}_3$ electrolyte in lithium-sulfur batteries

Ruby Epler, Department of Chemical Engineering, Columbia University, New York City, NY 10027

Ke Sun, Sustainable Energy Technologies Department, Brookhaven National Laboratory, Upton, NY 11973

Hong Gan, Sustainable Energy Technologies Department, Brookhaven National Laboratory, Upton, NY 11973

## ABSTRACT

For Lithium-Sulfur (Li-S) batteries,  $\text{LiNO}_3$  has been used as an electrolyte additive to protect the anode surface from side reactions, such as the polysulfide induced shuttling effect. Most past studies use low sulfur loading electrodes ( $\sim 1\text{-}2\text{ mg cm}^{-2}$  sulfur) and electrolyte solutions that contain only  $\sim 0.1\text{-}0.2\text{ M LiNO}_3$  additive. Recent studies using high sulfur loading electrodes ( $> 6\text{ mg cm}^{-2}$ ) indicate that the anode surface is not sufficiently protected by the standard electrolyte containing  $0.15\text{ M LiNO}_3$ . This project is targeted to investigate the  $\text{LiNO}_3$  concentration effect on high sulfur loading Li-S cells. Our results indicate that  $\text{LiNO}_3$  concentration as high as  $0.70\text{ M}$  is beneficial for high sulfur loading Li-S cell performance in terms of long cycle life and high coulombic efficiency. High  $\text{LiNO}_3$  concentration is also beneficial for high rate discharge. Based on the results of this study,  $0.7\text{ M LiNO}_3$  is incorporated in the future Li-S cell research. Along with this results we also uncovered a mechanism of sulfur cell internal shorting due to the type of separator material in combination with high sulfur cell loading. A revised cell design is incorporated to prevent Li-S cells from developing this internal short mechanism.

## I. INTRODUCTION

Lithium-sulfur (Li-S) batteries offer a promising future for sustainable energy storage due to their high theoretical specific energy ( $\sim 2600\text{ Wh kg}^{-1}$ ), and the abundance of cheap sulfur for the manufacture of cathodes.<sup>1</sup> To be competitive in the market place against the benchmark Li-ion batteries, sulfur cathodes with high sulfur loading ( $> 6\text{ mg cm}^{-2}$ ) are desirable. Current research focuses on identifying cell design factors that can impact high sulfur loading cell performance. One area of interest is the polysulfide shuttle effect; during cycling, soluble intermediate polysulfides interact with the lithium anode and can cause internal shorting in the cell.

Incorporating  $\text{LiNO}_3$  in the battery's electrolyte has been found to form a solid electrolyte interphase (SEI) layer on the Li anode, preventing the negative consequences of the polysulfide shuttle effect. The effect of  $\text{LiNO}_3$  concentration on Li-S cell performance has been reported in the past.<sup>23</sup> However, these reports only studied Li-S cells with sulfur loading of  $< 2\text{ mg cm}^{-2}$

sulfur.<sup>4</sup> The results of these past experiments show issues with ionic conductivity and viscosity at high  $\text{LiNO}_3$  concentrations that counterbalance the positive effects of the prevention of the polysulfide shuttle effect. Thus their conclusions place optimal concentration of  $\text{LiNO}_3$  between  $0.1$  and  $0.2\text{ M}$ .<sup>5</sup> However, cycling of higher sulfur loading cells will result in deeper cycling of the lithium anode. Since  $\text{LiNO}_3$  is consumed during cycling to repair the SEI layer on the anode, increased  $\text{LiNO}_3$  concentration in the electrolyte may improve high sulfur loading Li-S battery cycling performance. This experiment is geared to examine the

$\text{LiNO}_3$  concentration effect on high sulfur loading cell's electrochemical performance.

## II. EXPERIMENTAL

### A. Experimental Design

The focus of the experiment was to determine optimal  $\text{LiNO}_3$  concentration in the electrolyte of high sulfur loading cells. The maximum concentration of  $\text{LiNO}_3$  in  $1.0\text{ M LiTFSI/DOL:DME} = 1:1$  (v/v) electrolyte is about  $0.75\text{ M}$ .<sup>6</sup> In this experiment we are testing three levels of  $\text{LiNO}_3$  concentration,  $0.15\text{ M}$ ,  $0.40\text{ M}$  and  $0.70\text{ M}$  with Li-S coin cells of identical cell design (see cell build section). 2032 coin cells with high sulfur loading electrodes are assembled with electrolytes containing the above three  $\text{LiNO}_3$  concentrations. Once built, coin cells are tested on the Arbin battery cyclers in a series of rate and cycling tests. The impact of  $\text{LiNO}_3$  concentration on cell performances are compared.

### B. Cell Build

The sulfur cathode was prepared by casting the cathode slurry (containing 56% sulfur by weight) onto Aluminum current collector. The slurry coated electrode was air dried overnight in a dry room with a maximum dew point  $< -40\text{ }^\circ\text{C}$ , and then dried in an oven at  $50\text{ }^\circ\text{C}$  to drive off the solvent residue. The sulfur loading can be controlled by adjusting the gap of the doctor blade during electrode coating. The resulting cathode sulfur loading is  $\sim 8\text{ mg/cm}^2$ . Each cathode was punched to a standard size of  $1.27\text{ cm}^2$ , and then measured for thickness and weight. The separator for the first experiment was fiberglass. In addition to the fiberglass separator, the second experiment incorporated a Celgard separator on the anode side of the fiberglass. The anodes were made

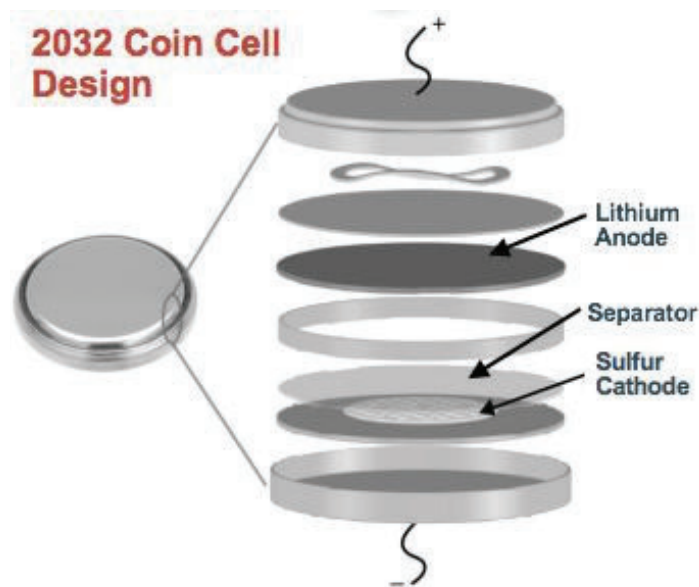


Figure 1: Cell design diagram.



of brushed lithium measuring 1.6 cm<sup>2</sup>. 2032 coin cell parts were used. See Figure 1 for a schematic of the cell stack. A standard electrolyte fill volume of 120 μL was used.

Each cell was built inside an argon filled glove box with water content <1 ppm, and oxygen content < 1 ppm.

### C. Standardized Testing Procedure

Each cell went through a series of two standard tests; rate, and cycling. Prior to testing, the cells were stored overnight to ensure they had time to calibrate. Coin cells are cycled from

1.8 V to 2.6 V. Throughout the tests, the charging procedure for each cycle is 1.0 mA/cm<sup>2</sup> to 2.6V, followed by holding at 2.6V until the current drops to below 0.1 mA/cm<sup>2</sup>. During discharge, cells are discharged at constant current until they reach 1.8 V.

#### 1. Rate Test

All cells are discharged once at a rate of 0.1 mA/cm<sup>2</sup>. Afterwards, cells are discharged twice at 0.2, 0.4, 1.0, 2.0, and 4.0 mA/cm<sup>2</sup> respectively. Sulfur utilization at each rate of discharge is calculated and compared for each LiNO<sub>3</sub> concentration.

#### 2. Cycling Test

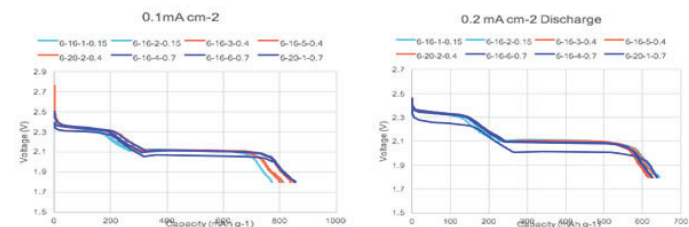
After the completion of the rate test, all cells are placed on cycling test. The discharge current is 1.0 mA/cm<sup>2</sup> for all cycles. Cells are charge and discharge cycled 100 times. Sulfur utilization over cycle number is calculated and compared for each LiNO<sub>3</sub> concentration. In addition Coulombic efficiency over cycle number is calculated and compared for each LiNO<sub>3</sub> concentration.

## III. RESULTS AND DISCUSSION

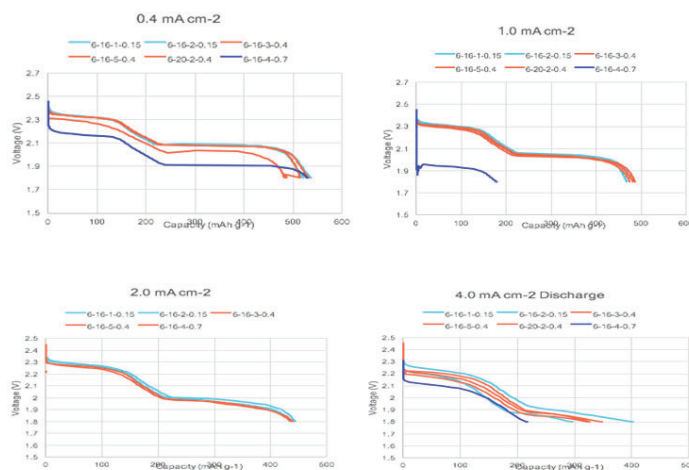
### A. Experiment One

#### 1. Cell Build Information

See Table 1.



Figures 2 and 3. Sulfur utilization for discharge rates of 0.1, 0.2, mA/h/cm<sup>2</sup>.



Figures 4-7. Sulfur utilization for discharge rates of 0.4, 1.0, 2.0, 4.0 mA/h/cm<sup>2</sup>.

### B. Rate Test Results

For rate test, all the cells exhibited similar discharge rate capability at all current densities (Figures 2-7). However, during the third charge cycle a majority of the cells shorted. The shorting occurred independent of LiNO<sub>3</sub> concentration. During charging, it's expected that cells will gain voltage overtime. However, the data shows that during the third charge cycle, the cell's voltage did not increase uniformly. For most cells, the voltage fluctuated. In other words, the cells shorted. While most cells were able to eventually recover, two of the 0.7 M cells failed permanently (see Figure 8). The interference of this cell shorting issue prevented immediate understanding of the effect of LiNO<sub>3</sub> concentration on rate performance capability.

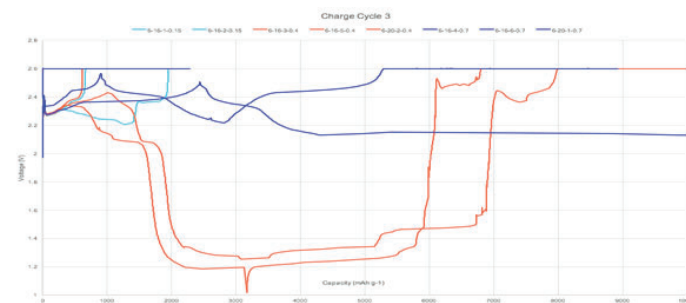


Figure 8. Shorting issues shown in voltage profile for the third charge cycle.

### Concentration Study Discharge Capacity

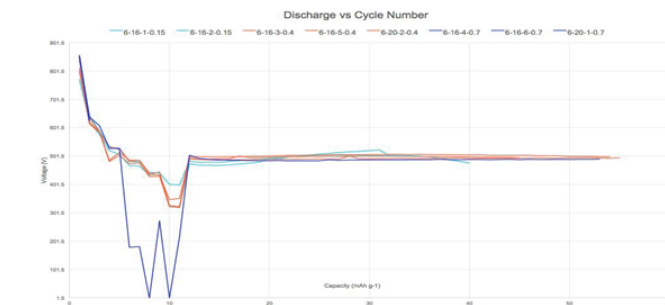


Figure 9. Cell cycling capacities during cycling.

### Coulombic Efficiency vs Cycle Number

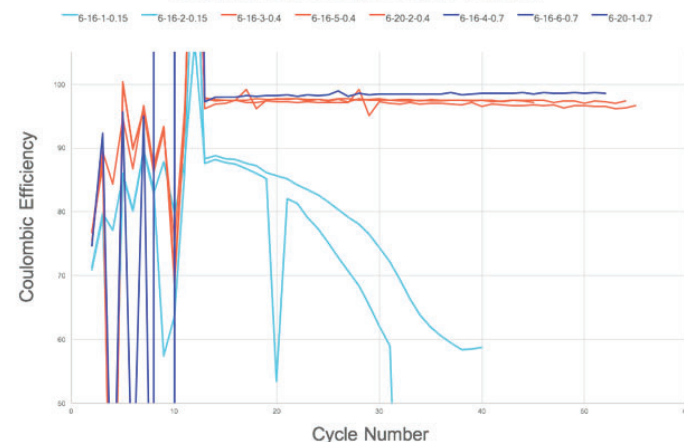


Figure 10. Coulombic efficiency data during cycling.

## C. Cycle Test Results

Partial data for cycle performance was taken from the recovered cells. While this data is incomplete, the existing data shows that the cell cycling capacities are similar for all the cells with very low capacity fade rate (see Figure 9). However, the coulombic efficiencies of the cells correlates to their LiNO<sub>3</sub> concentrations (see Figure 10). The higher the LiNO<sub>3</sub> concentration, the higher the cycling Coulombic efficiency.

## D. Experiment Two

The cell internal short issue (Figure 8) has prevented us to make conclusive result regarding the optimal LiNO<sub>3</sub> concentration. A follow up experiment is executed by modifying the cell design which geared to prevent the cell internal short (see cell design modification).

### 1. Cell design modification

The internal short issue is potentially caused by an interaction between the soluble polysulfide, fiberglass separator, and the lithium anode. To prevent this, an inert Celgard separator is added to the cell design. The new cell configuration incorporates both a fiberglass separator and a Celgard separator on the anode side.

### 2. Cell build data

See Table 2.

### 3. Rate Test Results

For rate test, all the cells exhibited similar discharge rate capability for current densities of 0.1, 0.2, 0.4 and 1.0 mAh/cm<sup>2</sup> (see Figures 11-14). However, at high current densities, there is a cor-

relation between LiNO<sub>3</sub> concentration and discharge rate capability; the higher the concentration, the higher the rate capability (see Figures 15-16). While this trend was seen, one of the 0.7 M cells shorted during the high rate discharge test for unknown reasons. It was able to recover during cycling testing.

## 4. Cycle Test Results

The data from the cycling test shows that the cell cycling capacities vary according to LiNO<sub>3</sub> concentration. Capacity fade rate is highest for the 0.7 M cells, medium for the 0.4 M cells and lowest for the 0.15 M cells (see Figure 17). The coulombic efficiencies of the cells also correlate to their LiNO<sub>3</sub> concentrations (see Figure 18). The higher the LiNO<sub>3</sub> concentration, the higher the cycling Coulombic efficiency. This confirms the partial coulombic efficiency data gathered from the first experiment.

## IV. CONCLUSION

Based on the experiments, the team concludes that LiNO<sub>3</sub> concentration influences high sulfur loading cell performance. Higher concentrations of LiNO<sub>3</sub> cause cells to have better cycle life and higher coulombic efficiency. Additionally, there was no observed detrimental effect of the viscosity of the 0.7 M electrolyte on the overall cell performance. Thus, high concentration electrolyte will be adopted in future high sulfur loading cell studies.

## V. ACKNOWLEDGEMENTS

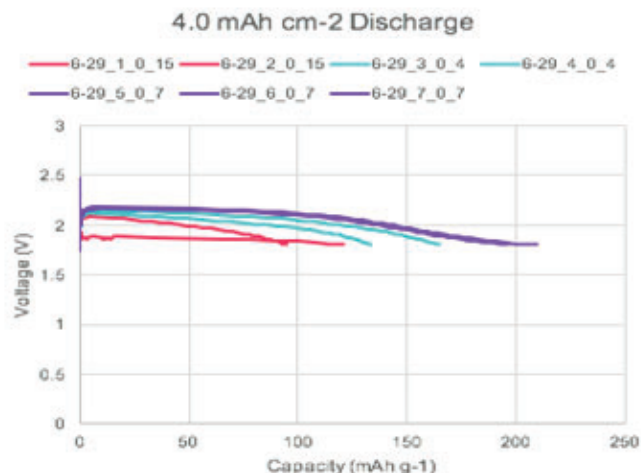
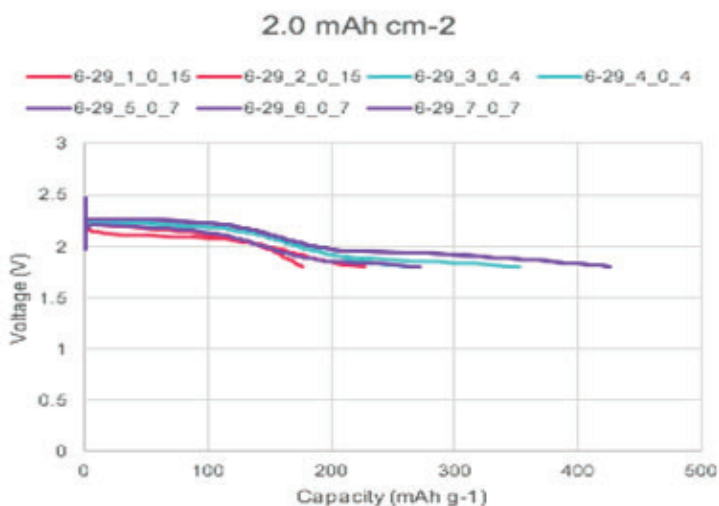
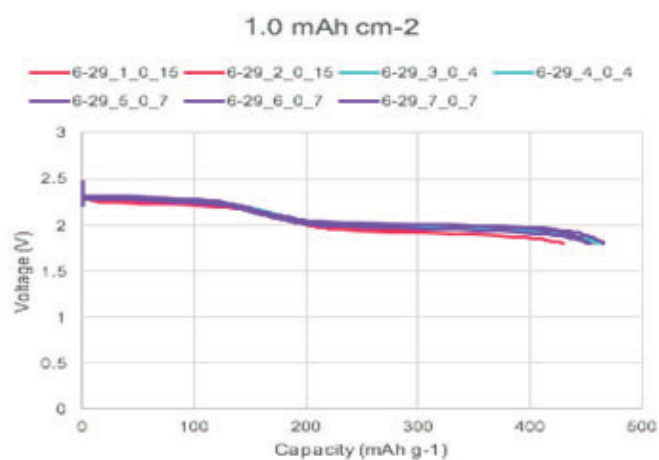
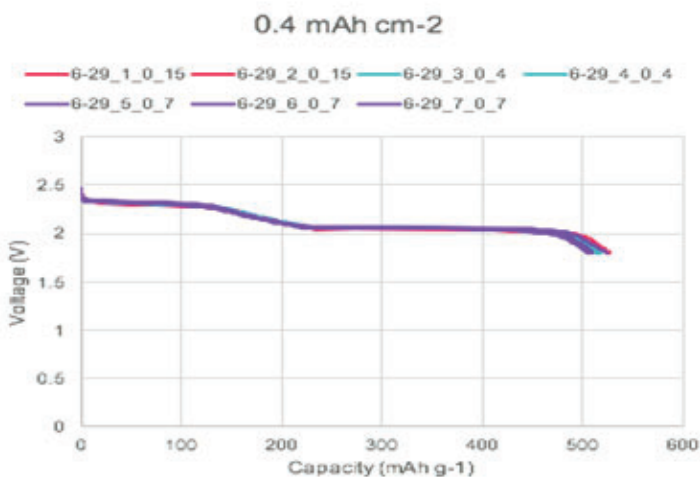
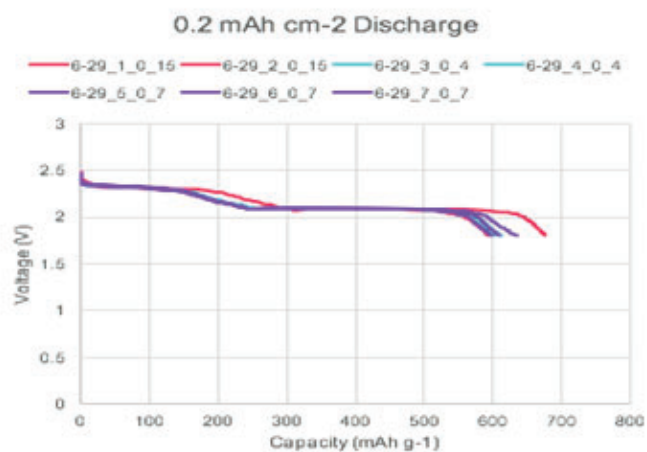
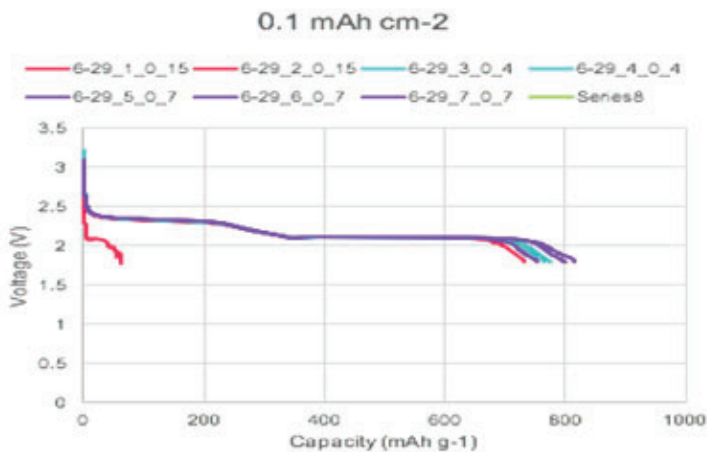
Thanks to my mentor, Dr. Hong Gan, for his professionalism and help during my research. I would also like to thank Dr. Ke Sun, a postdoc in the lab who helped to train me and provided hand on

Table 1.

Cell Name	Operator	[LiNO <sub>3</sub> ] M	Cathode Mass(mg)	S. Load (g/cm <sup>2</sup> )	Electrolyte (mg)
6/16-1-.15	Ruby	0.15M	18.48	8.15	121.24
6/16-2-.15	Ruby	0.15M	15.95	7.03	131.77
6/16-3-.4	Ruby	0.40M	15.71	6.93	121.72
6/16-5-.4	Ruby	0.40M	17.44	7.69	128.15
16/20-2-.4	Ruby	0.40M	16.42	7.24	123.49
6/16-4-.7	Ruby	0.70M	17.35	7.65	116.98
6/16-6-.7	Ruby	0.70M	17.75	7.83	116.39
16/20-1-.7	Ruby	0.70M	17.15	7.56	126.51

Table 2.

Cell Name	Operator	[LiNO <sub>3</sub> ] M	Cathode Mass (mg)	S. Load (g/cm <sup>2</sup> )	Electrolyte (mg)
6-29_1_015	Ke	0.15M	16.22	7.15	143.33
6-29_2_015	Ruby	0.15M	17.86	7.88	126.26
6-29_3_0_4	Ke	0.40M	18.47	8.14	136.24
6-29_4_0_4	Ruby	0.40M	18.49	8.15	136.85
6-29_5_0_7	Ke	0.70M	18.95	8.36	133.08
6-29_6_0_7	Ruby	0.70M	19.07	8.41	121.44
6-29_7_0_7	Ke	0.70M	19.02	8.39	135.57



Figures 11-16. Sulfur utilization for discharge rates of 0.1, 0.2, 0.4, 1.0, 2.0, 4.0 mAh/cm<sup>2</sup>.



assistance. In addition, I'm grateful to everyone at Brookhaven National Laboratory for hosting this program in conjunction with the Department of Energy. This project was supported in part by the U.S. Department of Energy, Office of Science, Office of Workforce Development for Teachers and Scientists (WDTs) under the Science Undergraduate Laboratory Internships Program (SULI).

## VI. END NOTES

- <sup>1</sup> Ke Sun, Christina A. Cama, Jian Huang, Qing Zhang, Sooyeon Hwang, Dong Su, Amy C. Marschilok, Kenneth J. Takeuchi, Esther S. Takeuchi, Hong Gan, Effect of Carbon and Binder on High Sulfur Loading Electrode for Li-S Battery Technology, *Electrochimica Acta*, Volume 235, 1 May 2017, Pages 399-408, ISSN 0013-4686, <https://doi.org/10.1016/j.electacta.2017.03.023>. (<http://www.sciencedirect.com/science/article/pii/S0013468617304875>)
- <sup>2</sup> Marzieh Barghamadi, Adam S. Best, Anthony F. Hollenkamp, Peter Mahon, Mustafa Musameh, Thomas R  ther, Optimising the concentration of LiNO additive in Cmpyr-TFSI electrolyte-based Li-S battery, *Electrochimica Acta*, Volume 222, 2016, Pages 257-263, ISSN 0013-4686, <http://dx.doi.org/10.1016/j.electacta.2016.10.169>. (<http://www.sciencedirect.com/science/article/pii/S0013468616322952>)
- <sup>3</sup> H.S. Kim, T.-G. Jeong, N.-S. Choi, Y.-T. Kim. The cycling performances of lithium-sulfur batteries in TEGDME/DOL containing LiNO<sub>3</sub> additive *Ionics*, 19 (2013), p. 1795
- <sup>4</sup> Ibid.
- <sup>5</sup> Ibid.
- <sup>6</sup> W. Li, H. Yao, K. Yan, G. Zheng, Z. Liang, Y. M. Chiang, Y. Cui. The synergetic effect of lithium polysulfide and lithium nitrate to prevent lithium dendrite growth, *Nature Communications*, Volume 6, 17 June 2015

## VII. REFERENCES

- Ke Sun, Christina A. Cama, Jian Huang, Qing Zhang, Sooyeon Hwang, Dong Su, Amy Marschilok, Kenneth J. Takeuchi, Esther S. Takeuchi, Hong Gan, Effect of Carbon and Binder on High Sulfur Loading Electrode for Li-S Battery Technology, *Electrochimica Acta*, Volume 235, 1 May 2017, Pages 399-408, ISSN 0013-4686, <https://doi.org/10.1016/j.electacta.2017.03.023>.
- Marzieh Barghamadi, Adam S. Best, Anthony F. Hollenkamp, Peter Mahon, Mustafa Musameh, Thomas R  ther, Optimising the concentration of LiNO additive in Cmpyr-TFSI electrolyte-based Li-S battery, *Electrochimica Acta*, Volume 222, 2016, Pages 257-263, ISSN 0013-4686, <http://dx.doi.org/10.1016/j.electacta.2016.10.169>.
- H.S. Kim, T.-G. Jeong, N.-S. Choi, Y.-T. Kim, The cycling performances of lithium-sulfur batteries in TEGDME/DOL containing LiNO<sub>3</sub> additive, *Ionics*, 19 (2013), p. 1795
- W. Li, H. Yao, K. Yan, G. Zheng, Z. Liang, Y. M. Chiang, Y. Cui, The synergetic effect of lithium polysulfide and lithium nitrate to prevent lithium dendrite growth, *Nature Communications*, Volume 6, 17 June 2015

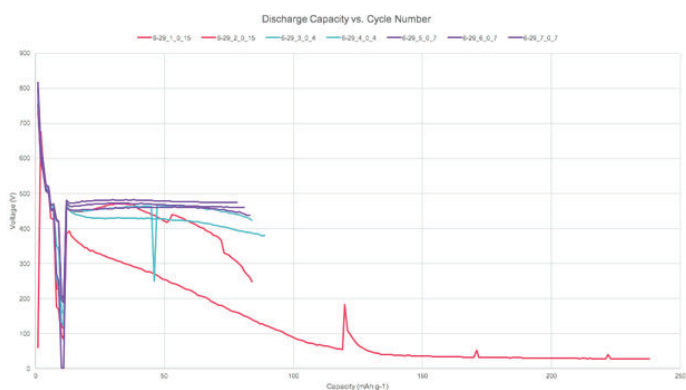


Figure 17. Cell cycling capacities during cycling.

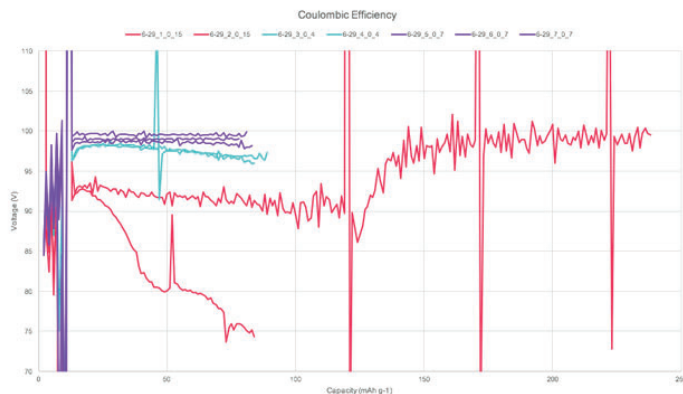


Figure 18. Coulombic Efficiency data during cycling.

# Pattern recognition in generalized continued fraction encodings of the Riemann Zeta zeros

Danielle Fieseler, Department of Mathematics and Computer Science, St. Joseph's College, Patchogue, NY 11772  
 Janelle Walker, Department of Mathematics, CUNY Medgar Evers College, Brooklyn, NY 11225  
 David Biersach, Information Technology Department, Brookhaven National Laboratory, Upton NY 11973

## Abstract

The objective of this experimental computational mathematics (ECM) research project at Brookhaven National Laboratory is to identify any possible patterns in the generalized continued fraction (GCF) representations of the zeros of the Riemann Zeta function, one which contains crucial information about the distribution of prime numbers, an element of the most asymmetric Internet encryption algorithms. As the perceived strength of modern Internet encryption depends upon the difficulty of factoring large numbers, finding a faster way to estimate Zeta zeroes by exploiting a hidden pattern in their GCF encodings might lead to improved factoring algorithms and warrant major revisions to current Internet encryption standards, an important part of our national security. Recent techniques to search for Zeta zeros are computationally expensive and lack the ability to quickly estimate much higher roots. Currently no known pattern exists in the decimals comprising the first 100,000 Zeta zeroes which have been calculated to 1,024-digit of precision using nine years of computer time. GCFs excel at compactly describing what appears to be a chaotic sequence of digits that go to an infinite amount of decimal places like the Zeta zeroes. In order to search for the best fit GCFs, specialized custom computer code will be implemented in C++ that uses threading wherever possible for a parallel speedup. If a "short cut" pattern can be identified it would significantly reduce the work effort required to calculate successive zeroes, however during the course of this research if the "short cut" is not identified our results will be inconclusive.

## I. Background

### A. The Prime Number Theorem (PNT)

A prime number is an integer greater than one whose factors are only one and itself.<sup>2</sup> From here, when there are functions of primes that is called "The Prime Counting Function". The Prime Counting Function, also known as  $\pi(x)$  ["pi of x"] is the number of primes less than a given number.<sup>1</sup> Figure 1 shows a graph of the prime number theorem.  $Li(x)$  is the logarithmic integral function and was discovered by Jacques Hadamard and Charles de la Vallé-Poussin in 1896. The function to the right of  $\pi(x)$ ,  $x/\log(x)$ , was discovered originally by Carl Friedrich Gauss. If the graph were to be extended further, one would see that the  $\pi(x)$  function would oscillate above and below  $Li(x)$ .

### B. Continued Fractions

A continued fraction (CF) is an expression that is received through an iterative process. There are three types of continued fractions; finite, infinite with a repeating sequence, or infinite with a repeating pattern. From this, CF's are either rational, irrational or transcendental numbers. The most commonly known irrational

and/or transcendental numbers that are used are  $e$ ,  $\phi$  (the golden ratio),  $\sqrt{2}$ , and  $\sqrt{3}$ .

Within continued fractions there are two types, Standard or Generalized Continued Fractions. A Standard Continued Fraction expression takes on the following form below, in which all the numerators are all ones.

$$a_1 + \frac{1}{a_2 + \frac{1}{a_3 + \frac{1}{\ddots + \frac{1}{a_n}}}}$$

The terms for all of the "a" terms can be generated by using the written code from C# below.

The long list of convergents that you see above in Figure 2 is inserted into the standard continued fraction form in order to get the formula. For example, if one were to look at the first Zeta zero, the index would be 0; the number of convergents would be 15; the Riemann Zeta zero would be 14.134725142; the convergents are 7, 2, 2, 1, 2, 1, 1, 1, 12, 32, 1, 4, 1, and 6. The form that this Standard Continued Fraction takes on is as followed,  $14 + \frac{1}{7 + \frac{1}{2 + \frac{1}{\dots}}}$ .

For the Generalized Continued Fraction the process is the same. A program is generated to find the "a" and the "b" terms, you are the one who has to come up with the formula.

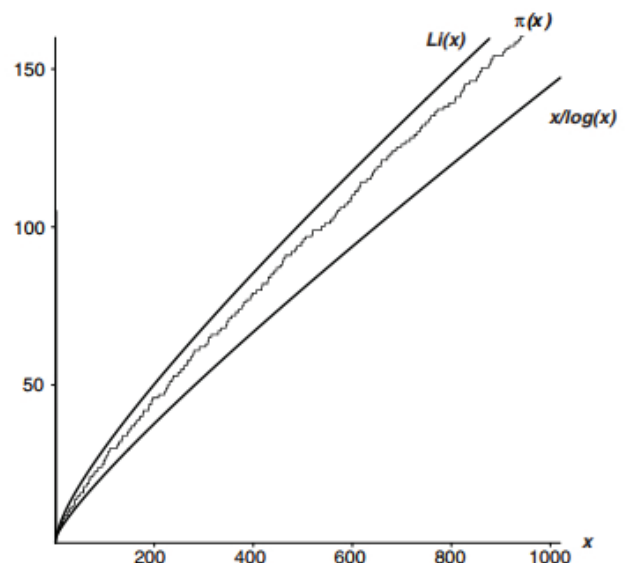


Figure 1. The Prime Number Theorem (PNT) -  $\pi(x) \sim Li(x)$

$$a_0 + \frac{b_0}{a_1 + \frac{b_1}{a_2 + \frac{b_2}{a_3 + \frac{b_3}{a_4 + \dots}}}}$$

When trying to create the form for the Generalized Continued Fraction, one has to use Figure 3 and 6 as a reference. Within Figure 3 one will be looking at the third Zeta zero, 25.010857580. All of the information should be directly taken from the chart and applied to the generalized continued fraction expansion shown in Figure 6. From there the Generalized Continued Fraction form for the third Zeta zero can be written. The Generalized Continued Fraction for the third Zeta zero is  $25 + \frac{5}{17 + \frac{-5}{1 + \frac{33}{\dots}}}$ .

### C. The Riemann Zeta function and the discovery of the Riemann Zeta Zeroes

$$\zeta(s) = \sum_{n=1}^{\infty} \frac{1}{n^s}$$

The Riemann Zeta function is defined as Zeta of s to be equal to the sum from n equals one to infinity of one over n to the s power.<sup>1</sup> For example, when s = 2, the Riemann Zeta function is equal to  $\frac{\pi^2}{6}$ . It was in 1998, when a mathematician by the name of Andrew Odlyzko discovered two data files at AT&T Laboratory while doing research that found the Riemann Zeta zeroes. The two data files that were released for the public to use for reference and research purposes are seen in Figures 4 and 5.

## II. Methods

### A. Overview

For this research project, code was written in C/C++, C#, and Code::Blocks (Linux). The focus was to use different methods to find a pattern (also known as pattern recognition). The pattern recognition techniques used were k-means clustering, longest repeated

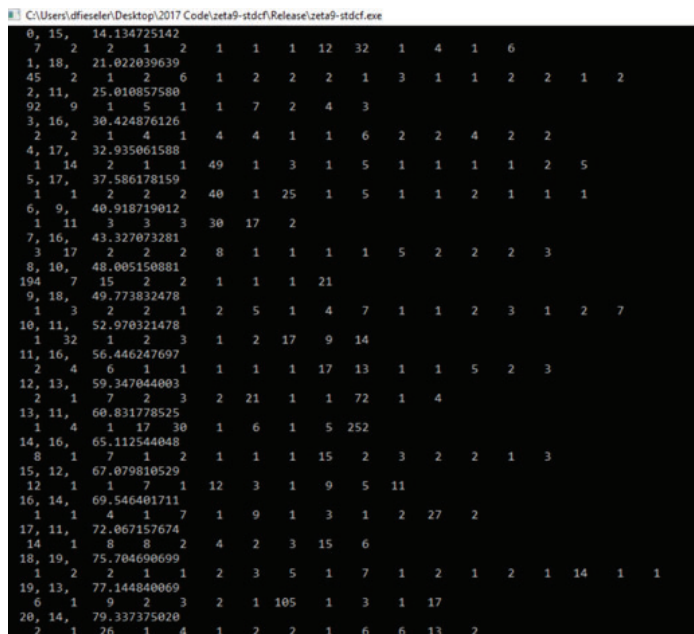


Figure 2. A program that finds the index number of the Riemann Zeta zero, the number of convergents, the Riemann Zeta zero number, and the convergents

ed substrings (LRSS) and longest repeated subsequence.

### B. K-means Clustering

The goal of k-means clustering was to break up the n observations into “k” clusters, where each cluster has its own  $\mu$  point. The  $\mu$  point of each cluster is called the centroid. The centroid changed until the cluster eventually reached convergence. Initially, what was searched for were several points grouped together. If there happened to be a data point that was an outlier from all of the clusters, it was either a data capture error or a statistical anomaly that could provide information regarding the function.

### C. Longest Repeated Substring and Longest Repeated Subsequence (LRSS)

The purpose of the longest repeated substring and the longest repeated subsequence was to look at each individual char, string, and integer, and find the longest recurring pattern of not only the generalized continued fraction, but for the standard continued fraction as well. This required dynamic programming, a way of solving a difficult problem by breaking it down into simpler and easier sub problems, and storing the solutions as one answer. This approach was done by comparing, contrasting and analyzing the columns and rows of the output of the generalized continued fraction.

## III. Data and Results

Through the use of k-means clustering, the data points for the Riemann Zeta function did not display an obvious pattern. Therefore, the use of k-means clustering was not effective. The next pattern recognition technique employed was the longest repeated substring (LRSS). This technique was used to analyze the standard continued fraction of the first thirty Zeta zeroes. When going through this code a pattern was improperly spotted. This occurred because the numbers being inputted were strings and the program looked at each individual number instead of the whole number.

For example, when the input was:

zeta += “2”;

zeta += “28”;

The output for the pattern happened to be 2, when it really should have been no pattern. Even though it was an error, it was

2	25.01086	19	24	5	7	-18	10	9	25.01086	2.8E-11	8
2	25.01086	22	24	2	1	19	7	14	25.01086	5.94E-11	6
2	25.01086	21	23	3	8	31	1	6	25.01086	1.34E-10	9
2	25.01086	16	24	6	-9	-2	13	3	25.01086	7.81E-10	5
2	25.01086	17	24	10	-10	16	2	14	25.01086	8.78E-10	11
2	25.01086	17	24	12	-14	44	6	9	25.01086	9.01E-10	4
2	25.01086	17	24	5	-13	-43	6	13	25.01086	9.01E-10	4
2	25.01086	25	16	-13	-1	-6	8	-3	25.01086	9.61E-10	11
2	25.01086	19	24	2	-7	37	-1	18	25.01086	1.53E-09	7
2	25.01086	19	23	15	-6	27	15	-7	25.01086	1.67E-09	5
2	25.01086	6	13	4	-10	-8	8	-6	25.01086	1.72E-09	9
2	25.01086	24	24	0	5	-14	11	13	25.01086	2.03E-09	4
2	25.01086	2	22	15	-2	-27	7	-5	25.01086	2.17E-09	10
2	25.01086	25	24	5	8	49	11	12	25.01086	2.36E-09	6
2	25.01086	12	23	7	2	30	14	-10	25.01086	2.44E-09	9
2	25.01086	23	23	-6	-10	2	14	-2	25.01086	2.6E-09	10
2	25.01086	21	24	-15	-15	-31	8	15	25.01086	2.63E-09	8
2	25.01086	5	17	8	14	-27	11	-10	25.01086	2.69E-09	5
2	25.01086	21	23	10	3	-24	8	3	25.01086	2.84E-09	7
2	25.01086	21	24	4	8	-41	2	20	25.01086	2.98E-09	4
2	25.01086	20	21	8	-14	-29	5	3	25.01086	3.17E-09	7
2	25.01086	16	22	-4	-15	2	6	1	25.01086	3.2E-09	8
2	25.01086	9	24	-4	14	48	7	-2	25.01086	3.26E-09	11
2	25.01086	16	22	5	8	-35	6	1	25.01086	3.5E-09	5
2	25.01086	24	23	6	12	18	6	4	25.01086	3.76E-09	11
2	25.01086	25	24	-5	-1	-34	7	19	25.01086	3.91E-09	6
2	25.01086	22	17	-6	-4	-33	7	0	25.01086	3.92E-09	11
2	25.01086	24	24	-7	-10	-35	1	25	25.01086	4.32E-09	7
2	25.01086	14	24	6	-10	37	4	8	25.01086	4.38E-09	8
2	25.01086	8	24	-8	-6	-7	12	-3	25.01086	4.43E-09	7

Figure 3. A CSV file of the Generalized Continued Fraction of the third Riemann Zeta Zero



extremely interesting to do a bunch of iterations of iterations of the columns. Another program that would need to be generated is called the longest repeated subsequence. If this code works, by applying the same process as described above it may find a pattern for the standard continued fraction.

For the generalized continued fraction, the GCF was expanded in an Excel table using the “h-k algorithm”. Within this table the columns were labeled in the following order; n, a, b, h, k, h/k, and delta. The initial values for the prior two rows were given by  $n = -2, n = -1, a(-1) = 1, h(-2) = 0, h(-1) = 1, k(-2) = 1, \text{ and } k(-1) = 0$ .

From the starting point, successive row values were calculated from the following recurrence relationships:

$$hn = bn * h(n-1) + a(n-1) * h(n-2)$$

$$kn = bn * k(n-1) + a(n-1) * k(n-2)$$

Figure 6 shows the full expansion using these two algorithms for the third Riemann Zeta zero, 25.01085758. Also, Figure 6 demonstrates that the successive h/k as produced by the recurrence relationships converged rapidly to the Riemann Zeta zero. Once the expansion was completed, the successive values oscillate above and below the true Zeta zero.

There has additionally been an unexpected discovery that certain GCFs can approximate the known zeta zeros using a b0 value that is not close to the floor of the zeta zero. This is important because though there is a known pattern in the floors of the successive zeta zeroes, there could be a pattern in the GCFs. Knowing the nearest integer of a given root will give any “root finding” coding a major head start in finding the remaining decimal digits of that root.

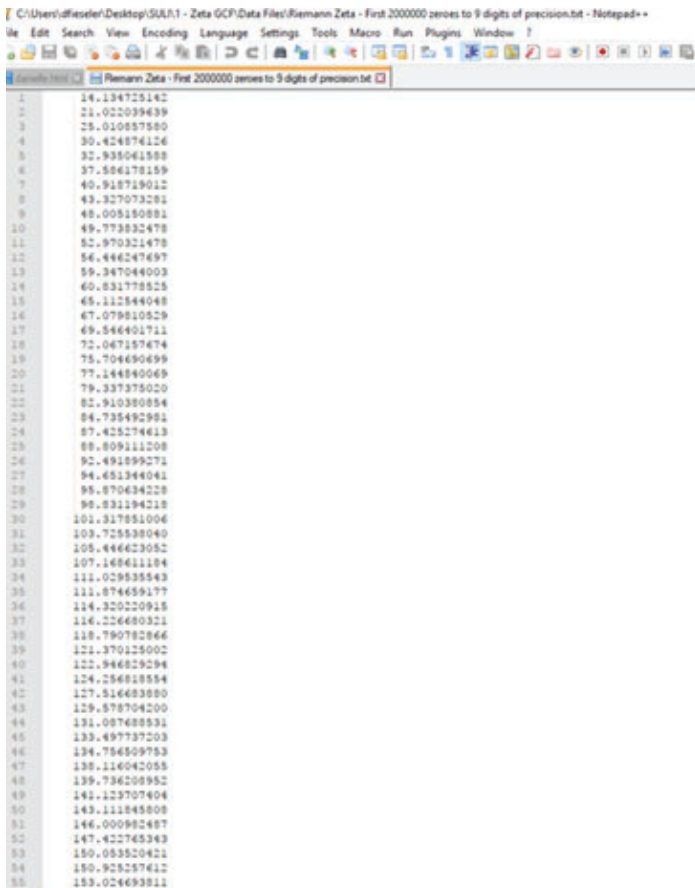


Figure 4. A data file that displays a portion of the first 2,000,000 Zeta zeroes to the 9 digits of precision

#### IV. Conclusion and Recommendation

Over the course of this ten week research project, the results were inconclusive. Although there were times in which a pattern was thought to be found for the standard continued fraction; these observations were in actuality an error. A huge gain has been made, however, in understanding how to reduce the time it takes to find the next Zeta zero.

For anyone doing further research, one would recommend doing a Discrete Fourier Transform (DFT). When doing this you should get a graph of the wavelength of the Generalized Continued Fraction of the Riemann Zeta function. From there it is up to you on how you choose to analyze the graph. Also, besides doing a DFT another concept that might want to be looked at that is in the mist of being researched and analyzed are iterated function systems (IFS) and their relationship to fractals. This concept can possibly lead to a pattern for the generalized continued fraction.

#### V. References

- Derbyshire, John. Prime Obsession: Bernhard Riemann and the Greatest Unsolved Problem in Mathematics. Washington: Joseph Henry, 2003. Print.
- Mazur, Barry, and William A. Stein. Prime Numbers and the Riemann Hypothesis. Cambridge: Cambridge UP, 2016. Print.

#### VI. Acknowledgements

I would like to give a special thank you to my mentor, David Biersach, for providing me with his insight and guidance on this project. Also, I would like to thank Noel Blackburn (Manager, University Relations and DOE Programs), Ken White (Manager, Office of Educational Programs), Mel Morris (Manager, Special Projects), and Sister Jane Fritz (Professor from the Computer Sci-

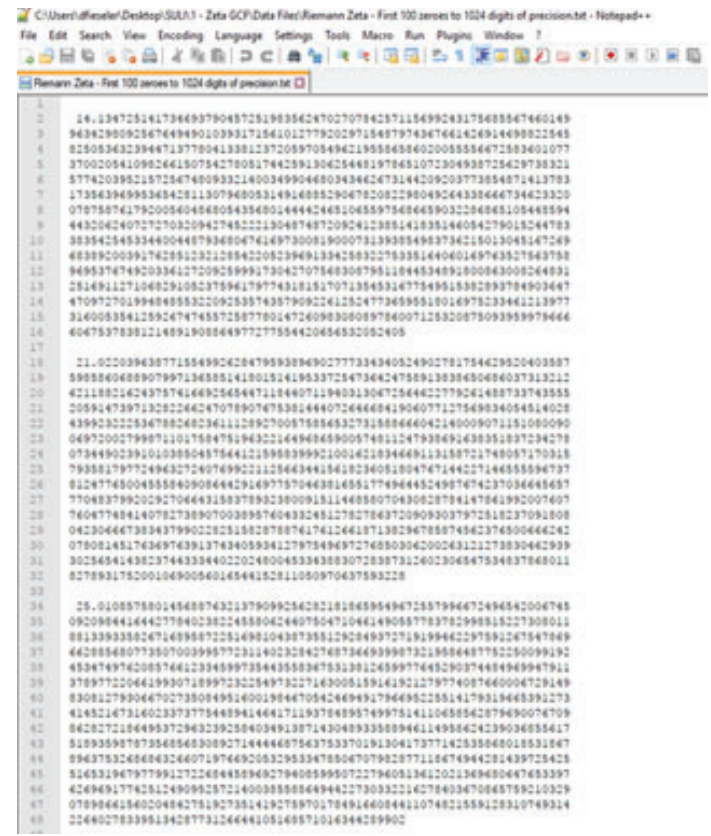


Figure 5. A data file that displays a portion of the first 100 Zeta zeroes to the 1,024 digits of precision



# Support structure design for the sPHENIX inner hadronic calorimeter

Howard Graham Giese, Mechanical Engineering, San Jose State, San Jose, CA 95192  
Donald Lynch, P.E., PhD Physics Dept., Brookhaven National Laboratory, Upton NY 11973

## Abstract

**The Pioneering High Energy Nuclear Interaction Experiment (PHENIX) was designed to detect subatomic particle collisions inside the Relativistic Heavy Ion Collider (RHIC) at Brookhaven National Laboratory. A new upgrade of the PHENIX project is being designed, called sPHENIX. My work with fellow interns and engineers will progress the design of the support structures for the Inner Hadronic Calorimeter (Inner HCal). This section of the detector resides within the large solenoid magnet of the sPHENIX and measures the energy of the hadrons produced during collision. The detector consists of a radial setup of long stainless-steel sectors, each estimated to weigh around one ton. Cost estimates and side-by-side comparisons have been looked at to choose the best design for the project, the main concern being how to attach the sectors to one another. Other factors that we analyzed were the strength of the materials, scale of manufacturing, accessibility to inner electronics, and finalization of design drawings. The Inner HCal went from concept to a planned design and installation process over the course of the summer. From this summer experience, I have grown in my technical, design, and communication skills as an engineer in the workplace. I have also expanded my networking skills and professional knowledge in programs such as AutoCAD, AutoCAD Inventor, ANSYS Simulation.**

## I. Introduction

The PHENIX project runs annually and as of summer of 2016 is set for a major upgrade. This upgrade, named sPHENIX, is planned to be a more accurate and efficient detector of high-energy particles and states of matter at Brookhaven National Laboratory. PHENIX is currently one of two large detectors on RHIC, the other being the STAR experiment. The proposed sPHENIX detector will not only improve the detection of particles, but also add many more applied sensor components and new implementations to the overall experiment. The previous detector is in the process of removal and repurposing to make way for this upgrade. The design and implementation of the sPHENIX project is planned to take five to six years, with a similar time of operation.

A hadronic calorimeter can record high-energy particles as they travel through the detector, essentially recording the energy lost as the particle travels through the calorimeter. The Inner HCal of sPHENIX uses a comb formation of stainless steel plates embedded with scintillating fibers. When a particle passes through these plates, it will slow down passing through the steel and interact while passing through the scintillating fiber causing light to be generated. This light can be recorded and analyzed with different interactions in the calorimeter to determine the speed and energy or the passing particle based on the energy a single particle loses as it travels. The sPHENIX Inner HCal consists of thirty-two

identical sections 171.26 inches in length and a weight of 2050 lbs. each. They are configured in a radial pattern and angled towards a central point to record the most interactions as possible. The sectors have limited space for attachment, so there are pin holes set into the endplates (figure 3). All the sectors together make up the whole of the Inner HCal; the detector nests inside a large solenoid magnet with smaller detectors nested inside of the Inner HCal (figure 3, cryostat coil)

## II. Methods and Design

### A. Splice Plates

#### 1. Overview

We proposed splice plates since they took up much less material than a full ring and would cost much less. This required two additional holes to the sector endplates to have enough contact points to keep the sectors stable. For assembly of the detector with splice plates, two steps are involved. The first step in assembly, the sectors would be lifted and placed onto a support cradle and then built up from the cradle until the full detector is assembled. The second step would involve lifting the entire calorimeter on a support beam and transferred inside the magnet for the final installation. For each process both lifting positions were simulated through AutoCAD Inventor's finite element analysis (f.e.a.) and compared Von Mises stress, max force applied, factor of safety, and displacement factor.

#### 2. Materials

The material for the Inner HCal is required to withstand the forces of the weight of the other detectors as well as the magnetic field produced by the solenoid magnet. Two non-magnetic materials were considered for the support structure. Aluminum 6061-T6 is a commonly used non-magnetic metal in building structures. It is cheaper to buy and manufacture than most other metals. With a density of 0.0975 lb/in<sup>3</sup>, tensile strength of 45 ksi, and a yield strength of 39 ksi, aluminum is light enough to move easily but doesn't have a high strength. The other material considered was stainless steel, series 310S. This specific type of austenitic steel was found to have low magnetic properties. The stainless steel has a tensile strength of 70 ksi, yield strength of 30 ksi, and a density of 0.285 lb/in<sup>3</sup> (1). Stainless steel is stronger than the aluminum, but also more dense. The possible added weight of material for the splice plates, approximately 530 lbs. total (calculated based on stainless steel), is not substantial when compared to the total weight of the sectors. These two materials were also considered while designing the ring cage assembly.

#### 3. Version 1 Analysis

The first version of the splice plate was a simple one-inch thick plate with the hole pattern cut into it (figure 5). The preliminary f.e.a. of the plate showed a factor of safety of less than 2 for



the aluminum and more than two for the stainless steel. The team working on sPHENIX values safety so any factor of safety values  $>2$  are considered unacceptable. After further discussion the shape of the ver. 1 splice plate needed to be changed to fit in electronics and brackets to later be placed on the sector endplate.

#### 4. Version 2 Analysis

The second version of the splice plate (figure 6) was shifted. Additional holes (figure 4) were added to the sector endplates so the splice was over the gap rather than across the whole face of the plate. There are two sets of smaller holes on this version of the splice plate, the larger of the holes aren't threaded and allow access to underlying bolt holes in the sector while the smallest holes are for plate separation in case the plate needs to be removed from its pins. The shape was changed and more extrusions were added to make room on the face of the plate. This hypothetically will also reduce the price of materials. The f.e.a. of a stainless-steel plate produced high stresses and a factor of safety of  $>2$ . The design wasn't enough to support the whole assembly when lifted.

#### 5. Version 3 Analysis

Version 3 of the splice plate had a similar shape to version two, but changed the shape to follow the curvature of the detector and a small adjustment to the hole placement on one of the holes of the inner HCal endplate (figure 7, 8). Analysis of this plate proved to be unacceptable based on the project expectations. Factor of safety values for assembly on the cradle had a minimum value of 1.31, whereas the factor of safety while lifting had a value of 0.65 (figures 9, 10, 11). The safety factor was effectively reduced by fifty percent when transitioning from sitting in the cradle to being lifted into the detector.

### B. Ring

#### 1. Overview

Assembly of the Inner HCal using ring supports involves a cage consisting of two rings nine feet in diameter, and sixteen support braces to make up the cage (figure 12). This method requires a large amount of material and precision machining, but less need for additional support while being assembled. The ring and the

Table 1.

Material:	Aluminum 6061	Stainless Steel 310S	Stainless Steel 310S	Aluminum 6061
Plate Thickness:	1 in	1 in	2 in	2 in
Max Stress:	15.71 ksi	20.7 ksi	12 ksi	11.64 ksi
Min Factor of Safety:	2.1	1.99	2.89	2.84
Max Displacement:	0.0389 in	0.0546 in	0.0455 in	0.0319 in

Table 2.

Material:	Stainless Steel 310S	Stainless Steel 310S
Plate Thickness:	1 in	2 in
Max Stress:	21.81 ksi	11.67 ksi
Min Factor of Safety:	1.42	2.83
Max Displacement:	0.0641	0.0321

full assembly are designed so that they may be put together on the same support structure used to transfer the Inner HCal into the magnet. Also, unlike the splice plate assembly, each sector can be lowered into the cage at the same angle. This would reduce the need for a rotation stand prior to placement in the detector. The proposed design is compatible with rotating the entire ring cage while attaching the sectors. The full ring covers the entire area of all thirty-two sectors end plates and is attached by pins, two pins per sector end for a total of sixty-four pin holes on each ring.

#### 2. Materials

The ring was considered using the same material information described in Section 1.a.iii. For large plates of the size needed for the ring material, the price of stainless steel plate (either 1-inch or 2-inch thickness) is roughly the same price per pound of material. The major factor in buying large material for the rings is the total area of the plate, since this part will most likely be custom-made. Making the full ring will use the most material. Splitting the ring into separate parts allows manufacturers to use smaller plates, possibly cutting multiple parts from the same plate. Possible cuts are shown in Figure 14.

#### 3. Full Ring Analysis

The full ring has an outer diameter of 108 inches (9 feet) and an inner diameter of 91 inches (7.58 feet). The total weight of the ring is 237.7 lbs. Analysis was based on two factors: material and thickness. The results of analysis are listed in Table 1 below.

Stainless steel has a higher yield stress (30 ksi) and less of a chance of deformation or failure. The added weight of the steel decreases the factor of safety compared to the aluminum ring; by increasing the ring thickness by an inch, this increases the strength of the ring by distributing contact forces. The two-inch stainless steel is the optimum choice for a full ring.

#### 4. Half Ring Analysis

For the half ring design, we split the ring into two halves and joined the halves with two relatively simple splice plates (Figure 15). The analysis compared the thickness of the plates. Stainless steel was the only material looked at due to the results from the

Table 3.

Material:	Stainless Steel 310S	Stainless Steel 310S
Plate Thickness:	1 in	2 in
Max Stress:	17.57 ksi	15.61 ksi
Min Factor of Safety:	2.06	2.12
Max Displacement:	0.0367 in	0.0334

previous simulations. Aluminum was projected to have similar stress readings and considered to be unacceptable for more complicated assemblies with splice plates. Based on the factor of safety values for the analysis, the two-inch plate halves are a better choice. Similar to the full ring analysis, the results for the half ring are listed in Table 2 below.

### 5. Quarter Ring Analysis

The smallest size of the split ring analyzed is when the support ring is in four parts. Note that the way the holes and sections are aligned the ring cannot be split into three parts without splitting a sector through the center. Having the ring split across the face of an end plate will cause additional stresses on the Inner HCal sector, which has already been approved to lift by the pin holes but not designed for twist and torque. The four plates are joined by the same splice plates as in the half rings. The results of analysis are listed in Table 3 Below.

### III. Future Work

This research done on the Inner HCal support structures directly impacts the design of the installation structures and the physical design of the detector. The analysis and estimates made in this report will assist in making decisions about the Inner HCal and how it will fit into the sPHENIX detector in the near future. This will also give the planning engineers and scientist a good idea of where to push the project and which areas of the design need more attention. Overall my work on the sPHENIX project has aided the upgrade of the project and contributed to new research soon to take place at the Relativistic Heavy Ion Collider.

### IV. Impact on Laboratory Missions

The research and design work done for the sPHENIX project directly impacts progress on multiple projects involving the par-

### VIII. Appendix:

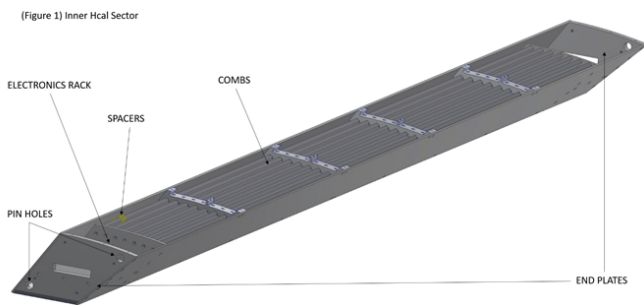


Figure 1 (above): Components of a single Inner HCal Sector:

Figure 2 (right): A view of the complete sPHENIX project

ticle collider at Brookhaven National Laboratory. Not only does this project show important data on the real world installment of the detector, but it directly contributes to the completion of the detector at the particle accelerator. Once sPHENIX is completed, the experiments at the detector will be valuable to the research done in high-energy physics at Brookhaven National Lab and the scientific community.

### V. Conclusions

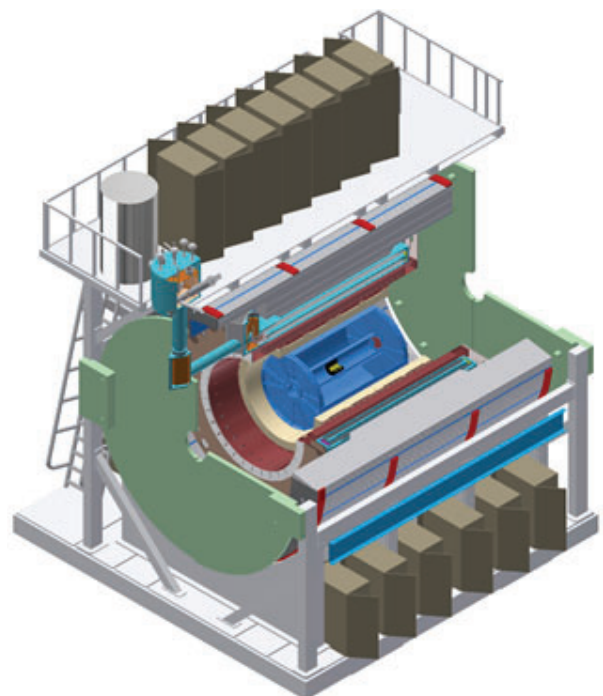
Analysis of materials and different designs of the Inner HCal has shown that, due to the size and shape of the detector, some methods are more desirable than others. We've concluded that Although aluminum is less costly the material doesn't hold up to factors of safety for the project. The optimum design for the support structure is the Half Ring assembly. This has the best values for stress reduction and safety. The splice plates stack up tolerances the more you have, so in the long run splice plates will need to have very high tolerances in able to fit together. With the half ring design, there is significantly less material used than cutting a full ring, and only two connection plates are used.

### VI. Acknowledgements

This project was supported in part by the U.S. Department of Energy, Office of Science, Office of Workforce Development for Teachers and Scientists (WDTS) under the Science Undergraduate Laboratory Internships Program (SULI). Also special thanks to Don Lynch (sPHENIX Chief Engineer), Rich Ruggiero (sPHENIX Chief Designer), Dan Cacace (sPHENIX Inter), Spencer Locks (sPHENIX Intern) and both the PHENIX and sPHENIX technicians and engineers for their help and guidance.

### VII. References

<sup>1</sup>Material Property Data. (n.d.). Retrieved June 31, 2017, from <http://www.matweb.com/search/DataSheet.aspx>



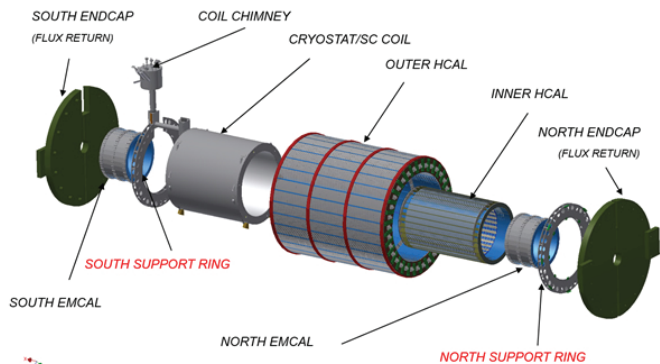


Figure 3: an explode view of the sPHENIX detector



Figure 4: Splice plate hole spacing, the endplates of the two sectors and the placement of their holes and set screws.

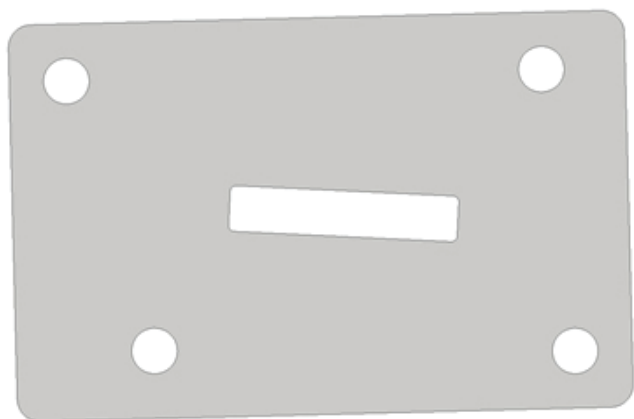


Figure 5: splice plate version 1

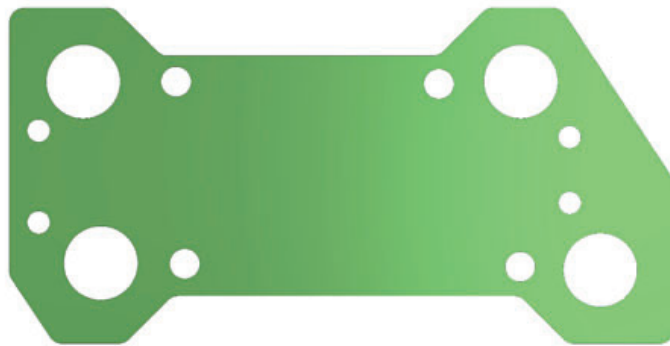


Figure 6: version 2 splice plate



Figure 7: version 3 splice plate

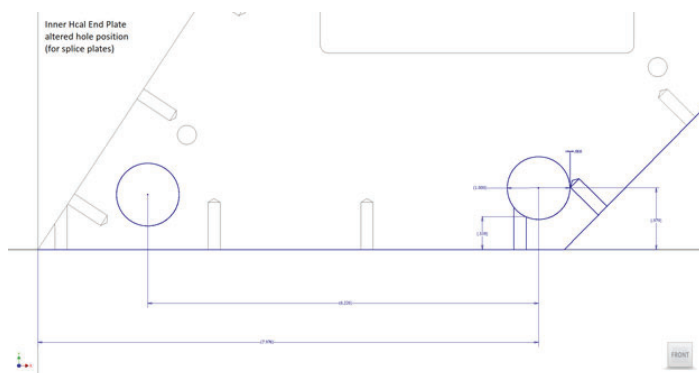
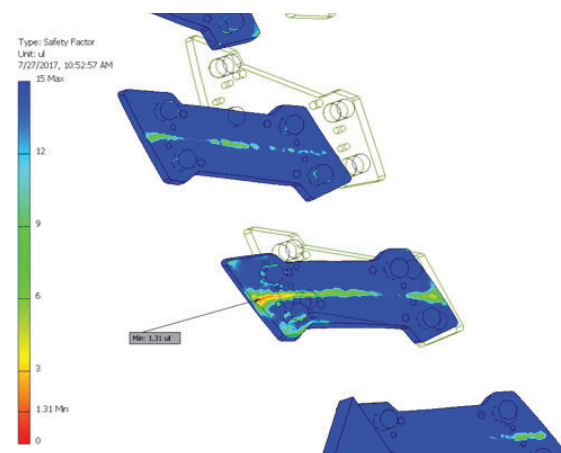
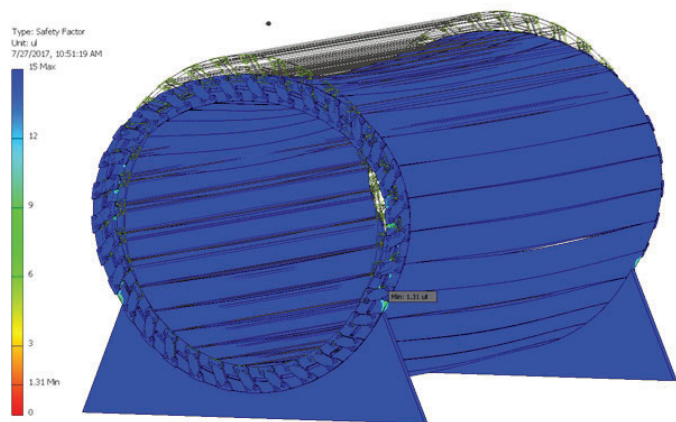


Figure 8: one of the holes on the Inner HCal endplate adjusted to create a larger area of support.



Figures 9, 10: finite element analysis of Version 3 splice plates sitting in a cradle setting.



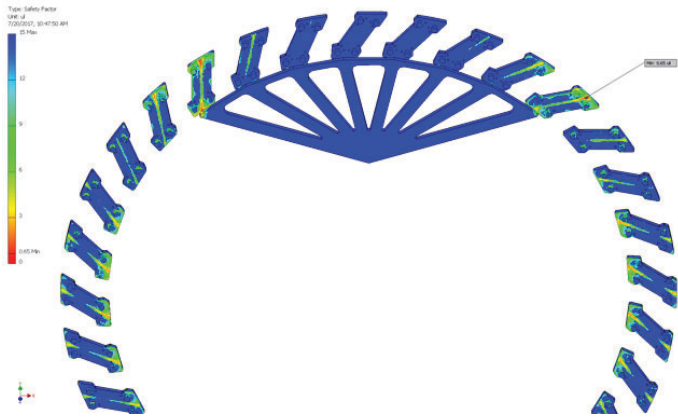


Figure 11: Version 3 splice plate analysis, lifting

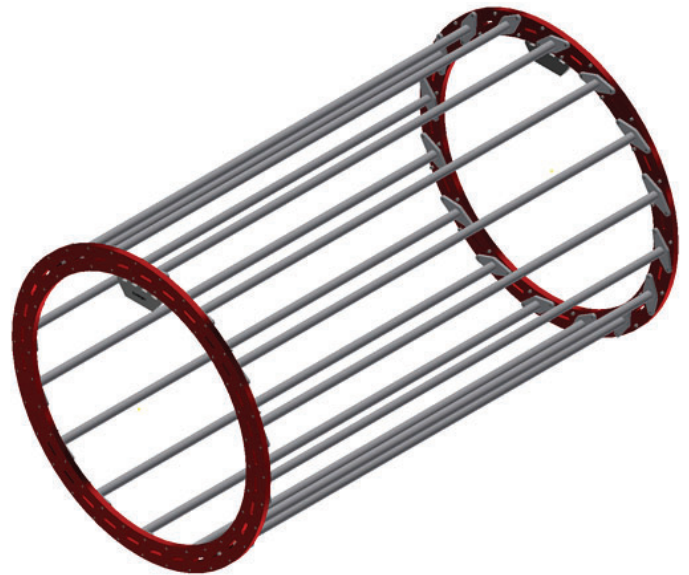


Figure 12: Ring cage

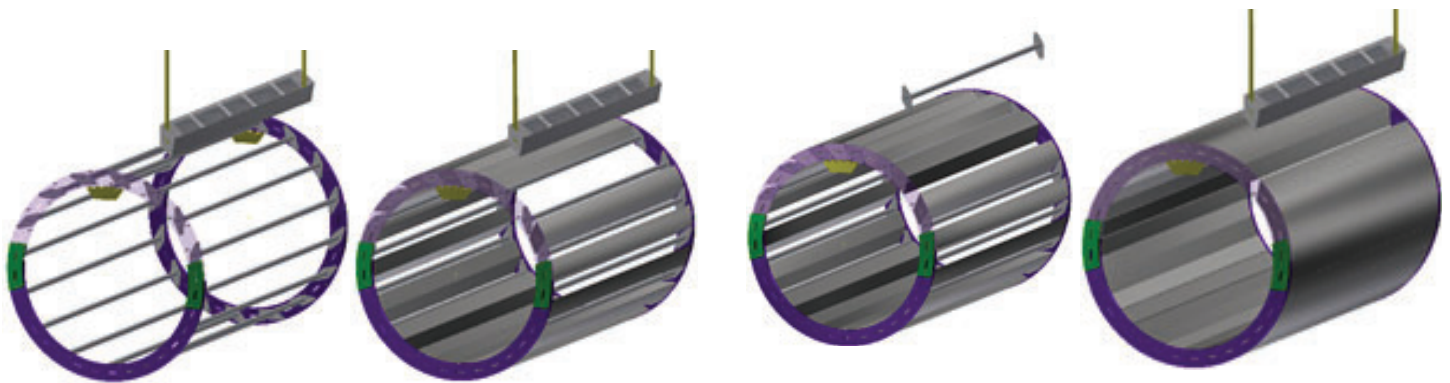


Figure 13: proposed assembly procedure for the ring cage.

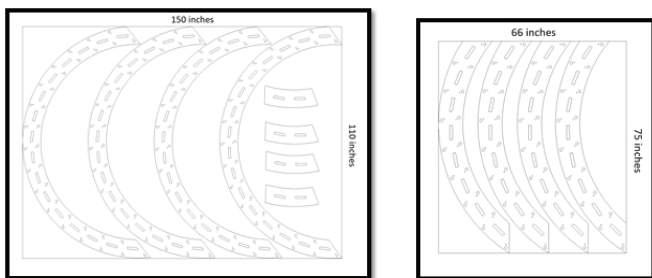


Figure 14: possible half ring cuts (left), possible quarter ring cuts (right)

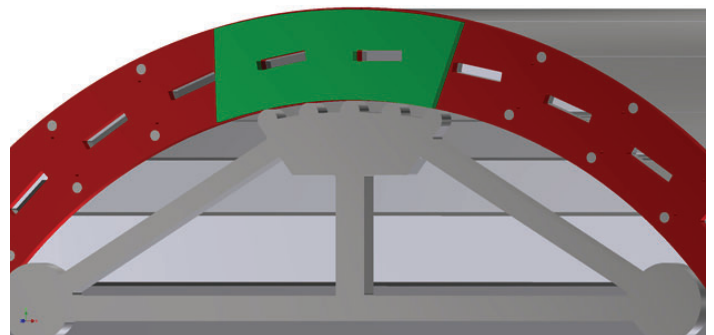


Figure 15: connector plate for the ring pieces

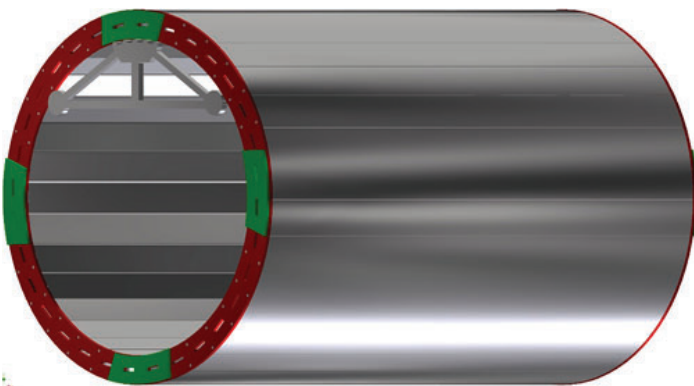


Figure 16: Inner HCal quarter ring assembly

# Examining transgenic poplar trees as a route towards improving cellulosic biofuel yields

Timothy Grace, Stony Brook University, Stony Brook, NY 11794

Chang-Jun Liu and Yunjun Zhao, Brookhaven National Laboratory, Upton, NY 11973

## ABSTRACT

A major aspect in the hesitation of turning towards renewable fuel sources rather than those which are petroleum based or otherwise unrenewable is the greater financial expense brought on as a penalty of the inefficiency of current cellulosic plant biomass digestion. Cellulosic plants include trees and plants with high woody biomass to total biomass ratios. There are advantages to using cellulosic biofuel feedstocks rather than non-cellulosic feedstocks, such as the ability for trees to grow on marginal land not suitable for crops such as corn, the ease of maintenance of the cellulosic plants, and avoiding the controversy of whether to use biofuel crops for food or for fuel. In order for cellulosic biofuel to become a more viable substitute, the ratio of energy invested during harvesting versus energy generated as a result must shift further to the production side for significant interest in the future of cellulosic biofuel to rise in the energy industry. Synthesis of plant-based biofuels such as ethanol is significantly inhibited by the presence of a structural polymer called lignin, which is present in cell walls of woody plants. Lignin is a hydrophobic molecule which restricts access of digestive enzymes from catalyzing the breakdown of the necessary polysaccharides within the cells into fermentable sugars to ultimately generate ethanol.

## I. INTRODUCTION

This experiment is aimed at the conversion of lignin into a less highly polymerized form as a result of changed composition in the transgenic poplars without experiencing adverse effects on the ability for the plants to survive. A popular technique to change the structure or formation of a polymer is by modifying its monomers in a way that alters their polymerization activity. By introducing genetic coding for an enzyme, MOMT4 (monolignol-4-*O*-methyltransferase) into the poplar trees, we have seen promising statistical evidence for the reduction in standard lignin production. This enzyme follows a methylation mechanism of the monomeric building blocks of lignin—*p*-coumaryl, coniferyl, and sinapyl alcohols—rendering them unable to polymerize normally [2]. The experiment has now progressed to the stage of introducing these mutant poplar trees into an outdoor field setting with little maintenance and exposed to the natural elements, as opposed to growth in a highly controlled environment within a greenhouse. The data to be gathered during these trials is vital, as it could demonstrate either the stability or fragility of the lessened structural support of the poplar trees, as well as potentially different growth rates versus the wild type poplars. Greenhouse data, while valuable, is not sufficient enough to present to industry, as they will grow their biofuel crops outside and will expect to see field data as well.

In Figure 1 molecule (a) shows the 3 different monolignol structures. Reaction pathway (b) displays the normal method of

polymerization for a coniferyl alcohol following dehydrogenation of the hydroxyl group at carbon (4). The methyltransferase catalytic action shown in (c) illustrates the inability for dehydrogenation of methylated coniferyl and sinapyl alcohols [1]

## II. METHODS

The poplar trees were organized into different genetic lines, each having differing capabilities of polymerizing lignin. The poplars were grown in Latin squares in both the greenhouse and the field to efficiently minimize the effect of the environment and individual placement on the growth of any of the lines of trees. Once a specimen is ready for study, stems carrying leaves from different lines were cut, dried, and ground to a very fine powder. These powder samples were then chemically treated for quantitative spectroscopic analysis of lignin content. Another examination of the plants was of their relative growth rates in the field. Once per week, they were groomed of any other vegetation near their base and their height was measured for genetic line comparison. Finally, 30-80  $\mu\text{m}$  cross-sections were sliced from different stems and stained using phloroglucinol and to observe total lignin composition.

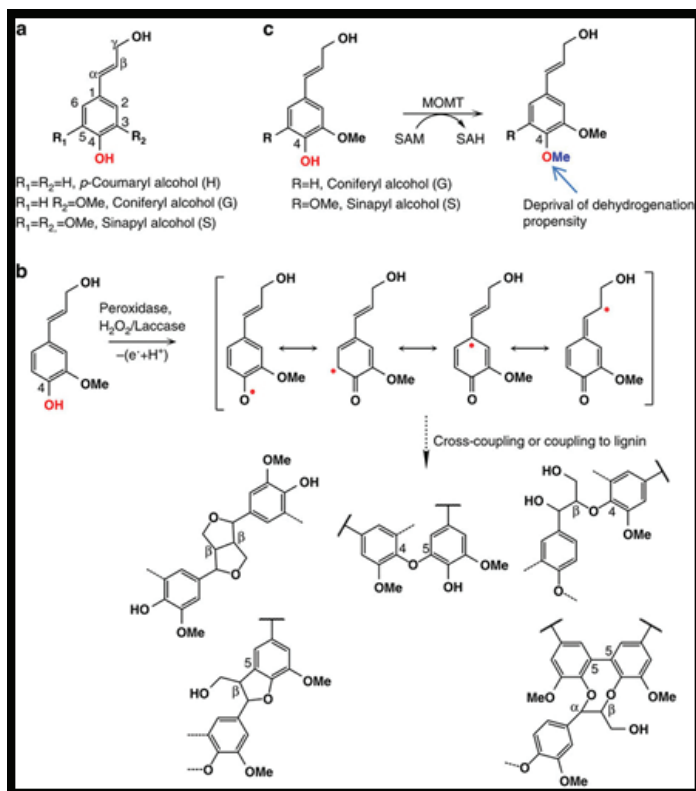


Figure 1.

### III. RESULTS

In Figure 2 the average height of the poplar lines are as expected, as the wild-type control finished the tallest after 7 weeks, and all genetic lines followed a highly conserved linear pathway during growth. Although the height data does seem linear, there are fluctuations that could be of interest and tell a deeper story about the growth of the different species of poplars. The heights of the poplars look promising, while none of the mutant lines exceeded the height of the wild-type control, none seemed to be incapable of growing past any certain height—just at a slower rate.

In Figure 3 the more interesting data set is the average growth, week by week, as it illustrates the deviations from the best fit line. The lines follow similar growth trends throughout the seven weeks of data collection; however, they do not follow exactly. We will assess environmental factors and arrive at a hypothesis as to why there was such a period of flux in the beginning of the data collection, followed by a highly conserved “V” shape pattern in the latter stages of the data collection.

In figure 4 looking at the time period between June 12th and June 16th, there is a dramatic decrease in temperature which the wild-type poplars may have sustained with minimal or no stress placed onto the plant, while other lines suffered as a result of the shock. Following that temperature drop, there is a period of slightly over one week in which the plants began thriving and increasing their weekly growth rates. I hypothesize that this phenomenon is due to prolonged temperatures in the high 70’s and low 80’s, which could be the preferred temperature for the poplars, both

wild type and transgenic. Over the next several weeks, there were oscillations in temperatures routinely reaching into the 90’s which corresponded to a decrease in growth rates for all lines of trees, which could be explained by the temperature/stress causation stated previously, in which even the wild-type control trees could not sustain their faster rates. Towards the latter stages of data collection, there is a large temperature drop into the 70’s which does not spike back up into the high 80’s or low 90’s; rather, it floats between the mid-70’s and mid-80’s. The growth data supports the hypothesis once more as the growth rates dramatically spike back up to approximately their fastest levels [3].

In attempting to correlate the relative humidity percentages to the growth data (Figure 5), it could be theorized that the plants experienced stress due to prolonged 95%+ relative humidity which caused the initial several weeks of turbulence in the data, however, I see no explanation for any causation for the other phenomena in the growth graph, therefore it is inconclusive as to whether or not the humidity played a factor in the growth rates of the poplars [3].

In Figure 6 the rainfall experienced by the trees seems almost backwards, as for the time period following intense rainfall, the growth of the plants began decreasing, and during times of drought, both increased and decreased. As with the humidity records, the precipitation records are not consistent enough with the weekly growth data to determine any conclusions of causation [3].

Analysis of dry harvested biomass from field grown poplars

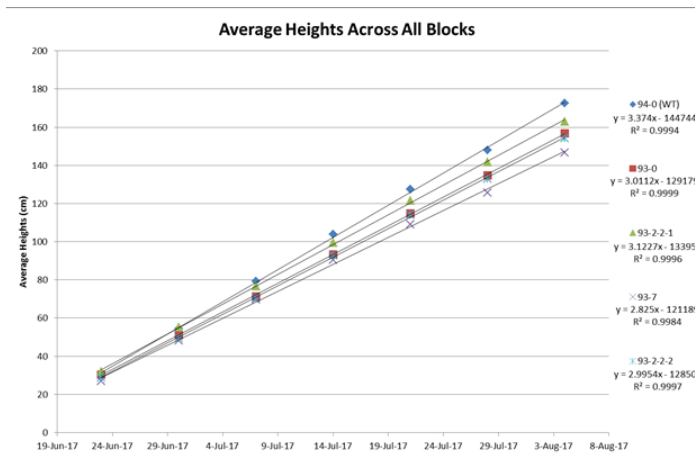


Figure 2.

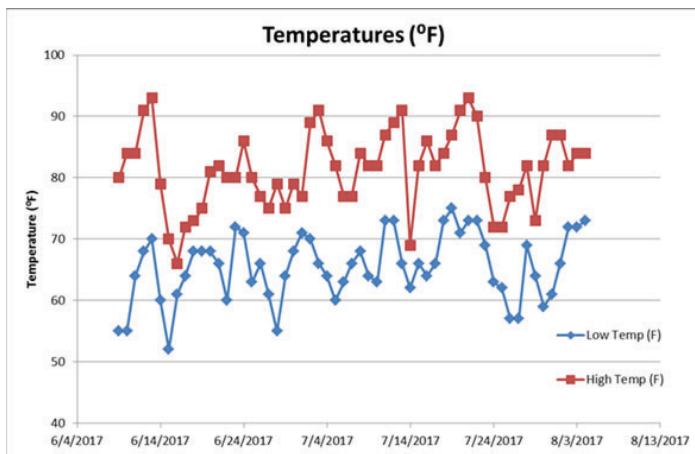


Figure 4.

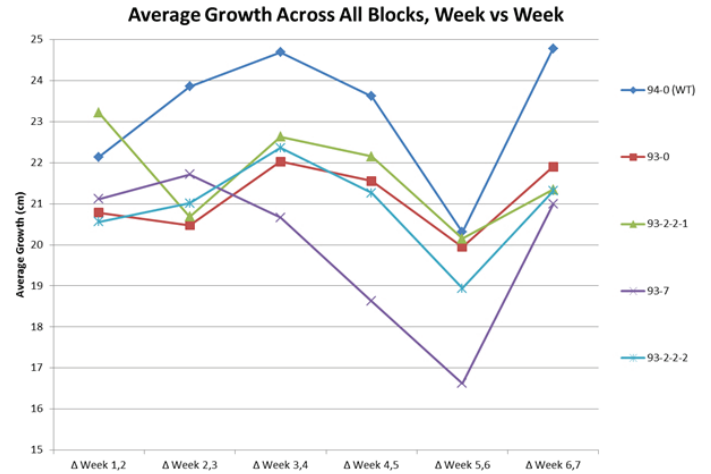


Figure 3.

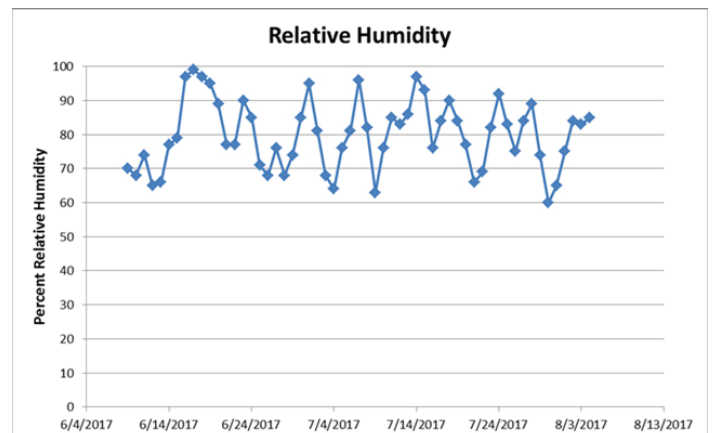


Figure 5.



demonstrates the growth inhibition experienced by only one line, 93-0 (Figure 7). Both 93-2-2 lines, as well as 93-7, grew reasonably close enough to the 94-0 wild-type control that it could be concluded that they did not endure seriously stunted growth. This is very promising data all around as we can now examine the genetic causations of both of these phenomena to further increase our knowledge of the activity and manifestation signs of the different expressions of the MOMT4 enzyme.

Phloroglucinol staining photographs qualitatively indicate the presence or lack of all lignin (Figures 8 and 9). The wild-type stem (on left) shows very dense regions of lignin shown in deep pink, while the transgenic over-expression line (on right) shows a clear reduction of lignin to the point where some of the structures visible in the wild-type photo are not able to be seen.

The Mäule staining results which show the presence of S-type lignin only are somewhat inconclusive (Figures 10 and 11). While the wild-type cross-section (on left) shows a vibrant red color, the mutant line (on right) may be slightly off color, but the density of stain is close enough to be called identical, coinciding with previously collected Mäule staining photos of the line.

#### IV. CONCLUSIONS

There are several main points to be taken away from this project. First, the field data did not completely reflect the previously collected greenhouse data; the transgenic lines were adversely affected in the field, just not significantly. Although there was not a drastic decrease in growth, the fact that they did grow more slowly is very valuable information going forward. The temperature in which the poplars are exposed to could potentially have a moderate impact on the growth rates of control and transgenic lines, a factor which industry will have to take into consideration if they choose to grow these transgenic poplars for biofuel. The phloroglucinol staining photographs are also new

pieces of data in this project which were not previously tested for the field grown poplars. The greenhouse staining pictures were not conclusive in demonstrating a clear reduction in the total presence of lignin, while the new staining photos clearly demonstrate a reduction. The future of this project looks bright as fermentation and ethanol yield data is collected and the most promising lines of MOMT4-expressed poplars can be promoted for industry.

#### V. ACKNOWLEDGEMENTS

This project was supported in part by the U.S. Department of Energy, Office of Science, Office of Workforce Development for Teachers and Scientists (WDTS) under the Science Undergraduate Laboratory Internships Program. I would also like to take a moment to thank CJ Liu and Yunjun Zhao for their inspiring level of dedication to their work, caring nature, and patience with me during my internship.

#### VI. REFERENCES

- [1] <https://www.nature.com/articles/ncomms11989>
- [2] <https://www.howplantswork.com/page/18/>
- [3] [https://www.wunderground.com/history/airport/KHWV/2017/8/7/DailyHistory.html?req\\_city=Upton&req\\_state=NY&req\\_statename=New+York&reqdb.zip=11973&reqdb\\_magic=1&reqdb.wmo=99999](https://www.wunderground.com/history/airport/KHWV/2017/8/7/DailyHistory.html?req_city=Upton&req_state=NY&req_statename=New+York&reqdb.zip=11973&reqdb_magic=1&reqdb.wmo=99999)

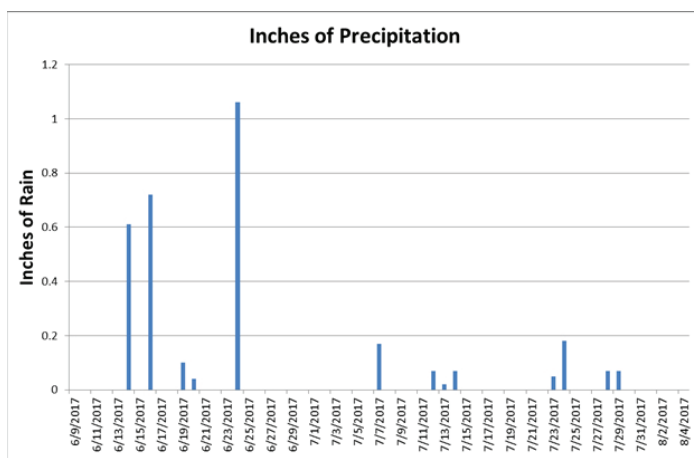


Figure 6.

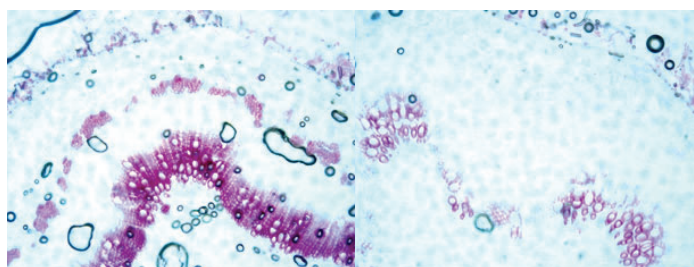


Figure 8 and 9.

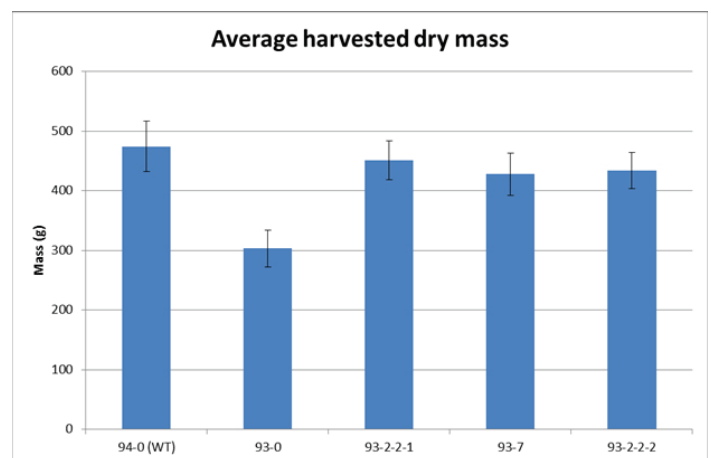


Figure 7.

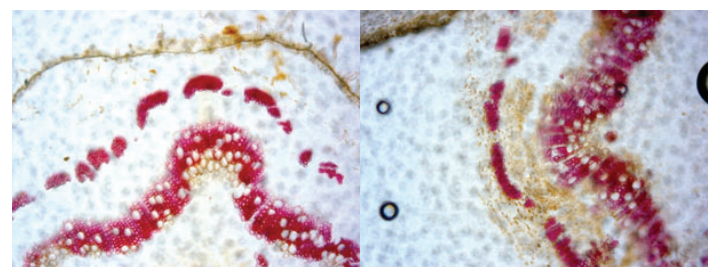


Figure 10 and 11.

# Low charge state ion beam production using a sub-nanosecond neodymium-doped yttrium aluminium garnet laser

Colin Guilbault, Department of Nuclear Engineering, Texas A&M University, College Station, TX 77843  
Masahiro Okamura and Takeshi Kanesue, Collider-Accelerator Department,  
Brookhaven National Laboratory, Upton, NY 11973

## Abstract

**The Laser Ion Source (LIS), at Brookhaven National Laboratory's Electron Beam Ion Source (EBIS) injector, is in operation to create singly charged heavy ion beams. To produce singly charged ion beams, the LIS currently uses a 6 ns, Neodymium-doped Yttrium Aluminium Garnet (Nd:YAG) laser. To function properly, the LIS must continuously operate for more than half a year, without major maintenance. The minimization of material consumption, by the LIS, is important in preventing maintenance of the LIS, and loss of costly material. Our study examined how different settings of a new sub-nanosecond Nd:YAG laser affected the fraction of singly charged ions created versus total material consumed. Three targets made of Aluminium, Iron, and Tantalum were used in the experiment. These targets were chosen in order to get results for materials of varying masses.**

## I. Introduction

Neodymium-Doped Yttrium Aluminium Garnet (Nd:YAG) lasers are often used in ion beam production. This is due to the Nd:YAG laser's ability to produce plasma, from materials. The Laser Ion Source (LIS), at Brookhaven National Laboratory's linear accelerator, uses a Nd:YAG laser, with a 6 ns pulse length. The LIS is set up to supply the rest of the linear accelerator facility with singly charged ion beams. In order to assure that the ion beams are singly charged, certain laser power densities are used by the LIS; however, ions that are more than singly charged are still created by the LIS. These non-singly charged ions must be removed from the ion beam, and thus waste target material. Previous experiments were conducted, at the LIS, to see if a sub-nanosecond pulse Nd:YAG laser could reduce the fraction of non-singly charged ions being produced; however, the experiment was unsuccessful, due to the instability of the ion beam that was produced [1]. A new sub-nanosecond Nd:YAG laser, produced by Ekspla, was introduced at the LIS. For my experiment, this new laser was tested to see if it could produce ion beams with 90% singly charged ions, what power density this fraction was reached, and how the laser could be implemented to replace the 6 ns pulse length Nd:YAG laser.

## II. Methods and Materials

There were four main parts to this experiment: preparing the target chamber, measuring the ion beams' current density, separating the current density measurement into the current densities of each ion, and analyzing the collected data. The target chamber incased the laser beam focusing lens, the target plate, and the axis system that positioned the target plate. The target plate help three element species: aluminium, iron, and tantalum. These element

species were selected, in order widely vary the atomic masses, of the target materials. Once the target chamber was prepared, the Faraday Cup was positioned to measure the current density of the ion beam. The target was shot ten times, in order to collect ten Faraday cup measurements. The Faraday Cup was then removed from the path of the ion beam, after the measurements. Then, the Electrostatic Ion Analyzer (EIA) was prepared. The EIA would apply an electric field to the ion beam, causing it to make a right turn towards the signal collector. Since the different ions had different charge to mass ratios, the electric field caused the ions to be separated by arrival time. A calculation involving the electric field strength, and charge to mass ratio was used to identify when different ions would arrive at the signal collector. EIA measurements were taken, until the Faraday cup signal could be reproduced, with the EIA signals. Then the Faraday Cup was repositioned, in the beam line, and ten more Faraday Cup signals were taken, in order to test if the ion beam signal had stayed steady for the length of the experiment. The majority of the analysis of the collected data was completed using OriginPro 8.1, an OriginLab software product. The signals from both the EIA and Faraday cup data were imported into OriginPro. The EIA signal peaks were then chosen manually. The Faraday Cup signals' magnitudes were averaged. Then, using the gathered data, previously written codes were run. These codes output the ion beam's current density, at different distances from the target, and the singly charged ion fraction. The codes also allowed the peak current density, and full width half max of the current density to be measured. Using the output results, the following test's variables would be selected. The figure to the right displays, from top to bottom, the test chamber, the Faraday Cup, and the EIA.

To select the power density for each test, the laser amplification and pulse length, and the lens' focal length were varied. These variables chose the laser energy, and laser spot size, respectively. The laser energy associated with each amplification setting were measured by collecting laser energy measurements from forty shots consecutively. From those forty shots, the mean laser energy was then calculated, and used as the actual laser energy. The mean laser energy values for each laser amplification can be seen in Appendix A. The spot size for each associated focal length, and laser amplification were measured by shooting burn paper with each laser setting, and then measuring the spot diameter, with a caliper. The diameter of the burn spots can be seen in Appendix B.

## III. Results

In total, nine tests were conducted, in order to measure at least three singly charged ion fractions, for each target material. The tests performed during this experiment, their test settings and their results are presented in Figure 1. The plot of singly charged

Test #	Material	Laser Energy (mJ)	Focal Length (mm)	Spot Diameter (mm)	Pulse Width (ps)	Power Density (W/cm <sup>2</sup> )	1+ Fraction
1	Al	64.00	150	2.97	170	5.43E+09	0.393
2	Al	34.90	150	2.97	570	8.84E+08	0.601
3	Ta	55.70	150	2.97	570	1.41E+09	0.794
4	Al	77.90	250	4.72	570	2.38E+08	0.924
5	Ta	102.80	250	5.15	570	2.86E+08	0.919
6	Fe	102.80	250	5.15	570	2.86E+08	0.910
7	Fe	171.50	250	5.33	570	4.35E+08	0.695
8	Fe	102.80	450	6.20	570	1.80E+08	0.969
9	Ta	102.80	450	6.20	570	1.80E+08	N.A.

Figure 1. Summarization of the tests performed

ion percentage versus power density is presented in Figure 2. The plot of the current density of aluminium, from its 90% singly charged ion test, the plot of the current density of iron, from its 90% singly charged ion test, and the plot of the current density of tantalum, from its 90% singly charged ion test are presented in Appendix C, D, and E respectively. The 90% singly charged ion threshold, for each target material, all coincided around the power density  $2.9 \cdot 10^8$  W/cm<sup>2</sup>. At the power density of

$1.8 \cdot 10^8$  W/cm<sup>2</sup> the ion beams became unstable. Thus, to produce an ion beam of at least 90% singly charged ions, the power density should be between  $1.8 \cdot 10^8$  W/cm<sup>2</sup> and  $2.9 \cdot 10^8$  W/cm<sup>2</sup>. The peak current densities and Full Width Half Maxes (FWHM), at one meter from the target, from each materials' 90% singly charged ion test were also recorded. Aluminium had a peak current density of 0.524 mA/cm<sup>2</sup> and a FWHM of 27 μs. Iron had a peak current density of 1.14 mA/cm<sup>2</sup> and a FWHM of 35 μs. Tantalum had a peak current density of 0.276 mA/cm<sup>2</sup> and a FWHM of 120 μs. An important note on lowering the power density from  $2.9 \cdot 10^8$  W/cm<sup>2</sup> comes from the  $1.8 \cdot 10^8$  W/cm<sup>2</sup> test on tantalum. The results from this test proved to be unusable, due to instability in peak ion beam current. The instability in the peak current was characterized by the presence of two dominant peak current values, instead of one. This caused the average peak current to be between both values, and representative of neither. This instability in peak current can be connected to the fact that the power density used in the stated test was near the plasma creation threshold. Thus, lowering the power density, in order to increase the singly charged ion percentage, can lead to the inability to create plasma.

#### IV. Discussion

The main purpose of this experiment was to examine the potential of the Ekspla sub-nanosecond Nd:YAG laser replacing the 6 ns Nd:YAG currently being used to produce the ion beams, at the LIS, for Brookhaven National Laboratory's linear accelerator facility. The results, from this experiment, proved that the Ekspla sub-nanosecond Nd:YAG laser is able to produce ion beams of 90% singly charged ions, from target materials of varying atomic mass; however, the peak current, and FWHM must match the necessary values that the LIS has set. Knowing that peak current decays in the form of one over the distance traveled cubed, and that the FWHM increases proportionally with distance travelled, the current distance between the target plate and the aperture is

3.361 m, and that the aperture the ion beam exits the LIS through has a radius of

7.5 mm, recommendations can be made to accompany the sub-nanosecond laser's ion beam output. Since a solenoid can be used to increase the peak current, the FWHM values are the first concern. For aluminium, the FWHM, at the aperture, from the experiment is 90.75 μs, while the set one is 50 μs. Thus, an aluminium target would have to be moved 1.5 m closer to the aperture.

For iron, the FWHM, at the aperture, from the experiment is 117.6 μs, while the set one is 100 μs. Thus, an iron target would have to be moved 0.5 m forwards. For tantalum, the FWHM, at the aperture, from the experiment is 403 μs, while the set one is 200 μs. Thus, a tantalum target would have to be moved 1.7 m forwards. Since the iron target needs to be moved the least distance forwards, to a position 2.86 m from the aperture, the calculation of the solenoid amplification was made from there. Aluminium would need to be amplified by a factor of 25, iron would need to be amplified by a factor of 5.8, and tantalum would need to be amplified by a factor of 4.8. All of the calculated multiplication factors are able to be produced by the current solenoid setup in the LIS. In order to summarize the previously listed values, the initial calculated peak current, and FWHM at the aperture are presented in Appendix F, the desired peak current, and FWHM are presented in Appendix G, and the peak current, and needed solenoid amplification, from 2.86 m away, are presented in Appendix H. Appendix I displays the dimensions of the current LIS configuration.

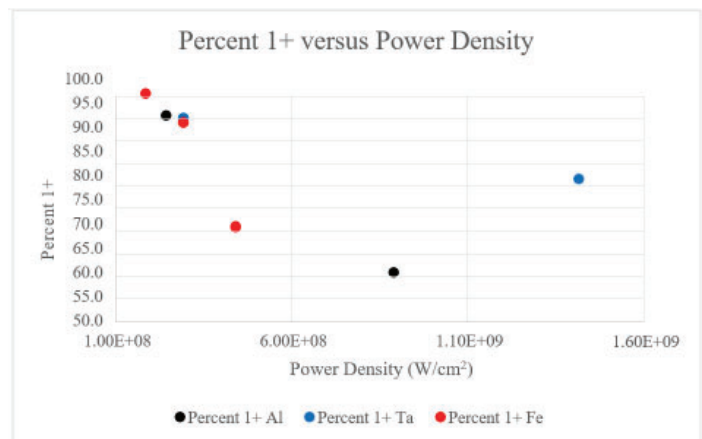


Figure 2. Singly charged ion percentage versus power density



## V. Acknowledgements

This project was supported in part by the U.S. Department of Energy, Office of Science, Office of Workforce Development for Teachers and Scientists (WDTS) under the Science Undergraduate Laboratory Internships Program (SULI).

## VI. Appendix

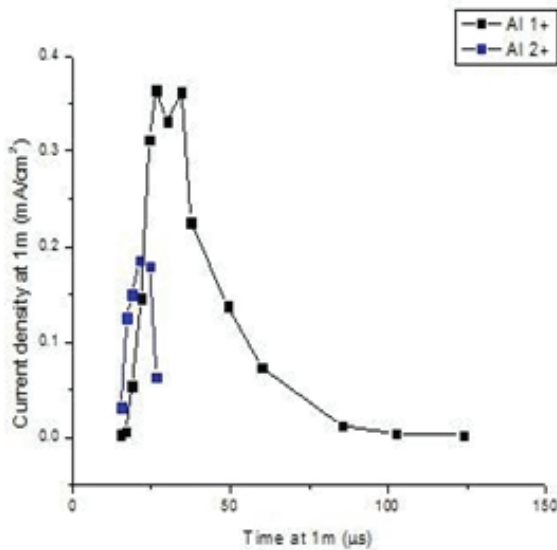
[A]

Laser Amplification	Laser Energy with 570 ps pulse (mJ)	Laser Energy with 170 ps pulse (mJ)
99%	228.90	248.20
90%	205.80	216.30
80%	171.50	184.80
70%	135.50	150.80
60%	102.80	123.80
50%	77.90	90.50
40%	55.70	64.00
30%	34.90	40.70
20%	17.54	21.93

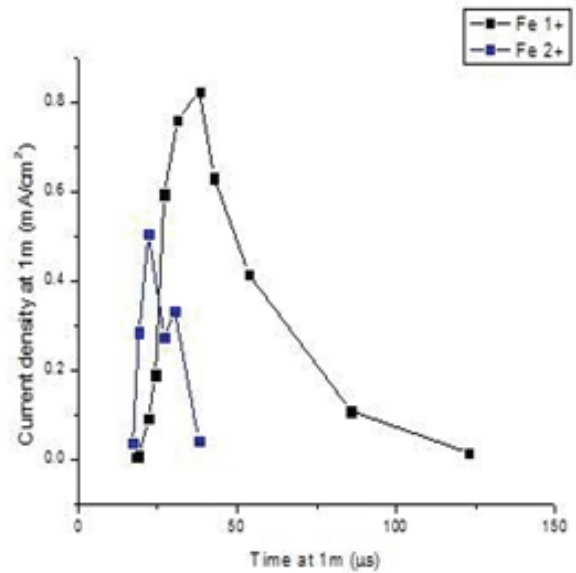
[B]

Laser Amplification	Spot Diameter of $f = 250$ mm (mm)	Spot Diameter of $f = 450$ mm (mm)
80%	5.33	6.50
60%	5.15	6.20
50%	4.72	6.15
40%	4.67	5.91
30%	4.33	5.70

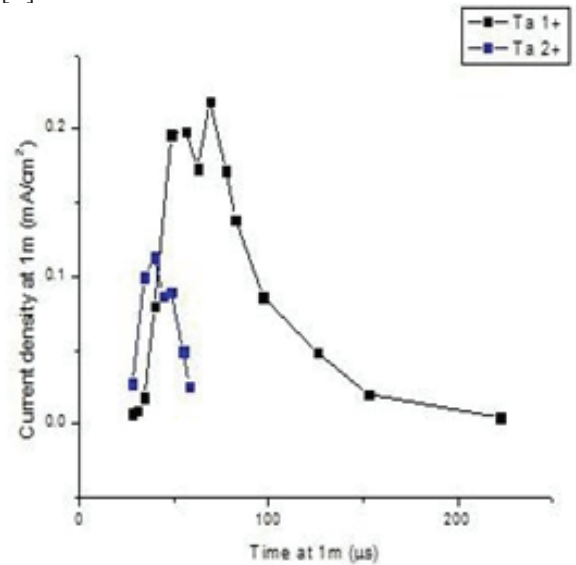
[C]



[D]



[E]



[F]

Material	Current at the aperture (mA)	FWHM at the aperture ( $\mu$ s)
Fe	0.0530	117.60
Ta	0.0128	403.32
Al	0.0244	90.75

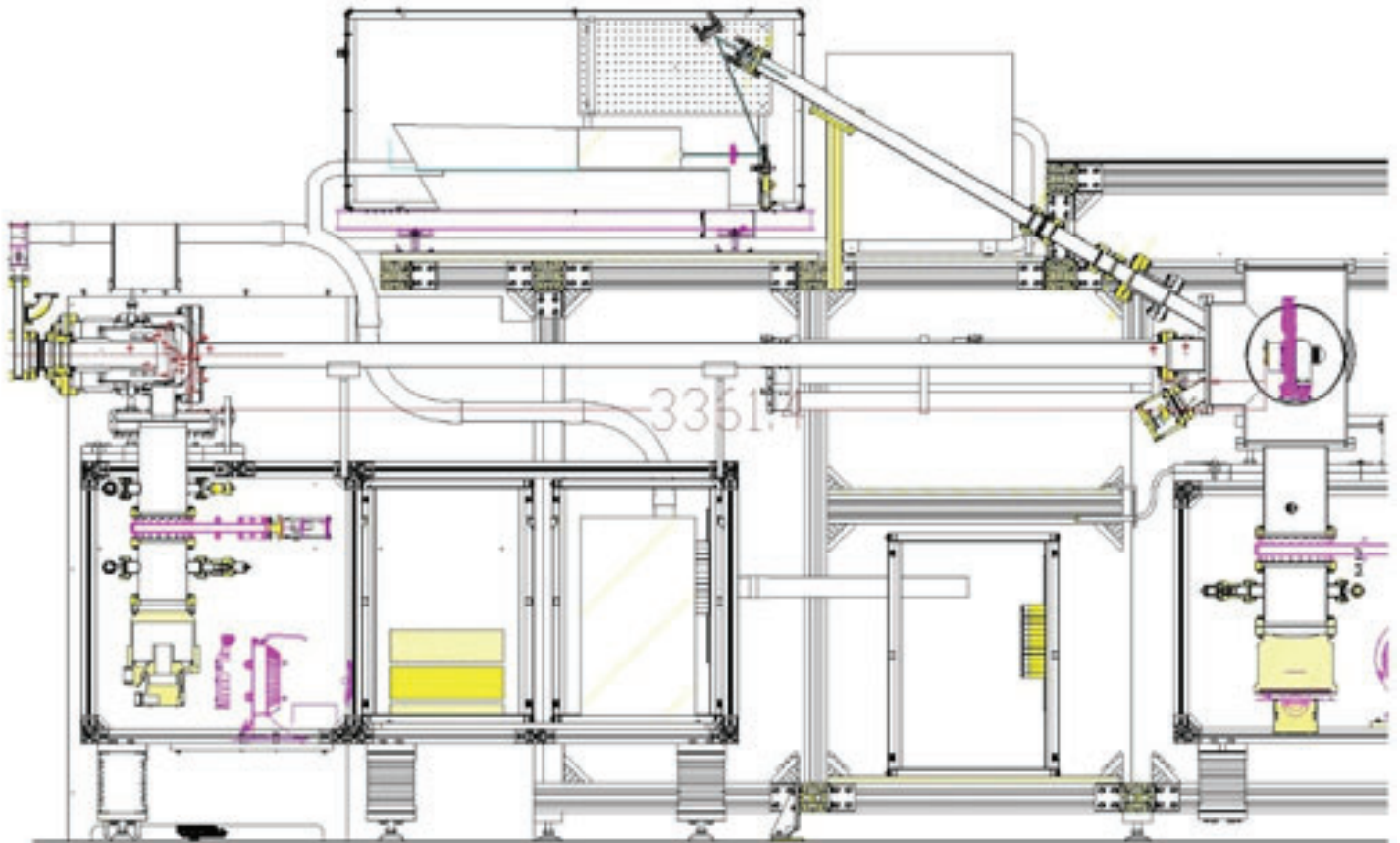
[G]

Material	Desired Current (mA)	Desired FWHM ( $\mu$ s)
Fe	0.5	100
Ta	0.1	200
Al	1.0	50

[H]

Material	Current from 2.86 m away (mA)	Solenoid Multiplication
Fe	0.0861	5.81
Ta	0.0208	4.80
Al	0.0396	25.28

[I]



## VII. References

- [1] Kanesue, T., et al. "Low Charge State Heavy Ion Production with Sub-Nanosecond Laser." *Review of Scientific Instruments*, vol. 87, no. 2, 2016, doi:10.1063/1.4935625.

# Study of the nonlinearity response for Large Synoptic Survey Telescope sensors

Thomas Hagan, Physics, Northern Michigan University, 1401 Presque Isle Ave, Marquette, MI 49855  
Andrei Nomerotski, Physics Department, Brookhaven National Laboratory, Upton, NY 11973

## Abstract

The Large Synoptic Survey Telescope (LSST), undergoing construction on a mountaintop in Chile, will be utilized for Astrophysics and Cosmology research to explore mysteries ranging from Dark Matter and Dark Energy to cataloging the Milky Way. Brookhaven National Laboratory (BNL) participates in the LSST construction by building the sensor modules, composed of Charge Coupled Devices (CCDs), needed for the telescope to operate. Before these sensors can be used, testing is required to ensure that the CCDs are operating properly. This study examines the nonlinearity response, a required test for implementation of the sensor modules, through the analysis of flux generation over time. With the aid of Python coding software, these values were measured and recorded. Outliers in the data were analyzed by checking light exposure levels on the CCDs to reveal drops in intensity during data collection. This indicated a failure in the sensor used to measure current generated from light exposure. These results will be used to understand the limitations on flux generation along with well capacity for the CCDs. Results will also aid in image processing and data analysis for LSST as well as other sensor testing at BNL.

## I. Background

### A. LSST and CCDs

Over the course of 10 years, LSST will conduct a survey of the night sky, the goal of which is to tackle unanswered topics about the universe<sup>1</sup>. Such topics to be examined include the origin of the universe, analysis of the elusive Dark Matter and Dark Energy, the structure of the Milky Way Galaxy, and many others. LSST will conduct a survey, measuring the entire sky every couple of nights, to identify objects that have changed in either position or state. These can be anything ranging from comets hurdling past the Earth, to the evolution of supermassive black holes.

LSST requires a special type of sensor for the analysis of light data, being such a powerful telescope. Each sensor must pass a number of tests with names such as read noise, serial and parallel charge transfer efficiency, and full well. Of these tests, nonlinearity is of particular interest as it relates to the ability of a sensor to collect data from incoming light at an extremely efficient rate. The purpose of this study was to analyze 13 E2V CCD sensors that failed a nonlinearity test and understand causes for their failure.

### B. Flux Generation

CCDs work under the properties of the photoelectric effect wherein photoelectrons are generated from incoming light onto a metal surface<sup>2</sup>. The number of photoelectrons generated, or flux on the surface of a pixel in the sensor, are measured over different exposure times. This is analogous to filling a bucket with water

and observing the change in volume of liquid within the container, assuming the rate of flow is constant. The average number of electrons generated, over all pixels within a specified region, is measured as the flux for a data point. Flux value is proportional to the product of an average current, from a photodiode sensor over a time interval, and the change in time itself for that trial.

A photodiode acts as a means of confirming the flux over a CCD. Current is generated from the photodiode as photoelectrons, which multiplied by a light exposure period, is proportional to the flux on the actual CCD. These values were utilized to generate a line of best fit for the data. A problem exists if the water bucket were to fill up to the top and begin to spill over. In CCD terminology this is referred to as blooming<sup>2</sup>, when a pixel fills up with generated photoelectrons. To avoid this issue, a limited range of the data must be used to avoid skewing the line of best fit. The term nonlinear defines any flux value, within the specified range, which falls more than 2% away from the generated line of best fit.

## II. Methods

### A. Overview of code analysis

Each CCD divides into 16 independent regions or segments. These segments are composed of an array of 517 pixels wide by 2048 pixels long. The data from each segment was extracted from Flexible Image Transport System (FITS) files via Python coding software. The FITS file contained flux values from each segment as well as current measurements at different time trials.

Plots were created using three calculated averages from the data: flux values, photodiode current values, and time change values. Figure 1 shows segment plots of CCD 107, depicting the average flux of each segment as a product of both average current

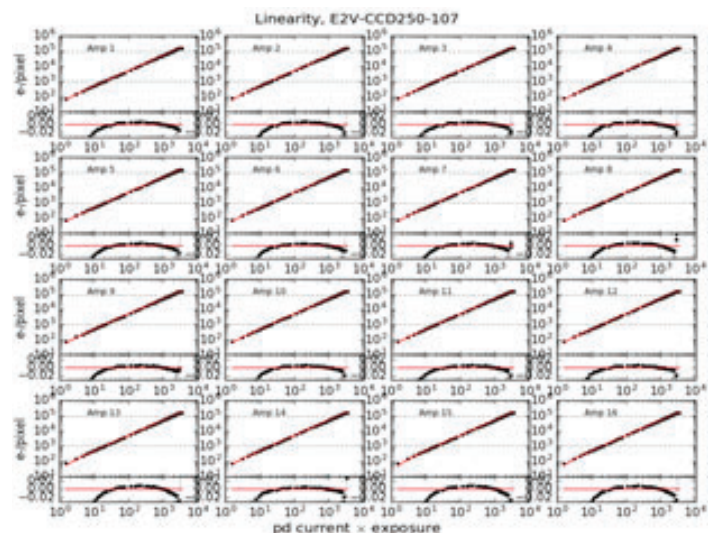


Figure 1. Change in flux (photoelectrons/pixel) as function of average photodiode current and time per trial for CCD 107, which passed nonlinearity. The x-axis is scaled logarithmically.



during a trial and the length of time of a trial<sup>3</sup>. The y-axis is produced from the average flux value from all pixels in a segment while the x-axis is produced from both the time change over a trial and the average current over a trial. Each plot is generated under the assumption that flux and time are the only variables being altered. This means the average current over all trials must remain constant to prevent errors from appearing in data. A line of best fit was generated for each plot with the residual information for each data point depicted underneath the plot. SAOImage DS9, a program used for converting FITS files into graphical images, displayed the flux values across all pixels on the CCD for visual confirmation of data.

### III. Data and Results

#### A. Analysis of plots

Examination of the CCDs failing nonlinearity revealed similarities across all segments of the same sensor but changes when comparing separate sensors. Analysis of residual information from failing segments reveal an upward trend of residuals at the lower boundary for allowed nonlinearity (lower boundary = -2% error from best-fit line). This occurred near the starting range of data (1000 – 2500 electrons/pixel). Figure 2 shows Segment00 plotted from CCD-195 that failed the nonlinearity test with its corresponding residual information, or distance of each data point away from the line of best fit. The upper plot shows the photoelectrons generated over time while the lower plot shows a logarithmic scale of the residual information from the top plot. A failure of nonlinearity results from residuals in flux generation to fall either above or below the horizontal dotted line, within the region of interest indicated by the two horizontal lines, as depicted in figure 2.

Current values measured from the photodiode were examined next. In theory, the only values that should change when plotting the flux, as in figure 2, are the time indexes. Measurements from the photodiode indicate both peaks and valleys in the current over time, which is inconsistent with flux values. If current values drop then flux at that point should also drop. Figures 3 and 4 show current over time comparisons, however, figure 3 is composed of multiple exposure trials within a single plot. Data points within figure 3 are calculated from the integration of current over time

measured by the photodiode while illuminated. Figure 4 shows current plotted over a specified time. Figure 4 represents one trial of data used to generate the values shown in figure 3. The red line in figure 3 represents the region of interest when determining a pass or fail of nonlinearity.

To ensure the oscillations in current are not a result of a bad experimental run, other sensors that failed nonlinearity were analysed. Flux values and photodiode measurements were examined for other E2V CCDs that failed. Figure 5 shows Segment00 from three additional sensors with their residuals. All three residual plots show similar results to figure 2. The three CCD sensors seen from left to right are CCD sensors 216,217, and 239.

Upon further examination, all failing sensors reveal the same oscillations when plotting the average photodiode measurements

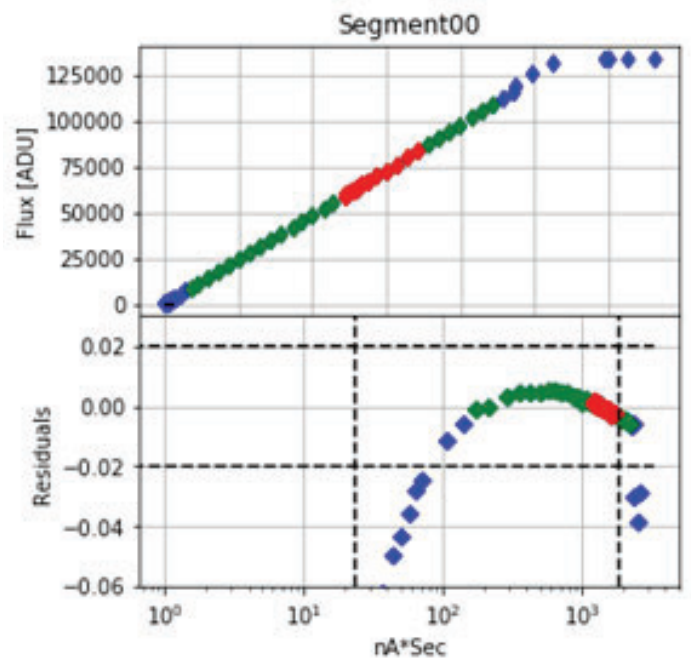


Figure 2. Change in flux (photoelectrons/pixel) as function of photodiode current and time per trial for Segment00 of CCD 195. Boundaries for the test are upper and lower horizontal dotted lines. Two vertical lines are the regions of interest.

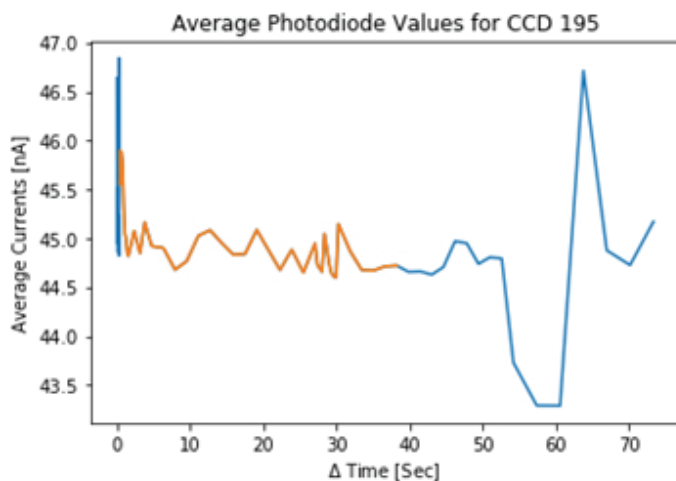


Figure 3. Plot of average current values per time period as a function of time that passes at each period. The red region of the plot contains the x-axis data points for figure 2 within the range of interest for nonlinearity.

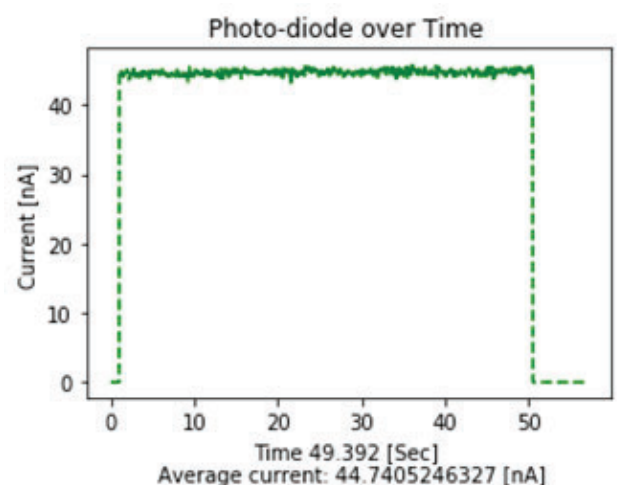


Figure 4. Plot of current as a function of time for a sample photodiode time period. Integration of this plot results in one data point on figure 3.

over time. Figure 6 shows the photodiode values for all CCDs tested that fail. In this figure, the integrated current values per time interval for all CCDs were plotted. The bottom right corner of the plot contains a label corresponding to each CCD tested. Interestingly, there was no consistency in max flux value among the different photodiode sensor measurements as well as no consistent length in exposure time.

The current measurements from the photodiode were removed from all flux generation plots to test if the residuals were being affected by oscillations in the photodiode currents. CCD 195 was the first sensor to be examined using this approach. Figure 7 contains two plots from Segment00 on this sensor. The plot on the left includes data from the photodiode, in the x-axis, while the plot on the right excludes data from the photodiode. After the removal of the photodiode current values, the residuals shifted such that no point fell above or below the line for allowed non-linearity.

All of the sensors failing nonlinearity were checked next. The flux generated over each sensor was examined, both with values from the photodiode measurements and without the photodiode, to determine if any of the other residuals would be affected by the lack of current averages. After removal of current, from the x-axis of all CCD plots, most CCDs pass the nonlinearity test. Figure 8 shows CCDs 216, 217, and 239 plotted with and without current values from the photodiode, similar to figure 7. All three CCDs show that if current is removed from the data, residuals for each segment pass the nonlinearity test. It is important to note

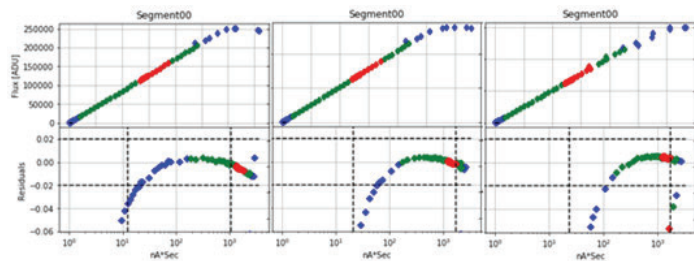


Figure 5. Change in flux (photoelectrons/pixel) as function of photodiode current and time per trial for Segment00 from CCDs 216, 217, and 239 with corresponding residual values. Boundaries for test are upper and lower horizontal dotted lines. Two vertical lines are the regions of interest.

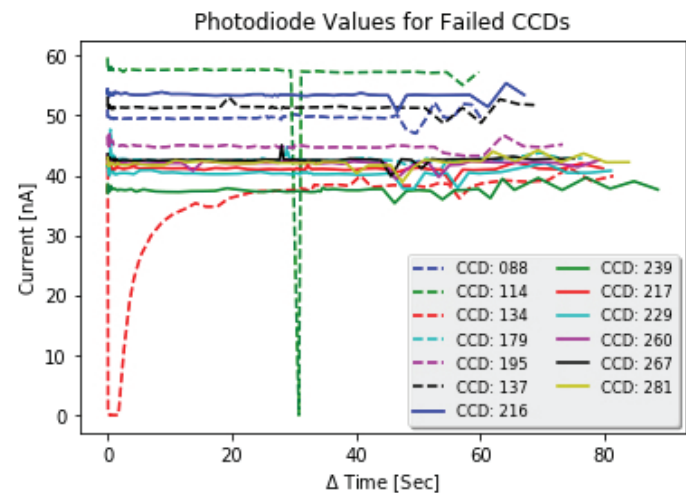


Figure 6. All photodiode values for 13 CCD sensors plotted as average currents per sensor integrated over exposure times. Each CCD is labeled according to its own photodiode measurements.

that, even though most residuals sensors were adjusted when removing issues from the photodiode, not all sensors were adjusted by removing current. This could be due to other effects when taking data.

#### IV. Conclusion and Recommendations

When analyzing the flux generation over time on a sensor, as long as there is a constant light source, the rate of photoelectrons generated should be relatively linear. Analysis of 13 CCDs reveal a potential issue with the method of data collection from the photodiode sensor. Measurements reveal oscillations in the current values over all trials. This poses a problem seeing as each sensor relies on a uniform current output for reliable data collection.

This issue could result from a number of problems with the photodiode. There could be an error with the sensor itself which would require an updated for future usage. There could also be a failure in ensuring the CCDs take data in a uniform environment resulting in unexpected light exposure. The photodiode needs to be examined for any future measurements in CCD tests. Examination of the photodiode and correction of potential issues will lead to an increase in quality for sensor testing. This can lead to higher accuracy in data collection for LSST collaboration at BNL.

#### V. References

- 1 "About LSST". *About LSST | The Large Synoptic Survey Telescope*. Np., n.d. Web. 04 Aug. 2017. <<https://www.lsst.org/about>>
- 2 Janesick, James R. *Scientific Charge-coupled Devices*. Bellingham (Wash.): pages 23-25 and 274-275, SPIE, 2001. Print.
- 3 Sensor 107 lsst eo testing report

#### VI. Acknowledgements

This project was supported in part by the U.S. Department of Energy, Office of Science, Office of Workforce Development for Teachers and Scientists (WDTS) under the Science Undergraduate Laboratory Internships Program (SULI).

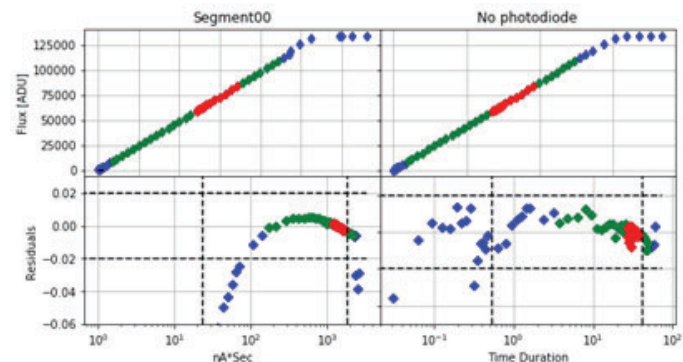


Figure 7. Plots of flux (photoelectrons/pixel) generated over time for Segment00 from CCD 195. The plots on the left include photodiode in the x-axis whereas the plots on the right exclude values from the photodiode. The horizontal dotted lines correspond to the nonlinearity boundaries for the residuals. The vertical dotted lines correspond to the range of relevant data for the trial.

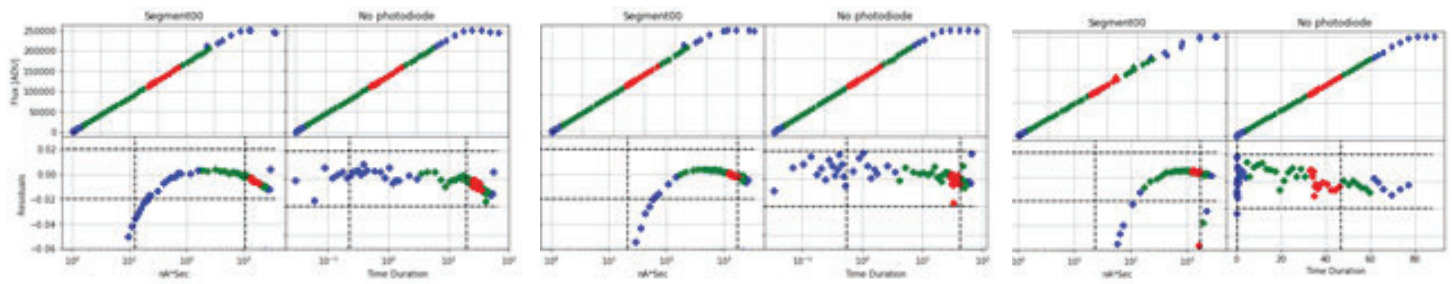


Figure 8. Flux generation over time for Segment00 of CCDs 216, 217, and 239 from left to right. The plot and residuals on the left portion of each plot contain current values from the photodiode while the plot and residuals on the right portion lack current values. The horizontal dotted lines correspond to the boundaries for nonlinearity and the vertical lines are the range limits.



# ZSM-5 supported molybdenum carbide and oxide catalysts for methane dehydroaromatization: elucidation of active sites and deactivation pathways

Leah Harper and Sheima Khatib, Department of Chemical Engineering, Texas Tech University, Lubbock, TX 79409  
Sanjaya Senanayake and Jose Rodriguez, Chemistry Department, Brookhaven National Laboratory, Upton, NY 1197

## Abstract

Heterogeneous metal oxide catalysts supported on zeolites can be used to directly convert methane into aromatic products in a process called Methane Dehydroaromatization (MDA). Work performed in our group demonstrates that molybdenum carbides ( $\text{MoC}_y$ ) supported on zeolites tend to outperform molybdenum oxides ( $\text{MoO}_x$ ) in activity and selectivity to benzene. The identity of the exact species responsible for the activation and selective conversion of methane to aromatics remains unclear. In this study, we investigated the nature of the active species and the deactivation mechanism of  $\text{MoO}_x$  and  $\text{MoC}_y$  catalysts supported on Zeolite Socony Mobil-5 (ZSM-5). Catalyst samples with 6 % and 10 % loadings of  $\text{MoO}_x$  and  $\text{MoC}_y$  were synthesized, structurally characterized, and tested in reaction at Texas Tech University. The surface chemistry of the samples was investigated by ex situ and in situ Soft X-ray Absorption Spectroscopy (sXAS) at NSLS II and Ambient Pressure X-ray Photoelectron Spectroscopy (AP-XPS) in BNL Chemistry. sXAS spectra taken at the carbon and oxygen K-edges suggest that  $\text{MoO}_x$  is converted to  $\text{MoC}_y$  during reaction, while the oxygen state of the zeolite support remains unchanged. AP-XPS data observed the carburization process in MDA. Future studies will investigate the effect of Fe promoter on  $\text{MoC}_y$  and  $\text{MoO}_x$  catalyst activity and selectivity, and Fe- $\text{MoO}_x$  mixed phase chemistry.

## I. Introduction

As illustrated in Fig. 1, there are two approaches to processing methane: direct and indirect. Indirect methods rely on the production of syngas as an intermediate product, before using other methods to manufacture products such as paraffins, olefins, and alcohols. Direct methods require only one processing step to convert methane to value-added products. Our study will be focused on methane dehydroaromatization, a process used to convert methane to benzene and hydrogen.

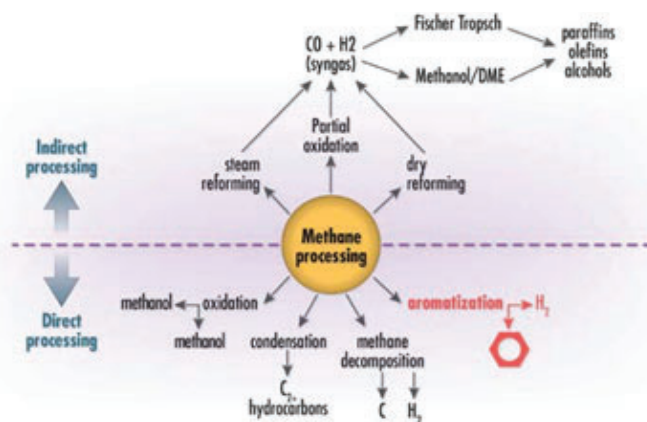


Fig. 1 Methane processing methods.

## II. Background

### A. Methane Dehydroaromatization

Methane Dehydroaromatization (MDA) is a direct method of processing methane that is still being developed at the laboratory scale. The reaction proceeds as shown in equation 1 below.



Methane ( $\text{CH}_4$ ) is transformed to hydrogen and benzene with no other reactants in the presence of a catalyst.  $\text{MoO}_x/\text{ZSM-5}$  was selected as the focus of this study because previous research has shown that they are the most effective catalysts for MDA.

The three stages of MDA, as outlined by Fig. 2, are induction, aromatization, and deactivation. During the induction period  $\text{MoO}_x$  is carburized into the active site,  $\text{MoC}_y$ . In this stage  $\text{CO}_x$  and  $\text{H}_2$  are produced, but no benzene is observed yet. During aromatization, the  $\text{CH}_3\text{-H}$  bond of methane is activated over the  $\text{MoC}_y$  site. These activated hydrocarbons oligomerize into longer chains over the Brønsted acid sites on the zeolite framework. These carbon chains are then linked into 6-membered aromatic rings, also over the acid sites. Finally, the catalytic activity succumbs to deactivation over time. The primary cause of catalyst deactivation is the deposition of carbon over active sites.

### B. Proposed Approach

Traditionally, researchers have prepared  $\text{MoO}_x$  supported on zeolite, then subjected it to reaction conditions. As illustrated in Fig. 3, we propose that by carefully carburizing  $\text{MoO}_x/\text{ZSM-5}$  to  $\text{MoC}_y/\text{ZSM-5}$  before exposing the catalyst to reaction, the sample will have a higher benzene yield with reduced catalyst deactivation. Additionally, because  $\text{MoC}_y/\text{ZSM-5}$  has already been carburized, we expect that this catalyst will have a shorter induction period.

## III. Experimental Methods

### A. Catalyst Synthesis

$\text{MoO}_x/\text{ZSM-5}$  and  $\text{MoC}_y/\text{ZSM-5}$  catalyst were synthesized at Texas Tech University. Samples with metal loadings of 3, 6, 10, 12, and 15 wt% were prepared using incipient wetness impregnation.  $\text{MoC}_y$  catalysts were carefully prepared from  $\text{MoO}_x$  by heating the oxide from room temperature to 700 °C (5 °C per

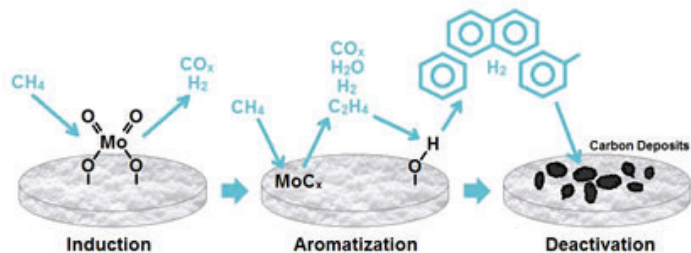


Fig. 2 Proposed mechanism for MDA.

min ramp rate) in the presence on hydrogen and methane. The sample was held at that temperature for 10-15 min under flow of pure methane, then allowed to equilibrate to room temperature under flow of helium.

## B. Activity and Selectivity Characterization

Tests were performed at Texas Tech University. The samples were reacted with methane at 700 °C until significant deactivation (reduction in benzene yield) was observed.

## C. Soft X-Ray Absorption Spectroscopy (sXAS)

Soft X-ray Absorption Spectroscopy (sXAS) scans were taken at CSX-2 at NLSL II. Samples were pressed into indium foil and mounted on a copper plate using carbon tape and then loaded into chamber, then the sample cell was evacuated. Spectra were recorded near the K-edges of C, O, Si, and Al, and the L2,3-edge

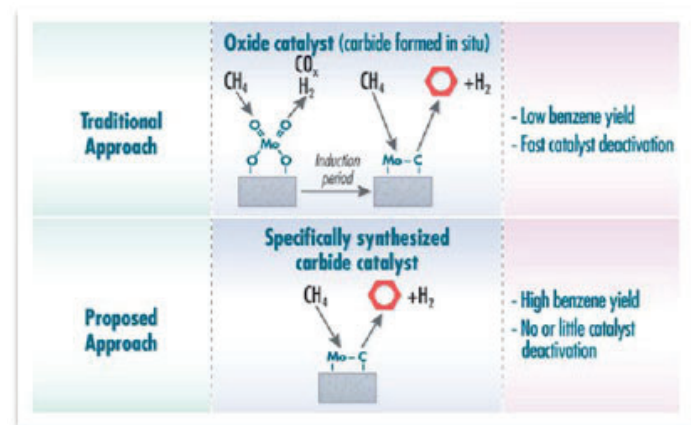


Fig. 3 Traditional versus proposed approach.

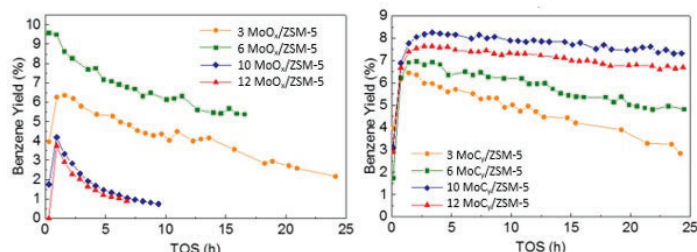


Fig. 4 Benzene yield with time on stream of 3, 6, 10, and 12 wt% loaded a) MoO<sub>x</sub> and b) MoC<sub>y</sub> on ZSM-5.

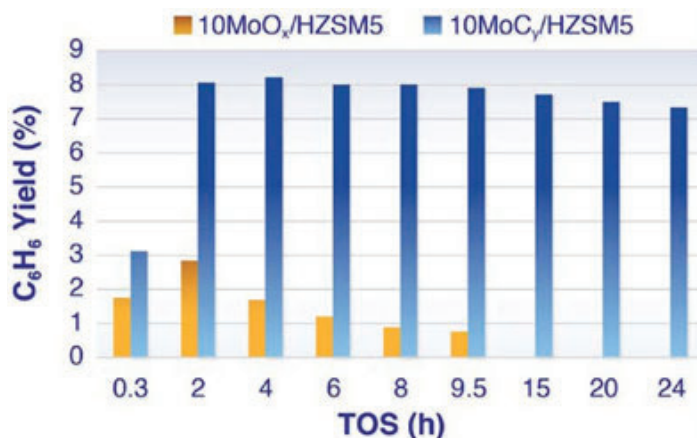


Fig. 5 Benzene yield with time on stream of 10 MoO<sub>x</sub>/ZSM-5 and 10 MoC<sub>y</sub>/ZSM-5.

of Fe. For spectra recorded at the C K-edge, an asynchronous photodiode measurement was used to normalize out background signals due to carbon contamination in the equipment.

## D. Ambient Pressure X-Ray Photoelectron Spectroscopy (AP-XPS)

Samples were pressed into approximately 150 mm diameter wafers on an aluminum plate. The foil was then spot welded onto a stainless-steel plate. The samples were loaded into the cell and the chamber was evacuated to UHV. Ex situ samples were measured under UHV. In situ samples were first annealed under UHV to 690 °C, then exposed to methane for a period of 2 hours.

## IV. Results

See figures 4 and 5.

### B. XRD

See figures 6 and 7.

### C. sXAS

See figures 8 and 9.

### D. AP-XPS

See figure 10.

## V. Discussion

MoC<sub>y</sub>/ZSM-5 catalysts show better catalytic properties (higher benzene yield and stability) compared to MoO<sub>x</sub>/ZSM-5 catalyst. XRD data shows a reduction in crystalline MoO<sub>x</sub> features after reaction. sXAS data suggests that MoO<sub>x</sub>/ZSM-5 transforms to MoC<sub>y</sub>/ZSM-5 under reaction conditions and that the oxygen chemical state of the catalyst surface is identical chemically and electronically. AP-XPS data observed the carburization process in MDA and show co-presence of molybdenum oxide and carbide species during reaction.

## VI. Conclusions

Reactivity studies showed that MoC<sub>y</sub>/ZSM-5 catalysts tend to outperform MoO<sub>x</sub>/ZSM-5 as they maintain a higher benzene yield

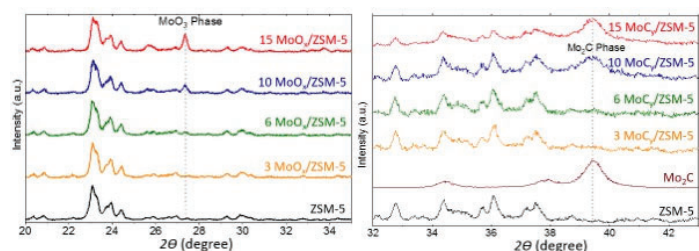


Fig. 6 XRD spectra of a) 15, 12, 10, 6, and 3 wt% loaded MoO<sub>x</sub>/ZSM-5, ZSM-5, b) 15, 12, 10, 6, and 3 wt% loaded MoC<sub>y</sub>/ZSM-5, Mo<sub>2</sub>C, and ZSM-5.

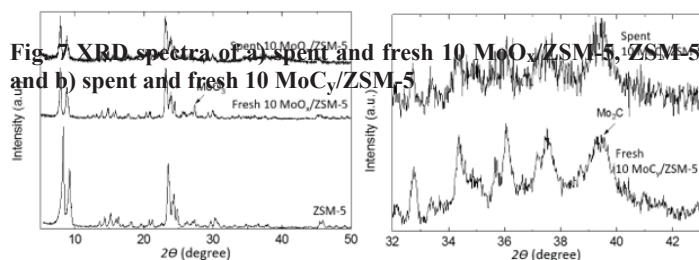


Fig. 7 XRD spectra of a) spent and fresh 10 MoO<sub>x</sub>/ZSM-5, ZSM-5, and b) spent and fresh 10 MoC<sub>y</sub>/ZSM-5.

and are less susceptible to deactivation. X-ray spectroscopy data supports our assessment that  $\text{MoO}_x/\text{ZSM-5}$  is completely carbided under reaction conditions, suggesting that  $\text{MoC}_y/\text{ZSM-5}$  is the active species in our catalyst.

## VII. Acknowledgements

This project was supported by: 1) the U.S. Department of Energy, Office of Science, Office of Workforce Development for Teachers and Scientists (WDTS) under the Visiting Faculty Program (VFP); 2) Texas Tech University.

## VIII. References

Shuqi Ma, Xiaoguang Guo, Lingxiao Zhao, Susannah Scott, Xinhe Bao, Recent progress in methane dehydroaromatization: From laboratory curiosities to promising technology, *Journal of Energy Chemistry*, Volume 22, Issue 1, January 2013, Pages 1-20, ISSN 2095-4956,

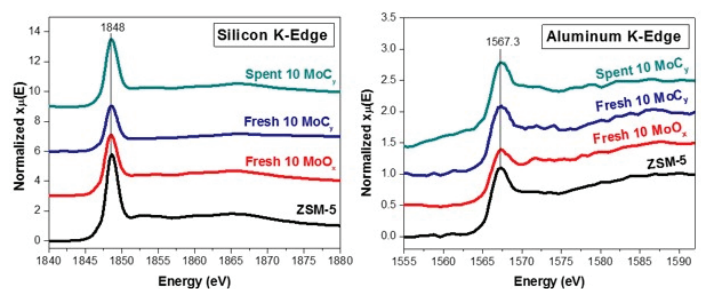


Fig. 8 sXAS spectra of a) the carbon K-edge of fresh 10  $\text{MoC}_y/\text{ZSM-5}$  and spent 10  $\text{MoO}_x/\text{ZSM-5}$  and b) oxygen K-edge of fresh 10  $\text{MoO}_x/\text{ZSM-5}$ , spent and fresh 10  $\text{MoC}_y/\text{ZSM-5}$ , and ZSM-5.

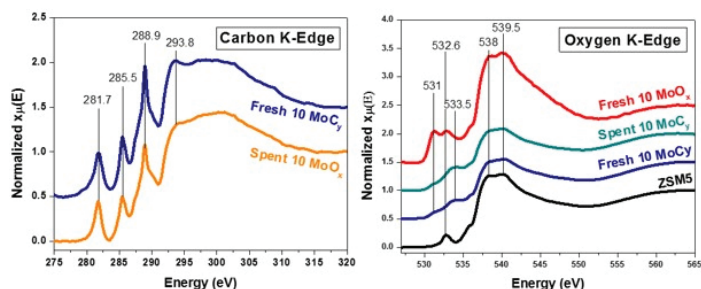


Fig. 9 sXAS spectra of a) the silicon K-edge and b) the aluminum K-edge of spent and fresh 10  $\text{MoC}_y/\text{ZSM-5}$ , fresh 10  $\text{MoO}_x/\text{ZSM-5}$ , and ZSM-5.

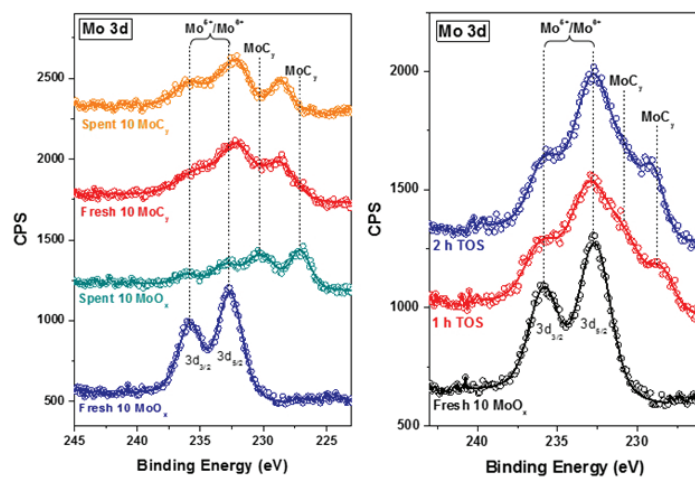


Fig. 10 AP-XPS spectra of a) *ex situ* measurements of spent and fresh 10  $\text{MoC}_y/\text{ZSM-5}$  and spent and fresh 10  $\text{MoO}_x/\text{ZSM-5}$ , and b) *in situ* measurements of fresh 10  $\text{MoO}_x/\text{ZSM-5}$  heated to 690 °C under methane.



# Calibration interval of truck scales within waste management

Matthew Harris, Business Administration, St. Joseph's College, Patchogue, NY 11772  
Steve Stein, Quality Assurance, Brookhaven National Laboratory, Upton, NY 11973

## Abstract

**This project involves extending the calibration intervals of three platform scales used by the Waste Management Division within Brookhaven National Laboratory (BNL). Currently, the scales are on an annual schedule of calibration. The intention of the analysis and report will be to extend this period to 18 to 24-months. One benefit of this interval extension would be to properly gauge whether the scale loses accuracy (considering that annual adjustments might be doing more harm than good to the product's lifespan), and to reduce costs within the department. The Calibration Subject Area allows for an interval extension up to 100%. To validate the consistency of these scales, the calibration data was extracted and analyzed using a statistical process control (SPC) chart in order to reveal variations in the year-to-year fluctuations which naturally occur. These fluctuations compared the post-adjustment measurement of one year, to the pre-adjustment measurement of the next. The difference between these two measurements reveals any tendencies of drift that occurs within the course of a year. The data used for the SPC chart reveals relatively small, cyclical variations. Additionally, the inspection test records show an out-of-tolerance reading occurring only once for one scale in May of 2017. To extend the calibration interval of the scales, a formal report must be submitted to the Waste Management program manager along with a monitoring plan to ensure that the scales maintain accuracy. Following approval of this project, the scales will be shifted to a 2-year interval, with initial 6-12 month monitoring, which will cut the calibration costs by 50%.**

## I. Introduction

Brookhaven National Laboratory's Waste Management Division focuses on handling radioactive, hazardous, and mixed waste. Waste Management is a part of BNL's Environmental Protection Division (EPD) whose main goal is to "[develop] and [deliver] environmental products and services for all Brookhaven stakeholders, including federal, state and local regulators, the public, the U.S. Department of Energy, and internal customers." (Brookhaven National Laboratory-Waste Management) Another support organization active within BNL is the Quality Management Office, which employs Quality Representatives throughout the laboratory. These representatives provide quality assurance services which aide in perfecting processes and ensuring effectiveness and efficiency in the department's methods. During my time at BNL, I have worked with a Quality Representative who has been matrixed out to the Waste Management department.

This project entails analyzing the calibration data on three of the Waste Management Division's truck scales, and performing a cost-benefit analysis to decide whether to extend the calibration interval versus keeping an annual cycle. This interval period

extension that I am initiating is in accordance with the Optimizing Calibration Intervals portion of the Calibration Subject Area, which notes that "If the calibration interval is consistently in tolerance for six to eight intervals, it is recommended that you extend the interval 50% to 100% of the current interval and monitor the results. The decision to increase the interval should be monitored until it is optimized." (SBMS- Calibration)

There are two primary functions for these three truck scales. The first is to weigh waste materials such as radioactive solid waste, and liquid materials that are flammable, corrosive, or toxic. The scales are used in this case to properly characterize the waste. The second function is to weigh waste containers (e.g., bins, drums, sealed containers, intermodals, and sacs). This is required for shipping purposes in compliance with Department of Transportation (DOT) regulations. In both cases, the uses of the scales qualify for an A2 risk rating, according to the Graded Approach Risk Matrix.

## II. Methods

- Extract the necessary data from the calibration reports of the scales (2005-2017 reports).
- Compile the data into a Microsoft Excel spreadsheet. This includes the date of calibration, the nominal value of the standardized weight, and the before and after adjustment values reported by the scales.
- Ensure the accuracy of the data. There was one recent instance of a technician and a supervisor signing off on a test report, despite the fact that the scale was bringing up an out-of-tolerance reading. It should be noted that the tolerance range compares the nominal standardized weight value against the weight reported by the scale (before and after adjustment).
- Calculate the percent change in yearly variations between the after adjustment reading of one year, and the before adjustment reading of the next. (ex. 2016, scale #040357, 1000 lbs.: The before adjustment value of 2016 [1000.8 lbs.] was subtracted by the after adjustment of the same weight range from 2015 [1000 lbs.]. That number was then divided by 0.2, being the resolution to which divisions were measured. Therefore, there have been 4 divisions between 2015 and 2016 for this scale.) This association shows the natural changes that occur in the scales overtime.
- Enter the divisions calculated in step #4 into a Statistical Process Control (SPC) chart. The procedure of utilizing the SPC chart is listed below:
  - Choose the appropriate control chart for your data.
  - Determine the appropriate time period for collecting and plotting data.
  - Collect data, construct your chart and analyze the data.
  - Look for "out-of-control signals" on the control chart.

When one is identified, mark it on the chart and investigate the cause. Document how you investigated, what you learned, the cause and how it was corrected.

- Continue to plot data as they are generated. As each new data point is plotted, check for new out-of-control signals.
- When you start a new control chart, the process may be out of control. If so, the control limits calculated from the first 20 points are conditional limits. When you have at least 20 sequential points from a period when the process is operating in control, recalculate control limits.

(Information received from Nancy R. Tague's The Quality Toolbox)

- Contact the manufacturer and/or distributor of the product to learn any additional recommendations or regulations that might have been overlooked.
- Once it is decided that the data indicates a stable scale, create a report to formally suggest the interval extension of the scale calibration interval. This report includes the above data, an explanation of the results, and an internal monitoring plan for the scales which will occur every 6 months indefinitely.

### III. Data/Results

The Subject Area allows for an interval extension under the condition that the scale has been within tolerance for the last 6 to 8 intervals. However, on two different occasions there have been out of tolerance readings for a scale (Scale serial #040357 for the year 2017 & serial #040358 for the year 2016). With these isolated events, this complicates the process of allowing an extended calibration interval. This requires further data analysis to ensure a stable condition for these scales. Additionally, it should be noted that when considering out of tolerance ranges, guard bans are put in place due to the nature of these scales use. These guard bans are a further safety measure which institute a much stricter tolerance

allowance than would be reasonably necessary to maintain accuracy and overall safety. These purposefully slight allowances of deviation from the standard ensure that true tolerance levels that would impact Waste Management functions never would be exceeded for these scales. Therefore, although the scales read as out of tolerance, they are still well within the legal allowable limit of variance. A calibration interval extension is still justifiable under the right circumstances.

A word on scale adjustments: adjustments are made periodically if the difference between the standard weight and actual weight is substantial. The scales' pre-adjustment readings are "as-found" while the post-adjustment readings are "as-left". If no adjustment was needed, then the "as-found" and "as-left" values are the same.

The data that was extracted for this report (figure 1) focuses on the "as found" readings compared to the standard in determining tolerance level. A further step was taken, and the difference between the "as left" readings of one year, and the "as-found" readings of the following year were also measured. This data tracks the natural upward or downward trend of the scale accuracy, and a scale that keeps these fluctuations within a reasonable level should be qualified for an extended calibration interval period. See the attached chart for the calibration data on the three scales, along with the Statistical Process Control (SPC) graphs which measured the year-to-year variations. These SPC graphs can be found with the Excel spreadsheet provided at the end of this section. (Figure 2)

An email correspondence with Paul Gerard, V.P. Sales of Advance Scales (distributor of Weigh-Tronix Scales) supports this extension of the annual calibration interval; he was open to the concept that this interval could be extended to an 18-month or 24-month cycle. Paul did not cite any company or regulatory mandates to oppose this extension; in his words "...it depends on the level of inaccuracy you can tolerate."

\*It should be noted that not all of the measurements taken in the calibration process used the same weight values, making it

Test Parameter	Test load	As found	As left	Tolerance d (+/-)	Tolerance (+/-)
<b>Increasing Load</b>	2000 lbs	2000 lbs	2000 lbs	2	4 lbs
	4000 lbs	4000 lbs	4000 lbs	2	4 lbs
	6000 lbs	6002 lbs	6002 lbs	3	6 lbs
	8000 lbs	8000 lbs	8000 lbs	3	6 lbs
	10000 lbs	10000 lbs	10000 lbs	5	10 lbs
<b>Decreasing Load</b>	8000 lbs	8000 lbs	8000 lbs	3	6 lbs
	6000 lbs	6002 lbs	6002 lbs	3	6 lbs
	4000lbs	4000lbs	4000lbs	2	4 lbs
	2000 lbs	2000 lbs	2000 lbs	2	4 lbs
<b>Shift Test</b>	4000 lbs	4000 lbs	4000 lbs	2	4 lbs
	4000 lbs	4000 lbs	4000 lbs	2	4 lbs

As found:  Accept  Reject      As left:  Accept  Reject

Comments: Scale in good condition.

Figure 1. Sample Calibration Report

difficult to compare some of the calibration data. Values that were not directly comparable, due to an absence of a unified standard, were given assumed values based on contextual data. It is not likely that these gaps in the data lead to any significant change.

\*It should also be noted that the company performing the calibrations shifted between 2012 and 2013, with Fairbanks Scales taking control after this date. Fairbanks uses more weight, in some cases more than twice the amount, than the previous company during the calibration process. While some would look at the data in the graph and infer that the scales have become less accurate and more prone to variability since 2012, it is more likely the case that Fairbanks is finding a more precise measurement of variability, which was not detected with the minimal weights used in prior years. The data maintains that all three of the scales are fit for a 24-month calibration interval period.

#### IV. Conclusion and Recommendations

In summary, data indicates that these three platform scales utilized by the Waste Management Division can hold calibration consistently. In accordance with the Calibration Subject Area, it is justifiable to suggest increasing the time period of calibration from 12 months to 24 months. This decision is based off historical data of calibration reports, statistical analysis of the calibration trends, and recommendation from the distributor of the product. Currently, the formal report which outlines this data and plan has not yet been approved by the department. Once approved, a plan will be enacted which includes a monitoring plan in which the Quality Representative within Waste Management will semi-annually perform calibration checks.

#### V. References

Brookhaven National Laboratory (Waste Management)-Brookhaven National Laboratory. (Environmental Protection Division). (U.S. Department of Energy),retrieved from <https://intranet.bnl.gov/esh/env/>

Brookhaven National Laboratory (Quality Management Office)- Brookhaven National Laboratory. (Planning, Performance, and Quality Management). (US Department of Energy), retrieved from <https://intranet.bnl.gov/qmo/>

Nancy R. Tague's The Quality Toolbox, Second Edition, ASQ Quality Press, 2005,pages 155-158. Retrieved from <http://asq.org/learn-about-quality/data-collection-analysis-tools/overview/control-chart.html>

SBMS. Calibration Subject Area, Optimizing Calibration Intervals. Retrieved from [https://sbms.bnl.gov/sbmsearch/subjecta/68/68\\_Exh7.cfm](https://sbms.bnl.gov/sbmsearch/subjecta/68/68_Exh7.cfm)

#### VI. Acknowledgements

I would like to thank my mentor, Steve Stein for his help and guidance throughout this program. A special thanks to the Waste Management Division and the Quality Management Office for their support and hospitality. This project was supported in part by the U.S. Department of Energy, Office of Science, and Office of Workforce Development for Teachers and Scientists (WDTS), under the Science Undergraduate Laboratory Internships (SULI) program.

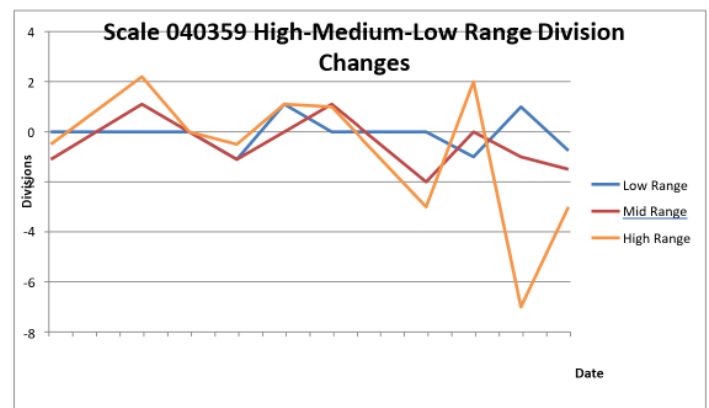


Figure 2.



# Analyzing meteorological measurements and determining the operational comparability

Brooke Hildebrand, Environmental and Climate Sciences Department, Suffolk County Community College, Selden, NY 11784

Scott Smith and John Heiser, Environmental and Climate Sciences Department, Brookhaven National Laboratory, Upton, NY 11973

## Abstract

**The Environmental and Climate Sciences Department at Brookhaven National Laboratory employs sensor systems mounted on a meteorological tower to take measurements of temperature, wind speed and wind direction, using identical sensors at multiple levels (ten, fifty and eighty five meters) that take simultaneous measurements at one minute intervals. Since the identical sensors do not always record equivalent measurements at the same time, the operational comparability is calculated to quantify the overall difference. The American Society for Testing and Materials (ASTM) published an article [“Standard Practice for Determining the Operational Comparability of Meteorological Measurements”] [1] that aided my success in finding the operational comparability among other measurements for the first time here at the lab, for every month’s collected data in 2015 and 2016. Using 2015s measurements, I was then able to create multiple graphs to efficiently display the results and observe where any specific trends or discrepancies occurred. I also created a chart to record all of 2015s operational comparability measurements by month and elevation, including the average and range. By doing so, I found that the fifty meter sensor has the highest variability, and the fifty meter wind direction contains the highest operational comparability measurements (less accurate). Furthermore, I concluded that there is not only an issue at 270 degrees for the fifty meter sensor as expected, but there is also a newfound issue around 200 degrees! These findings will enable the scientists and engineers associated with this project to easily assess the precision of the sensors and make adjustments if necessary.**

## I. Introduction

The sensors are connected to a data collection system where Campbell Scientific Loggernet software package collects the meteorological data. Campbell Scientific Loggernet database program, LNDB, forwards this data to a SQL database maintained by Brookhaven National Lab’s (BNL) Information Technology Division. The data is stored in this database until it is retrieved using the program HeidiSQL. It can then be post processed in any manner, or stored in another location. The tower was placed in an open field west of the majority of the Brookhaven building complex at latitude 40°52.20’N and longitude 72°53.35’W in May of 1981. The original sensors were used from this time until about 2010 when they were switched to the current sensors-R.M. Young Company, model number 05106 [2]. Since both types of sensors have been placed in operation (about thirty six years in total), the operational comparability of their measurements has never before been calculated. According to the ASTM article [1], the operational compatibility represents the root mean square of the difference between simultaneous readings from two systems measuring

the same quantity in the same environment. This is valuable information because if one sensor is unable to record data during a specific time period, the identical sensor’s measurements may possibly be used interchangeably if the operational comparability is within acceptable parameters. It also shows where any significant discrepancies occur between measurements which will allow for sensor adjustments to take place if necessary. The focus of this study is to find and evaluate the operational comparability of the wind sensors located at fifty and eighty five meters on the meteorological main tower, as well as assess a suspected issue that occurs when the wind direction measurement is equivalent to roughly two hundred and seventy degrees. I was able to successfully complete these tasks within my ten week internship through the use of specific software and the help of my mentors.

## II. Progress

### A. A. Technical Approach

The ASTM article [1] provides a lot of valuable information regarding the operational comparability including the correct sensor setup, data sampling, restrictions, equations to use, etc. These procedures produce measurement samples that I was then able to use for statistical analysis. See Figure 1 below for all of the terms and equations that have been applied to this project.

I started off my summer project by familiarizing myself with the terminology and equations discussed in the article [1] so that I could properly apply them to the desired data sets. I also familiarized myself with the software that I used to conduct my research including Microsoft Excel, Openoffice, and HeidiSQL. I then received data for every month in 2016 from my mentor, Scott Smith, including the wind speed, direction, temperature, etc. for sensor A and B at fifty and eighty five meters. In order to correctly input the equations as functions into Excel and Openoffice, I watched tutorials online and visited their help sites [3] [4]. Since the sensors record specific measurements every single minute, one month worth of data contains about forty thousand measurement values for one aspect (wind speed or direction, etc.). Therefore, working with the data is rather time consuming. Once I successfully created various spreadsheets with

May 1’s data and applied all of the necessary functions, I moved on to each month in 2016. While doing so, I had meetings with my mentors, Scott Smith and John Heiser, where we discussed special parameters regarding wind direction. See Figure 2 for a diagram to help understand. When dealing with wind direction, zero degrees is equivalent to three hundred and sixty degrees. By looking at Figure 2, it is clear to see that the shortest path between point A and B is the green path. However, if you were to subtract B’s value from A’s (like many of the equations require), the result would be two hundred and seventy degrees which is not the true distance between them. In order to fix this issue, we came up with an IF statement that I incorporated into ev-

ery single wind direction spreadsheet. The statement is as follows;  
 $= IF (ABS(B2 - C2) > 180; ABS((ABS(B2 - C2) - 360));$   
 $ABS(B2 - C2) )$ , which says that if the absolute value of the difference between the two sensor measurements is greater than one hundred and eighty degrees, then subtract three hundred and sixty

and take the absolute value for the actual distance, otherwise keep the given value. This guarantees that all of the values will be positive and less than or equal to one hundred and eighty degrees.

Once I finished and analyzed the measurements for every month in 2016, I observed that many months were either missing

Term	Variable	Equations
Systematic Difference	$d$	$d = \frac{1}{N} \sum_{i=1}^N (x_{ai} - x_{bi})$
Operational Comparability	$C$	$C = \pm \sqrt{\frac{1}{N} \sum_{i=1}^N (x_{ai} - x_{bi})^2}$
Estimated Standard Deviation of the Difference	$s$	$s = \pm \sqrt{C^2 - d^2}$
Skewness	$M$	$M = \frac{\sum_{i=1}^N ((x_{ai} - x_{bi}) - d)^3}{N^3}$
Kurtosis	$K$	$K = \frac{\sum_{i=1}^N ((x_{ai} - x_{bi}) - d)^4}{N^3}$

Figure 1; Terms and equations

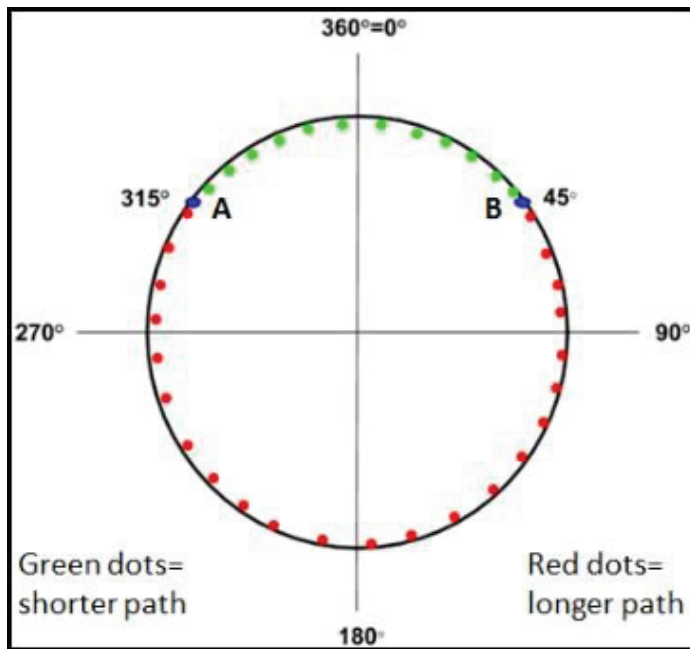


Figure 2; Wind Direction Specification

2015								
Month	O.C for WSat 50m (m/s)		O.C for WSat 85m (m/s)		O.C for WDat 50m (degrees)		O.C for WDat 85m (degrees)	
January	0.218981769	✓	0.389564858	✓	11.73026246	X	6.1367174	✓
February	0.227348079	✓	0.340937918	✓	12.21870994	X	8.756140265	X
March	0.333592756	✓	0.25389607	✓	15.39384878	X	6.184220426	✓
April	0.45497099	✓	0.725492719	OK	11.38668856	X	6.63062337	OK
May	0.269815169	✓	0.360822579	✓	11.81924081	X	6.680123105	OK
June	0.350465426	✓	0.863160036	X	10.1524447	X	6.055515429	✓
July*	0.153413939	✓	0.185490986	✓	5.713079128	✓	3.313975906	✓
August*	0.318819077	✓	0.280802604	✓	5.050468283	✓	3.722007449	✓
September	0.531317105	✓	0.707107474	OK	6.836859834	OK	3.986758338	✓
October	0.492565613	✓	0.598513939	✓	4.591460238	✓	4.149465787	✓
November	0.409959849	✓	0.523556792	✓	5.895413661	✓	3.673398977	✓
December	0.524835951	✓	0.640278305	✓	5.996712349	✓	4.289810444	✓
<b>Average</b>	<b>0.35717381</b>	✓	<b>0.489135357</b>	✓	<b>8.898765729</b>	X	<b>5.298229741</b>	✓
<b>Range</b>	<b>0.153413939</b>		<b>0.185490986</b>		<b>4.591460238</b>		<b>3.313975906</b>	
	-		-		-		-	
	<b>0.531317105</b>		<b>0.863160036</b>		<b>15.39384878</b>		<b>8.756140265</b>	
<b>*Key*</b>	✓ = Acceptable, within O.C parameters OK = Within one increment of te O.C parameters X = Not acceptable, not within O.C parameters							

Figure 3; Operational Comparability Record for 2015

data for a particular sensor or had -999 replacement values which indicates that the sensor was not recording data at that time. Under Scott's supervision, I then extracted the necessary data for all of 2015 using HeidiSQL. This year contains more reliable data and enabled me to give a better analysis. After spending an immense amount of time to complete all of 2015's spreadsheets, my next task was to gather all of the wind direction measurements for every month in 2015 and assemble them into one spreadsheet (~482,000 data points). By doing so, I was able to create multiple graphs to illustrate my findings and evaluate any noticeable trends or issues.

### III. Results

Once I calculated the operational comparability (O.C) for every month in 2015, I put the values into a chart to observe trends and compare to the acceptable parameters which are 0.6 m/s for wind speed, and 6 degrees for wind direction (parameters are half if using only one sensor) (See Figure 3). I found that the wind speed results for fifty meters are all acceptable for the entire year while the eighty five meter values are mostly acceptable besides three months- two are within one increment and one is unacceptable. The rough average O.C for fifty meters is .3572 m/s with a range of 0.1534-0.5313, and for eighty five meters it is 0.4891 with a range of 0.1855-0.8632. However, the O.C for the wind direction at fifty meters and eighty five meters are mostly not within the acceptable parameters (fifty meter sensor has the highest values by far and is completely off while a few values of the eighty five meter sensor are off) until a sensor alignment occurred between July and August that decreased the O.C by about half, which made the values within the acceptable parameters. The rough average O.C for fifty meters is 8.899 with a range of 4.591-15.403, and for eighty five meter it is 5.298 with a range of 3.314-8.756.

By comparing the graphs with no filter (Figure 4 and 6) to the graphs with a filter (Figure 5 and 7), it is clear to see that low values of windspeed (2.5 m/s or less) are where the highest variability in measurements occur, since the graphs without the filter have a greater amount of scattered points. The graphs that contain wind speed filters (Figure 5 and 7) show that the sensors are actually very precise above low wind speeds considering the lines are mostly uniform with only a few outliers. Furthermore, by creating these graphs I was able to confirm that there does seem to be a discrepancy around 270 degrees as expected, but only for the fifty meter sensor. Not only was I able to verify this, but I also came across a newfound issue around 200 degrees that was not anticipated! (See figure 4).

### IV. Conclusions

The chart I created for every month's operational comparability of 2015 demonstrates the importance and use of this function. When it is observed that values are not within the acceptable parameters, altering the position of the sensors accordingly results in an increased accuracy of measurements. The O.C data indicates that the fifty meter sensor has a higher variability in measurements than the eighty five meter sensor, which is plausible since at higher levels there is usually a larger wind force that would enable more precise measurements. The fifty meter graph (Figure 1) is very significant since it verifies that the issue around 270 degrees is real as well as a new found issue around 200 degrees, and that it should be taken care of. During my internship here at Brookhaven

National Lab, I have gained an immense amount of knowledge regarding meteorological processes and how to extract, interpret, and analyze data using valued software. I have also enhanced my personal abilities when dealing with problem solving, time management and recording impressive time logs.

### V. References

1. ASTM D4430-00(2015) Standard Practice for Determining the Operational Comparability of Meteorological Measurements, ASTM International, West Conshohocken, PA, 2015, <https://doi.org/10.1520/D4430-00R15>
2. "MarineWind Monitor." *R. M. Young Company :: Products :: MarineWind Monitor - Model05106*. R. M. Young Company, n.d. Web. 28 July 2017.
3. "Excel help center." *Excel help - Office Support*. Microsoft, n.d. Web. 28 July 2017.
4. "Welcome to Apache OpenOffice Support." *Apache OpenOffice*. N.p., n.d. Web. 31 July 2017.

### VI. Acknowledgments

I would like to thank the National Science Foundation for sponsoring this internship, the staff at Brookhaven National Lab for being such welcoming hosts, and the Department of Energy for giving me this opportunity. I would also like to send a sincere thank you to my mentors Scott Smith and John Heiser, as well as Noel Blackburn, Mike Stegman, Gregory Fries, and Candice Foley. "This project was supported in part by the U.S. Department of Energy, Office of Science, Office of Workforce Development for Teachers and Scientists (WDTS) under the Community College Internships Program (CCI)."

### VII. Appendix

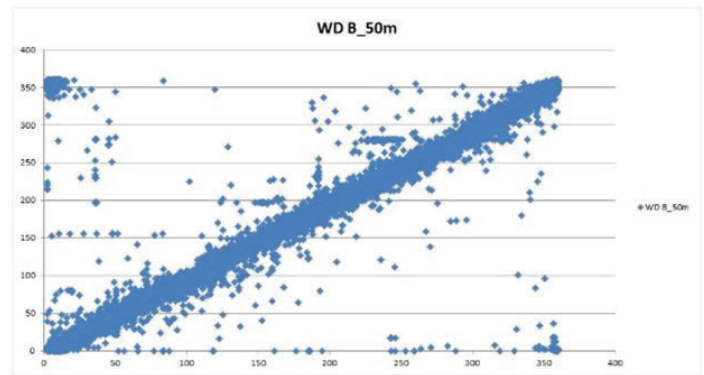


Figure 4; Graph of WD A\_50m (y-axis) vs. WD\_B 50m (x-axis), No filter



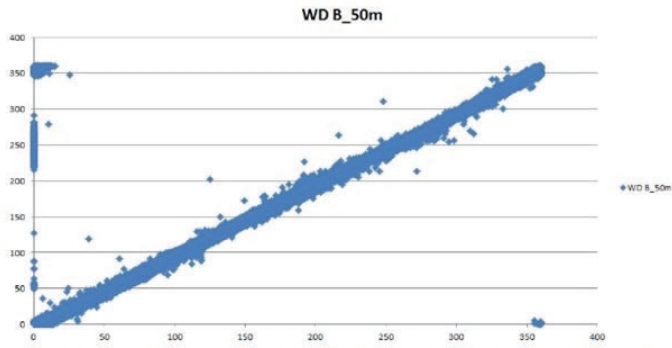


Figure 5; Graph of WD\_A\_50m (y-axis) vs. WD\_B\_50m (x-axis), Filter; only includes WD values with a wind speed greater than 2.5 m/s

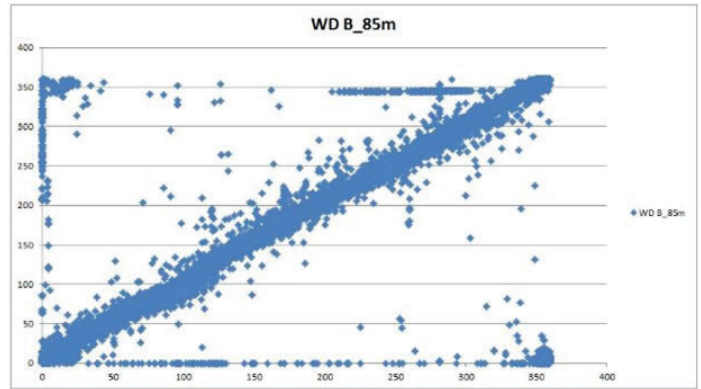


Figure 6; Graph of WD\_A\_85m (y-axis) vs. WD\_B\_85m (x-axis), No filter

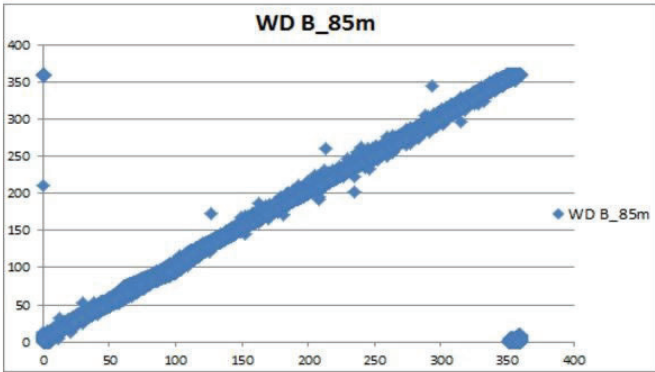


Figure 7; Graph of WD\_A\_85m (y-axis) vs. WD\_B\_85m (x-axis), Filter; only includes WD values with a wind speed greater than 2.5 m/s

# Vast challenge mystery at the wildlife preserve

Rumeel Jessamy Computer Science, Lincoln University, Lincoln, PA 19352

Dantong Yu/ Xu Wei, Computational Science Initiative, Brookhaven National Laboratory, Upton, NY 11973

The Visual Analytics Science and Technology Challenge is an annual contest with the goal of advancing the field of visual analytics. The challenge is designed to help researchers understand how software would be used to solve analytic tasks while determining what data transformations, visualizations, and interactions would be beneficial for each particular task. This year there are three mini-challenges and one grand challenge for us to attempt. The team I work with decided to complete one of the mini challenges. The subject of our investigation is the city of Mistford located to the southwest of a large nature preserve. There are signs that the number of nesting pairs of the Rose-Crested Blue Pipit are decreasing by large numbers. A post doc student gained access to several datasets that will help to identify a possible cause of the problem. The datasets I received was very large, so I used two python scripts to break them into smaller more manageable forms of data. Then I wrote another script that helped me check the dataset for any missing dates or possibly any missing reading. I then utilized a program called Tableau Public to graph the data in a way that everyone on the team can visually analyze the data. We then arrived at an answer for the first question of our mini challenge. The nine sensors surrounding the five factories were malfunctioning. They were missing over one hundred readings for the months of April, August, and December. This led us to our next question, which is what chemicals the sensor group is detecting, and what patterns of chemical releases do we see as being reported in the data? These challenges are open to participation by individuals and teams in industry, government, and academia.

Chemical	Date Time
AGOC-3A	20,027
Appluimonia	19,810
Chlorodinine	19,809
Methylosmolene	19,597

Fig. 1. Total Number of Records Per Chemical

In Figure 2, we plotted the count of hourly reading for each chemical at each monitor. It is very clear that there are also times that sensors performed double readings presented as a larger square in Figure 2 and no reading presented as blank in Figure 2 for the other chemical at the exact same time. Therefore, we did not count this missing data as above because we assume that one of the double readings presents the other chemical release.

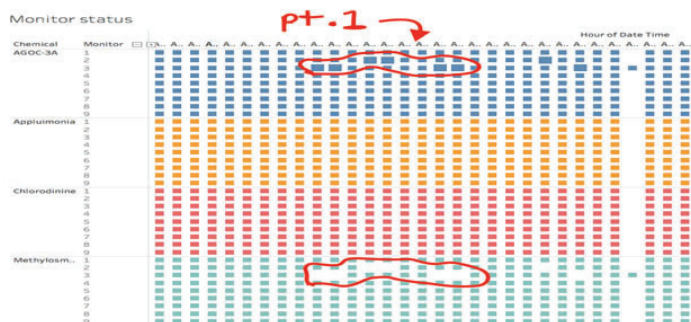
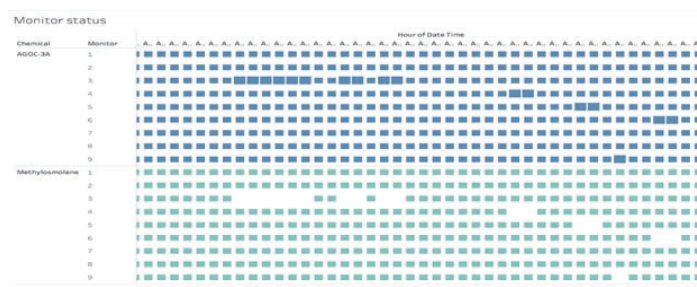


Fig 2. Double Reading and Blank Reading

Methylosmolene’s missing reading happened frequently for all three months in the dataset. We suspect one of readings regarding AGOC-3A is for Methylosmolene.

Double reading for AGOC-3A and missing reading for Methylosmolene are at exact same time. The most significant issue we saw was how many repeated readings there were for chemical AGOC-3A. This issue can be seen below where the blocks are larger than normal. When we compared that specific monitor’s time and date with the other chemicals; we found that the reading for Methylosmolene was missing for that exact same time and date. This issue can be seen in Figure 6 where blank space is located. This same pattern of AGOC-3A’s repeated readings and



Based on the provided dataset, we can conclude that all nine monitors are not running at maximum efficiency. This can be due to a variety of factors such as poor quality electronic components, instability over the temperature range, or inadequate engineer manufacturing. For the missing data this could be due to the monitors simply not picking up readings from any chemical for that hour of the day, or they could have shut down all production in all five factories at that time.

Additionally, we plotted the monthly heatmap representing the daily release amount and pattern for each chemical at each monitor. Figure 3 our x-axis is arranged in month with daily scale, while the y-axis organizes per chemical observation for each monitor. We observed that Monitor 3 consistently captures all chemicals in three months (so as Monitor 4 in month Aug and Dec).

Even when there is no wind blowing to the monitor there is

still a consistent level of release. We conclude it should be the chemicals from the environment.

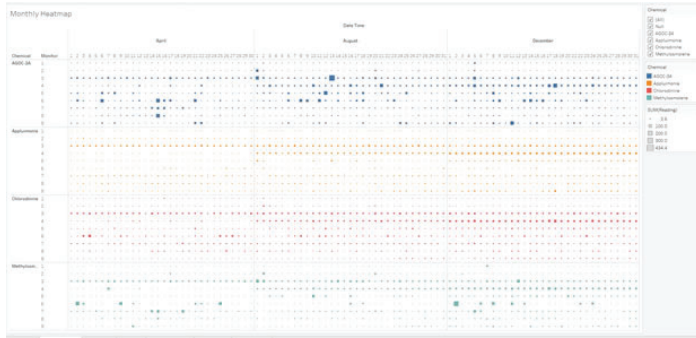
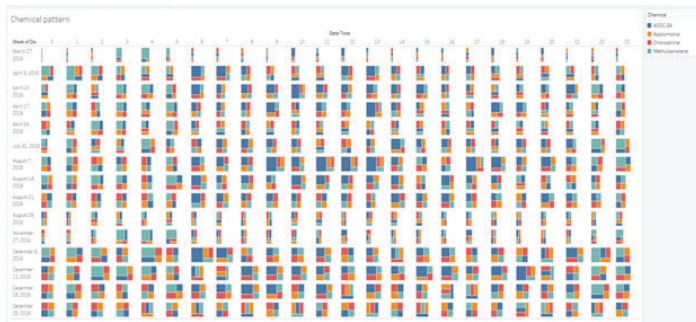


Fig 3

The rest of our analysis is based on cleaned up data that we removed double reading from the last figure, we can also observe, AGOC and Meth have more accumulated release than other chemicals.

In this figure, we can clearly see the release pattern per hours. In order to have a compact view, we summarize the pattern in a weekly manner. It is clear that between 6am to 21pm, the most captured chemical is AGOC-3. In contrast, between 22pm to 5am, the most captured chemical is Methylosmolene. This is the release pattern we found.



There are four chemicals, AGOC-3A, Appluimonia, Methylosmolene and Chlorodinine, that are detected by the sensor group. Chemical release of Appluimonia and Chlorodinine are consistent with no dramatic increase (see figure 3). Chemical release of AGOC-3A has many peak readings that are almost 19 times more than regular release of it and they are detected at both day and night in the 24-hour period (see figure 4). Chemical release of Methylosmolene also has many peak readings that are approximately 10 times over than the regular release of it, these peak readings are only detected during evening hour between 10pm-5am (see figure 5).

Fig. 3 Consistent chemical release for Appluimonia and Chlorodinine



Fig. 5. Chemical release of AGOC3 has many peak readings that are detected at either day and night

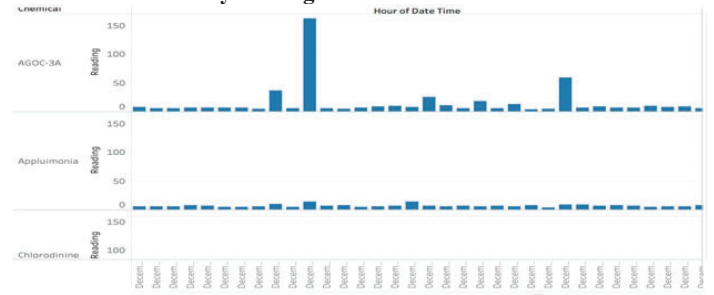
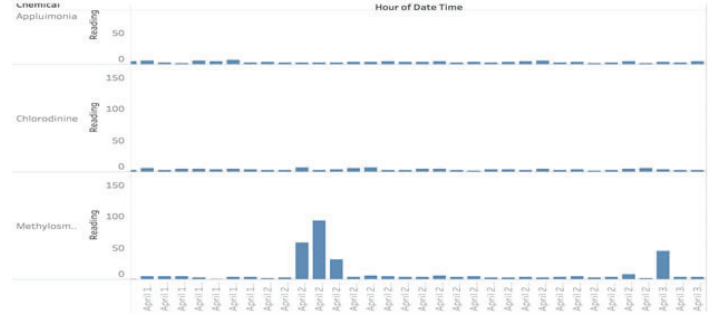


Fig. 5. Chemical release of Methylosmolene has many peak readings that are only detected during evening hour between 10pm-5am



Factory	1	2	3	4	5	6	7	8	9
Roadrunner	77.5	109.2	137.1	176.8	221.2	291.0	0.0	36.9	243.4
Kasios	90.0	120.3	145.0	175.2	179.0	265.2	3.2	48.8	234.1
Radiance	83.9	101.8	114.4	132.1	160.6	60.3	41.0	61.5	212.0
Indigo	89.0	103.5	113.4	125.7	141.0	90.0	58.5	71.9	177.1

We define the amount of contribution (we called possibility) of a factory to a sensor by relating with wind direction at given time. The value  $w$  can be considered as the unit vector of wind direction, and the value  $v$  can be considering the unit vector from factory to a sensor. The contribution is calculated as a dot product of the two vector as amount = dot( $w$ ,  $v$ ), which is equal to the cosine of the angle between two vectors. An example of this can be seen in the images below.

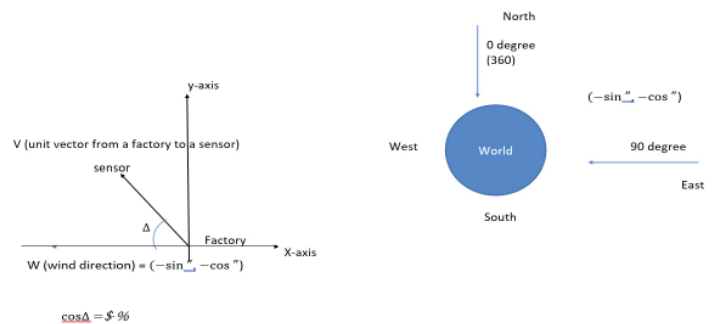


Figure 6

If two vectors are perfectly aligned, i.e. the location of a sensor is along the wind direction, the amount is 1 or zero angles between two vectors. As it is deviating from the perfect alignment (i.e. non-zero angles between two vectors), the amount is reducing by following cosine curve. Once it reaches 90 degrees, the amount is zero. In other words, the factory does not give any effects to the sensor. A negative value can be considered as zero effects.



Please note, we chose this simple model without considering the wind speed and the real distance in miles is because we didn't know the map scale when we started the project. We noticed that missing information was added some time in July, which we did not have time to complete. But theoretically, if we know the real distance between factory and sensor, we can adopt the wind speed, and compute an accurate arrival time of the chemical spread. This patch computation will shift the time of observation but won't change the linkage between chemical release and factories

Then we filter out small readings (<5), we select only "peak" readings, and we filter out small possibilities (<49%). This really helped us to remove environmental contribution as mentioned in question 1, and put our focus on only salient locations. We use two color trends to visualize that as in Figure 7. Bar charts show chemical release, while circles show possibilities. This is the overview in date time order. In the figure, the x-axis is the Date Time in hours, and the y-axis is monitor. We plotted both chemical readings and the possibilities in the same plot by adding the possibilities of factories as the second axis. The bar charts are for chemical readings which are colored in blue series, while the possibilities are plotted by circles whose colors represent factories and sizes represent possibility values

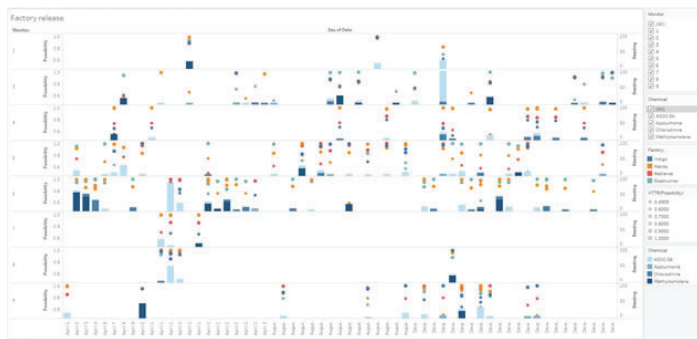


Figure 7

In order to better observe the possibility, we rearrange the data in descending order of possibility for each monitor. This effect is shown in the figure below.

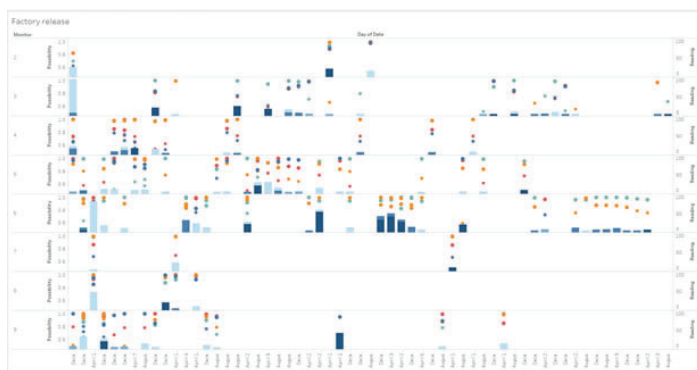


Figure 8

By highlighting each chemical in turn, for example "Appluimonia" as in the figure below, we quickly find that factory Indigo consistently has the most possibility shown as below.

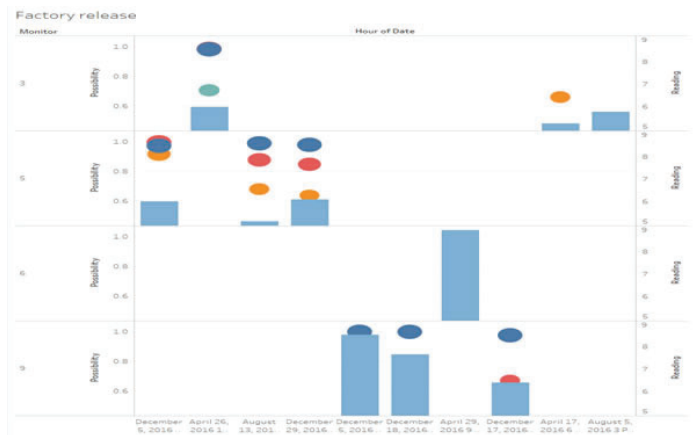


Figure 9

By following the same strategy, we summarize our finding as the figure below. the following table. In that, Indigo mostly re-released Appluimonia, Radiance mostly release AGOC-3A, Kasios and Roadrunner both released all the other chemicals.

	AGOC-3A	Appluimonia	Chlorodimine	Methylosmolene
Indigo				
Kasios				
Radiance				
Roadrunner				

# Implementing a Wire-Stretch test to locate the position of the electrical center of radio frequency cavities in operation in the RHIC

Wayne Johnson, Mechanical Engineering, Stony Brook University, Stony Brook, NY, 11794

Jean Clifford Brutus, Collider-Accelerator Department, Brookhaven National Laboratory, Upton, NY, 11973

## Abstract

A Wire-Stretch test will be implemented at Brookhaven National Laboratory (BNL) to help improve the overall effectiveness of Radio frequency (RF) cavities. RF cavities are used extensively throughout the Relativistic Heavy Ion Collider (RHIC) at BNL to alter the speed or energy spread of the particle beam. The electrical center of the cavity, which is where the particles undergo zero longitudinal force, is the optimal path for the beam of particles. The electrical center is designed to be equivalent to the mechanical center of the cavity; however, due to manufacturing limitations, this is normally not the case. Thus, determining the location of the electrical center is crucial in extracting the greatest performance from the cavities. Currently, BNL uses a Bead-Pull test to find this location. A small cylinder is fed through the cavity at different orientations and takes measurements iteratively. However, this method is both arduous and inaccurate. The Wire-Stretch test, which will be both simpler and more precise, will involve a conducting wire fed through the cavity. Then, both ends of the wire will be independently moved, using two sets of linear stages, while RF measurements are taken periodically. This pattern will repeat until the location of the electrical center is determined. The Wire-Stretch test will require a LabVIEW program, a search algorithm, and a physical modification of the current Bead-Pull test setup. The LabVIEW interface and search algorithm were completed, and we are confident that it will work as anticipated. However, we are still waiting for the cavity and several of the physical components for the test.

## I. Background

### A. A. RF Cavities and their Electric Centers

A radio frequency (RF) cavity is an enclosed metal structure which has specific electromagnetic (EM) properties. Used primarily in particle accelerators, such as the Relativistic Heavy Ion Collider (RHIC), their main purpose is to alter the beam of particles: some cavities accelerate the beam while others modify the bunching and energy spread of the beam. Inside of the cavity, EM waves become resonant and build a stable EM field. The particles entering the cavity, via the beam port, are impacted by the resulting force of the EM field, which will subsequently alter the particles trajectory.<sup>1</sup> Ideally, the beam should travel along the electrical center of the cavity, where the particles experience zero longitudinal forces; in other words, there is no radial force present.<sup>2</sup> In a perfectly built cavity, the mechanical center, which is the axis that the physical cavity is centered upon, would be equivalent to the electrical center. For this to happen at the demanding accuracy required for the operation of particle colliders, painstakingly precise manufacturing – usually on the order of micrometers – is required. However, due to the limiting nature of manufacturing, imperfections arise, which can cause the electrical center to shift

from the mechanical center. Since cavities are placed into the collider by its mechanical center, the performance of the cavity is limited. Thus, the Wire-Stretch test will improve the efficiency of the RF cavities in use.

### B. B. BNL's Current System to Locate the Electrical Center

A Bead-Pull test is used at BNL to determine the location of the electric center. The test consists of a non-conducting wire placed through the RF cavity. Attached to the wire is a small cylinder made of dielectric or metallic material. This wire is then fed through the cavity, usually aligned with the mechanical center of the cavity. The cylinder is pulled through the cavity at different orientations by means of a motor attached to one side. As the cylinder moves through the EM fields of the cavity, it causes small perturbations in the fields. These perturbations can be recorded by several instruments and can help to sample the field inside of the cavity, allowing physicists and engineers to determine the location of the electric center.

The Bead-Pull test in use at BNL, shown in Fig. 1, consists of two stands on each side of the cavity. Each stand has a pair of linear stages – one for back and forth, or x-direction movement, and one for up and down, or y-direction movement. These stages allow for the wire to be moved radially while remaining parallel to the mechanical center of the cavity. The wire and cylinder, which is mounted to the y-direction linear stage, is run through the beam port of the cavity; it has its own DC motor to pull the cylinder through.

## II. Methods

### A. A. Physical Requirements of the Wire-Stretch Test

The Wire-Stretch test will have a similar physical setup as



Figure 1: Current Bead-Pull Setup at BNL

the current Bead-Pull test, shown in Fig. 1. Instead of a non-conducting wire with a cylinder attached, a conducting wire will be fed through the cavity. This wire will have a signal sent through it, allowing it to mimic the beam inside of the cavity. With this configuration, the DC motor is not required. However, the two sets of linear stages will still be used, which will move the wire radially, just as they do in the current Bead-Pull test. However, unlike the current system, the two sets will be able to move independently from each other, which will allow us to determine if the electrical center is not horizontal. The motors will be controlled using a Newport ESP7000 Universal Motion Controller. An Agilent E8362B PNA Series Network Analyzer will be used to both send the signal through the wire and record the RF data to be analyzed by LabVIEW.

## B. LabVIEW Interface and Testing Algorithm

A LabVIEW program, or virtual instrument (VI), is required to complete this process automatically. The electrical center is when the maximum change in amplitude and phase at a given frequency is minimized; the location of the wire where this “peak” is the smallest is the electrical center. To find this position, LabVIEW implements a search algorithm combining the motion of the linear stages and the reading from the network analyzer. The search method compares the peak in the middle of the circle to the peaks of a specified number of points on the circle itself. To obtain these peaks, a global line is determined, and the maximum change in amplitude is found, as shown in Fig. 2. Then, the VI compares all of the values to see which is the lowest. If the center of the circle is the minimum peak, then the radius is halved, and the circular sweep is started again. If a point on the circle in the minimum peak, the center of the circle for the next iteration moves to that point, and a new sweep is performed with the same radius. The sets of motors operate in turn – one does a circular sweep, and then waits for the other to complete a sweep – until the radius falls below a specified stopping criterion of 0.01 mm.

The LabVIEW VI itself, shown in Fig. 3 above, is a completely autonomous method to find the electrical center. It has controls to initialize the motor groups, which allow the user to select which axes belong to which group. It also allows the user to set the velocity, acceleration, and deceleration of the group. Also, there are controls to setup the circular sweep: the user can specify the number of test points, the radius, the angle of sweep,

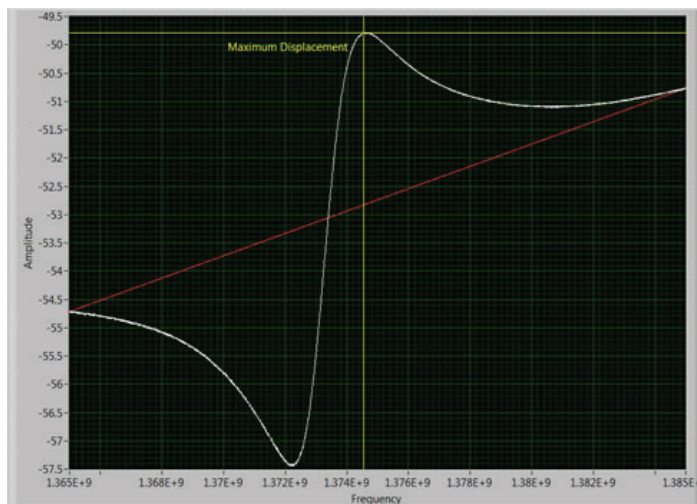


Figure 2: Graph showing the global line and the data from the network analyzer (this is amplitude data)

and the initial circle’s center coordinates. Additionally, there are controls for the E8362B: a measurement setup allows the user to select the type of data, the number of points, the power level, and the bandwidth. The threshold, seen in the Setup Measurement control, is for switching the data from amplitude to phase. When far away from the electrical center, the phase data is unreliable, while the amplitude data is reliable. However, once near the electric center, the opposite is true. A threshold of 0.1 means that if the peak in the center of the circle and the smallest peak on the edge of the circle are within 0.1 of each other, the data switches from amplitude to phase. Also, the user can specify the initial frequency range and the averaging factor.

## III. Data and Results

### A. A. BNL’s Tests

Unfortunately, we did not get the opportunity to complete this project during my summer stay. We are missing several key factors are missing. First, the four linear stages are not in our possession; we should be receiving them in early August. Additionally, the motion controller used – the Newport ESP7000 – is not the motion controller that will be used for the permanent test. Instead, we are having one built for us at BNL. This will require small tweaks to the already completed LabVIEW VI, but is overall not an issue. Lastly, the RF cavity to be measured, which is the 704 MHz cavity, is still at the manufacturer – Research Instruments in Germany – and should be arriving mid-to-late August. Once the electrical center is found, the same testing system will be used to map the transverse kick strength in an area around the center to accuracy unavailable with older testing methods. <sup>1</sup> Additionally, once the location of the electrical center is known, the beam can be guided through this center as to maximize the efficiency of the RF cavity.

## IV. Conclusion

The Wire-Stretch test, which is on course to be completed at Brookhaven National Laboratory sometime in the early fall, will assist physicists and engineers in finding the electrical center of RF cavities. This crucial result will help harness the maximum potential out of these cavities, allowing for better overall performance of the cavity and, subsequently, the entire RHIC.

## V. References

- “Radiofrequency Cavities.” *CERN*. N.p., 17 Sept. 2012. Web. 24 July 2017.
- Xin, Tianmu. “Background Introduction of Wire Stretching System for RF Dipole Mode Measurement.” 26 July 2017.

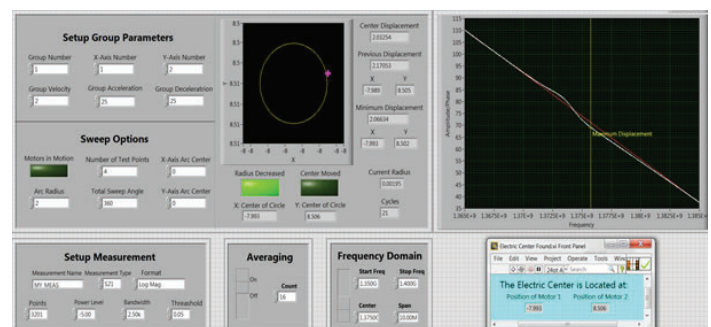


Figure 3: LabVIEW VI which implements search algorithm



# The importance of bees: an interdisciplinary unit for fifth grade students

Michelle Joseph, College of Education, University of Maryland College Park, College Park, MD 20742  
Bernadette Uzzi, Office of Educational Programs, Brookhaven National Laboratory, Upton, NY 11973

## Abstract

**Since 2006, a phenomenon now known as Colony Collapse Disorder (CCD) began to affect the world's bee population<sup>1</sup>. Many scientists have theorized some causes for this problem including mites, over exhaustion, pesticides, and habitat loss. Since bees are responsible for the pollination of billions of dollars' worth of crops, CCD is detrimental not only to beekeepers and farmers, but to the entire human population. The Science Learning Center (SLC) at Brookhaven National Laboratory (BNL) is devoted to educating the next generation of scientists on the relevant issues facing our world. My work with the SLC has led to the creation of a fifth grade interdisciplinary bee unit. I have spent my time assisting the setup and execution of their elementary school programs which has aided in my knowledge of lesson plan organization as well as given me practical teaching experience. When I was not at the SLC, I assisted a group of interns from the environmental department in conducting bee surveys which gave me the background information needed to craft my lessons to be thoughtful and engaging. The goal of this project is to educate the next generation not only on an important environmental issue but also how best to address them in a productive way.**

When most people are asked what humans benefit from having bees around, they will most likely answer "honey." Humans tend to think of other things in terms of how they directly relate to humans. However the true benefit humans get from these small insects is far greater than this one product and therefore the impact of declining bee populations will be far greater than most of us expect. The first step in battling any problem is to raise awareness, and what better place to do that than among the younger generation, the ones who will be left with our problems when we pass on. Getting students to internalize and engage in events that do not directly affect them can be a very daunting but beneficial task. In order for the next generation to aid in solving prominent issues in the world, educators must inspire a passion of these issues in our students. This lengthy process begins with teaching a background knowledge of the problem, the causes of the problem, an investment in the problem, and then creating possible solutions.

In the case of this bee unit, I began by relating bees to their everyday life by discussing insect stings, what insects are more likely to sting you, and how to best treat that sting. This is making the subject relevant to them, since most people are quite afraid of being stung. The next few lessons are meant to get the students to discover different kinds of bees, what each of them needs to survive, and the role that humans play in their lives. The conclusion of this education exploration specifically targets the problem of colony collapse disorder: what causes it and what can be done about it. I made sure not to make all of these lessons only science lessons. True learning utilizes a wide variety of knowledge and

skills. Within this bee unit, I have incorporated the subject of bees into geography, math, reading, writing, civics.

Before I could figure out what or how to teach students about bees, I had to learn about them myself. Prior to my internship at BNL, I knew very little about bees. I was afraid of them and had bought into many misconceptions about them such as 'all bees die after they sting you.' This fear and ignorance was soon replaced with awe and appreciation. During the beginning of my internship, I spent a good deal of time working with a group of interns working with the Environmental Department of BNL that were studying pollinators on site. Every day I was with them in the field, we went to different wildflower patches around the lab and caught and identified different types of bees and the flowers they were found pollinating using nets, vials, and field guides supplied to the pollinator group. This constant exposure to bees helped me realize that I had nothing to be afraid of in the first place. Even though we took the bees momentarily away from their work, once released they never even gave us a second thought. They merely went back to pollinating. On days spent indoors with the pollinator intern group, we used our field guides and other online sources to identify any unknown bees or flowers that we came across in the field. These days of hands on experience helped shape the types of questions to ask myself when crafting my lesson plans.

Now that I had a bit of background knowledge myself, I went back to the Office of Educational Programs ready to create a structure for my bee unit. The first topic that I wanted to know more about bee stings. When I was in the field, I was constantly worried about getting stung so I decided to look up which bees sting. I thought that this would be most people's initial reaction to bees so I made that the first lesson in the unit. What better way to start than to just people's main concern addressed. The next topic that came to mind as a result of field work was how bees related to math. The tracks we took to catch the bees were so organized and methodical that my mind began to think of different ways this related to math topics, such as locating bees on a coordinate plane, creating and interpreting bee data in different representations, and the symmetry of bees.

The structure of this unit changed a great deal over the latter half of my internship. Some of my initial ideas included more art and history lessons because I had a goal of making sure each discipline was utilized once in this unit. One of my earlier unit structure ideas culminated in a craft garden the students would make. It began with two lessons, one about the parts of a bee and another on the different types of bees. At the end of those the students would draw and label a bee which would be part of the garden. Next would be a lesson about pollination which would end in the students making flowers from cardboard rolls and tissue paper. The fourth lesson would be about beehives and other places bees live which would end in the students writing a bee poem in the shape of a hexagon to make a beehive. The unit would end

with the kids learning about colony collapse disorder and they would find a way to share this information through some form of artistic expression such as a poem, skit, song, or dance. Although I really liked this structure, I realized that the standards that aligned with it and the way I had them engaging with the information was for more first and second grade rather than the fifth graders I had in mind.

When I scrapped this initial plan, I discussed my new plan with one of the teachers in the office. She helped me realize that I don't necessarily need to make the lessons flow cohesively. Just having lessons about bees for teachers to take and insert into their syllabus would also be beneficial. So I set out to craft lessons that I thought would be valuable to insert at any time. I knew that a bee stings lesson would be great and engaging as well as one on bee habitats. I had also hoped to do an economics lesson about beekeepers and honey. Each student would be a beekeeper and they would have to run their finances for a month. I unfortunately could not find the information I was looking for in the allotted time I had. Another really interesting idea I had was a civics lesson that came to mind after I viewed a video about how bees make decisions about where to put their hive after they have overcrowded their current one. However this was another topic I could not find enough information on to make myself comfortable teaching it to others.

Eventually, I found a set of individual lessons that ended up flowing together as one cohesive unit anyway. My finished unit consists of an introductory lesson on bee stings. During this exploration students learn about what bees are more likely to sting you, what the difference is between a bee and a wasp, and how to properly treat an insect sting. The second lesson teaches the students about some of the different types of bees through bee centers placed around the classroom. The five bees the students learn about are bumble bees, honey bees, carpenter bees, squash bees, and southeastern blueberry bees. My third lesson stems from my many math ponderings in the field. The students learn about coordinate geometry and then must locate and plot bees on a coordinate plane. The fourth lesson addresses colony collapse disorder and the effect that will have on our earth. I didn't want to spell everything out for them in this lesson, so they are shown a video about the importance of bees and then map out the chain reaction that would play out if bees disappeared. This leads into a week-long writer's workshop: "A world without bees." For five days the students will expand their chain reaction maps and develop a five paragraph essay based on three big aspects of life that would be affected due to a loss of bees.

This unit, like most lesson plans, is intended to be a non-comprehensive living document. It is an example of one way that this information can be shared with students. Many different aspects can change depending on the needs of a specific classroom. Some modifications may depend on school resources. This unit is quite low-tech but there are different apps and websites available for students to engage in the same information is the technology is accessible. Possible extensions from this unit could include a field trip to a beekeeper's farm or a community bee garden. However, because of some people's allergic reactions to insect stings, this may be inadvisable depending on the people involved.

As a result of my time here at the lab, I have gained not only an increased knowledge of bees but also a better understanding of how scientific research is conducted. Being surrounded by so many experts who are passionately exploring their curiosity about

the universe has encouraged me to try to instill in my students a similar passion, persistence, and curiosity. My time working with summer camps at the lab has also let me see a different way that science can be taught. Rather than teaching to a test, I have seen science in action and the children's curiosity takes them much farther than I had expected. This freedom and innovation is what I plan to bring back into my own classroom. We should all be curious and passionate about something.

## **I. Acknowledgements**

This project was supported in part by the Brookhaven National Laboratory-Virginia Pond Scholarship Program under the VPSP-Supplemental Undergraduate Research Program (SURP). I would like to thank Bernadette Uzzi and Susan Frank who have supported me throughout this process and given me educational guidance as well as Timothy Green and the environmental department interns who aided in increasing my bee knowledge.

## **II. References**

<sup>1</sup>Colony Collapse Disorder. (2017, April 18). Retrieved August 09, 2017, from <https://www.epa.gov/pollinator-protection/colony-collapse-disorder>

# Assessing preference by white-footed mice (*Peromyscus leucopus*) for coarse woody debris

Eric Juers, Natural Science, Paul Smith's College, Paul Smiths, NY 12970

Jennifer Higbie, Environmental Protection, Brookhaven National Laboratory, Upton, NY 11973

## Abstract

**Research to expand current knowledge of habitat use by white-footed mice (*Peromyscus leucopus*) at fine spatial scales is needed given the species' widespread distribution in the United States and its prevalence as a reservoir for zoonotic pathogens like Lyme disease. Downed coarse woody debris, a structural component of forest floor habitat important for many small mammals, may be preferred by woodland dwelling *P. leucopus* because of its multiplicity of uses from cover, to landmarks that aid in spatial memory for navigation. To assess the role that downed woody debris plays in facilitating habitat preference of *P. leucopus*, Sherman box traps were deployed for live trapping and tagging of *P. leucopus* and coarse woody debris was surveyed in grids across various types of forest at Brookhaven National Laboratory during the summer of 2017. A Pearson correlation analysis produced no significant correlation between abundance estimates of *P. leucopus* population size and total volumes of coarse woody debris. In order to inform wildlife and forest management practices of the importance of woody debris in facilitating *P. leucopus* populations, more long-term studies are needed that can account for the interacting effects of other habitat characteristics like patch size and understory vegetation density. Over the course of the study I became proficient and confident in handling and processing *P. leucopus*, a useful skill to have for future studies in wildlife ecology.**

## I. Introduction

Lyme disease (LD) is a major public health issue in the United States with approximately 30,000 cases of LD being reported to the Center for Disease Control (CDC) every year, a number that has been increasing every year since 1995 (CDC 2015). Other research conducted in association with the CDC indicates that this number may actually be closer to 300,000 cases nationwide annually (Hinckley et al. 2014, Nelson et al. 2015). Because there is currently no vaccine for LD on the market and LD can cause debilitating acute and chronic symptoms and even be fatal, it poses a significant public health risk and is of the utmost importance for the scientific community to understand as much as possible about the underlying factors driving the disease.

The white-footed mouse (*Peromyscus leucopus*), an abundant generalist mammal species, is one of the most successful host reservoirs for LD and other zoonotic diseases like Babesiosis and Ehrlichiosis (LoGiudice et al. 2003, Shaw et al. 2003). *Borrelia burgdorferi*, the spirochete bacteria responsible for causing LD is benign to *P. leucopus*. However, once a blacklegged tick or "deer" tick (*Ixodes scapularis*) at the larval or nymph stage bites and consumes a blood meal to repletion (until it falls off) from an infected white-footed mouse, it has up to a 90% chance of becoming infected with the *B. burgdorferi* bacteria (Shaw et

al. 2003) and is subsequently more likely to become a vector to transmit the bacteria to a human and cause LD than when feeding on other host species. *P. leucopus*' effectiveness as a host reservoir may stem from its habitat use; microhabitat segregation between *P. leucopus* and the eastern chipmunk (*Tamiasciurus hudsonicus*) shows that *P. leucopus* is more likely to use tick-infested habitat and attract questing larval ticks and have much higher tick burdens than *T. hudsonicus*, despite significant grooming by *P. leucopus* (Shaw et al. 2003).

Given that *P. leucopus* is abundant in the Northeastern United States where cases of LD are high, assessing the relationship between habitat characteristics that may be preferred by *P. leucopus*, and *P. leucopus* abundance could inform wildlife and/or forest management by providing a quantifiable basis for forest areas to be designated as high-risk for LD because of its suitability for *P. leucopus*.

Numerous factors facilitate *P. leucopus* populations, from forest productivity and mast production (Ostfeld et al. 1996, Elias et al. 2004), to habitat patch edge-to-interior ratio (Anderson et al. 2003), connectivity (Rizkalla and Swihart 2007), and vegetation density (Monamy and Fox 2000). Downed coarse woody debris (CWD), a significant structural component of forest habitat, may be an important determinant of *P. leucopus* populations (Graves et al. 1988, Barnum et al. 1992). CWD is heterogeneous across the landscape and variable from one forest patch to the next due to the random effects and varying magnitudes inherent to different disturbance types (Harmon et al. 1986). For example: fire, a less frequent but significant disturbance, has the capacity to exacerbate the role of CWD in providing habitat structure by not only felling trees directly but by making surviving trees more susceptible to wind and insect infestations as well as "re-setting" the succession of herbaceous understory cover.

Small mammals utilize CWD in different ways but generally use it for cover from predators (Zollner and Crane 2003, Fanson 2010), foraging space, and nesting (Bowman et al. 2000). Research has also highlighted the importance of downed wood for *P. leucopus* by using CWD as "highways" or landmarks that aid in spatial navigation (Graves et al. 1988, Barnum et al. 1992, McMillan and Kaufman 1995). This knowledge sets a precedent to investigate the preference of *P. leucopus* for habitat containing relatively larger amounts of CWD. I hypothesized that *P. leucopus* populations are positively correlated with volume of CWD.

## II. Field Methods

To investigate the hypothesis that *P. leucopus* populations and volume of CWD are positively correlated, Sherman traps were deployed Monday- Thursday of each week between June 12th and August 4th 2017 to mark and recapture *P. leucopus* individuals and estimate their abundance at 16 different trapping sites around Brookhaven National Laboratory (BNL) in Upton, New



York (Figure 1). All sites were adjacent to roads, but set-up at least a few meters into the forest to reduce edge effect. Sites 11-16 constituted mixed oak and pitch pine (*Pinus rigida*) stands with blueberry (*Vaccinium corymbosum*) dominating the understory and contained relatively few fallen trees, forests gaps, or larger CWD. These sites have not been burned by wildfire or prescribed fires in recent decades.

Sites 9 and 10, near the Long Island Solar Farm, were similar to 11-16 but differed with a more heterogeneous understory of herbaceous groundcover and open/somewhat grassy patches as well as more treefalls and a taller canopy. Sites 7 and 8, near the sewage treatment plant at BNL both constituted large areas of open grasses mixed with patches of blueberry with some large treefalls. Site 7 in particular was about 1/3<sup>rd</sup> open canopy and grass. Sites 3 and 5 were within quadrants of forest between dirt roads that were subject to prescribed fires before trapping occasions in the first trapping session. Both exhibited similar vegetation to Site 4, an unburned site between the two burned quadrants with homogenous blueberry and generally taller and thicker understory with more treefalls, gaps, and large CWD. These quadrants were previously burned unsuccessfully in 2015. Site 6 was across a dirt road from site 5 and was not burned this summer or in the past.

It also contained homogenous blueberry understory with greater amounts of CWD. Site 1, had similar vegetation and canopy structure to sites 3-6 (pre-burn) and was burned by a wildfire in 2012.

Trap grids were 35m<sup>2</sup> and included 64 traps spaced 5m apart for a total of 8192 trap nights over the course of the study. Traps contained a cotton square and a peanut butter and oat bait. Trapped *P. leucopus* were tagged and ticks were removed and put into ethanol when found. Each grid was surveyed completely for CWD pieces at least 16cm in diameter and 60cm in length. Volume of CWD pieces were calculated based on the volume of a cylinder ( $V = \pi r^2 h$ ) and summed for a total volume of CWD for each grid.

Diameter was measured by eye-balling the middle of the CWD piece in an effort to reduce the error associated with the taper of downed pieces and calculating volume based on a uniform cylinder. When possible, multiple measurements were taken and recorded as separate pieces (for example, a downed tree where the main trunk splits into smaller branches) to further reduce this error. Pieces had to be at least half inside of the grid to be counted, and had to be resting at an angle less than 45° to be considered downed CWD.

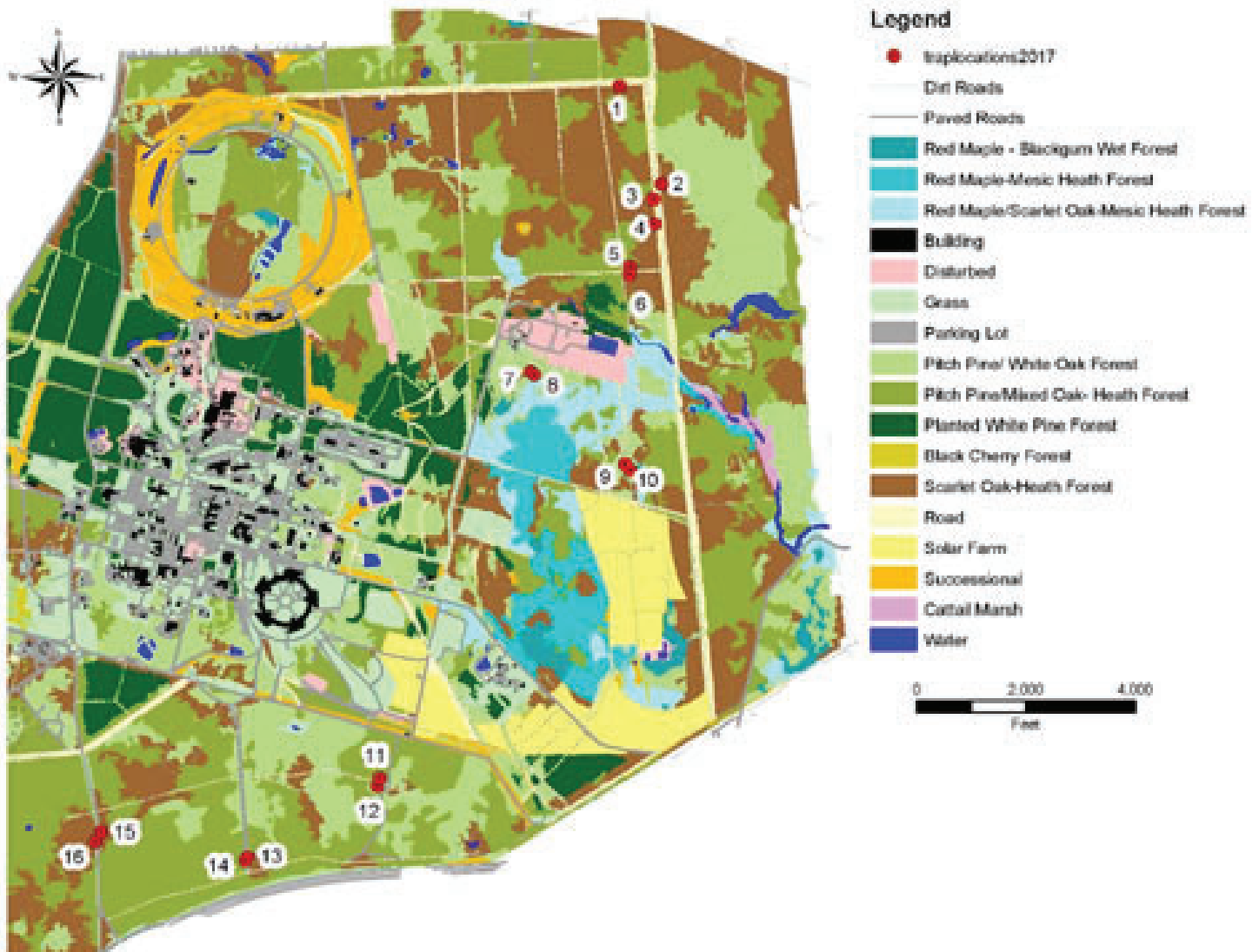


Figure 1. Map of Brookhaven National Laboratory including land cover types and the 16 trap sites for the study. Map courtesy of Leanna Thalmann.

### III. Statistical Methods

Population abundance estimates and 95% confidence intervals were produced by running a Huggins p and c robust design model (a population estimate that combines the closed model of Lincoln-Peterson and the open model of Jolly-Seiber (Huggins 1991)) in program MARK ver 6.1.7601. A Pearson correlation analysis was run in R Studio ver 1.0.136 to produce a correlation coefficient for CWD as an x variable and *P. leucopus* abundance as a y variable.

### IV. Results

The correlation between *P. leucopus* abundance and total volume of CWD across all trapping sites was weakly positive ( $r = 0.09$ , 95% CI [-0.35, 1]) and not statistically significant ( $p = 0.37$ ). A few sites with high abundance had high volumes of CWD while most others had low abundance and relatively high CWD or relatively high abundance and low CWD (Figure 2). Although Site 6, an unburned site, had the highest volume of CWD (1,920,791.74 cm<sup>3</sup>) as well as the highest estimate of *P. leucopus* abundance (35.58, 95% CI [21, 47.2]), wildfire site 1 ranked 4<sup>th</sup> overall for abundance (35.39, 95% CI [23.1, 2394.36]) as well as having a high total volume of CWD (1,374,011.68 cm<sup>3</sup>). The sites in the southern part of BNL (11-16) fell into the lower half of all sites for both abundance estimates and volumes of CWD. Both prescribed burn sites 3 and 5 exhibited low abundance estimates (3.35, 95% CI [2.44, 4.26], and 8.63, 95% CI [4.99, 10] respectively) but high volumes of CWD (1,463,817.24 cm<sup>3</sup> and 1,533,172.61 cm<sup>3</sup> respectively).

### V. Discussion

The structural and functional complexity of forest habitat makes focusing on one characteristic independent of all others difficult. Although CWD has been shown to be an important aspect of habitat for small mammals (Graves et al. 1988, Barnum et al. 1992, Bowman et al. 2000, Brannon 2005) the simultaneous and possibly interacting effects of other habitat components like understory vegetation density (Monamy and Fox 2000), habitat patch size and edge-to-interior ratio (Anderson et al. 2003), patch connectivity (Rizkalla and Swihart 2007), and mast production (Ostfeld et al. 1996, Elias et al. 2004) all work to influence small mammal abundance.

The low abundance estimates but high CWD volumes for both of the prescribed burn sites (3 and 5) most likely biased the results of the correlation analysis. Several of the downed trees surveyed in site 5 were cut by workers post-burn for safety reasons, and nearly half of all pieces surveyed in site 3 were also cut by workers post-burn which significantly influenced the total volumes calculated for both sites. Furthermore, although vegetation density and habitat structure have been shown to be better predictors of small mammal abundance post-disturbance (Monamy and Fox 2000) it is likely that adequate time had not passed since the prescribed burns to allow small mammal populations to fully re-colonization; other studies of how fire effects small mammal populations have sampled populations on the scale of months or years after fire (Vieira 1999), not within the same week/the weeks following the fire as was done here.

Abundance may not be the best parameter with which to study the preference of a small mammal species like *P. leucopus* for habitat structure like CWD. Spatially explicit models in tandem with habitat surveys that give accurate information about the

distribution of a habitat component within a trapping area would be more likely to reveal a use preference by a species because of the aforementioned number of variables that can contribute to influencing small mammal abundance. Many studies use florescent powder to mark and track the movements of small mammals within a habitat (McMillan and Kaufman 1995), a technique that could be used in tandem with trapping to elucidate habitat use preferences at a finer spatial scale.

The time and resource restrictions of this study limited CWD surveying to larger pieces ( $\geq 16$ cm in diameter and  $\geq 60$ cm in length) and excluding decay class from measurements of CWD pieces, another factor known to influence species specific preference for CWD (Bowman 2000, Brannon 2002). Furthermore, trapping occurred only twice at each site, limiting the accuracy with which local populations of *P. leucopus* could be estimated and stretching the assumptions of a robust design. Pollock (1982) states that at least 3 primary trapping sessions and 5 secondary trapping occasions for each primary session are required for using a robust design to estimate population size. Although our study incorporated a large number of secondary trapping occasions across different sites, there were only two primary trapping sessions because each site was only visited twice. This gave us a relatively large number of trap nights (8192), but between 2 sessions conducted over a relatively short period of time compared to other mark-recapture studies (Graves et al. 1988, Brannon 2005). This could have violated the assumption that individuals of the same species have the an equal chance of being captured, as condensed trapping occasions could have exacerbated behavioral responses by *P. leucopus* like being trap-happy or trap-shy.

Future studies using small mammal abundance as a parameter to correlate to volume of CWD must take place over longer spans of time to allow for more trapping sessions with longer intervals between sessions, as well as include surveys for multiple habitat characteristics that might influence *P. leucopus* abundance. If prescribed burns are going to be used to simulate disturbance and successional variables, adequate time must be given for small mammal populations to re-colonize before surveying an area after a burn. Running multivariate statistics to analyze the interacting effects between multiple habitat characteristics could better elucidate the role of CWD in facilitating populations of *P. leucopus* and by extension, forest areas at a higher risk of harboring *I. scapularis* infected with Lyme disease.

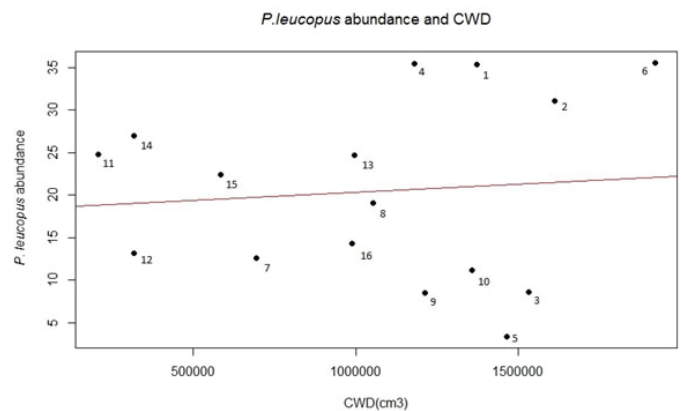


Figure 2. Correlation analysis of volume of CWD in cubic centimeters (x-axis) against *P. leucopus* abundance (y-axis). R coefficient = 0.09 (red line), p-value = 0.37. Black circles represent different trap sites and correspond to the trap numbers labeled in Figure 1.

## VI. Acknowledgements

This project was supported in part by the U.S. Department of Energy, Office of Science, Office of Workforce Development for Teachers and Scientists (WDTS) under the Science Undergraduate Laboratory Internships Program (SULI). I would also like to thank Jennifer Higbie for her guidance with conducting this research, as well as Sofia Vaca, Scarlett Alvarez, Leanna Thalman, Tre Wise, and Susanna Mann for their contributions to our trapping efforts this summer and to this paper.

## VII. Citations

- Anderson, C. S., A. B. Cady, and D. B. Meikle. 2003. Effects of vegetation structure and edge habitat on the density and distribution of white-footed mice (*Peromyscus leucopus*) in small and large forest patches. *Canadian Journal of Zoology*. 81(5):897-904.
- Barnum, S. A., C. J. Manville, J. R. Tester, W. J. Carmen. 1992. *Journal of Mammalogy*. 73(4):797-801.
- Bowman J. C., D. Sleep, G. J. Forbes, M. Edwards. 2000. The association of small mammals with coarse woody debris at log and stand scales. *Forest Ecology and Management* 129:119-124.
- Brannon, P. M. 2002. Distribution of *Sorex cinereus* and *S. fumeus* on north-and south- facing slopes in the Southern Appalachian Mountains. *Southeastern Naturalist*. 1(3):299-306.
- Brannon, P. M. 2005. Distribution and microhabitat of the woodland jumping mouse *Napaeozapus insignis*, and the white-footed mouse, *Peromyscus leucopus*, in the Southern Appalachians. *Southeastern Naturalist*. 4(3):479-486.
- Elias, S. P., J. W. Witham, and M. L. Hunter, JR. 2004. *Peromyscus leucopus* abundance and acorn mast: population fluctuation patterns over 20 years. *Journal of Mammalogy* 85:743-747.
- Fanson, B. G. 2010. Effect of direct and indirect cues of predation risk on the foraging behavior of the white-footed mouse (*Peromyscus leucopus*). *Northeastern Naturalist*. 17(1):19-28.
- Harmon, M. E., J. F. Franklin, F. J. Swanson, P. Sollins, S. V. Gregory, J. D. Lattin, ... & G. W. Lienkaemper. 1986. Ecology of coarse woody debris in temperate ecosystems. *Advances in Ecological Research*. 15:133-302.
- Hinckley A. F., N. P. Connally, J. I. Meek, B. J. Johnson, M. M. Kemperman, K. A. Feldman, J. L. White, P. S. Mead. 2014. Lyme disease testing by large commercial laboratories in the United States. *Clinical Infectious Diseases*. 59(5):676-681.
- Huggins, R. M. 1991. Some practical aspects of a conditional likelihood approach to capture experiments. *Biometrics*. 47:725-732.
- Graves, S., J. Maldonado, J. O. Wolff. 1988. Use of ground and arboreal microhabitats by *Peromyscus leucopus* and *Peromyscus maniculatus*. *Canadian Journal of Zoology*. 66:277-278.
- LoGiudice, K., R. S. Ostfeld, K. A. Schmidt, and F. Keesing. 2003. The ecology of infectious disease: effects of host diversity and community composition on Lyme disease risk. *Proceedings of the National Academy of Sciences*. 100(2): 567-571.
- McMillan, B.R. and D.W. Kaufman. 1995. Travel path characteristics for free-living white-footed mice (*Peromyscus leucopus*). *Canadian Journal of Zoology*. 73(8):1474-1478.
- Monamy, V., and B. J. Fox. 2000. Small mammal succession is determined by vegetation density rather than time elapsed since disturbance. *Austral Ecology*. 25:580-587.
- Nelson, C. A., S. Saha, K. J. Kugeler, M. J. Delorey, M. B. Shankar, A. Hinckley, ..., P. S. Mead. 2015. Incidence of clinician-diagnosed Lyme disease, United States, 2005–2010. *Emerging Infectious Diseases*. 21(9):1625-1631.
- Ostfeld, R. S., Jones, C. G., & Wolff, J. O. 1996. Of mice and mast. *BioScience*, 46(5), 323-330.
- Pollock, K. H. 1982. A capture-recapture design robust to unequal probability of capture. *The Journal of Wildlife Management*. 46(3):752-757.
- Rizkalla, C. E. and R. K. Swihart 2007. Explaining movement decisions of forest rodents in fragmented landscapes. *Biological Conservation*. 140:339-348.
- Shaw, M. T., F. Keesing, R. McGrail, and R. S. Ostfeld. 2003. Factors influencing the distribution of larval blacklegged ticks on rodents. *American Journal of Tropical Medicine Hygiene*. 68(4):447–452.
- Vieira, E. M. 1999. Small mammal communities and fire in the Brazilian Cerrado. *Journal of Zoology*. 249: 75–81.



# An assessment of bee diversity at “No-Mow” sites and the Long Island Solar Farm at Brookhaven National Laboratory

Julie Kapuvvari and Claire Y. O’Kane, College of Agriculture and Life Sciences, Cornell University, Ithaca NY 14850

Trevor McIntosh, Department of Natural Sciences, Southern University at New Orleans, New Orleans, LA 70126

Alexander Whittle, Department of Ecology and Evolution, Stony Brook University, Stony Brook, NY 11794

Tim Green, Environmental Protection Division, Brookhaven National Laboratory, Upton NY 11793

## Abstract

A majority of the agricultural crops that we eat depend on the valuable ecological services of pollinators. Unfortunately, anthropogenic influences have significantly disturbed pollinator populations worldwide, particularly bumblebee species. Therefore, conservation for these pollinators has been prioritized in recent years. Our research at Brookhaven National Laboratory evaluated the effects of two management areas: “no-mow” plots and “Solar Farm 1” of the Long Island Solar Farm (LISF). First, no-mow plots, or areas of vegetation protected from major human disturbances such as the use of lawn mowers, were established across BNL in order to promote wildflower growth and provide foraging opportunities for pollinator species. Second, “Solar Farm 1,” similar to the no-mow plots, is an area that hosts a wide variety of wildflower species that create an optimal habitat for bees. Our objective for conducting surveys in these two types of sites involved determining the richness of bees, as well as assessing the overall success of the areas in providing ample resources for bees to forage. Throughout the course of our study, our team collected and identified hundreds of bumblebees by their species using dichotomous keys, and recorded other bee species, such as honey bees. Obtaining data on abundance and diversity of bees, along with the flower on which they were found, led us to find correlations between bee species and their attraction to specific wildflower species. We found that the bumblebee were highly attracted to non-native wildflowers growing within the no-mow and solar farm sites.

## I. Introduction

Pollinators are exceptionally valuable to the environment and the global economy for the ecological services that they provide. Globally, pollination contributes to the reproduction of over 85% of the flowering plants, two thirds of which are significant crop species that humans depend on (“Pollinator Conservation”). According to a Cornell study in 2010, the economic value of pollinators was estimated to be equivalent to \$29 billion in farm income (Ramanujan, 2012). Unfortunately, many species of pollinators, particularly bumblebees (*Bombus* spp.) and honeybees (*Apis mellifera*), have experienced significant population declines over the past decade. This phenomenon, known as Colony Collapse Disorder (CCD), affects these eusocial bees alike; the adult worker bees will abandon the hive and leave the queen and brood to starve. The main culprits of CCD include the elevated use of pesticides, especially the ubiquitous neonicotinoids (Watanabe, 2008), commercial beekeeping transportation to monocultural farms, the fragmentation of viable habitats and wildflowers, the spread of pathogens, and climate change, which alters the species range and off-sets the timing of emergence (National Research Council).

While the term CCD is typically directed towards *Apis mellifera*, many species of bumblebees are in decline for the same reasons. In particular, *Bombus affinis*, or the Rusty-Patched Bumblebee, is the very first bee to ever be listed as endangered under the U.S. Endangered Species Act in January of 2017, and has been listed as critically endangered on the IUCN’s Red List (“Bumble bees”). A couple of the species found and observed in this study, *Bombus impatiens* and *Bombus bimaculatus*, seem have to have stable population growth according to geographic range analysis of North America (Cameron et al. 2011). Regardless, the ecosystem and the food supply cannot afford any further risk in losing bee richness and overall abundance, therefore this research assesses the abundance and diversity of bees and their species-specific attractions to the wildflowers at Brookhaven National Laboratory to enhance the administration’s pollinator management plan.

## II. Methods and Study Site

### A. A. Study Site

We conducted bee surveys at two different types of sites at Brookhaven National Laboratory: no-mow plots and Solar Farm 1 of the Long Island Solar Farm. No-mow plots are areas of tall grass that are undisturbed by current anthropogenic activities, such as mowing or pesticide use. They are located in small fields near or alongside the roads. We completed numerous bee surveys at five different no-mow plots of varying sizes, which are titled as and located within proximity of the following locations at BNL: “Cavendish,” “Compton,” “HFBR,” “NSLS-II,” and “Cornell” Avenue (Figure 1). The no-mow plots also varied in wildflower diversity. The second site that we visited to carry out pollinator surveys was Solar Farm 1, within the Long Island Solar Farm (Figure 2). Solar Farm 1 is the largest division of the six that make up the LISF. Within Solar Farm 1, solar arrays are arranged in many rows parallel with one another, separated by a dirt road running north-south near the center of the area. Surrounding all edges of Solar Farm 1 are high fences to prevent large wildlife as well as unauthorized people (ie. the public) from accessing this area, therefore the vegetation within Solar Farm 1 is protected from these external factors. Much of the vegetation grows underneath and all around the solar panel at varying heights, most of which are low lying wildflower species.

### III. Figure 2. Map of our site within LISF for pollinator surveys, Solar Farm 1.

#### A. A. Methods

To conduct our pollinator surveys at each of the five no mow plots, we established various walking transects of equivalent distances measured at approximately 200m. During our walks through the no mow fields, observed bumblebees were captured



Figure 1. Map of the five no mow plots selected across BNL where our pollinator surveys were conducted.



Figure 2. Map of our site within LISF for pollinator surveys, Solar Farm 1.



Figure 3. *Bombus bimaculatus* (Two-spotted bumblebee)



Figure 4. *Bombus fervidus* (Golden northern bumblebee)



Figure 5. *Bombus griseocollis* (Brown-belted bumblebee)



Figure 6. *Bombus impatiens* (Common eastern bumblebee)



Figure 7. *Bombus perplexus* (Confusing bumblebee)

with a net, transferred to a vial, identified by species, and released. In addition to recording bumblebee species, we also recorded the wildflower species each bee was observed foraging on, respectively, before being caught with our net. Other bees, such as honeybees and native bees, and their associated wildflower data were also recorded without requiring to be captured. At Solar Farm 1, the methods used to conduct pollinator surveys were almost identical. Rather than by distance, each of our surveys at the solar farm was limited by time. Each collection occurred for one hour in the late morning. Given the larger size of Solar Farm 1 compared to the no mow plots, different walking transects would be determined randomly for each survey in order to cover more ground and a higher diversity of wildflowers at the solar farm. The number of visitations for each site varied; therefore our data was normalized for analysis and comparison.

#### IV. Results

##### A. A. No-Mow Sites

The 5 different bumblebee species that we observed throughout our research include *Bombus bimaculatus* (Two-spotted bumblebee), *Bombus fervidus* (Golden northern bumblebee), *Bombus griseocollis* (Brown-belted bumblebee), *Bombus impatiens* (Common eastern bumblebee), and *Bombus perplexus* (Confusing bumblebee) (see Figures 3-7). In addition to these bumblebee species, we observed *Apis mellifera* (European honey bee) and other native bees.

Among the five different no mow sites that we visited in order to conduct pollinator surveys, the no mow site at NSLS-II had the highest diversity of bumblebee species (Figure 8). NSLS-II also had a higher diversity of bee species compared to Solar Farm 1. Of the six species of pollinators focused on in our study, indi-

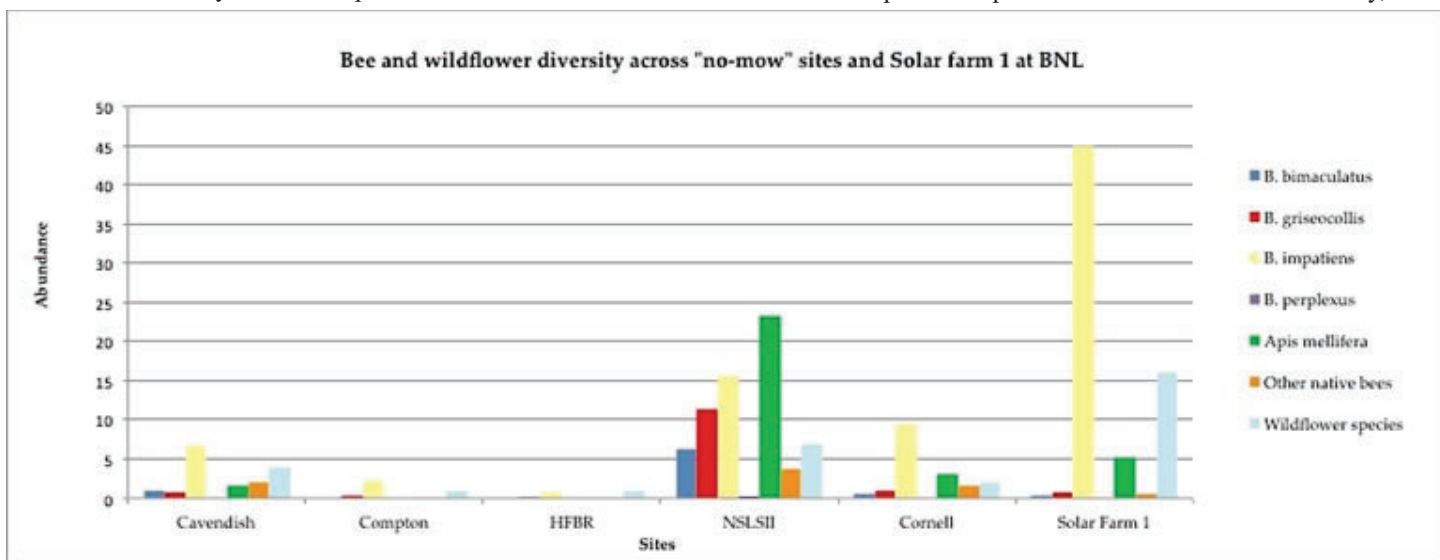


Figure 8. Bee species abundance and wildflower diversity across all no-mow sites and Solar Farm 1. Data is represented as the average number of individuals per bee species per visit and total number of wildflower species per site.



No-mow sites

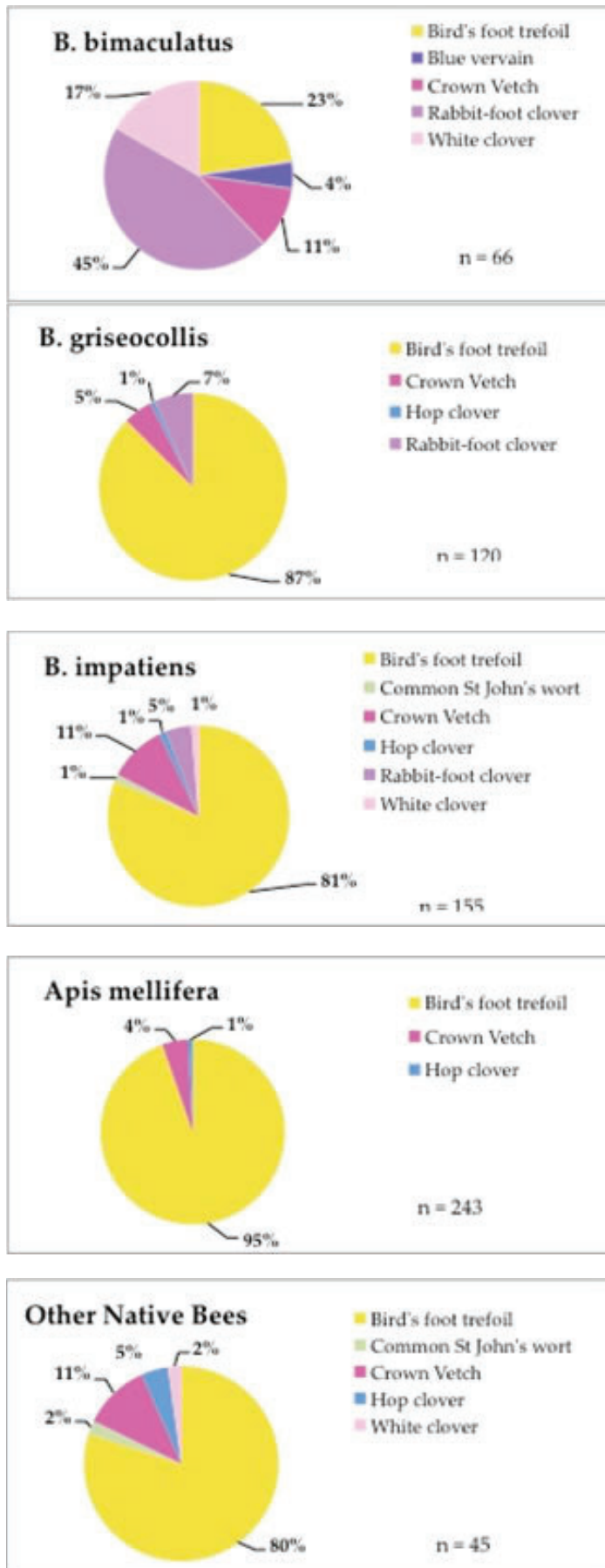


Figure 9a. : Wildflower preferences of bee species at no-mow sites

Solar Farm 1

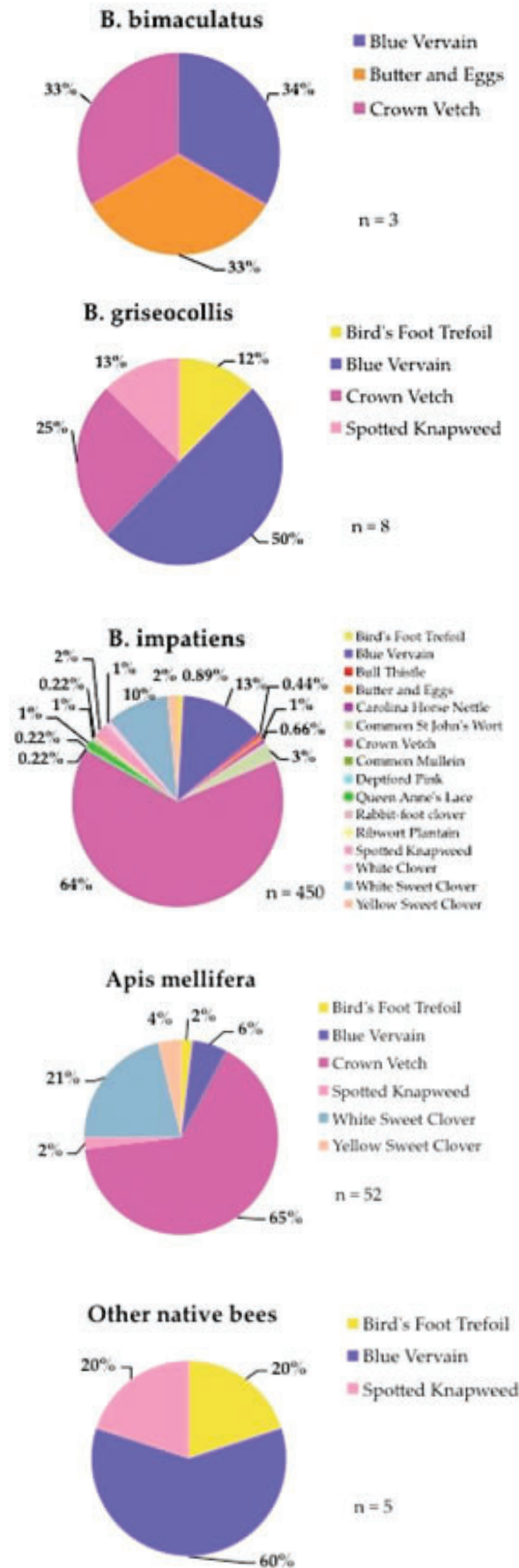


Figure 9b. : Wildflower preferences of bee species at Solar Farm 1



viduals of five of the species were recorded more than once at NSLS-II. On average, NSLS-II also had the highest species abundance per visit compared to the other four no mow sites and the solar farm, with the exception of *Bombus impatiens*. While there was lower bee diversity at Solar Farm 1 as well as the highest wildflower species diversity, we observed the highest abundance of any pollinator species recorded estimated at approximately 45 *B. impatiens* per one visit. Other no mow sites such as HFBR and Compton had very low pollinator abundance and diversity. The analysis of the species-specific preferences of bees at the no-mows revealed that many of the bees we observed favored *Lotus corniculatus* (Birds-foot Trefoil) (Figure 9a). In contrast, many of the bees in Solar Farm 1 preferred *Securigera varia* (Crown Vetch) over most of the other wildflowers present, including Birds-foot Trefoil (Figure 9b).

## V. Discussion

Overall, no-mow sites vary in their success as foraging sites for pollinators. We found that the bumblebee species were highly attracted to non-native wildflowers growing within the no-mow and solar farm sites, with the exception of *Verbena hastata* (Blue vervain), which is native to eastern North America (Figure 10 and 11). Based on the no-mow data, there is a general wildflower preference for each bumblebee species observed. *Bombus bimaculatus* was observed on *Trifolium arvense* (Rabbit-foot clover) most frequently, and *Bombus griseocollis*, *Bombus impatiens*, *Apis mellifera*, and other native bees were observed on *Lotus corniculatus* the most (Figure 9a). This trend could be attributed to the fact we visited NSLS-II, which had a very high relative abundance of *Lotus corniculatus*, on 10 separate occasions, while other sites were visited only 2-5 times. As for our Solar Farm 1 findings, *Bombus impatiens* had the highest relative abundance, which may be attributed to the site's overall high wildflower diversity (Figure 9b). Therefore due to the high diversity wildflowers that this species visited during our observations, we have concluded that *Bombus impatiens* is a generalist forager. Compared to the abundance of *Bombus impatiens*, there was a very low abundance of other bumblebee species such as *B. bimaculatus*, *B. griseocollis*, and *B. fervidus*. *Bombus fervidus* is not shown in our figures since there was only one sighting in Solar Farm 1. Subjectively, we also observed that *Securigera varia* (Crown Vetch) had the highest relative abundance in Solar Farm 1, which could be the reason this wildflower species was the highest preferred among *B. impatiens* and *Apis mellifera*. Despite the dedication of this land to solar energy production, we believe that our data shows that this area acts as a sanctuary for optimal wild pollinator habitat.

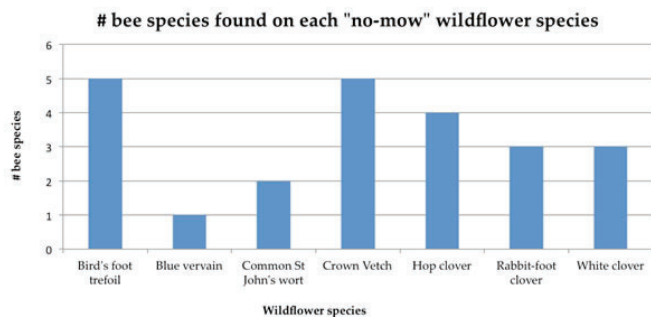


Figure 10. the number of different bee species that was observed on each wildflower species in the no-mow sites

## VI. Acknowledgements

We would like to thank Michelle Joseph and Lindsey McKenna for their help in conducting our pollinator surveys. This project was supported in part by the U.S. Department of Energy, Office of Science, Office of Workforce Development for Teachers and Scientists (WDTS) under the Science Undergraduate Laboratory Internships Program (SULI) and by the National Science Foundation (NSF), Louis Stokes Alliance(s) for Minority Participation (LSAMP) at Southern University at New Orleans under the LSAMP Internship Program at Brookhaven National Laboratory.

## VII. References

“Bumble Bees: Rusty Patched Bumble Bee (*Bombus Affinis*).” The Xerces Society for Invertebrate Conservation, 2017, [xerces.org/rusty-patched-bumble-bee/](http://xerces.org/rusty-patched-bumble-bee/).

Cameron, S. A., Lozier, J. D., Strange, J. P., Koch, J. B., Cordes, N., Solter, L. F., & Griswold, T. L. (2011). Patterns of widespread decline in North American bumble bees. *Proceedings of the National Academy of Sciences of the United States of America*, 108(2), 662-667. doi:10.1073/pnas.1014743108

“Pollinator Conservation.” The Xerces Society for Invertebrate Conservation, The Xerces Society, [xerces.org/pollinator-conservation/](http://xerces.org/pollinator-conservation/).

National Research Council. “Summary.” *Status of Pollinators in North America*, National Academies Press, pp. 1–12.

Ramanujan, Krishna. “Insect Pollinators Contribute \$29 Billion to U.S. Farm Income.” *Cornell Chronicle*, Cornell University, 22 May 2012, [news.cornell.edu/stories/2012/05/insect-pollinators-contribute-29b-us-farm-income](http://news.cornell.edu/stories/2012/05/insect-pollinators-contribute-29b-us-farm-income).

Watanabe, Myrna. “Colony Collapse Disorder: Many Suspects, No Smoking Gun.” *BioOne*, American Institute of Biological Sciences, 2008, [www.bioone.org/doi/full/10.1641/B580503](http://www.bioone.org/doi/full/10.1641/B580503).

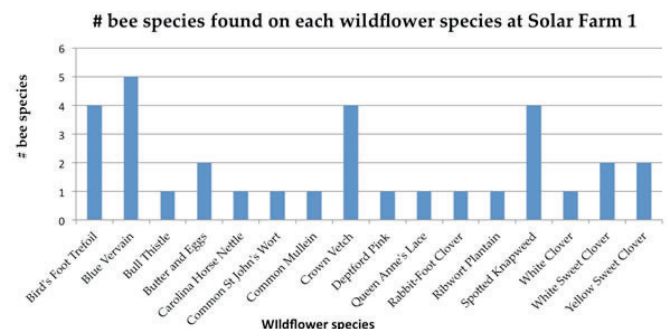


Figure 11. the number of different bee species that was observed on each wildflower species at Solar Farm 1

# Dose assessment of radiation fields inside 8-ID-A first optical enclosure at the National Synchrotron Light Source-II

Kalifa O. Kelly, Chemistry, Texas Southern University, Houston, TX 77004

Jessie R. Zapata, and Mark C. Harvey, Physics, Texas Southern University, Houston, TX 77004

Steve A. Coleman, Environment, Safety & Health/ Radiological Control Division, Brookhaven National Laboratory, Upton, NY 11973

## ABSTRACT

The National Synchrotron Light Source II (NSLS-II) at Brookhaven National Laboratory (BNL) produces high energy x-rays for imaging and high-resolution energy analysis. X-rays are transported through beamlines to experimental enclosures where experiments are conducted. The purpose of this experiment was to measure the stray radiation dose contribution from energetic gammas produced inside the first optical enclosure (FOE) of beamline 8-ID-A at NSLS-II for the first time. In addition, an assessment for stray neutrons was also performed. Measurements of radiation inside of this enclosure were performed using the following equipment: 451P survey meters for gammas, SWENDI-E600 for neutrons, and thermoluminescent dosimeters TLDs. Prior to TLD placement, 451P survey meters and SWENDI detectors were placed inside of the FOE near the collimating mirror tank to assess the maximum rates. Radiation dose rates within the FOE of the 8-ID-A beamline has only been predicted using Monte Carlo simulations to date. Hence, Monte Carlo simulations were used to determine the nominal placement of the survey instruments. Our preliminary results suggest that the measured dose rates with the 451P survey meter around the first mirror tank were less than 90 mrem/h; however, a maximum TLD dose rate of 2819 mrem/h was measured downstream of the mirror tank near the double crystal monochromator. Furthermore, the neutron dose rates measured with the SWENDI 2 detector was below 20 mrem/h. These measurements will be compared with Monte Carlo results in future work.

## I. INTRODUCTION

The National Synchrotron Light Source II (NSLS-II) at Brookhaven National Laboratory (BNL) produces x-ray radiation of ultra-high brightness and energy resolution, while also providing advanced insertion devices and optics to increase the scientific yield<sup>1</sup>. The x-ray beam is transported from the synchrotron storage ring through an insertion device to each beamline's first optical enclosure (FOE) for specific experiments. An insertion device (e.g., an undulator or wiggler) consist of rows of alternating polarity magnets, which are installed along the section straight of the electron beam orbit. The magnetic field of the undulator is relatively low, yet allows for a nominal beam at a certain peak intensity. By contrast, the wiggler provides a high magnetic field producing a wide spectrum of extremely intense and continuous radiation of short wavelength. The insertion devices provide for the high-performance demands of NSLS-II, where optical focusing of the x-rays provide high quality beam to each beamline<sup>2</sup>. (add paragraph from Klaus). The main stray radiation considered in this study include the following: bremsstrahlung radiation cre-

ated during electron beam interactions in the synchrotron storage ring with residual gas molecules, secondary neutron production by high energy bremsstrahlung photons and synchrotron radiation from the insertion devices and bending magnets, respectively<sup>1</sup>. Primary gas bremsstrahlung accompanied by synchrotron radiation can interact with various components along the beamline resulting in cascade showers through the materials that make up the beamline components<sup>3</sup>. The radiation doses inside FOE 8-ID-A produce the most significant contribution of scatter dose at NSLS-II and were calculated using the FLUKA Monte Carlo code<sup>4</sup>. Prior to measurements presented in this paper, FLUKA was also used to calculate the radiation levels for occupiable regions (dose rate < 5 $\mu$ Sv/h)<sup>5</sup> of the experimental floor due for errant electron beam conditions and to simulate particle transport through shielding materials to assess their efficacy<sup>6</sup>. Of note is that the FLUKA calculations and simulations have been the only tool utilized at NSLS-II to estimate radiation dose within the enclosures. Hence, it is of high importance to validate these calculated results against measured data to better understand the shielding and design efficacy of the beamline enclosures at NSLS-II. The purpose of this work was to measure the bremsstrahlung spectrum and stray radiation dose contribution from energetic x-rays produced inside the FOE of beamline 8-ID-A at NSLS-II for the first time. In addition, a dose assessment of the stray neutron contributions was also performed. These measurements were compared with two independent Monte Carlo codes: FLUKA<sup>7</sup> and GEANT4<sup>8</sup>.

## II. METHODS AND MATERIALS

The stray radiation dose generated by energetic gamma and neutron secondaries produced inside the FOE of beamline 8-ID-A at NSLS-II was measured for the first time. Dose rate measurements were performed with ion chamber survey meters, a gamma dose and spectrometer unit and neutron detectors primarily around the main contributing source of radiation inside the FOE. Measurements of radiation inside of this enclosure were carried out using the following equipment: 451P survey meters for gammas, a Wide Energy Neutron Detector and accompanying survey meter Eberline E600 (SWENDI-2-E600) and REM Ball for neutrons, a spectrometer unit for both gamma spectroscopy and dosimetry, and thermoluminescent dosimeters (TLD). The FLUKE 451P survey meter has dimensions of 4.0 in x 8.0 in x 6.0 in with a 230 cm<sup>3</sup> ionization chamber pressurized to 125 psi for gamma detection above 25 keV. The SWENDI-2 detector consisting of a polyethylene cylindrical shell (9.0 in diameter x 8.3 in length) and an inner <sup>3</sup>He proportional tube (dimensions 0.6 in x 1.0 in), which is surrounded by tungsten powder was coupled to an E600 survey meter and used to measure the neutron ambient dose equivalent rate with detection capabilities ranging from thermal energies up

to 5 GeV. The NRD neutron ball from Thermo Fisher Scientific was coupled to the ASP2e Eberline survey meter and consists of a 9 in diameter outer spherical shell of cadmium loaded polyethylene and a  $\text{BF}_3$  tube (dimensions 0.6 in X 1.0 in) measured the secondary neutron dose rate from thermal energies up to 10 MeV. A Canberra InSpector™ 1000 hand-held Multichannel Analyzer with a LaBr probe (1.5 in x 1.5 in) was used for both gamma spectroscopy and dosimetry measurements over an energy range of 30 keV to 3 MeV. Harshaw TLD badges (8814 A/B type) were used to map the secondary gamma dose along the FOE beamline in 8-ID-A. The TLD card is comprised of four LiF:Mg, Ti hot-pressed chips positioned between Teflon sheets on an aluminum substrate. Measurement of the gamma dose and neutron rates was conducted near the collimating mirror tank in FOE 8-ID-A, where the main contribution of radiation was predicted from FLUKA calculations. The detectors were initially placed at different locations laterally with respect to the beamline center between the mirror tank and outer wall of the FOE to assess the gamma dose rates. Following the initial study, two 451P survey meters, SWENDI-E600, NRD neutron ball, and InSpector 1000 detector were placed on the top of the mirror tank to measure the dose rates and bremsstrahlung spectrum, respectively. The SWENDI-E600 measured the most energetic directional neutrons over a wider energy range ( $> 50$  MeV), while the NRD ball measurements evinced the isotropic neutrons (7 – 10 MeV). Finally, TLDs were mounted along the beamline of the FOE and some were also hung vertically by string above the center of the mirror tank to measure the elevation dosimetric spread of radiation. Results obtained from the experiment were compared with both FLUKA and Geant4 calculations.

### III. RESULTS

Figure 1 shows an example of the measurement setup in the FOE of 8-ID-A with the FLUKE 451P, SWENDI and Canberra InSpector™ 1000 detectors positioned at the mirror tank. Figure 2 illustrates the Geant4 (version 10.3) simulation the main beam line components contiguous with the corresponding measurements points in the FOE. In Figure 3, a plot of the gamma dose rate measured with the FLUKE 451P gamma survey meter about 1.8 m above the floor of FOE 8-ID-A is shown as a function of the distance away from the upstream wall relative to the central beamline axis at a mean beam current of 325 mA. (The line is included in Figure 3 to guide the eyes). The dose rate peaked at  $11.4 \pm 0.17$  mrem/h at the center of the collimating mirror tank, which was approximately 3.8 m downstream of the FOE front wall. A small increase in the gamma dose rate of  $0.79 \pm 0.073$  mrem/h was also observed around 7.7 m downstream just after the monochromator. The measured bremsstrahlung spectrum is shown as a function of energy in Figure 3 about 1.8 m above the center of the collimating mirror tank with the maximum gamma energy occurring at 270 keV. Figures 5a and 5b show a linear increase in the mean gamma rate with increasing beam current at the front and top collimating mirror tank, respectively. The curves are linear fits to the data. Figure 6 shows an event from the Geant4 simulation of the scattered radiation indicating that the majority of the scatter dose is produced between the first and second collimating mirrors, where the most measurements were emphasized. The largest mean dose rate of  $79 \pm 0.44$  mrem/h was measured nearly 4.4 m downstream of the mirror tank about 1.5 m above the floor at 325 mA. However, a maximum TLD dose rate of 2819 mrem/h was

measured at the DCM. (see Fig. 7)

### IV. CONCLUSION

In conclusion, dose rates and gamma spectrum were measured for the first time inside FOE 8-ID-A. Our data suggests that the radiation inside of this FOE was comparable to previous Monte Carlo results. Furthermore, measurements of the dose rates with increasing beam current showed a clear linear dependence and exceeded predicted values in some areas. Of note is that the largest dose rate calculated with FLUKA was approximately 10 mrem/h at an operating current of 500 mA between collimating mirrors one and two<sup>9</sup>. However, the dose rates measured in this work at 325 mA were nearly an order of magnitude greater.

Limitations of this experiment included (1) performing data measurements in parasitic mode, which was a time constraint limiting access to the FOE to position detectors and assess radiation dosimetry, and (2) inadequate remotely monitoring capability for the spectrometer and neutron devices preventing real time data acquisition of the gamma spectra and neutron dose rates, respectively.

The NSLS-II facility has not been fully constructed; therefore, the data obtained in this experiment may provide additional insight into hutch enclosure design and potentially lead to a reduction of shielding material and monitoring costs by decreasing safety redundancy and time in the future.

### V.

#### REFERENCES

- [1] Job P.K., Casey W.R., 2011, Radiological considerations for bulk shielding calculations of national synchrotron light source-II, Nucl. Instr. and Meth. in Phys. Res. A 660 1 - 6
- [2] Tanabe, Toshi, Charles Kitegi, Ping He, Marco Musardo, Oleg Chubar James Rank, Peter Cappadoro, Huston Fernandes, David Harder, and Todd Corwin. "The Latest Status of NSLS-II Insertion Devices." Journal of Physics: Conference Series 493 (2014): 012031. Web.
- [3] Asai, J., and H. Hirayama. "Shielding Design Study against Gas Bremsstrahlung for the CLS first Optics Enclosures." N.p., 2007. Web.
- [4] Ahmed, A.S., Benmerrouche, M. Cubbon, G., 2015, Monte Carlo simulation study to calculate radiation dose under beamloss scenarios in Top-up operation mode for HXMA beamline at Canadian Light Source, Radiat Meas 74 31-38
- [5] Devienne A., Aymerich N., Garcia-Fuste M.J., Queralt, X., 2015, A comparative radiation study at ALBA synchrotron facility between Monte Carlo Modeling and radiation monitors dosimetry measurements, Radiat Phys and Chem 116 365-367
- [6] Job P.K., Casey W.R., 2011, Radiological implications of top-off operation at national synchrotron light source-II, Nucl. Instr. and Meth. in Phys. Res. A 648 15 - 21
- [7] Battistoni, G. et al. "Applications of FLUKA Monte Carlo Code for Nuclear and Accelerator Physics." Nuclear Instruments and Methods in Physics Research Section B: Beam Interactions with Materials and Atoms 269.24 (2011): 2850-856.
- [8] Agostinelle, S. et al. 2003
- [9] private communications



## VI. ACKNOWLEDGMENTS

The authors would like to thank Klaus Attenkoffer, Mohamed Benmerrouche, Noel Blackburn, Shawn Buckallew, Sean Carr, Sunil Chitra, Steve Coleman, Gregory Condemi, Henry Kahnhauser, Robert Lee, Andrew Levine, Reid Smith, Eli Stavitski, Geraldine Townsend, and Kimberly Wehunt for their assistance and helpful discussions with this project. This project was supported in part by the National Science Foundation (Grant No. HRD-1407736) Louis Stokes Alliance(s) for Minority Participation (LSAMP) at Texas Southern University under the LSAMP Internship Program at Brookhaven National Laboratory.

TLD No.	Cumulative deep dose (rem)	Dose rate (mRem/h)
1	0.00	0.00
2	1.75	24.4
3	0.11	1.54
4	0.52	7.26
5	0.04	0.558
6	0.01	0.139
7	0.02	0.279
8	0.38	5.30
9	1.15	16.1
10	0.01	0.139
11	1.57	21.9
12	0.52	7.26
13	0.08	1.12
14	0.18	2.51
15	0.26	3.63
16	0.17	2.37
17	0.40	5.58
18	1.21	16.9
19	0.73	10.2
20	202	2819
21	0.08	1.12
22	0.17	2.37
23	0.14	1.95
24	0.04	0.558
25	0.04	0.558

Table 1. Subset of the deep cumulative dose and deep dose rates measured with TLDs along the FOE of the 8-ID-A beamline.

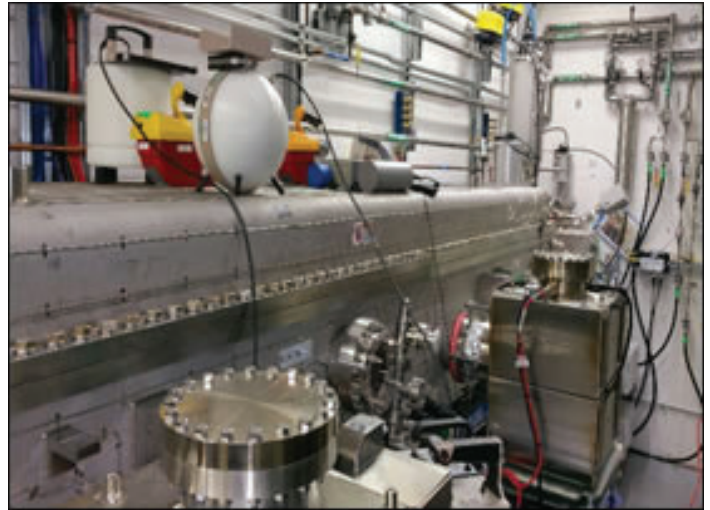


Figure 1. The FOE of 8-ID-A is shown with the detectors positioned at the mirror tank at NSLS II. Measurements were performed at fixed positions along the longitudinal and lateral directions of the beamline.

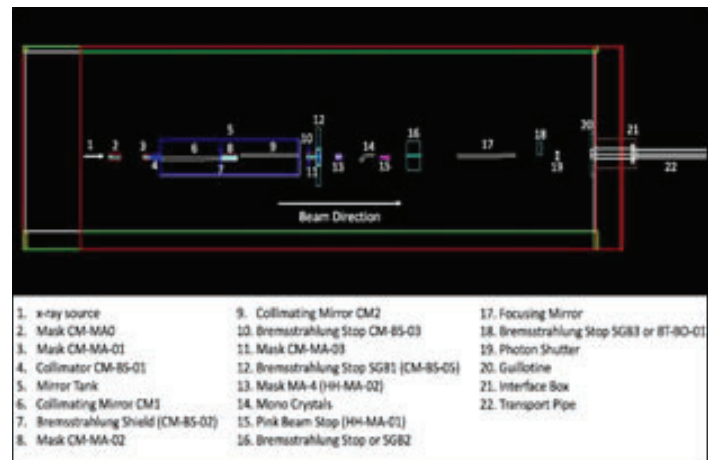


Figure 2. Side view of the FOE of 8-ID-A at NSLS II using the Geant4 Monte Carlo toolkit. The main beamline components are indicated by numbers.

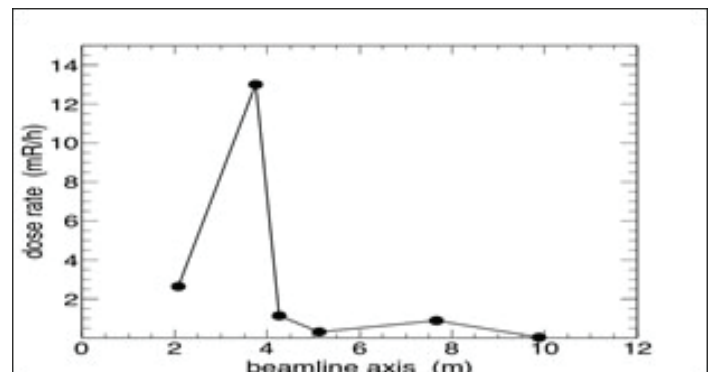


Figure 3. The mean gamma dose rate produced along the beam components of FOE 8-ID-A is shown as a function of the distance away from the front wall. These measurements were performed about 1.8 m above the floor at fixed positions along the beam line axis.

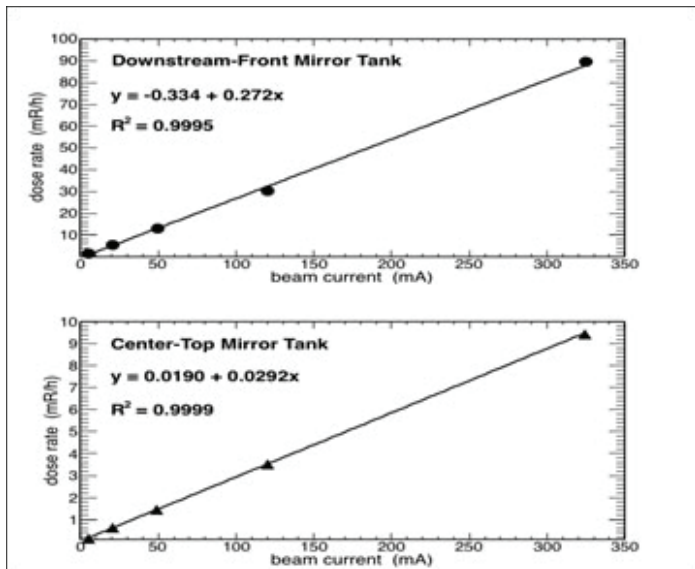


Figure 4. The mean gamma dose rate is shown as a function of the mean beam current for measurements performed with the FLUKE 451P survey meter (a) directly in front of and (b) on top of the mirror tank. The dose rate scales linearly with increasing current. The curves are linear fits to the data.

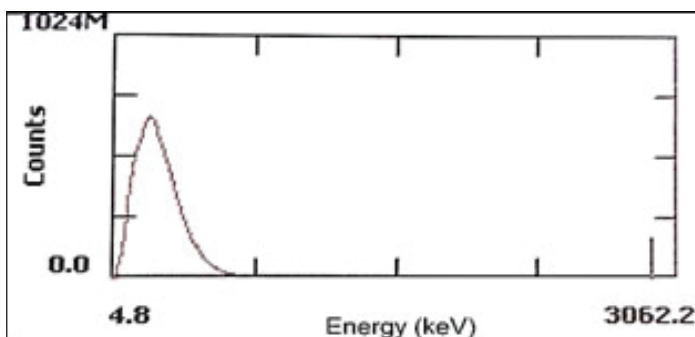


Figure 6. Bremsstrahlung spectrum measured with the Canberra Inspector 1000 hand-held MCA about the center of the mirror tank approximately 1.8 m above the floor.

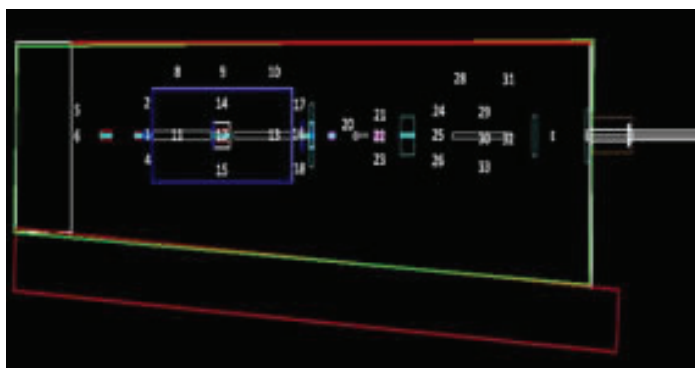


Figure 7. Top view of the FOE of 8-ID-A at NSLS II using the Geant4 Monte Carlo toolkit. The numbers indicate TLD positions. Note that TLDs 3, 7, 19 and 27 were positioned below the beam pipe.

# Microhabitat and vegetation selection of eastern box turtles (*Terrapene carolina carolina*)

Katherine Kennedy, Environmental Protection Division, University of Vermont, Burlington, VT 05405  
Timothy Green, Environmental Protection Division, Brookhaven National Laboratory, Upton, NY 11973

**The eastern box turtle (*Terrapene carolina carolina*) is a small, terrestrial turtle that utilizes its microhabitat to thermoregulate and prevent excess water loss. The microhabitat of *T. c. carolina* is not thoroughly understood and many studies do not characterize the microhabitat relative to the surrounding habitat. This summer, we used radio telemetry to track nine different eastern box turtles on the grounds of Brookhaven National Laboratory. We closely examined the diagnostic characteristics of the microhabitats by measuring vegetation preference, number of standing dead trees (snags), amount of downed woody debris, ground cover, and canopy cover within a 3-m radius of each turtle's location. We identified the species composition of the trees understory surrounding the turtle to assess overall vegetation preference. We measured the diameter at breast height (DBH) of the surrounding trees within the 3-m radius, and recorded the species of these trees. We also recorded the number and species of trees that had a DBH less than 2.5 cm. We measured humidity and temperature at standing height (152 cm), and at the height of the turtle, to assess how turtles may utilize the microhabitat to prevent water loss. There is not a preferred tree species, however, there is evidence that suggests eastern box turtles prefer areas of downed woody debris, and being covered by either leaf litter or thick vegetation, such as barberry or green brier. Understanding the characteristics of microhabitat provides greater context for preferred habitat in a species, making it essential to conservation and management.**

## I. Introduction

Eastern box turtles are terrestrial turtles typically found in grasslands or mesic forests of eastern and central United States. These turtles behaviorally thermoregulate by utilizing different microhabitats to regulate body temperature, prevent water loss, and maintain homeostasis<sup>2</sup>.

Their microhabitats are characterized by factors such as leaf litter, vegetation, canopy cover, and downed woody debris<sup>5</sup>. At higher temperatures, or other unfavorable climatic conditions, eastern box turtles create "forms", or small depression in the leaf litter shaped by the carapace. These forms create an environment with more moisture<sup>3</sup>. In addition to the form, eastern box turtles also seek microhabitats beneath thick vegetation or downed woody debris.

Understanding the conditions of different microhabitats is important to developing different management strategies for the species. This study investigates the conditions of the microhabitat within the greater context of the available macrohabitat with an emphasis on preferred vegetation.

## II. Methods & Materials

### A. A. Study Site

We conducted this study at Brookhaven National Laboratory, in Upton, New York, in central Long Island. The area of the laboratory campus is 2,130 hectares, with approximately 1,361 hectares of undeveloped land. The Long Island Solar Farm comprises approximately 81 hectares of land on site. Land cover type includes vegetation of varying successional stages, wetland, and grassland areas.

### B. B. Radio telemetry

We used radio telemetry to track nine out of the 20 turtles that have been situated with radio transmitters as individuals of ongoing research through the laboratory's Environmental Protection Department. The transmitters are mounted on the posterior end of each turtle's carapace using an epoxy glue, and make up about 5% of the turtle's total mass. Our study was conducted over the span of seven weeks throughout the months of June, July and August. Four turtles were tracked twice a day between 9 AM to 12 PM and 1 PM to 3 PM. The other five turtles were tracked twice every week within the same time blocks on Tuesdays and Thursdays.

### C. C. Vegetation and microhabitat

We defined microhabitat as the 3-m radius of the turtle, and collected data on the vegetative characteristics within that area. Canopy cover was measured using a spherical crown densiometer, and ground cover by estimating the percent that was not leaf litter or bare ground. Each species in the understory or on the ground was recorded. Within the ground cover, we estimated the percent of which downed woody debris was present within the ground cover. Each tree that was greater than 2.5-cm DBH was identified and measured. We also recorded the number and species of each tree that was present that was less than 2.5-cm DBH and greater than 1.2-m tall. We recorded the number of standing dead trees, or snags, present, as well as whether either leaf litter, downed woody debris, or thick vegetation covered the turtle.

To provide greater context for the total available habitat, we selected random plots by using the Random Points Tool on the GIS platform, ArcMap 10.1. This tool selected more than 1500 random coordinates. Within these random coordinates we selected land cover where the turtles would most likely not be found: buildings, parking lots, roads, water, grass, disturbed areas, and the solar farm. Although we found turtles on the grounds of the solar farm in the past, due to the smaller sample size and the large area of the solar farm, the data collected from locations in the solar farm would most likely skew the results. When these land cover types were eliminated, there were 1054 points remaining in the land cover types Red Maple-Blackgum Wet Forest, Red Maple-Mesic Heath Forest, Red-Maple Red Oak-Mesic Heath Forest, Pitch Pine/White Oak Forest, Pitch Pine/Mixed Oak-Heath Forest, Planted White Pine Forest, Black Cherry Forest, Red Oak-



Heath Forest, Successional, and Cattail Marsh. With these points, we used a random number generator to select 30 random numbers from 1-1054. These 30 numbers were the plots where we collected vegetation data.

### III. Results

We used a one-sample t-test to compare the number of trees, average DBH, density of canopy cover, and percent of downed woody debris in the ground cover at the plots with turtles present and the random plots. We found that there was 8.62% more downed woody debris cover at the plots where turtles were present ( $t(113)=2.13, p=0.018$ ). There were more trees found at the random sites ( $t(113)=-0.68, p=0.245$ ) with an overall smaller average DBH ( $t(113)=0.25, p=0.402$ ), however the difference was not significant. There was a higher canopy cover density at plots with turtles ( $t(113)=0.48, p=0.316$ ), but these results were not significant.

At the sites with turtles, the most frequently sighted tree species were red oak (*Quercus rubra*) and red maple (*Acer rubrum*), while commonly sighted species were also white oak (*Quercus alba*) and sassafras (*Sassafras albidum*). The most frequently sighted tree species at random sites were pitch pine (*Pinus rigida*) and red oak (*Quercus rubra*). The two different plot types overall had trees that represent almost completely different forest types.

Lowbush blueberry (*Vaccinium angustifolium*) was the most abundant understory species at turtle plots found at both plot types, followed by green brier (*Smilax rotundifolia*), highbush blueberry (*Vaccinium corymbosum*), and huckleberry (*Vaccinium ovatum*). The most abundant understory species at random sites was lowbush blueberry (*Vaccinium angustifolium*), followed by huckleberry (*Vaccinium ovatum*), and various species in the grass family (Poaceae).

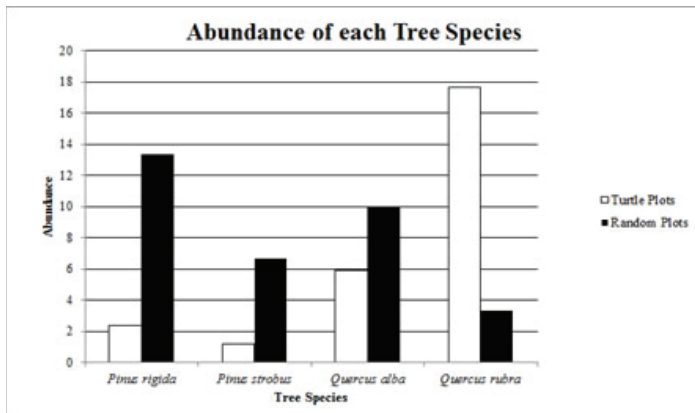


Figure 1. Normalized abundance of each tree species that was found at both the turtle sites and the random sites.

Tree Species	Total	Random Plots	Total
<i>Acer rubrum</i>	12	<i>Cornus florida</i>	1
<i>Carya cordiformis</i>	2	<i>Pinus rigida</i>	4
<i>Nyssa sylvatica</i>	2	<i>Prunus serotina</i>	1
<i>Pinus rigida</i>	2	<i>Quercus alba</i>	2
<i>Pinus strobus</i>	1	<i>Quercus rubra</i>	3
<i>Quercus alba</i>	5	<i>Robinia pseudoacacia</i>	1
<i>Quercus rubra</i>	15		
<i>Quercus velutina</i>	2		
<i>Sassafras albidum</i>	3		

Table 1. The total number of sightings of each tree species, including those that were not shared between the two different plot types

### IV. Discussion

Overall, these results suggest that the turtles are selecting areas with a greater percentage of downed woody debris, as well as fewer small trees (DBH < 2.5-cm), a denser tree canopy, and more trees with an overall greater average DBH.

Downed woody debris provides a wide range of habitat depending on the vegetation species composition of the larger habitat<sup>4</sup>. Therefore, an area of this study to expand on would be to consider if there is a correlation between microhabitat selection, and the decaying period of the species in the surrounding macrohabitat.

The tree species found most frequently surrounding the turtles was red oak and red maple, both of which are associated with mesic forests in eastern North, where box turtles are known to typically be found. These forests are also associated with patchy canopy cover, an abundance of downed woody debris for cover, and moisture retaining soil<sup>3</sup>. The varying densities of canopy cover provide the eastern box turtles with opportunities to bask, while also allowing them to remain out of the sunlight for large spans of time<sup>3</sup>. The tree species found at the random sights are largely associated with early successional and grassland habitat. Pitch pine, black cherry (*Prunus serotina*), and black locust (*Robinia pseudoacacia*), are all shade intolerant species, while white oak (*Quercus alba*) and red oak are classified as having an intermediate shade intolerance<sup>1</sup>. This suggests that the eastern box

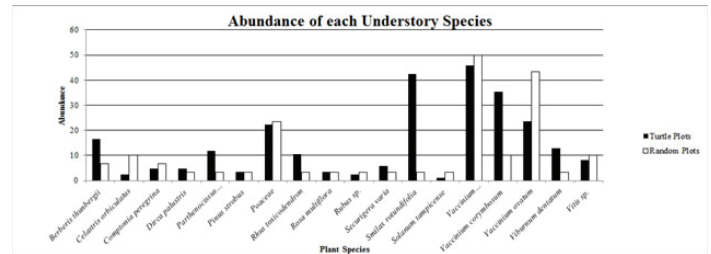


Figure 2. Normalized abundance of the understory species found at both the turtle sites and the random sites. These plants include trees that were <2.5-cm DBH, herbaceous and woody plants found on the ground and in thickets, and tree saplings.

Turtle Plots	Total	Random Plots	Total
<i>Asclepias syriaca</i>	2	<i>Berberis thunbergii</i>	2
<i>Berberis thunbergii</i>	14	<i>Celastris orbiculatus</i>	3
<i>Boehmeria cylindrica</i>	1	<i>Comptonia perigrina</i>	2
<i>Celastris orbiculatus</i>	2	<i>Dirca palustris</i>	1
<i>Clethra alnifolia</i>	22	<i>Lyonia ligustria</i>	2
<i>Comptonia perigrina</i>	4	<i>Parthenocissus quinquefolia</i>	1
<i>Dirca palustris</i>	4	<i>Pinus rigida</i>	3
<i>Gaultheria procumbens</i>	1	<i>Pinus strobus</i>	1
<i>Juncaceae</i>	1	<i>Poaceae</i>	7
<i>Lonicera sp.</i>	1	<i>Prunus serotina</i>	1
<i>Oxalis stricta</i>	2	<i>Quercus alba</i>	2
<i>Parthenocissus quinquefolia</i>	10	<i>Quercus rubra</i>	1
<i>Pinus strobus</i>	3	<i>Quercus ilicifolia</i>	3
<i>Poaceae</i>	19	<i>Rhus toxicodendron</i>	1
<i>Rhus toxicodendron</i>	9	<i>Rosa multiflora</i>	1
<i>Rosa multiflora</i>	3	<i>Rubus sp.</i>	1
<i>Rubus sp.</i>	2	<i>Securigera varia</i>	1
<i>Securigera varia</i>	5	<i>Smilax rotundifolia</i>	1
<i>Smilax rotundifolia</i>	36	<i>Solanum tampicense</i>	1
<i>Solanum tampicense</i>	1	<i>Trifolium pratense</i>	1
<i>Vaccinium angustifolium</i>	39	<i>Vaccinium angustifolium</i>	15
<i>Vaccinium corymbosum</i>	30	<i>Vaccinium corymbosum</i>	3
<i>Vaccinium ovatum</i>	28	<i>Vaccinium ovatum</i>	13
<i>Viburnum dentatum</i>	11	<i>Viburnum dentatum</i>	1
<i>Vitis sp.</i>	7	<i>Vitis sp.</i>	3
<i>Wisteria frutescens</i>	3		

Table 2. The total sightings of each understory species at both plot types, including the species that were sighted only at one plot type and not the other.

turtles we were studying selected habitats associated with more shade, adequate sun exposure, and soil with greater moisture retention.

However, there were instances when we found turtles in open grass fields, and therefore a more extensive study, with a greater sample size, would be beneficial to understanding the choices made by the eastern box turtle.

Green brier, lowbush blueberry, highbush blueberry, huckleberry, and coastal sweet pepper bush (*Clethra alnifolia*) were the most common understory plants found at the turtle plots. Individuals were often found occupying dense thickets of greenbrier, which suggests the turtles were utilizing the species for cover and increased moisture.

To better assess if there is an active selection occurring in eastern box turtles at Brookhaven National Lab, we will need to increase our sample size of both the number of times visiting plots with a turtle present, as well as number of random plots on grounds of the lab. The results of this study also do not represent eastern box turtles in their full geographical range, and therefore any conclusions drawn may only be specific for the turtles at the Laboratory. We also only tracked female box turtles in the southeastern region of the Laboratory grounds. This study is nearly a foundation for understanding the choices made by eastern box turtles in terms of vegetation and microhabitat.

## V. Acknowledgements

This project was supported in part by the U.S. Department of Energy, Office of Science, Office of Workforce Development for Teachers and Scientists (WDTS) under the Science Undergraduate Laboratory Internships Program (SULI). I would also like to extend my gratitude to Dr. Timothy Green and Dr. Russell Burke for their additional support and guidance during this study.

## VI. References

- Abrams, Marc D., and Mark E. Kubiske. "Leaf structural characteristics of 31 hardwood and conifer tree species in central Wisconsin: influence of light regime and shade-tolerance rank." *Forest Ecology and Management* 31, no. 4 (1990): 245-253.
- Adams, Nadine A., Dennis L. Claussen, and John Skillings. "Effects of Temperature on Voluntary Locomotion of the Eastern Box Turtle, *Terrapene carolina*." *Copeia* 1989, no. 4 (1989): 905-15. doi:10.2307/1445976
- Dodd, C. Kenneth. *North American box turtles: a natural history*. Vol. 6. University of Oklahoma Press, 2002.
- Harmon, Mark E., Jerry F. Franklin, Fred J. Swanson, Phil Sollins, S. V. Gregory, J. D. Lattin, N. H. Anderson et al. "Ecology of coarse woody debris in temperate ecosystems." *Advances in ecological research* 15 (1986): 133-302.
- McKnight, Donald T. "Observed plant preferences of eastern box turtles (*Terrapene carolina carolina*) in a Maryland forest." *Herpetology Notes* 4 (2011): 97-102.

# Electromagnetic calorimeter quality control and mechanical design for the sPHENIX Project

Spencer Laddy-Locks, Mechanical Engineering, Stony Brook University, Stony Brook 11790  
Donald Lynch, Sean Stoll, and William Lenz, Physics Dept., Brookhaven National Laboratory, Upton, NY 11973

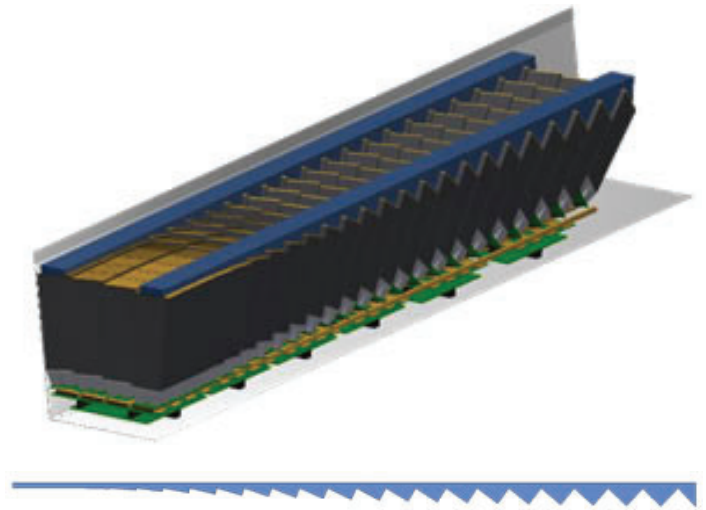
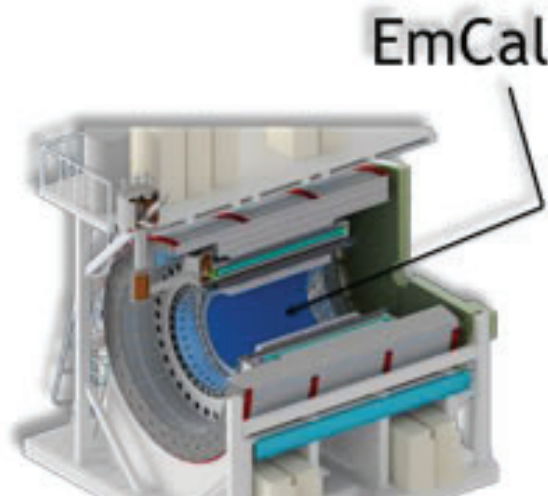
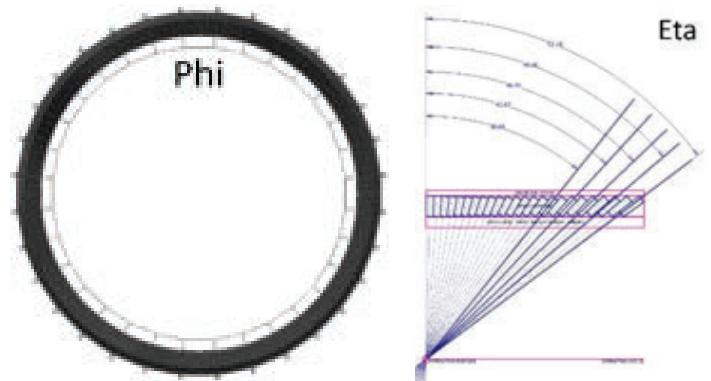
## Abstract

An electromagnetic calorimeter (EmCal) is going to be one type of calorimeter in the sPHENIX detector at Brookhaven National Laboratory. Continuing this year, the PHENIX project will be undergoing removal and repurposing to make room for the newest upgrade to the Relativistic Heavy Ion Collider (RHIC). The sPHENIX project includes the EmCal, which will allow scientists and physicists to analyze the electromagnetic particles that are emitted by quarks and gluons after a collision. The detector will accomplish this by utilizing 6,144 triple tapered tungsten blocks (64 sectors, with 96 blocks each) which internally, have 2,668 scintillating fibers each. My engineering focusses this summer was to design and test how these blocks would be mechanically mounted inside of the final detector, and how to confirm that the blocks were produced within tolerance. I used Autodesk Inventor to design an aluminum “sawtooth” which would provide a faceted mounting surface for each block in a sector. This method has reduced the number of unique machined parts from 88 to 26. I have also developed a matlab program that is able to process an image of a completed block and provide vital information pertaining to the optical quality of the block. The work that I have done over this summer will continue and may be implemented in the final detector. While working with great engineers and scientists, I have not only increased my understanding of mechanical engineering and collaboration, but I have also contributed to a large project that has and will continue to help push our understanding of science forward in great strides. Additionally, while working on the sPHENIX project at BNL I have gained experience that will carry through my career and invaluable connections that will last a lifetime.

## I. Background

The electromagnetic calorimeter converts electromagnetic particles into photons. These photons can then be read by a silicon photomultiplier (SiPM) sensor which converts the light into an electronic signal. This is used to calculate the energy of the particle. To do all of this in sPHENIX, the proposed EmCal will use 6,144 tungsten epoxy composite blocks. These blocks must be triple tapered to provide the detector resolution and efficiencies desired. The first two tapers allow for the blocks to point close to the interaction point when the blocks are rotated about the phi and eta direction. The third taper permits the blocks to fit inside of the stainless-steel sector assembly box, which has a taper of its own. These blocks have complex geometric features which makes designing the mounting system a unique challenge.

Each block internally has 2,668 scintillating fibers. It is important to ensure that the manufacturing process successfully placed each of these fibers to allow for proper readout using the SiPM. This presented another engineering challenge.





## II. Mechanical Mounting

### A. A. T-Stock

The original method for attaching all 96 blocks to the top of the stainless-steel assembly box utilized aluminum T-stock material. The T-stock would be precisely machined and epoxied onto the top surface of each block. Due to the complex geometries of these blocks, this method would require there to be 88 different machined parts. This could lead to high costs and a higher possibility of assembly error due to the many slightly different parts.

### B. B. Sawtooth

Utilizing an aluminum sawtooth mounting piece, the number of unique parts would be reduced from 88 to 26. This method would consist of 22 different thin aluminum mirrored plates (shown as gold), and at most, four different aluminum sawtooths (shown as blue). Due to the reduced number of unique parts, cost and complexity is reduced. The probability of a misplaced part in the assembly also decreases which will result in a faster assembly process.

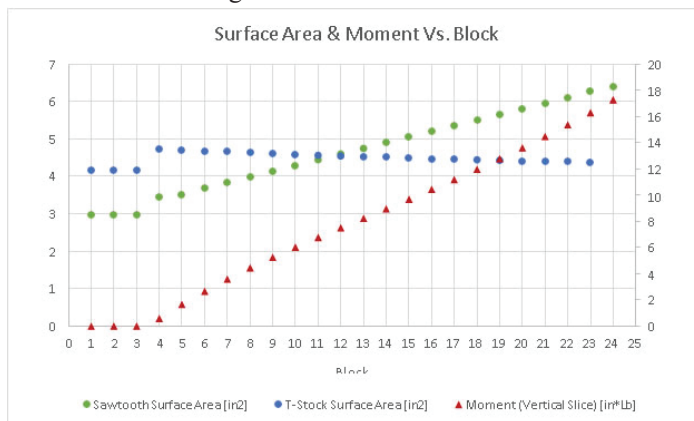
Another benefit that results from this method is the increase in epoxied surface area as the moment of the block increases. Below is a plot that shows how the sawtooth bonding surface area increases linearly after block 3 with respect to block position. The moment induced by gravity follows a similar trend, and is plotted in red. Blocks 1-3 are geometrically the same, this is why there are 96 block, and only 88 unique T-stock that would be needed if that method were chosen.

The sawtooth method would have two epoxied joints, one more than the T-stock method. The joint between the mirror aluminum plate and the block will utilize an optical epoxy, and industrial epoxy will be used to cement the sawtooth to the back of the mirror plate, of which both surfaces will be media blasted for an ideal bonding surface.

## III. Testing

### A. A. Stress Analysis

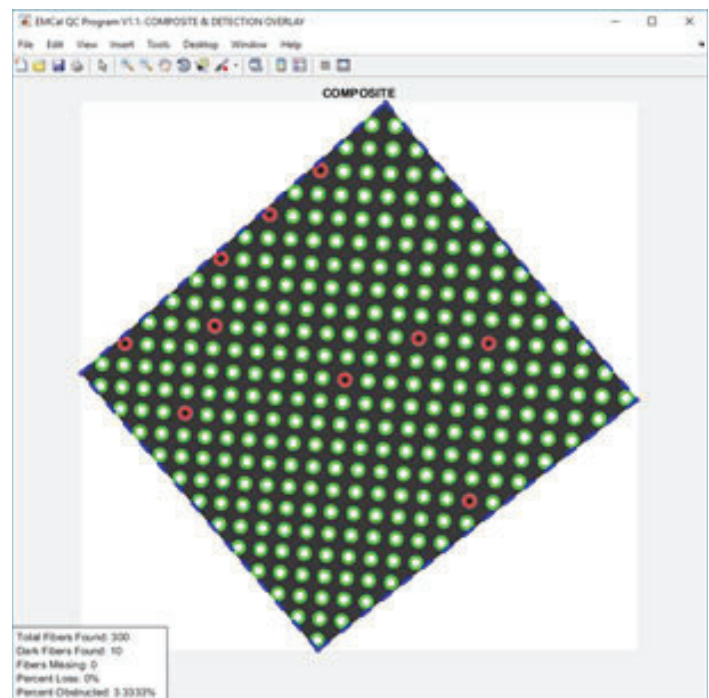
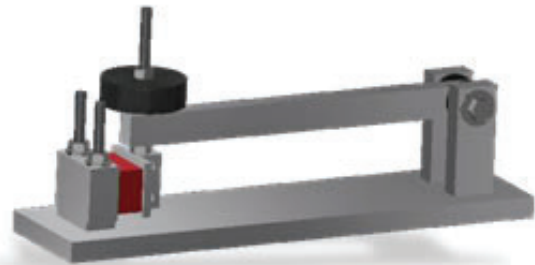
Testing was conducted to analyze the bond strength of different epoxies that could be used in the detector. Each EMCal block weighs about seven pounds. It is imperative that the epoxied joints in the detector can withstand not only the forces that will be seen due to gravity, but also the forces seen during installation. Three methods of testing were proposed, tensile, bending, impact. Each of these tests will be conducted first as a control. Further testing will involve the same three tests after the test specimens are subjected to thermal cycling and radiation exposure. This will be done to ensure that the epoxy bonds will remain within acceptable tolerances throughout the life of the detector.



### B. B. Quality Control

To ensure that the finished EMCal blocks are within the required size and quality tolerances to be accepted into the detector, quality control must be implemented. An optical test program was written to provide information about the light transmission quality of each EMCal block. The program, which was written in matlab, obtains a photo of a backlit block and processes the number of illuminated fibers. There are three states of a fiber that the program can detect. The first state is the best state, where the fiber is transmitting the light from the back of the block. This fiber will show up white on the image and the program will categorize it as a good fiber.

The second state is a dark fiber. This fiber is being blocked off on the back end by un-machined tungsten and epoxy composite. This fiber can still transmit light by itself, but will not be as efficient as a bright fiber that can take advantage of the mirrored surface that will be epoxied on after. The third and worst state of a fiber is one that doesn't show up in the image at all. This fiber is completely covered on the readout end of the block. This fiber will not contribute anything to the energy sum, and thus is a bad fiber. By implementing a program like this, the quality of the detector will increase significantly without the need for arduous checking of each fiber by eye. I am planning on designing a desktop device that will allow for an ideal photo of a block to be taken. This device would hold the block at the right distance from the camera and provide all of the light needed for the picture to be clear enough to process using matlab.



#### IV. Results

Although further testing is required to accurately conclude the final design of the support structure for the EMCal blocks, the progress made this summer with the sawtooth design has brought the EMCal's overall conceptual design to a more defined level. The sawtooth will result in lower costs of production, and decrease possibility of an error being made during the assembly of an EMCal sector.

Block quality control will be a major component of EMCal block production. With the new program that has been developed this summer, checking each block's mechanical and optical performance parameters will not only be more accurate, but will also require less time and resources. This will speed up production and allow for more testing and validation, which is key when developing a new design.

#### V. Recommendations

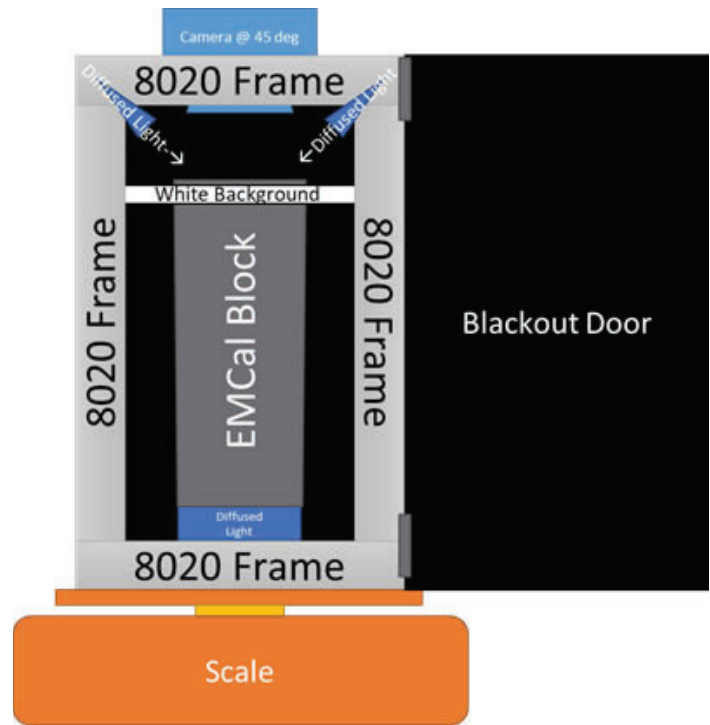
The most important aspect regarding design when working on the EMCal is design iteration. Many designs have been proposed for the structural support of each block inside of the sector assembly box. Each design had its benefits and downfalls. When working on an engineering challenge, incorporating the best of many different designs can lead to the best final product. Each previous design or idea helped the next become that much more ideal. That is why I recommend that time be assigned to researching more ways to mount the EMCal blocks into place. The sawtooth method is extremely promising, and it likely would be. However, even the best idea can be improved when looked at from a different angle.

More testing is needed to prove out the two epoxy bonded joints. More specifically, how they will react to the environment seen in the interaction room has yet to be fully determined. Some tests that will help simulate the interaction room's environment may include thermal cycling, radiation hardening, and time degradation. The progress thus far on the EMCal quality control and mechanical design has and will continue to help develop the EMCal for a full sector prototype in the near future.

#### VI. Acknowledgements

This project was supported in part by the Brookhaven National Laboratory (BNL), (sPHENIX, Physics) under the BNL Supplemental Undergraduate Research Program (SURP).

I would also like to especially thank Cindi Biancarosa, Tina Walsh, Melvyn Morris, Noel Blackburn, Mike Stegman, Nicholas Bonura, and everyone at the Office of Educational Programs at Brookhaven National Laboratory who make the program run as smoothly as it does.



# Improving machine-learning classification accuracy of x-ray scattering images

Ronald Lashley<sup>c</sup>, Nicole Meister<sup>a, b</sup>, Ziqiao Guan<sup>b</sup>, Bo Sun<sup>f</sup>, and Dantong Yu<sup>c, d</sup>

<sup>a</sup>Stony Brook University, <sup>b</sup>Centennial High School,

<sup>c</sup>Brookhaven National Laboratory, <sup>d</sup>New Jersey Institute of Technology,

<sup>e</sup>Lincoln University (PA), <sup>f</sup>Rowan University

## Abstract

In technology, image recognition software uses various methods to extract information from an image. X-ray scattering images contain visual features such as rings, spots, and halos. Using machine learning, we are proposing to increase the accuracy of image classification by increasing the amount of data. Due to the real dataset being hard to get and/ or not being ready, we use synthetic x-ray scattering images that are generated using physics for training and testing purposes. The synthetic images are as close to possible to the real dataset making it efficient enough to use. Previously, synthetic images that have been generated have a size of 256 x 256 pixels. Now, we have increased the resolution of the synthetic images by generating synthetic images with a size of 1,000 x 1,000 pixels. Increasing the resolution of the image provides us with more information of the attributes, increasing our ability to recognize and classify the images by tagging them. Here at the Computer Science Initiative, we have changed a few parameters in the previous python code that was used for the original dataset size to increase the size of the generated images to 1,000 x 1,000 pixels. We used the generated synthetic images to train and test our machine learning system that classifies and tags the x-ray scattering images. The real dataset that needs to be classified and tagged are from the National Synchrotron Light Source II (NSLS-II) at Brookhaven National Laboratory (BNL). Once the training and testing is verified to be efficient enough we will apply the machine learning with the real dataset.

## I. Introduction

X-ray scattering is a powerful technique for probing the physical structure of materials at the molecular and nanoscale, where strong X-ray beams are shined through a material to learn about its structure at the molecular level. This can be used in a wide variety of applications, from determining protein structure

to observing structural changes in materials. Modern x-ray detectors can generate 50,000 to 1,000,000 images/ day, thus it's crucial to automate the workflow as much as possible. Our goal is to build and automatic machine learning pipelines for data analysis tasks including a hierarchical physics aware learning, streaming and real-time learning capabilities, experiment and decision making assistance.

Machine Learning, figure 1, itself is undergoing a shift with a re-thinking from traditional, naive neural networks, towards deep learning models where the neural hierarchy is more rational, optimized, and informative. This has already led to clear advances in several fields including computer vision and speech recognition, and we aim to demonstrate similarly transformative gains with respect to scientific image streams. The core idea in deep learning is to design multiple levels of representations corresponding to a hierarchy of features, wherein the high-level concepts and knowledge are derived from the lower layers.

For machine-learning, there are two types of datasets that are used. The first is real dataset, which is collected by shining powerful x-rays through a material and the attribute is labeled by material experts. The second type dataset is synthetic scattering dataset, where the data is generated by simulation software. Real data for be hard to get in the quantity needed or it can just not be ready of yet. Because of this, we generate synthetic x-ray scattering images for training and testing of the image recognition and tagging software. The simulation software can generate synthetic scattered images based on physics laws making it as close to the real dataset as possible.

Previously, the synthetic images, figure 2, that were generated had a size of 256 x 256 pixels as seen in Figure 2. Now, we believe if we increase the size of the synthetic images that we generate, we will be able to obtain more information/ data to improve the classification and tagging of the images. If this is seen to be true and efficient then the scientist at the National Synchrotron Light Source II (NSLS-II) can build an x-ray machine or calibrate

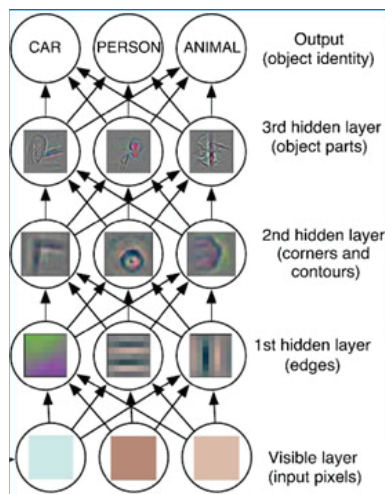


FIGURE 1

These methods will be used in real-time to extract hierarchical and physically-meaningful insights from scientific datasets collected at NSLS-II beamlines:

- 1) Low-level: identifying characteristic features in a diffraction image;
- 2) Intermediate-level: detecting the occurrence of a physical process from a sequence of images; and
- 3) High-level: learning and predicting scientifically-meaningful trends.

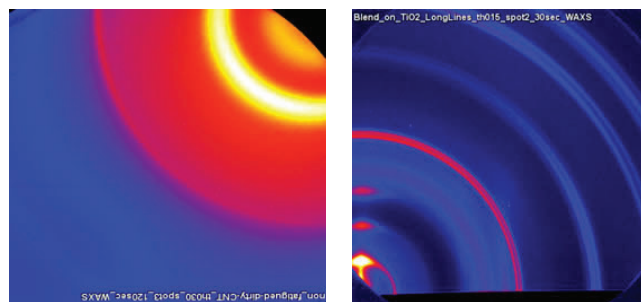


FIGURE 2

Examples of false color images with the "Ring" tag. Tags can include a diverse selection of images, which makes classification of x-ray scattering images difficult



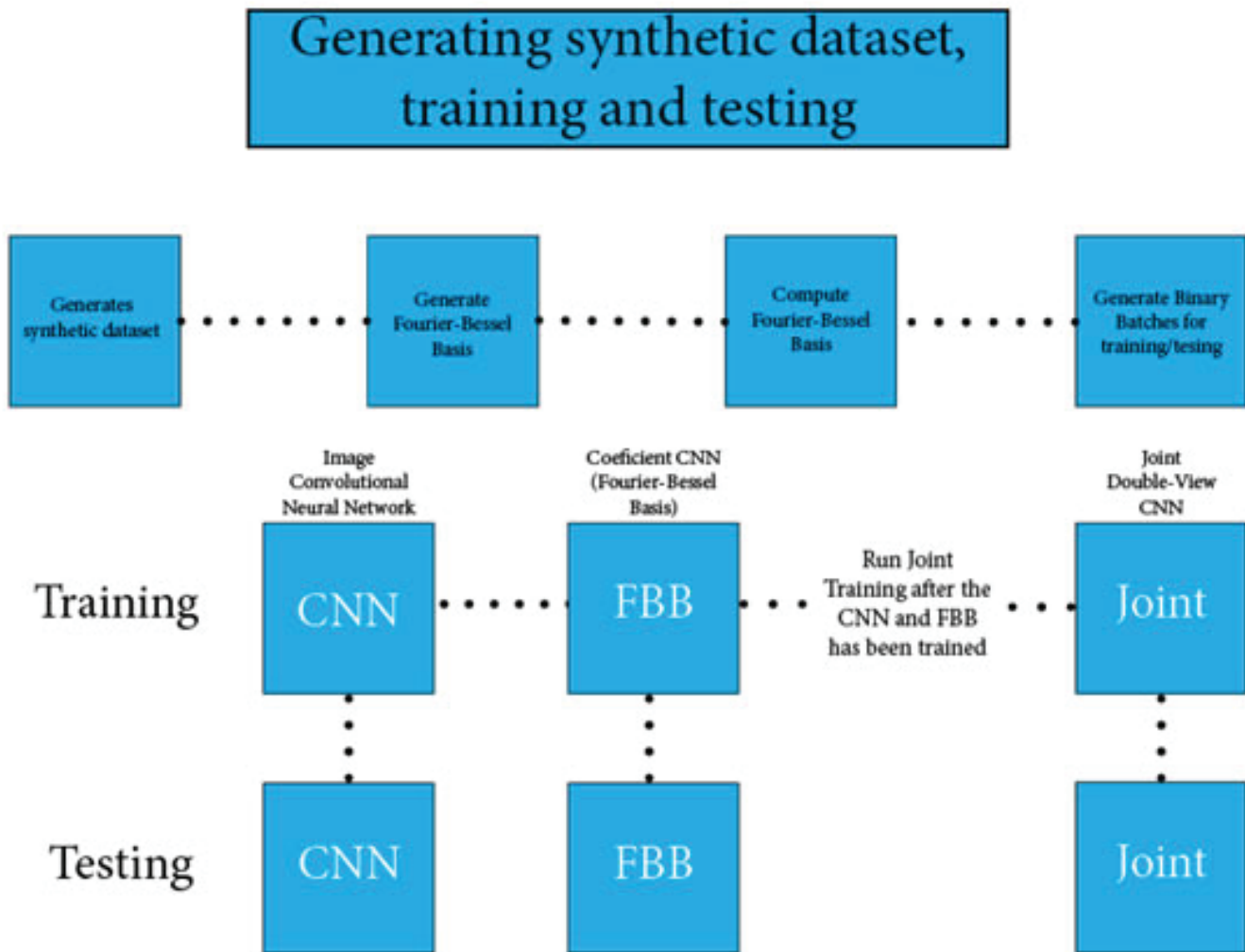


FIGURE 3  
Process for generating, training, and testing of synthetic x-ray scattering images.

it to get larger images. The size of synthetic data that we have increased to are 1,000 x 1,000 pixels.

## II. Methods

### A. A. Simulation

First, we will generate synthetic images to use for testing and training. The synthetic images will be generated using various experiments that have certain variables placed to develop x-ray scattering images. Some of these variables are constant and will be the same across an experiment(s). These experiments use physics properties to generate the data and images. It also uses randomization to avoid creating duplicate images which would be no help when it comes to training. The randomization also helps when it comes to running multiple jobs to generate the data. Without the randomization, there would be a chance that each job would produce identical datasets. Previously, the image size that was generated were 256 x 256 pixels. Now we have changed a few parameters so that the image that is generated is 1,000 x 1,000 pixels. The benefit of generating a larger image with a higher resolution is that it provides us with more information of the attributes, increasing our ability to classify the images.

### B. B. Big Data Issues

When generating larger synthetic images, we believed that it will take longer which was true. The cluster/ server we are working on only allows us to run jobs for 24 hours and then they will be

killed. Because of this, we had to generate the images by running multiple jobs on the server. We produced 50K images for both the 256 x 256-pixels size images and the 1k x 1k images. To generate 1 experiment with 200 images, it took 85secs (1 min 25 secs) for the 256 x 256-pixel and 435secs (7 mins 15secs) for 1 experiment with 200 1k x 1k- pixel images. To generate 5 experiments of 200 images 224 (3 mins 44secs) for 256 x 256-pixel images and 2040 secs (34 mins) for 5 experiments of 200 1k x 1k-pixel images. To generate an experiment with 200 images, it takes the 1k-pixel size image approximately 5 times as long as the 256-pixel size images. To generate 5 experiments with 200 images each, it takes the 1k-pixel size images approximately 9 times as long as the 256-pixel size images. From this rate shown in figure 4, we can see that to produce 50k images of the 1k x 1k-pixel size will take a lot longer than producing 50k images with 256 x 256-pixel size.

### C. C. Fourier-Bessel Basis

After running the simulation code, which generates the synthetic images we generate and then compute the Fourier-Bessel Basis. This is slow and could take a day or approximately a few days with the original dataset of 256 x 256-pixel images, therefore we assume it will take much longer for the larger dataset. When it came time to compute the Fourier-Bessel Basis, we had to make some changes in the code. Instead of using the Multiprocessing pooling python module like we did with the 256 x 256 dataset, we had to use a loop for parsing. This change had to be made because

of the multiprocessing pooling module not being able to handle the larger size dataset.

#### D. D. Convert Fourier-Bessel Basis

Following that we generated Binary Batches for training and testing. There are 10 batches that are generated which each contain data from the images. We condense all the generated data in batches of raw data records for fast I/O in TensorFlow. Batch files are divided into fixed length byte intervals that save a (tags, image pixels, FBT) tuple each. Each batch consist of 5000 images each, which is a set parameter in the convert FBB (Fourier-Bessel Basis) program.

### III. Training and Testing

Once the batches were completed we entered training. The 3 types of training are Image Convolutional Neural Network, Coefficient Convolutional Neural Network, and Joint Double View Convolutional Neural Network (combination of the two). For the 256 x 256 dataset, Image CNN can achieve mean average precision of approximately 0.5-0.6 with training. The Coefficient CNN can outperform Image CNN by approximately 0.1. The Joint double-view CNN should be slightly better than both. From this we predict that the results will be proportionally the same with the Joint Double-view CNN being better than both the Image CNN and Coefficient CNN individually. For each type of training we used 9 of the 10 batches and saved the 10th batch for testing. Image CNN and Coefficient CNN must be trained before we trained the Joint Double-view CNN but we were able to train the Image CNN and Coefficient CNN simultaneously. We monitor the training (learning) progress by the means of observing learning error (console output) and tensor-board. Training error will stop descending and stay (roughly) constant at one point. Once we notice this, we no longer need to wait for the preset training steps to finish so we can kill the process. Training creates checkpoints so that if we add new data for training, we will be able to pick up from where we left off. This keeps us from having to restart training from the beginning if it is not necessary.

Once Training is complete we can test the machine learning. With the synthetic data, we will use the tenth batch (batch-9) for testing. This batch has been saved or testing purposes and wasn't included in the training to avoid the system from being bias.

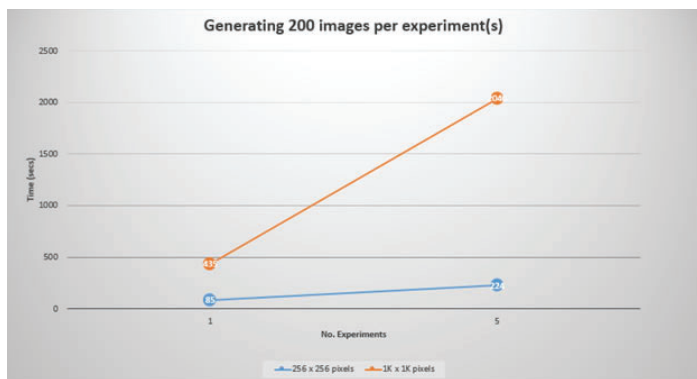


**FIGURE 4**  
Sample display of time to generate images of 256x256-pixel size and 1k x 1k-pixel size. This has been test for 1 experiment of 200 images and 5 experiments with 200 images each.

### IV. Conclusion

Due to the length of time it takes to generate and prepare the data for training and testing, we haven't yet trained or tested the system with the 1k x 1k images. There are modules that cannot be used for the 1k x 1k-pixel images like they were used for the 256 x 256-pixel images. The goal is to find python modules that are compatible with large data sizes. This will allow the code to be used on all systems and avoid changes when using a larger dataset. We believe this will be an ongoing problem due to us wanting to max out infinite amounts of data.

After training and testing was complete and the accuracy error rate was satisfactory, we can now use the real dataset from NSLS-II to test the system. Once that is done and is satisfactory, we will look to increase the data size again from 1,000 x 1,000-pixel size to 2,000 x 2,000-pixel size. We are looking to gain even more data to improve machine learning classification of x-ray scattering images. With the dataset now being larger, we need to convert from using Alexnet to using VGGnet. VGGnet is suitable for larger data sizes while Alexnet is suitable for smaller data sizes. The process of using Alexnet was successful for the 256 x 256-pixel images. By switching to VGGnet, we expect the training and testing to be more efficient. Also, we intend to use Google TensorFlow as a pre-processing tool and GPU computing to speed up pre-processing.

### V. Acknowledgements

This project was supported in part by the National Science Foundation, Louis Stokes Alliances for Minority Participation (LSAMP) at Lincoln University of Pennsylvania under the LSAMP Internship Program at Brookhaven National Laboratory. I wish to thank my host, Dr. Dantong Yu, for his professionalism and generosity during the NSF program. I would also like the thank my Visiting Faculty Professor and Mentor, Dr. Bo Sun, for her assistance, guidance, and for selecting me as the student to join her team. Further, I would express my gratitude to the Office of Science Education Program, and all who continue to so willingly assist interns in that branch. I very much appreciate the efforts of the National Science Foundation, LSAMP at Lincoln University of Pennsylvania for their support. Finally, I wish to acknowledge the hospitality and kindness of Brookhaven National Laboratory and the Department of Energy.

### VI. References

Computer Science Initiative, Brookhaven National Laboratory  
Department of Computer Science, Lincoln University of Pennsylvania  
Department of Computer Science, Stony Brook University  
National Science Foundation (NSF), Louis Stokes Alliances for Minority Participation (LSAMP)  
National Synchrotron Light Source II (NSLS-II) at Brookhaven National Laboratory

# Morphological effects of the nanostructured ceria support on the activity of Cu/CeO<sub>2</sub> catalysts for the reverse water-gas shift reaction

JinYing Lin, Department of Material Science and Chemical Engineering, Stony Brook University, Stony Brook, NY 11790

José A. Rodriguez, Chemistry Department, Brookhaven National Laboratory, Upton, NY 11973

## Abstract

CO<sub>2</sub>, an abundant and harmful greenhouse emission, has the potential to be used for the synthesis of valuable chemicals. This process requires the catalytic reduction of CO<sub>2</sub> directly into fuels such as CO via the Reverse Water-Gas Shift reaction (RWGS), but this process is as yet not realized at an industrial scale. Cu/CeO<sub>2</sub> catalysts are promising new catalysts for this reaction due to their low cost, abundance, and high activity. We studied three Cu/CeO<sub>2</sub> catalysts with different nanostructured ceria morphologies, including nanospheres, nanocubes, and nanorods, loaded with 5 wt% Cu. Their catalytic performance in the RWGS reaction was investigated using a Clausen cell reactor connected to Mass Spectrometry-Residual Gas Analyzer (MS-RGA). Cu supported on the ceria nanospheres exhibited the highest activity when compared with nanocubes and nanorods ceria catalysts, showing that the support morphology can influence reactivity. In addition, the Cu/CeO<sub>2</sub> (nanospheres) catalyst was examined with diffuse reflectance infrared Fourier transform spectroscopy (DRIFTS) and ambient-pressure x-ray photoelectron spectroscopy (AP-XPS) to perform a study analysis. These results showed that the active state of the catalyst was Cu<sup>0</sup> and partially reduced ceria (Ce<sup>3+</sup>/Ce<sup>4+</sup>), while the ceria nanospheres were the most reducible and likely responsible for improved reactivity.

## I. Introduction

Carbon dioxide (CO<sub>2</sub>), a major greenhouse gas, is released into the atmosphere continuously due to the combustion of carbonaceous fuels, such as fossil fuels. The rapid increase in the atmospheric CO<sub>2</sub> concentration leads to an enhanced greenhouse effect and its detrimental consequences. Thus, stabilization of atmospheric CO<sub>2</sub> level, which requires both a significant cut in emission as well as active removal of CO<sub>2</sub> from the atmosphere, has become urgent. As CO<sub>2</sub> is a cheap, non-toxic, and abundant carbon resource, utilizing CO<sub>2</sub> in a catalytic reduction process to produce economically valuable fuels and chemicals is a promising strategy to reduce CO<sub>2</sub> emission [1][2].

CO<sub>2</sub> can be converted directly to CO via the reverse water gas shift (RWGS) reaction, methanol via the methanol synthesis, and hydrocarbons via Fischer-Tropsch (FT) reactions [1]. Among the three CO<sub>2</sub> hydrogenation pathways, the RWGS is the most promising and flexible method because CO produced from the RWGS reaction could be a powerful intermediate for methanol synthesis and FT reactions [1].

RWGS is an equilibrium endothermic reaction and thus requires high temperatures [2]:



Generally, RWGS catalysts are composed of a metal-oxide support and an active metal dispersed on the support, such as Cu/ZnO. There are two mechanisms proposed for the RWGS reaction. One is the redox mechanism, and the other is the formate decomposition mechanism. In the redox mechanism, metallic copper, Cu<sup>0</sup>, is oxidized by CO<sub>2</sub> to generate CO and Cu<sup>+</sup>, and then Cu<sup>+</sup> is reduced by H<sub>2</sub> to generate Cu<sup>0</sup> and H<sub>2</sub>O. In the formate decomposition mechanism, CO<sub>2</sub> is hydrogenated to formate, and then the C=O bond is cleaved and formate is decomposed to form CO [1].

Copper catalysts have received a great interest in previous studies for the RWGS reaction and methanol synthesis from CO<sub>2</sub> hydrogenation, due to their low price, high activity, and have been used as industrial catalysts for the water-gas shift (WGS) reaction [3]. CeO<sub>2</sub> is a rare earth metal oxide with high reducibility and high intrinsic activity toward CO<sub>2</sub> adsorption [1]. The surface oxygen of CeO<sub>2</sub> can be reduced by H<sub>2</sub> or other reductants to form oxygen vacancies, which are crucial in catalytic reduction reactions. The introduction of copper can improve the reducibility and oxygen vacancies formation of CeO<sub>2</sub>, consequently improve the catalytic activity in CO<sub>2</sub> hydrogenation [2].

The activity of Cu/CeO<sub>2</sub> catalysts for the WGS reaction and methanol synthesis was well-reported in previous studies [4][5]. In these studies, the results show that the morphology of the nanostructured ceria support can affect the activity, selectivity, and stability of Cu/CeO<sub>2</sub> catalysts for the WGS reaction [4] and methanol synthesis [5]. Cu/CeO<sub>2</sub> (nanospheres) exhibited the highest activity and stability for the WGS reaction [4], while Cu/CeO<sub>2</sub> nanorods showed the highest catalytic performance for methanol synthesis [5]. Thereby, we hypothesize that the morphology of the nanostructured ceria support can influence the Cu/CeO<sub>2</sub> catalyst activity for the RWGS reaction.

This summer, we studied three Cu/CeO<sub>2</sub> catalysts with different nanostructured ceria morphologies, including nanospheres, nanocubes, and nanorods, loaded with 5 wt% Cu. The catalytic activity of three Cu/CeO<sub>2</sub> catalysts was evaluated using a Clausen Cell reactor. The surface analysis of the most active RWGS catalyst was performed by using diffuse reflectance infrared Fourier

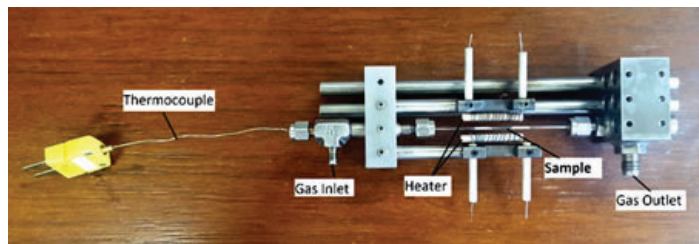


Figure 1. A Clausen Cell reactor.



transform spectroscopy (DRIFTS) and ambient-pressure x-ray photoelectron spectroscopy (AP-XPS).

## II. Experimental Methods

### A. A. Catalyst preparation

As described in the previous study<sup>[4]</sup>, ceria nanospheres were prepared by a microemulsion method. Distilled water was mixed with n-heptane to form a reverse microemulsion using Triton X-100 as the surfactant. Then cerium (III) nitrate was introduced to this reverse microemulsion. After stirring the microemulsion for 1 hr, a tetramethyl ammonium hydroxide (TMAH) alkali solution was added to the microemulsion as a precipitant. After adding the TMAH alkali solution, the mixture was stirred for 24 hr to allow the precipitation reaction completed. The precipitate was collected as the product through centrifugation and decantation. And then the product was rinsed with methanol and dried overnight at 100 °C. Ceria nanorods and nanocubes were prepared by a hydrothermal method. The cerium (III) nitrate precursor was dissolved in a NaOH aqueous solution with stirring. The mixture was introduced into a stainless steel autoclave and kept at 100 °C and 180 °C for nanorods and nanocubes, respectively, for 24 hr. The precipitates were further separated, washed, and dried at 60 °C overnight. All three ceria supports were calcined in air at 500 °C for 2hr after they were dried. Cu/CeO<sub>2</sub> catalysts were prepared by incipient wetness impregnation using the as-prepared ceria supports and copper nitrate as the precursor, loaded with 5 wt% Cu. The samples were dried overnight at 100 °C and calcined in air at 500 °C for 2 hr<sup>[4]</sup>.

### B. B. Catalyst activity test

The catalyst activity of the three Cu/CeO<sub>2</sub> catalysts in the RWGS reaction was tested in a Clausen Cell reactor connected to the Mass Spectrometry-Residual Gas Analyzer (MS-RGA, SRS-RGA 300) at the Chemistry Division of Brookhaven National Laboratory (BNL). A Clausen Cell reactor is a plug flow reactor used for time-resolved, temperature dependent studies of reaction activity at high temperatures. As shown in Figure 1, ~4 mg of the catalyst sample was loaded between two quartz wool beds into a capillary (0.9 mm ID). Then the capillary was mounted in the Clausen Cell reactor and reactant gases were allowed to flow into the capillary through the gas inlet. The gas outlet was connected to the MS-RGA for measuring the concentration of the components in the product gas over the experiment. Two resistance

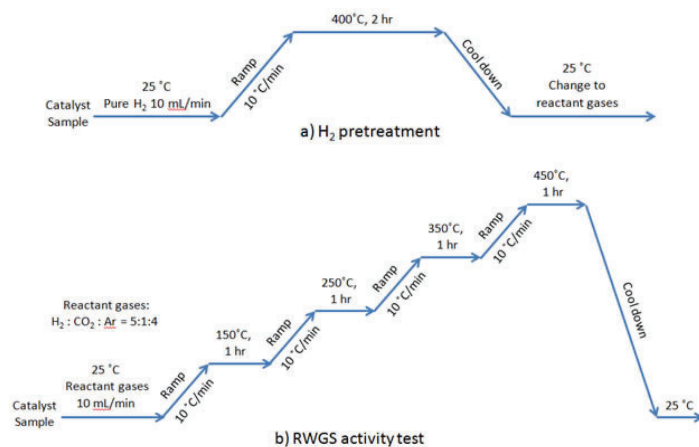


Figure 2. Schematic procedures for a) H<sub>2</sub> pretreatment and b) RWGS activity test at different temperature stages.

heating coils were installed on the two opposite sides next to the capillary and connected to a power supply for heating the sample evenly. A K-type thermocouple was placed inside the capillary in the vicinity of the quartz wool bed closed to the gas inlet and connected to a temperature programmable controller (Eurotherm) in order to control and monitor the catalyst temperature<sup>[6]</sup>.

In a typical activity test experiment, as shown in Figure 2a, a pure H<sub>2</sub> stream (10 mL/min) was introduced to the flow cell system at the beginning, and then the sample was heated to 400 °C with a heating rate of 10 °C/min and maintained at 400 °C for 2 hr. After the reactor was cooled down to 25 °C, the gas stream was changed to a desired reactant gas mixture consisting of H<sub>2</sub> (5 mL/min), CO<sub>2</sub> (1 mL/min), and Ar (4 mL/min) (H<sub>2</sub>:CO<sub>2</sub>:Ar = 5:1:4). As shown in Figure 2b, under the reactant gas flow, the sample was stepwise heated to 150 °C, 250 °C, 350 °C, and 450 °C at a heating rate of 10 °C/min and stayed at each temperature stage for 1 hr.

### C. C. Transmission electronic microscopy (TEM)

The high-resolution TEM images were collected at 200 kV using a Cs-corrected (1mm) JEOL JEM 2100F instrument located at the Center for Functional Nanomaterials at BNL. Fresh catalyst samples were dispersed as a suspension in deionized water, sonicated for 60 sec and introduced onto a Holey-C and Lacey-C grid, followed by air dry<sup>[4]</sup>.

### D. D. Diffuse reflectance infrared Fourier transform spectroscopy (DRIFTS)

*In-situ* measurements were performed for detecting the reaction intermediates over the Cu/CeO<sub>2</sub> (nanospheres) catalyst, which was the most active catalyst in the RWGS activity test, under reaction conditions. *In-situ* DRIFTS spectra were collected using an FTIR spectrometer (Thermo Fisher Scientific, Nicolet 6700) equipped with a Harrick cell and an MCT detector at the Chemistry Division of BNL. The spectra were expressed in units of Kubelka-Monk (K-M), in which only bands attributed to adsorbed species were shown<sup>[7]</sup>. 33.2 mg of the most active catalyst was placed into the Harrick cell. Similar to the activity test procedures shown in Figure 2, the catalyst was reduced in a mixture of H<sub>2</sub> (10 mL/min) and He (10 mL/min) at 400 °C for 40 min, and then cooled down to 25 °C. After reaching 25 °C, the gas stream was changed to H<sub>2</sub> (10 mL/min), CO<sub>2</sub> (2 mL/min), and He (8 mL/min) (H<sub>2</sub>:CO<sub>2</sub>:He = 5:1:4). The catalyst was stepwise heated to 250 °C, 350 °C, and 450 °C at a heating rate of 10 °C/min and stayed at each temperature stage for 30 min, followed by cooling down to room temperature.

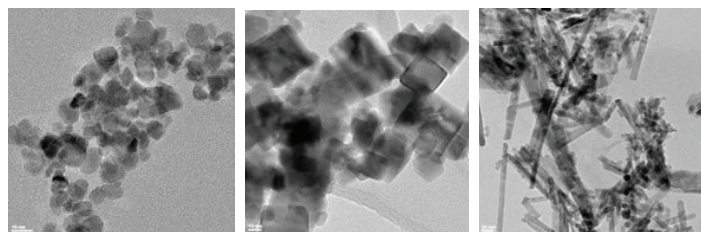


Figure 3. TEM images of the Cu/CeO<sub>2</sub> (nanospheres), Cu/CeO<sub>2</sub> (nanocubes), and Cu/CeO<sub>2</sub> (nanorods) catalysts (from left to right).

## E. Ambient-pressure x-ray photoelectron spectroscopy (AP-XPS)

A commercial SPECS AP-XPS chamber equipped with a PHOIBOS 150 EP MCD-9 analyzer at the Chemistry Division of BNL was used for XPS analysis (Resolution:  $\sim 0.4$  eV). The Ce 3d photoemission line with the strongest  $Ce^{4+}$  feature (916.9 eV) was used for the energy calibration. The Cu/CeO<sub>2</sub> (nanospheres) catalyst powder was pressed on an aluminum plate and then loaded into the AP-XPS chamber. The sample was heated with 0.001 mTorr O<sub>2</sub> at 500 °C for 30 min. 45 mTorr of H<sub>2</sub> was used to pre-treat the sample at 400 °C for 30 min, before 40 mTorr of H<sub>2</sub> and 8 mTorr of CO<sub>2</sub> was introduced into the reaction chamber at 25 °C through a high precision leak valve. Ce 3d, Cu 2p, Cu LMM, O 1s, and C 1s XPS regions were collected at 25 °C, 350 °C and 450 °C under the reaction gas environment.

## III. Results and Discussion

### A. TEM

The TEM images, shown in Figure 3, confirm the morphology of the Cu/CeO<sub>2</sub> catalysts as desired: nanospheres (8-15 nm), nanocubes (10-20 nm), and nanorods (10-20 nm). Copper particles are barely visible and are highly dispersed on the surface of the nanostructured ceria supports.

### B. Catalyst activity

Around 4 mg of each 5 wt% Cu/CeO<sub>2</sub> catalyst with different ceria morphologies was used in the catalytic activity test. The reactants and products gas evolution during the RWGS reaction was recorded by MS-TGA and was shown in Figure 4. When the RWGS reaction took place, the intensity of CO<sub>2</sub> decreased as CO<sub>2</sub> was consumed and the intensity of CO and H<sub>2</sub>O increased as they were produced. The near intact H<sub>2</sub> level over the experiment comes from the abundance of H<sub>2</sub> than CO<sub>2</sub> in the feed gas as the

H<sub>2</sub>/CO<sub>2</sub> ratio was 5:1 and the insensitivity of H<sub>2</sub> change by the MS-RGA.

Based on the MS-RGA data, the RWGS catalytic activity is characterized by CO<sub>2</sub> conversion, CO production, and H<sub>2</sub>O production, using the equations below, and the results are shown in Figure 5.

$$CO_2 \text{ Conversion } \%_{T_i} = \left( \frac{P_{RT} - P_{Ti}}{P_{RT}} \right) / m_{catalyst} * 100 \quad \text{Eq. 2}$$

$$\text{Normalized } H_2O \text{ Production }_{T_i} = \left( \frac{P_{RT} - P_{Ti}}{P_{RT}} \right) / m_{catalyst} \quad \text{Eq. 3}$$

As shown in Figure 5a, the Cu/CeO<sub>2</sub> (nanospheres) catalyst appeared to be active at 250 °C, while the RWGS reaction over the nanocubes and nanorods catalysts started to take place at 350 °C. All catalyst activities increased with temperature because RWGS is an endothermic and kinetic-limited reaction and requires high temperature to overcome the limit [1]. At 350 °C, the nanospheres catalyst was significantly more active than the nanocubes and nanorods catalyst, as the CO<sub>2</sub> conversion over the nanospheres catalyst is almost twice the conversion over the nanocubes catalyst. At 450 °C, although the nanocubes catalyst is more active than the nanospheres catalyst, the difference between their CO<sub>2</sub> conversions is very small.

CO production and H<sub>2</sub>O production, shown in Figure 5b and 5c, are consistent with the catalyst activities represented by CO<sub>2</sub> conversion, expect that the H<sub>2</sub>O production over the nanocubes catalyst at 450 °C. It was twice the H<sub>2</sub>O production over the nanospheres and nanorods catalysts at the same temperature, while the CO production over the nanocubes was greater than others with relatively smaller difference. It happened might because H<sub>2</sub> not only reduced CO<sub>2</sub> to form CO and H<sub>2</sub>O but also reduced the ceria to form H<sub>2</sub>O.

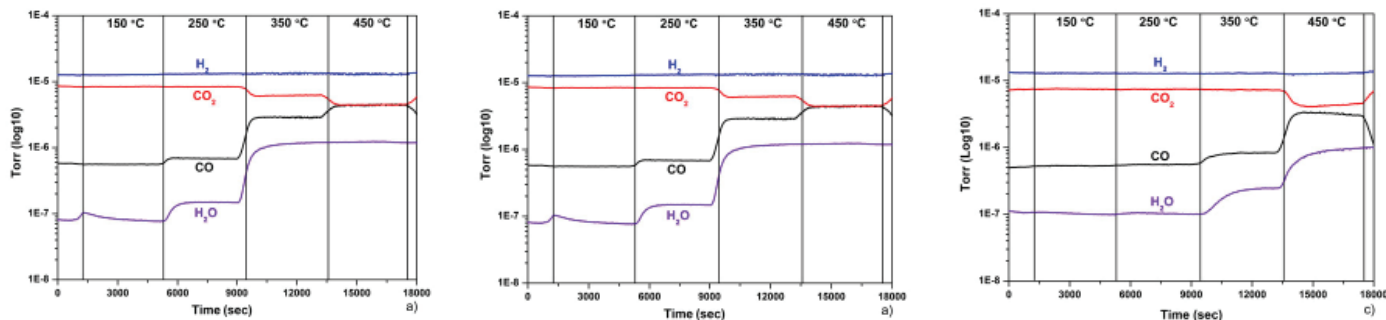


Figure 4. *In-situ* MS-RGA data collected during the RWGS reaction for the 5 wt% a) Cu/CeO<sub>2</sub> (nanospheres), b) Cu/CeO<sub>2</sub> (nanocubes), and c) Cu/CeO<sub>2</sub> (nanorods) catalysts at different temperatures.

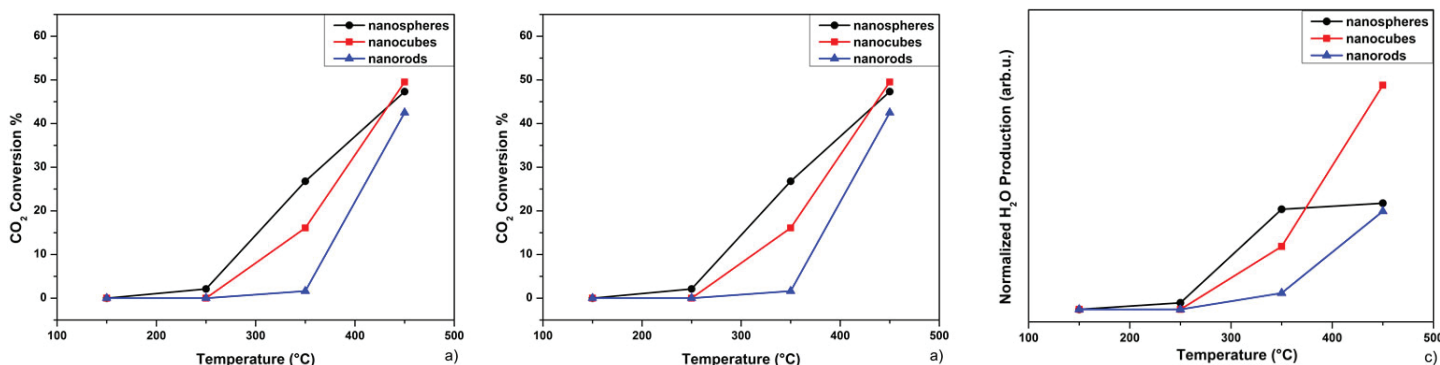


Figure 5. RWGS activities, calculated as (a) CO<sub>2</sub> conversion, (b) CO production, and (c) H<sub>2</sub>O production, over the 5 wt% Cu/CeO<sub>2</sub> (nanospheres), Cu/CeO<sub>2</sub> (nanocubes), and Cu/CeO<sub>2</sub> (nanorods) catalysts at different temperatures.

Based on the RWGS activities, the Cu/CeO<sub>2</sub> (nanospheres) catalyst exhibited the highest activity, compared to nanocubes and nanorods catalysts. Overall catalyst activity ranking is nanospheres > nanocubes > nanorods. As the nanospheres catalyst is the most active in the activity test, we studied its surface chemistry via DRIFTS and surface chemical state via AP-XPS over RWGS.

### C. C. DRIFTS data

Figure 6 shows the *in-situ* DRIFTS spectra were obtained in the surface study of the Cu/CeO<sub>2</sub> (nanospheres) catalyst during the RWGS reaction, and expressed in units of K-M, in which only bands attributed to adsorbed species were shown [7]. In Figure 6, there are 5 regions of frequency where most intense bands are detected.

Based on CO<sub>2</sub> and CO IR spectra in the literature [8], the bands in the region 3733 – 3620 cm<sup>-1</sup> and in the region 2400 – 2250 cm<sup>-1</sup> are related to CO<sub>2</sub>, and the bands in the region 2175 – 2115 cm<sup>-1</sup> are related to CO. The intensity of the bands in the region 3733 – 3620 cm<sup>-1</sup> gradually decreased as the temperature increased from 25 °C to 450 °C. This shows that more CO<sub>2</sub> was consumed in the RWGS reaction as temperature increased. The bands for CO appearing in the spectra for 350 °C and 450 °C also confirm the CO formation from RWGS. The attenuated CO<sub>2</sub> peaks together with intensified CO peaks demonstrate the improved catalytic activity as temperature goes up, which agrees with the result of catalytic activity tests.

The bands around 2840 cm<sup>-1</sup> are associated to with formate species adsorbed on the ceria support [4][9][10]. The intensity reduction of these bands from 250 °C to 450 °C. It might result from the increase of formate decomposition as the temperature went up, or the decrease in the adsorbed amount of formate on ceria support at high temperature.

The bands in the region between 1800 – 850 mostly result from the stretching vibration modes of the COO group of formate and mono-, bi-, or tridentate carbonate OCO species [4][9][10]. The band around 1750 cm<sup>-1</sup> is associated to bridged carbonates and it appears in the spectra except 25 °C. The complexity of the band

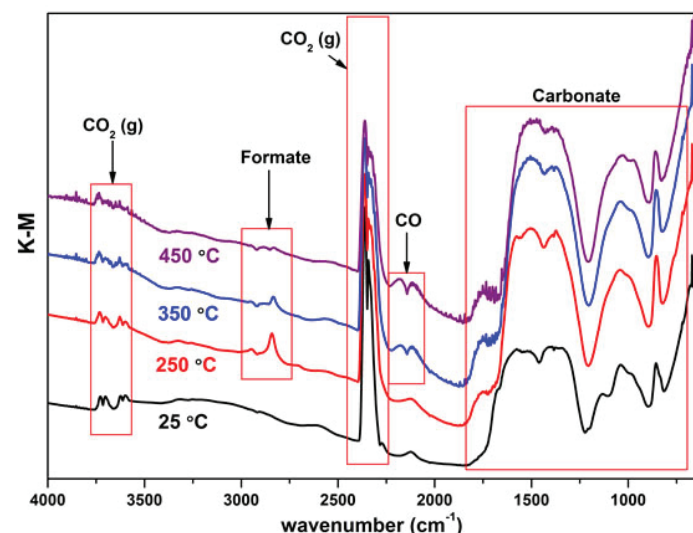


Figure 6. *In-situ* DRIFTS spectra collected during the RWGS reaction over a 5 wt% Cu/CeO<sub>2</sub> (nanospheres) catalyst at different temperatures.

structure in this region makes it difficult to assign the peaks, therefore the interpretation of this region is not attempted.

Based on the DRIFTS spectra, formate and bridged carbonates species were formed as intermediates during the RWGS reaction over the Cu/CeO<sub>2</sub> (nanospheres) catalyst. It implies that the RWGS reaction over the Cu/CeO<sub>2</sub> (nanospheres) catalyst involves the formate decomposition.

### D. D. AP-XPS data

AP-XPS is a useful tool for investigating the chemical composition of solid surfaces and it allows us to study the surface chemical state over the catalyst. As mentioned above, a surface analysis of the Cu/CeO<sub>2</sub> (nanospheres) catalyst during the RWGS reaction was performed using AP-XPS. Figure 7 shows the Cu 2p, Ce 3d, and Cu LMM Auger XPS spectra were collected before and after H<sub>2</sub> pretreatment and during the RWGS reaction. The normalized intensity of the Cu 2p spectra is doubled in order to display the clear change.

Based on the Handbook of XPS, in the Cu 2p spectra, Cu<sup>2+</sup> can be identified by the two satellite peaks in the spectrum, however, because of the similar line shapes and close binding energy of metallic Cu and Cu<sup>+</sup>, it is difficult to distinguish these two species during the reaction. As a result, the Cu LMM Auger spectra are utilized to determine the chemical state of copper. From the Handbook, the kinetic energy of metallic Cu is 918.7 eV, of Cu<sup>+</sup> is 916.2 eV, and of Cu<sup>2+</sup> is 918.1 eV [11]. It helps us to determine the chemical state of copper by the location of peaks, as shown in Figure 7. The XPS spectra show that copper on the catalyst surface was reduced from Cu<sup>2+</sup> to metallic Cu after H<sub>2</sub> pretreatment and was mainly metallic Cu during the RWGS reaction.

Based on the Ce 3d spectra for CeO<sub>2</sub> and Ce<sub>2</sub>O<sub>3</sub> in the reference paper [12], the peaks in the Ce 3d spectra are assigned for Ce<sup>3+</sup> and Ce<sup>4+</sup> as shown in Figure 7. From the Ce 3d spectra in Figure 7, cerium was reduced from Ce<sup>4+</sup> to a mixture of Ce<sup>3+</sup> and Ce<sup>4+</sup> after H<sub>2</sub> pretreatment at 400 °C because H<sub>2</sub> molecules took away O atoms on the ceria surface, and oxygen vacancies were formed. After CO<sub>2</sub> and H<sub>2</sub> were introduced to the XPS chamber at 25 °C, the intensity of the Ce<sup>4+</sup> peak increased and of the Ce<sup>3+</sup> peak decreased because CO<sub>2</sub> molecules were adsorbed to the ceria surface and reoxidized part of the Ce<sup>3+</sup> to Ce<sup>4+</sup>. The Ce<sup>4+</sup> peak intensity decreases as the Ce<sup>3+</sup> peak intensity increases while ele-

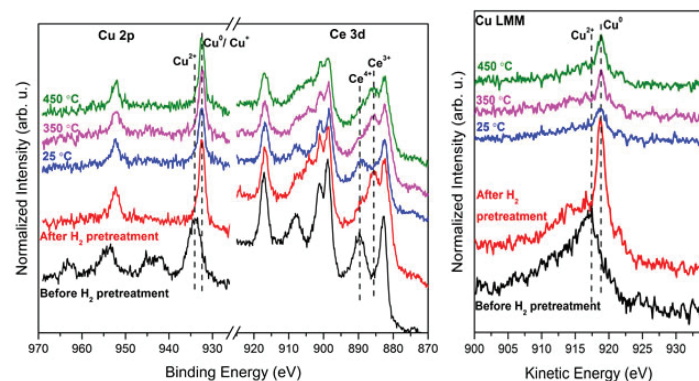


Figure 7. Cu 2p (x2), Ce 3d, and Cu LMM Auger *in-situ* AP-XPS spectra of a 5 wt% Cu/CeO<sub>2</sub> (nanospheres) catalyst, before H<sub>2</sub> pretreatment (black line), after H<sub>2</sub> pretreatment under 45 mTorr of H<sub>2</sub> at 400 °C (red line), under 8 mTorr CO<sub>2</sub> and 40 mTorr H<sub>2</sub> at 25 °C (blue line), and subsequent heating to 350 °C (pink line) and 450 °C (green line). The excitation energy was 1253.6 eV.



vating temperature from 25 °C to 450 °C, and this is because the abundant H<sub>2</sub> (H<sub>2</sub>:CO<sub>2</sub> = 5:1) generates stronger effect on the CeO<sub>x</sub> support and reduces Ce<sup>4+</sup> to Ce<sup>3+</sup> again at higher temperature.

#### IV. Conclusion

The Cu/CeO<sub>2</sub> (nanospheres) catalyst is the most active catalyst in activity tests, compared with the Cu/CeO<sub>2</sub> nanocubes and nanorods catalysts. The result of activity tests shows that the morphology of the ceria support can influence the catalyst reactivity for the RWGS reaction. The *in-situ* DRIFTS spectra show that formate and carbonate species were formed as intermediates during the RWGS reaction over the Cu/CeO<sub>2</sub> (nanospheres) catalyst, and the formate decomposition mechanism was involved in the reaction. AP-XPS spectra show copper is mainly metallic Cu and cerium is mixture of Ce<sup>3+</sup> and Ce<sup>4+</sup> over the RWGS reaction.

#### V. Acknowledgements

We greatly appreciate the support we received from Feng Zhang, Robert M. Palomino, and Sanjaya Senanayake.

This project was supported in part by the U.S. Department of Energy, Office of Science, Office of Workforce Development for Teachers and Scientists (WDTS) under the Science Undergraduate Laboratory Internships Program (SULI).

#### VI. References

- <sup>1</sup>Porosoff, M.D., B. Yan, and J.G. Chen. "Catalytic reduction of CO<sub>2</sub> by H<sub>2</sub> for synthesis of CO, methanol and hydrocarbons: challenges and opportunities." *Energy & Environmental Science*, Vol. 9, No. 62 (2016): Pg. 62-73.
- <sup>2</sup>Dai, B., G. Zhou, S. Ge, H. Xie, Z. Jiao, G. Zhang, and K. Xiong. "CO<sub>2</sub> reverse water-gas shift reaction on mesoporous M-CeO<sub>2</sub> catalysts." *The Canadian Journal of Chemical Engineering*, Vol. 95 (2017): Pg. 634-642.
- <sup>3</sup>Jurkovic, D.L., A. Pohar, V.D.B.C. Dasireddy, and B. Likozar. "Effect of copper-based catalyst support on reverse water-gas shift reaction (RWGS) activity for CO<sub>2</sub> reduction." *Chemical Engineering Technology*, Vol. 40, No. 5 (2017): Pg. 973-980.
- <sup>4</sup>Yao, S.Y., W.Q. Xu, A.C. Johnston-Peck, F.Z. Zhao, Z.Y. Liu, S. Luo, S.D. Senanayake, A. Martinez-Arias, W.J. Liu, and J.A. Rodriguez. "Morphological effects of the nanostructured ceria support on the activity and stability of CuO/CeO<sub>2</sub> catalysts for the water-gas shift reaction." *Phys. Chem. Chem. Phys.* Vol. 16 (2014): Pg. 17183-17195.
- <sup>5</sup>OuYang, B., W. Tan, and B. Liu. "Morphology effect of nanostructure ceria on the Cu/CeO<sub>2</sub> catalysts for synthesis of methanol from CO<sub>2</sub> hydrogenation." *Catalysis Communications*, Vol. 95 (2017): Pg. 36-39.
- <sup>6</sup>Zhao, F.Z., Z.Y. Liu, W.Q. Xu, S.Y. Yao, R. Si, A.C. Johnston-Peck, A. Martinez-Arias, J.C. Hanson, S.D. Senanayake, and J.A. Rodriguez. "Pulse Studies to Decipher the Role of Surface Morphology in CuO/CeO<sub>2</sub> Nanocatalysts for the Water Gas Shift Reaction." *Catalyst Letter*, Vol. 145 (2015): Pg. 808-815.
- <sup>7</sup>Kattel, S., B.H. Yan, Y.X. Yang, J.G. Chen, and P. Liu. "Optimizing Binding Energies of Key Intermediates for CO<sub>2</sub> Hydrogenation to Methanol over Oxide-Supported Copper." *Journal of The American Chemical Society*, Vol. 138 (2016): Pg. 12440-12450.

<sup>8</sup>Coblentz Society, Inc. CO<sub>2</sub> and CO IR spectra. NIST Chemistry Webbook. Web, 10 Aug 2017.

<sup>9</sup>Meunier, F.C., D. Tibiletti, A. Goguet, and R. Burch. "DRIFTS-MS-SSITKA study of the Reverse Water-Gas Shift Reaction." *Oil & Gas Science and Technology*, Vol. 61, No. 4 (2006): Pg. 497-502.

<sup>10</sup>Wang, X.Q., J.A. Rodriguez, J.C. Hanson, D. Gamarra, A. Martinez-Arias, and M. Fernandez-Garcia. "In Situ Studies of the Active Sites for the Water Gas Shift Reaction over Cu-CeO<sub>2</sub> Catalysts: Complex Interaction between Metallic Copper and Oxygen Vacancies of Ceria." *Journal of Physical Chemistry B*, Vol. 110 (2006): Pg. 428-434.

<sup>11</sup>J. F. Moulder, W. F. Sticle, P. E. Sobol, and K. D. Bomben, *Handbook of X-ray Photoelectron Spectroscopy*. Physical Electronics, Perkin-Elmer Corporation, Minnesota, 1992.

<sup>12</sup>Mullins, D.R., S.H. Overbury, and D.R. Huntley. "Electron Spectroscopy of single crystal and polycrystalline cerium oxide surfaces." *Surface Science*, Vol 409 (1998): Pg. 307-319.

# Characterization of *Arabidopsis thaliana* mutants defective in starch synthesis and lipid turnover

Tiffany Lin, Chemical Biology, University of California Berkeley, Berkeley, CA 94704

Jilian Fan and ChangCheng Xu, Biology Department, Brookhaven National Laboratory, Upton, NY 11973

## Abstract

Improving renewable energy production to replace fossil fuels has been considered a major, worldwide goal. Although plant oils have already been used as a source of biofuel, the quantity of lipids produced naturally by oil-producing plants has not been sufficient enough to meet the large demand.<sup>1</sup> With genetic engineering as a key mechanism, our study aims to increase the yield of energy rich triacylglycerol (TAG) in *Arabidopsis thaliana*. *A. thaliana* has been studied as a model organism for plant biology research at Brookhaven National Laboratory (BNL) due to its sequenced genome, easily accessible mutant lines, and rapid life cycle.<sup>2</sup> In one experimental procedure, the leaf tissues of a F2 *A. thaliana* population of *adg1-2* crossed with S012432 were stained with an iodine solution and the DNA run through a polymerase chain reaction (PCR) to select for a specific double mutant. This double mutant carries a defect in a chloroplast lipase in addition to a lack of starch production that is believed to cause an increased synthesis of other lipids to compensate. The coupling of these two mutations was tested in the hopes that knocking out the lipase would reveal the increased accumulation of TAG. Analysis from thin layer chromatography (TLC) revealed that this lipase was actually not responsible for degradation of TAG but possibly another phospholipid; however this information may lead us to better understand what role each mutated gene plays in the survival of the plant and how we can synergistically manipulate these genes towards a higher TAG yield. Knowledge of the genes involved in fatty acid synthesis and degradation can be applied to other biomass plants for a more efficient production of biofuels. Completion of my experience at BNL has allowed me to gain considerable proficiency with procedures for DNA extraction, PCR, DNA gel electrophoresis, and TLC.

## I. BACKGROUND

Plants produce their own food using sunlight and carbon dioxide as energy and carbon sources through a process called photosynthesis. During the day, the products of photosynthesis are stored as sugar polymers named starch and as lipids such as oils. At night when photosynthesis is not possible, starch is hydrolyzed to release sugars to support growth, metabolism, and respiration. The goal of this project is to understand how plants survive without starch, how lipid metabolism is affected in plants deficient in starch accumulation, and whether plants can use lipids as alternative energy sources in the absence of starch. Multiple *A. thaliana* plants with mutations in various genes were constructed and analyzed over the course of this project; however the ones of highest interest are double mutants defective in both starch synthesis and lipid turnover.

Loss of starch in these mutants was thought to possibly trigger an increase in metabolism towards synthesis of other lipids

like TAG to compensate the loss of energy source.<sup>3</sup> With an increased lipid production rate comes an increased lipid degradation rate. In order to determine whether the starch mutation was actually linked to lipid synthesis rates, this mutation was crossed with another mutation in a certain chloroplast lipase thought to be responsible for the degradation of TAG before any significant increase was allowed to accumulate.<sup>4</sup> Therefore, this double mutant was tested in the hopes that knocking out the lipase would reveal a linkage between increased production of TAG and loss of starch. Iodine staining was used to visualize starch accumulation in leaf tissue and PCR to identify mutants carrying transfer DNA (T-DNA) that resulted in the lipase defect.

## II. METHODS, DATA, AND RESULTS

### A. A. Phenotype identification

Typically, the first course of action in identifying the double mutants in a F2 generation cross is to search for any obvious changes in phenotype, for example a yellowish color or premature withering in leaf tissue. The two particular mutations of interest in this project do not have these distinctive phenotypes but instead give the same appearance as the *col-2* wild type so relying purely on phenotype differences to distinguish the mutants will not work in this case. Additionally, it is known that older, more mature leaf tissues tend to accumulate more lipids as well as display a yellowish color in the leaves (Figure 1). In order to ensure any lipid accumulation changes occur from the mutation and not merely the age of the plant, an older *adg1-2* *A. thaliana* plant is set as a control.



Figure 1. The *adg1-2* S012432 double mutant, shown on the left, has no distinctive phenotype from the *col-2* wild type. The further aged *adg1-2*, shown on the right, has a distinctive yellow color on the tips of the leaves and is used as a lipid accumulation control for the double mutants.

## B. Iodine staining

Since there is not a distinctive phenotype visible that differs from the wild type in *adg1-2* S012432 double mutants, a series of techniques are required to select for the desired mutations. Staining of leaves from a F2 population of *adg1-2* crossed with S012432 with an iodine solution revealed which carry the mutation that causes a lack of starch production. The largest, oldest leaf tissues were removed and placed in ethanol while heated at approximately 65°C to remove the green pigments off the leaves. After rinsing with water, the individual leaf tissues were placed in an iodine solution and allowed to soak for several minutes before another rinse with water. The resulting leaf tissues in individual micro centrifuge tubes clearly reveal which contain starch and which do not. Leaves that contain starch stain much darker than those that do not have starch (Figure 2).

## C. PCR and DNA gel electrophoresis

The plants that don't contain starch were selected out and run through a PCR followed by DNA gel electrophoresis to select for the mutation in the chloroplast lipase. Since this is a T-DNA mutation, PCR is the simplest way to reveal which plants carry the S012432 insertion. Amplification of the small amount of DNA extracted from the leaf tissue is done with three different primers that will multiply both the wild type and the mutational DNA. Since the T-DNA contains a known DNA sequence, a left border (LB) primer can be designed to amplify the DNA that contains the mutational sequence.<sup>5</sup> For all the other DNA strands that don't contain the insertion, the left primer (LP), designed for a sequence in the wild type DNA, will amplify these other segments. Both the LB and LP are paired with the same right primer (RP) that can amplify the complimentary strand of DNA going in the opposite direction (Figure 3).

Since the LB primer begins amplification on the left border of the T-DNA insertion, the LB to RP segment is about 500 base pairs shorter than the wild type LP/RP sequence and thus will run faster in the gel and result in a band further from the loading wells. A band in the gel only for the LB/RP indicates that the plant is homozygous for the mutation and a band only for LP/RP indicates that the plant does not contain the mutation at all, while a band in both LB/RP and LP/RP indicates the plant is heterozygous for the mutation (Figure 4). Visualization of the electrophoresis gel under UV light will reveal the presence of the DNA bands. The plants homozygous for the lipase mutation are selected out and the final batch of plants are the desired double mutants (Figure 5).

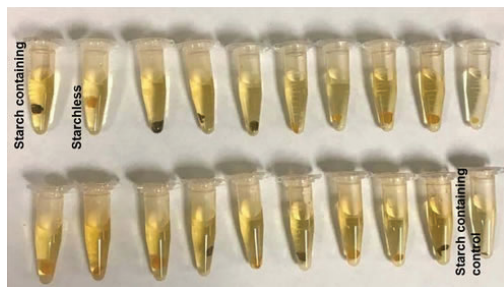


Figure 2. Iodine staining results of leaf tissue collected from the F2 generation of *adg1-2* S012432. The first sample shown in the upper left has a dark brown appearance from the staining which indicates that the leaf tissue contains starch. The second sample, next to the first, has a light tan appearance as a result of the staining which indicates that this leaf tissue does not contain starch. A leaf tissue known to contain starch, shown on the lower right, is used as a control.

## D. Thin layer chromatography

To determine whether there is actually a change in TAG accumulation in the leaf tissue of these double mutants, a TLC plate is run with all the double mutants that were distinguished alongside a *adg1-2* control that contains only the starch mutation but not the lipase mutation. Also dotted on the TLC plate were lipids extracted from the F2 *adg1-2* S033146, a double mutant similar to the *adg1-2* S012432 with the difference being the exact position of the T-DNA insertion. The lipids were extracted out of the mutants with a 2 methanol: 1 chloroform: 0.1 formic acid extraction solvent. A 1 M KCl, 0.2 M H<sub>3</sub>PO<sub>4</sub> solution was then added to dissolve the non-lipid components into an aqueous layer while allowing the lipids to be retained in the organic layer. To distinguish each individual type of lipid, the organic layer of each mutant sample was dotted out on a TLC plate and separated by the silica on the plate and a 70 ml hexane: 30 diethyl ether: 1 acetic acid solvent mobile phase.

The position on the plate indicative of the presence of TAG revealed no significant differences between the double mutants and the mutants containing only the starch defect. In fact, the TAG accumulation was even lower than in the *adg1-2* controls in some of the *adg1-2* S012432 double mutants (Figure 6). This result leads us to believe that this chloroplast lipase is not involved in the degradation of TAG but possibly another lipid, like phospholipid.

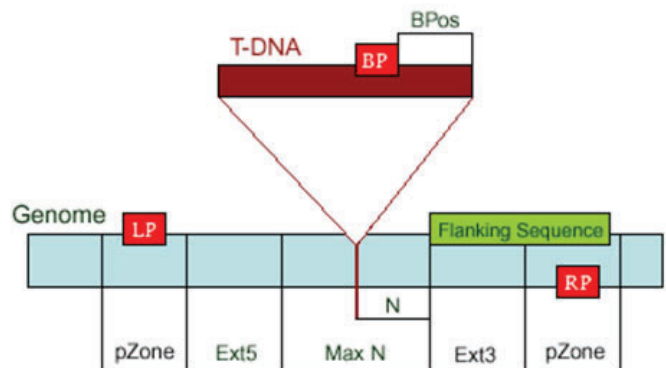


Figure 3. Graphic depiction of the positions within a DNA sequence that the LB (BP in the figure), LP, and RP begin amplification at and the specific sequences they select for that allow for the distinction of the T-DNA. Both types of DNA contain the same RP sequence but differ in that only the sequence containing the T-DNA will be able to amplify using the LB.<sup>6</sup>



Figure 4. Example of DNA gel electrophoresis scan that shows the 900 base pair band indicating wild type DNA, ~410 base pair band indicating homozygous mutational DNA, and the presence of both bands indicating heterozygous DNA.<sup>6</sup>



### III. DISCUSSION AND CONCLUSION

#### A. Results of experimentation

We successfully generated several double mutants defective in various aspects of lipid turnover in starch-less mutant backgrounds. One example is the double mutants between starch-less mutants and a chloroplast lipase. Although the function of the chloroplast lipase we chose to examine was not what was anticipated, the conclusions we can draw from the results still reveal information about the role of certain genes in plant survival and how this component fits into the grand mechanism of lipid metabolism. Further testing can be done to conclude whether or not this lipase we focused on is actually responsible for phospholipid degradation. If so, we can more definitively map what this particular gene encodes for. Future studies to further analyze these double mutants will provide new information about the genes involved in lipid turnover, the role of lipids in energy production via respiration, and the role of lipids in plant growth and survival.

#### B. Suggestions for further studies

With so much still unknown about the function of genes in *A. thaliana* the best approach we have now is to create transformational and single base pair mutations both individually as well as paired with other mutations at different gene loci and then to genotype the mutation to discover what alteration has been made in the plant. For example, the effect mutated genes have on other biological components of *A. thaliana*, including the closing and opening of the leaf stomata and how they respond during harsh conditions, may be examined. Studying the plant from this aspect, which may not seem directly related to lipid production, can lead to the overall understanding of how the plant alters its fundamental functions to adapt and survive.

### IV. ACKNOWLEDGEMENTS

I would like to give a special thanks to Jilian Fan and Chang-Cheng Xu for their valuable guidance and insight on this project. This project was supported in part by the U.S. Department of Energy, Office of Science, Office of Workforce Development for Teachers and Scientists (WDTS) under the Science Undergraduate Laboratory Internships Program (SULI).

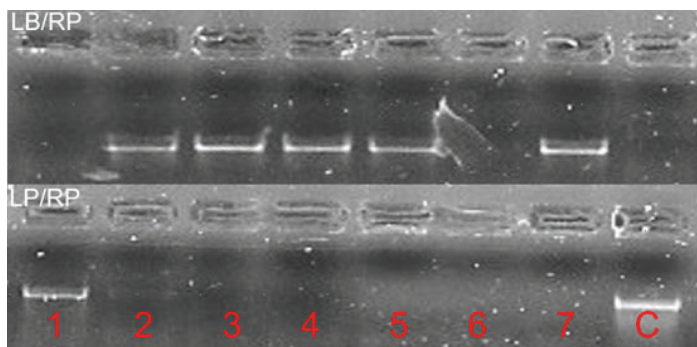


Figure 5. Gel electrophoresis scan of 7 *adg1-2* S012432 plants alongside a control. Presence of only the LB/RP band and not LP/RP in samples 2-5 and 7 indicate that these plants were homozygous for the lipase mutation. Presence of only the LP/RP band in sample 1 indicates that this plant was homozygous for no mutational insertion, or wildtype. The control has only the LP/RP band, which is expected since the control cannot have the T-DNA insertion.

### V. REFERENCES

- J. Ohlrogge and K. Chapman, *The Biochemical Society* 34 (2011).
- J. Fan, C. Yan, X. Zhang, and C.C. Xu, *The Plant Cell* 25, 3506 (2013).
- J. Ohlrogge and J. Browse, *The Plant Cell* 7, 957 (1995).
- L. Heinrichs, J. Schmitz, U.I. Flugge, and R.E. Hausler, *Front Plant Sci.* 3, (2012).
- R.C. O'Malley, C.C. Barragan, and J.R. Ecker, *Methods in molecular biology* 1284, 323 (2015).
- G.E.B.D., *T-DNA Primer Design* (2005).

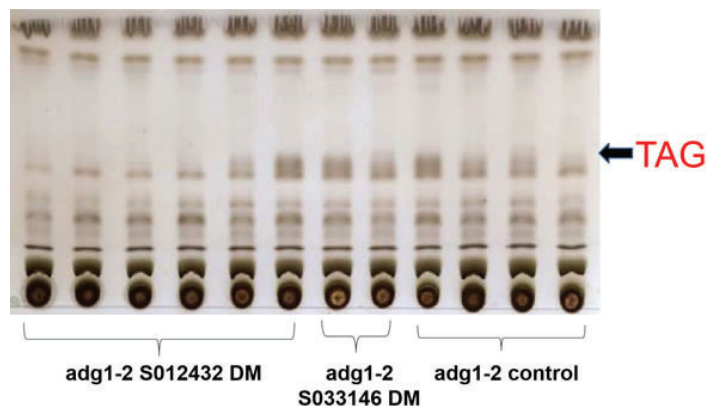


Figure 6. TLC results of 6 *adg1-2* S012432 double mutants (DM), 2 *adg1-2* S033146 DM, and 4 *adg1-2* controls. Row where the position of TAG should be along the plate is indicated with a labeled arrow. TLC results indicate that the first 4 DM samples had barely any TAG accumulation while the next 4 DM samples had some accumulation but not a significant enough amount to surpass the controls.

# Exploring $\Delta^{12}$ fatty acid desaturase (FAD) family protein interaction specificity

Katherine Lo, College of Arts and Science, Stony Brook University, Stony Brook, NY 11790

Yuanheng Cai, and Jon Shanklin, Department of Biology, Brookhaven National Laboratory, Upton, NY 11973

## Abstract

Previous studies showed that heterologous expression of the *Ricinus communis castor* fatty acid hydroxylase (RcFAH12) in *Arabidopsis thaliana* resulted in a far lower concentration of the ricinoleic acid product than in its native castor plant. We hypothesize RcFAH12 and *Arabidopsis* fatty acid desaturase (AtFAD2) interaction could impair both enzymes' activity, decreasing product accumulation. Here, the mating-based split-ubiquitin system (mbSUS) was employed to investigate the interactions amongst AtFAD2, RcFAH12, and unusual fatty acid desaturases acetylenase, conjugase, and epoxygenase to gain insights into interaction specificity and mechanisms of these enzymes. This study is the initial step to understand why transgenic plants produce less unusual fatty acids heterologously, which can facilitate mass production of biofuels and beneficial seed oils.

## I. Introduction

Plant desaturases are comprised of two classes, a structurally well classified soluble class and a poorly structurally characterized integral membrane class. Both classes require iron and oxygen for activity and are inhibited by azide and cyanide (Lou et al., 2014). The  $\Delta^{12}$  integral membrane desaturases introduce a *cis* double bond into fatty acyl chains using oxygen and electron donor NADH. The  $\Delta^{12}$  integral membrane desaturases contain a diiron active center and are localized in the endoplasmic reticulum membrane in cells. Enzymes in this family are structurally similar, but have a variety of functions. A member of the desaturases, *Arabidopsis thaliana* fatty acid desaturase (AtFAD2) converts the monounsaturated oleic acid (18:1) into a polyunsaturated fatty acid linoleic acid (18:2), an essential fatty acid precursor in human health, by introducing a secondary *cis* double bond at the  $\Delta^{12}$  position, 12 carbons from the carboxylic end (Figure 1).

Unusual fatty acids, another derivative of oleic acid desaturases, are a class of fatty acids containing functional groups such as hydroxyl, epoxy, acetylenic groups or conjugated bonds (Fig-

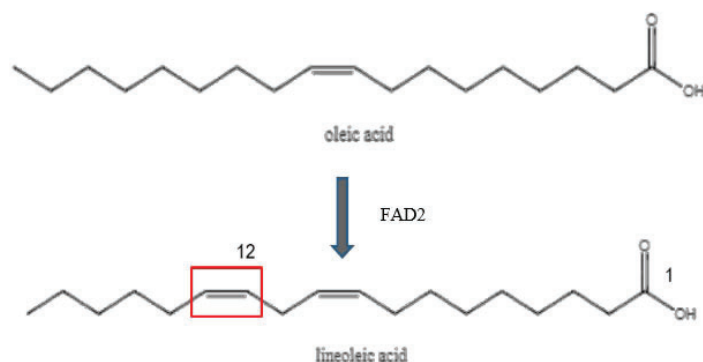


Figure 1 AtFAD2 desaturates oleic acid (18:1) at the  $\Delta^{12}$  carbon, creating a secondary *cis* double bond. This produces linoleic acid (18:2).

ure 2). These fatty acids are produced by the  $\Delta^{12}$  integral membrane desaturase family proteins, hydroxylase, epoxygenase, acetylenase, and conjugase, respectively. They are only found in a small number of organisms and possess various industrial importance, such as use in lubricants, emulsifiers, nylon precursors, and drying agents. Unusual fatty acids are conventionally produced from petrochemicals; however, with the growing consumption of the earth's petrochemical reserves, it is of considerable interest to produce these chemicals by transgenic plants to serve as petrochemical substitutes.

Previous studies by Burgal et al. (2008) showed that heterologously overexpressed *Ricinus communis* fatty acid hydroxylase (RcFAH12) in *Arabidopsis thaliana* resulted in a maximum ricinoleic acid accumulation of 17% out of the total seed oil production in the seed, a much lower concentration of ricinoleic acid than in its native plant, the castor. For this phenomenon, we hypothesized that the overexpression of RcFAH12 inhibits AtFAD2 function and thus, a decrease of ricinoleic acid product accumulation in *Arabidopsis*. Our preliminary investigations using the mating-based split ubiquitin system (mbSUS) show that AtFAD2 and RcFAH12 can form strong homodimers with itself and heterodimers with each other (Figure 3). We then further investigated the interactions between AtFAD2 and RcFAH12 and other  $\Delta^{12}$  integral membrane desaturases acetylenase, conjugase, and epoxygenase using mbSUS. Here, we demonstrate that all  $\Delta^{12}$  integral membrane desaturase proteins can interact with itself and one another at varying degrees of strength.

## II. Materials and Methods

**Preparing Electrocompetent Cells** A fresh culture was grown overnight in YENB media, shaken at 37°C. The cells were harvested at OD<sub>600</sub> between 0.5 to 0.9. Cells were then chilled on ice for 5 minutes and spun at 4000xg for 10 mins at 4°C. The medium was aspirated and the cells were washed twice with 100mL of cold water. Cells were then centrifuged and the supernatant was discarded. The cells were resuspended in 2-3mL of 10% glycerol. The competent cells were aliquoted and then frozen in the -80°C freezer.

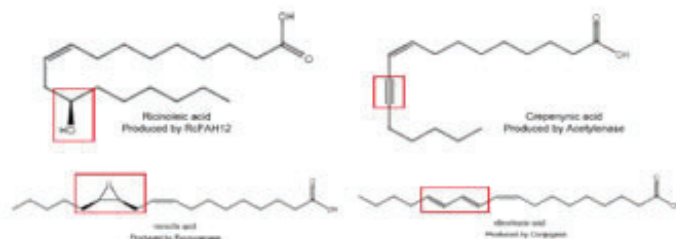


Figure 2 Unusual fatty acids are produced by different  $\Delta^{12}$  integral membrane desaturases.

**Polymerase Chain Reaction (PCR)** The sequences for acetyle-nase, conjugase, and epoxygenase as well as the vectors 810, 813, 814, and 935 were used as template for PCR Phusion with their respective primers to amplify the fragments. The amplification occurred over 37 cycles of 98°C (30s), 55°C (30s), and 72°C (10min). PCR products were run on a 1.2% agarose gel for 12 mins and visualized with ethidium bromide.

**Gibson Assembly** The target fragments of the PCR product were digested with DPN1, leaving only the PCR copy in the product. 1µL of Pst1 was placed in 37°C for an hour. The product was then concentrated using the ethanol precipitation method and re-suspended in 3µL of 60% glycerol and run on a 1.2% agarose gel. A gel extraction was performed on the target band.

The purified PCR product were placed in 1µL of 2X Gibson Assembly Buffer, 0.5 µL of one of the vector backbones (810, 813, 814, or 935) and 0.5µL of one of the PCR product (acetyle-nase, conjugase, or epoxygenase). The mixture was then incubated in 50°C for 1 hour.

**Bacterial Transformation** 50 µL of the electrocompetent cells (BL21(DE2) Gold strain) were added with 0.5 µL of DNA into a 1mm pore transformation cuvette. The cuvette was placed in the Bio-Rad Gene Pulser and electroshocked at 1.35 kilovolts. 200 µL of YENB was added and the cells were then shaken at 37°C for 1 hour. The cells were then spun at 4000xg and removed the supernatant. They were then resuspended in 50-100 µL YENB, spread onto a YENB agar petri-dish containing tetracycline antibiotic and incubated in the 37°C shaker overnight.

**Yeast Transformation** The plasmid was isolated from the transformed bacterial cells following the manufacturer's instructions for the Zippy Plasmid Prep Kit from the Zymo Research company. 10 µL of yeast competent cells were added with 1 µL of plasmid DNA, 1 µL of carrier DNA, and 100 µL of PEG/LiAc mix. The mixture was placed in 30°C for 30 mins. 2 µL of DMSO was added and then placed in 42°C for 15 mins. After spinning at 1700xg, the supernatant was removed and the cells were resuspended in 500 µL of 0.9% NaCl. 50 µL of the suspension was spread onto petri-dishes of synthetic-defined agar deficient of tryptophan (SD-W) and deficient of leucine (SD-L). After overnight growth, selected yeast colonies were inoculated and shaken in 200µL of SD-LUW media at 30°C overnight. 300 µL of SD-LUW and 15 µL of each bait and prey protein were mixed and placed in 30°C shaker overnight.

**Yeast Colony Growth** SD-LUW and SD-ALUWHM agar plates were made by adding 6.7g/LYNB, 20g/L glucose, and 10g/L Agar. 1.29g/L of amino acid mix without ALMWUH and 1.37g/L of amino acid mix without AHLUMW and additional A and H were added into the agar mixture for SD-ALUWHM and SD-LUW respectively. 1 µL of inoculated yeast mating colonies were spotted onto both SD-LUW and SD-ALUWHM plates. The plates

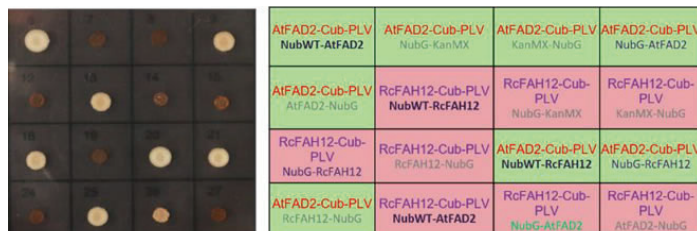


**Figure 3** Preliminary data using mBSUS in transgenic yeast colonies show that AtFAD2 and RcfAH12 can form strong homo- and heterodimers.

were then incubated at 37°C for 5 days.

**X-Gal Overlay Assay** Z buffer stock solution was made using 16.1 g/L Na<sub>2</sub>HPO<sub>4</sub>•7H<sub>2</sub>O, 55 g/L Na<sub>2</sub>HPO<sub>4</sub>•H<sub>2</sub>O, 0.75 g/L KCl, and 0.246 g/L MgSO<sub>4</sub>•7H<sub>2</sub>O. The pH was then adjusted to 7.4.

For the X-Gal Overlay assay, 0.25g of agarose was dissolved in 50mL of Z Buffer and heated until the solute was dissolved. The mixture was cooled in a 50°C water bath. 1 mL of 10% SDS and X-Gal stock (final concentration 2 µg/mL) was added. The solution was poured over diploid yeast cells in SD-ALUWHM agar and incubated in 37°C.

**Sodium Dodecyl Sulfate Polyacrylamide Gel Electrophoresis (SDS PAGE)** Yeast mating colonies were inoculated in a 30°C shaker overnight. The freshly inoculated were washed twice with water. After spinning at 4000x g, the supernatant was removed and the cells were resuspended in 400 µL of 20mM HEPES (pH 7.0), 150mM NaCl, and 10% Glycerol mix and 40 µL of 10X Complete (1 tablet of Complete and 1mL HEPES (pH7.0), 150mM NaCl and 10% Glycerol). 400 µL of unwashed glass beads (Sigma Life Sciences) were added to the sample. The samples were then homogenized in the Mini-Bead Beater four times. 100 µL of 6X SDS with loading buffer was added and the proteins and beads were separated. A 1.0mm 12% polyacrylamide gel was prepared by combining 3.2mL of ddH<sub>2</sub>O, 0.75mL of 2,2,2-trichloroethanol, 4mL of 30% Acrylamide/Bis-acrylamide, 2.6mL 1.5M Tris (pH 8.8), 0.1mL 10% SDS, 100 µL 10 ammonium persulfate, and 10 µL of TEMED. The solution was then placed into the SDS PAGE appa-

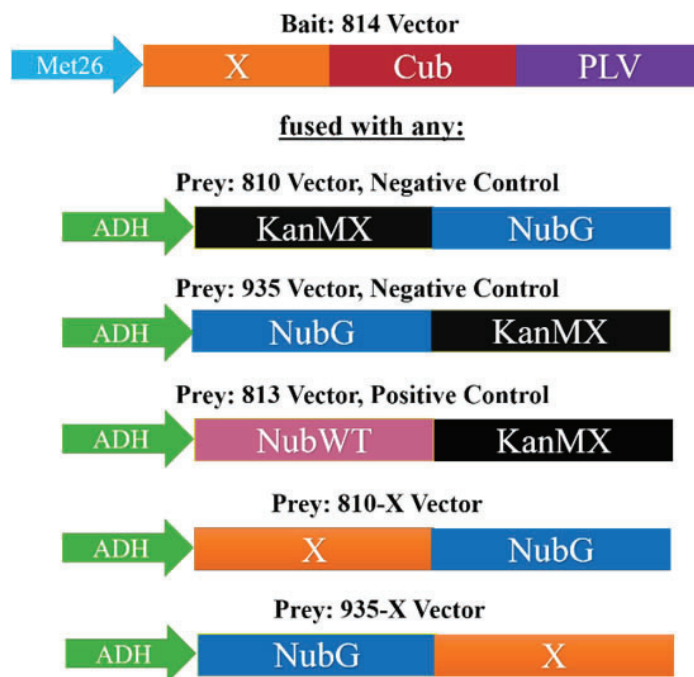


**Figure 4** The bait and prey vectors were placed under promoters Met26 and ADH respectively. The 814 bait vector contains the gene of interest (X), the mutated C-terminus ubiquitin (Cub) and PLV. Vectors 810-X and 935-X contain the mutated N-terminus ubiquitin (NubG) and the gene of interest. NubG will only interact with CubG if the gene of interest in the bait and prey interact. Negative control vectors 810 and 935 have Kanamycin (KanMX) instead of the gene of interest. KanMX should not interact with the bait and therefore, will not activate the downstream reporter genes. On the other hand, the 813 vector contains the wildtype N-terminus ubiquitin (NubWT). The NubWT will strongly interact with the Cub regardless if the genes of interest interact and acts as the positive control.



ratu and left to solidify. The stacking gel was also prepared using 2.975mL of ddH<sub>2</sub>O, 1.25mL of 0.5 Tris-HCl (pH 6.8), 0.05mL of 10% SDS, 0.67mL of 30% Acrylamide/Bis-acrylamide, 0.05mL 10% ammonium persulfate, and 0.005mL TEMED. The stacked gel was then added on top of the solidified separating gel and allowed to solidify with a 15 well comb. The gel was placed in the SDS-PAGE separation apparatus, 10  $\mu$ L of sample were loaded, and it was allowed to run on 80V for 20 min and then 130V for 2.5 hours.

**Western Blot** The 12% polyacrylamide gel was placed on top of a membrane and placed in the Bio-Rad membrane transfer apparatus. The 12% polyacrylamide gel was allowed to transfer onto the membrane for 2 hours or until all the proteins were transferred. The membrane was then placed in blocking buffer 2.5% nonfat dry milk in 50mL tris-buffered saline and tween 20 (TBST) prepared with 50mM Tris, 150 mM NaCl, and 0.1% Tween 20 adjusted to pH 7.6 for 30 mins. The membrane was then washed 5 times in TBST and then incubated in 50mL of blocking buffer with the primary antibody overnight. The membrane was then washed TBST 5 times and then continued to incubate in blocking buffer and secondary antibody solution for 2 hours. After, the membrane was treated with 300  $\mu$ L of peroxide solution and luminol enhancer (Thermo Fisher Scientific).

### III. Results

Mating based split-ubiquitin system (mbSUS) confirms interaction between  $\Delta^{12}$  integral membrane desaturase family proteins. We employed the split ubiquitin system to probe for potential interactions between the  $\Delta^{12}$  integral membrane desaturase family proteins. To understand their interactions, AtFAD2, RcFAH12, acetylenase, conjugase, and epoxygenase were cloned into a bait vector and fused with the C-terminus of ubiquitin (Cub) and the artificial transcription factor PLV (protein A-LexA-VP16) at its C terminus (Figure 4). Different vector schemes were created to test protein-protein interactions.

When the Cub and NubG are brought into close proximity by their fusion partners' interaction, the formation of the fully functional ubiquitin is recognized by ubiquitin-specific proteases (USP). USPs then cleave PLV which activates downstream ADE2, HIS3 and lacZ. When transformed yeast colonies are placed into adenine and histidine deficient media, growth of yeast mating colonies indicates activation of ADE2 and HIS3 genes and therefore, interaction between the two target proteins. Activation of the lacZ gene can be detected using the X-Gal overlay assay. All constructs are able to grow on SD-L-U-W media, but growth on SD-A-L-U-W-H-M are only allowed by the interaction of the

Bait Vector	Prey Protein	Interaction	Bait Vector	Prey Protein	Interaction	Bait Vector	Prey Protein	Interaction
B10	B10		B10	B10		B10	B10	
B10	B15		B10	B15		B10	B15	
B10-AtFAD2	B10-AtFAD2	Strong	B10-AtFAD2	B10-AtFAD2	Strong	B10-AtFAD2	B10-AtFAD2	Strong
B10-AtFAD2	B15-AtFAD2	Strong	B10-AtFAD2	B15-AtFAD2	Weak	B10-AtFAD2	B15-AtFAD2	Strong
B10-AtFAD2	B15-AtFAD2	Strong	B15-AtFAD2	B10-AtFAD2	Very weak	B15-AtFAD2	B15-AtFAD2	Very weak
B10-RcFAH12	B10-RcFAH12	Strong	B10-RcFAH12	B10-RcFAH12	Strong	B10-RcFAH12	B10-RcFAH12	Strong
B10-RcFAH12	B15-RcFAH12	Strong	B10-RcFAH12	B15-RcFAH12	Strong	B10-RcFAH12	B15-RcFAH12	Strong
B10-RcFAH12	B15-RcFAH12	Strong	B15-RcFAH12	B10-RcFAH12	Weak	B15-RcFAH12	B15-RcFAH12	Weak
B10-Acetyl	B10-Acetyl	Strong	B10-Acetyl	B10-Acetyl	Strong	B10-Acetyl	B10-Acetyl	Strong
B10-Acetyl	B15-Acetyl	Strong	B10-Acetyl	B15-Acetyl	Weak	B10-Acetyl	B15-Acetyl	Very weak
B10-Acetyl	B15-Acetyl	Strong	B15-Acetyl	B10-Acetyl	Very weak	B15-Acetyl	B15-Acetyl	Very weak
B10-Conj	B10-Conj	Strong	B10-Conj	B10-Conj	Strong	B10-Conj	B10-Conj	Strong
B10-Conj	B15-Conj	Strong	B10-Conj	B15-Conj	Very weak	B10-Conj	B15-Conj	Weak
B10-Conj	B15-Conj	Strong	B15-Conj	B10-Conj	Very weak	B15-Conj	B15-Conj	Weak
B10-Epoxy	B10-Epoxy	Strong	B10-Epoxy	B10-Epoxy	Strong	B10-Epoxy	B10-Epoxy	Strong
B10-Epoxy	B15-Epoxy	Strong	B10-Epoxy	B15-Epoxy	Strong	B10-Epoxy	B15-Epoxy	Strong
B10-Epoxy	B15-Epoxy	Strong	B15-Epoxy	B10-Epoxy	Very weak	B15-Epoxy	B15-Epoxy	Weak

**Table 1** Summary of mbSUS interactions. The rows show the bait vector scheme and protein used to interact with the prey vector scheme and its respective protein (column).

bait and prey proteins.

Our results show that all  $\Delta^{12}$  integral membrane desaturase proteins have the ability to interact with each other (Table 1). While AtFAD2 and RcFAH12 showed strong interactions in producing homo- and heterodimers, the other unusual fatty acids acetylenase, conjugase, and epoxygenase displayed generally weak.

**Western Blot supports mbSUS data** For the weak interactions seen in acetylenase, conjugase, and epoxygenase, it was uncertain if the result was due to a absence/low concentration of protein in the cell or due to the lack of protein interaction. We performed Western blots on a selection of bait-prey interaction samples to determine if there were any target proteins in the yeast cells. Our results (Figure 5) show that there is protein at around our target molecular weight.

### IV. Discussion

The mbSUS results support the conclusion that all  $\Delta^{12}$  integral membrane desaturase proteins have the ability to interact with each other, but at varying degrees of strength. Generally, homodimers of each enzyme interact the strongest and since most of the  $\Delta^{12}$  integral membrane desaturase proteins have a highly similar structure, it is possible that the similar structures facilitate the ability for  $\Delta^{12}$  integral membrane desaturase proteins to interact with one another, but possibly more weak than the homodimer. For example, AtFAD2 and RcFAH12 interact strongly to form homodimers with itself and can form heterodimers with other  $\Delta^{12}$  integral membrane desaturase proteins. However, acetylenase, conjugase, and epoxygenase generally have weak interactions in both their homo- and heterodimers. The Western blot data has proven that there is a presence of protein in the cell, thus, this is due to weak protein-protein interactions. However, more research can be done to understand the strength of the binding between these proteins.

Further research could include studies performing lipid analysis on the concentration of these enzymes in the cell and potentially find a ligand which blocks the formation of homo- and heterodimers of the  $\Delta^{12}$  integral membrane desaturase proteins to increase target fatty acid accumulation in transgenic plants.

### V. Acknowledgements

I would like to thank Dr. Yuanheng Cai and the Shanklin Lab for their mentorship and guidance throughout this project. This project was supported in part by the U.S. Department of Energy,

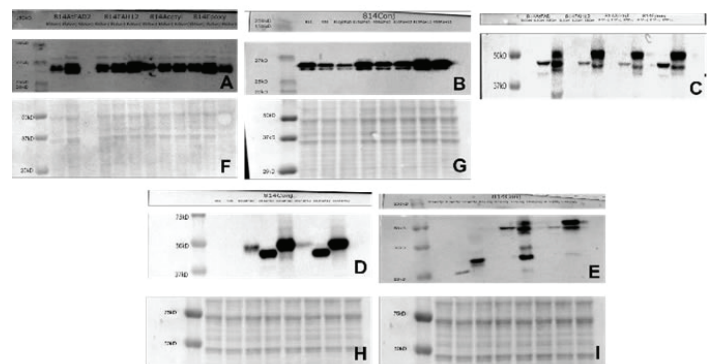


**Figure 5** The anti-VP16 and anti-HA antibodies were used to probe bait and prey proteins respectively. A and B are detected with anti-VP16; C, D, and E with anti-HA. F, G, H, and I are IarePonseau stains showing that similar amounts of proteins were loaded.

Office of Science, Office of Workforce Development for Teachers and Scientists (WDTS) under the Science Undergraduate Laboratory Internships Program (SULI).

## VI. References

Burgal J., Shockey J., Lu C., Dyer J., Larson T., Graham I., & Browse J. (2008). Metabolic engineering of hydroxy fatty acid production in plants: RcDGAT2 drives dramatic increases in ricinoleate levels in seed oil. *Plant Biotechnology Journal*, 6(8), 819–831.

Chapman K., Austin-Brown S., Sparace S., Kinney A., Ripp K., Pirtle I., and Pirtle R. (2001). Transgenic Cotton Plants with Increased Seed Oleic Acid Content. *Journal of the American Oil Chemists' Society*, 78(9), 941-947.

Grefen C., Lalonde S., and Obrdlik P. Split- Ubiquitin System for Identifying Protein-Protein Interactions in Membrane and Full-Length Proteins. Oct 2007. *Current Protocols in Neuroscience*. 5.27.1-5.27.41

Lou Y., and Shanklin J. 2010. Evidence that the Yeast Desaturase Ole1p Exists as a Dimer *in Vivo*. *Journal of Biological Chemistry*. 285(25): 19384-19390.

Lou Y., Schwender J., and Shanklin J. 2014. FAD2 and FAD3 Desaturases Form Heterodimers that Facilitate Metabolic Channeling *in Vivo*. *Journal of Biological Chemistry*. 289(26):17996-18007.

# Evaluating the radiation dose around a hot cell after the bombardment of a Thorium target

Juliana Mendes, Department of Physics, Applied Physics and Astronomy, Rensselaer Polytechnic Institute, Troy, NY 12238

Kin Yip, Collider Accelerator Department, Brookhaven National Laboratory, Upton, NY 11973

## Abstract

While Actinium-225 is promising for radiotherapeutic cancer treatments, there is a limited supply available for clinical trials. The proton spallation of Thorium is a method used to induce the production of Ac-225 as one of the daughter products in order to make this treatment more available. It is essential to evaluate and control the radiation dose during the process. The combination of Monte Carlo N-Particle eXtended (MCNPX) and CINDER90 was used as tools for simulating the bombardment of the Thorium target at 200 MeV for ten days. MCNPX is a transport code that tracks all the events and outcomes of each particle involved in the process. CINDER90 employed the resulting neutron flux data along with the production and destruction of isotopes to provide the decay gamma spectrum for requested time steps. The gamma spectrum is then used as a radiation source in MCNPX to evaluate the radiation dose at different locations near the modeled hot cell room in which the Thorium target was placed after the bombardment. Doses were measured in MCNPX immediately, three days and five days after the bombardment. This project has provided valuable information for the radiation safety of the workers around the hot cell room. It has also given me the opportunity to enhance my knowledge about nuclear physics and learn how to run Monte Carlo simulations in a supercomputer platform.

## I. Introduction

The short half-lives of Actinium-225 (10 days) and its daughter product, Bismuth-213 (43 minutes), are ideal for cancer therapy treatments since its long enough for transportation to patients and short enough to avoid long-term storage in medical facilities. The benefits of these alpha-emitting isotopes are that unlike commonly used beta-emitting isotopes, they release highly energetic alpha particles in a short range, hence effectively eliminating the cancerous cells while leaving less healthy tissue harmed.<sup>1</sup> While these isotopes are very promising, they are scarce throughout nature. Oak Ridge National Laboratory (ORNL) provides enough Actinium-225 to treat about 50 patients per year, but it is estimated that nearly 30 times as much is needed to conduct clinical trials.<sup>2</sup> At Brookhaven National Laboratory (BNL) isotopes for medical applications like these can be produced at the Brookhaven Linac Isotope Producer (BLIP). Small puck-shaped targets can be bombarded with highly focused beams of energetic protons at BLIP.<sup>2</sup> This proton spallation method is used to produce more Actinium-225 by inducing decay in Thorium.

Although this bombardment has already been done at BLIP for many years, a different hot cell room has been proposed to place the irradiated target in the future. The gamma radiation emitted by the isotopes in the target can be a hazard to those who are around the hot cell room, and thus it is important to evaluate

the dose rates. MCNPX version 2.7.0 and CINDER'90 can be used as tools to simulate the bombardment and estimate the dose rates at different locations that receive gamma radiation. MCNPX is a transport code that was developed at Los Alamos National Laboratory. It serves a purpose to track all the events of the particles present and to provide the probability of particle interactions by the use of physics models and a cross section library.<sup>3</sup> CINDER is a transmutation code that constructs a sequence of nuclide interactions to provide a gamma spectrum for different time steps by using the data from MCNPX. The CINDER'90 package includes three additional components that allow the proper execution of the simulation: the "activation script", the "tabcode" and the "gamma source script". The "activation script" gathers necessary information from the MCNPX output files to prepare the execution for CINDER. The post-processing code, "tabcode", then employs these files to obtain the gamma spectra of the isotopes and the isotope inventory. The "gamma source script" combines the gamma spectra and provides the new source information for a new MCNPX input file. Once the hot cell room is modeled in the new MCNPX file, the simulation is then run again to evaluate the dose rates at different points around the hot cell room.

## II. Methods and Process Outline

The first step of the process is modeling the target that will be bombarded at BLIP. The MCNPX input file is divided into three sections: cell cards, surface cards and data cards. The surface cards provide the geometric information of the stacked layers while the material cards provide the elements present in each material. The shape of the target is a right circular cylinder. This information is combined in the cell cards to construct the complete

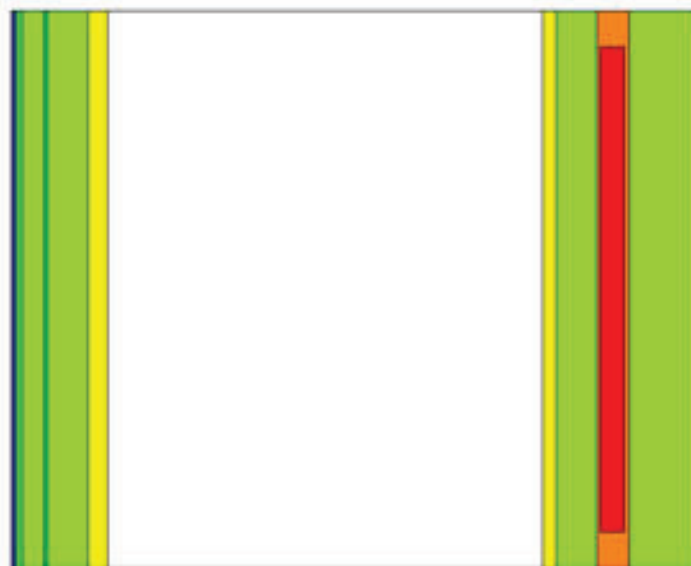


Fig. 1: 2-D image of the target modeled in MCNPX for bombardment.



target. The details of the stacked materials can be seen in Table 1 and the 2-D image of the modeled target can be seen in Figure 1.

MCNPX is then run to simulate the bombardment with 200 MeV protons for 10 days. The proton is placed in front of the first layer of the target and was aligned in the z-axis. All the events caused by the particle interactions are recorded in a MCNPX output file called “histp”, which will later on be used to extract information for CINDER to obtain cell based isotope production and destruction rates. The simulation is run until 100 million events are recorded.

**Table 1: List of materials used for target**

Layer Number	Material	Thickness (cm)	Density (cm/g <sup>3</sup> )
1	Beryllium	0.0305	1.85
2	AlBeMet	0.0305	2.10
3	Stainless Steel	0.0787	8.0
4	Water	0.2682	1.0
5	Stainless Steel	0.0510	8.0
6	Water	0.5080	1.0
7	Copper	0.2410	8.96
8	Vacuum	5.4580	0
9	Copper	0.1580	8.96
10	Water	0.5080	1.0
11	Inconel	0.4070	8.43
12	Thorium	0.3050	11.7
13	Water	0.8100	1.0
14	Stainless Steel	0.0508	8.0

A shell script is used to execute the MCNPX file by providing the input and output file names. Two output files, “histpa”<sup>a</sup> and “histpb”, are made to hold the information about the neutron fluxes averaged over the Inconel and thorium cells and the production and destruction rates of isotopes.

A shell script was used to execute the more complex “activation script”, which is written in Perl. All the necessary input and output files created from the CINDER package are placed in a separate directory for each cell in which the activation was performed. The first step for the activation process is reading the MCNPX output file to find the neutron fluxes and the material information for each cell. One of the files created in this directory contains the data of the neutron fluxes that provides the integral of all the fluxes and the fluxes separated into bins. All of these binned

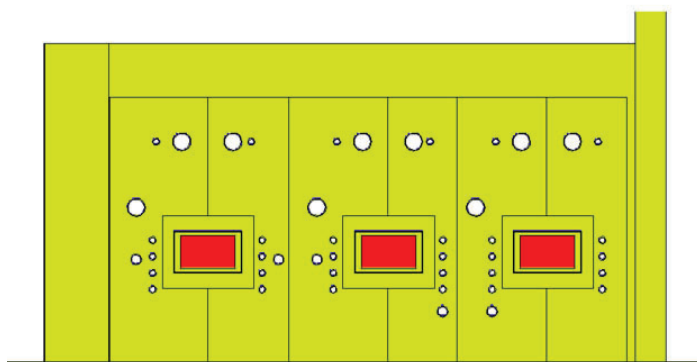


**Fig. 2: Front view of the hot cell room beneath the outside steel liner modeled in MCNPX.**

fluxes are multiplied by a normalization constant specified in the activation file which indicates the number of protons per second. To obtain this constant, the current of 200  $\mu\text{A}$  is divided by the proton charge, resulting in  $1.243\text{E}15$  protons/s. The next step uses the code provided by the MCNPX package called “HTAPE3X”. This code is executed by the activation script three times to evaluate the “histp” files. The code initially separates the information needed to generate the isotope production, gas production and isotope destruction data into files named “int8”, “int14” and “int15”, respectively. Each file is then evaluated by the same code to generate the mentioned data in the files “outt8”, “outt14” and “outt15”, respectively. The activation script then proceeds to read these output files in order to create a file containing the spallation products of each cell. The last file required for the execution of CINDER contains the information of the library path that contains a total of 3400 nuclides.<sup>4</sup>

After all these files are created in the directories made by the activation script, CINDER is finally ready to be executed. The main output of this process contains the initial and final nuclide information for each time step along with the total atom density activity for the Thorium and Inconel cells. The post-processing step utilizes “tabcode” to provide the final isotope inventory in different tables and the gamma spectra of the isotopes separated into 25 different energy bins for the requested time steps. After this process is done, a file indicating the cell numbers in which an activation calculation was performed, the total volume, density and the directory name with the input and output files from the process is created.

The “gamma source script”, also written in Perl, utilizes that last file to locate the necessary files for its execution. The gamma spectrum acquired from the “spectra” file for each cell is combined to act as a photon source for the gamma radiation for the different time steps. The probability of the gamma radiation coming from either cell is determined by the cell weight, which is obtained by multiplying the weight per unit volume in the “spectra” file for

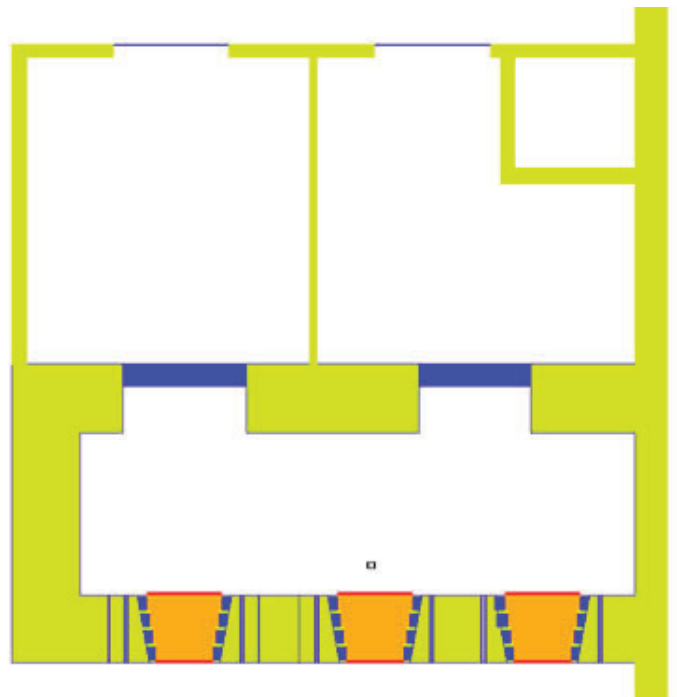


**Fig. 3: Top view of the hot cell room modeled in MCNPX.**

each cell and its volume. The kinetic energy of the source is now a function of the energy bins and their probabilities. To obtain the probability of the energy of the photon coming from each bin, the gamma source script multiplies the cell weight by the gamma spectrum corresponding to each bin. Each source information for the different times will then replace the initial source information used for the target bombardment.

Since we want to know the dose rates outside of the hot cell room where the target gets placed in after the bombardment, it must also be modeled in MCNPX. The front view of the modeled hot cell room can be seen in Figure 2.

The target is placed 1.5' from the middle lead glass window and 3' above the floor. The hot cell room has a length of about 27', height of 15' and a width of about 10'. The room located behind the hot cell room was also modeled with the same length and height, but with a width of 17'. The top view of the hot cell room can be seen in Figure 3. The inside and outside of the hot cell room had a stainless steel liner 3/8" thick. The two steel doors

leading to the back area were each 1' thick, while the other two steel doors leading to the outside of the modeled area were 8". Three sides of the hot cell room were 3' thick and made out of heavy concrete. The right side wall is 1.4' thick. To account for the uncertainty of the material, two MCNPX files were made for the hot cell room, where one included heavy concrete for that wall and the other contained normal concrete. The material properties represented by the different cell colors can be seen in Table 2.

**Table 2: Material properties of hot cell room**

Cell Color	Material	Density (g/cm <sup>3</sup> )
Green	Heavy Concrete	3.9
Blue	Stainless Steel	8.0
Orange	Lead Glass	6.2
Red	Non-browning Lime Glass	2.7
None	Normal Concrete	2.35

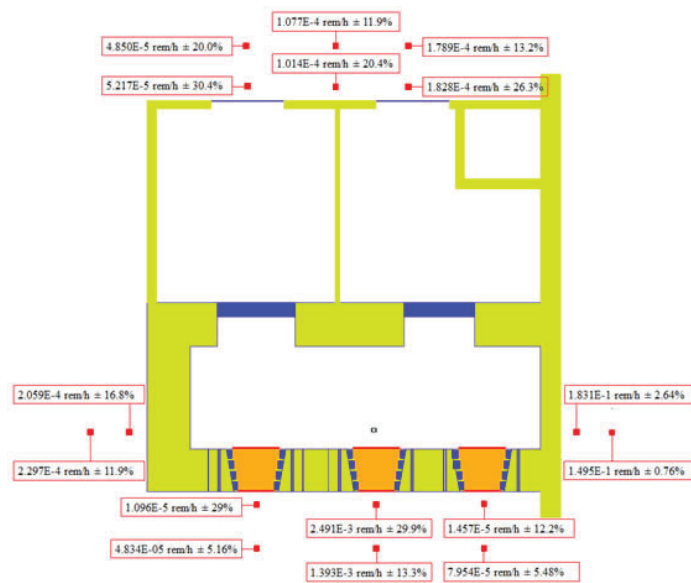


**Fig. 4: Dose rates immediately after the bombardment.**

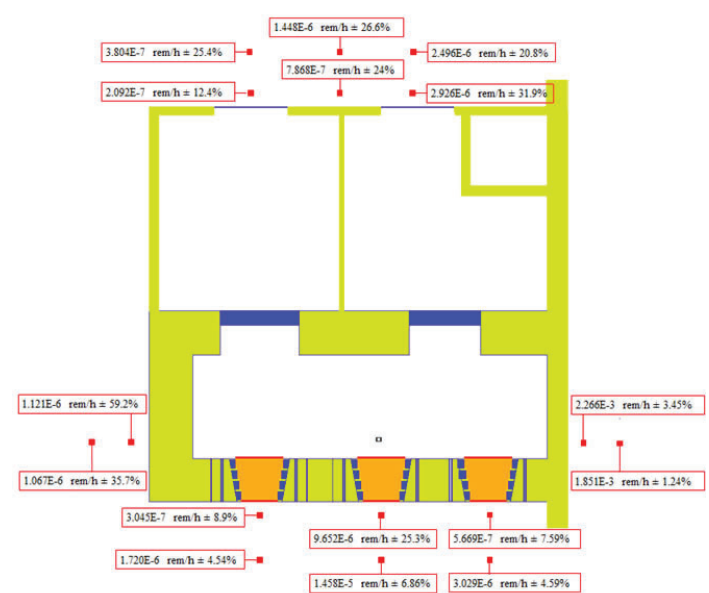


**Fig. 5: Dose rates three days after the bombardment.**

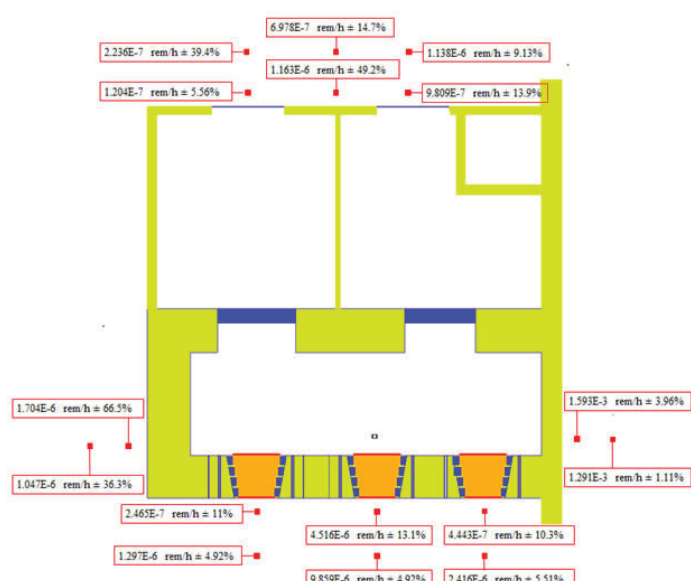


**Fig. 6: Dose rates five days after the bombardment.**

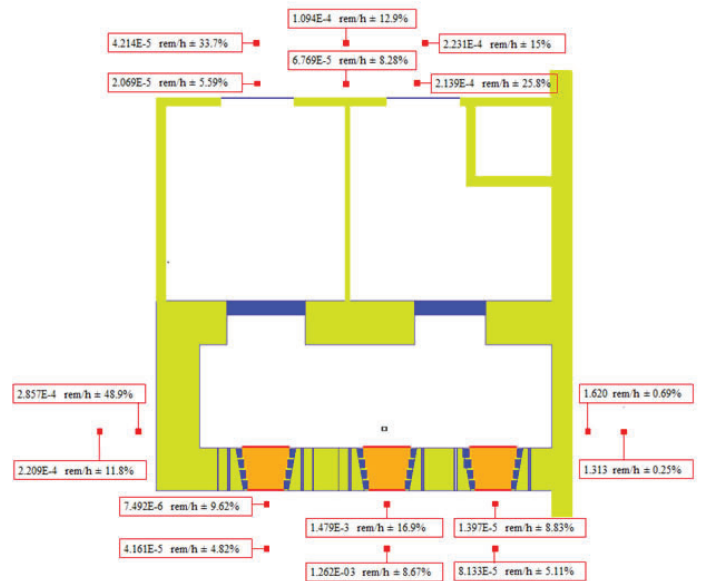


**Fig. 7: Dose rates immediately after the bombardment with normal concrete for the right wall.**

To evaluate the dose rates at different locations around the modeled room, detection tallies (F5) were implemented in the MCNPX input file to request 18 different point detectors. Each detector was either 10 cm or 1.5' from the outside wall of the hot cell room. A dose function card was also included in the file to convert photon fluxes to the standard flux-to-dose conversion given by ICRP-21 1971.<sup>5</sup> A super computer platform named Cori at the National Energy Research Scientific Computer Center (NERSC) is utilized to run this simulation. Four sets of simulations are run with the irradiated target inside of the hot cell room: three with the right side wall made out of heavy concrete for immediately, three days and five days after the bombardment and one immediately after the bombardment with normal concrete for the right side wall. Each simulation is run until 2 billion events were done.

### III. Results and Discussion

The dose rates at the different time steps around the outside of the hot cell room in which all walls are made out of heavy concrete can be seen in Figures 4, 5 and 6. The dose rates immediately after the bombardment with normal concrete for the right side wall can be seen in Figure 7.

Although only 16 points can be seen in the figures above, the last two detectors are placed directly above the location of the target, at 10 cm (detector #17) and 1.5' (detector #18), above the roof of the hot cell room. The estimated dose rates for these points at the different time steps can be seen in Table 3.

**Table 3: Dose rates for the points located above the hot cell room**

Time step of detection	Tally Number	Dose rates (rem/h)	Standard Deviation (%)
Immediately (Heavy Concrete)	17	1.629E-4	21.1
	18	2.124E-4	24.4
Immediately (Normal Concrete)	17	1.607E-4	23.9
	18	1.956E-4	17.1
Three Days	17	1.970E-6	62.9
	18	1.279E-6	34.0
Five days	17	8.776E-7	39.4
	18	9.048E-7	33.9

It can be seen that the highest dose rates are located near the right side wall in all time intervals. This was expected since this wall is thinner, allowing more gamma radiation to escape. When the simulation was run with normal concrete instead of heavy concrete for the right side wall, the estimated dose rate nearest to the wall increased from 0.183 rem/h  $\pm$  2.64% to 1.620 rem/h  $\pm$  0.69%, which is nearly 9 times higher. The other area with higher dose rates is directly in front of the middle window, where it was estimated to be 1.48E-3 rem/h  $\pm$  16.9% (closer point) and 1.26E-3 rem/h  $\pm$  8.67% (further point) immediately after the bombardment as seen in Figure 7. This was also predicted to be one of the areas of higher gamma radiation since it is the location closest to the irradiated target. There were many steel pipes inside the front wall, as seen in Figure 2, which could also have been a reason for the higher dose rates.

The reason why some of the standard deviations are relatively high is due to the fact that the corresponding dose rates or the Monte Carlo statistics are very low, causing small deviations to

result in a high percent difference.

From the results mentioned above, it can be seen that one should avoid going close to especially the right side wall if the target is placed inside the hot cell room immediately after the bombardment. Moreover, to reduce the radiation hazard, one can delay placing the target in the hot cell room after the bombardment; or one can build an additional shielding on the right side wall. The CINDER simulation provides a file containing an inventory of all isotopes resulted from the process. A sample of the acquired isotopes with the highest total activities can be seen in the Appendix in Table A1.

### IV. Conclusion

The combination of MCNPX and CINDER was used as a tool to initially simulate the bombardment of a Thorium target and then to estimate the dose rates around the hot cell room where it is proposed to be placed after being irradiated in the future. The initial target was a stack of different elements, but then only the Thorium puck surrounded by Inconel was placed in the hot cell room for the simulation. The sets of simulations were run in a supercomputer platform until 2 billion events were done. The highest dose rate was estimated as 1.620 rem/h  $\pm$  0.69% at the location near the right side wall when made out of normal concrete. If the actual material is heavy concrete, then this dose rate was estimated to be 0.183 rem/h  $\pm$  2.64%. Workers around the hot cell room should especially avoid going near this area immediately after the bombardment. An inventory of the isotopes was also obtained throughout this process.

### V. Acknowledgements

This project was supported in part by the U.S. Department of Energy, Office of Science, Office of Workforce Development for Teachers and Scientists (WDTS) under the Science Undergraduate Laboratory Internships Program (SULI)."

### VI. Appendix

**Table A1: Sample of Isotope Inventory from CINDER**

Isotope	Total Activity (Curies)	Isotope	Total Activity (Curies)	Isotope	Total Activity (Curies)
Cs138	5.118	Fr216	2.937		
Th231	39.680	Ac228	5.116	Te133	2.895
Th233	18.510	La142	4.822	I 136	2.851
Ra222	13.160	Te129	4.792	Tl208	2.819
Rn218	13.140	Fr221	4.723	Ac220	2.791
Th226	11.500	<b>Ac225</b>	<b>4.635</b>	Ce146	2.696
Bi211	9.738	Ce143	4.633	Pb209	2.654
Tl207	9.712	At217	4.597	Pr147	2.651
At215	9.109	Bi210	4.589	Po213	2.559
Fr219	9.109	<b>Bi213</b>	<b>4.582</b>	Rn217	2.559
Ac223	9.096	Te127	4.556	Ra221	2.557
Bi212	7.843	Te132	4.363	Ba143	2.467
Ac224	7.640	Te131	4.281	La145	2.403
Po214	7.277	Ba141	4.228	Ba144	2.356
Ac231	7.267	Pa233	4.182	Th227	2.356
Rn220	7.258	I 135	4.108	I 137	2.329
Ra224	7.256	Pr145	4.057	Xe140	2.313



Po216	7.201
Ac226	7.086
Pb212	7.014
Fr218	6.347
I 132	6.166
At214	6.122
Xe135	6.054
I 133	5.900
At213	5.751
Fr217	5.750
La141	5.745
Ac229	5.696
Ac221	5.571
Ac222	5.457
Ba139	5.305

I 131	4.045
Cs139	3.948
Xe138	3.752
La143	3.751
Cs140	3.681
Xe137	3.678
Ba142	3.659
Pa229	3.561
Pr146	3.327
Ac230	3.303
La144	3.285
Te134	3.273
Ce145	3.148
Cs141	3.065
La140	3.013

Pm149	2.268
Ba140	2.259
Xe139	2.241
Cs142	2.219
At211	2.045
Po211	2.020
I 138	2.009
Pr148	1.991
Nd149	1.917
Pr143	1.914
Ce147	1.890
Te136	1.844
Fr215	1.781
Po212	1.771
Rn216	1.769

Te137	0.929
Cs129	0.910
I 123	0.894
Nd152	0.875
La148	0.866
Pr144	0.851
Rn214	0.851
Te118	0.227
I 144	0.224
Cs126	0.223
Sm158	0.223
La151	0.222
Ra230	0.219
Nd140	0.219
Gd161	0.217
Pr138	0.217
Cs148	0.215
Eu156	0.215
Pr154	0.212
Tb161	0.210
Po210	0.205
Th228	0.204
Pr137	0.199
Ba150	0.197
Tb163	0.197
I 125	0.186
Pm157	0.186
Xe127	0.184
Eu160	0.184
Gd162	0.173
Ce134	0.172
Xe123	0.166
I 145	0.165
Dy165	0.165
Ho166	0.165
Ho167	0.164
Ba128	0.163
La131	0.161
Pm148	0.160
Nd156	0.157
I 120	0.151
Te141	0.150
Ba129	0.146
Po206	0.146
Cs149	0.145
La152	0.144
Tb164	0.144
Sm159	0.138

Te140	0.537
Fr214	0.527
Rn213	0.515
Pr139	0.515
Ba148	0.505
Nd153	0.494
Ra216	0.491
Eu161	0.135
Te117	0.132
Dy166	0.132
Ho168	0.131
Cs125	0.131
Pm142	0.131
Ce153	0.130
Po207	0.126
Pr155	0.122
Bi206	0.122
Ac232	0.120
Pm158	0.118
Ce154	0.114
Gd163	0.113
Ac217	0.113
Xe147	0.109
Tb165	0.108
Ce144	0.107
Eu162	0.101
Xe122	0.100
Pr136	0.100
Te144	0.098
Dy167	0.098
Tl209	0.097
Nd139	0.096
Tb166	0.095
Xe148	0.094
Fr212	0.093
I 119	0.089
Er171	0.088
Gd164	0.088
Te116	0.088
Ho169	0.088
Nd157	0.088
Ra213	0.085
Th223	0.083
Dy168	0.083
Tm172	0.082
La153	0.082
Pa225	0.082
Pm141	0.080

Pm156	0.259
Eu159	0.255
Pa226	0.254
Te142	0.251
Ra214	0.244
La132	0.243
Te139	0.241
La130	0.079
I 146	0.078
Te143	0.077
Fr223	0.075
Ba127	0.075
Fr222	0.074
Pm159	0.074
Sm161	0.072
Nd138	0.072
Rn209	0.071
Tm173	0.069
Tb155	0.069
Ba152	0.068
Ce139	0.068
Nd158	0.068
Ba151	0.068
Er172	0.067
Pr156	0.065
Er169	0.065
At208	0.064
Er165	0.063
Tb167	0.062
Sm162	0.058
Tm174	0.058
Fr224	0.058
Eu163	0.058
Gd165	0.058
Cs150	0.058
Ho171	0.057
Ce132	0.057
Dy157	0.057
Ho170	0.055
Tb156	0.054
Gd166	0.054
Cs124	0.054
Ho164	0.053
Yb175	0.052
Ho162	0.052
Ba126	0.051
Pr135	0.051
Dy169	0.050

Te135	1.738
Th225	1.705
I 130	1.620
Pa228	1.576
I 128	1.556
Ac219	1.552
Pm151	1.539
La146	1.531
Xe141	1.529
Pr149	1.524
Cs143	1.490
Ce148	1.469
Nd147	1.462
Pa232	1.408
Ba145	1.406
Pa230	1.396
La147	1.357
Ce141	1.262
Rn219	1.255
Ra223	1.254
Cs144	1.168
Xe142	1.164
Ba146	1.130
Pr150	1.116
I 139	1.105
Nd151	1.104
Pm152	1.079
La135	1.063
Te138	1.029
Sm153	1.003
Ce149	0.962
I 140	0.950

Pa227	0.846
Ra218	0.827
La136	0.809
Pm153	0.806
Cs136	0.801
Rn215	0.800
Pr151	0.798
Ra219	0.789
Cs132	0.781
Ce150	0.760
Cs145	0.759
Pr140	0.752
Cs130	0.728
Ce137	0.699
Ra227	0.695
Cs131	0.690
La134	0.661
Ba147	0.644
Pr142	0.644
At210	0.643
I 141	0.640
I 124	0.638
Po215	0.630
Pb211	0.629
Th224	0.617
Xe144	0.599
La149	0.595
Rn212	0.595
Sm155	0.585
Cs128	0.553
Pr152	0.546
Cs146	0.539

I 126	0.483
Ra217	0.479
I 142	0.477
Xe125	0.476
Eu157	0.465
Xe143	0.462
La133	0.452
Ce151	0.442
Sm156	0.440
Ac218	0.421
Ra225	0.413
Pm155	0.407
At209	0.394
La150	0.389
Nd154	0.380
Cs127	0.379
I 143	0.365
Cs147	0.364
Gd159	0.362
Ra229	0.352
Nd141	0.349
I 121	0.344
Pm150	0.335
Eu158	0.333
Rn211	0.332
Ce135	0.289
Te121	0.280
Ra215	0.278
Rn210	0.272
Xe145	0.270
Tb162	0.260
Ba131	0.259

## VII. References

- <sup>a)</sup> If there are too many events, there will be additional “histp” files (such as “histpa”) produced.
- <sup>1</sup> Idaho National Laboratory. “Medical Actinium for Therapeutic Treatment (MATT).”  
< <http://www4vip.inl.gov/factsheets/docs/matt.pdf>>.
- <sup>2</sup> Walsh, K. M. “Producing radioisotopes for medical imaging and disease treatment.” Mar 2017. < <https://www.bnl.gov/newsroom/news.php?a=212043>>.
- <sup>3</sup> Hughes, H. G. & James, M. R. Los Alamos National Laboratory. “MCNP6 Class”. Feb 2014. < <http://permalink.lanl.gov/object/tr?what=info:lanl-repo/lareport/LA-UR-14-21281>>.
- <sup>4</sup> Trellue, H. R., Fensin, M. L., & Galloway, J. D. Los Alamos National Laboratory. “Production and Depletion Calculations Using MCNP” < [https://mcnp.lanl.gov/pdf\\_files/la-ur-12-25804.pdf](https://mcnp.lanl.gov/pdf_files/la-ur-12-25804.pdf)>.
- <sup>5</sup> Biswas, D. Westinghouse Safety Management Solutions LLC. “Rad-in-Tissue versus Rad-in-Air” < <http://sti.srs.gov/fulltext/ms2002472/ms2002472.html>>.

# Electron multiplying charge coupled device calibration for the NSLS-II soft inelastic x-ray scattering beam line

Lorena Mezini, Astronomy and Physics, Stony Brook University, Stony Brook, NY 11794  
Ivan Kotov, Instrumentation, Brookhaven National Laboratory, Upton, NY 11973

## Abstract

The National Synchrotron Light Source II (NSLS-II) at Brookhaven National Laboratory (BNL), recently opened for operation in 2015, produces beams which are used to study material properties. The Soft Inelastic X-ray Scattering (SIX) beamline at the light source will produce a soft x-ray beam with energy between 165 to 2300 eV. This beamline uses a RIXS-Cam2 electron multiplying charged coupled device (EMCCD) as a x-ray detector. Two EMCCD sensors are adjoined to get larger angular coverage. In order to make accurate measurements, the EMCCD must be properly calibrated. The goal of this research is to find the optimal voltage setting for EMCCD operation so that the greatest signal to noise ratio can be achieved by the detector. Data for calibration of this detector were obtained with Iron 55 as a source of x-rays. An existing C++ code is used to identify and measure bright pixel clusters where x-rays from this source were incident on the detector. It is observed that some of the pixels in the images taken by the EMCCD at high gain voltage settings are followed by a tail of dimmer pixels. Modifications that I added to the C++ code are used to identify and measure these inline pixel clusters. The implementation of these findings in the future when the beam line is up and running will allow for better measurements of samples brought in by visiting scientists.

## I. Introduction

The Soft Inelastic X-ray Scattering (SIX) beamline at the National Synchrotron Light Source II (NSLS-II) at Brookhaven National Laboratory (BNL) utilizes a soft x-ray beam with energy in the range of 165 to 2300 eV. This beamline will be used for techniques such as x-ray absorption spectroscopy, x-ray inelastic scattering, and x-ray emission spectroscopy. These soft x-ray

techniques are of interest in the fields of condensed matter physics and materials sciences since they can be used to characterize the surface layers and structures of materials and molecules. During beamline experiments, a sample is placed at the end of the x-ray beam which allows the x-rays to excite electrons in the sample and cause them to emit light. This light is detected by a RIXS-Cam2 electron multiplying charged coupled device (EMCCD) and converted into a digital signal which can then be analyzed. The accuracy of these measurements is dependent on the resolution achieved by the detector. For this reason, it is necessary to calibrate this detector so that the greatest signal to noise level can be achieved.

## II. EMCCD

### A. A. Sensors

The RIXSCam2 used in beamline SIX contains two E2v technologies CCD-207 devices. These sensors each have 1632x1608 pixels that are  $16 \times 16 \mu\text{m}^2$  in size. The sensors are back-illuminated and mounted on a movable stage that can be tilted so as to change the effective size of the pixels. Figure 1, from David Colebrook [9], shows how the sensors are held in the RIXSCam2. These sensors do not have any anti-reflective coating as this would hinder its response to soft x-rays.<sup>[8]</sup>

Photons produced during beamline experiments are incident on the silicon layer of the EMCCD sensor where they interact and create electron-hole pairs.<sup>[1]</sup> Electrons are collected in potential wells located at each pixel of the EMCCD camera and are transferred from one pixel to the next by applying different voltages at the gates of the EMCCD register.<sup>[1]</sup> Unlike regular CCDs, EMCCDs contain an added gain, or multiplication, register situ-

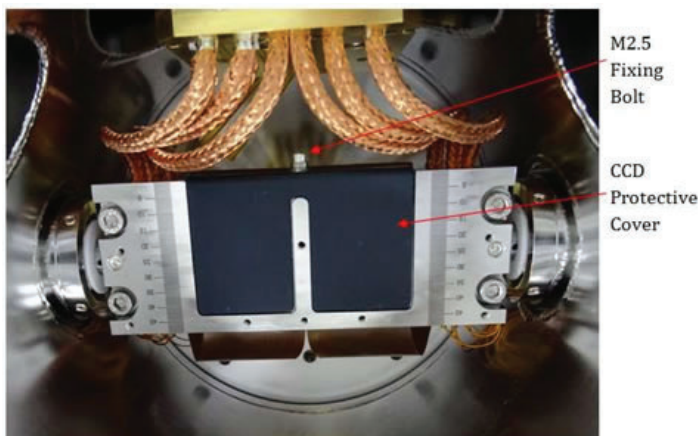


Figure 1: RIXSCam2 EMCCD bench

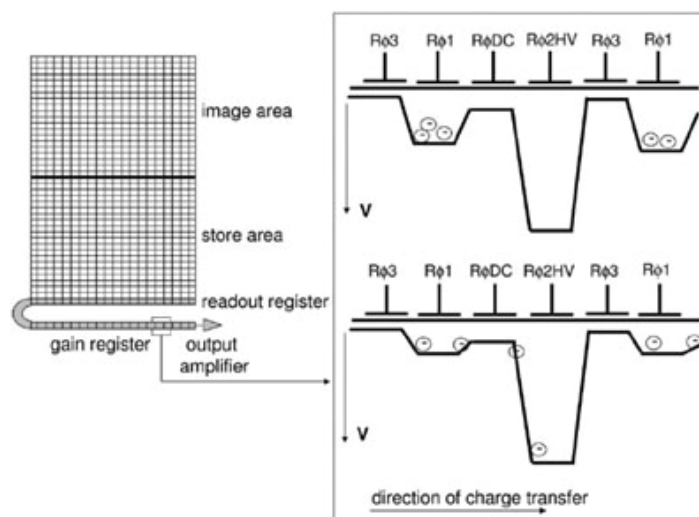


Figure 2: EMCCD Schematic



ated after the readout register.<sup>[5]</sup> In the RIXSCam2 EMCCD, this register is referred to as the LS register, and the register without the additional gain feature is the HR register. The multiplication register serves to amplify signals by creating large potential differences between the gates in this register so that electrons can undergo impact ionization.<sup>[5]</sup> This is shown schematically in figure 2 from Gerralt A. De Vree, *et al.*<sup>[4]</sup> As this process repeats for all pixels in the multiplying register, the number of electrons increases. Finally, this charge is converted into voltage at the output amplifier at the end of this register and gets measured.<sup>[1]</sup> For our purposes, one of the sensors has a 0.1V higher voltage setting.

### B. B. Noise

There are several noise sources in EMCCDs. They are shot noise, readout noise, and dark current.<sup>[3]</sup> Shot noise is due to statistical fluctuations in the number of x-ray generated electrons. These fluctuations come about as a result of the quantum nature of light.<sup>[3]</sup> Dark current noise is due to the thermal generation of electrons in the silicon of the EMCCD. We are able to suppress the contribution from dark current by cryogenically cooling the EMCCD sensors down to -100°C. The readout noise is created by the circuitry in the EMCCD.<sup>[3]</sup> Its effect can be minimized by increasing the voltage at the gain register to amplify the signal, but, this would also amplify the noise collected during the prior charge transfer process. The resolution, R of an EMCCD can be described by the following equation assuming no dark current contribution:

$$R = \frac{\sigma_{\text{signal}}}{A_{\text{signal}}} = \sqrt{\frac{2N_e F - \frac{N_e F}{M} + \frac{\sigma^2}{M^2}}{N_e}} \quad (1)$$

where  $N_e$  is the number of electrons produced in the EMCCD by an incoming x-ray, F is the Fano factor, M is the multiplication factor,  $\sigma$  is the noise due to readout, and  $A_{\text{signal}}$  is signal peak position.

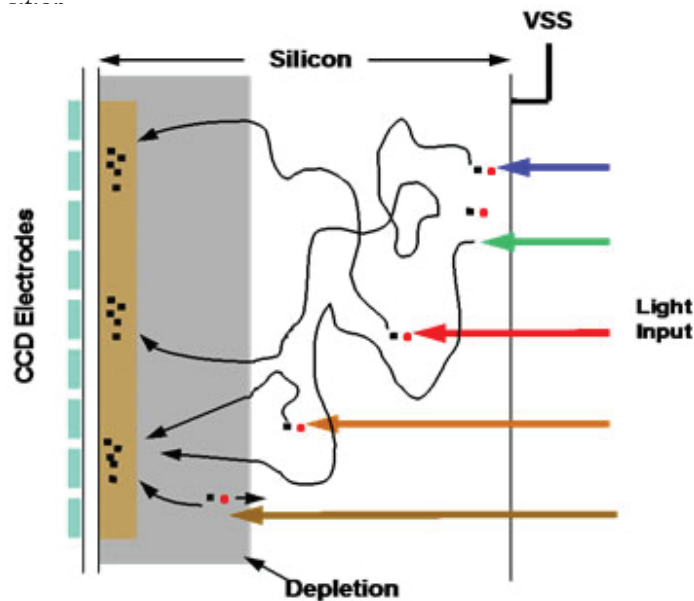


Figure 3: Incoming light rays will interact at different depths in the EMCCD silicon depending on their frequency and produce a single electron. If this interaction takes place in the non depleted region, the electron will travel along a random path until it reaches the depleted region and enters into a pixel. For x-rays, a group of electrons is produced during a single interaction instead. Similarly, these electrons will move randomly causing the group to disperse as it travels to the depleted region and enters into a diffused cluster of pixels.

## III. DataCollection

### A. A. Calibration source

Iron55 is currently being used as a source of x-ray radiation for the EMCCD calibration process. The source active material, <sup>55</sup>Fe is deposited on the holder and sealed by a film. The holder is placed a distance away from the detectors. According to a table put together by Lund University and Lawrence Berkeley National Laboratory, source emissions are 16.2% <sup>55</sup>Fe K<sub>α1</sub>, 8.5% <sup>55</sup>Fe K<sub>α2</sub>, and 1.98% <sup>55</sup>Fe K<sub>β1</sub>.<sup>[7]</sup> Only a fraction of these x-rays are actually incident on the detector. Because the x-rays are emitted from the source in all directions, many will never see the detector. In addition, there is also a probability of the emitted x-rays being absorbed by the iron or the material of the surrounding film. The iron 55 will emit 5.19 keV auger electrons approximately 60% of the time.<sup>[2]</sup> Almost all of these electrons will be absorbed by the iron 55 due to its high density and high probability of interaction with the electrons. Any electrons that make it out will then mostly be absorbed by the film surrounding the iron source.

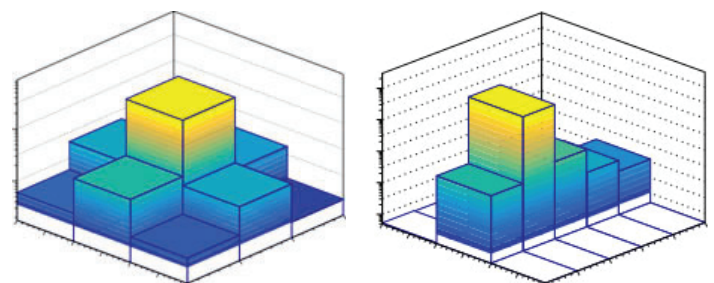
### B. B. Images

Calibration data are collected in the form of EMCCD images of the x-rays emitted from iron 55 decays. These images are taken with 5 second exposure times and with different voltages applied to the multiplication register. Two main data sets were used for analysis. The first set contains 36 images total, 4 taken at low voltages in the range of 20V to 35V and 32 taken at high voltages in the range of 40V to 45.3V. The second set is a high statistics set and contains 118 images for each of 7 different voltage settings between 42V and 44.6V.

### C. C. Clusters

In the images, the x-rays appear as clusters of bright pixels. These clusters come in two different forms. A compact cluster is a group of few bright pixels, most often a single bright pixel followed by a tail of several dimmer ones in the direction of readout. A diffused cluster is a bright pixel surrounded on all sides by dimmer ones. One possible cause of the events with a "tail" is very high voltage applied at the multiplication register so that impact ionization generates more electrons than the well capacity can hold and electrons begin to overflow into neighboring pixels.

The diffused clusters occur when x-rays interact in the field free region of the EMCCD.<sup>[6]</sup> The electrons that are produced in this region spread apart as they travel to the depleted region and enter into different pixels.<sup>[6]</sup> Figure 3 shows this process for incoming light rays which only produce one electron, as opposed to x-rays which produce many at a time. The appearance of these two types of events in the EMCCD images is shown in figure 4



(a) Diffusedcluster

(b) Inlinecluster

Figure 4: Histogram (a) shows the average shape of a diffused cluster and histogram (b) shows the average shape of an inline cluster.

where (a) is an average diffused cluster and (b) is an average compact cluster. The distribution of the number of these two types of clusters is shown in figure 5.

#### IV. Software and Data Analysis

An existing C++ code is used to identify and measure the signal levels of clusters seen in the data images. Before this process begins, the code does a baseline reduction of the image by subtracting some constant amplitude from all pixels and effectively setting the minimum pixel amplitude to zero. At the same time, it calculates a root mean square (rms) value for the noise. Because the pixel amplitudes in the data are all in analog-to-digital-units (ADU), the gain should be specified in the code in order to convert amplitudes to number of electrons. In order to pick out the clusters, this code searches for the brightest pixels in the image, one at a time, and creates a box (n pixels on a side) surrounding this pixel. The dimensions of the box can be adjusted but are always odd numbered so that the bright pixel is located at the center. There is also the option of increasing the dimensions of the box by adding a tail in order to encompass wider clusters. For our analysis, a 3 by 3 box with a 2 pixel long tail was used. The signal level of each cluster is measured by summing the amplitude of the pixels in the box or rectangle. The minimum signal threshold can be adjusted by the user of the code. Once a cluster has already been used it cannot be counted again. If another cluster overlaps with one that has been previously measured, both will be discarded. This ensures that double counting does not take place.

In order to identify inline clusters only, each general cluster picked up by the code must satisfy several conditions that were added for the purposes of this research. The code checks to see if any of the pixels in the row above and below the brightest have amplitudes greater than approximately 3 times the noise level. Any pixel that passes this threshold is flagged and the entire cluster is no longer qualified as an inline event. Because of the small pixel size, when an x-ray is incident at the boundary between two pixels, some of the electrons produced will enter one pixel and the rest enter the other.<sup>[6]</sup> For this reason, the check described above is not required for the pixel immediately next to the brightest in serial shift direction. Any other pixels beyond this one must also pass the test described. The histograms in figure 8 show what the

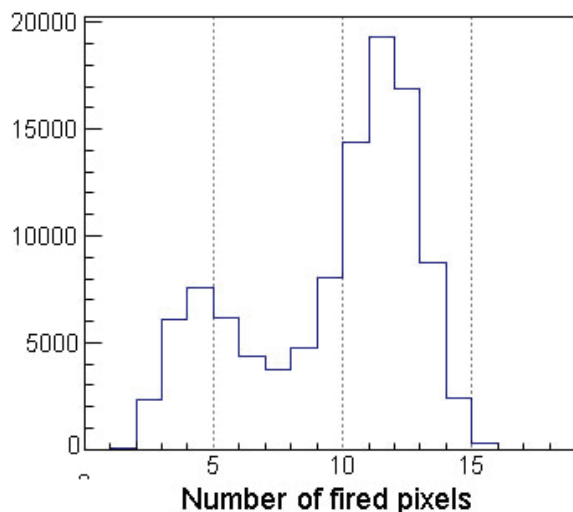


Figure 5: The cluster size distribution (number of pixels above the noise). Two groups are clearly visible, left peak corresponds to compact clusters and the right to diffused clusters.

average shape of one of these clusters looks like. Each of the 7 histograms used 118 images taken with the same settings. The histograms were created by averaging the amplitude of each pixel in the inline cluster over the number of clusters identified. CERN ROOT data analysis framework is used to make all histograms.

In order to analyze the spectrum of the x-ray emission, the sum of the amplitudes of the brightest pixel, the pixel to the left, and the pixel to the right of the brightest is taken for each inline cluster and put into a histogram. Such histograms will have two peaks which are a result of  $K_{\alpha}$  and  $K_{\beta}$  emission from the iron source. Figure 6 shows 7 of these histograms created using data taken at different voltage settings from the high statistics data sets. In order to measure the width and the signal peak value, we fitted the peaks with Gaussians. The mean value of each Gaussian is our measure of the signal peak. The ratio width/mean calculated from the Gaussian versus the multiplication factor is shown in figure 7(a) for the  $K_{\alpha}$  peak.

In order to calculate the multiplication for each voltage setting, the instrument's conversion factor between electrons and ADU must be known. To find this, the code is run only on data taken at very low voltage settings, 20V, 25V, and 30V, which would not introduce multiplication. The following equation is used to find the conversion value:

$$Conversion = \frac{N_2}{Mean(ADU)} \quad (2)$$

where the numerator is the number of electrons produced by an interaction of  $K_{\alpha}$  or  $K_{\beta}$  emission in the EMCCD and the denominator is the mean value in ADU taken from a Gaussian fit of the very low voltage data. Next, the multiplication factor is found by using the conversion in the following equation:

$$M = \frac{Mean(ADU) * Conversion}{N_e} \quad (3)$$

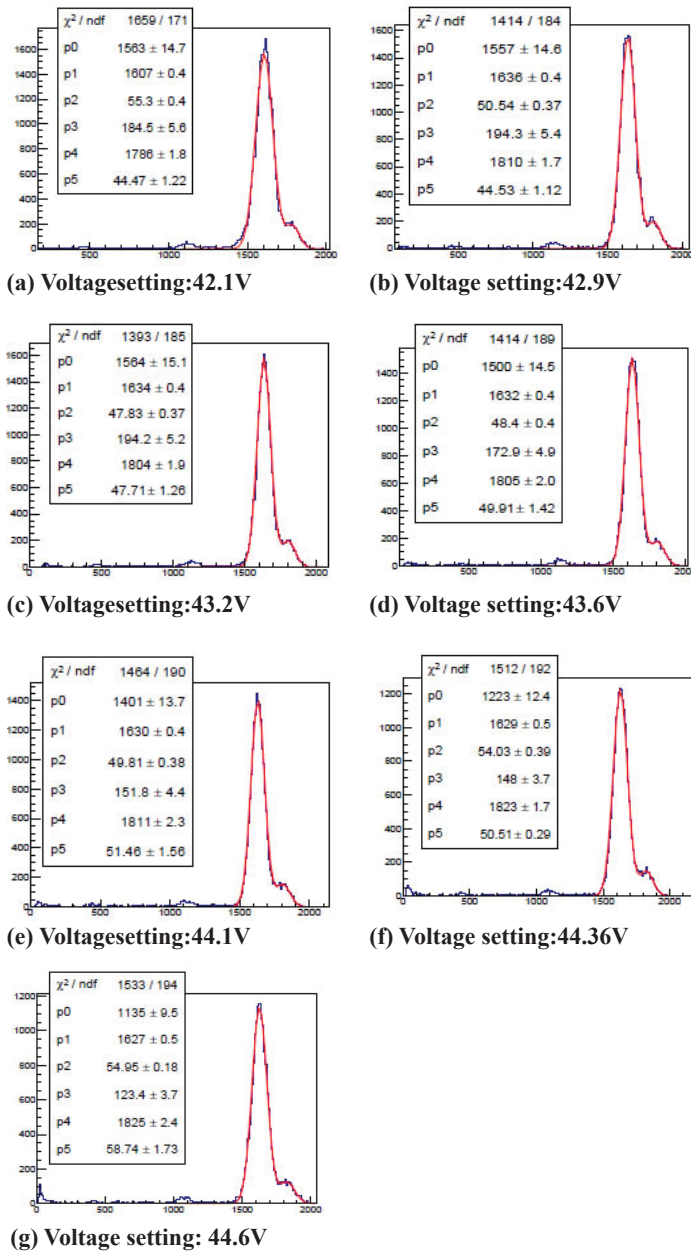
where this time the mean is taken from data with voltage settings high enough to introduce multiplication.

#### V. Results

The graph in figure 7(a) shows the resolution achieved by the RIXSCam2 sensors at the 7 different voltage settings. The minimum of this graph indicates that the most optimal voltage setting to use is 43.2V which corresponds to a multiplication value of 18.5. The resolution was found using Gaussian fits of  $K_{\alpha}$  peaks in figure 6. We calibrate our data so that all measurements are in units of electrons and the  $K_{\alpha}$  peak of the histograms in 6 is centered at approximately 1613 electrons. It is the number of electrons produced by  $K_{\alpha}$  interactions in Silicon. This calibration step allows us to make cross comparisons between graphs from different settings.

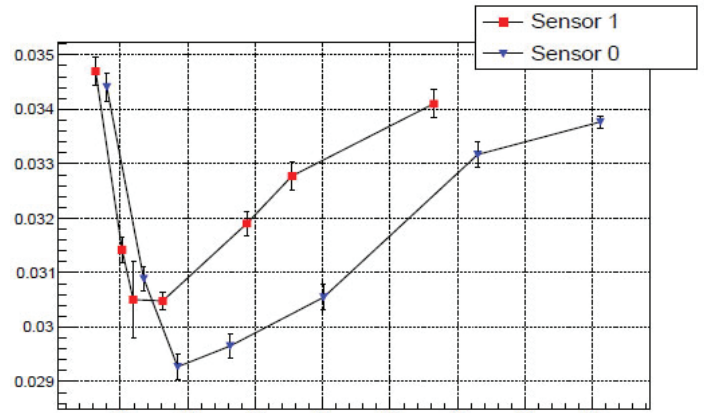
Figure 7(b) shows the resolution calculated using equation 1 that is expected with the readout noise levels from sensor 0, red curve. The blue line shows the ultimate resolution that can be achieved in the limit of very large M. The steep, negative slope near zero in the theoretical plot is similar to that of the experimental plot. The slope of the experimental plot turns positive before  $M=20$  whereas the theoretical continues its downward trend until it hits a minimum. Figure 7(c) is a close up of the minimum of this graph located at  $M=236.771$ .

Figure 8 shows the average shape of inline clusters at 7 different high voltage settings. These histograms were created using only contributions from the  $K_{\alpha}$  clusters in figure 6.

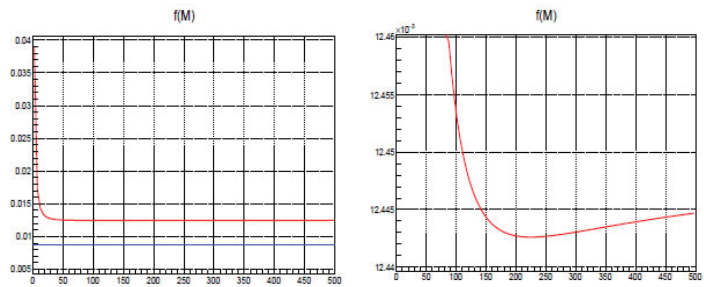


**Figure 6:** X-ray spectra obtained with compact clusters in sensor 0 for 7 different voltage settings. The x-axis is in electrons. The vertical axis is number of clusters. The tallest peak is from  $K_{\alpha 1}$  and  $K_{\alpha 2}$  emissions and the second tallest is from  $K_{\beta}$  emissions. P0 to P3 in the legend are the amplitude, mean, and sigma from the Gaussian fit of the  $K_{\alpha 2}$  peak, and P3 to P5 are the same for the  $K_{\beta}$  peak.

We calculate the ratio between the total amplitude of the 5 pixels making up the cluster and the difference between the first and third pixels which are located on either side of the brightest. Because it is equally probable for x-rays to interact at the boundary of any two pixels, it is expected that the first and third pixels have similar average amplitudes as a result of charge sharing with the brightest pixel. Therefore, any additional amplitude in the third pixel indicates the presence of a "tail". These ratios are shown in table 1. The "tail" is present at the level of  $\sim 10^{-2}$  of the total signal. For comparison, the table also shows the same ratio taken for images that were read out from the HR register which has no multiplication. The "tail" in HR clusters is at the level of  $\sim 3 \times 10^{-4}$ . These numbers show that the ratio decreases as multiplication is increased.



**a)** The  $K_{\alpha}$  line resolution, red points for sensor 1 and blue points for sensor 0, as a function of M. The voltage setting for sensor 0 is 0.1V greater than that of sensor 1.



**b)** The theoretical resolution calculated using equation (1) is plotted in red as a function of M using measured values of read-out noise from the RISX-Cam2 sensor 0. The blue line shows the limit of the function at very large values of M.

**(c)** The function minimum is located at  $M=236.771$ .

**Figure 7**

Voltage Setting (V)	Multiplication	Ratio ( $10^{-3}$ )	Number of $K_{\alpha}$
HR register	1	0.2951 $\pm$ 0.0445	67482
42.1	7.99	15.31 $\pm$ 0.23	17568
42.9	13.5	13.43 $\pm$ 0.23	17775
43.2	18.5	11.70 $\pm$ 0.39	17910
43.6	26.3	11.32 $\pm$ 0.20	17903
44.1	40.1	10.99 $\pm$ 0.14	17656
44.36	63.0	8.223 $\pm$ 0.655	17668
44.6	81.1	7.725 $\pm$ 0.620	17600

**Table 1:** The trailing pixels statistics.

Each individual pixel in the clusters is further analyzed in figure 9. Figure 9(a) was created using 42.1V data and (b) was created using 44.6V data. Both (a) and (b) contain histograms for each of the 15 pixels measured in the 3 pixel by 5 pixel cluster search rectangle. The histograms in the central column are those corresponding to the inline cluster pixels whereas the outer columns are pixels with amplitudes below approximately 3 times the noise level. These outer histograms all have distributions with means around 0. The center histograms have means that are shifted over to the right of 0. Inline clusters with more prominent tails exhibit



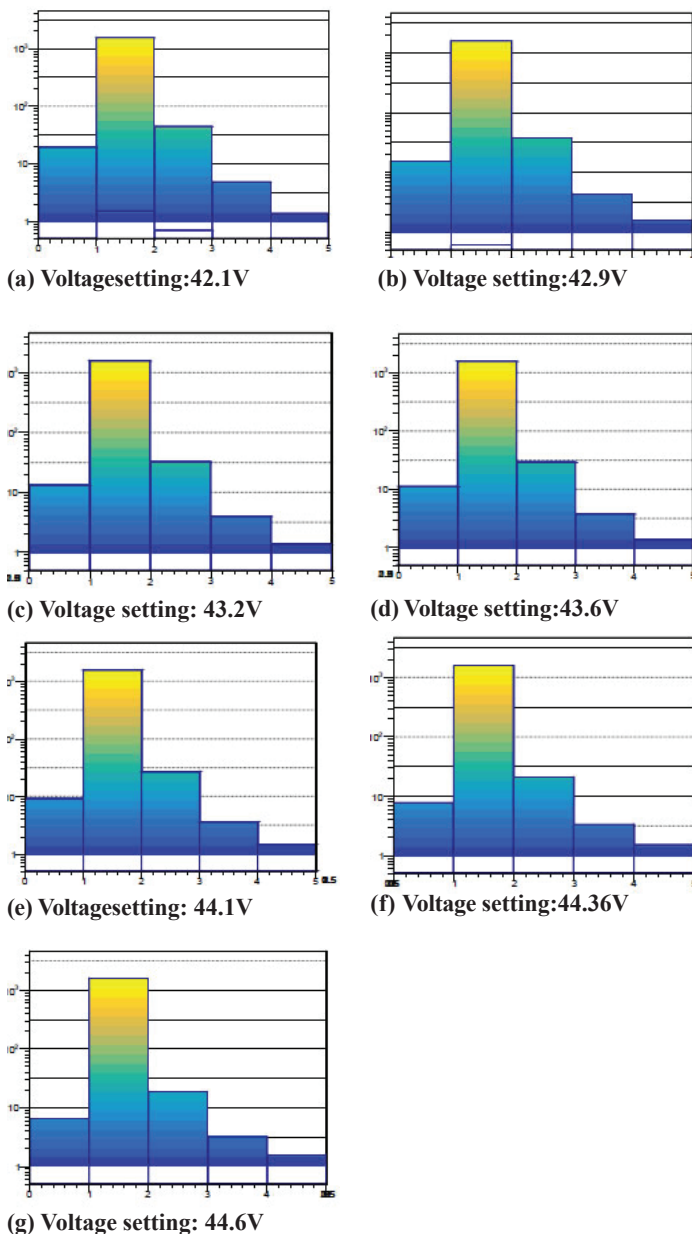


**Figure 8:** The average shape of inline clusters for different voltage settings.

larger shifts in their means to the right. The second histogram of the central column is the one which corresponds to the brightest pixel. This histogram along with the one above and below it all exhibit tails which is due to the sharing of electrons that takes place between these pixels. It can be seen that the brightest pixel histogram has a mean value of around 1600 which is almost equal to the number of electrons produced in the a  $K_{\alpha}$  interaction. The sum of the means of the 5 central histograms is equal to the calibrated mean value of the  $K_{\alpha}$  peak used in the analysis. For (a) this value is 1609 and for (b) this value is 1628.

Two main differences can be seen between the sets of histograms in 9(a) and (b). The histograms in (a) contain wider distributions than those in (b) and the central histograms in (a) have means that are shifted to more positive values than those in (b). The smaller means at higher voltages indicate that the tails are becoming smaller with increased voltage.

The histograms in figure 10 show the total amplitude of different size clusters. Figures (a) and (c) show the total amplitude from clusters that are 1 to 3 pixels in size for data with no mul-

tiplication read out from the HR register and data with multiplication read out from the LS register respectively. Figures (b) and (d) show the same for clusters that are 5 pixels or larger in size. These larger size clusters are usually from diffused events. Since  $K_{\alpha}$  interactions in the EMCCD silicon produce 1613 electrons, we expect the peak of these histograms to be located at this value. A shift in the mean of the peak with the Gaussian fit to smaller amplitudes can be seen from (a) to (b) and (c) to (d). This shift indicates a charge loss in diffused clusters. This loss is calculated to be  $169.89 \pm 0.29$  electrons for the multiplication data and  $96.750 \pm 0.013$  electrons for the HR register data.

## VI. Acknowledgements

This project was supported in part by the U.S. Department of Energy, Office of Science, Office of Workforce Development for Teachers and Scientists (WDTS) under the Science Undergraduate Laboratory Internships Program (SULI).

## VII. References

- <sup>1</sup>James R. Janesick. *Scientific Charge-coupled Devices*. SPIE Press, 2001. isbn: 9780819436986.
- <sup>2</sup>Esam M. A. Hussein. *Handbook on radiation probing, gauging, imaging and analysis*. Springer, 2003.
- <sup>3</sup>David Dussault and Pual Hoess. “Noise performance comparison of ICCD with CCD and EMCCD cameras”. In: *Proc.SPIE 5563* (2004), pp. 195–204. doi: 10.1117/12. 561839.
- <sup>4</sup>Gerralt A De Vree et al. “Photon-Counting Gamma Camera Based on an Electron- Multiplying CCD”. In: *IEEE TRANSACTIONS ON NUCLEAR SCIENCE 52.3* (2005), pp. 580–587. doi: 10.1109/TNS.2005.851443.
- <sup>5</sup>P.A. Jerram et al. “Electron Multiplying CCDs”. In: *SNIC Symposium 0.a* (2006), pp. 3–6. doi: n.
- <sup>6</sup>M.R. Soman et al. “Improving the spatial resolution of a soft X-ray Charge Cou- pled Device use for Resonant Inelastic X-ray Scattering”. In: *SNIC Symposium 13.a* (2011), pp. 3–7. doi: 10.1088/1748-0221/6/11/ C11021.
- <sup>7</sup>Huo Junde. *Table of Radioactive Isotopes*. url: <http://nucleardata.nuclear.lu.se/toi/nuclide.asp?iZA=260055>.
- <sup>8</sup>XCAM Ltd. *Camera Systems*. url: <http://www.xcam.co.uk/camera-systems>.
- <sup>9</sup>*System Operating Manual for RIXSCam2 System 2014-00003*.

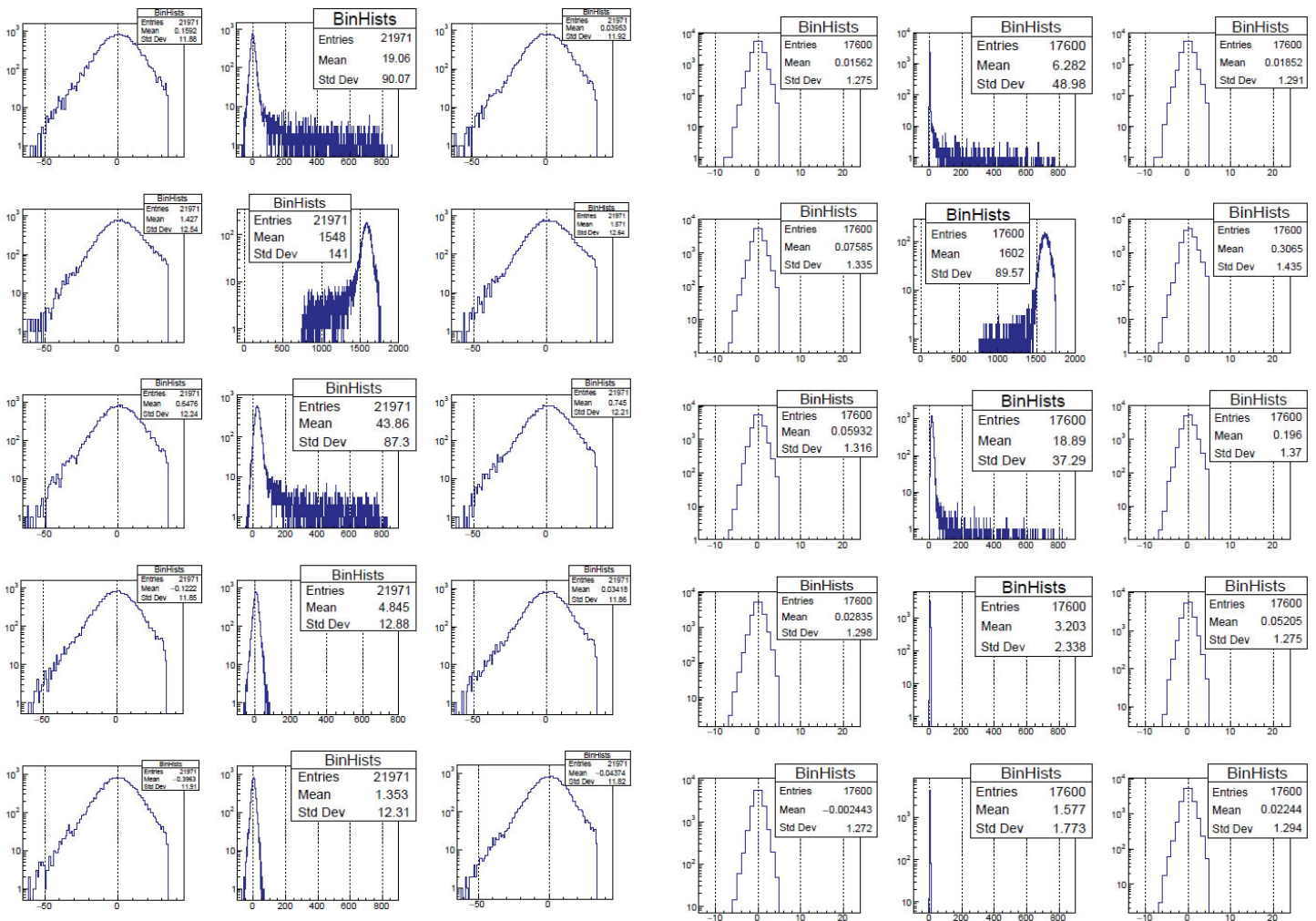


Figure 9: The amplitude distributions in individual pixels of compact clusters, (a) for the 42.1V setting and (b) for the 44.6V setting. The histograms are aligned vertically with the brightest pixel located in the second row.

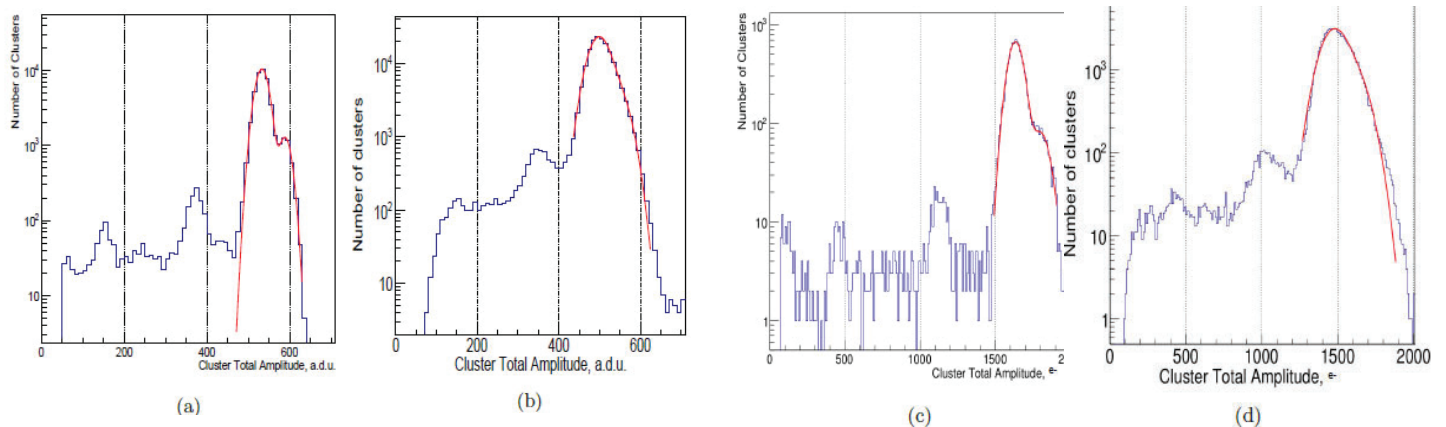


Figure 10: X-ray spectra. (a) and (b) plots made using data read out through the HR register. The amplitudes of compact clusters are shown in (a) and the amplitudes of 5 or greater pixel clusters are shown in (b). The histograms in (c) and (d) show the same plots for data from the LS register with voltage setting 43.2V

# A study of digital signal processing algorithms for time extraction from digitized multi-Gap Resistive Plate Chamber waveforms

Abioye Mohammed and Brendyn Van Demark, Computer & Information Science, Cheyney University of Pennsylvania, Cheyney, PA. 19319

Mickey Chiu, Physics, Brookhaven National Laboratory, Upton, NY 11973

Marcus Alfred, Physics & Astronomy, Howard University, Washington, DC, 20059

## ABSTRACT

At Brookhaven National Laboratory we are working on research and development for a possible new time-of-flight detector for the Super Pioneering High Energy Nuclear Interaction Experiment (sPHENIX), an upgrade of the PHENIX detector, that will take data from the Relativistic Heavy Ion Collider (RHIC) starting in 2022. sPHENIX is focused on identifying how the interactions of the smallest building blocks of matter gives rise to the properties of “quark-gluon plasma” – a hot, dense state of matter formed from the collision of heavy ions at RHIC. For this specific project, we are investigating digital signal processing algorithms to extract a time of arrival from waveforms using digital Constant Fraction Discrimination (dCFD) and Finite Impulse Response (FIR) filters. Digital Signal Processing (DSP) is the analysis and conversion of sampled and discrete input signals using digital computers and special purpose digital hardware to yield discrete useful results. In implementing the code required to analyze the digital signal processes, we used CERN ROOT’s data analysis framework along with the C++ programming language. ROOT is an object-oriented program with its library developed by CERN and mainly written in C++ but integrated with other languages such as Python. The resolution received from the use of these techniques will be investigated for different signal shapes (rise time) and signal to noise ratios then compared to the nominal best value that can be extracted with the waveform fits in offline analysis.

## I. INTRODUCTION

In the 10-20 ps mRPC detector being proposed for the sPHENIX detector upgrade, the time of arrival must be extracted from waveforms of the mRPC detector signals since the readout is based on the DRS4 waveform digitizer. This can be done by waveform fits via a chi-squared minimization technique, which is time consuming, but it maximizes the use of the information available. Having a much faster algorithm for extracting the time of arrival would enable the ability to have this task executed using a field-programmable gate array (FPGA). This would make possible a time of flight (TOF) trigger to select high momentum particles in a collider detector and possibly enable reduction in data required.

## II. METHODS

In investigating the digital signal processing algorithms, we used the constant fraction discrimination technique. For this project, we generated simulated signals that were based on real signals read out from actual mRPC detectors. The simulated signals were generated with variations in specific parameters such as the am-

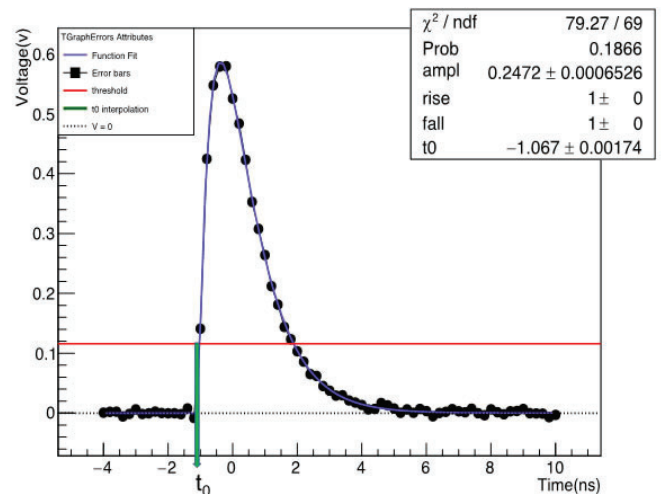
plitude, the different signal shapes (rise time and fall time), and with varying levels of noise from 1-4 mV. The simulated signal was stored using a TGraph in ROOT, and consisted of data points every 200 ps to simulate a 5 GHz sampling rate. The time of arrival of this digital signal is extracted using a dCFD algorithm, where a threshold sets when the pulse arrives. This threshold is a fraction of the amplitude of the pulse, and the time when the signal reaches that level is taken to be the time of arrival of the pulse  $t_0$ . A linear interpolation between the two data-points that intersects the threshold level is used to determine the  $t_0$  in the dCFD. The  $t_0$  is then subtracted from the known simulated signal TOA and the root-mean-squared (RMS) spread of this difference is used to determine the resolution of the  $t_0$  extraction. We also fit the digitized signal using the signal function to extract a  $t_0$ , and compare this result to the dCFD.

### A. The Simulated Signals using TGraphErrors

This plots the pseudo-data, the fitted function and the signal and background components at the best-fit values. In case of a TGraphErrors object, when x errors are present, the error along x, is projected along the y-direction by calculating the function at the points  $x_{\text{exlow}}$  and  $x_{\text{exhigh}}$ . The chisquare ( $\chi^2$ ) as shown on the graph above is then computed as the sum of the quantity below at each point:

$$\frac{(y-f(x))^2}{\sigma_y^2 + (1/2(\sigma_x + \sigma_{\text{ex}}) f'(x))^2}$$

where  $x$  and  $y$  are the point coordinates, and  $f'(x)$  is the derivative of the function  $f(x)$ . Hence to fit the TGraphErrors, the parameters of the fit function was initialized and the options used as the fit parameters were specified using as “R” -> use the range specified in the function range and “Q” -> quiet mode requiring minimum printing respectively. The parameters used in fitting the





TGraphErrors with their values are explicitly stated as amplitude (ampl), rise time and fall time of waveforms, and t0 which represents the interpolation of the threshold and the fit.

### III. RESULTS

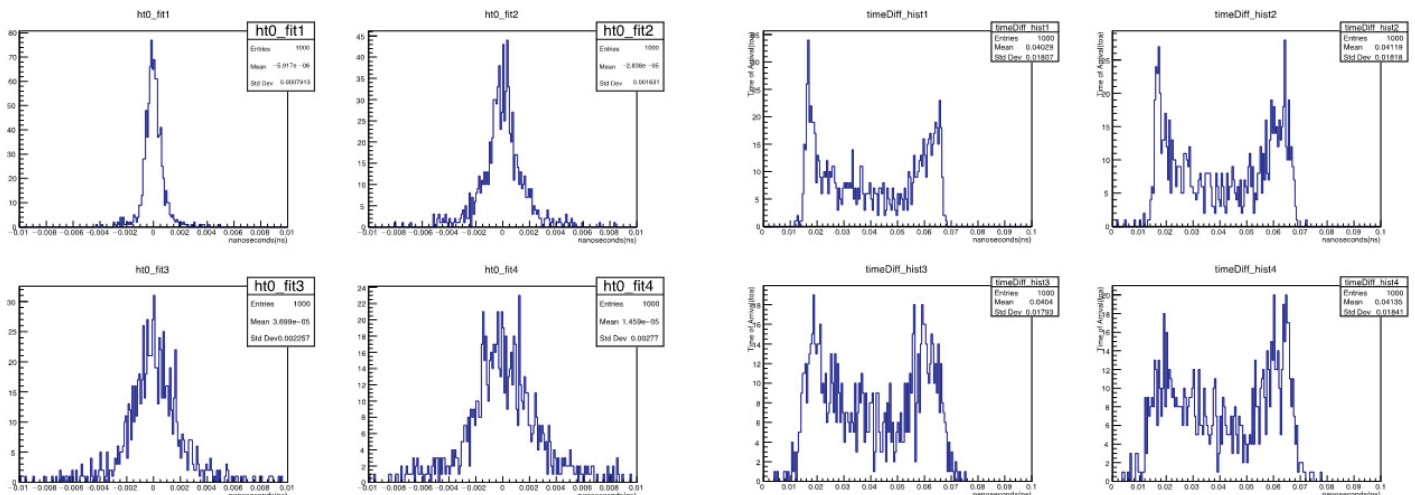
We have found that the Fit function has extremely good time resolution of 0.8 ps– 2.7 ps for 1 to 4 mV of noise respectively (a difference of 1.9 ps between the lowest and highest levels of noise). It is extremely costly on computational resources, while the dCFD function we created that uses linear interpolation, has lower time resolution of 18 ps but at a much lower computational cost. The lower computational cost and simplicity in the implementation can allow for the use of FPGAs to potentially give data in real-time as opposed to having to wait for offline computing to convey data.

The first graph in the Fit function (hto\_fit) graphs has the lowest amount of simulated signal noise, and subsequently encounters the lowest amount of deviation from the actual signal parameters. The fourth graph in the Fit function (hto\_fit) graphs has the highest amount of simulated noise, and the highest amount of deviation from the actual signal parameters accordingly. We can make the conclusion from the data received that the resolution seemingly drops in relation to an increase in noise distorting the signal when using the Fit function.

The second set of graphs show the results of using the dCFD function (timeDiff\_hist) we developed, and can be compared to those of the Fit function. When analyzing the results for these simulations, the data falls into two distinct peaks instead of the previous single peak encountered when analyzing the Fit function. We think this may be caused by the way the algorithm is almost a perfect fit between the two points taken for the linear interpolation, but encounters noticeable error once the curve of the signal is encountered. One major observation that we made regards the signal deviation in relation to the addition of higher noise levels. The dCFD function has a much lower time resolution than the Fit function, and a very similar overall deviation to the actual signal like the Fit. The one place where the dCFD really stands out is the reliability of the calculations it makes during the introduction of noise. The overall difference between the lowest and highest time resolutions for the dCFD function with the data we received was roughly a mere .48 ps, while the difference in time resolutions between the fastest and slowest readings for the Fit function were roughly 1.9 ps, which is quite a considerable difference in the re-

liability of the time resolution. We feel that more testing could be done to improve the overall analysis in performance, such as running more simulations to add to the data set, and even increasing the amount of noise in the simulation to observe if there is a true correlation between the Fit function’s increase in deviation of time resolution and the increase in noise with the signal, and to observe if the dCFD function we developed will continue to remain relatively stable under the introduction of more noise to the signal. The low time resolution calls for improvements in the algorithm or a change in digital signal processing technique to improve the time resolution and bring it down into the 10 ps range instead of the 18 ps range it’s maintaining now.

Potential improvements on the time resolution of the algorithm we created could come in the form of using a quadratic interpolation instead of a linear interpolation like we did in this instance. This would most likely give the function much better time resolution by being able to calculate the curves of the signal much more efficiently than taking what is essentially a straight line between each data point. We are aware that the increase in resolution due to this technique will lead to an increase in the processing power required for the calculations. We have also considered implementing FIR filtering techniques in place of the dCFD technique to see what sort of time resolution we could achieve. We are also aware that this technique will most likely require more processing resources, although we are unsure of the exact amount required to implement this technique.



# Designing a high-temperature superconducting magnet compression fixture

Patrick O'Donnell, Mechanical Engineering, Stony Brook University, Stony Brook, NY 11790  
Michael Anerella and John Cozzolino, Superconducting Magnet Division, Brookhaven National Laboratory, Upton, NY 11973

## Abstract

Over the course of the summer, I have been working to design a fixture that tests the capabilities of superconducting coils when placed under compressive loads. The fixture is vital to the success of ongoing operations on the solenoid magnet which will be used by the Institute of Basic Science to conduct experiments involving high magnetic fields causing high compression loads on the coils. My fixture will be utilized in a 20 in. diameter open top dewar that will simulate the conditions of the full solenoid at a temperature of 77 K. The parts for the fixture must be carefully designed to withstand large stress concentrations in a low temperature environment. I used PTC Creo 3D modeling software to design and create the drawings for each part of the fixture. In addition, we used ANSYS Finite Element Analysis to run tests on our model along with hand calculations. My design was sent to be manufactured at the central shops after being thoroughly reviewed by my mentor, Michael Anerella, as well as other engineers of the Superconducting Magnet Division. The fixture was then put together according to my assembly drawing specifications and tests on coils will be run later this week.

## I. Background

The Institute of Basic Science (IBS) in South Korea is currently planning to conduct research involving a dark matter search experiment. One of the tools IBS desires for their research is a magnet that can produce a high magnetic field in a large volume. The Superconducting Magnet Division at BNL has a great deal of experience in designing these types of magnets. BNL proposed a single layer solenoid design with fourteen double pancake coils. The design is proposed to have “no insulation” which means there is no turn to turn insulation. However, this does not mean that there is no insulation between the double pancakes and each of the

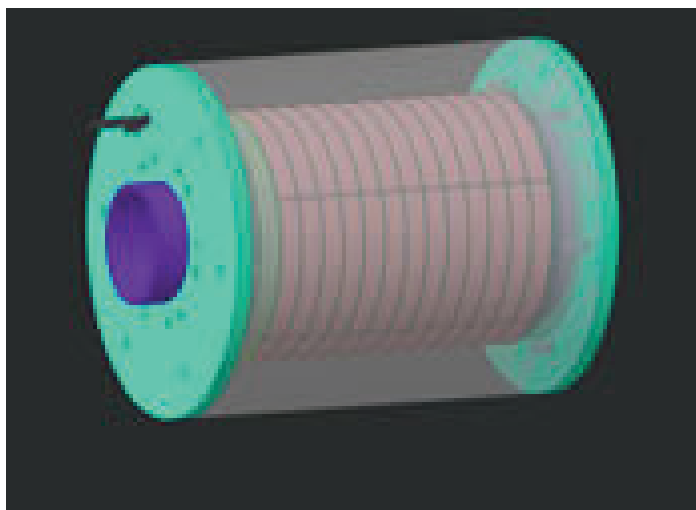


Figure 1a.- IBS Solenoid Isometric View

coils. Figure 1a and 1b display the insulation as well as the overall design of the agent itself. Their magnet design was proposed to produce a magnetic flux of 25 T at 4.2 K.

A design with such a high magnetic field must be analyzed thoroughly to insure its stability. Magnetic structural analysis done by John Cozzolino showed compressive mechanical stresses between the double pancake coils as high as 205 MPa, higher than limits proven safe by testing to date. Figure 2 shows this ANSYS analysis. A similar test in 2011 was done by Dr. W.B. Sampson on a similar type of coil that reached up to 100 MPa. His results showed only reversible effects to the coil and no effect on its current carrying capabilities.

Moreover, a fixture is needed to assess the ability of these coils to perform under these high compressive loads shown in the design analysis. My task was to design such a fixture that is capable of withstanding such high loads and assuring its ability to produce an accurate assessment of the a test coil specimen's response to such loads.

## II. Design

### A. Features

This test fixture needed to be able to place approximately 8-9 m of wound conductor (approx. 70 micrometers thick) under at least 200 MPa of stress. Two items in stock at the Magnet Division initially became crucial to my design process. The first being a Enerpac RCH 302 hydraulic cylinder with max capacity of 30 Tons. A component capable of producing this magnitude of force was crucial because it satisfies the requirement of produce at least 200 MPa to the wound coil's top surface. The other component was a double walled vacuum insulated stainless steel cryogenic dewar capable of producing a 77 K liquid nitrogen bath for the coil to placed in.

### B. Concept

The hydraulic cylinder rests on top of the cryogenic dewar using a support plate. A partially threaded rod goes through the

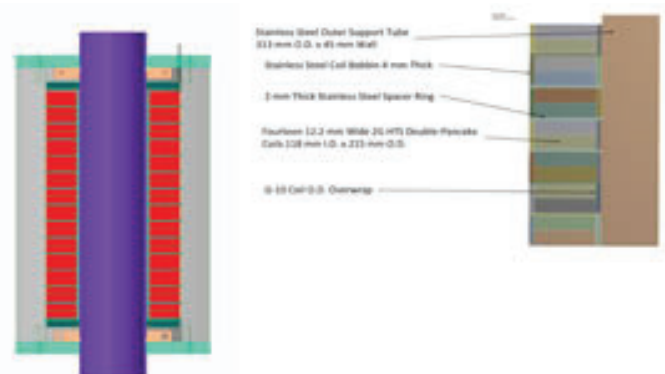


Figure 1b.- The pictorial on the right displays a quarter section of the cross section shown on the left.

center shaft of the cylinder the runs down into the dewar. The basic concept behind the design is to have the center rod to go into tension as the cylinder pulls the center shaft upwards from its base. This action of the center shaft causes the platens supporting the coil specimen to go into compression under a force magnitude equal to the tensile load on the center rod. Most of the parts were designed with stainless steel due to its desirable properties in magnetic operations which include its low magnetism and low thermal conductivity. Figure 3 displays the solid model of my design.

### C. Compression Tube

The design of the compression tube was crucial to my design. The tube needed to be long enough to reach down to the bottom of the dewar with minimum clearance in order to keep the coil fully submerged in a liquid nitrogen bath. Selection of the tube's inner diameter, outer diameter, and length was key to maintain its structural capacity. Another important feature of the tube is two relief cuts for hangers that will support the weight of the tube when the lower flange nut is not assembled to keep the bottom components of the fixture in place. Figure 4 displays the solid model of the thick walled compression tube.

### D. Coil Subassembly

A structurally stable structure around the test coil specimen was crucial for a proper test to be done on these coils. Shown in Figure 5 is a solid model of the cross section of the coil subassembly. The upper and lower platen apply the compressive loads to the edge of the conductor. The conductor is wound on either a stainless steel or aluminum bobbin. Advantages of winding on a metal bobbin are increased mechanical stiffness in the axial direction as well as lower thermal conductivity, as shown by data collected by Dr. H. Song. Winding on such a bobbin also simulates what the actual coil will be wound on in the IBS solenoid magnet design.

Initially, the coil was to be wound in a bifilar configuration which meant that both entering and exiting lead would come out

on the outer edge of the wound coil. This configuration would produce no magnetic field. After further observation and analysis, it was concluded that a regular wound coil would better simulate the conditions of the solenoid magnet design being proposed. Therefore, it became necessary to accommodate the T-spliced coil specimen leads (sample T-splices displayed in Figure 6) using an angular chamfer cut on the outside edge of the upper platen and a broached keyway slot on the inner age, as shown in Figure 5.

### E. Other Structural Components

A few other structural components of the design are outlined below:

- Two high strength steel nuts threaded to the specifications of the center rod were used to hold the fixture components in proper position along the rod.
- A stainless steel support plate was used to position the fixture on top of the cryogenic dewar.
- Two eyebolts were assembled into the support plate for the purpose of lifting and strapping down the fixture for testing.
- The center rod material was an A286 high strength stainless steel.

## III. Engineering Analyses

Before the fixture could be manufactured and assembled, it was necessary to confirm acceptable mechanical stresses to the magnitude at which the test requires.

### A. Compression Tube

The thick walled compression tube was analyzed through ANSYS (Figure 7) and checked for buckling by hand calculations (Figure 8). The formula used for buckling analysis was the Johnson Formula as opposed the normal Euler critical load formula. This was due to the fact that the compression tube slenderness ratio was less than the critical slenderness ratio. It is clear from Figure 7 that the general state of stress in the thick walled tube is in the greenish blue area, lower than the yield stress of stainless steel.

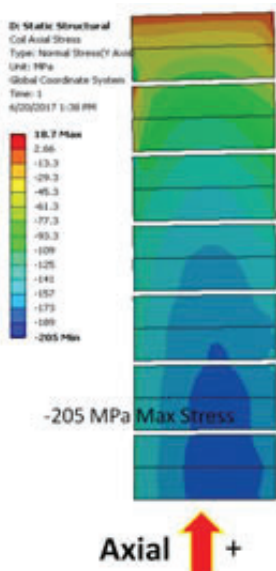


Figure 2- Magnetic structural ANSYS model of a quarter section of the IBS solenoid.



Figure 3- CAD model of compression fixture assembly



Figure 4- CAD model of thick walled compression tube

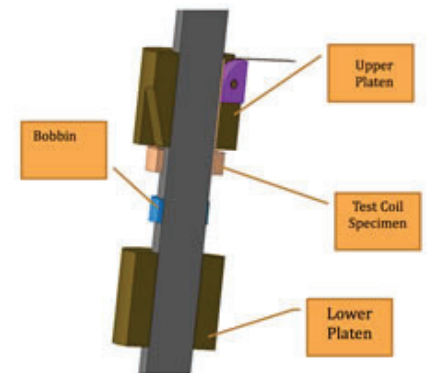


Figure 5- CAD model of coil subassembly



## B. Tensile Stress in Center Rod

The center rod's tensile mechanical stress calculations are shown in Figure 9.

## C. Axial Deflection of the Coil

A calculation was done to assess how much the coil deflects in the axial direction under the working stress of the fixture shown in Figure 10.

## IV. Results

Engineering calculations showed no issues with the high loads being applied the fixture. The fixture was then manufactured and assembled and is shown in Figure 11. Tests will be conducted on test coils by Dr. W.B. Sampson using this compression fixture. These tests are crucial to the design of the IBS Solenoid because there is no data showing that the coils will be able to handle such high loads. Design of IBS Solenoid will proceed after the results of these compression tests.

## V. Acknowledgment

I would like to thank and acknowledge my mentor, Michael Anerella, as well as John Cozzolino of the Superconducting Magnet Division here at Brookhaven National Lab for their guidance and leadership this summer. Thanks also to Dr. Ramesh Gupta, Principal Investigator for the Institute of Basic Science (IBS) Project, for funding this work. This project was supported in part by the Brookhaven National Laboratory (BNL) Superconducting Magnet Division under the BNL Supplemental Undergraduate Research Program (SURP).

## VI. References

- <sup>1</sup>Dr. W.B. Sampson "The Effect of Axial Stresses on YBCO Coils" (2011)
- <sup>2</sup>Dr. H. Song "2G HTS Coil Technology Development at Superpower Inc." (2012)
- <sup>3</sup>Analysis and Presentations made by J. Cozzolino
- <sup>4</sup>Designs for IBS Solenoid made by J. Schmalzle

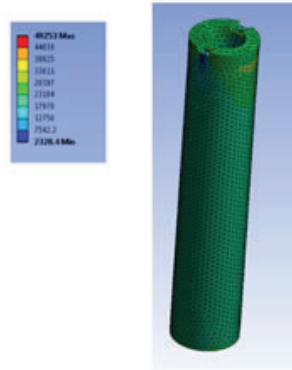


Figure 6- Sample conductor with T-splices

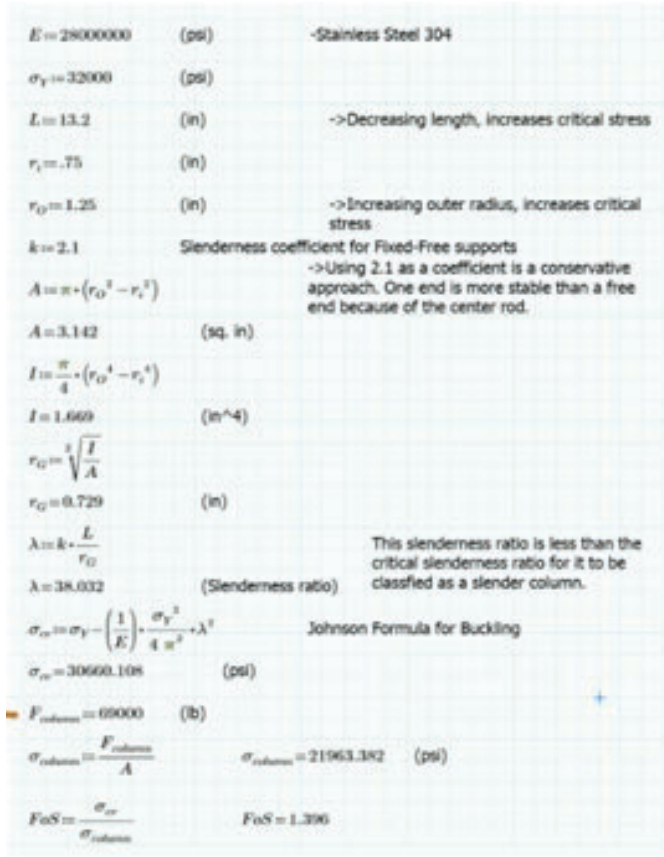


Figure 7- ANSYS Static Structural Analysis of Compression Tube

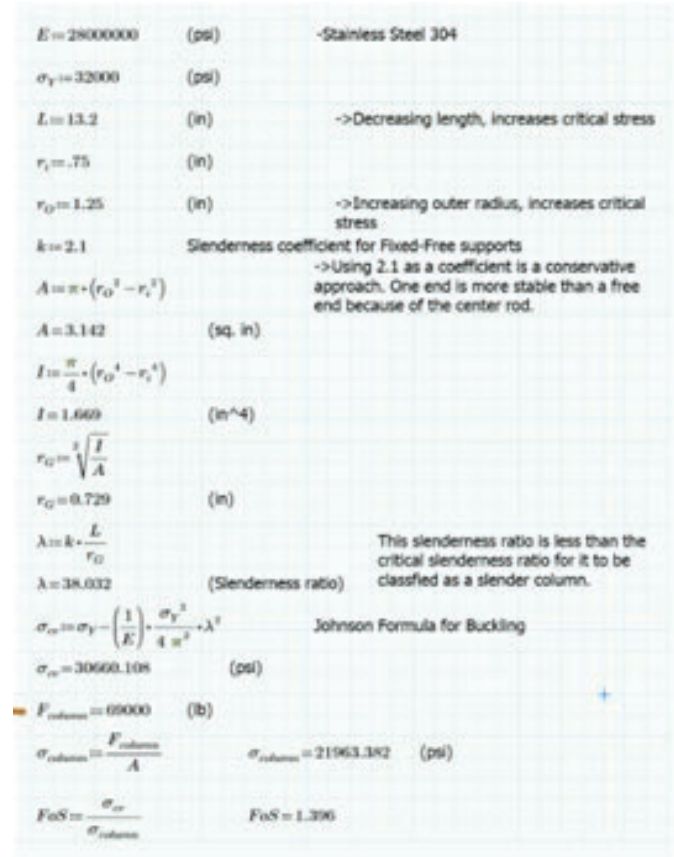


Figure 8- Buckling Analysis of Compression Tube

$$A_r := .969 \text{ (in}^2\text{)} \quad \text{Stress area for 1.25-7 UNC thread}$$

$$\sigma_y := 7 \cdot 10^4 \text{ (psi)}$$

$$F_{rod} := 45000 \text{ (lb)}$$

$$\sigma_{rod} := \frac{F_{rod}}{A_r} \quad \sigma_{rod} = 46439.628 \text{ (psi)}$$

$$FoS_{rod} := \frac{\sigma_y}{\sigma_{rod}} \quad FoS_{rod} = 1.507$$

Figure 9-Tensile Stress Calculation for Center Rod

$$F_{coil} := -45000 \text{ (lb)}$$

$$d_i := 1.5625 \text{ (in)}$$

$$d_o := 1.88585 \text{ (in)}$$

$$A_{coil} := \frac{\pi}{4} \cdot (d_o^2 - d_i^2)$$

$$A_{coil} = 0.876$$

$$\sigma_{coil} := \frac{F_{coil}}{A_{coil}} \quad \sigma_{coil} = -51385.245 \text{ (psi)}$$

$$E_{coil} := 21755660.66 \text{ (psi)} = 150 \text{ GPa}$$

$$\epsilon_{coil} := \frac{\sigma_{coil}}{E_{coil}} \quad \epsilon_{coil} = -0.002$$

$$t_{coil} := .484252 \quad \Delta t_{coil} := \epsilon_{coil} \cdot t_{coil} \quad t'_{coil} := t_{coil} + \Delta t_{coil} \text{ (in)}$$

$$t'_{coil} = 0.483 \text{ (in)}$$

Figure 10- Axial Deflection of the Coil



Figure 11- Assembled Compression Fixture

# Laser energy absorption efficiency as a function of laser intensity

Haejun Oh, Physics & Astronomy Department, University of Rochester, Rochester, 14627

Masahiro Okamura, Department of Collider and Accelerator, Brookhaven National Laboratory, Upton, NY 11973

## Abstract

The project was to characterize the best condition for laser energy absorption, which will improve plasma production for the laser ion source for the electron beam ion source (EBIS) at Brookhaven National Laboratory (BNL). Since, in many cases, a significant portion of the beam is reflected because the laser cannot penetrate the high-density part of the plasma, the project was to characterize the best condition for laser energy absorption, in order to improve plasma production for the laser ion source for EBIS. Furthermore, since the laser ion source does not use magnetic field confinement and the induced plasma continues to expand, the velocity of the plasma expansion directly influences the laser energy absorption process. Therefore, we measured the laser energy absorption efficiency via a calorimeter stationed inside the vacuum chamber while altering the laser power density on iron target material. As a result of this investigation, we were able to find the relationship between laser incident energy and laser energy absorption to target.

## I. Introduction

The electron beam ion source (EBIS) at Brookhaven National Laboratory (BNL) is a heavy ion-pre-injector for other experiments occurring within BNL such as the Relativistic Heavy Ion Collider and NASA Space Radiation Laboratory. The primary ion source provider for EBIS is the laser ion source. When producing the ion source, beams from Nd: YAG lasers are focused on various target materials with estimated power density up to  $10^{12}$  or  $10^{13}$  W/cm<sup>2</sup> [1]. From previous investigations, it has been found that plasma formation occurs at irradiance above  $10^8$  W/cm<sup>2</sup> [1].

Once the ablation begins, the target material, aligned to the laser beam inside the vacuum, absorbs the laser energy. As the target material begins to increase in temperature, electrons in the outer most shells leave their atoms, beginning of ionization [2]. A cloud of ions and electrons are formed in front of the target material with certain density, which was call plasma. However, during the plasma generation process, a significant portion of laser incident energy is known to reflect instead of absorbing into the target material. We assume that this is due to the high-density parts of the plasma generated, which the laser beams cannot penetrate. Due to this characteristic, the typical range of absorption percentage is anywhere between 10% and 80% of the incident energy [2]. Therefore, laser energy absorption efficiency is dependent on the initial plasma generation conditions.

Additionally, laser irradiation conditions are known to be non-uniform for different element materials. Therefore, defining the threshold level for plasma generation is an important characteristic when different types of radiation or laser beams are in demand.

## II. Methods

### A. Overview of Detectors

This experiment is comprised of two important measurements. One is the reflected energy from the target material. The reflected energy was detected by a calorimeter stationed inside of the vacuum chamber with a corresponding angle of reflection. Two is the plasma detection signal from faraday cup (FC) and ring terminal from different locations. Both FC and ring terminal was used to detect the amount of charge as a function of time. Therefore, the total charge detected proportional to the total charge produced by plasma generation can be calculated from integrating the area of the signals detected.

### B. Experimental Set-Up

For our experiment, Fe plates were ablated with a solid state Nd:YAG laser (Quantel laser brilliant B) with 1064 nm and 6 ns pulse length. Iron was chosen as the target material since iron ion beams can be used for NSRL science program for cosmic ray simulations. To find the threshold level at which plasma would be generated, laser energy intensity was varied with each trial. Consequently, while using a Plano-convex lens ( $f = 2500$ mm, 4000mm), spot sizes of each laser energy intensity varied. The laser beam ablated the target material with 30° from the axis perpendicular to the target material. With the assumption that the reflected laser beam has 30° of angle and with the help of neon laser, the calorimeter was stationed. To measure the plasma current inside of the vacuum, two different detectors were set up. The FC was stationed at the end of the 3.69 m of solenoid tube. The ring terminal detector ran along the ceiling of the vacuum chamber and at the end, the small ring terminal hovered in front of the opening to the solenoid tube – 187 mm from the target material. A schematic diagram of the laser, vacuum chamber, and solenoid is shown in Appendix A.

### C. Measurements

Two iron plates of 50 mm and 100 mm was placed on the target holder, and then screwed on the linear stage. Once FC, ring terminal detector, and calorimeter were all set up inside of the vacuum chamber, the chamber was sealed and the pressure was pumped down to a magnitude of  $10^{-4}$  Pa by a turbo-molecular pump. The purpose of this step is to decrease the possibility of recombination effect. If there are background molecules inside the chamber, the possibility of ions in the plasma recombining and therefore mindreading the total plasma charge increases. Therefore, decreasing the pressure is an important step in the plasma generation/detection process. In order to begin firing the laser, at first, Nd: YAG laser was warmed up to a temperature of 38°C. Changing the q-switch delay ( $\mu$ s) of Nd:YAG laser changed the laser energy. The maximum energy possible is related to 210  $\mu$ s q-switch delay. Again, our objective was to find reflected laser



energy while the laser incident energy was changing. Therefore, it was essential to fire consistent number of shots for consistently fresh new areas on the target material. Consequently, 40 shots were fired for each measurement at fresh new spots on the iron material. The linear stage moved horizontally 9 mm for each measurement.

### 1. First Trial

The Plano-convex lens had a focal length of 2500 mm. When recording the data, an oscilloscope connected with the FC signal. For each laser shot, the signal was saved onto a USB drive, which was directly connected to the oscilloscope. For low laser incident energies, near 0.1 J, high impedance of 1k $\Omega$  was used. For higher laser incident energies, 50 $\Omega$  was used.

### 2. Second Trial

The Plano-convex lens had a focal length of 4000 mm. When recording the data, both of the FC and the ring terminal signal were connected to the oscilloscope. Again, for each laser shot, the signal was saved onto a USB drive. For low laser incident energies, 1k $\Omega$  was used. For higher laser incident energies, 50 $\Omega$  was used.

Reflected laser energy parameters were recorded when the calorimeter monitor automatically calculated mean, standard deviation, minimum and maximum for each 40 shots. A computer

program called Origin was used to analyze the FC and ring terminal data.

## III. Data and Results

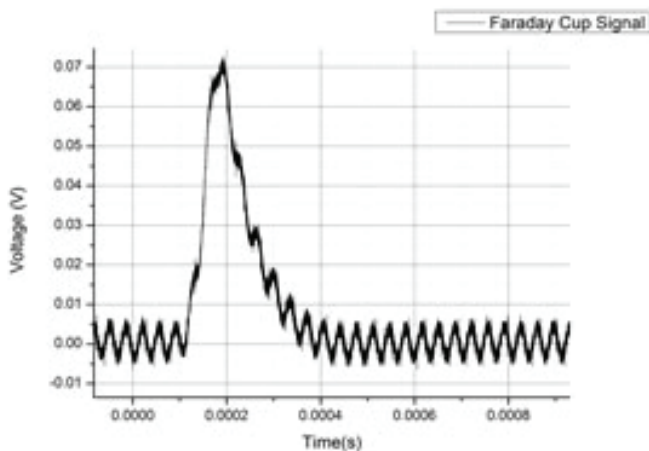
### A. Results

We are interested in lower laser energies where the percentage of energy, which was reflected, may show some evidence of specific threshold level. The first trial using 2500 mm focal length lens and only FC data showed signals of plasma detection from 0.6 J to 0.13 J. In order to investigate lower energy levels near 0.1 J, in the second trial, 4000 mm focal length lens was used instead. Increasing the focal length increases the spot size of the laser ablation, which in turn increases possible plasma creation for lower energies. Both FC and ring terminal detectors were considered. Appendix B shows the q-switch delay ( $\mu$ s), laser energy (J), and reflected laser energy (J).

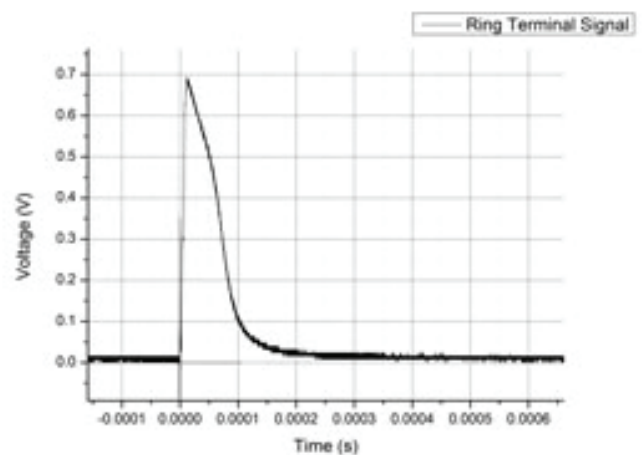
The following figure shows an example of the raw signal from the FC and ring terminal detectors. It is apparent that the FC signal is non-existent at 300  $\mu$ s q-switch delay (figure 1.c). Because of this, we decided to not use data from FC cup and use the ring terminal signals only.

### B. Data Analysis and Results

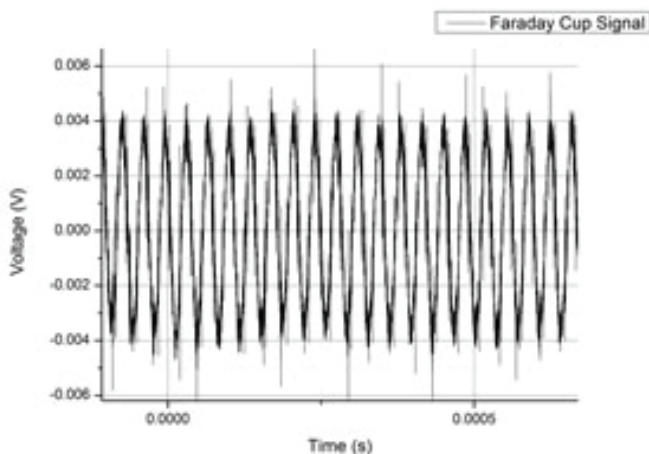
In order to measure the total plasma current generated inside the vacuum chamber, the plasma signal we receive must be inte-



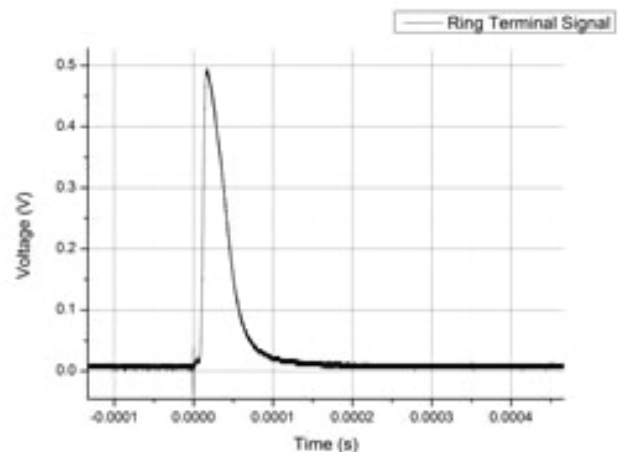
a) Faraday Cup signal – 270  $\mu$ s delay



b) Ring Terminal signal – 270  $\mu$ s delay



c) Faraday Cup Signal – 300  $\mu$ s delay



d) Ring Terminal Signal – 300  $\mu$ s delay

Figure 1: Comparison between the signals detected from both FC and ring terminal in two different q-switch delays.

grated (voltage\*seconds), and then divided by the impedance to find total charge (voltage\*seconds/ohms = charge). Since there were 40 shots, the integrated signals were averaged over 40 giving a true average total charge detected by the ring terminal detector. Fig 2 shows the relationship between calculated average total charge detected by the ring terminal and laser incident energy on the right y-axis. On the opposite y-axis is a graphical representation of the percentage of laser energy reflected.

#### IV. Conclusion

We pursued to answer the following question: How can we understand the fundamental process of plasma production by measuring the reflected energy? How can we characterize the threshold level at which plasma is initially generated? At laser incident energies higher than 0.1 J the percentage of the reflected energy decreased at a slow rate. This trend was expected since laser energy is mostly absorbed in order to generate plasma. However, what was not expected was the decrease in the percentage of the reflected energy as laser energies decreases less than 0.1 J. Coincidentally, at the same point, the total charge detected by the ring terminal detector neared zero. Therefore, we concluded that

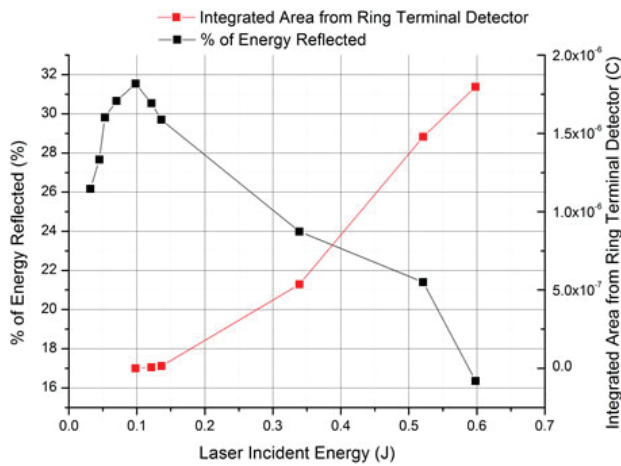


Figure 2: Showing two relationships: between laser incident energy and charge from integrated signal area, and between laser incident energy and percentage of energy reflected. For energies lower than 0.1 J, the average total charge detected was zero or near zero.

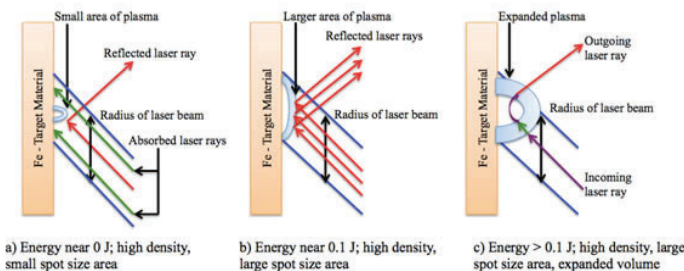


Figure 3: Three figures show the progression of plasma generation at points of different energy levels, which in consequence shows different plasma shape, which determines the amount of laser energy reflected/absorbed. Green arrows show laser rays absorbed, while red arrows show laser rays reflected. The purple laser beam shows incoming laser ray. The blue arrows show the width of the Nd: YAG laser beam. The blue circumference of the plasma shows low density and white circumference shows high density.

there are other reasons than plasma generation that caused this decreasing trend for energies lower than 0.1 J.

One possible reason for this behavior is the density and volume of the plasma. Initially, plasma is too dense and too small in volume; it cannot absorb the laser energy efficiently. Once the laser energy is increased, the volume of the plasma also increases. Then, the laser beam penetrating the outer, low-density areas of the plasma has higher possibility of absorption. Continuing the penetration, the laser beam approaching the inner, high-density area of the plasma, will be repelled and reflected. This phenomenon is illustrated in figure 3.c.

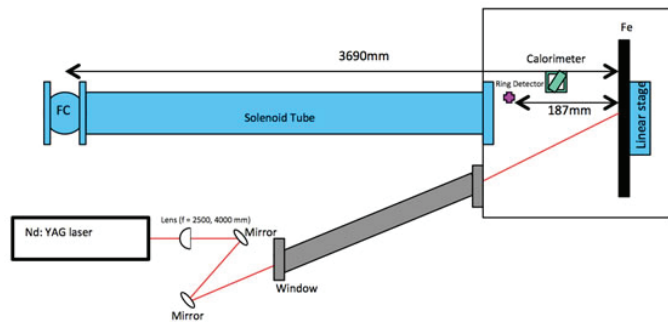
Another possibility is that, at laser energies lower than 0.1 J, the amount of reflected energy depends on the spot size area on the iron target material. Due to the non-uniformity in the laser, only small part of the target is ionized and only small plasma is produced. Therefore, most energy was absorbed (illustrated in Fig 3.a). However, once the laser energy increased to nearly 0.1 J, spot size area increased significantly, which increased the percentage of energy reflected (illustrated in Fig 3.b).

#### V. Acknowledgements

I wish to thank my mentor, Dr. Masahiro Okamura, and the rest of his research team for their generosity, guidance, and knowledge throughout the SULI program. Furthermore, I would like to thank the U.S. Department of Energy, Office of Science, and Office of Workforce Development for Teachers and Scientists (WDTS) under the Science Undergraduate Laboratory Internships Program (SULI) for their support in this internship.

## VI. APPENDIX

### A: Schematic of experimental set-up.



The Nd: YAG laser produces a beam, which passes through Planor-convex lens, then two mirrors and through a window to the vacuum chamber on the right. Then the beam proceeds to travel and ablate the Fe target holder. Then the reflected beam is detected by the calorimeter. The ring detector and/or FC measured the plasma, as shown by the figure. Haejun Oh made this schematic diagram.

### B: Table of laser energy and reflected energy according to the q-switch delay.

Q-Switch Delay	Laser Energy	Reflected Energy	% of Energy Reflected
( $\mu$ s)	(J)	(J)	(%)
210	0.620	0.1014	16.35
250	0.541	0.1158	21.40
270	0.474	0.1137	23.99
290	0.398	0.1182	29.70
300	0.354	0.1081	30.54
320	0.266	0.0840	31.54
340	0.172	0.0528	30.66
350	0.141	0.0421	29.82
400	0.076	0.0209	27.67
430	0.034	0.0089	26.17

## VII. References

- <sup>1</sup>Kondo, K., Yamamoto, M. Sekine, and M. Okamura. "Laser Ion Source with Solenoid for Brookhaven National Laboratory-electron Beam Ion Source." *Review of Scientific Instruments* 83.2 (2012): n. pag. Web.
- <sup>2</sup>Ditmire, T., R. A. Smith, J. W. G. Tisch, and M. H. R. Hutchinson. "High Intensity Laser Absorption by Gases of Atomic Clusters." *Physical Review Letters* 78.16 (1997): 3121-124. Web.



# An assessment of butterfly diversity at the Long Island Solar Farm

Claire Y. O’Kane and Julie Kapuvári, College of Agriculture and Life Sciences, Cornell University, Ithaca NY 14850

Trevor McIntosh, Department of Biology, Southern University at New Orleans, New Orleans, LA 70126

Alexander Whittle, Department of Ecology and Evolution, Stony Brook University, Stony Brook, NY 11794

Tim Green, Environmental Protection Division, Brookhaven National Laboratory, Upton NY 11793

## Abstract

People typically associate pollinators with bees, but there are many other animals that contribute to this crucial ecosystem service, such as Lepidopterans (butterflies and moths). Our research at Brookhaven National Laboratory focused particularly on butterflies. In the face of global butterfly population declines in recent decades, conservation for butterfly habitat is becoming even more critical. The Long Island Solar Farm located at Brookhaven National Laboratory features a variety of wildflower species that butterflies are attracted to. Our team conducted surveys on the species abundance of all butterflies found within the boundaries of “Solar Farm 1” and determined which wildflower species are most favorable. To obtain our data, we walked through the site for approximately one hour every day in the late morning, identifying the butterfly species and the wildflower species they were observed on. With data on butterfly diversity, we were able to analyze the important role that “Solar Farm 1” plays as a sanctuary for these important pollinator species. Extensive Lepidopteran surveys at BNL have not been performed since 2005, thus our data will update and expand the database, and most importantly inform the solar farm administration how to best approach vegetation management to best support butterflies and other pollinators. While performing our daily surveys, we learned how to create a protocol for collecting vast amounts of data in the field and how to accurately identify both wildflowers and butterflies using credible field guide books.

## I. Introduction

Lepidoptera is an order of insects that includes butterflies and moths, which play crucial roles in the ecosystem as pollinators. Butterflies in the northeastern United States provide pollination to a wide variety of flowering crops and wildflowers, act as agents of biological pest control, and serve as prey for a vast range of vertebrates, such as birds, wasps, and rodents. Over the last decade, the overwintering populations of butterflies, including the popular Monarch, have been mainly threatened by habitat loss, as a result of elevated herbicide usage alongside the advent of genetically modified crops (Pleasants & Oberhauser, 2013), as well as the extreme temperature fluctuations of climate change, which disrupt their migration and reproduction patterns (WWF, 2015). Thus, many butterfly species nationwide are listed under the IUCN “Red List” for threatened and endangered species (Xerces Society). According to the U.S. Fish & Wildlife Service, the population of the Eastern Monarch in the Northeast has declined by about 90 percent in the last 25 years (U.S. Fish & Wildlife Service, 2015). Further plunges in butterfly populations would negatively impact the balance within the food chain. This ex-

perimental survey explores the diversity of butterflies and their observed preferences to certain wildflowers within the confines of Solar Farm 1 of the Long Island Solar Farm in order to improve the pollinator protection and wildflower management plan at Brookhaven National Laboratory.

## II. Methods and Study Site

### A. Study site

The Long Island Solar Farm (LISF) is the largest photovoltaic power plant in the eastern United States, and was established at Brookhaven National Laboratory under the collaboration of the Department of Energy, BP Solar, and the Long Island Power Authority (LIPA). The 32-megawatt photovoltaic system has been delivering power to the LIPA grid since 2011. LISF covers approximately 200 acres of land and helps New York State to meet its goals in producing clean energy and reducing carbon output. It is also an area of interest for various ecological studies, including our research on butterfly diversity. Butterfly surveys were conducted exclusively around the solar panels at “Solar Farm 1,” one out of six divisions within LISF. This study site was chosen because of its high diversity of short wildflower species growing underneath and around the panels. Each division of LISF, including Solar Farm 1, is surrounded entirely by high fences. Therefore, there are little to no major impacts on the vegetation within the study site due to human activity or other large wildlife species such as deer.

### B. Methods

For approximately one hour in the late morning during each of our data collections, we walked alongside the solar panels and through the small fields adjacent to the panels at random, searching for butterflies within the solar farm. Using a Kestrel anemometer, we took daily information of air temperature (°C), wind speed (m/s), and relative humidity (%). We also noted cloud cover through observation. During our walks, we counted the number of each butterfly species that we were able to identify using field guides and took down the wildflower species they were observed on. Additionally we noted butterfly species that we observed flying nearby. If necessary, we sometimes used a handheld tally counter to take data on butterflies present in large abundances. With data from our surveys on overall butterfly abundance, species richness, and relative abundance distributions, we were able to determine what kind of role the solar farm plays as an ecological foraging habitat for native butterfly species.

## III. Results

We organized the data from the butterfly surveys into three categories: species abundance of butterflies, number of butterfly

species observed on each wildflower species, and total number of butterflies observed on each wildflower species. To determine species abundance, we simply counted the observed number of butterflies of each species. The species with the highest species abundance was found to be the Duskywing butterfly, with between 250 and 300 individuals observed, followed by the Orange Sulphur, with between 150 and 200 individuals observed, and so on. In determining the number of butterfly species on each wildflower species, we found that Blue Vervain (*Verbena hastata*) attracted the most butterfly species at fifteen, followed by crown vetch at ten, Queen Anne's Lace (*Daucus carota*) and White Sweet Clover (*Melilotus albus*) at eight, and so on. In determining the total number of butterflies on each wildflower species, we found that blue vervain attracted the most individuals at between 300 and 350, followed by White Sweet Clover at approximately 100, Crown Vetch (*Securigera varia*) at between 50 and 100, and so on. It should be noted that for each of the latter two categories in which we organized our butterfly survey data, we created two bar graphs that feature the same numerical data, but have the wildflower species arranged in different ways: relative abundance (see Figure 4 & 5) and alphabetically (see Figure 2) for random arrangement. For the other category, species abundance of butterflies, we created only one bar graph (see Figure 1), which arranges the butterfly common names in alphabetical order.

#### IV. Discussion

Despite the ubiquity of non-native wildflowers in Solar Farm 1, the native butterflies species visited Blue Vervain, which is a native perennial herb, the most out of our pool of mostly non-na-

tive wildflowers. However, this correlation could be attributed to a number of factors, such as preferred nectar reward, color, smell, shape, or locality, which we did not investigate in this experiment. It was observed that the two wildflowers with the most butterfly visitations, Blue Vervain and White Sweet Clover, have a similar physiological structure-- slender and elongate-- which makes landing, grasping, and feeding on nectar relatively easy. Based on our subjective observations, Blue Vervain is larger and attracted a vast size range of butterflies (from the large Swallowtails to the medium sized Duskywing), while White Sweet Clover attracted many smaller butterflies, such as Eastern Tailed Blue and Pearl Crescent. In sum, the Solar Farm hosted a high diversity of non-native wildflowers, yet still attracted a high diversity of butterflies. Therefore, we would determine that this area is a successful sanctuary for important pollinating butterflies, some of which are threatened and in need of optimal habitat.

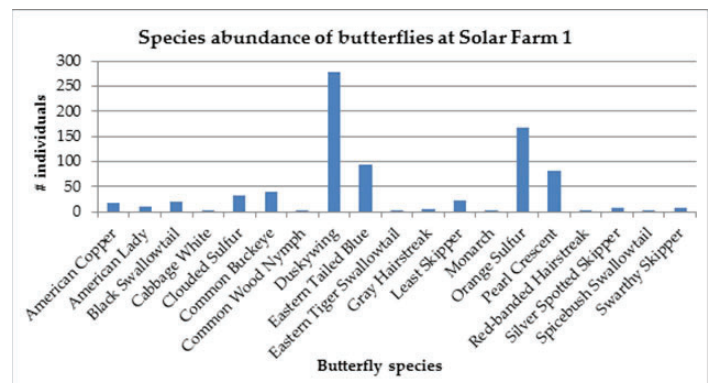


Figure 1: The overall abundance of each butterfly species that were found within Solar Farm 1, arranged alphabetically.

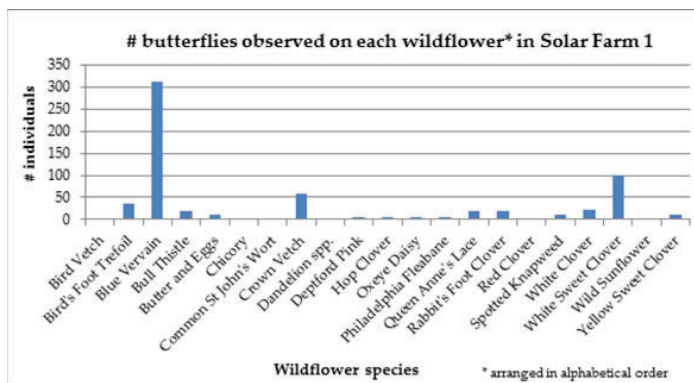


Figure 2: The overall number of individual butterflies that were found on each wildflower species within Solar Farm 1, arranged alphabetically.

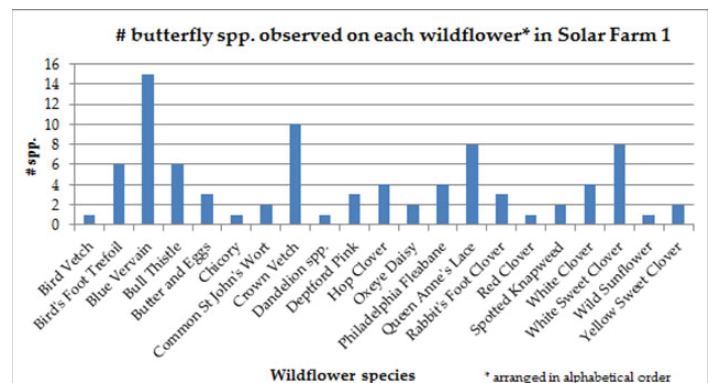


Figure 3: The overall number of butterfly species that were found on each wildflower species within Solar Farm 1, arranged alphabetically.

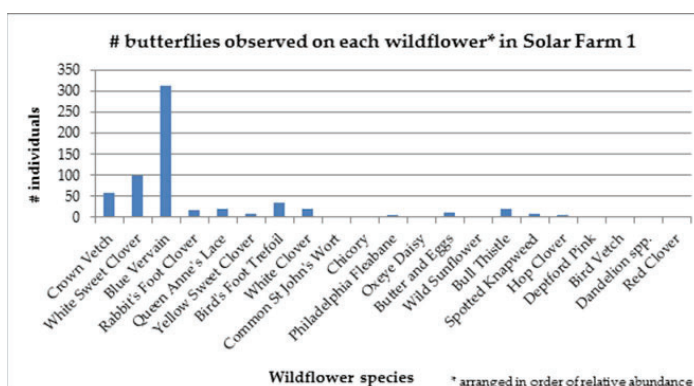


Figure 4: The overall number of individual butterflies that were found on each wildflower species within Solar Farm 1, arranged by our judgement of abundance in comparison to other wildflowers.

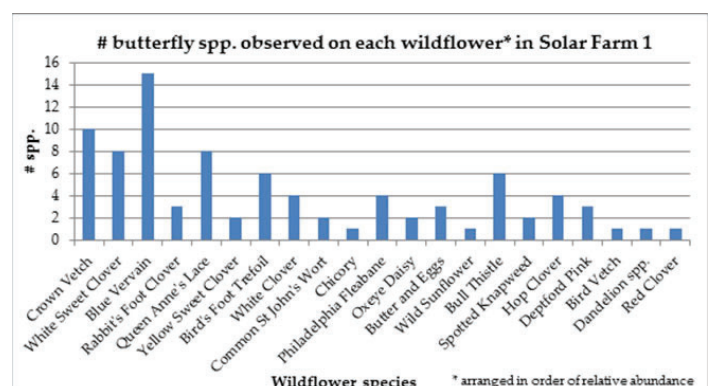


Figure 5: The overall number of butterfly species that were found on each wildflower species within Solar Farm 1, arranged by our judgement of abundance in comparison to other wildflowers.

## V. Acknowledgements

We would like to thank Michelle Joseph and Lindsey McKenna for their help in conducting our pollinator surveys. This project was supported in part by the U.S. Department of Energy, Office of Science, Office of Workforce Development for Teachers and Scientists (WDTS) under the Science Undergraduate Laboratory Internships Program (SULI) and by the National Science Foundation (NSF), Louis Stokes Alliance(s) for Minority Participation (LSAMP) at Southern University at New Orleans under the LSAMP Internship Program at Brookhaven National Laboratory.

## VI. Reference

- Pleasants, J. M. and Oberhauser, K. S. (2013), Milkweed loss in agricultural fields because of herbicide use: effect on the monarch butterfly population. *Insect Conservation and Diversity*, 6: 135–144. doi:10.1111/j.1752-4598.2012.00196.x
- U.S. Fish & Wildlife Service. “Northeast Region Monarch Update.” *U.S. Fish & Wildlife Service*, July 2015, <[www.fws.gov/northeast/monarchupdate.pdf](http://www.fws.gov/northeast/monarchupdate.pdf)>
- WWF. “Monarch Butterflies and Climate Change.” World Wildlife Fund, 2015, <<https://www.worldwildlife.org/pages/monarch-butterflies-and-climate-change>>
- Xerces Society. “Red Listed Butterflies of North America.” *Red List of Butterflies and Moths*, Xerces Society, <[xerces.org/red-list-of-butterflies-and-moths/](http://xerces.org/red-list-of-butterflies-and-moths/)>



# Mass and mobility diameter classification of emissions from a wood-burning boiler

Kristen Okorn, Department of Mechanical Engineering, Stevens Institute of Technology, Hoboken, NJ 07030  
Rebecca Trojanowski, Sustainable Energy Technologies Department, Brookhaven National Laboratory, Upton, NY 11973

## Abstract

Wood burning boilers are known to emit aerosols such as black carbon that are detrimental to human health when inhaled and warm the Earth when present in the atmosphere. While these heating systems have been endorsed as a carbon-neutral renewable energy technology in the past few decades, they have instead become the number one source of particulate emissions in New York State. Thus, the objective of this project was to classify emissions produced by a wood boiler in order to determine how best to mitigate them. A two-stage outdoor wood boiler integrated with a catalyst was fired, and all sampling occurred during its steady state phase. Emissions were sampled from a dilution tunnel, and the aerosol particles were then charged using Krypton-85. A Differential Mobility Analyzer (DMA) was then used to classify the charged particles by mobility-equivalent diameter. Next, a Centrifugal Particle Mass Analyzer (CPMA) was used to classify emissions by their mass. As a result, the varying masses of aerosol particles with the same mobility diameter during the boiler's steady state period were able to be determined. The distribution of these microphysical properties varied significantly through the course of the burn; this information is vital to understanding and reducing emissions. This experiment was the first instance of a CPMA being used at BNL, which is significant to meeting state energy needs without compromising environmental standards. As a consequence of this research, I have added the ability to operate a CPMA, DMA, and Condensation Particle Counter to my skillset. Additionally, I am now well-versed in Igor programming and the various methods for testing wood-burning hydronic heaters (WHH).

## I. Introduction

According to the 2010 United States (US) Census, wood is the nation's fastest growing heating fuel, showing a 34% increase between 2000 and 2010<sup>1</sup>. This is no surprise, since residential wood heating is significantly cheaper than the current leading sources - natural gas, oil, and propane. Wood is also endorsed as a renewable, carbon-neutral energy resource; all the carbon dioxide a tree absorbs during its lifetime is released as it burns, and a new tree planted in its place can cycle back the same amount of carbon. By comparison, fossil fuels will take millions of years to regenerate, and are predicted to be depleted within the next century<sup>2</sup>.

Despite these apparent benefits, wood smoke also drives climate change. When wood undergoes incomplete combustion, in addition to yielding water and carbon dioxide, excess carbon atoms combine to form carbonaceous particles, which aerosolize with the rest of the smoke. One particle of this type, Black Carbon, consists solely of pure carbon and acts as a climate forcer, absorbing a million times more solar radiation per unit mass than

carbon dioxide<sup>3</sup>.

In addition to these adverse effects in the atmosphere, the inhalation of wood smoke can be detrimental to human health. The cumulative effects of long-term inhalation are known to cause respiratory complications and can increase the risk or mortality from pre-existing conditions such as lung cancer and heart disease<sup>4</sup>. These risks are even greater in developing countries, where indoor air pollution from burning wood kills 4.3 million people per year<sup>5</sup>.

## II. Methods

### A. Outdoor Wood Fired Hydronic Heater

An outdoor wood boiler with a 102,400 Btu/hr maximum nominal rating was used for this experiment. Rather than cycling, where a boiler shuts down when it produces more heat than the demand, the boiler used for this experiment modulates by controlling its air dampers and fan speed to help slow combustion until it decreases to the desired amount. The two-stage boiler improves efficiency; the first chamber is designated for fuel combustion, and any exhaust gases not burned during this stage are passed to the second chamber in order to be combusted. The hot water jacket around the boiler of 55 gallons is heated and then piped out to be used for both heating and hot water.

Additional measures are taken within this particular WHH in order to reduce emissions. Excess gases exiting the combustion chamber are mixed with a stream of oxygen in an injection tube to ensure complete combustion, curbing the production of particulate matter (PM). This air stream is then passed through a catalyst, a honeycomb-shaped ceramic coated with a catalytic metal such as platinum, which undergoes a redox reaction with the emissions, lessening the concentration of harmful pollutants present. So long as the catalyst is heated to the correct temperature and the coating is intact, it can significantly reduce these emissions.

After passing through the catalyst, the exhaust travels upwards through the stack. At the end of the stack, the effluent enters the dilution tunnel, where its behavior in the atmosphere is mimicked by mixing it with room air, allowing semi-volatile and volatile organics to condense as the gas travels the length of the tunnel before sampling it. A schematic of the dilution tunnel is shown in Figure 1:

In this experiment, the boiler was fed red oak cordwood, with each piece cut to a length of approximately 21 inches. The average moisture content of each log was 21.4%, and the maximum bark content for each piece was 20%. The boiler was first lit with approximately 1.3 pounds of cardboard and paper kindling. Once burning, approximately 7.5 pounds of wood, cut into thin pieces for kindling, was added. Once the catalyst temperature reached 750° F, where it enters its temperature region of highest efficiency, 60 pounds of the cordwood was added to the fire chamber, approximately 50% of the boiler's maximum load.

Once running, emissions were classified for approximately 3.5 hours during the boiler's "steady state" period. At this condition, the catalyst temperature is between 1200 and 1700 °F and is therefore most effective. Classification began immediately after the load was added to the fire chamber, and ceased before the catalyst temperature dropped below this range.

## B. Classification Method: Differential Mobility Analyzer (DMA) and Centrifugal Particle Mass Analyzer (CPMA)

The Differential Mobility Analyzer (DMA) is one of the most widely used devices for classifying aerosol particles by their microphysical properties. A schematic is shown in Figure 2:

Pre-charged aerosol particles enter the DMA in an airstream between two charged electrodes. For particles of a user-set mobility diameter, the electric and drag forces on the particle will be equal, and it will be able to exit out a slit at the end of the airstream. This relationship between the forces acting on the particle is shown in Equation 1, where  $q$  is the particle's charge,  $E$  is the electric field,  $\eta$  is the viscosity of air,  $U$  is the velocity of the airstream, and  $D_{mob}$  is the particle's mobility diameter:

$$\frac{q}{D_{mob}} = \frac{3\pi\eta U}{E} \quad (1)$$

Thus, the only variable dependent on the particle's microphysical properties is its mobility diameter; all other variables are subject to the DMA and pre-charger. Particles of all other mobility diameters will become lodged to the sides of the electrodes.

Rather than relying on mobility diameter, the Centrifugal Particle Mass Analyzer (CPMA) classifies aerosol particles by their mass. A schematic is shown in Figure 3:

Pre-charged particles enter a region between two cylindrical, concentric, rotating electrodes. For particles of a user-selected

mass, the electric and centrifugal forces on the particle will equal, and they will be able to pass through the electrodes and exit. This relationship between the forces acting on the particle is demonstrated in Equation 2, where  $q$  is the charge on the particle,  $M$  is the particle's mass,  $R$  is the center radius,  $\omega$  is the rotational speed at the center radius, and  $E$  is the electric field:

$$\frac{q}{M} = \frac{\omega^2 R}{E} \quad (2)$$

The only particle property in this equation is its mass; all other variables are functions of the CPMA. While particles with these forces equal will pass through the device, all other particle masses will become stuck to the walls of the cylinders.

Although both the DMA and CPMA classify aerosol particles by their microphysical properties, the information they provide can vary significantly. For perfectly spherical particles, mobility diameters and masses will be directly related. However, the emissions of wood burning boilers are rarely perfectly spherical. Black carbon particles in particular are fractal, meaning that their shape is more wispy and branchlike, not necessarily akin to any one shape. Thus, the diameters of these particles do not necessarily correlate to their mass.

This lack of agreement between particle diameter and mass is precisely why the DMA and CPMA were coupled in this experiment. Emissions were first classified by the DMA, such that only particles of a specific mobility diameter exited the instrument. This stream of size-selected particles was then classified again by the CPMA, this time on the basis of mass. Thus, the mass distribution of particles of the same mobility diameter was determined.

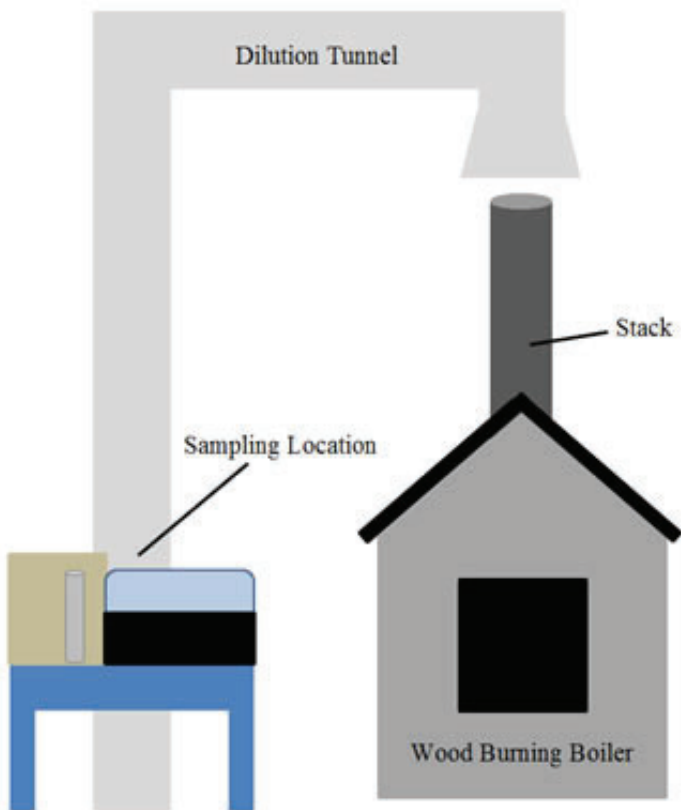


Figure 1: Schematic of boiler and dilution tunnel.

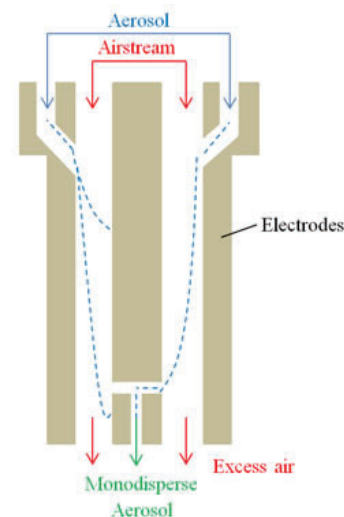


Figure 2: A schematic showing how a DMA selects particles by mobility diameter.

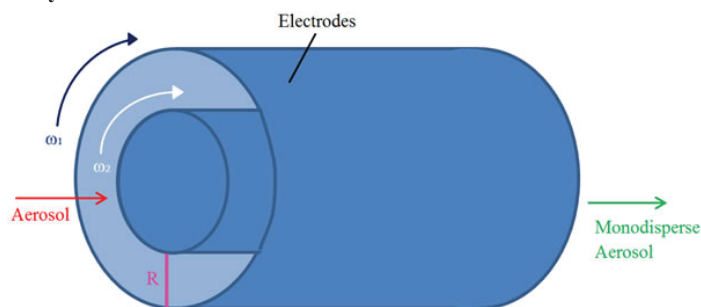


Figure 3: A schematic showing how a CPMA classifies aerosol particles by their mass.

### C. Experimental Plan

In order to classify emissions from the wood burning boiler with the DMA and CPMA, a few other instruments were needed. The full setup can be seen in Figure 4:

Emissions were sampled from the dilution tunnel (1), and the concentration of particles was artificially reduced using a high-efficiency particle arrester (HEPA) filter, referred to as a diluter (2). This ensured the Krypton-85 neutralizer (3) was not overloaded with more particles than it was capable of charging at a time. This pre-charging was necessary because both the DMA and CPMA employ electrodes in order to classify the particles.

Next, particles entered the DMA (4) for classification by mobility diameter. Immediately following, they were further classified by mass in the CPMA (5). A flowmeter (6) integrated with the CPMA was used directly downstream of it to ensure proper flow through the instrument. A Condensation Particle Counter (CPC) (7) was employed in order to count the number of particles that passed through both the DMA and CPMA. Within the CPC, butanol is condensed onto the individual particles such that they are large enough to be detected by a laser. A pump was also employed to pull the sample downstream through this entire apparatus.

For this experiment, the DMA was set to select particles with a mobility diameter of 150 nm. On the CPMA, the “Step Scan” classification method was utilized. The unit alters its rotational speed and voltage to select particles within a range of masses rather than just a single mass, in this case 0.5 femtograms (fg) to 3 fg. This size range is consistent with the expected mass distribution for spherical particles of the given mobility diameter.

## III. Results and Discussion

### A. Typical Mass Distribution for Mobility Diameter Selected Particles

An example of a typical scan is shown below in Figure 5. Despite all particles being pre-selected for the same mobility diameter, particles clearly appear over a range of masses. Note these masses are presented on a logarithmic scale. The green line, located at approximately 2.65 fg, represents the equivalent mass for spherical particles of the set mobility diameter, assuming a density of 1.5 g/cm<sup>3</sup>, which is typical for particulate emissions.

These results illustrate that over the three minutes it took to complete the scan, particles of the same mobility diameter do not all occupy a single mass, nor is this distribution centered at the expected mass for spherical particles. It is unlikely that the boiler’s output changed significantly over this short time period. This is

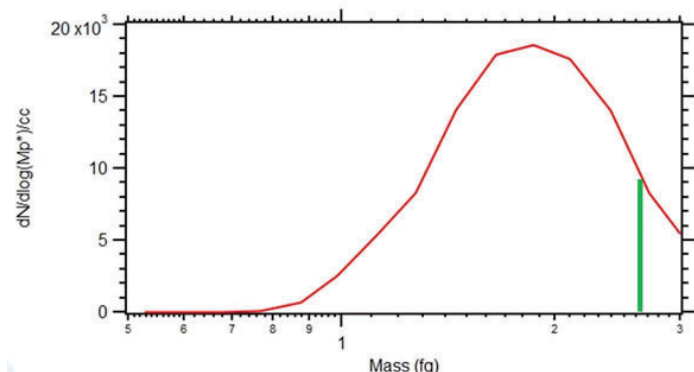


Figure 5: Mass distribution for a scan of particles pre-selected by diameter. The green line indicates the equivalent mass of 2.65 fg for spherical particles with a density of 1.5 g/cm<sup>3</sup>.

indicative that the particles classified have varying densities and fractal dimensions, characteristic of fractal particles such as BC.

### B. Mass Distribution as a Function of Boiler Output

Beyond this variation of mass within an individual scan, sequential scans proved to be even more inconsistent. The results of a series of scans from the beginning of the experiment are shown in Figure 6. Each individual scan represents the mass distribution of particles over the set range of masses, again plotted on a logarithmic scale. Each scan was conducted one immediately after the other, with the first labeled Scan 1 and the last Scan 6.

Over the twenty-minute period it took to complete these scans, the mass distribution is highly variable, sometimes unimodal with varying diameter width and concentration, and other times bimodal. It was hypothesized that this disparity was caused by changes in boiler operation over time; thus the particle masses emitted were not uniform.

To test this hypothesis, several key metrics of the boiler’s operation were plotted over the first hour of its steady state period, as shown in Figure 7. The concentrations of carbon monoxide, carbon dioxide, and hydrocarbons as measured in the stack are plotted, as well as the temperature of the catalyst. Note that the stack concentration of carbon dioxide was divided by a factor of 100 before being plotted to improve visual clarity.

Throughout the first hour of the boiler’s steady state operation, it certainly does not appear steady; it modulates approximately every 12 minutes to achieve the correct output without shutting off entirely when it spikes too high. Thus, individual scans only captured masses at certain times throughout these cy-

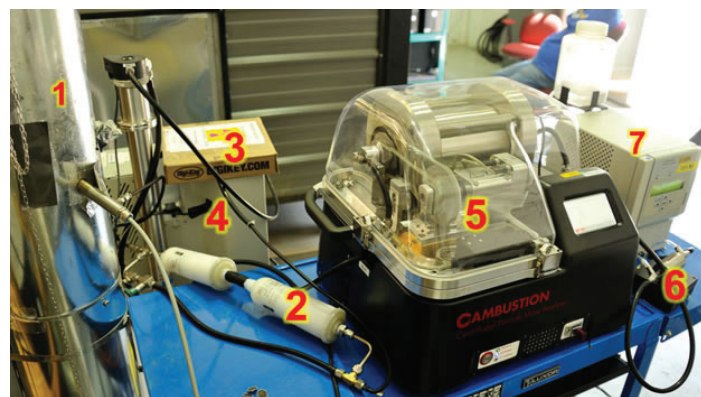


Figure 4: Emissions sampling and classification setup: 1 dilution tunnel; 2 diluter; 3 neutralizer; 4 DMA; 5 CPMA; 6 flowmeter; 7 CPC.

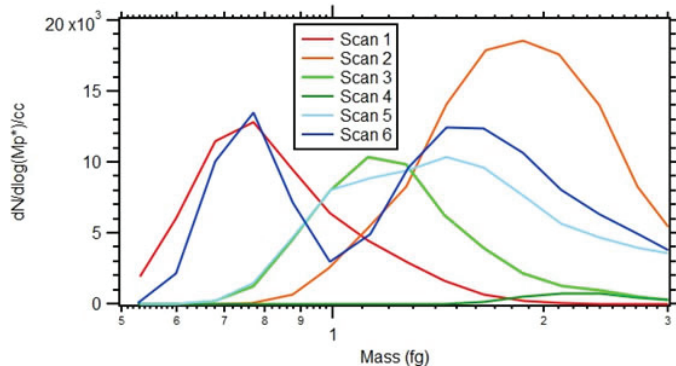


Figure 6: Mass distribution of mobility diameter selected particles during the first 20 minutes of the experiment. Each of the six scans occurred sequentially with time.



cles and alone do not provide reliable information on the complete burn. It is suspected the boiler controls were not operating properly as the boiler hunted for its sweet spot. Conversations with the manufacturer to discuss this possibility have begun.

### C. Full Mass Distribution of Mobility Diameter-Selected Particles during Steady State

Figure 8 shows the mass distribution of the 150 nm pre-selected particles over the entire three-hour course of the boiler's steady state. The results of continuous scans were combined in order to examine overall patterns in the distribution in spite of boiler modulation. Red regions indicate the highest particle concentrations; purple indicates low concentrations, and in white areas, no particles of the pre-selected diameter were present.

The mass modes vary significantly throughout the steady state period. This again implies that the particles sampled were fractal, so particles with the same diameter had completely different masses, and therefore unique densities and fractal shapes. These mode changes occur over longer periods of time than it took for the boiler to modulate, and persist even after the end of modulation. Thus, the types of particles emitted do not seem dependent on the boiler's self-regulation.

### D. Modified Combustion Efficiency

To explain the inconsistency of masses measured by the CPMA, the modified combustion efficiency (MCE) of the boiler was calculated according to Equation 3, where  $[CO_2]$  and  $[CO]$  are the concentrations of each gas as measured from the stack:

$$MCE = \frac{[CO_2]}{[CO_2] + [CO]} \quad (3)$$

By comparing how much of the fuel has burned completely to how much of the fuel has burned, the MCE is a measure of how efficiently the wood is being utilized. This method is commonly used in studying wildfire emissions, another large source of carbonaceous aerosols in the US. The result was plotted against the mass distribution in Figure 9 to see if there was any correlation between burn efficiency and the microphysical properties of the emissions.

Although the MCE is most transitory during the first hour when the boiler was modulating, there is no clear correlation between the two plots.

## IV. Conclusions and Future Work

Using the DMA and CPMA in series provided more information on the microphysical properties of the boiler emissions than either could have separately. The mass distributions for particles of the same mobility diameter have wide ranges, implying that fractal particles such as BC were abundant in the emissions. Even during steady state the boiler's output varies greatly. The Modified Combustion Efficiency does not appear to correlate with the varying mass sizes. This suggests that the fractal dimension, density or both of particulate emissions vary with some other factor of boiler output.

In future iterations, comparing the mass distribution with more comprehensive measures of boiler efficiency, such as the Stack Loss Method, might reveal a stronger correlation between emissions and boiler output. Varying the cut of wood or moisture content might produce a different emissions profile. In addition, rather than simply classifying emissions during steady state, this method could also be employed during the startup and burnout portions of the burn, during which emissions are typically worse. Using this classification method in conjunction with a Single Particle Soot Photometer (SP2) could verify that the fractal emissions observed are BC.

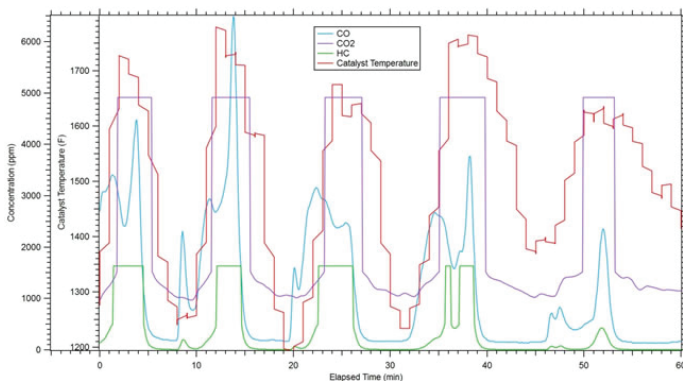


Figure 7: Time series of stack concentration of carbon dioxide ( $CO_2$ , divided by a factor of 100), carbon monoxide (CO), hydrocarbons (HC), and the catalyst temperature.

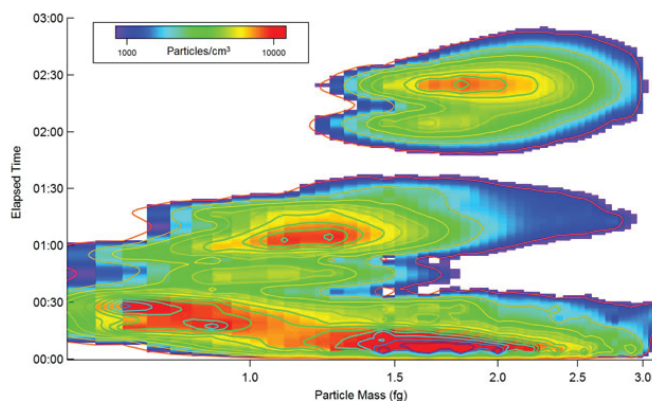


Figure 8: Mass distribution of diameter-selected particles for boiler's entire steady state period.

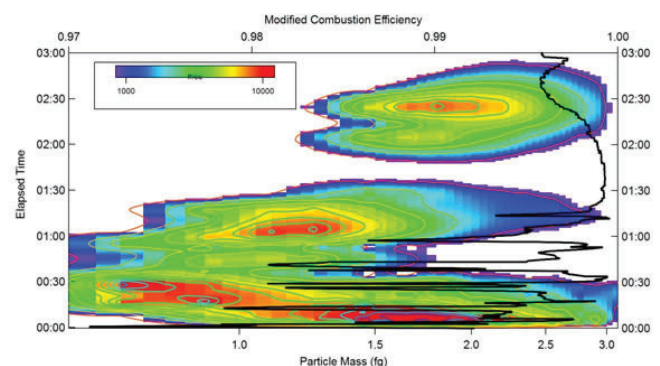


Figure 9: MCE plotted against the full steady state mass distribution.

## V. References

- <sup>1</sup> Alliance for Green Heat. (2011). 2010 Census Shows Wood is Fastest Growing Heating Fuel in U.S. [online] Available at: <http://www.forgreenheat.org/resources/press.pdf>
- <sup>2</sup> Shahriar Shafiee and Erkan Topal, "When will fossil fuel reserves be diminished?" Energy Policy. 36 (1), 181-189 (2009).
- <sup>3</sup> Environmental Protection Agency. (2017). Black Carbon Basic Information. [online] Available at: <https://www3.epa.gov/airquality/blackcarbon/basic.html>
- <sup>4</sup> Environmental Protection Agency. (2016). Black Carbon Research. [online] Available at: <https://www.epa.gov/air-research/black-carbon-research> [Accessed 31 Jul. 2017]
- <sup>5</sup> World Health Organization. (2017). Household (Indoor) Air Pollution. [online] Available at: <http://www.who.int/indoorair/en/>

## VI. Acknowledgements

Many thanks to Ernie Lewis and Arthur Sedlacek for their expertise in aerosol science and allowing us to collaborate with the Environmental and Climate Sciences Department for this project. Thank you to Thomas Butcher, George Wei, Yusuf Celebi, and Jake Lindberg for their work on the boiler tests. Thanks to Robert Bullard and Chongai Kuang for their help with atmospheric instrumentation. Additional thanks to the Office of Educational Programs at Brookhaven National Laboratory for making this project possible.

This project was supported in part by the U.S. Department of Energy, Office of Science, Office of Workforce Development for Teachers and Scientists (WDTS) under the Science Undergraduate Laboratory Internships Program (SULI).

# Analysis of micrometeorites at the National Synchrotron Light Source II; introducing secondary education teachers to beamline science

Lauren Osojnak, Physics Department, Vassar College, Poughkeepsie, NY 12604

Bernadette Uzzi, Office of Educational Programs, Brookhaven National Laboratory, Upton, NY 11973

## Abstract

A group of high school science teachers from Long Island were granted beam time on the Submicron Resolution X-Ray Spectroscopy (SRX) Beamline at the National Synchrotron Light Source II (NSLS-II) at Brookhaven National Laboratory to analyze micrometeorites. I collaborated with this group to facilitate the data analysis of their micrometeorite samples and to introduce secondary education teachers to the NSLS-II. This project has both a scientific and educational purpose. Scientifically, analyzing micrometeorites with the NSLS-II may provide insight into the origin of our universe. Educationally, this was an opportunity to demonstrate how to conduct a science research project to teachers and students using the NSLS-II. Spatially resolved X-ray Absorption near edge Structure (XANES) and X-Ray fluorescence spectroscopy were used to identify specific elements in micrometeorites in this experiment. The beam used during this experiment was an undulator beamline that enables x-ray fluorescence and nanometer spatial resolutions. Micrometeorites (MMs) are 2-100 $\mu$ m in diameter and slowly fall to the Earth trapped in atmospheric wind and rain. These teachers, along with their students, created their own experiments to collect these MMs and the samples were brought to the NSLS-II to be analyzed. I used PyXRF, a python based analysis package, to analyze the data from the beamline. The Athena Program will also be used which has the capabilities to process data from X-Ray Absorption Spectroscopy. This data analysis is still in process, but should confirm that some of the samples collected are MMs and provide more comprehensive data analysis of the composition of MMs in general. This was both an educational and scientific opportunity for me as I worked with high school science teachers and beamline scientists. I added new data analysis programs to my repertoire and spent time with science teachers who were eager to continue experimenting as well as sharing that passion with their students.

## I. Introduction

Micrometeorites (MMs) are cosmic dust particles that have survived atmospheric entry.<sup>1</sup> There is no official classification for MMs as the investigation into their composition is just beginning.<sup>2</sup> The scientific purpose of this research was to begin the classification of MMs by comparing their composition using the National Synchrotron Light Source II. This data is limited by a small sample size from one area of the globe. This cannot provide anywhere near a full classification of MMs but it can begin the process and delve deeper into their composition and thus the composition of the early universe. The educational component to this research was to teach students and teachers to be able to incorporate beamline science into public secondary school education. On a wider scope, this was a way to have teachers and

students perform hands-on beamline science and bring it back to the classroom outside of the textbook. This was also limited to a small group of teachers who were able to work directly with scientists on the beamline floor but it will hopefully encourage further participation.

## II. Methods

This research utilized the National Synchrotron Light Source II and MM samples previously collected by students and teachers. These samples were collected using plastic wrap, neodymium ring magnets, plastic buckets with lids and fine grid net. The MMs are rich in Iron to allow for magnetic susceptibility.<sup>3</sup> The samples were washed with ethanol before being mounted for the X-ray beams of the NSLS-II. At the NSLS-II students learned to work the undulator beamline to collect the X-ray spectroscopy and XANES data. Teachers were also given a chance to directly use the computer that controls the beamline. The teachers were taken through a data analysis seminar to learn the Python-based program PyXRF to analyze the X-ray fluorescence data from the beamline. The teachers were taught this higher level data analysis to then be able to show the students the raw data in Excel to analyze. My knowledge of Python allowed me to provide instructional support as I demonstrated to teachers how to work the program and further analyze the samples using PyXRF. This gave insight into the MM composition and classification. I analyzed extra samples of the MM data to demonstrate to the teachers and students and to begin classification. This classification was based on comparing element composition, element mapping, and element coexistence within the samples. I also reviewed the exit surveys that the teachers and students were given by the Brookhaven National Lab Office of Educational Programs to identify the positive and negative aspects of the workshop from an educational standpoint. The data analysis and the surveys provided a more concrete way to analyze the workshop from both a scientific and educational viewpoint.

## III. Results

### A. Scientific Results

The following figures show the data analysis of MM samples, yet the teachers analyzed many more samples for this project. All four samples analyzed have pronounced Iron spectrum lines in the spectrum view between 6 and 8 keV. MM sample 5623, 5640, and 5651 have Calcium present in their spectrum. All four samples have a lower level of Zinc and Terbium in their spectrum. MM sample 5640, 5638 and 5651 have Titanium in their element composition as well as Aluminum. This composition of MM samples can be used for classification systems in future experiments due to their consistency throughout samples in large quantities. MM sample 5638 and 5640 have similar dispersion of elements in their element maps. The concentration of elements is



high in large areas represented by great quantities of hot red and yellow areas on the element map. MM sample 5623 and 5651 have similar element maps with sectionalized hot and cool zones.

It is important to note that the scales of the element map are not the same, but that this is not a necessity when comparing relative concentrations.

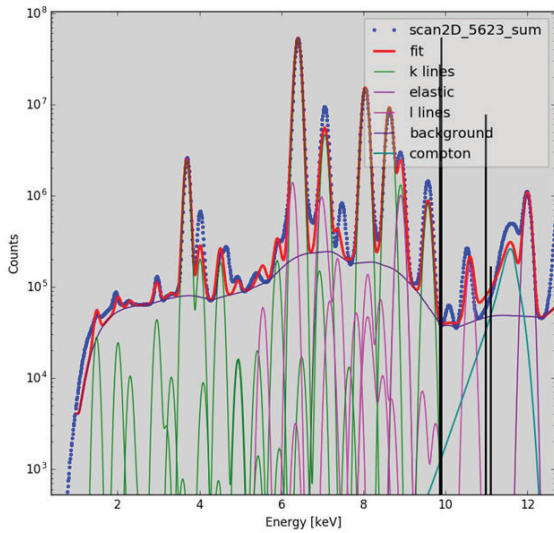


Figure 1A: This shows the spectrum view for the 5623 MM sample. The thick red line represents the fitted spectrum line and the peaks represent different elements present in the sample. The pronounced black lines are used to match the peaks to the specific elements.

scan2D\_5623\_fit

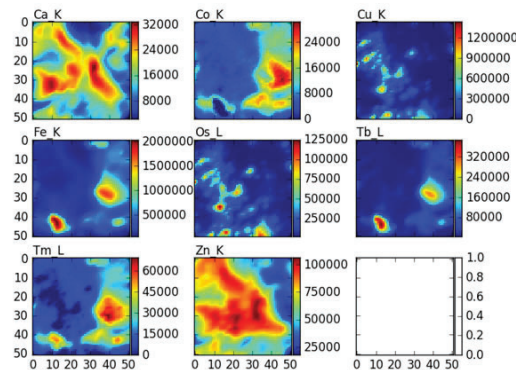


Figure 1B: This shows the element map for the scan 5623 fit. The red areas represent higher concentrations of the element in the sample and the cooler blue areas represent the lower concentrations. The white boxes can be ignored as excess of the PyXRF program but no element was observed in this sample.

scan2D\_5623\_fit

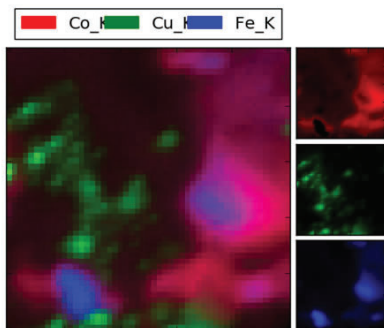


Figure 1C: This shows the element RGB for MM sample 5623. I analyzed Cobalt, Copper and Iron in this particular sample. The mixing of colors, the purple area, shows where the elements Co and Fe are coexisting in the sample. The three boxes on the right show each element existing independently.

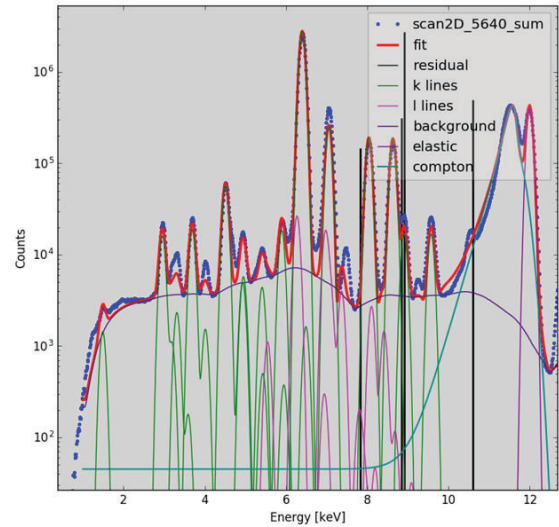


Figure 2A: This shows the spectrum view of MM sample 6540. The large peak at the 12keV is due to the Compton effect and is not representative of the MM element composition. The largest counts are for the Iron peaks which are the two peaks outlines in both red and blue between 6 and 8 keV.

scan2D\_5640\_fit

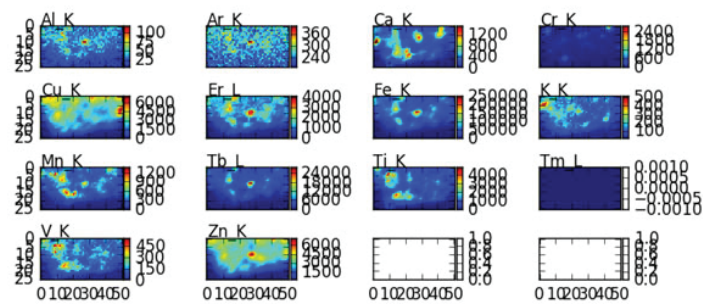


Figure 2B: This shows the element map for the MM 5640 sample. The white boxes can be ignored as excess PyXRF data; they are not representative of the MM element composition. This sample did not have significant composition of these elements as shown by the mostly cool blue areas. Zinc and Copper seem to be the most pronounced elements from this element map.

scan2D\_5640\_fit

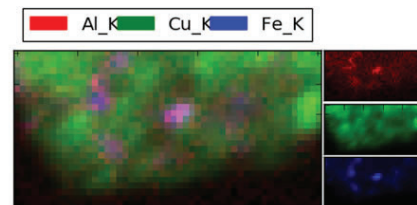


Figure 2C: This shows the element RGB for MM sample 5640. The elements Aluminum, Copper, and Iron were analyzed in this RGB. The small patches of purple represent where the Al and Fe coexist in the sample.

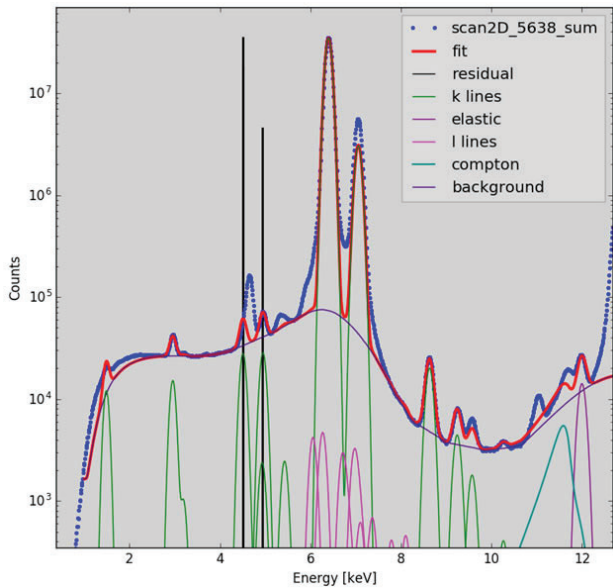


Figure 3A: This graph shows the spectrum view of the MM sample 5638. This spectrum does not contain many L-Lines and thus the MM is not composed of many of these elements associated with the L-lines.

scan2D\_5638\_fit

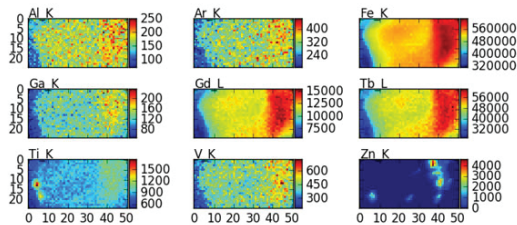


Figure 3B: This shows the element map of MM sample 5638. There are high concentrations of Iron in this sample as shown from this element map. This agrees with the spectrum view which shows strong Iron spectrum.

scan2D\_5638\_fit

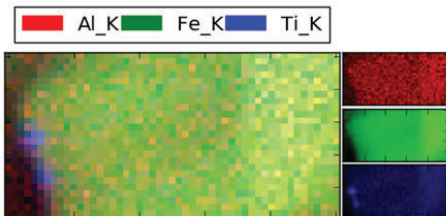


Figure 3C: This shows the element RGB for MM sample 5638. I chose to analyze the elements Aluminum, Iron, and Titanium for this RGB. There is significant coexistent of these elements dispersed throughout this sample as seen from this RGB.

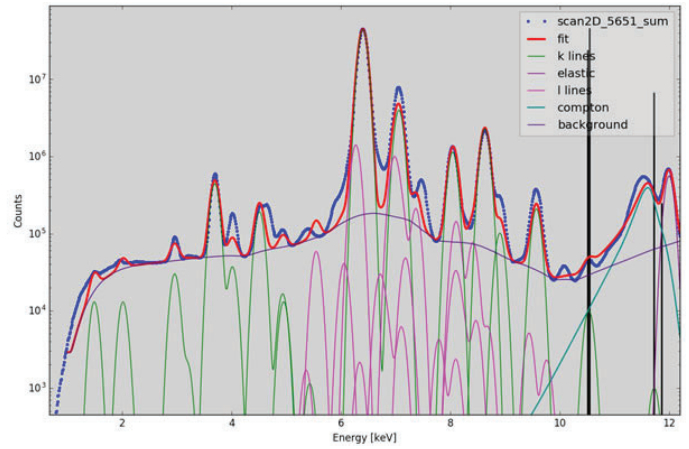


Figure 4A: This shows the spectrum view for MM sample 5651. This sample shows significant L and K spectral lines. There is also a pronounced count of background, shown by the purple line, in this spectrum.

scan2D\_5651\_fit

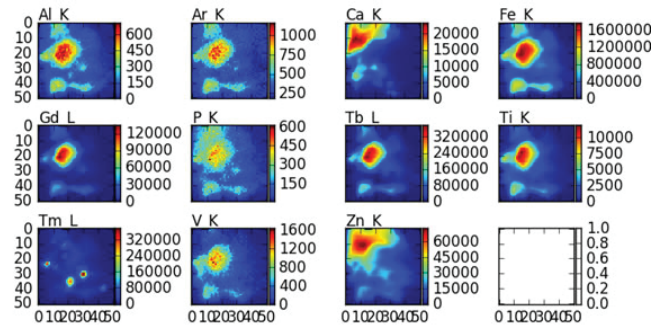


Figure 4B: This shows the element map for MM sample 5651. This shows high concentrations of Aluminum, Iron and Titanium in a similar area of the sample.

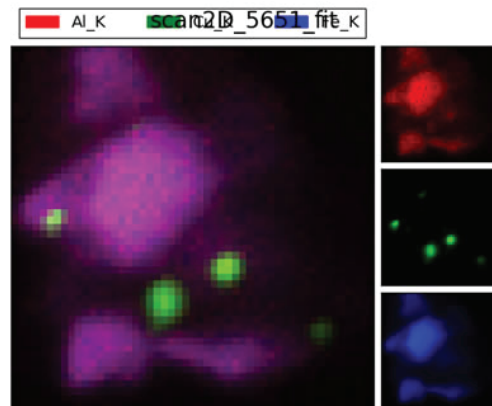


Figure 4C: This shows the element RGB for MM sample 5651. Elements Aluminum, Copper and Iron were analyzed in this RGB. The purple section in the larger image represents a coexistence of Aluminum and Iron in the sample. This is also demonstrated in Figure 4B by the element map of this MM sample.

## B. Educational Results

The students and teachers at the NSLS-II workshop were given anonymous surveys by the Brookhaven National Lab Office of Educational Programs about their experience during the week and for suggestions on how to improve this workshop for the future. I compared these surveys and I also found some common ideas in the surveys. A concern that many of the teachers had was that they did not have enough time in the weeklong workshop to fully comprehend the data and beamline analysis that they were being taught. Yet, the student surveys did not have this concern. Over 75% of the surveys, both teachers and students, ranked “Excellent”, the highest ranking possible, in all categories which shows a very positive outcome for the workshop as a whole. All surveys reported that the \$450 charge for the workshop was a reasonable amount to pay. An idea was also proposed to offer the workshop for NY Master teacher training credits. This would make the cost of the program even more worthwhile. Some teachers indicated on their surveys that they wanted a simplified version of the material for their high school students because they felt that the beamline science lessons that they were given were too in depth for the students to fully comprehend. There were also suggestions to make the material more applicable to the real world.

## IV. Discussion

Although the teachers must still perform their analysis of their MM spectroscopy to further the classifications and comparisons of the MMs, this project has thoroughly exposed me to Python-based beamline data analysis. I have been able to learn a computer program with enough confidence to help teachers who were uncomfortable to begin even inputting their data into. The beauty of this project was multi-level collaboration. Scientists at the NSLS-II took the time to collaborate with the Office of Educational Programs, of which I am an intern. Our office collaborated with Long Island schools to bring in teachers to the beamline and these teachers were able to create lessons to implement in their very own classrooms. A concern that came up a few times in the teacher surveys regarded submitting proposals to the NSLS-II in the future. The teachers’ concern was not having enough support from their school districts. Collaboration was cited as a crucial aspect to this workshop. As schools collaborate with each other and with scientific staff, we can bring more students and teachers to the NSLS-II with more research proposals. The importance of this project is the goal of making modern, high-level science research accessible to public school students. Hopefully these students will come back as interns or even scientists with the knowledge of beamline science, data analysis or even simply a passion for discovery.

## V. References

- <sup>1</sup>Brownlee, D. E. (2016). Cosmic dust: building blocks of planets falling from the sky. *Elements*, 12(3), 165-170.
- <sup>2</sup>Genge, M.J., Engrand, C., Gounelle, M. and Taylor, S. (2008), The classification of micrometeorites. *Micrometeorites and Planetary Science*, 43; 497-515.
- <sup>3</sup>Sauvet, C., J. Gattacceca, P. Rochette, N. Perchiazzi, L. Folco, J. Duprat, and R. P. Harvey (2009), Magnetic properties of micrometeorites, *J. Geophys. Res.*, 114, B04102.
- <sup>4</sup>Maurette, M. (1998). Carbonaceous Micrometeorites and the origin of life. *Origins of Life and Evolution of the Biosphere*, 28(4-6), 385-412.

<sup>5</sup>Noever, D.A., Phillips, J. A., Horack, J. M., Jerman, G., & Myszka, E. (1999). An ET Origin for Stratospheric Particles Collected during the 1998 Leonids Meteor Shower.

<sup>6</sup>Flynn, G.J. & Sutton, S.R. (1990). Synchrotron X-Ray fluorescence analysis of stratospheric dust: new results for chondritic and low-nickel particles.

## VI. Acknowledgements

I would like to give a special thanks to my mentor Bernadette Uzzi for her guidance and generosity supporting me with this project. I would also like to give a special thanks to Aleida Perez for her dedication to helping me through the research. I would like to thank the Robert Noyce Teacher Scholarship Program for funding my summer experience. This project was supported in part by the Brookhaven National Laboratory (BNL), Office of Educational Programs, under the BNL Supplemental Undergraduate Research Program (SURP). I would additionally like to thank the Office of Educational Programs Staff on a whole for making this experience possible.



# Optimization of geometry and a radiation damage study of acrylic lightguides

Zackary S. Parsons

Department of Physics, California State University, San Bernardino, California 92407-2630

Sean Stoll and Craig Woody

Department of Physics, Brookhaven National Laboratory, Upton, New York 11973-5000

## ABSTRACT

**The Pioneering High Energy Nuclear Interaction eXperiment (PHENIX) detector for the Relativistic Heavy Ion Collider (RHIC) at Brookhaven National Laboratory (BNL) is undergoing a major upgrade under the project name sPHENIX. Among the proposed upgrades is a new electromagnetic (EM) calorimeter which measures the energy of electrons and photons created from heavy-ion collision events. A critical component of the calorimeter design is the acrylic light guides. This part is the last step in directing 450 nm scintillation light onto Silicon Photomultipliers (SiPMs) where the light is converted to an electronic signal. The shape and material of these light guides are both important considerations to achieve maximum uniformity and efficiency of the detector. In order to improve light guide-light guide boundary efficiency, a 2 mm extension normal to the collection face is considered. The addition of the step showed a slight improvement on the boundary efficiency, and it could offer other useful manufacturing benefits. In addition to geometric concerns, the current choice for the light guide material, acrylic, is known to be susceptible to radiation damage. A study is performed to compare how ultraviolet-transmitting (UVT) acrylic compares to non-UVT acrylic under increasing doses of gamma radiation. Two possible manufacturing methods, resin-casting and injection-molding, are also considered as they could have different effects on the radiation hardness of the plastic. Results show that UVT acrylic is the better choice for the transmission of the 450 nm scintillation light, up to a gamma radiation dose of 1 Mrad. There is also evidence that using a more gentle production process, such as resin-casting instead of injection-molding, slightly improves the resistance to radiation damage.**

## I. INTRODUCTION

The Pioneering High Energy Nuclear Interaction eXperiment (PHENIX) detector for the Relativistic Heavy Ion Collider (RHIC) at Brookhaven National Laboratory (BNL) is undergoing a major upgrade under the project name sPHENIX. Among the proposed upgrades is a new electromagnetic (EM) calorimeter which measures the energy of electrons and photons created from heavy-ion collision events. These particles lose energy in dense tungsten blocks which are embedded with longitudinal optical fibers. Some of this energy is deposited in the optical fibers which scintillate at a peak wavelength of 450 nm. The light is then channeled through acrylic light guides and onto Silicon Photomultipliers (SiPMs) which convert the light to an electronic signal. The purpose of this study is to investigate and improve the geometry and radiation hardness of the acrylic light guides.

One of the most important aspects of the light guide design

is the balance between uniformity and efficiency. Uniformity is a measure of how much light is collected by the SiPMs as a function where the particle enters the tungsten block. This is important as it is one of the factors affecting the energy resolution of the detector. If the signal variation across a single light guide is too large, this will degrade the energy resolution of the EM calorimeter as a whole. The other design concern is the overall efficiency, or the measure of how much of the light exiting the embedded fibers is collected by the SiPMs. Efficiency is less of a concern since it can be more easily corrected in the data analysis stage. However, increasing the efficiency will give a higher signal-to-noise ratio, which should improve the detection of lower energy hits. Ideally, we would maximize both efficiency and uniformity, but in reality one must be traded for the other.

Along with light guide geometry optimizations, there remained a concern regarding the effects of radiation damage on the acrylic material. Poly(methyl methacrylate) (PMMA or acrylic), is desirable choice for the light guides in the EM calorimeter due to its low cost and ease of manufacture. However, this material known to be susceptible to radiation damage, which has the effect of pushing the ultraviolet (UV) absorption band into the visible region of the electromagnetic spectrum<sup>2</sup>. This is an especially important consideration because the light generated in the scintillating fibers peaks at 450 nm, which is close to the UV absorption edge of acrylic. In order to understand and improve the longevity of the light guides, a radiation damage study is performed to compare ultraviolet-transmitting (UVT) acrylic and non-UVT acrylic. Manufacturing methods are also compared as these might introduce different stresses and impurities which could affect the radiation hardness of the material.

## II. LIGHT GUIDE GEOMETRY OPTIMIZATION

Previous work at BNL on the optimization of the light guide geometry has narrowed the shape of the light guides to a rectangular frustum (Fig. 1a). The planar surfaces of the rectangular design allow for cheaper and more reliable manufacturing. The current dimensions are  $22 \times 24$  mm for the larger collection face,  $14 \times 14$  mm for the smaller exit face, and these two faces are 28 mm apart. This is a relatively short light guide due to the limited radial space within the sPHENIX magnet. With four SiPMs attached to the smaller face, each with an active area of  $9 \text{ mm}^2$ , this design gives a geometric light collection efficiency of 20 percent.

One major issue with this design is the sharp edge at light guide-light guide boundaries. A previous beam test carried out on a prototype calorimeter with similar light guides shows a dip in the efficiency at these boundaries. A proposed solution to this issue is to add a 2 mm step outward on the larger collection face (Fig. 1b). This would in theory allow light, which would have

been lost at the sharp boundary, to instead be shared between the two light guides. Another potential benefit of the step is that it prevents the optical binding epoxy from wicking up between light guides, which would further spoil boundary efficiency.

### A. Light guide and SiPM response scan setup

In order to test the effects that the addition of the 2 mm step would have on uniformity and efficiency, we needed to create a similar setup to that in the final detector design. Each channel in the EM calorimeter consists of about 700 of optical fibers directing light into a single light guide and onto four SiPMs. The SiPMs are then summed electronically before being amplified and digitized to create the readout signal. To simplify our testing, we only used a single fiber and LED to shine light into the collection face of the light guides. The fiber position was controlled with a (X, Y) stepper-motor scanner in a dark box. Since we were primarily concerned with the boundary efficiency, only two adjacent light guides were used with four SiPMs each. All sixteen SiPMs were summed together in order to measure the absolute collection efficiency of both channels.

### B. Light guide geometry optimization results

The addition of the step has the effect of increasing the efficiency directly at the boundary, but the wider reduction in the efficiency is still present. The scan of the “no step” light guide (Fig. 1a) shows a good overall efficiency (Fig. 2a), close to the maximum geometric efficiency of 20 percent. The uniformity follows the expected profile, peaking in the center of each light guide and falling off near the edges. Note that the light guide-light guide boundary is at  $Y = 2$  mm in Figure 2. Despite the central efficiency spike when the fiber was at the boundary, a previous beam test carried out on a EM calorimeter prototype with similar light guides shows that this effect is smoothed out. The wider dip in the efficiency around the boundary has a much more pronounced affect on the response due to the larger shower cross section.

## III. ACRYLIC RADIATION DAMAGE STUDY

Two main types of acrylic were looked at, ultraviolet-transmitting (UVT) acrylic and non- UVT acrylic. The primary difference between these two materials is that the UVT acrylic is opaque to light below 300 nm while the non-UVT variety is opaque below 400 nm, as shown in Figure 4. Another study has shown that when acrylic damages, the UV absorption band begins to move into the visible spectrum<sup>2</sup>. Presently, the light guide prototypes are manufactured using non-UVT acrylic. Since we are concerned primarily with 450 nm light transmission, switching to a UVT acrylic could provide a buffer which protects this critical wavelength from the effects of radiation damage.

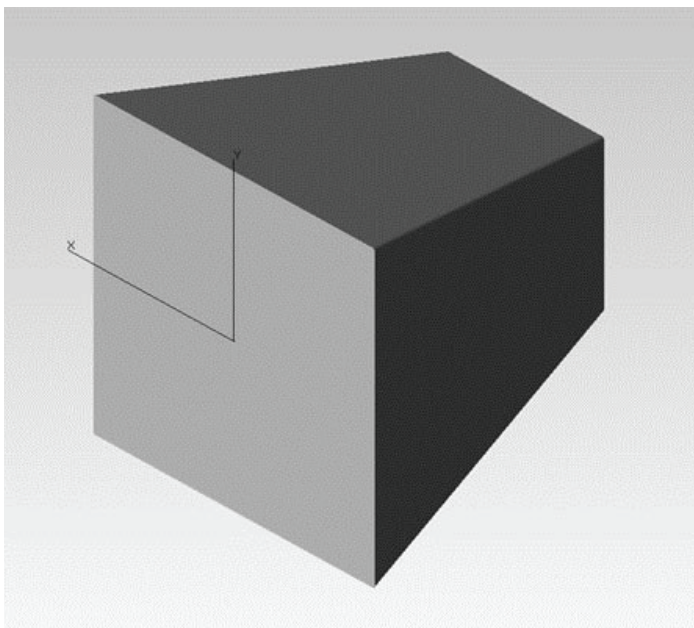
Another possible factor which could affect how the light guides damage is how they are manufactured. Different manufacturing processes introduce certain mechanical and thermal stresses, and this could affect the radiation hardness of the acrylic. Resin casting is a slower, less abrupt method, while injection-molding involves high temperatures and pressures. Injection-molding has already been selected to produce the final light guides. However, comparing the radiation damage of samples made with these two different techniques will provide useful insight into the effects we can expect to see in the final detector.

### A. Radiation damage methods

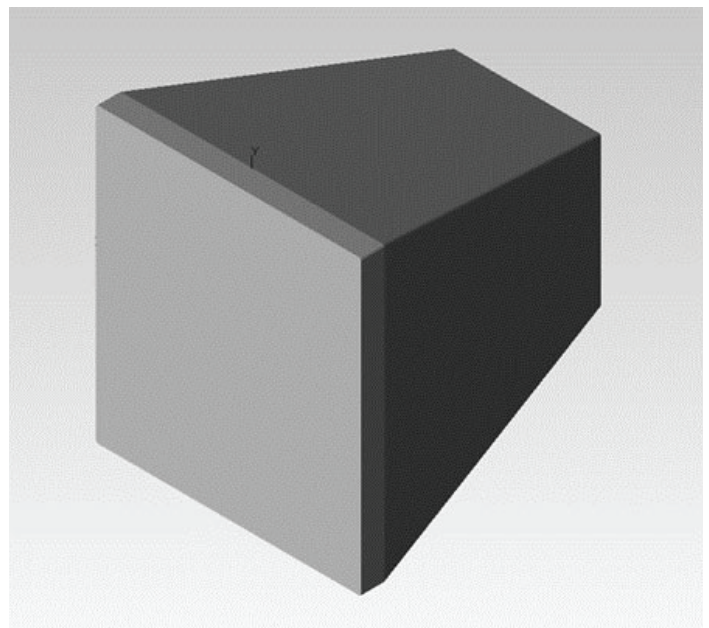
Four acrylic samples were selected to undergo doses of gamma irradiation from a Cobalt- 60 source. Two of the samples were used to compare the UVT and non-UVT varieties of acrylic, and the other two samples, both non-UVT, were selected to compare resin-cast and injection-molded acrylic. An initial spectral transmission scan from 800-190 nm was obtained for each sample to be used as a baseline comparison. Then, each sample was irradiated and re-scanned after 1, 10, 100, and 1000 krad doses.

### B. Radiation damage study results

The results were characterized using the radiation induced absorption coefficient<sup>1</sup>,



(a) Current light guide w/ no step



(b) Updated light guide w/ 2 mm step

FIG. 1: Proposed light guide geometries

$$dk = \frac{1}{l} \ln \left( \frac{T_{initial}}{T_{irr}} \right),$$

where  $l$  is the sample length,  $T_{initial}$  is the initial, undamaged transmission at 450 nm, and  $T_{irr}$  is the transmission at 450 nm after some radiation dose. At low radiation doses, 100 krad, little variation was observed between the four samples. The most notable differences occurred at the highest dose of 1 Mrad. As expected the UVT acrylic sample damaged much less than each of the non-UVT samples (Fig. 3). At 1 Mrad, the UVT stock acrylic reached a  $dk$  of  $13.4 \text{ m}^{-1}$ , implying an  $e^{-1}$  attenuation length of  $7.45 \text{ cm}$ . While the non-UVT stock acrylic reached a much worse  $dk$  of  $25.8 \text{ m}^{-1}$ , an attenuation length of just  $3.90 \text{ cm}$ . This implies that about 26 percent of the 450 nm light would be lost in the  $2.8 \text{ cm}$  light guide. The resin-cast non-UVT acrylic sample performed slightly better than the injection-molded sample, as expected.

#### IV. CONCLUSION

The addition of the 2 mm step to the collection face showed a slight improvement on the boundary collection efficiency. In addition to this result, the step provides some useful mechanical benefits, such as the prevention of the optical bonding epoxy from wicking up between the light guides. The extra material also allows for the removal and polishing of surface defects from manufacturing. The 2 mm step will be added to the final light guide design, but future studies should look at the effects of larger step sizes on boundary efficiency. Given the data, switching to a UVT acrylic would improve protection of 450 nm light transmission from radiation damage. There was also an observed effect based on how the acrylic was manufactured. Ideally, a more gentle process, such as resin casting, would also improve radiation damage resistance. However, cost and time are also important factors in the production of the light guides. Future studies should look into reducing mechanical and thermal stresses, and cutting down on impurities introduced during the production of the light guides.

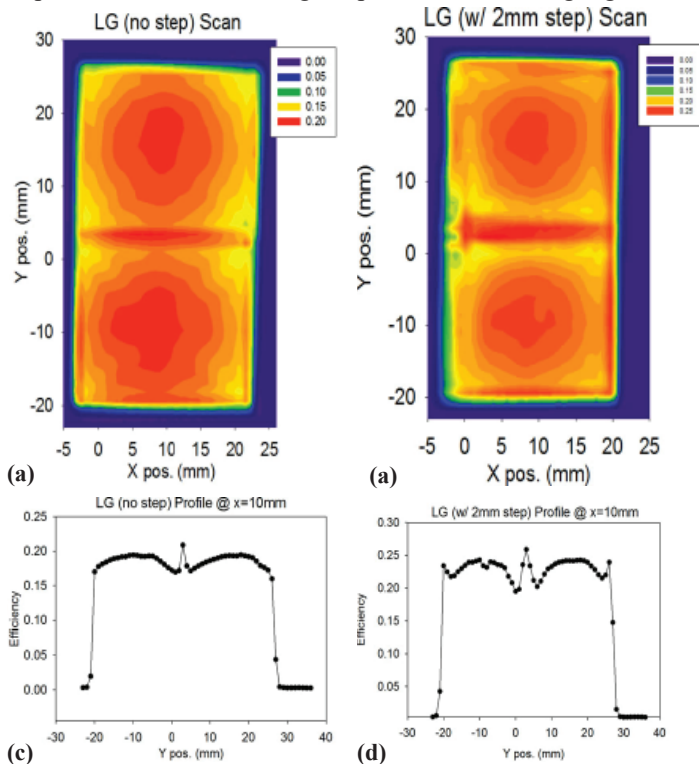


FIG. 2: Single fiber scans of side-by-side light guides

#### V. ACKNOWLEDGMENTS

This project was supported in part by the U.S. Department of Energy, Office of Science, Office of Workforce Development for Teachers and Scientists (WDTS) under the Science Undergraduate Laboratory Internships Program (SULI).

#### VI. REFERENCES

- <sup>1</sup>Fegan, S., Auffray, E., Battaglieri, M., Buchanan, E., Caiffi, B., Celentano, A., Colaneri, L., D'Angelo, A., Vita, R. D., Dormenev, V., Fanchini, E., Lanza, L., Novotny, R., Parodi, F., Rizzo, A., Sokhan, D., Tarasov, I., and Zonta, I., Nuclear Instruments and Methods in Physics Research Section A: Accelerators, Spectrometers, Detectors and Associated Equipment **789**, 101(2015).
- <sup>2</sup>Zorn, C., IEEE Transactions on Nuclear Science **37**, 504 (1990).

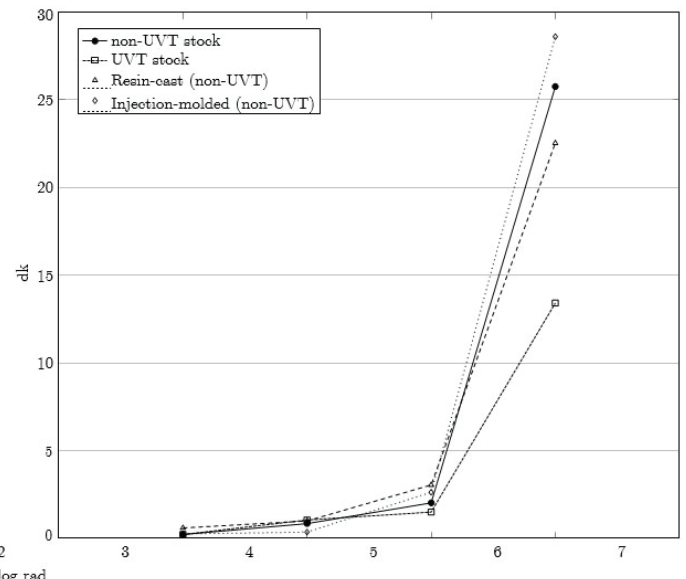


FIG. 3: Normalized radiation induced absorption coefficients;  $dk$  versus  $\log \text{ rad}$

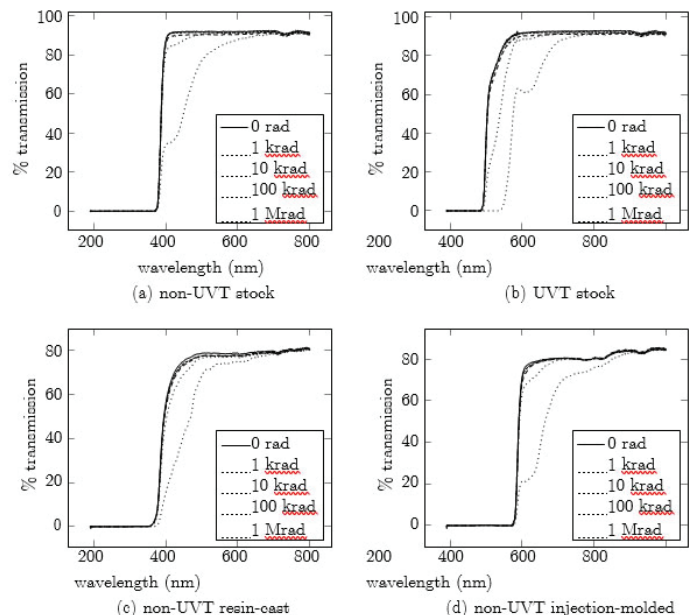


FIG. 4: UV-VIS spectral scans - Percent transmission versus wavelength



# 3-D printed multi-gap resistive plate chamber development

Abigail Paysinger and Marcus Alfred

Physics, Howard University, Washington, DC 20059

Gaylon Robinson

Computer Science, Howard University, Washington, DC 20059

Mickey Chiu

Physics Department, Brookhaven National Laboratory, Upton, NY 11973

## Abstract

Here at Brookhaven National Laboratory, we are working on research and development for the new Time-of-Flight (TOF) detector for the Super Pioneering High Energy Nuclear Interaction Experiment (sPHENIX). sPHENIX is an upgrade of the PHENIX detector and will take data at the Relativistic Heavy Ion Collider (RHIC) starting in ~2022. In particular, we plan to build and test ultra-thin glass multi-gap resistive plate chambers (mRPC), using glass of 160  $\mu\text{m}$  or thinner. The goal of our TOF research is to improve the time resolution from the ~100 picoseconds of existing detectors to 10 picoseconds, thus dramatically improving their capability for particle identification. The way we plan on getting this better timing resolution is by adding more gas gaps and making them more narrow in the mRPC. Currently, we are testing a 3D-printed ABS plastic mRPC to demonstrate that 3D-printed boards can be used as a future way of making mRPC's. The mRPC is inserted into a gas mixture composed of 95% R 134-A, 4.5% Isobutane, and 0.5% Sulfur Hexafluoride and read out using very high bandwidth (6-8 GHz) amplifiers, and digitized using DRS4 evaluation boards. After testing the 3D-printed mRPC, development and testing of a glass mRPC will follow.

## I. Background

### A. sPHENIX Upgrade

PHENIX was a particle detector stationed at the 8 o'clock collision point along RHIC's 2.4 mile long beamline. The experiment has been recently shut down for an upgrade to the sPHENIX detector. The goal of the PHENIX/sPHENIX project is to probe The Quark-Gluon Plasma, a state of matter that was present in the very early universe. sPHENIX will detect photons, electrons, and hadrons produced in high-energy collisions, and uses information obtained from these particles to deduce what happened in any particular event. Among the information, one can extract from these

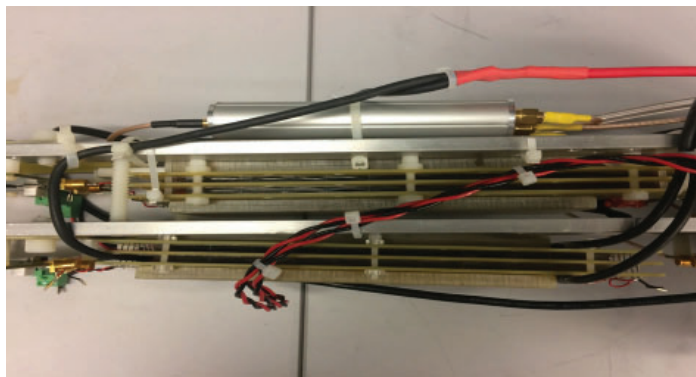


Figure 1: 3D-printed mRPC (side-view)

particles is time of flight, which along with tracking information lets one determine a particular velocity. With velocity and momentum, one can determine a particle's density via its mass, using the relation  $p = mv\gamma$ . Timing resolution is critical to determining the velocity of a detected particle. A primary goal of the proposed TOF detector is to bring timing resolution capabilities from 100 picoseconds down to 10 picoseconds, thus dramatically improving their capability for particle identification. As of today, ~20 picosecond timing resolution has been achieved. To squeeze out even better performance, improving the mRPC technology deployed in the detector has been the focal point of development.

### B. Brief Overview on Multi-Gap Resistive Plate Chambers and TOF

The PHENIX projected initially utilized scintillators in its TOF detectors. These detectors were able to achieve a timing resolution of 100 picoseconds. This timing resolution is insufficient for sPHENIX, since the TOF detector has to be much closer in sPHENIX (85 cm vs 500 cm in PHENIX). Multi-gap Resistive Plate Chamber (mRPC) technology is the prime candidate of interest for the proposed TOF detector in sPHENIX. In short, when a charged particle passes through an mRPC it sparks an "electron avalanche" that creates a distinct image current that can then be read out by electronics. As of date, mRPC development has achieved a timing resolution of ~20 picoseconds. To squeeze out extra performance, the next stage of development is to create

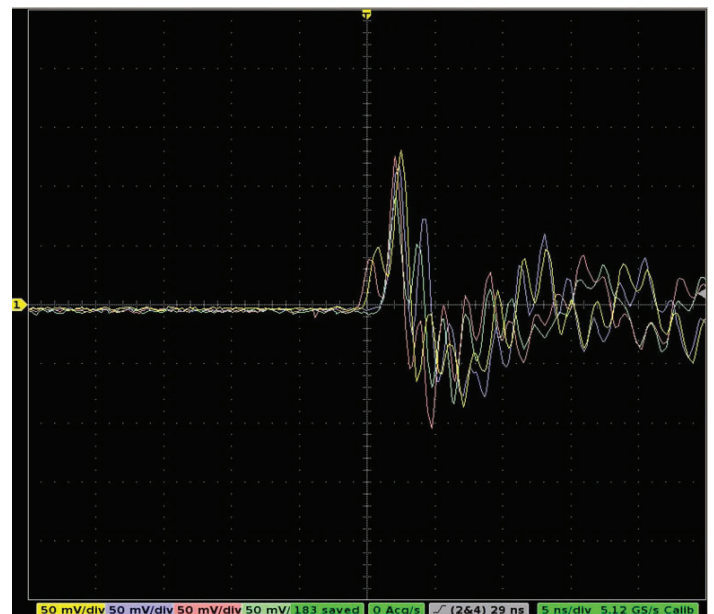


Figure 2: Real-time signals detected from cosmic rays.

a thin-glass mRPC. The ultra-thin glass will allow for more gas gaps in the mRPC which directly correlates to a higher signal, and therefore improved performance.

### C. Different Materials used for building the mRPC

The material mainly used for building the mRPC is glass. Different types of glass and different sizes are being tested to see which can be used since the thinner the glass gets, the more expensive it becomes and more difficult it makes to keep the glass from breaking. For this reason, other materials are being tested instead of glass that could be better alternatives. The one option being looked into is 3D printed mRPC, which is what we mainly researched this summer. 3D printed material is a lot less expensive than glass; building 2 pieces of the 3D printed material is about \$25 compared to float glass which would cost \$108. Testing is currently being done to see how effective a 3D-printed mRPC is. The only issue with 3D printed material is that the 3D printing technology is not able to print the gas gaps as thin as we need them to. Currently the gas gaps are at 0.3mm. However, we expect this technology to continuously be developed by industry, so that in the future one may be able to print thinner gas gaps.



Figure 3: Glass Results (from left to right): 160 um glass after attempt at cutting, 160 um glass before, 200um glass after

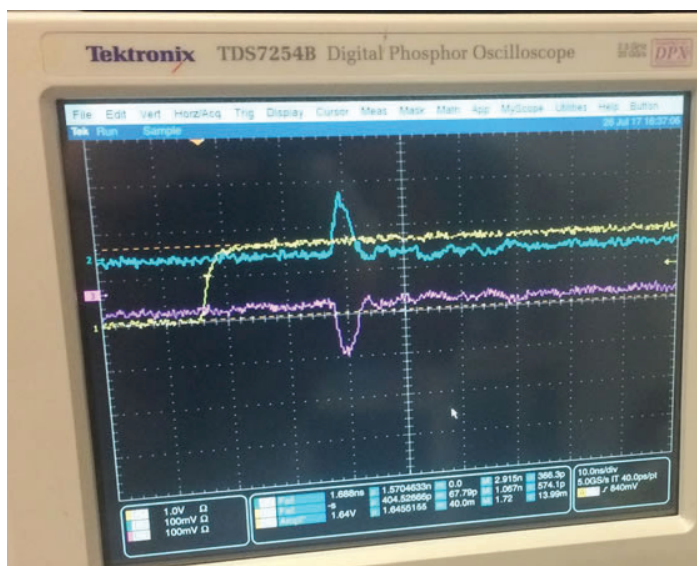


Figure 4: Signals with the reflections

## II. Methods

### A. Testing the 3D printed mRPC

The 3D printed mRPC was first outfitted with a DRS4 board so to digitize the waveforms produced for readout. We then tested each preamplifier and replaced Ch.4's, which was found to be bad. Next, the chamber was sealed and gas mixture of 95% Freon 134-A, 4.5% Isobutane, and 0.5% Sulfur Hexafluoride was flowed into the mRPC for 24 hours to ensure that the air originally inside had been completely flushed out.

### B. Thin-Glass Development

iPhone screen protector glass was used for the development as it was cheap and available with extremely thin widths.. Two thicknesses of glass were obtained, 200 um and 160 um. Initial processing of the glass consisted of meticulously peeling off the plastic layer adhered to one side of each screen protector. To dimension the glass to fit the printed circuit boards (PCBs) we used a diamond-tipped cutter. We first cut 12 pieces of glass at 200um so that they fit into existing mRPC PCBs. We taped the glass before cutting to reduce cracking. We then attempted to apply the same method to the 160 um glass, but since the 160um glass was tempered, we found that they cracked very easily. At this point our development stopped since the only way to cut this is to use a CO<sub>2</sub> laser.

### C. Reflection Mitigations

To remove the reflections present in the signal readout of the 3D-printed mRPC, we elected to investigate this issue using a larger mRPC in the lab. We configured a system to imitate a typical signal that could be seen if read out from an mRPC during actual testing. Using a waveform generator we ran a +15 mV signal through a comparator chip. This chip allowed us to increase the signal's rise time and render it detectable by the oscilloscope. Next, we tackled removing the reflections displayed on the oscilloscope. This meant that we had to match the resistance of the

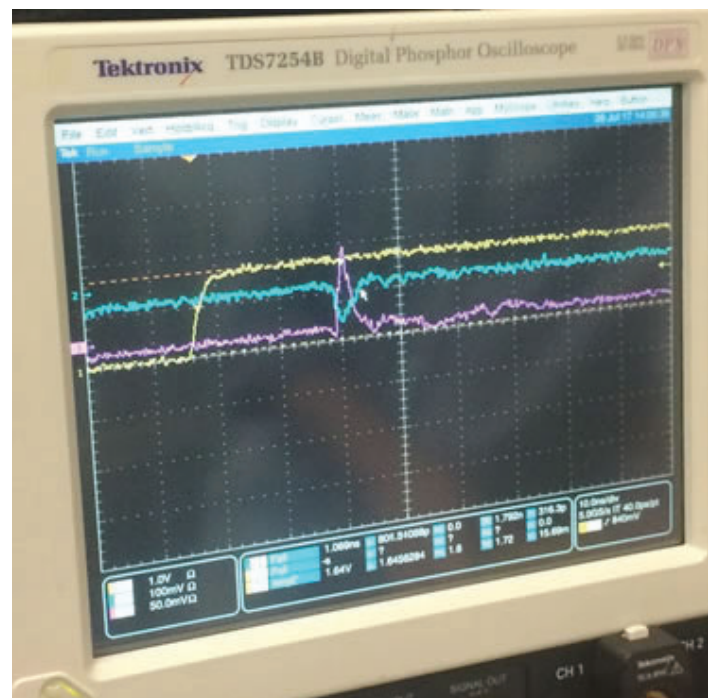


Figure 5: Signals after applying a resistor in parallel

output with the impedance of the input. We constructed a new cable that would allow us to attach two potentiometers connected in parallel across the mRPC. We then tuned the resistance until the reflections in the signal were removed.

### III. Data & Results

#### A. 3D-printed mRPC Results

We successfully received real signals using the 3D-printed mRPC. However, an unacceptable level of reflections was present in the signals. These reflections needed to be removed. It was a very unique experience for us to receive real signals using the 3D-printed mRPC since it had never been done. The only testing before has been running a signal through the 3D mRPC, but not itself actually detecting real signals. Although this experiment was successful and was a less expensive option than the glass mRPC, its printed materials were not as thin as we wanted.

#### B. Glass Cutting Results

The first set of glass we cut, the 200 um thick glass, was successfully dimensioned to 11 x 5 cm<sup>2</sup> rectangles with a handheld diamond-tipped cutter. The 160 um glass, however, was unfortunately too thin and would shatter when subjected to this method. The glass was also tempered, further increasing the likelihood of this shattering. Research showed that a CO<sub>2</sub> laser is used by the manufacturer to cut this glass. Consequently, the new plan is to build larger PCB boards to fit the glass without having to cut it.

#### C. Reflection Mitigation Results

We were able to successfully eliminate the reflections using the two potentiometers connected in parallel across the mRPC. This demonstrated that it was indeed possible to remove these reflections, and that what we were seeing was not just excess noise. However, this particular configuration is not ideal for mRPC stacks with more than 2 PCB's since in this case some signal traveled backward down one of the strips. We attempted to connect the resistors in series to reduce this effect, but this method had problems with reflections. Solving this issue remains an open question.

### IV. Conclusion & Recommendations

In summary, we were able to successfully record real signals using the 3D-printed mRPC. At the time that this mRPC was created, 3D-printing technology only permitted printing gaps of 300 microns in thickness. However, this field is progressing rapidly on its own and we see 3D-printing as a viable option for creating future mRPCs with optimal specifications. To handle the signal reflections, we matched the resistance of the output with the impedance of the input as mentioned above, but a different solution is still needed to suit mRPC stacks with more than 2 PCB's. We were successfully able to cut the 200um glass, but not the 160um glass. In the future, we would recommend cutting the glass using a CO<sub>2</sub> laser.

### V. References

- Chiu, Mickey. "10 picosecond Timing Detector Development". Powerpoint Presentation.
- Shimek, Taylor. "Time-of-Flight Method Using mRPC Technologies to Detect Particles with Reasonable Time Resolution and Cheaper Materials". Final Paper.

Mitchell, Jeffery T. ". " *PHENIX: An Introduction*. N.p., n.d. Web. 7 Aug. 2017.

### VI. Acknowledgments

This project was supported in part by the National Science Foundation, Louis Stokes Alliance(s) for Minority Participation (LSAMP) at Howard University under the LSAMP Internship Program at Brookhaven National Laboratory.



# Efficient full-stack web development for multidimensional scientific data visualization

Miguel Rodriguez, Computer Science, SUNY Oswego, Oswego, NY

Sungsoo Ha and Wei Xu, Computational Science Initiative, Brookhaven National Laboratory, Upton NY

## Abstract

This research project was a study of efficient full-stack web development for multidimensional scientific data visualization in the Computational Science Initiative(CSI) at Brookhaven National Laboratory(BNL). The CSI department at BNL is dedicated to developing new algorithms and data visualizations to help users explore their data. We conducted a study on improving the performance and functionalities of a full-stack web application to manage and visualize synchrotron-based scientific data including; raw image set, analysis results, and metadata. Such an application consists of two parts, the front-end performs visualizations of the data and supports user interactions, while the back-end manages the data analysis, storage, and the communication with the front-end. Specifically, for the back-end side, we installed a MongoDB database to manage large scale datasets. We used python to query and handle the MongoDB database and provide the data to the front-end. For the front-end side, we improved a visualization interface to help scientists readily explore and understand the data. For the efficient visualization with many data points to render, we employed the React framework. In this study, we focused on developing a histogram that shows the distribution of large scale data with user interactions to zoom in/out the data ranges. We explored three aspects of the interactive histogram. First, the two different data encoding schemes, which are height and color, are compared in terms of its compactness and readability and we found that encoding by color is more compact and encoding by height is more readable. Second, we tested the interaction performance with and without the React framework and we concluded that React is faster than D3. Lastly, readability and reusability of the implemented code were evaluated by comparing it with a traditional approach that is not built with the React framework. This allowed us to prove that React is more readable and reusable than the D3 framework. Extension of our full-stack web-based data visualization application framework allows users to efficiently explore the data further.

## I. Background

### A. Data Visualization and Traditional Methods

In a world driven by overwhelmingly large amounts of data, it is extremely important now more than ever to gain insight from this data. Human beings are visual creatures in that we can more quickly understand visual data. These are some of the reasons why the field of data visualization is becoming more and more popular. Scientists are gathering data every day from experiments with state of the art equipment such as the National Synchrotron Light Source (NSLS) at BNL. This data needs to be studied and explored to make predictions and discoveries, and data visualization can help achieve that by representing the data in graphs that

humans can understand easily. To visualize the data, we developed a full-stack web application. This application is composed of the back-end which handles the data and provides the data to the front-end, which visualizes the data. To code this application there are many different frameworks and languages to choose from. The traditional way of visualizing data would be using D3 for the front-end and any other programming language for the back-end. D3 stands for data driven documents and is a JavaScript framework created by Mike Bostock. This library has been adopted as the main way of visualizing data because of its specialization in data visualization. However, as the web changes and technology changes we need to find more efficient ways of visualizing data.

### B. React and full-stack web development

For an efficient visualization with many data points we employ the React framework. React is a JavaScript library developed by Facebook and Instagram. The main goal of React is to make the building of web user interfaces easier and more efficient. One of the main features of React is the implementation of a virtual Document Object Model(DOM) and the way it updates the real DOM. The virtual DOM is like the real DOM in structure but it doesn't render anything to the web browser making it faster when making changes. In React the process of rendering and updating the DOM is called "Reconciliation". When using traditional methods such as D3, every time something changes in our application, D3 renders the whole DOM. In React when something changes in our web app the reconciliation process begins. It starts by updating the virtual DOM based on the changes made; it then compares the previous virtual DOM with the current virtual DOM using the diff algorithm. The diff algorithm parses the two virtual DOM's line by line and when it sees something different between the two, it takes it and updates the real DOM respectively. This process is more efficient since we are just updating parts of the real DOM which increases speed in our full-stack data visualization web applications significantly.

### C. Interactive Histogram to visualize multidimensional data

To prove the performance of React over D3 we developed an interactive histogram to visualize data. This histogram was built using the two different frameworks. It was composed of horizontal bars which represented bins as shown in figure 1 or 2 below. Each bin had many data samples which fall between a range which was represented by the horizontal axis. The vertical axis represented the maximum number of samples within each bin.

User interactions were also implemented to test the updating performance and speed. We decided to implement a zooming function that allows users to zoom in/out horizontally. When zooming, the axis range position, the rectangles width, and horizontal position of the bars would change accordingly. This will

cause the DOM to update, allowing us to record the speed to make our educated decision to which one is faster. We studied to different bar encodings, encoding the bars by color or by height in terms of readability and compactness. Then, we decided to compare the code for readability, reusability, and scalability.

## II. Methods

To study the efficiency of a data visualization full-stack web application we adopted different methods. Specifically, we tested and studied an interactive histogram developed in the D3 and React frameworks for efficiency.

### A. React and D3 readability

When comparing the readability in both frameworks React has better readability than D3. This is accomplished by using components and XML like syntax called JSX. In react we can create components that mean something, such as a bar chart component that creates a bar chart. We also can have a data series component that handles all the data and then pass it through props to the child components. This makes it simple to understand that we have two components and one handles the data and the other one handles building the bar chart. For people that have a background programming using OOP, learning React would be a little familiar. In D3 we built the bar chart step by step by using method chaining and bind our data which can be overwhelming and time consuming trying to read and understand every single function used. An example of this can be the code below in Figure 3, which shows the same code in both frameworks. As you can see, in React we only have two components that received the data through “props” to build the bars and labels. However, for D3 it is a more tedious process since we have many different functions chained to each other and then assigned to some variables.

### B. React and D3 reusability

When it comes to reusability React outperforms D3. React makes use of components which makes the code more modular and less dependable. This is similar to Object-Oriented Programming in that we can have many different classes that work together to achieve a common goal. React has a top down data flow as shown in Figure 3, meaning that one can define a parent component that stores all the data and then is passed to child components via props. The child components are only dependable to the data being passed from the parent component. Therefore, by

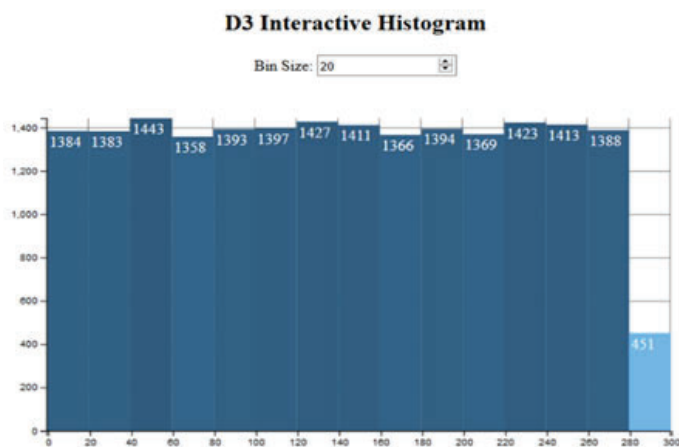


Figure 1. Traditional D3 interactive histogram

making little changes we can reuse components easily in React, making our web applications more cost effective when making future modifications. D3 has a different approach when it comes to program structure since it uses method chaining to call all the different functions available.

### C. React and D3 scalability

D3 has very limited capabilities when handling enormous amounts of data. This is because it renders elements directly to the real DOM and It updates the entire DOM each time, making it almost impossible to handle large sums of data. React on the other hand, incorporates a virtual DOM which is faster than the real DOM hence updating it takes less time. The process is called “Reconciliation” and It uses a Diff algorithm to compare the previous DOM with current DOM and when it sees a difference it updates the real DOM. This makes the process of updating the DOM and handling large amounts of information faster and more scalable.

### D. Interactive histogram bar encoding

When encoding the histogram by height, it is easily understood, because people are very familiar with bar charts and the higher the bar the higher the number that it represents and the lower the bars the lower the number that they represent. When it comes to compactness, encoding the histogram by the height do not saves space since there are empty gaps in the SVG because of the bars being of distinct heights.

If we color encode the histogram users, will need to stop and study the legends provided to be able to understand what the graph is conveying. When it comes to the compactness of the graph is more compact because the bars can be the same height meaning that we will have less to none white space shown in our SVG.

### E. React and D3 performance speed

During the React application initial render, and using a histogram generating 20000 random numbers between the ranges of 0-300. The “performance.now” JavaScript function was used to test the web app during five different occasions. For the first attempt, I recorded a time of 44.1050ms, for the second 50.5600ms, for the third 44.2050ms, for the forth 44.4500ms and for the fifth attempt I recorded 43.6750ms which yields an average time of 45.399ms.

When it comes to updating the histogram in React and

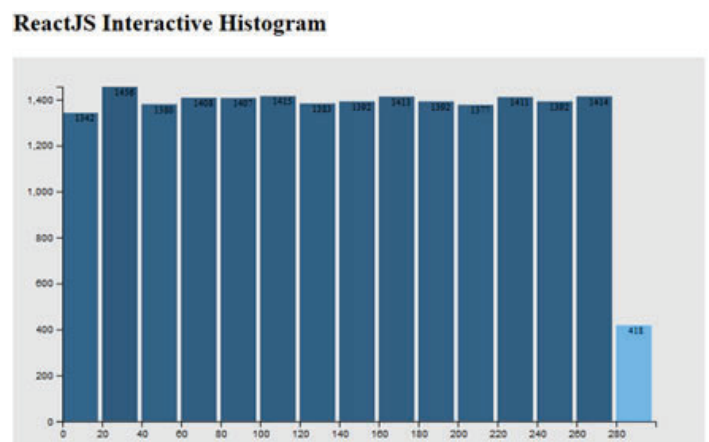


Figure 2. React interactive histogram

```

//creates a Bar component as a child
class Bar extends React.Component {
  render() {
    return (
      <rect fill={this.props.color}
        width={this.props.width} height={this.props.height}
        x={this.props.x} y={this.props.y}/>
    );
  }
}

//creates a Label component as a child
class Label extends React.Component {
  render() {
    return (
      <text className="bar_text" style={text_style}
        x={this.props.x}
        y={this.props.y}>{this.props.label}</text>
    );
  }
}

```

```

var bars = svg.selectAll('rect')
  .data(dataArray)
  .enter()
  .append('rect')
  .style('fill', function(d,i){
    return colors(d);
  })
  .attr('height', function(d,i){
    return yScale(d);
  })
  .attr('width', binSize * 2.09)
  .attr('x', function(d,i){
    return xScale(i);
  })
  .attr('y', function(d,i){
    return height - yScale(d);
  })
  .attr("class", "bar")

var labels = d3.select('svg').append('g')
  .attr('class', 'labels')
  .selectAll("text")
  .data(dataArray)
  .enter().append("text")
  .attr('fill', 'white')
  .text(function(d) {return d;})
  .attr('x', function(d,i){
    return xScale(i) + ((barOffset + 8) + margin.left);
  })
  .attr('y', function(d,i){
    return ((height + 17)+ margin.top) - yScale(d) ;
  });

```

Figure 3: React code syntax shown on the left side and D3 code syntax shown on the right

while zooming and increasing the zoom level by one I recorded a time of 0.6800ms for the first attempt, 0.3850ms for the second, 0.7000ms for the third, 1.3050ms for the fourth and 0.4600ms for the fifth attempt getting an average time of 0.706ms.

Initial rendering and testing a D3 histogram and generating 20000 random numbers between the range of 0-300. Using the “performance.now” function I recorded a time of 51.6200ms for the first attempt, 47.4350ms for the second, 48.0600ms for the third, 50.4450ms, and 47.6100ms for the fifth attempt getting an average time of 49.034ms.

When zooming in D3 and increasing the level by one I recorded a time of 5.9000ms for the first attempt, 2.9000ms for the second, 2.3900ms for the third, 3.4650ms for the fourth, and 2.5000ms for the fifth attempt which yields average time of 3.431ms.

### III. Data and Results

While testing these two different JavaScript frameworks I wasn’t surprised by the benchmarking results. For React the average initial render time was 45.399ms and for D3 it was 49.034ms meaning that React is 3.635ms faster than D3. For the update time, I acquired 0.706ms for the average of React and 3.431ms for the average of D3 meaning that React is 2.725ms faster than d3 when updating the DOM. This proves that React is significantly faster than D3 when updating the DOM because it uses a virtual DOM. This time difference might not seem a lot but in our experiment, we tested a simple interactive histogram. If we were to test a more complex web application we would see a much larger performance increase.

As far as readability is concern, React has the upper hand since it uses components and XML like syntax called JSX while D3 uses method chaining to call and nest all different functions needed. React is also more reusable because of the components and the top down data flow as shown below in figure 4. It is more scalable in terms of handling large amounts of data because of the virtual DOM making the updating process efficient. By encoding

the bars by height, the visualizations are more readable and if encoded by color the graphs are more compact saving space.

### IV. Conclusions and Recommendations

Performing experiments with cutting edge technologies often yields large amounts of data that scientists must use to make predictions. During this project, we used synchrotron-based scientific data to develop a full-stack web application to visualize multi-dimensional scientific data. To visualize large amounts of data we must employ different methods to make the process more efficient for scientists to learn and explore the data for further analysis. While traditional visualization methods such as d3 are good, there are many other methods that are better in terms of performance, readability, scalability and reusability. One of those methods is visualizing data using the React framework which increases the performance by using a virtual DOM to make changes which D3 does not provide. We still use D3 to do the data computations but not to handle the DOM manipulations which makes our applications faster during initial render and update. React also has other advantages which include being more reusable, scalable and readable making the process easier for future modifications.

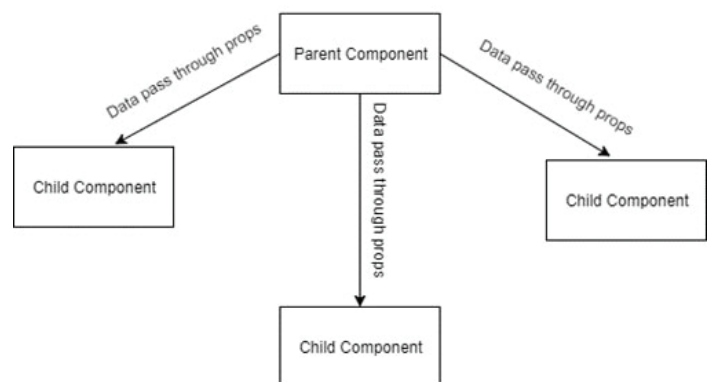


Figure 4. React unidirectional data flow



## V. References

- <sup>1</sup> D3.js Official Page. <https://d3js.org/>
- <sup>2</sup> React.js Official Page. <https://facebook.github.io/react/>
- <sup>3</sup> Reconciliation: <https://facebook.github.io/react/docs/reconciliation.html>
- <sup>4</sup> Virtual DOM vs Real DOM. <https://www.accelebrate.com/blog/the-real-benefits-of-the-virtual-dom-in-react-js/>
- <sup>5</sup> Scalability in React. <https://blog.codecentric.de/en/2016/05/how-react-makes-web-development-scalable/>
- <sup>6</sup> Reusability in React. <https://medium.com/walmartlabs/how-to-achieve-reusability-with-react-components-81edeb7fb0e0>

## VI. Acknowledgements

This project was supported in part by the U.S. Department of Energy, Office of Science, Office of Workforce Development for Teachers and Scientists (WDTS) under the Science Undergraduate Laboratory Internships Program (SULI).

Thank you to the DOE and BNL for encouraging me to pursue research and supporting me along my academic journey. Also, I thank you my mentor Wei Xu, PhD and Sungsoo Ha for their assistance and for giving me the opportunity to collaborate and extend my research experience. I would also like to thank the OEP at BNL for their assistance and support during this project.

# Characterization of Co-CeO<sub>2</sub> powder catalysts for the dry reforming of methane into synthesis gas

David Salazar

Engineering, Queensborough Community College, Bayside, NY 11364

Feng Zhang

Materials Science Department, Stony Brook University, Stony Brook, NY 11794

Dimitriy Vovchok

Chemistry, Stony Brook University, Stony Brook, NY 11794

Zongyuan Liu, Sanjaya D. Senanayake, and Jose A. Rodriguez

Chemistry, Brookhaven National Laboratory, Upton, NY 11973

## Abstract

This study investigates the role of Cobalt-Ceria powder catalysts for the Dry Reforming of Methane (DRM) reaction,  $\text{CH}_4 + \text{CO}_2 \rightarrow 2\text{H}_2 + 2\text{CO}$ , an important chemical process with the potential to be used in industry for converting methane, the main component of natural gas, into synthesis gas ( $\text{CO} + \text{H}_2$ ). Temperature-programmed reduction (TPR), residual gas analysis (RGA), and in situ x-ray diffraction (XRD) Rietveld analysis were used to obtain information on the reducibility, catalytic performance, and corresponding catalyst structural changes that occur during the reaction. The loadings of Co tested, include 1%, 10%, and 30% on CeO<sub>2</sub>. TPR results showed that the 10% CoCeO<sub>2</sub> sample had the optimum methane activation when compared to the 1% and 30% Co loadings. RGA analysis showed that the 10% CoCeO<sub>2</sub> produced the most product under DRM conditions when compared to the 1% and 30% Cobalt loadings. With in situ Synchrotron XRD analysis and Rietveld refinement, it was found that the active state of the 10% CoCeO<sub>2</sub> catalyst under DRM conditions was composed of metallic cobalt, Co<sup>0</sup>, on a CeO<sub>2</sub>x partially reduced support (Ce<sup>3+</sup> / Ce<sup>4+</sup>). TPR analysis was conducted in order to quantitatively learn about surface and bulk reducibility behavior of the CoCeO<sub>2</sub> catalysts, an important indicator of catalyst performance. In the TPR studies, pure

methane, CH<sub>4</sub>, was flown into the different catalyst samples at 8 cc/min with a temperature ramp of 10 °C/min from 30 °C to 700 °C. Temperature programmed reduction is an important experimental technique that was used to learn about the reactivity of catalysts, and Rietveld analysis was conducted to obtain information about catalyst structure under reaction conditions.

## I. Introduction

Natural gas is an underutilized and abundant fossil fuel that may be used in industry for the production of commodity chemicals, and as a chemical fuel for generating electricity. Methane is the main component of natural gas, and it is the cleanest hydrocarbon that produces more heat per unit mass (55.7 kJ/g) with a heat of combustion of 891 kJ/mol. It is for these reasons that dissociating the stable C-H bonds in methane represent a challenge. The Dry Reforming of Methane (DRM) reaction, [ $\text{CH}_4 + \text{CO}_2 \rightarrow 2\text{CO} + \text{H}_2$ ], is used in this study for analysis of hydrogen formation from methane dissociation. This reaction has the potential to be used in industry, but the catalytic process is not well understood. It has been reported that Group VIII transition metals such as Ru, Rh, Pd, Ir, and Pt based catalysts work best for the DRM reaction. However, it is not cost effective to use such transition metals, because they are scarce and expensive, and the downside of using

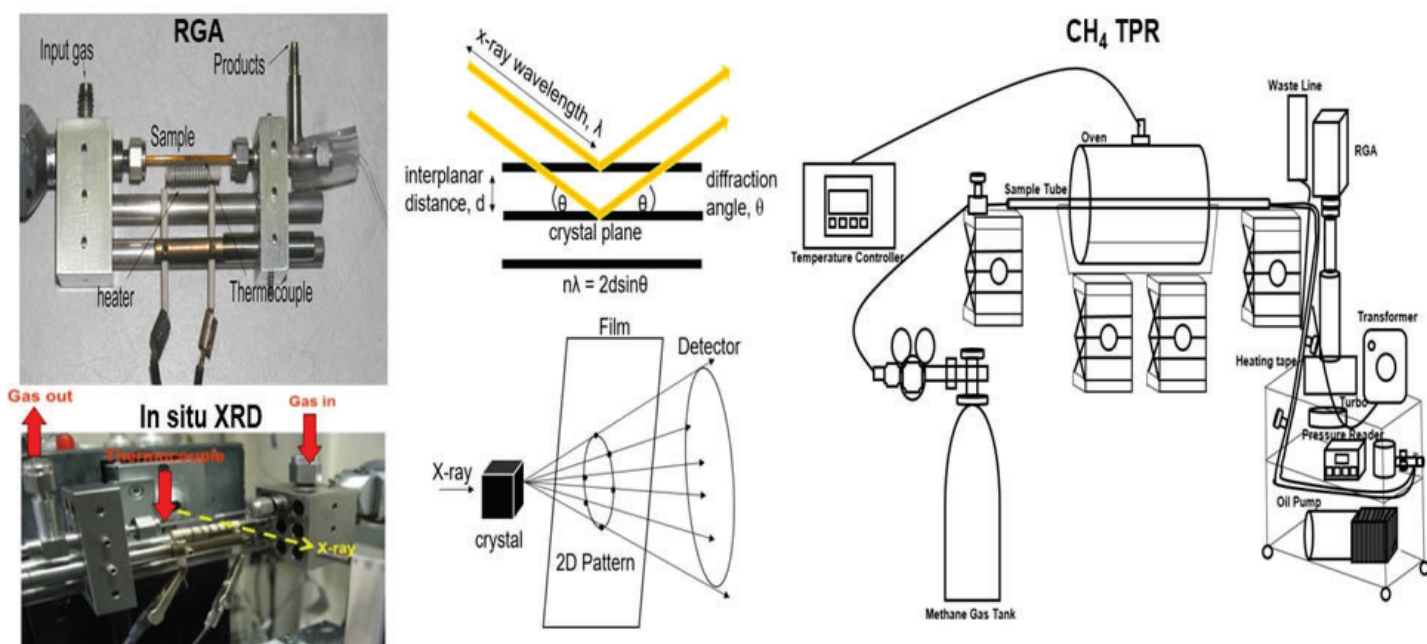
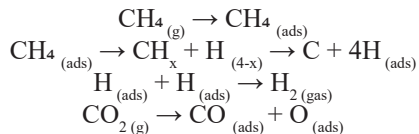


Figure 1: RGA, in situ XRD, methane temperature-programmed reduction

them is their deactivation issues from carbon deposition, and particle sintering. The focus of this investigation involves the cost effect Cobalt-Ceria,  $\text{CoCeO}_2$ , catalysts which have been reported to be active under DRM reaction conditions in the temperature range of 25 – 500 °C. The Cobalt found in  $\text{CoCeO}_2$  catalysts, dissociates the C-H bonds in methane, and the Cerium oxide takes an active role to support and disperse Cobalt, and this metal oxide support is likely to help activate the  $\text{CO}_2$ , and dissociate it into CO.

### Reaction Mechanism:



## II. Experimental

Temperature-programmed reduction (TPR) data was collected at Brookhaven National Laboratory (BNL). (See Figure 1.) Pure  $\text{CH}_4$ , was flown into 1%, 4%, 10%, and 30% Cobalt-Ceria samples as well as bare Ceria at 8 cc/min from room temperature to 700 °C at 10 °C/min. In situ and ex situ XRD data was obtained at the Advanced Photon Source (APS) at Argonne National Laboratory. Transmission Electron Microscopy (TEM) data was obtained at the Technical University of Catalonia, Barcelona, Spain. Residual Gas Analysis (RGA) studies were conducted

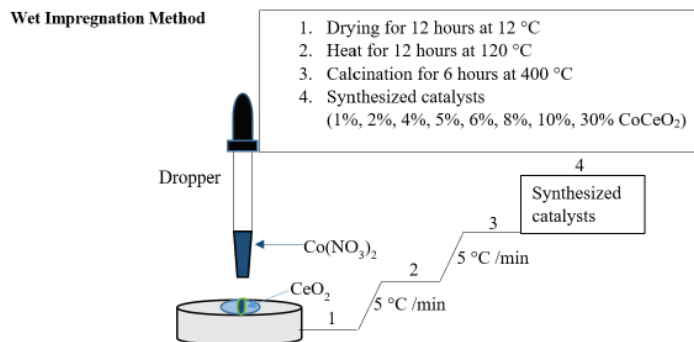


Figure 2

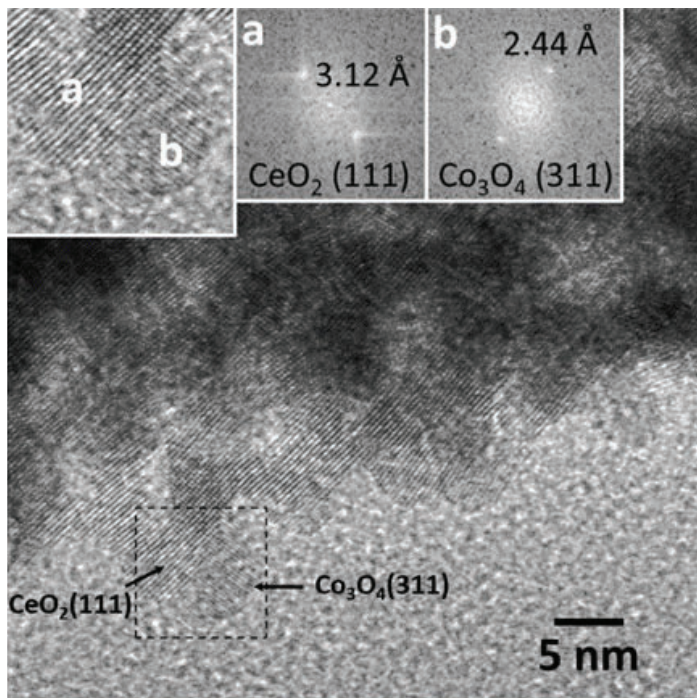


Figure 3:

at Brookhaven National Laboratory. The Cobalt loadings tested were 1%, 2%, 4%, 6%, 8%, 10%, and 30% on  $\text{CeO}_2$  under DRM reaction conditions. The 10%  $\text{CoCeO}_2$  sample was pretreated in  $\text{H}_2$  (10 c) for an hour from room temperature to 550 °C at 10 °C/min, and cooled down to room temperature (10 °C/min). The same procedure was performed for the rest of the samples, but with a maximum pretreatment temperature of 450 °C. Qualitative information was monitored by RGA using a mass spectrometer.

### Catalyst Preparation

Figure 2: By using the wet impregnation method, Cobalt Nitrate was dissolved in deionized water at room temperature and this was added drop-wise to 1 gram of Ceria ( $\text{CeO}_2$ ) and mixed. A slurry is obtained and procedures (1, 2, 3, and 4) were applied to obtain the 1% to 30 % Cobalt loadings.

### Evaluation of Reducibility: $\text{CH}_4$ temperature-programmed reduction (TPR)

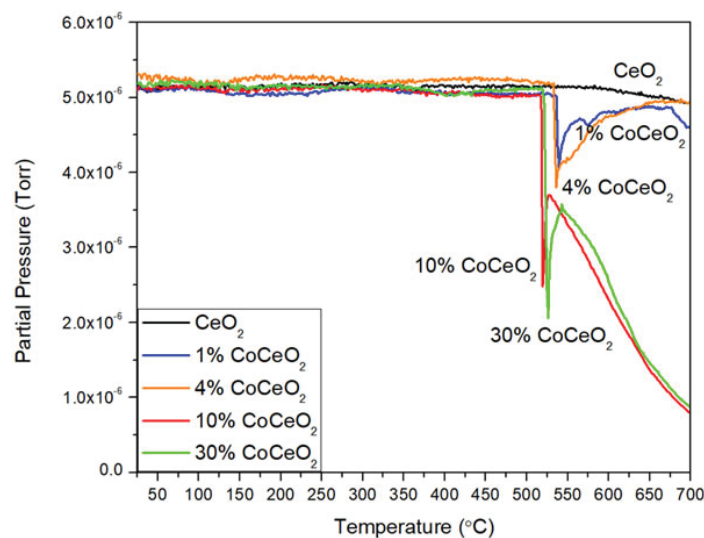


Figure 4a: Methane consumption of different cobalt loadings

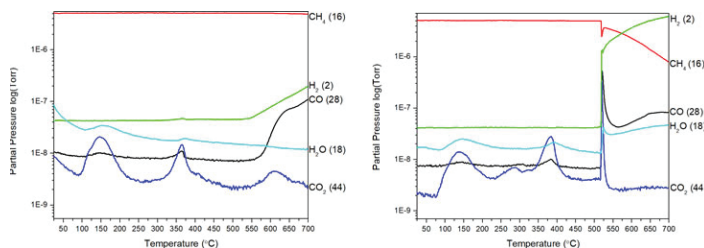


Figure 4b: Comparison of product formation between bare  $\text{CeO}_2$  and the 10%  $\text{CoCeO}_2$

### Catalyst Structural Properties: ex situ and in situ x-ray diffraction (XRD)

#### Ex situ XRD Analysis

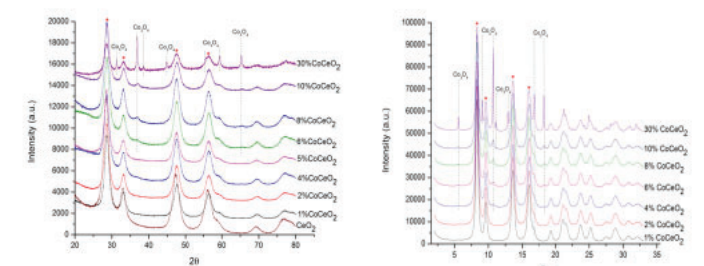
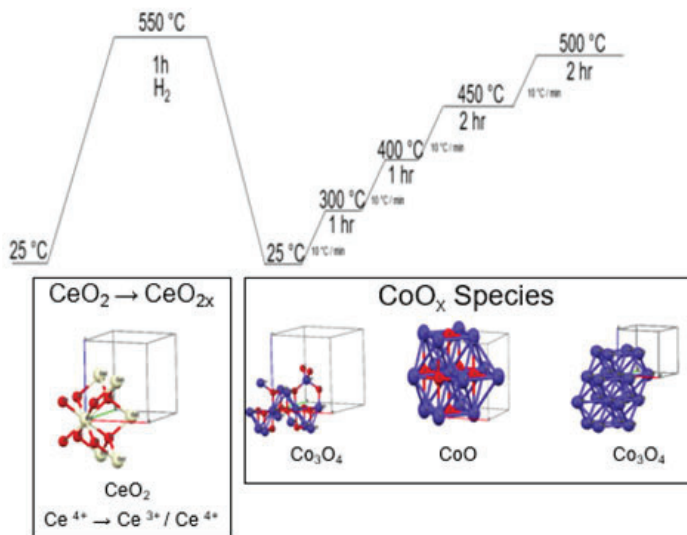


Figure 5a: Ex situ laboratory XRD Figure 5b: Ex situ Synchrotron XRD



**In situ Experiment**



**As Prepared → Pretreatment in H<sub>2</sub> → DRM reaction**

Figure 6a: Reaction Temperature Ramp

**In situ XRD: 10% Co-CeO<sub>2</sub>**

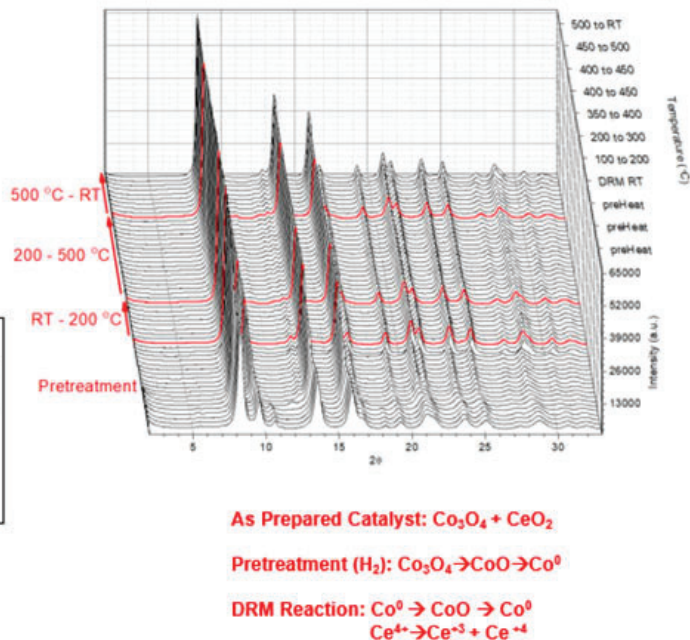
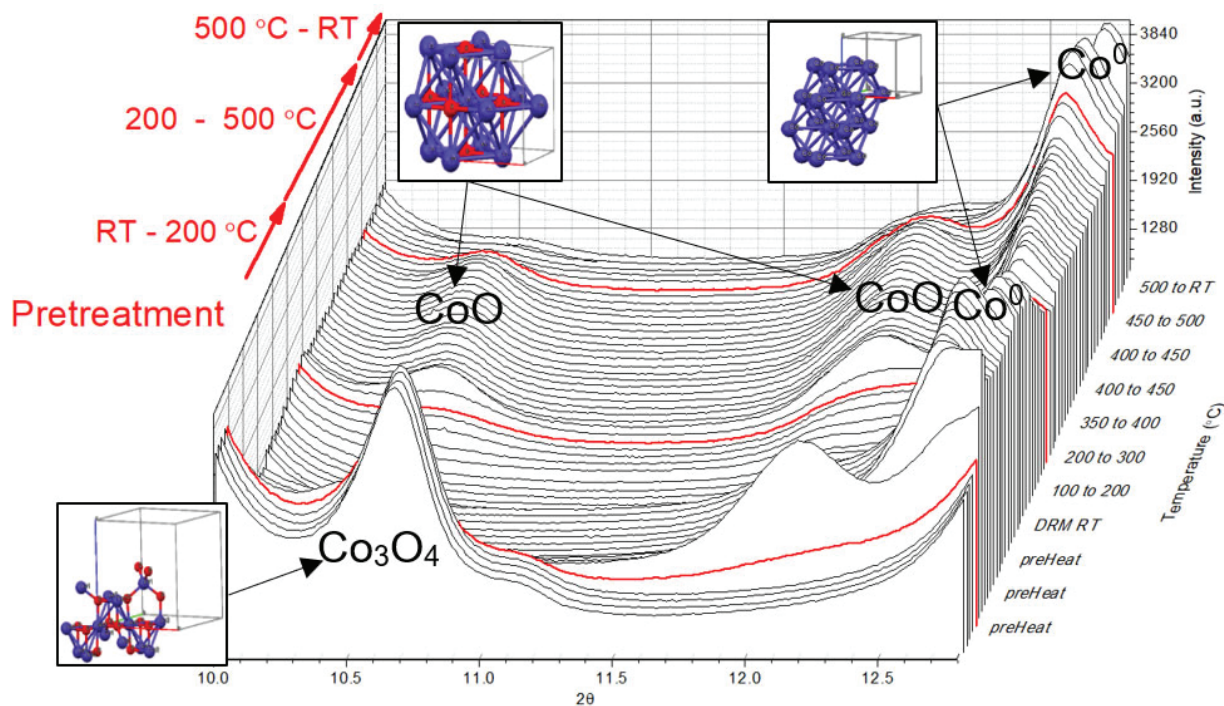


Figure 6b: In situ XRD for 10% CoCeO<sub>2</sub>



**As Prepared Catalyst: Co<sub>3</sub>O<sub>4</sub> + CeO<sub>2</sub>**

**Pretreatment (H<sub>2</sub>): Co<sub>3</sub>O<sub>4</sub> → CoO → Co<sup>0</sup>**

**DRM Reaction (CH<sub>4</sub> + CO<sub>2</sub>): Co<sup>0</sup> [RT] → CoO (d)/Co<sup>0</sup> [200 °C] + CoO/Co [200 - 500 °C] → Co<sup>0</sup> (d) [500 °C]**  
**Ce<sup>4+</sup> → Ce<sup>3+</sup> + Ce<sup>4+</sup> [RT - 500 °C]**

**RT= room temperature**  
**(d)= dominant species**

Figure 6c: In situ XRD for 10% CoCeO<sub>2</sub>

### III. Results

#### Catalyst Morphology

Figure 3: Transmission Electron Microscopy (TEM) was used to study the 2% CoCeO<sub>2</sub> catalyst to look at the size of the crystalline CeO<sub>2</sub> and Co<sub>3</sub>O<sub>4</sub> nanoparticles in the as prepared catalyst. A sharp interface between the two nanoparticles is clearly visible.

Figure 4a shows that the 10% CoCeO<sub>2</sub> activated CH<sub>4</sub> at the lowest temperature (519 °C), and this is when the catalyst has been reduced from as prepare Co<sub>3</sub>O<sub>4</sub> to Co<sup>0</sup>. CeO<sub>2</sub> on its own did not show any CH<sub>4</sub> consumption. The products obtained from CH<sub>4</sub> were plotted in Figure 4b, and it was observed that as Cobalt loading was increased, methane consumption lead to CO, CO<sub>2</sub>, and H<sub>2</sub> production at the temperature of 519 °C.

Ex Situ laboratory XRD results (Figure 4a) show that with Cobalt loadings between 1% and 5%, there is no visible CoO<sub>x</sub> phases. 2θ values corresponding to the Ceria, CeO<sub>2</sub> [\*], remain constant. Co<sub>3</sub>O<sub>4</sub> formation is visible when the Cobalt loading is equal to or higher than 6% for the ex situ laboratory XRD data. Ex Situ synchrotron XRD analysis (Figure 4b) shows CoO<sub>x</sub> phases with better resolution compared to ex situ laboratory XRD (Figure 4a) along with the CeO<sub>2</sub> [\*] diffraction patterns. CoO<sub>x</sub> patterns were clearly visible with the 4% CoCeO<sub>2</sub> sample in the ex situ synchrotron XRD data. Both results (Figures 4a & 4b) show that the 30% CoCeO<sub>2</sub> sample contained well-defined crystalline CoO<sub>x</sub> features as shown by the sharpness of their peaks.

Figure 5a shows the temperature ramp for the experiment along with the CoO<sub>x</sub> phases that form during the reaction. Figure 5b shows the changes happening to the structure of the 10% CoCeO<sub>2</sub> catalysts during the pretreatment and under DRM reaction conditions. By applying Rietveld analysis, it was found that the catalyst was in its active state at 500 °C which is Co<sup>0</sup> on partially reduced CeO<sub>2x</sub> support (Ce<sup>3+</sup> + Ce<sup>4+</sup>). Figure 5c provides a detailed description of what structural changes are taking place in the 10% CoCeO<sub>2</sub> catalyst during the DRM reaction.

Figure 7: Rietveld sequential refinement shows there is no significant CeO<sub>2</sub> reduction after the pretreatment (150 minutes or 2.5 hours).

Residual gas activity (RGA) analysis shows the catalytic performance of the different Cobalt loadings under DRM reaction conditions. Figure 6a shows that at 500 °C, the 10% CoCeO<sub>2</sub> cata-

lyst had highest production of CO, and this is the catalyst's active state which is composed of Co<sup>0</sup> (metallic), on partially reduced CeO<sub>2x</sub> (Ce<sup>3+</sup> + Ce<sup>4+</sup>). Figure 6b shows the results plotted for each catalysts in the temperatures of 300 °C, 400 °C and 500 °C. CO formation was highest for the 10% CoCeO<sub>2</sub> sample at 450 °C and 500 °C.

### IV. Conclusions

- The 10% CoCeO<sub>2</sub> was the best catalyst of this study.
- TPR analysis showed that the 10% CoCeO<sub>2</sub> catalyst had the best methane activation at the temperature of 519 °C.
- The active state of the catalysts was determined to be Co<sup>0</sup> (metallic) on partially reduced CeO<sub>2x</sub> (Ce<sup>3+</sup> + Ce<sup>4+</sup>) with Rietveld analysis on in situ XRD measurements.
- The partially reduced Ceria (CeO<sub>2</sub>) support contains oxygen vacancies that play an important role in the activation of CO<sub>2</sub> which leads to the production of CO.<sup>1,2</sup>
- Co-CeO<sub>2</sub> catalysts are potential cost-effective candidates for the Dry Reforming of Methane reaction.

### V. References

- <sup>1</sup>Liu, Z et al. Angew. Chem., Int Ed. 2016, 55 7455-7459
- <sup>2</sup>Lustemberg, P.G. et al. ASC Catal. 2016 6, 8184-8191

### VI. Acknowledgements

This project was supported in part by the U.S. Department of Energy, Chemical Science Division (DE-SC0012704), Office of Science, and Office of Workforce Development for Teachers and Scientists (WDTS) under the Community College Internship Program (CCI).

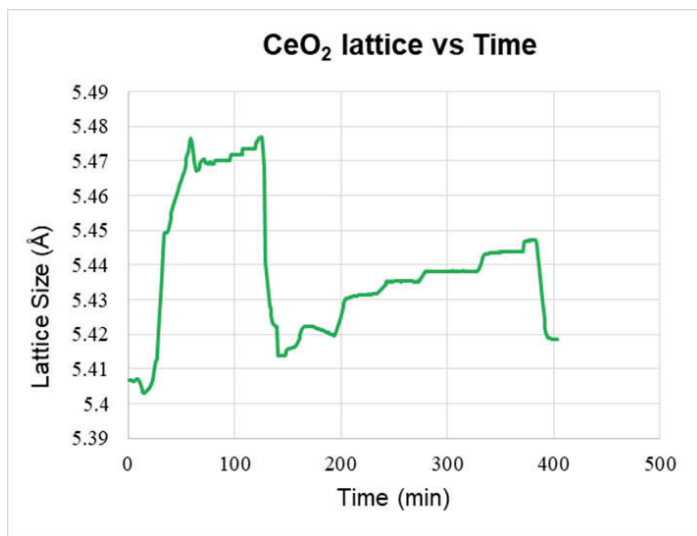


Figure 7

### Catalytic Performance in DRM, CH<sub>4</sub> + CO<sub>2</sub> → 2CO + 2H<sub>2</sub>: Residual Gas Activity (RGA)

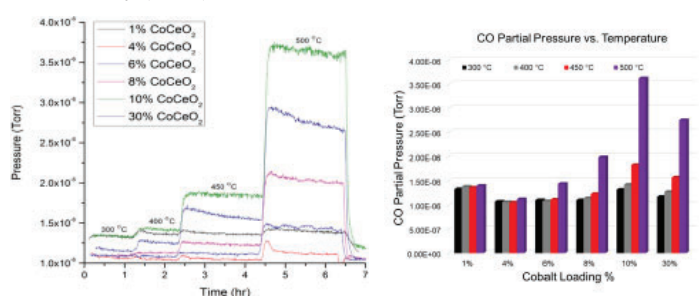


Figure 8a: RGA data of Carbon Monoxide formation for the different Cobalt loadings. Figure 8b: RGA analysis of Carbon Monoxide formation.

# Using Advanced Metering Infrastructure for improved grid phase balancing

Hayden Sierra

Electrical Engineering, University at Buffalo, State University of New York, Buffalo, NY, 14260

Robert Lofaro and Xiaoyu Wang

Sustainable Technologies Department, Brookhaven National Laboratory, Upton, NY, 11973

## Abstract

**Advanced Metering Infrastructure (AMI) is a system of meters installed in the electric grid that track power usage in real time and relay the information to both the utility and consumer. This data can then be used to make real world adjustments to improve the efficiency of the distribution grid. One application of AMI technology is improved phase balancing, in which power losses that occur today will be greatly reduced. By modeling the Route 110 electrical system on Long Island using CYME software, we at Brookhaven National Laboratory (BNL) demonstrated how balancing the load on each phase using AMI data results in fewer losses than conventional balancing methods. AMI is expensive to install and most utilities do not currently have it in their systems, but this is changing as modernization of the electric grid is performed. Results from this study show that using AMI technology to perform phase balancing decreased power losses and allowed for grid changes that could save utilities up to 184,000 kWh a year that would have been lost.**

## I. Background

### A. Advanced Metering Infrastructure

AMI technology is a new innovation in the power distribution world. Normally there is a meter installed in a house or commercial building that records how much power is used per month or per day and nothing else. It does not identify days when more or less power was used, or if the power is out. AMI technology is the next iteration of standard meters that will help pave the way to the adoption of Smart Grid across the country. The infrastructure includes smart meters, communication networks in different levels of the infrastructure hierarchy, Meter Data Management Systems, and the means to integrate the collected data into software application platforms and interfaces [1]. Access to this information in real time as opposed to once a month could al-

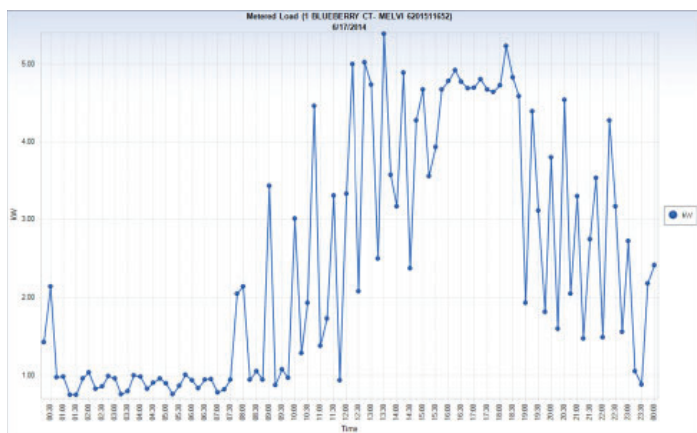


Figure 1. Example of AMI data collected over the course of June 17, 2014

low for more accurate billing and faster response time to outages, as well as many other applications.

For this study, data from multiple AMIs installed in the Route 110 distribution grid were collected on power usage to feed a CYME simulation of a sample distribution feeder. Without the real usage data, CYME would instead generate a generic load flow, which may not have resulted in reliable outputs. Figure 1 shows an example of the data collected from an AMI device over the course of one day.

### B. Load Balancing

When a power plant generates power, it generates three different phases, and each phase goes on a separate wire with a common ground for all of them. The power on these three wires then gets stepped up to high voltage lines to be able to cross long distances with minimal losses. The high voltage wires eventually lead to a substation where the power is stepped down to a lower voltage to be transported to various consumers. The three wires, each carrying one phase, then service different customers individually. The customers use the power to operate different loads, such as motors, appliances, lights, etc. Depending on the situation, some customers may have more loads than other customers, and may draw more power. This could result in one of the phases providing more power than the other phases.

Since the power plant is generating each of the three phases evenly, if one phase is supplying more power to customer loads than any of the other two, it could strain the generator by creating an unbalanced system. Figure 2 shows a decomposition of unbalanced and balanced loads, and Figure 3 shows an example of one method to calculate the unbalance factor. Strain on the generator then causes decreased efficiency and power generation losses, which leads to a loss of revenue for the utility. This is why it is important for utilities to keep the phases balanced. Utilities periodically balance the phases to account for new loads placed on the system over time to avoid such problems; however, they typically have limited load data available so they may not know the unbalance factor accurately.

With the current power grids that we have today, the only way to balance the loads is by manually switching where the power is flowing based on just peak and off-peak conditions. Upgrading to

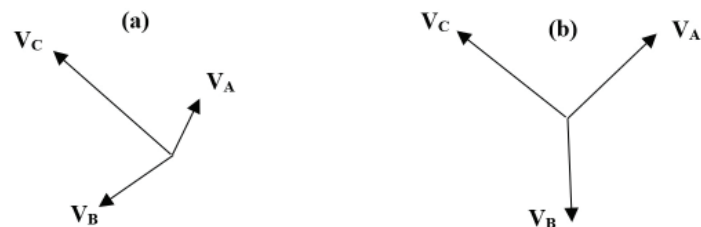


Figure 2. Decomposition of unbalanced (a) and balanced (b) loads



Smart Grids with AMIs installed will make this process as simple as looking at the load conditions of the grid in real time and then rerouting power where it needs to go with the push of a button. This can save utilities money that is being lost every year due to unbalanced loads.

- IEEE Std. 936 (1987): Phase voltage unbalance rate.

$$IEEE_{V_{936}} = \frac{\text{Maximum of } \{V_{an}, V_{bn}, V_{cn}\} - \text{Minimum of } \{V_{an}, V_{bn}, V_{cn}\}}{\text{Mean of } \{V_{an}, V_{bn}, V_{cn}\}} \times 100$$

Figure 3. Example of IEEE unbalance factor calculation [2]

## II. Methods

### A. Overview of the Study

This study consisted of using CYME to run simulations of the Route 110 power distribution grid using the data collected from AMIs in 2014 in an attempt to use load balancing algorithms to reduce power loss. The first step was to create the model in CYME. CYME Power Engineering Software offers “an extensive line of Power Engineering Software that feature some of the most advanced analysis tools for transmission, distribution and industrial power systems.”[3] This powerful tool is what makes the analysis of the Route 110 distribution grid possible. CYME can simulate power flows through the transmission grid by using profiles that contain the power consumption of all the consumers on the grid. AMIs and CYME work together to make a better system possible.



Figure 4. The Route 110 distribution system recreated in CYME

Every wire, transformer, and substation is present in the model including wire density, length, and diameter. Every detail about the distribution grid was modeled in CYME. Figure 4 shows what the full Route 110 model looks like in CYME, and Figure 5 shows the geographical area that the model encompasses. A phase balancing base case was run using the methods utilities use today to balance their grids. Then multiple simulations were run using AMI data to help balance the grid. The differences in savings were then compared between the two methods.

### B. Simulation Process

The first simulation to run was a default control load flow on electrical feeder 7UM657 with no load balancing changes. Figure 6 shows the South Farmingdale part of the grid where feeder 7UM657 is located. After running the simulation and recording the power losses, load balancing was applied based on a single specific time point during one year, the peak load instance for example, which is the way utilities balance their grids today. Due to the data availability, we randomly selected one time point in this study as the base case. The power losses before balancing and after balancing using the utilities’ method were then used to find the total savings due to load balancing. The next simulation instead used AMI data collected on June 17, 2014 to feed the simulation.

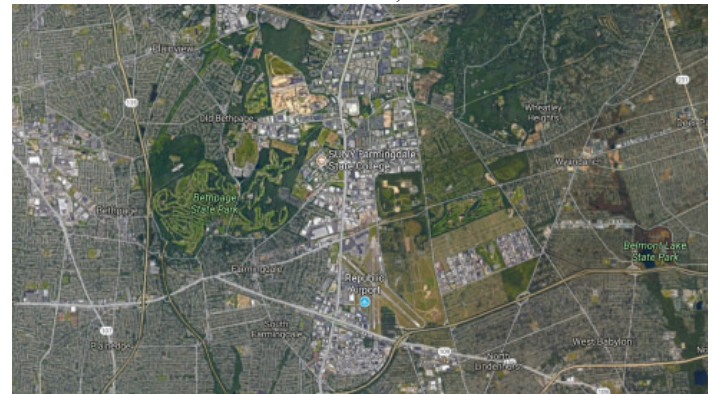


Figure 5. The geographical area of the Route 110 distribution grid [4]

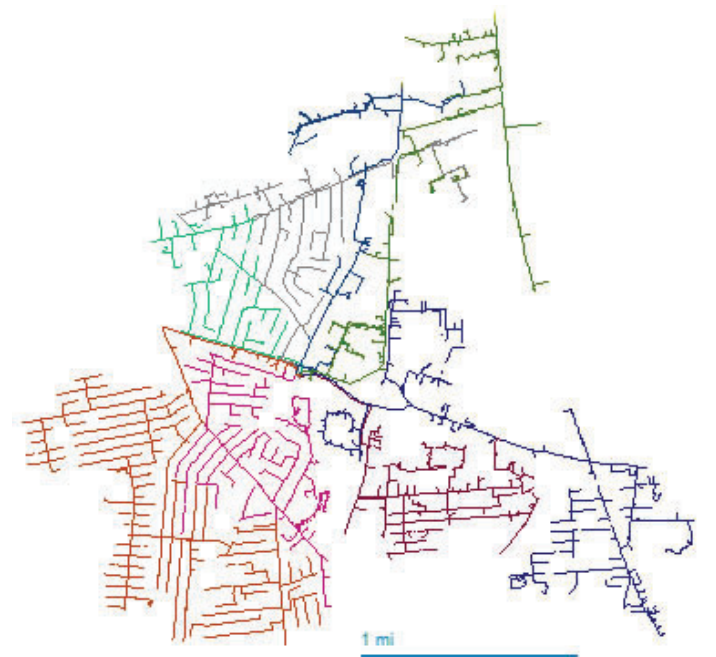


Figure 6. The South Farmingdale part of the Route 110 distribution system

on June 17, 2014. After running the base AMI simulation, data was collected and set aside for later comparison against the load balanced results.

The next step was running the load balancing algorithms provided in the CYME software. There are four options to choose from with regards to how to prioritize balancing the loads, but a minimum kVA unbalance factor of 1% was chosen for this experiment. Along with choosing what to prioritize, there are also different outputs that can be selected. For this experiment a standard summary report and a kVA profile graph of feeder 7UM657 were chosen. The balancing algorithm was then allowed to run using AMI data. Once the balancing program was done, it listed changes that could be made to certain feeders on the grid to route the power in a more effective way. The changes suggested to feeder 7UM657 by the balancing algorithm were then made, and the load flow was again run through the simulation to see if efficiency was in fact improved.

The next simulations that were run were done so to show the benefits of using AMI data to do load balancing over the conventional method of load balancing. One group of simulations focused on six different feeders and the effects that two different load balancing techniques have on the power savings over the course of a day, and another group of simulations focused on how AMI data can be used over a period of five months.

### III. Data and Results

#### A. Load Balancing on Feeder 7UM657 with Utility Balancing Method used Today

The resulting losses for the unbalanced load flow simulated through feeder 7UM657 were 205kW. Multiplied by 24 hours this value becomes 4,910kWh per day. After the utility balancing method was used, which is balancing the load based on what the load is at one specific time point, the resulting losses were reduced to 202kW, or 4,855kWh per day. Taking the difference between the losses before and after balancing results in a total of 55kWh per day saved. This comes out to a savings of 20,075kWh per year, which is enough to power almost 2 more homes. [5]

#### B. Load Balancing on Feeder 7UM657 with AMI Data

The results of the load flow with the AMI data before any balancing shows that there is a total loss of 683kW, or 16,392kWh per day. The higher losses recorded are a result of the accuracy of the AMI data. Utilities can only tell what the losses are at a single time point, while AMI data can find the losses accurately over an entire day. Figure 7 shows the kVA profile of feeder 7UM657 before any load balancing is done. From this graph it can be seen that the power from phase C of the distribution grid is much higher at a peak of 4,075 kVA compared to phases A and B which stay below 3,000 kVA. In an ideal system these three phases would be overlapping each other. In order to bring these phases closer together, changes must be made to the loads each phase serves that are suggested by the load balancing algorithms.

After running the load balancing algorithms with AMI data, the program outputs a table of all the feeders that can be adjusted

Location summary										
		Phase A (kVA)	Phase B (kVA)	Phase C (kVA)	Phase A (A)	Phase B (A)	Phase C (A)	Ineutral (A)	Total Losses (kW)	Average kVA Unbal.
7UM657	Before	2643.31	2690.47	3764.38	330	338.09	473.77	146.24	683.45	24.13%
	After	3036.09	3028.26	3029.48	377.17	374.02	373.38	35.87	662.36	0.16%
7UM658	Before	1265.46	2125.55	1461.42	157.98	267.1	183.93	95.37	683.45	31.41%
	After	1616.97	1620.03	1617.9	200.87	200.09	199.4	30.1	662.36	0.11%
7UM656	Before	1193.41	1655.62	1874.61	148.99	208.05	235.93	77.28	683.45	24.21%
	After	1568.52	1581.16	1571.5	194.85	195.29	193.68	14.29	662.36	0.47%
7UM655	Before	3131.71	3160.04	2859.53	390.97	397.1	359.89	26.46	683.45	6.26%
	After	3054.92	3036.48	3049.69	379.5	375.03	375.87	7.33	662.36	0.35%
7UM911	Before	1151.94	880.78	1282.66	143.99	109.99	160.94	46	474.54	20.30%
	After	1100.12	1118.04	1098.7	137.43	139.93	137.62	9.66	473.92	1.12%

Table 1. Location summary of feeder that could be adjusted after running the load balancing software

Recommended rephasing for location : Source HN_7UM657 (7UM657) (* means applied by user)													
Section ID	Rephasing (kVA)				Phase A (kVA)	Phase B (kVA)	Phase C (kVA)	Phase A (A)	Phase B (A)	Phase C (A)	Ineutral (A)	Total Losses (kW)	Average kVA Unbal.
	A	B	C										
*C.03230.9891_OH(101116-1)			to A 479.35	Before	2644.26	2687.55	3759.99	329.2	334.65	468.62	138.97	671.99	24.07%
				After	3189.57	2665	3236.84	396.43	329.51	398.35	31.56	662.78	12.06%
*C.03248.1125_OH(101776)			to B 185.8	Before	3190.23	2664.13	3236.59	397.03	328.97	398.3	31.08	662.69	12.08%
				After	3199.59	2860.88	3033.85	398.2	353.93	372.66	16.7	662.59	5.63%
*A.03248.8730_OH(101725)	to B 151.48			Before	3200.47	2859.96	3034.03	398.76	353.22	372.89	17.85	662.64	5.66%
				After	3036.64	3029.59	3028.39	377.57	374.93	372.21	39.9	663.64	0.17%

Table 2. The specific changes made to feeder 7UM657 after running the load balancing software

on the part of the grid that is being simulated, as well as what specific changes to make to them. This table can be seen in Table 1. For the purposes of this experiment, only feeder 7UM657 will be adjusted. Table 1 also shows that due to the changes made by the load balancing algorithms, total losses go from 683kWh to 662kWh. This results in a total savings of 504kWh per day and 183,960kWh per year. That's enough to power over 15 homes. [5] The changes suggested by the load balancing software consist of shifting certain amounts of power from one phase to another. A detailed table of these changes can be seen in Table 2.

Once the balancing changes were applied to feeder 7UM657, the simulation was run with the same load flow as the control grid. The results were what was expected after looking at the location summary. As can be seen in Figure 8, all three phases are now much closer to each other, and even overlap at some points. The range that the phases stay within is now 3,100 kVA to 3,400 kVA, instead of 2,700 kVA to 4,075 kVA as before. Since the loads are more evenly balanced, there is less strain on the generator to keep up with one phase in particular. This leads to the 21.09 kW per day decrease in losses.

### C. Load Balancing on Feeders with AMI Data Using Two Balancing Techniques

Two feeders from the three different sections of the Route 110 transmission grid were selected for this batch of simulations. Two different balancing techniques were used to balance the loads of the feeders, and the resulting power savings were compared. The two balancing techniques used were 1 kW loss reduction and 1% unbalance factor. The results of the simulations can be seen in Table 3.

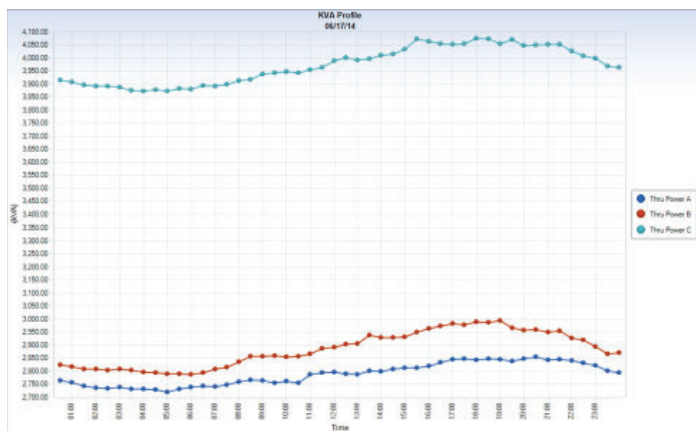


Figure 7. The kVA profile of feeder 7UM657 before load balancing

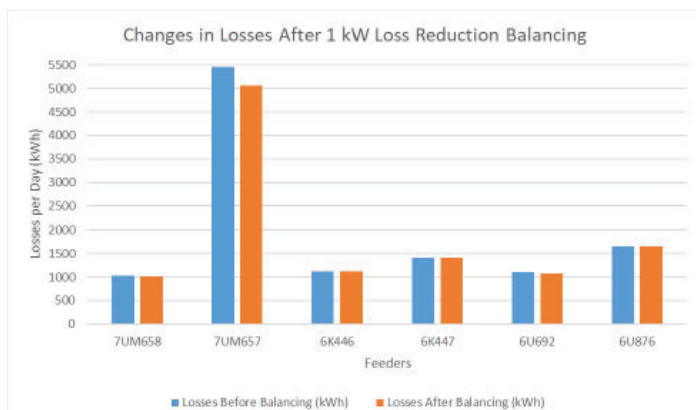


Figure 9. Graph of change in losses after 1 kW loss reduction load balancing

Savings were calculated using the residential rate of \$0.36 per kWh as charged by PSEG LI. [6] As can be seen by the results in Table 3, different feeders responded differently to the two different balancing criteria. Some improved, worsened, or stayed the same. The benefit that AMI data provides is that a utility can pick which balancing criteria they want to use based on the results of simulations. AMI data allows options when it comes to balancing loads. Figures 9 and 10 show the change in losses due to the two different balancing methods.

Using tools like CYME Power Engineering Software and AMI data gives utilities more information about power flow than ever. They can then use this information to improve the efficiency of the grid using whatever balancing criteria saves the most power.

### D. Load Balancing on Feeder 7UM120 with AMI data over 5 Months

For the last batch of simulations we looked at how AMI data over the course of 5 months could help improve the grid. Feeder 7UM120 was selected as the focus of this experiment. The simulation was run for 5 months with no balancing. Then the load was balanced using a 1% unbalance factor criteria and run again. Figures 11 and 12 show the kVA profile of feeder 7UM120 before and after balancing.

Energy losses were reduced from 10,334kWh daily to 9,873kWh daily. That results in 168,265kWh saved over the course of a year. Using AMI technology allows for simulations of this length because utilities will have the exact data instead of just estimates of when peaks and lows will occur. Utilities could also

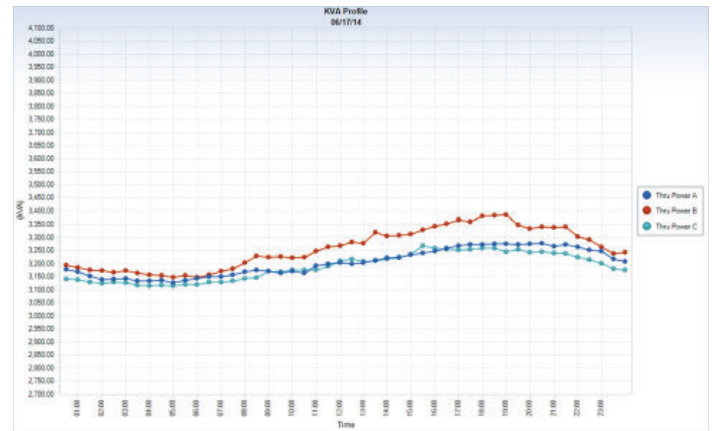


Figure 8. The kVA profile of feeder 7UM657 after load balancing

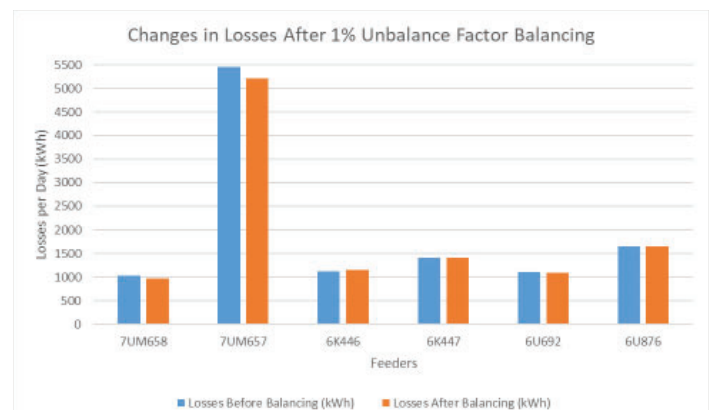


Figure 10. Graph of change in losses after 1% unbalance factor load balancing



Voltage Drop - Unbalanced	South Farmingdale	7UM657	Unbalance Factor	4:00 PM	345.08	324.875	7.21	143.07	52220.55			
				4:00 PM - 12:00 AM	345.96	325.845	7.24					
				12:00 AM - 8:00 AM	1747.13	1614.595	47.71					
			1 kW Loss Reduction	8:00 AM - 4:00 PM	1830.86	1712.525	42.6	87.46	31922.9			
				4:00 PM - 12:00 AM	1883.615	1737.05	52.76					
				12:00 AM - 8:00 AM	1747.13	1670.585	27.56					
			1% Unbalance Factor	8:00 AM - 4:00 PM	1830.86	1747.59	29.98	0	0			
				4:00 PM - 12:00 AM	1883.615	1800.515	29.92					
				12:00 AM - 8:00 AM	360.135	360.135	0					
Newton-Raphson - Unbalanced	State School	6K446	1 kW Loss Reduction	8:00 AM - 4:00 PM	377.53	377.53	0	-12.09	-4412.85			
				4:00 PM - 12:00 AM	381.835	381.835	0					
				12:00 AM - 8:00 AM	360.135	373.095	-4.67					
			1% Unbalance Factor	8:00 AM - 4:00 PM	377.53	387.485	-3.58	0	0			
				4:00 PM - 12:00 AM	381.835	392.505	-3.84					
				12:00 AM - 8:00 AM	458.99	458.99	0					
			Voltage Drop - Unbalanced	Ruland Road	6U692	1 kW Loss Reduction	8:00 AM - 4:00 PM	368.975	361.175	2.81	8.41	3069.65
							4:00 PM - 12:00 AM	368.68	360.895	2.8		
							12:00 AM - 8:00 AM	368.69	360.925	2.8		
1% Unbalance Factor	8:00 AM - 4:00 PM	368.975				364.675	1.55	4.63	1689.95			
	4:00 PM - 12:00 AM	368.68				364.395	1.54					
	12:00 AM - 8:00 AM	368.69				364.425	1.54					
Voltage Drop - Unbalanced	State School	6K447				1 kW Loss Reduction	8:00 AM - 4:00 PM	476.755	476.755	0	0	0
							4:00 PM - 12:00 AM	477.875	477.875	0		
							12:00 AM - 8:00 AM	458.99	459.535	-0.2		
			1% Unbalance Factor	8:00 AM - 4:00 PM	476.755	474.475	0.82	0.8	292			
				4:00 PM - 12:00 AM	477.875	477.385	0.18					
				12:00 AM - 8:00 AM	524.67	524.67	0					
			Voltage Drop - Unbalanced	Ruland Road	6U876	1 kW Loss Reduction	8:00 AM - 4:00 PM	564.565	564.565	0	0	0
							4:00 PM - 12:00 AM	567.315	567.315	0		
							12:00 AM - 8:00 AM	524.67	524.38	0.1		
1% Unbalance Factor	8:00 AM - 4:00 PM	564.565				564.145	0.15	0.44	160.6			
	4:00 PM - 12:00 AM	567.315				566.8	0.19					
	12:00 AM - 8:00 AM	524.67				524.38	0.1					

Table 3. A summation of the results from running simulations on 6 feeders with 2 different balancing criteria

choose to look at when the peak and low occur over the course of a few months and balance based on those times to save even more power.

#### IV. Conclusions and Recommendations

By utilizing data collected from AMI technology, utilities can decrease power losses, resulting in large energy savings per year. The money saved using AMI data can then be used to upgrade other power grids with AMI technology and repeat the process to further improve all parts of the grid. Based on the results of this study, it is recommended that all utilities invest in bringing their grids into the modern era. Upgrading to Smart Grids with AMI technology will be expensive, but the savings can be tremendous. Utilities should also invest in a power engineering software to help them balance the grid with the use of data collected from the AMI devices. These enhancements will help propel the United States into the forefront of electric distribution, and will keep it there for years to come.

#### V. References

- [1] National Energy Technology Laboratory for the U.S. Department of Energy. Advanced metering infrastructure, NETL modern grid strategy; 2008.
- [2] Wang Yaw-Juen, Yang Ming-Jer. Probabilistic modeling of three-phase voltage unbalance caused by load fluctuations. IEEE Power Eng Soc Winter Meet 2000;4(January):2588–93.
- [3] “CYME International Inc. - Home.” *CYME Power Engineering Software and Solutions*. Eaton, 2017. Web. 27 June 2017. <<http://www.cyme.com/>>.
- [4] *Google Maps*. N.p., n.d. Web. 27 June 2017. <<https://www.google.co.in/maps/@40.7484423,-73.4050885,11809m/data=!3m1!1e3>>.
- [5] U.S Energy Information Administration, Home Energy Usage. <https://www.eia.gov/tools/faqs/faq.php?id=97&t=3>
- [6] (n.d.): n. pag. Common Residential Electric Rates. PSEG, 2017. Web. 29 June 2017. <[https://www.psegliny.com/files.cfm/rates\\_resi.pdf](https://www.psegliny.com/files.cfm/rates_resi.pdf)>.

#### VI. Acknowledgements

I would like to thank my mentor Robert Lofaro for letting me be a part of his team at the Sustainable Technologies Department. Also I want to thank Xiaoyu Wang and Pat Looney along with the rest of Building 815 for their guidance during my project. Thank you to Zachary Dahl for his contributions and help in the office. Lastly, thank you to my Dad and the rest of the Table for making lunch entertaining as always. This project was supported in part by the Brookhaven National Laboratory (BNL), Sustainable Technologies Department under the BNL Supplemental Undergraduate Research Program (SURP).

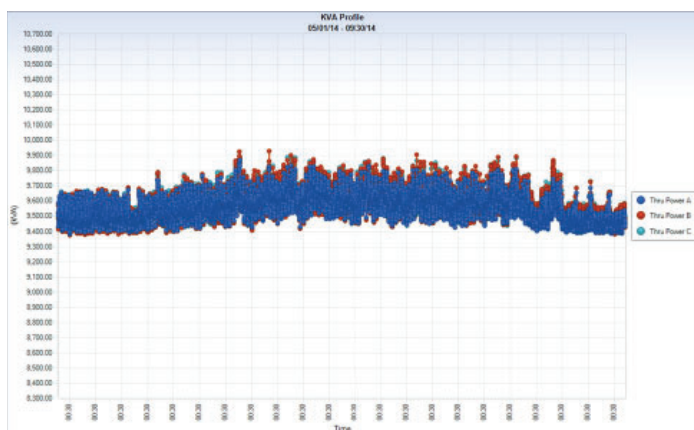


Figure 11. Feeder 7UM120 over 5 months before balancing

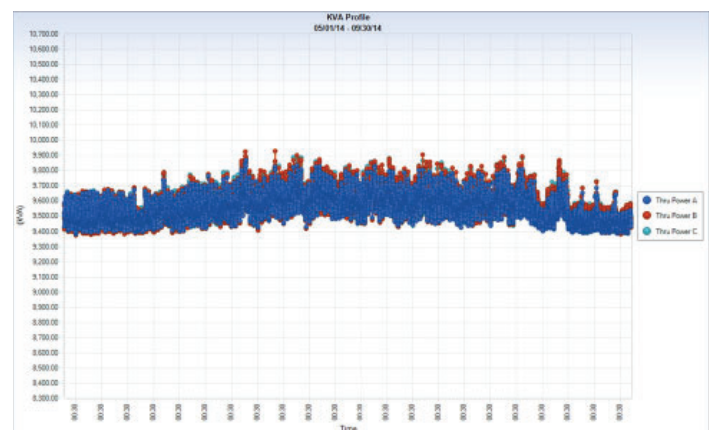


Figure 12. Feeder 7UM120 over 5 months after balancing

# Automated data verification and validation using zero-power nuclear reactors

Sukhjinder Singh

Nuclear Engineering, Rensselaer Polytechnic Institute, Troy, NY 12180

David Brown

Nuclear Science and Technology, Brookhaven National Laboratory, Upton, NY 11973

## ABSTRACT

Nuclear data is used in many facets of the nuclear industry, from determining reactor criticality to waste disposal. For these applications, the Evaluated Nuclear Data File/B (ENDF/B)[1] nuclear data library, is produced by the Cross Section Evaluation Working Group (CSEWG). Data validation is an important step of the process, but it is not uncommon for data to go untested for an extended period of time after being added to the ENDF/B data repository. As a result, the National Nuclear Data Center (NNDC) at BNL created the ADVANCE continuous integration system to automatically run checks on all changes made to the ENDF/B data repository. The goal of this project is to extend the checks available for the ADVANCE system to benchmark the data against critical nuclear reactor simulations. These critical simulations are a diverse set of models of zero-power nuclear reactors that can be simulated with a high degree of credibility. This extension of ADVANCE will set up the runtime environment for autonomous communication between the ADVANCE server, the NNDCs computing cluster, and the nuclear transport codes that run the simulations. To tailor a testsuite to a specific change set, the user can query a database of the available critical assemblies for the assemblies containing materials relevant to the change set. After each revision of the ENDF/B library, the ADVANCE server will run all the relevant simulations on the NNDCs computing cluster, collect the results of the simulations, and publish them on the main build report website. These results will then be available for analysis to study how a change impacts the behavior of the simulated assemblies.

## I. INTRODUCTION

### A. Importance of Nuclear Data

Nuclear data is the cornerstone of any system that undergoes nuclear reactions, including nuclear reactors, radiation detectors and dosimeters, machinery used in nuclear medicine, and even weapons and defense systems. In the United States, the Evaluated Nuclear Data File (ENDF/B), produced by the Cross Section Evaluation Working Group (CSEWG), is the primary nuclear data library used in many of these systems. Other libraries such as the Joint Evaluated Fission and Fusion File (JEFF) in Europe and the Japanese Evaluated Nuclear Data Library (JENDL), produced by the Japan Atomic Energy Agency (JAEA) are also prominent in other parts of the world. CSEWG collaboration is coordinated by Brookhaven National Laboratory (BNL), and the ENDF/B library is managed by the National Nuclear Data Center (NNDC).

ENDF/B contains a variety of nuclear reaction data, such as data for different cross-sections, angular distributions, photo atomic reaction data, and thermal neutron scattering ( $S(\alpha, \beta)$ ) data. If a developer wishes to commit a new set of data obtained from doing an evaluation, the developer could commit the changes

to the ENDF/B source repository located on GForge[2].

In the past, data verification took place as part of CSEWG's peer review. Reviewers verified new evaluations by running individual tests on every new data set. PHASE I testing refers to the pen and paper peer reviews of new evaluations while PHASE II testing took place during larger CSEWG meetings and conferences and involved users running benchmarks on the new data in order to validate it[3].

### B. History of ADVANCE

The JAEA Nuclear Data Center began the process of creating a nuclear data verification and validation system using criticality benchmarks in 2007, but they were not able to fully automate the process[4]. However, ENDF/B-VII.0 first introduced partial automation of data verification using the EMPIRE reaction code.

In order to test the newly committed data as it was committed, the NNDC developed the Automated Data Verification and Assurance for Nuclear Calculations Enhancement (ADVANCE) system. ADVANCE generates build reports that then tell a data evaluator whether the data that was committed passes basic checks run by ADVANCE[5]. These checks include basic ENDF checking codes such as STAN, STANEF, CHECKR, FIZCON, PSYCHE, and INTER[6] as well as checks with processing codes such as PREPRO, Fudge, and NJOY[7]. ADVANCE utilizes buildbot, a continuous integration system, with a boss-worker configuration[8]. The boss queries the NNDC GForge source repository for any changes that have been made in the data. Once a change is detected, the boss assigns its workers different tasks, such as running different checks on the newly committed data. Once all the checks have been completed, ADVANCE publishes the full build report on the ADVANCE webpage[9] for developers to view.

The deployment of the ADVANCE continuous integration system allows for data to be tested upon every commit, which then leads to smaller changes that need to be processed. There is no need to wait for experts that know how to use each processing code. Running each check on the nuclear data allows for small errors to be detected in both the data and in the processing codes themselves, which in turn leads to better performance of each revision of the ENDF/B library.

### C. Importance of criticality benchmarks

The purpose of this project was to extend the tests available for ADVANCE to include criticality simulations of zero-power nuclear reactors. These zero-power reactors are models based on assemblies from International Handbook of Evaluated Criticality Safety Benchmark Experiments[10]. These assemblies are zero-power nuclear reactors that contain fissile material such as plutonium or highly enriched uranium. These critical assemblies can be modeled with very high fidelity and simulated using neu-



tron transport codes to produce a variety of outputs, including the average neutron multiplication factor ( $k_{eff}$ ). Figures 1 and 2 show two typical, but very different, test cases.

The neutron multiplication factor,  $k_{eff}$  describes the ratio of neutrons from one generation of fission events to another generation of events. This is important in nuclear reactors because it allows us to determine how far a reactor deviates from criticality ( $k_{eff}=1$ ), which in turns provides us with information regarding the state of the reactor. A  $k_{eff}$  of 1 describes a reactor as exactly critical, meaning the number of neutrons produced through fission equal the number of neutrons absorbed to induce fission. A  $k_{eff}$  greater than 1 implies a reactor is supercritical, meaning more neutrons are being produced than being absorbed in the reactor. A  $k_{eff}$  of less than 1 implies a reactor is subcritical, meaning less neutrons are being produced than being being absorbed in the reactor. In order to control a sustained nuclear reaction, a reactor must be delayed-critical, meaning the  $k_{eff}$  is equal to one once the delayed neutron contribution is taken into account. The presence of these delayed neutrons allows for precise reactor control in modern nuclear power reactors.

The ICSBEP produces benchmark  $k_{eff}$  values for each critical assembly, usually hovering at or close to a value of 1 depending on the critical assembly. These  $k_{eff}$  are determined through experimental evaluation after constructing the critical assembly. These evaluations often involve evaluators using accelerators to collect different reaction data for an isotope. Using neutron transport codes such as COG or MCNP, a user can compare the output  $k_{eff}$  value calculated from the simulation to the benchmark experimental  $k_{eff}$  value. By comparing the two  $k_{eff}$  values, one can study if a set of changes caused the output  $k_{eff}$  values to shift closer to or further from the accepted benchmark values, which provides additional insight to the performance of the latest revision of the ENDF/B data repository.

## II. METHODS

Whenever a data evaluator comes out with a new set of data obtained from performing an evaluation of an isotope, that data is committed to the NNDC's GForge source repository. AD-

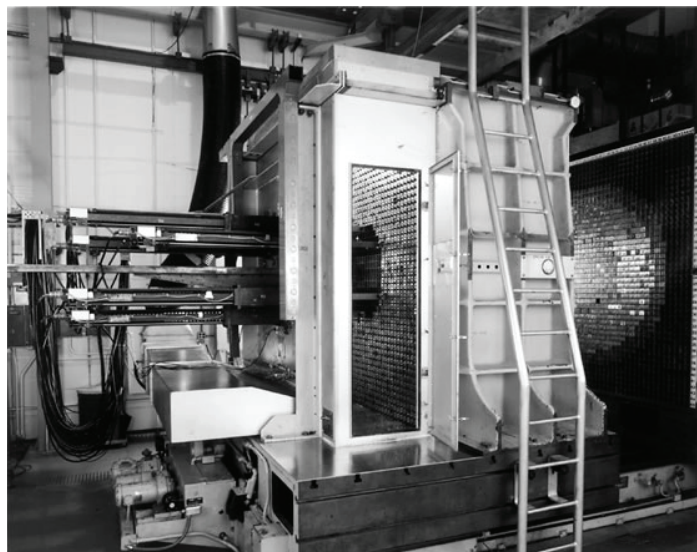


Figure 1: HEU-MET-FAST-067 - HEU (93%  $^{235}\text{U}$ ) cylindrical cores with tungsten, graphite, and aluminum diluents with a dense aluminum reflector[10]

VANCE uses buildbot to continuously poll for changes detected in the source repository. When a change is detected, ADVANCE then deploys build workers to perform various tasks. One of these workers will be deployed in order to run the criticality simulations. Before the worker is deployed, the NJOY processing code formats the raw ENDF/B evaluations into ACE files that can be used by the rest of the system. The conversion process includes resonance reconstruction and doppler-broadening of cross sections, incorporation of radiation heating, use of thermal scattering data, generation of unresolved resonance probability tables, and use of other relevant NJOY modules. The critical assemblies are then simulated using neutron transport codes.

Neutron transport codes use Monte-Carlo methods to perform calculations on the critical assemblies. For this project, COG11 was provided by Lawrence Livermore National Laboratory (LLNL)[11]. Currently, COG11 has the ability to track photons, electrons, and neutrons. It is an export-controlled code that is also licensed for use in nuclear applications such as criticality safety. COG11 uses custom data files known as libraries to define the nuclear data that it uses. In order to use the latest data available from the NNDC's GForge, it is necessary to compile these libraries for COG using a program known as LibMaker. Currently, LibMaker uses ACE files to compile data libraries relevant to the fast and unresolved resonance regions, and ENDF files for thermal neutron scattering. LibMaker uses three different programs to compile different types of libraries, URRtoCOG, ACEtoCOG, and SABtoCOG. URRtoCOG and ACEtoCOG both use neutron ACE files and an input file with a list of all relevant data as inputs

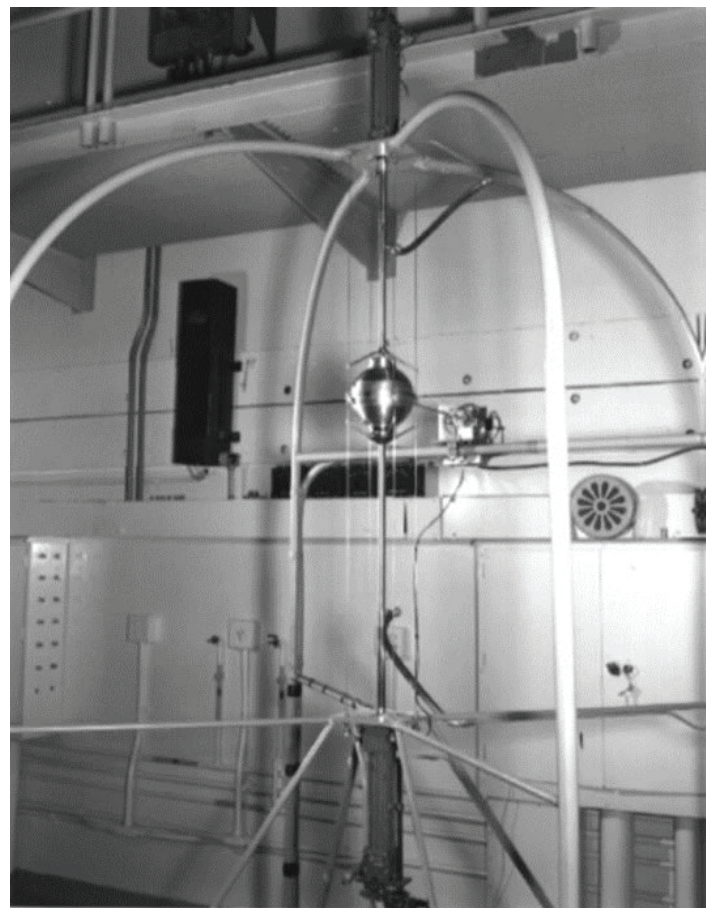
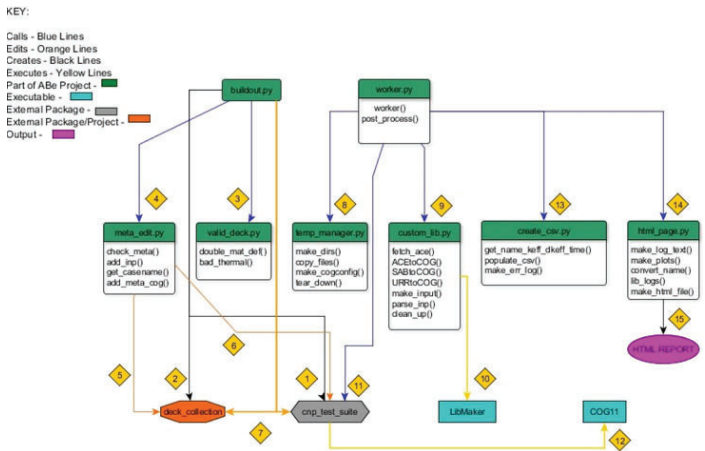


Figure 2: 240Pu JEZEBEL - A bare sphere of Plutonium-239 Metal[10]



**Figure 3: Generalized workflow diagram of the entire system ties together. The steps of the process are detailed below in text. The functions that create the system are show, with the primary two being worker.py and buildout.py.**

to compile a single output data library. SABtoCOG uses thermal scattering ENDF/B files and an input file with a list of relevant data and corresponding stoichiometry values in order to compile a custom thermal scattering library. Each transport code has its own syntax, so models of critical assemblies must be replicated for use with multiple transport codes. For use with COG11, we were given an in-house test suite, a collection of 145 Plutonium (PU) and 350 highly-enriched Uranium (HEU) test cases. The section below will detail how the various Python scripts and components of our system all tie together.

## A. Architecture

### 1. Automated benchmarking scripts

Figure 3 highlights how the system works to generate an output HTML report after a set of changes has been committed on the NNDC’s GForge. It is first necessary to set up the appropriate runtime environment for the run, so a call to buildout.py starts building this environment. It first creates a virtual Python environment so that packages such as buildbot can be installed without administrator privileges. It installs buildbot and initializes a build worker. A JSON formatted configuration file containing information such as usernames and the path to a COG installation is read in by buildout.py. After buildout.py is done setting up the user’s run environment, worker.py then goes through the process of running the relevant assemblies on the NNDC’s computing cluster. The following steps detail the process of setting up the runtime environment for worker.py.

- After confirming that there is a valid installation of COG available on the user’s account, buildout.py begins to checkout LLNL’s cnp test suite using subversion. This is a Python package that is used to determine which assemblies to run and to communicate with the NNDC’s computing cluster. More details on the workflow of cnp test suite are given in the following section.
- buildout.py then checks out deck collection from NNDC’s GForge using git. This is the suite of critical assemblies for COG provided to us by LLNL.
- buildout.py iterates through every critical assembly to verify that there are no errors in the input files. Errors that are currently being detected include the presence of new

thermal materials that do not have corresponding data and syntax errors pertaining to how materials are defined in the critical assembly. If there is an error, the program terminates prematurely with an appropriate exit message.

- buildout.py calls meta edit.py.
- meta edit.py appends metadata to all of the critical assemblies in order for them to be able to be indexed by cnp test suite. This metadata includes the name of the case being tested, the expected runtime for the test, the number of nodes to run on, whether to run this test interactively or not, the type of test being carried out on the assembly, the name of the person who added metadata to the assembly, and the transport code to run the case with.
- meta edit.py appends .inp file extensions to all of the test cases in deck collection for use with cnp test suite.
- buildout.py symbolically links all of the test cases into cnp test suite. Doing so preserves the ability for a user to manually update the deck collection project and allows changes in the source repository of deck collection to be reflected under the appropriate directories in cnp test suite.

It is only necessary to run buildout.py once every few days or weeks in order to update the deck collection and cnp test suite projects if needed. worker.py goes through the process that is run for each commit to the source repository. The following steps detail the steps worker.py takes in order to run all of the relevant critical assemblies on the NNDC’s computing cluster.

- worker.py sets up a run directory in the same directory as itself and a temporary directory under the temporary space on the mother node of the NNDC’s cluster. This space is used for temporarily storing LibMaker output files in order to avoid running into Fortran runtime errors. It then creates a cogconfig11 file that is used by COG in order to point to the correct directory containing the data for that particular run.
- worker.py then calls custom lib.py to start generating custom data library files for COG using LibMaker. It grabs the most recent ACE neutron data and ENDF thermal scattering data in the form of two tarballs. It creates an input file for LibMaker to use, and moves the output library files into the appropriate run directory once LibMaker has finished compiling the libraries. The standard output and error are saved in different files for later use.
- In custom lib.py, ACEtoCOG(), SABtoCOG(), and URRtoCOG() all point to different LibMaker executables to create different library files. COG uses three different types of data libraries in an input critical assembly. These three assemblies include fast neutron data, thermal scattering (sab) data, and unresolved resonance data.
- worker.py then calls cnp test suite, a separate Python package whose workflow is detailed in the next section.
- cnp test suite communicates with COG11 and tells it which critical assemblies to run out of all the available assemblies. These simulations are run on the NNDC’s supercomputing cluster and may take hours or even days to complete depending on the materials changed, so cnp test suite monitors the status of the simulations until completion. COG11 is run in parallel using MPI on the NNDC’s cluster, which allows the Monte-Carlo simulation to be sped up by allowing COG to utilize multiple processors for each simulation.



The NNDC's cluster consists of 25 nodes and 248 total processors, and of those 248 processors, 64 are reserved.

- Upon completion of the jobs on the NNDC's cluster, worker.py creates a csv file by parsing through the run directory to search for an output file for each run. The output file is then parsed for an output keff value. An error log with all errors from running each test case is also created.
- Using the output csv file, html page.py uses matplotlib to generate a plot for each case type and compiles all of the error logs from running all of the critical assemblies.
- All of this information is compiled into an output HTML page which can be viewed in a web browser. These reports have yet to be integrated into the full ADVANCE website.

## 2. cnp test suite

cnp test suite is a Python package that was adapted to BNL's batch system and to COG. It first creates an SQLite3[12] database using a user can query using SQL commands. In our system, a database is generated that consists of critical assemblies containing the material that was changed on the NNDC's GForge. For example, if a change in Zirconium is committed to the source repository, the 4 critical assemblies containing Zirconium will be run as opposed to all 495 available assemblies. Using the output from the database query, cnp test suite communicates with the NNDC's computing cluster until the jobs have been completed. The following steps detail how the package ties together with the rest of the system. The following list details how cnp test suite works by following Figure 4.

- worker.py first makes a call to make db.py. The primary function of this script is to create an output SQLite3 database file.
- make db.py calls various functions from funcs.py in order to make material substitutions to match the existing database. For example, if a material is defined in the input decks using weight percent or number density, it must be converted into atomic fraction.
- funcs.py references the critical assemblies symbolically linked from the deck collection
- project in order to parse through the decks and make material and za substitutions if needed
- make db.py creates the database after parsing through all of the available input decks.

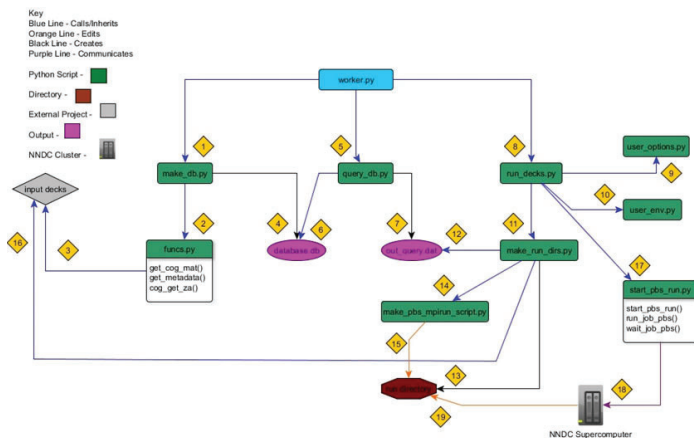


Figure 4: Workflow of cnp test suite. The steps below are numbered to match the flow in the diagram. The various functions in cnp test suite are shown.

- worker.py calls query db.py with an SQL command. This command will be used to pull only the critical assemblies containing the changed za.
- Using the material's ZAID identifier that describes the change on the NNDC's GForge, only the relevant assemblies are pulled from the database.
- An output .dat file is created using the database query. This is a text file containing a list of the assemblies containing the material that was changed.
- worker.py then calls run decks.py while passing on information such as where the cogconfig11 file is located and where the run directory for this library revision is located.
- run decks.py reads in pre-defined runtime options defined in user options.py, such as time until a job is treated as "timed-out", or how many jobs to submit to the NNDC's cluster at one time.
- run decks.py reads in more pre-defined options such as the path to the user's COG executable.
- run decks.py calls make run dirs.py.
- make run dirs.py reads each critical assembly from the output dat file generated by query db.py.
- make run dirs.py creates a subdirectory (in the main run directory) for each critical assembly in the dat file.
- make run dirs.py call make pbs mpirun script.py to create a PBS shell script compatible with the NNDC's batch scheduling system for the supercomputing cluster. This shell script includes commands that define the amount of computing resources each critical simulation will use and includes the command to tell COG to run in parallel using MPI.
- make pbs mpirun script.py moves the PBS script for that critical assembly into the existing subdirectory for that critical assembly.
- make run dirs symbolically links the critical assembly input file and the COG executable into the subdirectory for that critical assembly
- run decks.py calls start pbs run.py in order to begin submission of the jobs to the NNDC supercomputing cluster. start pbs run.py first creates lists of a size defined in user options.py that will represent how large each wave of submitted jobs will be. It then iterates through these lists and submits each PBS script in each critical assembly subdirectory to

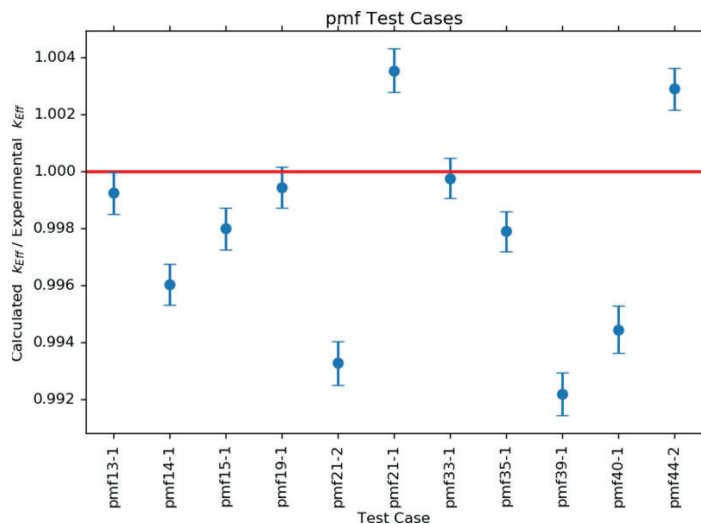


Figure 5: PU-MET-FAST graph generated by matplotlib[13] for Iron



the NNDC cluster.

- The NNDC cluster runs the jobs submitted from start pbs run.py and is polled continuously for completion of that batch of jobs. The PBS scripts provide the various nodes on the cluster with the instructions to execute a COG run using the appropriate critical assemblies. The cluster is continuously polled by start pbs run.py for the completion of those jobs.
- The NNDC computing cluster dumps the output files from the simulations in the appropriate run directories.

After the simulations have all been completed, the worker.py starts the process of creating a csv file containing information from the run and generated the HTML report. Currently, our system has not published these final HTML reports to the ADVANCE website due to time constraints. In the future, we plan to fully integrate the HTML reports into the main ADVANCE website after restructuring the how the website is currently organized to create a tab to view these HTML reports. We would also need to successfully deploy a build-worker to carry out the tasks detailed above by adapting the main ADVANCE scripts in order to accommodate for another build-worker.

### III. RESULTS

As a result of each revision to the source data repository, ADVANCE generates an html webpage displaying the results from each run. Currently, there are some issues with compiling the  $S(\alpha, \beta)$  data for COG, and a majority of the input decks throw different errors that stem from this issue. Error logs from LibMaker are added to the bottom of the webpage. By using subversion revision tracking, one can study if a new revision to the data on the NNDC's GForge shifted the output keff closer to or further from 1, which would tell us if there are any potential errors in the newly

committed data. Figures 5 and 6 show the results generated from a run using iron as the changed material.

Figure 5 shows a sample output graph that shows the calculated over experimental keff for each test case using matplotlib. The desired keff ratio is 1, as that tells us the simulated input decks have resulting keff values that match the associated benchmark values.

Figure 6 shows a webpage that includes the final graphs broken up by case type and the corresponding error logs from LibMaker and the execution of the input decks.

Currently, the NNDC is working towards an iron evaluation, and the results shown above agree with the results obtained by the NNDC for the test cases that overlap. The results generated with COG extend the cases that were tested by the NNDC while testing the new Iron data. There are some test cases that deviate from the desired keff ratio of 1, such as PU-MET-INTER-002, which presented a keff ratio of 1.018, representing an almost 2% deviation from the desired keff ratio. These anomalies may be caused by a variety of issues, including errors in the reactor model, iron data table issues, or even issues with materials other than Iron that are used in those reactor simulations. These results provide additional insight to where any issues with new evaluations may stem from and are saved so that current and past library performance can be compared to look for improvements in performance.

### IV. CONCLUSIONS

Although this system is new and not yet fully integrated into ADVANCE, it has already complemented the tests currently carried out by ADVANCE. The Nuclear Criticality Safety Program (NCSP) identified automated data verification using the breadth of ICSBEP benchmark data as one of its 5-year goals in FY14[14]. Completion of this project satisfies that goal, as the simulations run are modeled after cases in the ICSBEP handbook. As a result of the availability of criticality tests to ADVANCE, the performance of the ENDF/B library releases will improve as data testers now have a powerful tool to quickly identify issues in the reaction data or the processing of the data. In the case of Iron, the system has already helped validate the accuracy of the latest available reaction data. Future additions to this system can include compatibility with more transport codes such as MCNP and OpenMC and overcoming the issues associated with the compilation of thermal scattering libraries. The completion of this system is a stepping stone towards an even wider variety of applications past criticality benchmarks, including astrophysics applications, shielding benchmarks, or even defense applications.

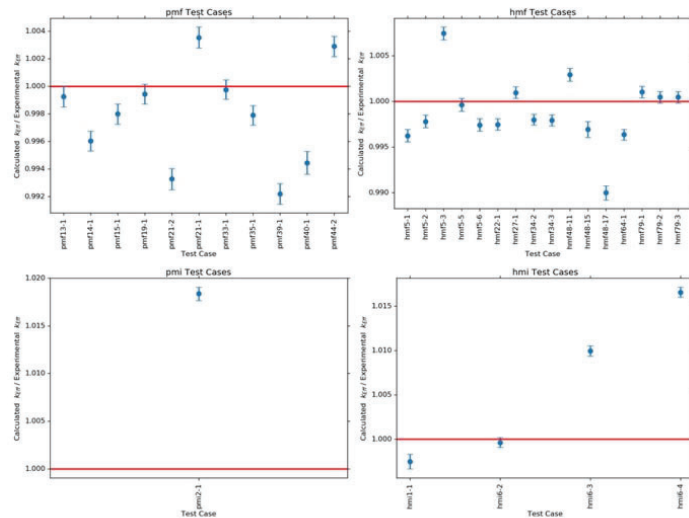
### V. ACKNOWLEDGEMENTS

This project was supported in part by the U.S. Department of Energy, Office of Science, Office of Workforce Development for Teachers and Scientists (WDTS) under the Science Undergraduate Laboratory Internships Program (SULI). In addition, I would like to thank my mentor, David Brown, and everyone at the National Nuclear Data Center as well as everyone from Lawrence Livermore National Laboratory who played a role in the completion of this project.

#### COG Runs for ZA: 1149

ADVANCE Library Revision Number: 26000

C/E keff plots



The following COG Decks did not have corresponding benchmark keff values

Case Name	keff
hrcb1-6	0.9891101 +/- 0.0005693
hmf15-1	0.9949635 +/- 0.0006152
hmf25-4	1.0041819 +/- 0.0006062
hmf10-01	0.9975032 +/- 0.0006298
hmi1-1	0.9808957 +/- 0.0005723
hmf25-2	1.0008277 +/- 0.0006041
hmf31-1	1.0012 +/- 0.0005901
hmf25-3	1.0047027 +/- 0.000614

COG Input Deck Errors

Figure 6: HTML report page generated for Iron

## VI. References

- [1] M. Chadwick, M. Herman, P. Obložinský, et al. "ENDF/B-VII.1 nuclear data for science and technology: Cross sections, covariances, fission product yields and decay data". Nuclear Data Sheets, 2011.
- [2] MyGforge Home. <https://ndclx4.bnl.gov/gf/>. NNDCensemble.
- [3] D. Brown. ADVANCE advances. PowerPoint Presentation given on ADVANCE.
- [4] N. Yamano, J. Katakura, K. Kato, and M. Igashira. "Integrated nuclear data utilization system for innovative reactors nuclear data processing and utilization system". 2007. International Conference on Nuclear Data for Science and Technology.
- [5] R. Arcilla, D. Brown, and M. Herman. "Continuous Integration and Deployment Software to Automate Nuclear Data Verification and Validation". Nuclear Data Sheets, Apr 2014.
- [6] A. Trkov. "Guidelines For Nuclear Data Verification and Validation". Aug 2005. International Atomic Energy Agency.
- [7] R. E. MacFarlane and A. C. Kahler. "Methods for processing ENDF/B-VII with NJOY". Nuclear Data Sheets, Dec 2010. <https://njoy.github.io/NJOY2016/>.
- [8] Brian Warner. buildbot. <https://buildbot.net/>. Buildbot - the continuous integration framework.
- [9] The advance continuous integration system. <http://www.nndc.bnl.gov/endl/b7.dev/qa/index.html>. ADVANCE: the ENDF/B continuous integration system.
- [10] Nuclear Energy Agency. International Handbook of Evaluated Criticality Safety Benchmark Experiments, Nov 2016.
- [11] The Regents of the University of California. COG, 1993. <https://cog.llnl.gov/>.
- [12] SQLite. <https://www.sqlite.org/>. SQLite.
- [13] John D. Hunter. matplotlib. <https://matplotlib.org/>.
- [14] NNSA. "The mission and vision of the United States Department of Energy Nuclear Criticality Safety Program", 2014.

# Value engineering: defining a beamline's basic control system

Aliyah Smith

Mechanical Engineering, University of Notre Dame, Notre Dame, IN, 46556

Julian Adams

Photon Sciences, Brookhaven National Laboratory, Upton, NY, 11973

## ABSTRACT

**Performing value engineering for the basic control system (BCS) used at the National Synchrotron Light Source II (NSLS-II) beamlines at Brookhaven National Laboratory (BNL) allows future beamlines to develop efficiently and effectively. The BCS allows a user to control the fully automated beamline at a workstation while performing experiments by using networked hardware and software in a way that can move components, detect changes in the beamline, and provide user-friendly data. The key to building a BCS involves understanding the boundaries of the BCS so that a work breakdown structure (WBS) can be used to estimate the cost of the deliverable and align with the actual cost. Defining a better WBS deliverable leads to better estimates of the actual cost for the BCS and presents opportunities to improve the development of a BCS. I interviewed project members to understand what a BCS is, how it is developed, and common issues encountered. The information from the interviews was organized in a Function Analysis System Technique (FAST) diagram. Any proposal I came up with needed to be cheaper, produce the same or better quality, and encourage compliance throughout the process. I came up with four proposals: make the definition of the BCS more specific in the WBS dictionary; have a generic template of activities in the WBS deliverable to consistently translate the WBS definition; make a crosscut schedule for controls personnel; and use a process and instrumentation diagram (PID) for connecting the BCS's cables. Each of these alternatives need little to no money to implement, promote uniformity and community among the project members and controls personnel, and promotes a consistent and efficient process which will result in better cost estimates and quality. During this internship at BNL, I learned how to do value engineering and earned value management, which included understanding and executing a FAST diagram, project tracking, a WBS, and a BCS.**

## I. INTRODUCTION

Value engineering on the basic control system (BCS) for the beamlines built in the National Synchrotron Light Source-II (NSLS-II) is necessary to improve the development process and its efficiency. A BCS is a network of hardware and software that allows for a user to control movement of beamline components, detect any changes along the beamline, and provide data in a user-friendly way. In order to complete a project such as this, a cost needs to be estimated and scheduled in the work breakdown structure (WBS) to understand what needs to be done and when to complete this deliverable. I used value engineering techniques to better define the WBS and improve the method of aligning the estimated cost to the actual cost. I also proposed ideas for improving the process for developing the BCS.

## II. PROJECT OBJECTIVE

Before a BCS can be built and implemented to control a beamline, the cost of the project needs to be estimated. The way to get the estimated cost to align with the actual cost of the project through the resource loaded schedule and WBS. This allows for project managers to organize the project into activities that can be scheduled into a timeline and track its progress using earned value management. In order to get the best function-to-cost ratio out of a project, also called value, the WBS needs to reflect the actual project in both cost and time. In order to better define the WBS for the BCS and improve its development, I followed a seven-step value engineering process. Since the value engineering process takes more time than I had at the internship, I completed the first five steps: Gathering Information, Measure, Analyze, Generate, and Evaluate.

## III. METHOD

I applied the typical value engineering structure that is used to perform value engineering for any project to the BCS.

### A. Gathering information

In order to better define the WBS deliverable, I conducted interviews with some members of the BDN portfolio and NSLS-II to understand what makes up the BCS. From the interviews, I learned that the BCS can be broken down into four major levels: the workstation, the input-output controller (IOC), the counter hardware, and the other hardware. The hardware includes all of the components of the beamline that need to be controlled and monitored. This includes the motors to move the mirror and slits, the vacuum system to remove the air molecules in the beamline, and detectors and cameras for the beam and the surrounding area. The beamline also includes two protection programmable logic controller (PLC) systems, which are eventually connected in the beamline's network, but it is separate task from the BCS deliverable. Each piece of hardware is connected to a controller that tells the hardware what to do. The controllers are networked such that the hardware can talk to one another and to the beamline user. The software used to store all the data from the beamline and allow for the user to send commands to the hardware is called Experimental Physics and Industrial Control System, or EPICS. EPICS converts machine units to engineering units, engineering units to human units, which can be read at the workstation, a series of monitors and computers that display information about the beamline in a user-friendly manner. Understanding what a basic control system is and the tasks required to get it to work is important in trying to define the WBS deliverable.

I made a Function Analysis System Technique (FAST) diagram to organize the information collected in my interviews, as seen in the Appendix. The FAST diagram is a chart of functions,



where a function is an active verb followed by a measurable noun, which describes the span of a project from its purpose to the basic tasks required. This tool is used in value engineering to organize a project and its tasks by asking three questions: *How do you achieve this function? Why did you do this function? When you do this function, what other functions must you do?* (Value) Using the FAST diagram makes it easy to understand what tasks are necessary or if tasks are done efficiently. I also used this diagram as a reference for suggesting a better definition for the WBS deliverable and improving the development process of the BCS.

With the BCS broken down clearly in a FAST diagram, I was able to understand what areas of the project needed improving. The personnel I interviewed brought up common issues and areas that need improvement related to the WBS deliverable for the BCS and its process. One issue is that the definition for the BCS in the WBS dictionary is too general, which allows for multiple interpretations of what the deliverable should be. Another issue is with the interpretation of the WBS deliverable itself. The activities listed in the WBS for each beamline is different, and does not reflect a uniform interpretation of the definition. Some of the activities are too unclear to accurately track its progress. There were two obvious issues with the development process. The first I noticed was the lack of community among the controls personnel. The controls division is possibly understaffed but they still have the same demand of work, if not more now due to NSLS-II becoming more operational. This goes beyond the scope of the BCS, but it is essential to the efficiency of the process. Another area of improvement is the cable installation. Cables usually are long and expensive, especially the custom ones used at NSLS-II. They can cause a lot of problems if they are not pulled and terminated properly. These issues should be easily resolved, and will have a measurable impact on the value of the end product.

## B. Measure

Before I could begin brainstorming ideas and working on proposals, I defined how to measure the value of each proposal. Since value is defined as a function-to cost-ratio, any solution I come up with needs to improve the value of the BCS. Therefore, the alternatives are measured by cost, quality, and compliance. Anything that needs to be implemented into the process or the WBS itself needs to be cheap or make the final cost cheaper. These alternatives should improve the completed BCS, or at least maintain the final product. A very important factor to improving the process is to make it easy for prospect members to follow and perform the same tasks with the same efficiency for each beamline built.

I was able to come up with four alternatives that will improve the basic control system's WBS and its process. The first proposal is to make the definition for the WBS deliverable more specific. The current WBS definition is too general and allows for various interpretations of the BCS deliverable. The WBS definition needs a uniform interpretation so that there is a clear understanding of what needs to get done to complete the deliverable. Even though I propose a more specific definition for the BCS, it still needs to be generic enough that there is room for adaptability for what the deliverables need to be. A way to make the WBS definition more specific is to include which groups or WBS sections are related to the BCS deliverable. This will ensure a uniform interpretation that can be specifically adjusted to each beamline.

The second alternative is to use the new proposal workbook tool with a fixed template to estimate the cost of the BCS. As seen in Figure 1, this tool includes the WBS deliverable for a project that would include template of activities that are typical for a BCS. The activities can reflect what task needs to be done and who needs to perform the task. In addition, any activity that requires a multistep process, for example, procuring hardware,

B	C	E	F	G	H	I	J	K	L
ACT ID	WBS	Activity Name	Cost Total	Duration Type	Working Duration	Calendar Duration	Work Group	Resource 1	Hours Direct \$
+ BDN-Project Name.06 - Controls			\$ -						
BDN-Project Name.06.01 - Basic System Controls			\$ -						
Pr_27010		Controls Design- Requirements	\$ -	Working Days					
Pr_27020		Controls Design- Cable Studies	\$ -	Working Days					
Pr_27030		Controls Design- EPS logic layout	\$ -	Working Days					
Pr_27040		Controls Design- motion/ hutch a	\$ -	Working Days					
Pr_27050		Controls Design	\$ -	Working Days					
Pr_27060		Controls Design	\$ -	Working Days					
Pr_27070			\$ -	Working Days					
Pr_27080		Controls Proc/Fab- Motion Components (Labor)	\$ -	Working Days					
Pr_27090		Controls Proc/Fab- Dection Components	\$ -	Working Days					
Pr_27100		Controls Proc/Fab- Vacuum Components	\$ -	Working Days					
Pr_27110		Controls Proc/Fab- Motion Shipment (Vendor)	\$ -	Working Days					
Pr_27120			\$ -	Working Days					
Pr_27130		Controls Hardware- Motion installation/ hutch a	\$ -	Working Days					
Pr_27140		Controls Hardware- Motion configuration/ hutch a	\$ -	Working Days					
Pr_27150		Controls Hardware- EPS installation	\$ -	Working Days					
Pr_27160		Controls Hardware- PPS installation	\$ -	Working Days					
Pr_27170		Controls Hardware	\$ -	Working Days					
Pr_27180		Controls Hardware	\$ -	Working Days					
Pr_27190			\$ -	Working Days					
Pr_27200		Controls Cabling- pulling/ hutch a	\$ -	Working Days					
Pr_27210		Controls Cabling- termination/ hutch a	\$ -	Working Days					
Pr_27220		Controls Cabling-	\$ -	Working Days					
Pr_27230		Controls Cabling-	\$ -	Working Days					
Pr_27240		Controls Cabling-	\$ -	Working Days					
Pr_27250			\$ -	Working Days					
Pr_27260		Controls Software- IOC Config and CSS development	\$ -	Working Days					
Pr_27270		Controls Software- Motion IOC Config. & testing	\$ -	Working Days					
Pr_27280		Controls Software-Vacuum IOC Config. & testing	\$ -	Working Days					
Pr_27290		Controls Software-	\$ -	Working Days					

Figure 1. The WBS with a template of activities

can be further broken down to its own separate activities, such as shipment and assembly. This will help reflect periods of activity and non-activity. One other activity that should be included in the WBS is an individual design review for the BCS deliverable. A design review will get the personnel involved with the deliverable together to make sure all groups involved are on the same page. With the WBS activities organized this way, there will help interpret the BCS deliverable uniformly and better align the estimated cost to the actual cost of the project.

The third alternative would promote more support and community among controls personnel. A crosscut schedule for controls personnel would have a timeline of all the beamlines, both controls in construction and in operations, where the priorities are set with defined deadlines. The creation of a database for controls personnel and beamline tasks, and where all the EPICS packages in use of NSLS-II would be organized and include who is an expert with each package. This will make it easier to find packages and find personnel who can help. The schedule can be adaptable and updated to better communicate what is happening within the controls group at NSLS-II. A crosscut schedule will help re-define job accountabilities to help with the facility's transition from construction to operation. It will make it easier for controls personnel to collaborate and support one another to complete the tasks that need to be completed.

The final alternative is to have a process and instrumentation diagram (PID) for cabling. A PID is a layout of how a system is organized and connected. The data is complex and the connections need to be understood so it can be implemented properly in order for the BCS to work, a PID will communicate those connections to all personnel to understand easily and uniformly. This will make cabling and instrumentation easier and minimize the chance of mistakes coming from poor interpretation.

### **C. Analyze and Generate**

In order to put these alternatives into effect, group leaders and other personnel involved with the basic control system need to meet to agree on WBS definition and the WBS activities. It seems like simple adjustments to the process and the WBS, but it could take time to get quantitative feedback. To adapt to NSLS-II going from construction oriented to operational, re-define job roles and accountabilities. It will also help to see where support is needed and where it can come from, especially for controls. Any available personnel who deal with the BCS needs to help implement whatever is decided on to improve the process.

### **D. Evaluate**

I proposed the alternatives to better define the WBS deliverable for the basic control system to BDN portfolio members and other NSLS-II personnel in a presentation at the BDN weekly meeting. These alternatives are simple fixes that will help improve the process and aligning the estimated cost and the actual cost of the project. The personnel at the meeting gave positive responses, and they seemed to really consider taking action to implementing the ideas.

## **IV. CONCLUSION**

The basic control system for the beamlines at NSLS-II controls the beamlines in a user-friendly way. The alternatives that I propose will better communicate what the basic control system is, what it does, and how it should work. They will help translate

WBS definition into the WBS deliverable so that the estimated cost will better align with the actual cost. Re-defining job roles and accountabilities that is understood by all personnel will encourage there to be support and a united community working towards a common goal. By better aligning the cost estimation and improving the process, this will make building and implementing a basic control system easier, cheaper, and more uniformly for future beamlines to come.

## **V. REFERENCES**

Ehrlich, Steve, Chanaka DeSilva, Ryan Tappero, Wah-Keat Lee, Milinda Abeykoon, Oksana Ivashkevych, Larry Carr, Greg Fries, Zhijian Yin, Andy Broadbent, Rob Petkus, and Chris Stebbins. "Value Engineering :The Basic Control System." Personal interview. June 2017.

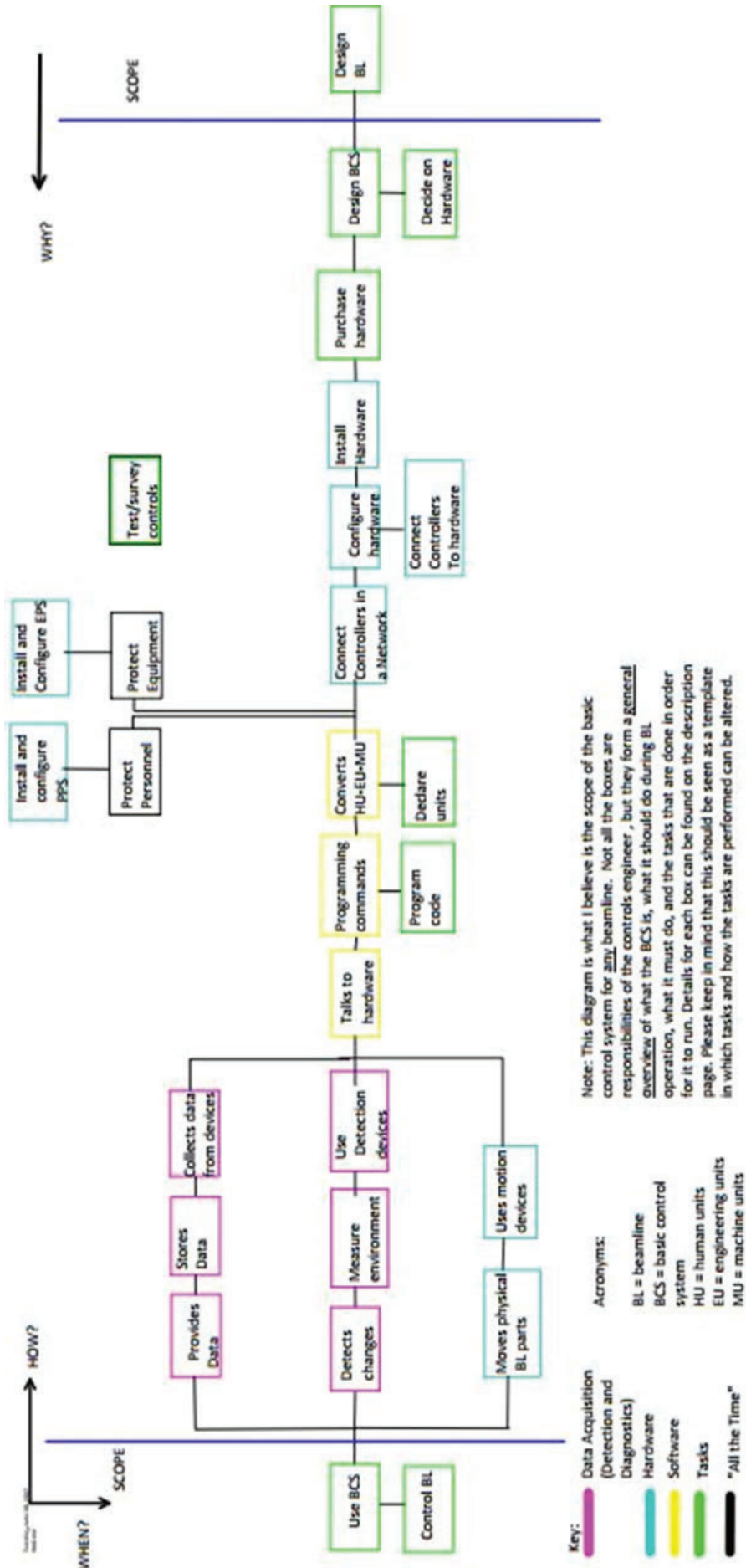
"Function Analysis System Technique (FAST)Search." *Value Analysis Canada*, [scav-csva.org/fast.php](http://scav-csva.org/fast.php).

## **VI. ACKNOWLEDGMENTS**

I would like to thank BDN portfolio and NSLS-II for their time and assistance.

"This project was supported in part by the U.S. Department of Energy, Office of Science, Office of Workforce Development for Teachers and Scientists (WDTS) under the Science Undergraduate Laboratory Internships Program."

## VII. APPENDIX: FAST Diagram of the BCS and Descriptions





## A. Description for FAST Diagram

### Software:

- Talks to hardware
  - Using a HMI at the workstation that displays and allows the user to access data and make adjustments to all the working components of the beamline
  - Using CSS to see all this data in a user-friendly way
  - Using BOY to display performance
- Program commands
  - This is the middleware component, EPICS
  - EPICS is used to access the data collected from the devices in a user-friendly manner
- Converts HU-EU-MU
  - EPICS takes the commands from the user, uses a conversion to change the units to engineering units (EU), then converts (N, m, kg, etc.) into “counts”. The counts are how motors and other hardware track how they move.

### Tasks:

- Use BCS
  - The whole point of using a BCS is for a user to be able to access data, move parts, and detect the environment within the beamline and the hutches where the beam actually operates without physically being present in a high-risk area for radiation.
- Control BL
  - There needs to be a user-friendly interface that scientists can use to perform their experiments and extract data seamlessly.
  - CSS and BOY implemented on a HMI
- Program Code
  - This code is for the middleware, EPICS
    - A working code needs to be implemented
    - Packages are available for upload on a “forum” of sorts (I think it’s a mailing list), and are found using keywords
    - Still there are some codes still needed to be written
- Declare units
  - EPICS application. The amount of counts should correlate with how far a motor moves the component, the pressure in the BL, the position of the beam, etc. Tested by controlling the hardware via the controller
- Purchase Hardware
  - Vendors should be the same for each type of hardware (ie. Motors, vacuum, etc.)
  - Takes time to get all of the components here
  - Are checked by the vendors then by BL team members
- Design BCS
  - The basic control system is broken down into four components: the Work Station, the IOC, the Counter Hardware, and the Hardware itself.
  - Profile manager and discuss requirements, costs, scheduling, etc.
- Decide on hardware
  - Decide on where\_ to get the hardware and in what condition(cost, efficiency, compliance with EPICS)
    - At BNL
    - From vendors
    - Reused
    - Brand new

- Design BL
  - Portfolio manager and “group leaders” discuss requirements, costs, scheduling, etc.
  - Need to know how the beamline functions in order to understand the BCS needed for it to work.
- Commercial
- Custom
- Cabling needed

### “All the Time”:

- Protect Personnel
  - PPS is implemented
  - Safety is always priority
  - Scheduling coordinates what groups are working where
- Protect Equipment
  - Safety limits are decided and implemented
  - Requirements established per BL for EPS; and implemented
- Test/survey controls
  - Hardware, software, controllers, cables, etc.
- Data Acquisition:
  - Provides Data
    - User can access data from workstation
  - Stores Data
    - EPICS database holds the info collected from devices
  - Collects data from devices
    - The devices are connected to controllers which is connected in the BL network
  - Detects changes
    - When the BL is in operation, gases and radiation are present. Detectors make sure that there aren’t any dangerous amounts that will affect the synchrotron, the BL or the personnel
  - Measures environment
    - Safe limits are implemented to make sure any changes are still low-risk
  - Uses detection devices
    - Detectors and diagnostics tools are placed along a BL and in the hutches to detect the beamline, any unwanted gas or radiation exposure, etc.
- Hardware:
  - Moves physical BL parts
    - Mirrors, stages, slits, etc. need to move to focus and align the beam, etc.
  - Uses motion devices
    - Motors/ axis to move the components in different directions
  - Connect controllers in a network
    - Cables need to be pulled and terminated
  - Configure hardware
    - PMAC software is used for testing hardware and making sure it functions how the controllers tell it.
  - Connect controllers to hardware
    - Cable pulling and termination
  - Install hardware
    - Put on stages, connected to other hardware, etc.

# Assessing the cryptographic strength of RSA moduli using algorithmic entropy reduction in sequenced binary quadratic forms

Nicole Soder

Applied Mathematics and Statistics, Stony Brook University, Stony Brook, NY 11794

Danielle Fieseler

Mathematics and Computer Science, St. Joseph's College, Patchogue, NY 11772

David Biersach

Information Technology Department, Brookhaven National Laboratory, Upton, NY 11973

## ABSTRACT

This research effort aims to develop a novel approach to factoring binary composites, those numbers that are the product of two and only two smaller primes. These numbers are at the heart of the RSA encryption method used to secure web server traffic. Our technique is based upon the theory of Algorithmic Entropy Reduction in Sequenced Binary Quadratic Forms (AERISBQ). Essentially, multiplication is treated as a form of lossy compression and, hence, this factoring method amounts to restoring the information bits lost during the production of the composite. Working computer code was generated to implement the method as it is currently established using the computer resources provided by Brookhaven National Laboratory (BNL), and a detailed analysis of the efficiency of AERISBQ compared to other well-known specialized and general purpose factoring algorithms was conducted. Our goal was to develop a fifth step to the AERISBQ method which would require finding an efficient way to solve binary quadratic forms. While no such approach was found, if any method is eventually developed, this feat would be considered a significant breakthrough to both the scientific community at BNL and the globe at large. Additionally, through this project we have been given the opportunity to learn and consistently work with C++, a skill that will serve both my colleagues and myself throughout our professional careers.

## I. BACKGROUND

### A. RSA Encryption

The first public-key encryption algorithm was developed in 1977 by Ron Rivest, Adi Shamir, and Leonard Adleman. Prior to this invention many different algorithms had been proposed, yet RSA quickly proved to be the easiest to understand and implement. The method has undergone years of thorough cryptanalysis, but its security has yet to be disproved. As a result, our research project aims to discover whether the currently established algorithm is sufficient to protect the extent of information concealed by RSA as there is still speculation regarding its potential pitfalls. The current encryption process proceeds as follows:

- Generate a public key by multiplying two large prime numbers, known as  $p$  and  $q$ , where  $p < q$ . Only the product of these two numbers,  $N$ , is known to the public. The security of RSA encryption lies in the inherent difficulty in factoring this number which is often millions of digits long.
- Randomly choose the encryption key,  $e$ , such that  $e$  and  $(p-1)(q-1)$  are coprime.
- Use the extended Euclidian algorithm ( $ax+by = \gcd[a,b]$ ) to

compute the decryption key,  $d$ , such that  $ed \equiv 1 \pmod{(p-1)(q-1)}$ .

- $N$  and  $e$  are the public keys and  $d$  is the private key. To encrypt a message,  $m$ , it must be divided into numerical blocks. Usually these blocks are the largest power of 2 smaller than  $N$ . From here,  $m$  becomes the encrypted message, known as  $c$ , by means of the formula  $c_i = m_i^e \pmod n$  where  $i$  is the block number.
- The receiver can decipher the encrypted message by calculating  $m = c^d \pmod N$ .

### B. Security of RSA

It is possible that there is a different way to break RSA encryption other than factoring  $N$ . A cryptanalyst could find the value of  $(p-q)(q-1)$ , but this technique requires just as much work as factoring  $N$ . One could also try using every possible value of  $d$ . However, this method is less efficient than factoring  $N$ . For the purposes of this research project, we will solely focus on the factorization of  $N$ .

### C. Current Factorization Methods

The most efficient factoring algorithm to date is the Number Field Sieve (NFS) which can factor numbers larger than  $10^{100}$ . This algorithm was developed by John Pollard and is the quickest in terms of number of steps required to factor  $N$ . The code implemented in this research effort is accordingly compared to NFS.

### D. AERISBQ Overview

Algorithmic Entropy Reduction in Sequenced Binary Quadratic Forms (AERISBQ) is a new method to factor  $N$ . AERISBQ seeks to systemically reduce the entropy inherent in the binary expression of  $N$ , produced through the multiplication of  $p$  and  $q$ ,

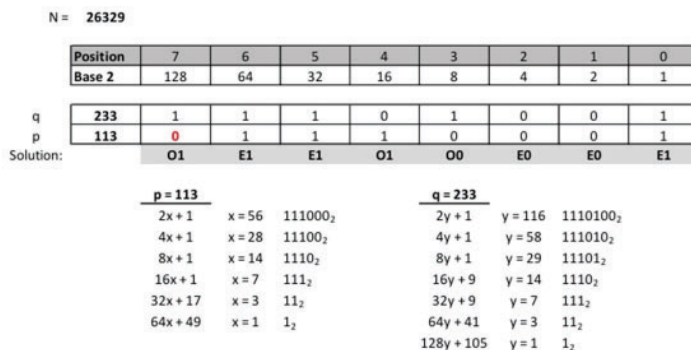


Figure 1. Chart representing the valid  $p$  and  $q$  forms through successive rounds of AERISBQ

AERISBQ Round # 1 for $p = 113$ , $q = 233$ , $N = 26329$			
GOOD		BAD	
$(4x+1)(4y+1)=26329$		$(4x+3)(4y+3)=26329$	
Step 1: $4xy+x+y=6582$		Step 1: $4xy+3x+3y=6580$	
x	y	x	y
0	6582	-6583	-1
28	58	-59	-29
58	28	-29	-59
6582	0	-1	-6583
Step 2: $-u^2+v^2+v=6582$		Step 2: $-u^2+v^2+3v=6580$	
x	y	x	y
$\pm 6582$	-6583	$\pm 6582$	-6584
$\pm 6582$	6582	$\pm 6582$	6581
$\pm 30$	-87	$\pm 30$	-88
$\pm 30$	86	$\pm 30$	85
Step 3: $-4x^2+4xy+y=6582$		Step 3: $-4x^2+4xy+3y=6580$	
x	y	x	y
0	6582	-6583	-6584
28	86	-59	-88
58	86	-29	-88
6582	6582	-1	-6584
Step 4: $-2x^2+4xy+y=3291$		Step 4: $-x^2+4xy+3y=1645$	
x	y	x	y
0	3291	-6583	-1646
28	43	-59	-22
58	43	-29	-22
6582	3291	-1	-1646

Figure 2. Chart representing the failure of a trivial reject path and success of a correct form's path



in order to recover these original factors. The method proceeds by inferring the binary digits (bits) of  $p$  and  $q$  (from least significant bit on the right-hand side to most significant bit on the left-hand side) by determining if a valid solution can exist for a given binary quadratic form (BQF). Rather than attempting to calculate exact integer solutions for any given BQF, AERISBQ searches for a quick way to prove that a given BQF is not solvable in integers. The two factors,  $p$  and  $q$ , are represented as forms based upon the binary numbering scheme (base 2). However, the form's coefficients are still expressed using standard decimal digits (base 10). Each round of AERISBQ starts by expressing  $p$  and  $q$  in this pseudo-binary form and then expanding their product to ultimately produce a binary quadratic in terms of  $x$  and  $y$ . The "remainders" of each round are carried forward into the next round's BQF and four new BQFs are created and tested. By determining the solvability of each successive BQF, another bit of  $p$  and  $q$  is ascertained. The goal of each round of AERISBQ is two-fold: to enable trivial rejection of forms which are impossible and to systematically reduce the current value of  $N$ .

## II. METHODS

### A. Solving Binary Quadratic Forms

We first compared the efficiency of AERISBQ to NFS in terms of number of steps required to factor  $N$ . While NFS still runs more quickly than AERISBQ, only step one is currently functional in the AERISBQ code. This is because in order for steps 2-4 to have purpose, a fifth step is required that would efficiently solve binary quadratic forms. Several approaches were taken to solve these BQFs. For example, we attempted to solve a given BQF for  $y$  and break the terms by numerator into separate fractions, leaving each with the same denominator. From there, we solved each of these equations independently for integer values, which is a much simpler task than finding  $x$  and  $y$  in binary quadratic form. However, we later realized that this process would eliminate solutions that yield decimal values for two or more terms. For instance, if non-integers  $n/Bx + D$  and  $-Ax/Bx + D$  when added together yield an integer value, its solution would be excluded through the process when in actuality it is valid.

### An AERISBQ Round – Step 4

$$A_4x^2 + B_4xy + C_4x + D_4y = n_4$$

$$B_4xy + D_4y = n_4 - A_4x^2 - C_4x$$

$$y = \left[ \frac{n_4 - A_4x^2 - C_4x}{B_4x + D_4} \right]$$

$$\text{set } g = \text{GCD}\{n_4, |A_4|, |C_4|\}$$

since  $y \in \mathbb{Z}^+$  and  $p = B_4x + D_4 \Rightarrow p \nmid g$   
 $\therefore$  we can reduce  $n_4, A_4, C_4$  by  $g$

$$n_4 = \frac{n_4}{g} \quad A_4 = \frac{A_4}{g} \quad C_4 = \frac{C_4}{g}$$

Figure 3. The necessary steps required to complete Step 4 of an AERISBQ round

## B. Python Code

We also created a different factoring algorithm apart from AERISBQ and NFS. This method stems from two fundamental principles: every prime number must be in the form  $6x \pm 1$ , and  $p$  is less than  $\sqrt{N}$  and greater than  $\sqrt{N}/4$ . In order for this code to successfully factor  $N$ , the user must input a file of all primes smaller than  $(\sqrt{N}/4-1)/6$ , values which are nominal compared to the size of  $N$ . The code creates an array of all numbers in the form  $6x \pm 1$  within the range of  $p$ , deletes those that are not prime, and tests to see which are factors of  $N$ . This method decreases the search space for factors as it includes only those in the category  $\text{floor}(\sqrt{N}/4-1)/6$  to  $\text{floor}(\sqrt{N}+1)/6$ , representing the range of  $p$  in terms of  $x$ . This algorithm was written in Python and does not currently exceed the efficiency of AERISBQ or NFS, but may have the potential to surpass both in the future.

## III. DATA AND RESULTS

### A. AERISBQ Behavior

AERISBQ exhibits an unexpected behavior in that there are certain bit values of  $N$  for which the number of work steps plateaus and then jumps. For example, when the bit length of  $N$  is 256, AERISBQ takes an average of three steps to factor  $N$ . But, when the bit length doubles to 512, the number of steps jumps to four, staying there until bit length 1024 and jumping again to five at bit length 2048. However, it is peculiar that the algorithm would take an equal number of steps to factor  $N$  for only certain bit lengths. Additionally, there are times when this plateau does not occur. For instance, the series  $N=262144$ , steps=8;  $N=524288$ , steps=9;  $N=2097152$ , steps=10 does not follow this pattern. If one were to draw a line of best fit through the current AERISBQ logarithmic graph, the original function would oscillate above and below the trend line. Perhaps if we tested all possible bit values of  $N$  rather

```

BQF* BQF::InitChild(int64_t a, int64_t r, int64_t s, int64_t b, int64_t c, int64_t n)
{
    // Step 1: Skip each TR (trivial rejection)
    int64_t num = n - r*s - b*c - b*s - c*r;
    if (num % a != 0) return nullptr;
    int64_t n1 = num / a;
    auto thisBQF = new BQF(a, r + b, s + c, n);

    // Step 2: UV-substitution
    thisBQF->a2 = a;
    thisBQF->b2 = c + s;
    thisBQF->c2 = b + r;
    thisBQF->n2 = n1;
    Reduce(thisBQF->a2, thisBQF->b2, thisBQF->c2, thisBQF->n2);

    // Step 3: L-substitution
    thisBQF->a3 = -thisBQF->a2;
    thisBQF->b3 = thisBQF->a2;
    thisBQF->c3 = -2 * (thisBQF->b2 - thisBQF->c2);
    thisBQF->d3 = 2 * (thisBQF->b2 + thisBQF->c2);
    thisBQF->n3 = 4 * thisBQF->n2;
    Reduce(thisBQF->a3, thisBQF->b3, thisBQF->c3, thisBQF->d3, thisBQF->n3);

    // Step 4: Reduction
    thisBQF->a4 = 4 * thisBQF->a3;
    thisBQF->b4 = -4 * thisBQF->a3;
    thisBQF->c4 = -2 * thisBQF->c3;
    thisBQF->d4 = thisBQF->c3 + thisBQF->d3;
    thisBQF->n4 = thisBQF->n3;
    Reduce(thisBQF->a4, thisBQF->b4, thisBQF->c4, thisBQF->d4, thisBQF->n4);

    int64_t g = GCD(thisBQF->n4, GCD(abs(thisBQF->a4), abs(thisBQF->c4)));
    thisBQF->a4 /= g;
    thisBQF->c4 /= g;
    thisBQF->n4 /= g;

    if (thisBQF->n4 < 0)
        return nullptr;

    return thisBQF;
}

```

Figure 4. Code for steps 1-4 of AERISBQ

than just doubling the bit value for each trial, AERISBQ would display a different or clearer trend. The reason for the current behavior has yet to be determined, but might provide a gateway for improvement in this novel approach.

## B. Python Code Results

I additionally found in the Python factoring code that there is a surprisingly significant amount of numbers in the form  $6x \pm 1$  that are not prime. While these numbers were not tested as potential factors of  $N$ , it is possible that the continual “weeding out” of non-primes within the array caused the code to be of secondary efficiency to AERISBQ. For example, when  $N = 181 \cdot 191$ , there were 20 values within the  $6x \pm 1$  form array that were not applicable factors of  $N$ . As  $N$  increases this value will only increase as well. While this method eliminates those primes not contained within a certain form, AERISBQ takes a contrary approach and seeks to find the exact form of  $p$  and  $q$ .

## IV. CONCLUSION AND RECOMMENDATIONS

Our goal was to develop a fifth step to the current AERISBQ method which would require finding an efficient way to solve binary quadratic forms. While no such approach was found, if any

```

1 import math
2 N = 181*191
3 all_numbers = []
4 imported_primes = [5, 7, 11, 13, 17, 19, 23, 29, 31]
5 removed = []
6 new_all_numbers = []
7 for x in range(math.floor((math.sqrt(N)/4)-1)/6), math.floor((math.sqrt(N)+1)/6)+1):
8     c = (6*x)+1
9     d = (6*x)-1
10    all_numbers.append(d)
11    all_numbers.append(c)
12    for x in range(0, len(all_numbers)):
13        for y in range(0, len(imported_primes)):
14            if all_numbers[x] % imported_primes[y] == 0:
15                removed.append(all_numbers[x])
16    print("All numbers in form:", all_numbers)
17    print("Numbers removed:", removed)
18    for j in range(0, len(all_numbers)):
19        if all_numbers[j] not in removed:
20            new_all_numbers.append(all_numbers[j])
21    print("Number lost:", len(all_numbers)-len(new_all_numbers))
22    for i in range(0, len(new_all_numbers)):
23        if N/new_all_numbers[i] == int(N/new_all_numbers[i]):
24            if N/new_all_numbers[i] > new_all_numbers[i]:
25                p = new_all_numbers[i]
26                q = int(N/new_all_numbers[i])
27                print("p:", p, "q:", q)
28                break
29            else:
30                q = new_all_numbers[i]
31                p = int(N/new_all_numbers[i])
32                print("p:", p, "q:", q)

```

Figure 5. Code for Python factoring algorithm

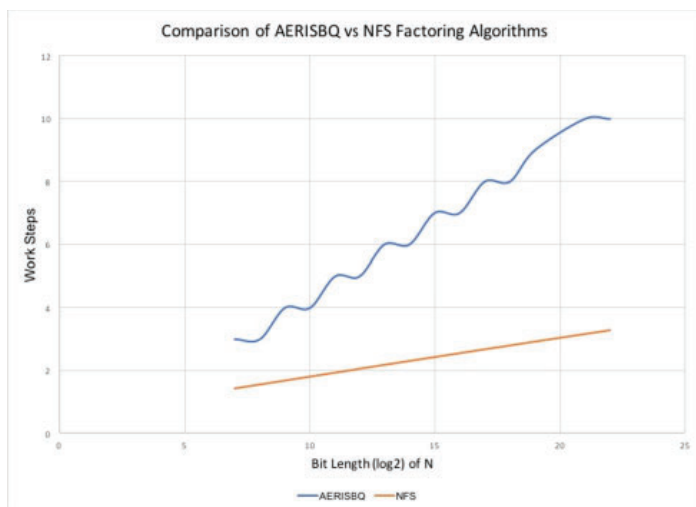


Figure 6. Logarithmic graph comparing the efficiency of AERISBQ to NFS

working method is eventually developed, steps 2-4 of the code can become functional and potentially turn AERISBQ into the fastest running factoring algorithm. For individuals looking to further pursue this research, I would recommend implementing any of the known methods of solving binary quadratic forms into the AERISBQ code. Though they are time consuming, these extra lines of code could produce unexpected results and possibly cause the factoring algorithm to execute more quickly than the current code or even NFS. I would also recommend attempting to turn AERISBQ into a recursive algorithm. Currently, AERISBQ proceeds horizontally rightward from least significant bit to most significant bit to determine bits of  $p$  and  $q$ . However, if step 4 involved the addition of an asymmetric BQF with a missing  $y^2$  term, then a new branch would begin downward, delving into the specific  $x$  and  $y$  of that particular step 4. If  $x$  was represented as either  $2x'$  or  $2x'+1$  and  $y$  as either  $2y'$  or  $2y'+1$ , four new but even smaller right-hand side values- some of which some might be invalid- would be created. These sub-BQFs would have new  $x$  and  $y$  unknowns, but again, drilling deeper, could be represented by  $2x''$ ,  $2x''+1$ ,  $2y''$ , and  $2y''+1$ . Only one of the two bivariate polynomials for any given top-level round (finding bits of  $p$  and  $q$ ) would be valid. If each path is further investigated, one of the bivariate polynomials would have some sub-BQF where all future forms are unsolvable. This feat would be a significant breakthrough to both the scientific community at BNL and the globe at large.

## V. ACKNOWLEDGEMENTS

I would like to thank David Biersach for his guidance and mentorship throughout this internship. This project was supported in part by the U.S. Department of Energy, Office of Science, Office of Workforce Development for Teachers and Scientists (WDTS) under the Science Undergraduate Laboratory Internships Program (SULI).

```

All numbers in form: [41, 43, 47, 49, 53, 55, 59, 61, 65, 67, 71,
73, 77, 79, 83, 85, 89, 91, 95, 97, 101, 103, 107, 109, 113, 115,
119, 121, 125, 127, 131, 133, 137, 139, 143, 145, 149, 151, 155,
157, 161, 163, 167, 169, 173, 175, 179, 181, 185, 187]
Numbers removed: [49, 55, 55, 65, 65, 77, 77, 85, 85, 91, 91, 95,
95, 115, 115, 119, 119, 121, 125, 133, 133, 143, 143, 145, 145,
155, 155, 161, 161, 169, 175, 175, 185, 187, 187]
Number lost: 20
p: 181 q: 191

```

Figure 7. Output of Python code for  $N = 34571$

# Combining microscope images on a common coordinate system

Tunisia Solomon

Mathematics, SUNY Farmingdale, Farmingdale, NY 11735

Randy Smith and Dan Allen

Photon Sciences, Brookhaven National Laboratory, Upton, NY 11973

## Abstract

**The National Synchrotron Light Source II (NSLS-II) at Brookhaven National Laboratory can offer micro- and nano-focused x-ray beams to visiting scientists. The focused x-rays can be used to take images of samples, revealing elemental and chemical information for innovative discoveries in fields including ecology, applied science, and engineering. Navigating samples and locating regions of interest at the beamline can sometimes be difficult due to the need to visualize the sample in both a global zoomed-out view and a high resolution zoomed-in view. Taking visible light microscope images beforehand can be helpful, but keeping track of where each visible image was taken can be difficult. Combining the microscope images on a common coordinate system that could be matched to the beamline coordinate system would help visiting scientists navigate their samples more easily. I created an application that will be useful to visiting scientists when navigating their sample at the beamline using images previously taken by lab-based microscopes starting with visible microscopes and expanding to electron microscopes.**

**Python is the programming language I used to carry out the building of this application due to its many features and extensive library. As of now, I have successfully created an application to display images taken with a lab microscope on a lab microscope micron coordinate system. This application then converts the lab microscope coordinate system to that of the beamlines through user interaction. The plan for this app is to be able to select spatial regions of interest (ROI) and output coordinates of the ROI as well as applying directional translations, rotation, and flipping transformations of the coordinate systems. Overall, this process will provide for more efficient examination of data, thus expediting the groundbreaking innovative research conducted at NSLS-II.**

## I. Motivation and Introduction

Many x-ray microscope scientists spend a lot of time searching for areas of their sample to scan. One main contributing factor to this issue is that the lab light microscope and beamline x-ray microscope have different coordinate systems. The question arises, how can we make sample navigation easier?

If scientists could take images of their sample using the lab light microscope and map out regions of interest before their beam time, their time spent in beamtime would be used more efficiently. This process could be carried out by converting the lab light microscope coordinate system to that of the beamline so that the images taken at the lab can be used as a reference before and during beamtime.

## II. Methods

Over forty images of polymer beads were captured at 10x

zoom with the Nikon Eclipse LVDIA-N light microscope, Nikon DS-Ri2 camera and the NIS-Elements Ar v4.40 software in the mesoscale imaging laboratory. The images were then uploaded into Python 3.3 using the Jupyter Notebook environment. Each image was uploaded as a TIFF file (Tag Image File Format) containing metadata for each image. From the metadata, the microns per pixel conversion factor and x and y coordinates of each image were extracted; the x and y coordinates are of the bottom left corner of each image.

First, the images were displayed on a pixel coordinate system due to the ease of the images already being measured in pixels. I had to convert the coordinate system to pixels, using the micron per pixels conversion that was extracted from the image metadata, in order for the images to be displayed in their proper locations on the coordinate system. In addition, each image was flipped horizontally to fit the orientation of the converted coordinate system. To display the images in microns on the lab micron coordinate system, I went into the mesoscale imaging lab to better understand the coordinate system of the images taken at the light microscope. This investigation led me to conclude that the y-axis in my application needed to be inverted to match the lab micron coordinate system. This information was vital to development of my application because without it the image plotted on the coordinate system in a non-uniform manner. After all images were displayed on the micron coordinate system in their proper location, in order to convert the lab coordinate system to the beamline coordinate system nine conditional statements were implemented for each images translation; these nine conditional statements accounted for all possible translations of images on the axes from one point to another.

Next, to test the coordinate system conversion would work, we employed a graphical user interface (GUI) command that enables a reference point to be clicked on one image on the lab coordinate system. Then, a new beamline location of the same point was entered that would represent the beamline coordinate of the same fiducial point. These two coordinate sets were passed through the conditional statements and difference between the clicked location and the new beamline location were calculated. The x and y offsets were then used to calculate the difference between the old x and y coordinates and the new desired location of the same x and y coordinates. Lastly, each image was translated to their new respective locations and through an auto-scale feature the lab micron coordinate system was converted to the beamline x-ray micron coordinate system.

Finally, the images were plotted and displayed in their proper location on the beamline x-ray micron coordinate system. A save command was added to the application that captured images of each coordinate system with images plotted on them. This command increased the resolution of images by saving the images as a jpg file with 800 dots per inch. Additionally, a feature that provid-



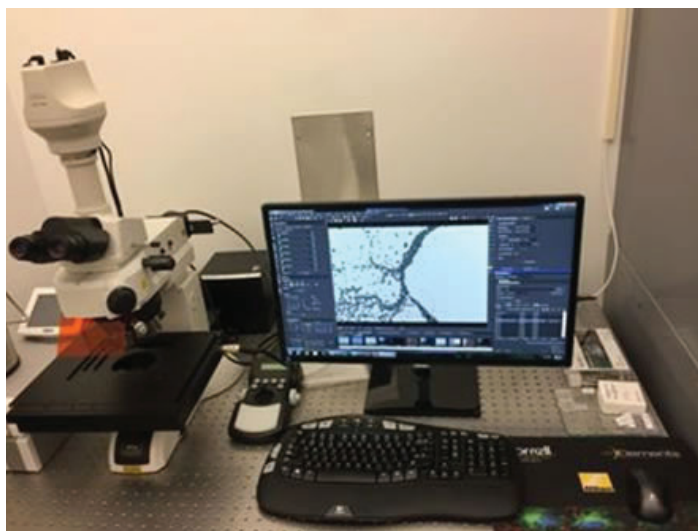


Figure 1. Lab Visible Light Microscope

ed zoom capabilities was added. This feature was tested by zooming in exclusively on a single image and saving the figure as a jpg. When the saved figure was opened, the image of the polymer beads was clear with high resolution and plotted on the local coordinate system relative to the beamline micron coordinate system.

### III. Results

After testing this application with over 40 images taken at the lab light microscope, it successfully assembled the images in their correct location providing a global zoomed out view of the Polymer beads. The images were plotted in pixels on a pixel coordinate system as well as in microns on the lab microscope micron coordinate system. A correction factor was applied to all images and was used to convert the clicked reference point to the coordinate (0,0). In all, the lab light microscope micron coordinate system was converted to the beamline x-ray micron coordinate system.

### 40+ New Sample Images at 10x zoom

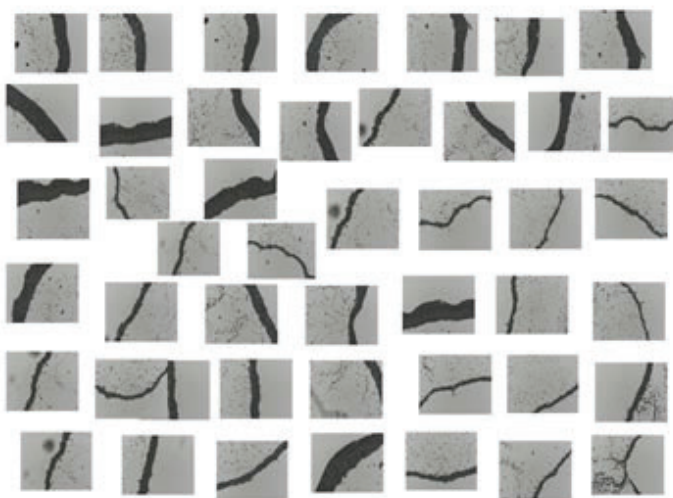


Figure 3: 40+ images of Polymer beads taken in mesoscale imaging lab with the Nikon DS-R12 microscope. Top right corner-zoomed out view of a Polymer bead.

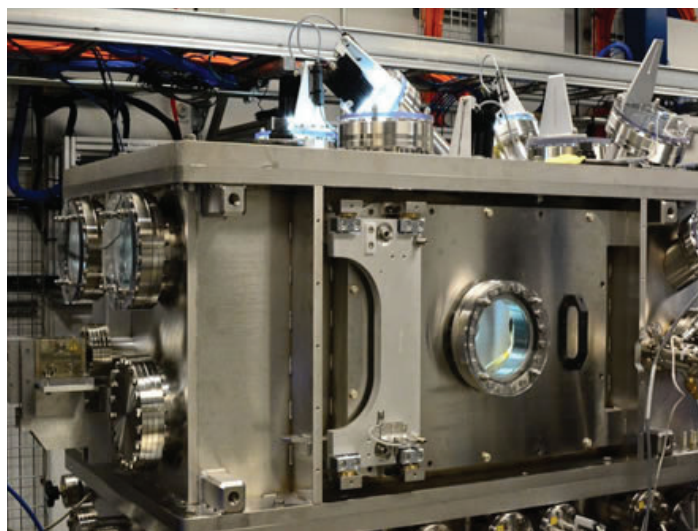


Figure 2. HXN X-ray Microscope

### IV. Summary

In conclusion, the need for a faster transfer of coordinates from the lab light microscope to the beamline x-ray microscope is satisfied with the application that I created. So far, the application organizes lab microscope images and displays the images in pixels on a pixel coordinate system as well as in microns on the lab microscope micron coordinate system. Through user interaction, a simple mouse click and input of new beamline location, the lab micron coordinate system is transferred to the beamline x-ray coordinate system. All composite images were captured and saved as jpg files with 800 dots per inch, increasing the resolution of the images. Additionally, an added zoom feature allows for zooming in to a specific region that depicts the image on a local coordinate system. This process could solve the issue of sample navigation being a challenge at the beamline for scientists in NSLS-II due to the different coordinate system between the lab microscope and the beamline x-ray.

### V. Future Work

In the future, we plan to integrate another GUI that would allow for scientists to click a reference point on an image on the lab microscope micron coordinate system and drag the cursor to

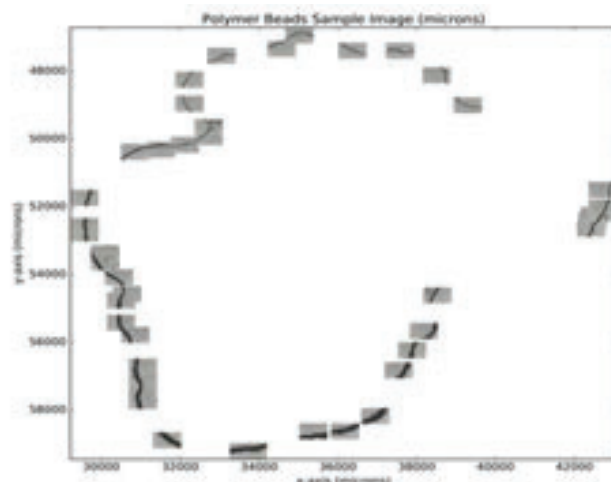


Figure 4: Polymer Beads assembled on lab micron coordinate system using x and y coordinates of bottom left corner of every image.

create a rectangular spatial region of interest. The code would then output x and y coordinates of four outmost corners of the region of interest. In addition, more translations options in regards to converting the lab microscope micron coordinate system to that of the beamline coordinate system would be implemented. Some of these would include directional translations, rotation, and flipping transformations of the coordinate systems.

## VI. References

Figure 2. (Sept., 2015) "NLSL II HXN (16)." *Flickr Photos*  
Tagged *Nslsii*, [farm1.staticflickr.com/741/20788934893\\_f472fb3757\\_b.jpg](http://farm1.staticflickr.com/741/20788934893_f472fb3757_b.jpg).

## VII. Acknowledgments

This project was supported in part by the U.S. Department of Energy, Office of Science, and Office of Workforce Development for Teachers and Scientists (WDTS) under the Science Undergraduate Laboratory Internships Program (SULI). Thank you to my mentor Randy Smith for all of his guidance throughout this research endeavor this summer 2017 and to Dan Allen for all of his direction and tips in imaging techniques. I would also like to express gratitude to Angela and OV Solomon for unparalleled support.

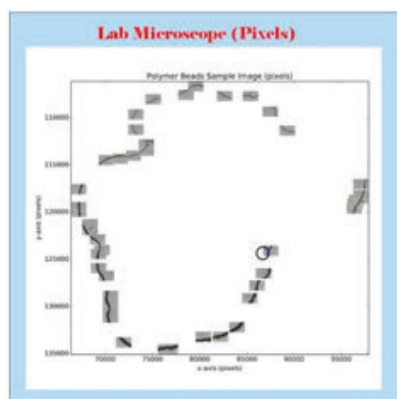


Figure 5: Polymer bead at 10x zoom plotted in pixels on pixel coordinate system

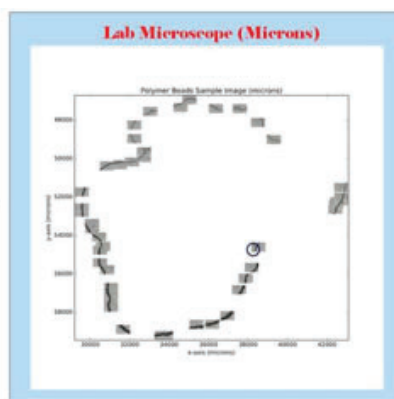


Figure 6: Polymer bead at 10x zoom plotted in microns on micron coordinate system

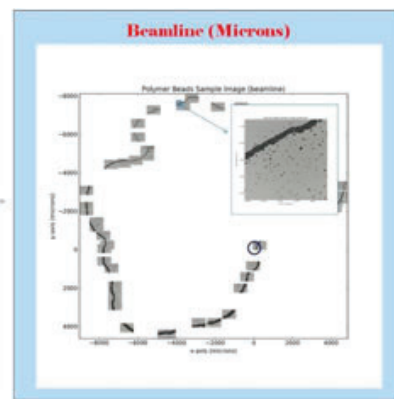


Figure 7: Polymer bead images translated to beamline micron coordinate system. Top right corner image shows zoom capability.

# Synthesis, activity, and characterization of Cu loaded ZSM-5 catalysts for the water-gas shift reaction

James Tata

Chemical Engineering, Texas Tech University, Lubbock, TX 79409

Dimitriy Vovchok

Chemistry, Brookhaven National Laboratory, Upton, NY 11973

Department of Chemistry, Stony Brook University, Stony Brook, NY, 11794

S.J. Khatib

Chemical Engineering, Texas Tech University, Lubbock, TX 79409

S.D. Senanayake

Chemistry, Brookhaven National Laboratory, Upton, NY 11973

Jose Rodriguez

Chemistry, Brookhaven National Laboratory, Upton, NY 11973

## Abstract

The water-gas shift reaction (WGSR:  $\text{CO} + \text{H}_2\text{O} \leftrightarrow \text{CO}_2 + \text{H}_2$ ) has the potential to enable hydrogen fuel cell technology through the production of pure  $\text{H}_2$  and simultaneous removal of the catalytic poison, CO. Additionally, the WGSR is currently used in industrial processes for CO purification and the balance of  $\text{H}_2$  and CO. We prepared Cu impregnated zeolite socony mobil-5 (ZSM-5) catalysts for use in the WGSR, then studied their activity and characterized their chemical properties. Nominal loadings of 1, 3, 5, and 10% were synthesized using the wetness impregnation technique. Samples were loaded into a quartz capillary tube in a modified Clausen flow cell. A mixture of 5% CO/ 95% Ar was passed through a gas bubbler to introduce approximately 3%  $\text{H}_2\text{O}$  into the reactant stream. Qualitative analysis of the product concentrations was carried out using a residual gas analyzer (RGA). Production of  $\text{CO}_2$  was observed between 150°C and 500°C, indicating that the catalysts are active and have a complex role for Cu and the ZSM-5 support. Diffuse reflectance infrared Fourier transform spectroscopy (DRIFTS) was utilized to study the surface chemistry of the catalysts under WGSR con-

ditions. DRIFTS revealed CO bound to  $\text{Cu}^+$  in two distinct locations within the ZSM-5 lattice. The amount of  $\text{Cu}^+$  species in each location were observed to be dependent on temperature, nominal loading, and WGSR conditions. X-ray photoelectron spectroscopy (XPS) was used to determine how the Cu species evolves throughout the temperature program. The Cu 2p and Auger data revealed that Cu is reduced from a higher oxidation state to its metal phase as the temperature is increased.

## I. Background

### A. Hydrogen and the WGSR

Hydrogen is an important chemical commodity that is widely used in many industries, such as the synthesis of ammonia, methanol, and hydrocarbons. However, the main obstacle to overcome is how expensive it is to produce. The WGSR is one way that this is accomplished. For example, the CO found in syngas ( $\text{CO} + \text{H}_2$ ), a common byproduct of oil reforming, can be reacted with  $\text{H}_2\text{O}$  in the presence of certain catalysts in order to produce  $\text{CO}_2$  and hydrogen. The  $\text{CO}_2$  can then be separated for further processing, leaving only the hydrogen.

## II. Methods

### A. Synthesis

The catalyst support used is ZSM-5 (Product # CBV 3024E, Zeolyst International). This support was chosen in part due to its near-atomic sized pores, which allow for individual metal atoms to be isolated and placed within the lattice structure. ZSM-5 is also inert by itself, meaning any activity seen will be solely from the loaded metal. The ZSM-5 is calcined by ramping from room temperature to 600°C at 2°C/min, holding at 600°C for 6 hours, and then naturally cooling to room temperature.

The metal chosen for the catalyst was Cu because of its known WGSR activity, as well as its relatively cheap price. The 1%, 3%, 5%, and 10% Cu by weight samples all require wet impregnation due to the low solubility of copper(II) acetate. These samples use copper(II) acetate dissolved in excess water. Calcined ZSM-5 is mixed with the solutions in separate roundbottom flasks, then the majority of the water is evaporated off using a rotovap. The flasks are then left to dry overnight in the oven at 120°C to remove the remaining water.

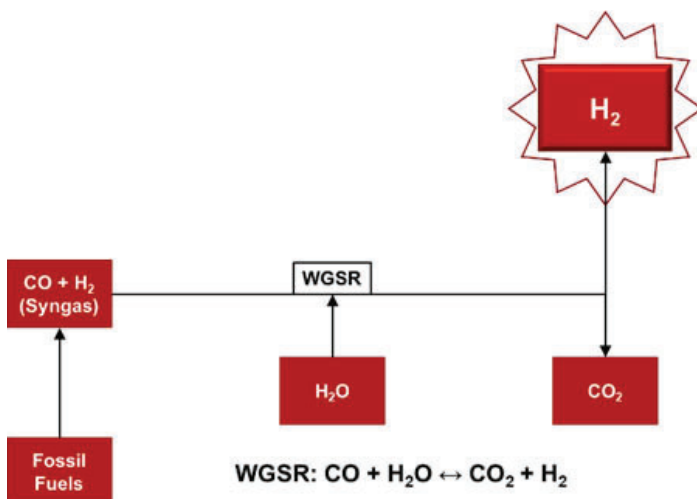


Figure 1: General diagram of WGSR using a syngas feed.



All dried impregnated ZSM-5 samples are crushed to a fine powder, then calcined by ramping from room temperature to 110°C at 1°C/min, holding at 110°C for 2 hours, ramping to 500°C at 1°C/min, holding at 500°C for 5 hours, then naturally cooling to room temperature.

## B. Activity Testing

To test the activity of the catalyst, a Clausen flow cell was used. The device is used to hold a quartz reactor tube containing the catalyst while the WGSR reactants are flowed through it. There is a pair of heating coils on either side of the tube, and when used with a thermocouple inserted into the reactor, they can control the temperature to within tenths of a degree. After the gas has flowed through the cell, it is analyzed by the RGA mass spectrometer. The amount of CO<sub>2</sub> which appears in the analysis is proportional to how active the catalyst is. All sample loadings were tested, including the bare ZSM-5 to confirm it wasn't contributing to the reaction. A pretreatment study was also carried out using the 5% Cu/ZSM-5 in order to see if they would increase the activity.

## C. Surface Characterization

*Ex situ* and *in situ* surface analysis was performed with AP-XPS. The X-rays are directed towards the sample plate, exciting electrons on the surface, which are then ejected and analyzed by the sensor cone. This method allows for the analysis of chemi-

cal species on the surface of the catalyst, such as the oxidation state of the copper. This equipment also allows for the addition of the WGSR conditions in order to study how these species change over the course of the reaction.

## D. Surface Mechanism

The *in situ* DRIFTS study allows for the various chemicals on the surface of the catalyst to be seen evolving under WGSR conditions. This study allows for a look into the mechanisms involved in the reaction, as well as a quantitative view of CO bound to Cu<sup>+</sup> in two distinct locations inside the ZSM-5 lattice structure.

## III. Results

### A. Activity data

The pretreatment analysis did not result in any significant increase in activity, so no pretreatment was utilized for the rest of the testing. All metal loadings were tested, with light off of the catalyst occurring at 150 °C. In every loading, the activity increased as the temperature increased, with the highest activity being seen at 500 °C. The metal loading affected the activity as well, with the 10% loading being more active at every temperature step.

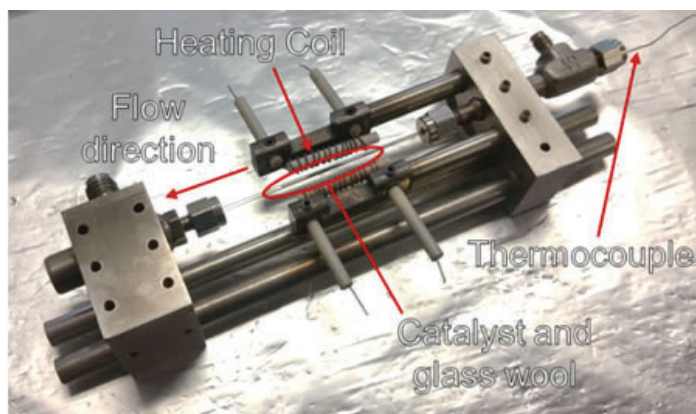


Figure 2: Clausen flow cell used for flowing reactant mixture through the catalyst

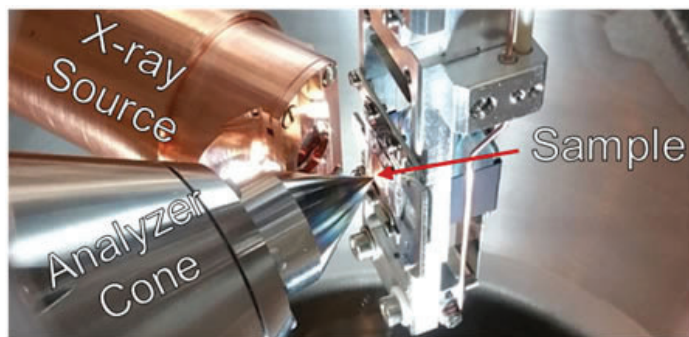


Figure 3: AP-XPS analysis equipment

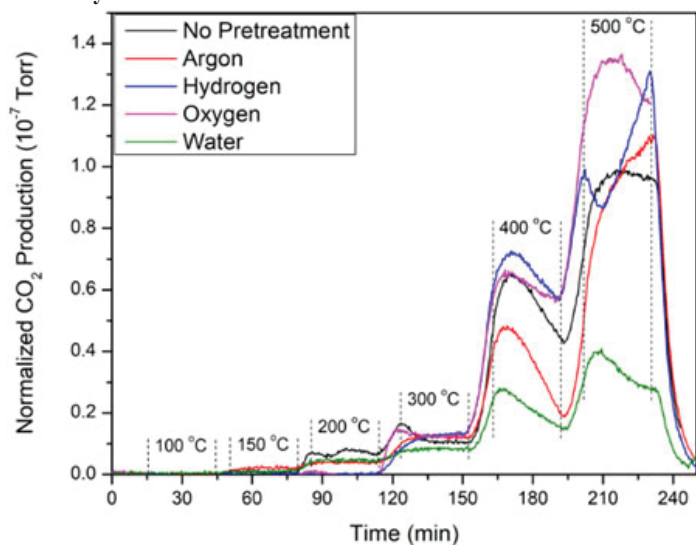


Figure 4: Evaluation of the effects of various pretreatments on activity

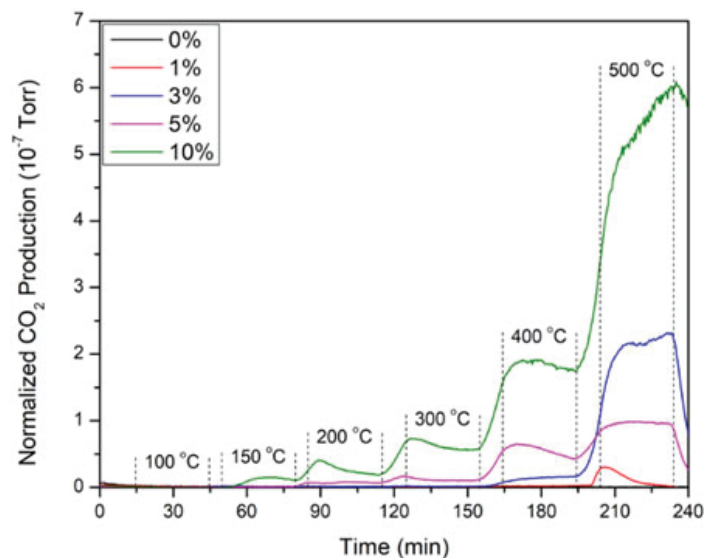


Figure 5: Evaluation of the effects of Cu loading on activity

## B. AP-XPS and Auger data

In the *ex situ* data, the main peaks observed in both the Cu 2p and Auger data suggest that the main copper oxidation state on the fresh catalyst in ambient conditions is  $\text{Cu}^{2+}$ . As the WGSR conditions were introduced to the catalyst, a transition occurs. The  $\text{Cu}^{2+}$  gets reduced to  $\text{Cu}^+$  at 150 °C to 300 °C, and then a transition to Cu metal at 500 °C.

## C. Surface Mechanism

From the DRIFTS spectra, the WGSR reactants can be seen being consumed as the temperature increases, and products can be clearly seen forming at higher temperatures. There are also some hydroxide and carbonate intermediates that can be observed. With further analysis, a full mechanism of the reaction on the catalyst

may be able to be formed. The peaks corresponding to CO bound to  $\text{Cu}^+$  is what was focused on for this analysis. When the data has the Kubelka-Munk mathematical transform applied to it, a more quantitative look at the two peaks can be analyzed. The peak at 2157  $\text{cm}^{-1}$  corresponds to CO bound to  $\text{Cu}^+$  in the oxygen 5-membered rings. The peak at 2138  $\text{cm}^{-1}$  corresponds to CO bound to  $\text{Cu}^+$  in the intersections of the main channels of the structure.

## IV. Conclusion

The RGA measurements confirm that the catalyst is active, as  $\text{CO}_2$  production is clearly observed. In the 5% Cu/ZSM-5 pretreatment experiment, no significant increases in activity were observed. However, the  $\text{H}_2\text{O}$  pretreatment appeared to dramatically decrease the catalysts performance. When running the activity

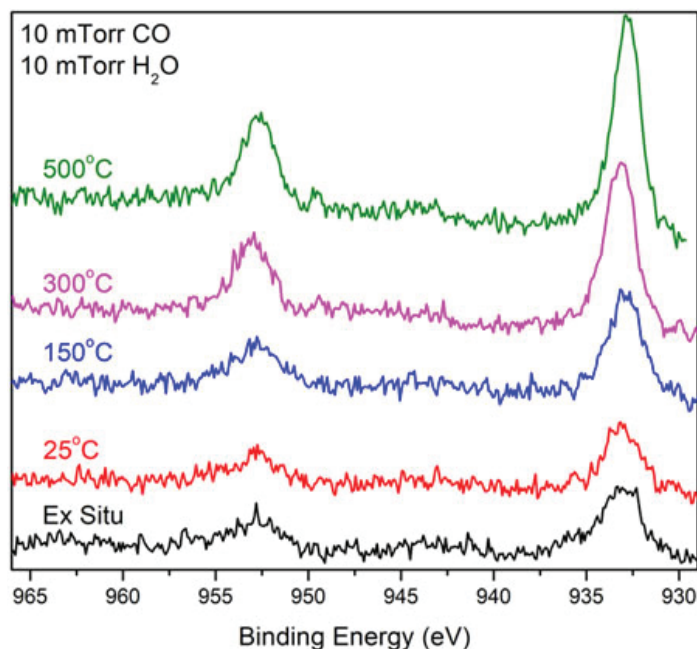


Figure 6: Ex situ and in situ Cu 2p data in WGSR conditions

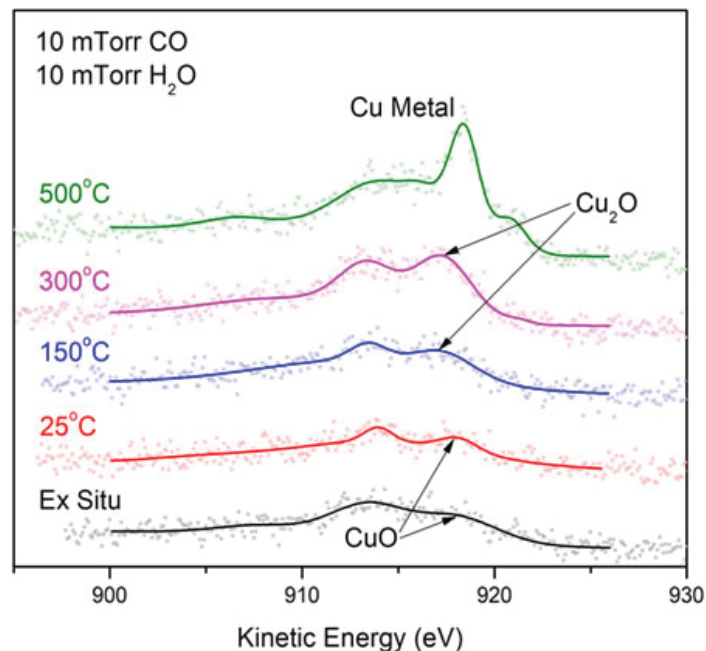


Figure 7: Ex situ and in situ Cu LMM Auger data in WGSR conditions

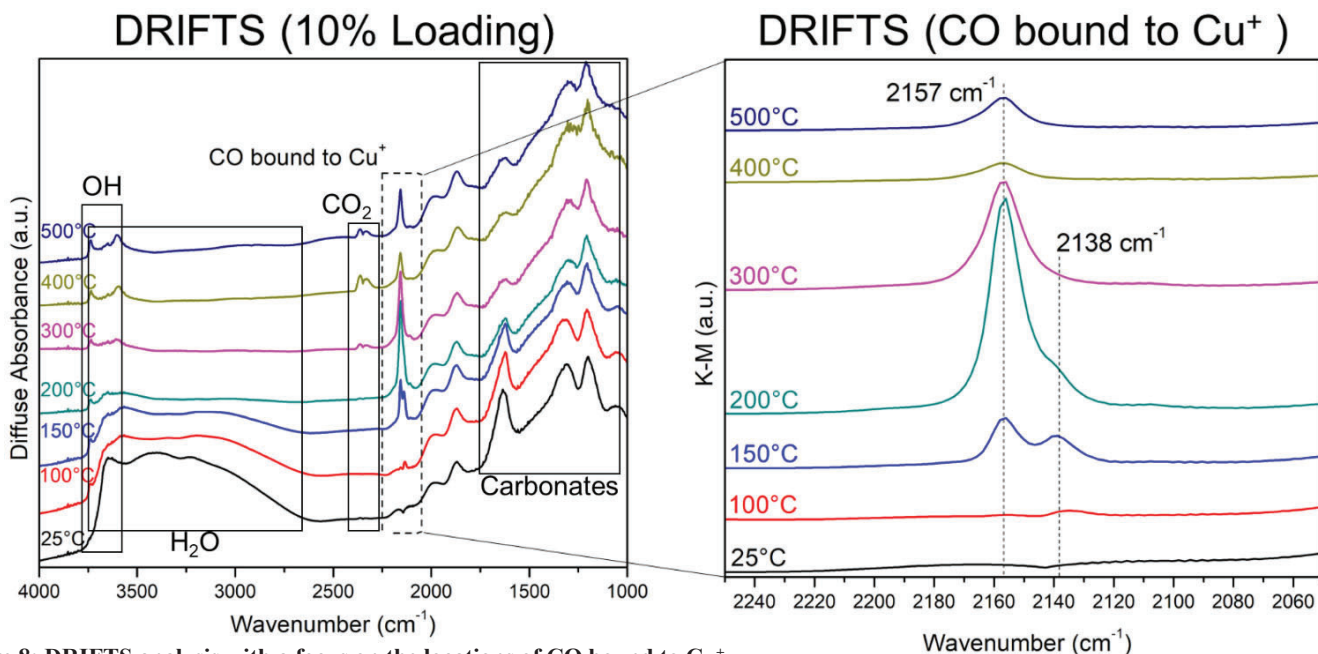


Figure 8: DRIFTS analysis with a focus on the locations of CO bound to  $\text{Cu}^+$

tests with varied loadings, no pretreatment was used. The 10% Cu/ZSM-5 showed the highest level of conversion at every temperature step, and was therefore selected for further testing.

DRIFTS revealed two locations of  $\text{Cu}^+$  bound to CO. The peak at  $2138\text{ cm}^{-1}$  corresponds to the intersection of the main channels in the ZSM-5 structure. The peak at  $2157\text{ cm}^{-1}$  corresponds to the interior of the oxygen 5-member rings. If the IR data is plotted using the Kubelka-Munk transformation, quantitative amounts of CO bound to  $\text{Cu}^+$  can be measured. The data from both peaks through the temperature program show an initial increase in this bound Cu phase, followed by a decrease as higher temperatures are reached. At  $500\text{ }^\circ\text{C}$ , our most active temperature, only the oxygen 5-membered ring peak is seen. This leads to the conclusion that this is where the actual reaction is taking place within the support.

The in situ AP-XPS data shows that as the temperature increases from  $25\text{ }^\circ\text{C}$  to  $500\text{ }^\circ\text{C}$ , the copper is reduced from  $\text{Cu}^{2+}$  to  $\text{Cu}^+$  then finally to Cu metal. This information fits with what is seen in the DRIFTS data, where  $\text{Cu}^+$  is seen to be the dominant phase at midrange temperatures. The greatest levels of activity in any loading are seen at  $500\text{ }^\circ\text{C}$ , which suggests Cu metal as the most active state.

## V. References

- I.C. Hwang, D.H. Kim, and S.I. Woo, *Catalysis Letters* 42, 177 (1996).  
XPS Interpretation of Copper. <http://xpssimplified.com/elements/copper.php#aboutthiselement>  
D.K. Chakrabarty, SlidePlayer (2016). <http://slideplayer.com/slide/9248538/>

## VI. Acknowledgements

I would first like to thank Sheima Khatib and Texas Tech University for providing me with the opportunity to be part of the Visiting Faculty Program (VFP), which has taught me valuable lessons about research that I will take with me to graduate school. I would also like to thank Dimitriy Vovchok and Sanjaya Senanayake for being outstanding mentors this Summer. This project was supported in part by the U.S. Department of Energy, Office of Science, Office of Workforce Development for Teachers and Scientists (WDTS) under the Visiting Faculty Program (VFP). The research carried out at Brookhaven National Laboratory was supported by the U.S. Department of Energy, Office of Science and Office of Basic Energy Sciences under contract No. DE-SC0012704.

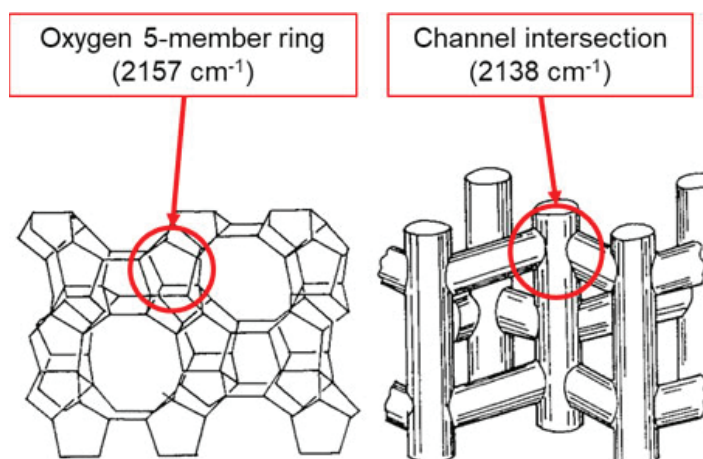


Figure 9: Locations of CO bound to  $\text{Cu}^+$  corresponding to DRIFTS data



# The effects of human-made disturbances on small mammal populations

Leanna Thalmann

Center for Earth and Environmental Science, SUNY Plattsburgh, Plattsburgh, NY 12901

Jennifer Higbie

Environmental Protection Division, Brookhaven National Laboratory, Upton NY 11973

## Abstract

Since small mammals are important indicator of ecological health and also provide insight on tick populations and Lyme disease, it is important to understand the effects of human-made disturbances on white-footed mouse (*Peromyscus leucopus*) populations. This summer at Brookhaven National Laboratory (BNL), I conducted research on small mammals and the disturbances they encounter, specifically roads. The goal of the study was to determine if trap location and recapture rates are affected by the distance to roads. Each week, four separate 35 meter square plots were set with 64 Sherman traps at each site. Each trap was five meters apart and marked with a flag. The GPS location of each plot was recorded and mapped with Geographic Information Systems (GIS). The population density was determined and graphed according to the sites distance from the nearest road and then compared across each site. This research will help determine how small mammal populations are effected by roads. The skills I learned include setting up Sherman traps, handling small mammals, and using mark and recapture methods to determine population size. This research has helped me grow professionally by allowing me to work with scientists and see how proper science is completed.

## I. Introduction

Small mammals are good indicators of ecological health. It is important to understand the effect of anthropogenic or human-made disturbances on local animal populations. White-footed mice (*Peromyscus leucopus*) populations are effected by varying anthropogenic disturbances. Disturbances that are human-made cause stress, fragmentation of habitats, and create patches and isolation to other habitats; increases in fragmentation can lead to high population densities in edge habitats (Mathis et al. 2004). Roads have been found to act as barriers to small mammal movement, including movement of white-footed mice (*Peromyscus leucopus*), the focal species in this study (Rytwinski, T. and Fahrig, L. 2007). High road densities can limit white-footed mice (*Peromyscus leucopus*) population densities and abundance. Forman (2000) estimated that about one-fifth of the United States land area is directly affected ecologically by the network of public roads and that this fraction is increasing. Brookhaven National Lab has roads that have been used since World War One. Since then the lab has grown and more human-made disturbances have been introduced. This study aims to document the effects of roadways on white-footed mice (*Peromyscus leucopus*) populations. Some objectives for this study include learning how to properly handle white-footed mice (*Peromyscus leucopus*), and record data correctly, and to determine the population density. I hypothesized that plots further away from roads will have a higher white-footed mice (*Peromyscus leucopus*) population density.

## A. Site Description

The study area was Brookhaven's 5,321-acre campus located in Long Island's Central Pine Barrens region and within the watershed of one of Long Island's four major rivers, the Peconic River. Often described as Long Island's last remaining wilderness, the Central Pine Barrens covers more than 100,000 acres of public and privately-owned land in Suffolk County. The Pine Barrens are a unique ecosystem dominated by groundcover, shrub thickets, a variety of oaks and pitch pine trees which grow in sandy, acidic, and infertile dry upland soils. The Pine Barrens also contain a diverse range of wetland communities such as marshes, coastal plain ponds, bogs, and river corridors ("Brookhaven National Laboratory").

## II. Methods

Small mammal population surveys were conducted at Brookhaven National Laboratory (BNL) in Upton, NY throughout June, July and August 2017. All mice were captured using Sherman live traps at sixteen study plots within BNL's campus over an eight week period. At each site a 35 meter x 35 meter grid was established of 64 traps each marked with a flag and spaced 5 meters apart. The GPS location of each site was recorded. Traps were baited with a peanut butter/oat mixture. Animals were trapped at each site over four consecutive nights during two alternate weeks for a total of 8 days. The total trap nights were 8192. Traps were checked each morning; captured animals were weighed, sexed, and marked with individual ear tags. Recaptured individuals were noted. All attached ticks were removed and preserved. Each site was measured from its center to the road and recorded. Using this data the GPS location of each plot was mapped with ArcMap 10.1 a Geographic Information Systems (GIS). The population density was determined and graphed according to each sites distance from the road and then compared across each site.

Program MARK Version 8.1, robust design model was used for a parameter estimate of white-footed mice abundance at each site. The robust design model considers the time interval between trapping sessions as "open" and the time interval during trapping as "closed" (Cooch and White 2006). Program DENSITY Version 5.0 was also used to predict the size of white-footed mice population using the spatially explicit capture-recapture data collected (Efford 2012).

## III. Results

There was no significant relationship between the sizes of the populations of mice calculated from program MARK and the distance from the road at each site (Fig 1A;  $R^2= 0.86$ ,  $p = 0.27$ ,  $n=16$ ). Additionally, the basic linear regression showed there was not a significant relationship between the density of mice calculated from program DENSITY with distance from the road at each site (Fig 2A;  $R^2= 0.71$ ,  $p = 0.02$ ,  $n=16$ ).

Table 1. GPS coordinates (Universal Traverse Mercator units) of the sixteen sites used in the study. See figure 1.

Plot	Latitude	Longitude	Plot	Latitude	Longitude
Site 1	0678997	4524445	Site 9	0681104	4527788
Site 2	0679011	4524464	Site 10	0681231	4528161
Site 3	0679730	4524870	Site 11	0681098	4527741
Site 4	0679742	4524914	Site 12	0681239	4528025
Site 5	0680555	4527194	Site 13	0678160	4524539
Site 6	0680575	4527175	Site 14	0678191	4524599
Site 7	0681117	4526649	Site 15	0681273	4528249
Site 8	0681090	4526683	Site 16	0681033	4528793

#### IV. Discussion

*Peromyscus leucopus* is a keystone species in relation to *Ixodes scapularis* and *Borrelia burgdorferi* bacteria in major Lyme disease infection regions (Tsao et al., 2004). Therefore, understanding the ecological relationships that affect their populations are crucial to assessing Lyme Disease risks. I predicted that the closer the site was to the road the lower the abundance and density of mice. The hypothesis formed in this study was not supported. This conclusion may be due to varying human-made and natural disturbances that includes vegetation type, and cover, weather and prescribed fire burns. In another similar study they found no significant relationship, between road density and the presence of *P. leucopus* during the early spring (Rytwinski, T. & Fahrig, L 2007). They also found that there study was the first to test

their hypothesis making no other published reports to which they could compare their findings (Rytwinski, T. & Fahrig, L 2007).

Other experiments may replicate this study using more sites to determine how greatly roads effect *Peromyscus leucopus* populations. Some potential modifications to this experiment's replication may include sites located in other areas besides BNL and more variable distances used. Although this experiment was well-designed, there are a few possible sources of error that should be considered. Possible sources of error may include mistakes with

Site	Abundance of mice from MARK analysis	Densities of mice calculated from program DENSITY	Distance from the road (m)
1	31.1	30.5	40
2	35.4	27	46
3	3.3	6	37
4	35.4	35	48
5	8.6	9	46
6	35.6	18.5	36
7	12.6	18.5	23
8	19	19	31
9	11.1	13.5	21
10	8.5	12.5	36
11	13	12.5	49
12	24.8	27	36
13	26.9	31.5	32
14	20.5	26.5	24
15	14.3	13.5	30
16	22.3	24	38

Table 2. Abundance of mice calculated from MARK recapture analysis, and Program Density from each encounter at each site. Compared to the distance from the center of the plot to the road of each site.

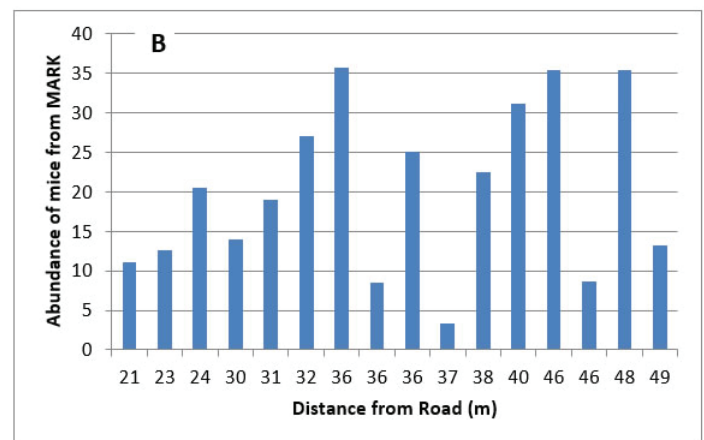
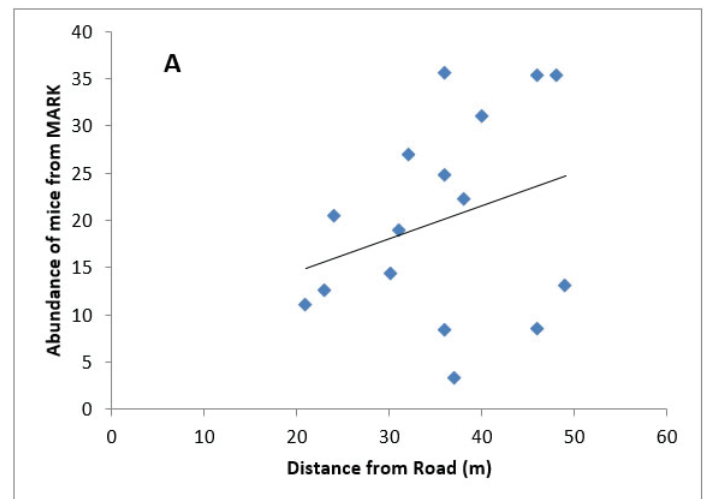


Figure 1 A- Each sites distance from the road in relation to the abundance of mice from MARK recapture analysis at each site as a linear regression. B- Each sites distance from the road in relation to the abundance of mice from MARK recapture analysis at each site as a bar graph sorted from smallest to largest.

baiting, raids by other wild animals, trap failure, misreading ear tags and escapees which could potentially skew data in plots and miscalculations made using the collected data.

## V. Acknowledgments

I would like to give a special thanks to Jennifer Higbie for all of her support and guidance on this project. This project was supported in part by the U.S. Department of Energy, Office of Science, Office of Workforce Development for Teachers and Scientists (WDTS) under the Science Undergraduate Laboratory Internships Program (SULI).

## VI. Citations

- Cooch, E., & White, G. (2006). Program MARK: a gentle introduction. Available in pdf format for free download at <http://www.phidot.org/software/mark/docs/book>.
- Efford, M. G. (2012). DENSITY 5.0: software for spatially explicit capture–recapture. *Department of Mathematics and Statistics, University of Otago, Dunedin, New Zealand* <http://www.otago.ac.nz/density>.
- Forman RTT (2000) Estimate of the area affected ecologically by the road system in the United States. *Conserv Biol* 14:31–35
- Mathis, C., Blalock, R., Virk, M., Compton, S., Coe, S, Derting, T. 2004. The effect of anthropogenic disturbance on the health of white-footed mice (*Peromyscus leucopus*). *Journal of the Kentucky Academy of Science*. 65: 62-63.
- Brookhaven National Laboratory “Our Natural Resources.” *BNL*

| *Natural Resources*, [www.bnl.gov/about/sustainability/naturalresources.php](http://www.bnl.gov/about/sustainability/naturalresources.php)

Rytwinski, T. & Fahrig, L. *Landscape Ecol* (2007) 22: 1501. <https://doi.org/10.1007/s10980-007-9134-2>

Tsao, J. I., Wootton, J.T., Bunikis, J., Luna, M.G., Fish, D., & Barbour, A.G. (2004). An ecological approach to preventing human infection: vaccinating wild mouse reservoirs intervenes in the Lyme disease cycle. *Proc. Natl. Acad. Sci. U.S.A.*, 101(52), 18159–18164.

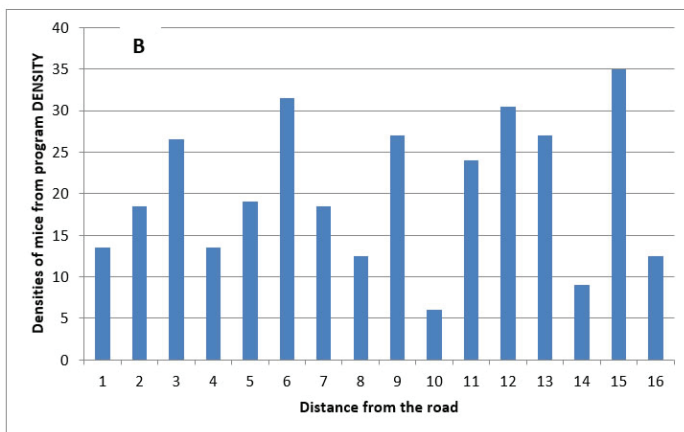
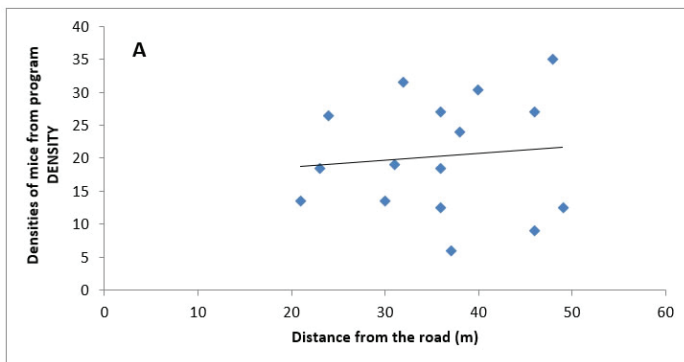


Figure 2 A- Each sites distance from the road in relation to the density of mice calculated from Program DENSITY at each site as a linear regression. B- Each sites distance from the road in relation to the density of mice calculated from Program DENSITY at each site as a bar graph.

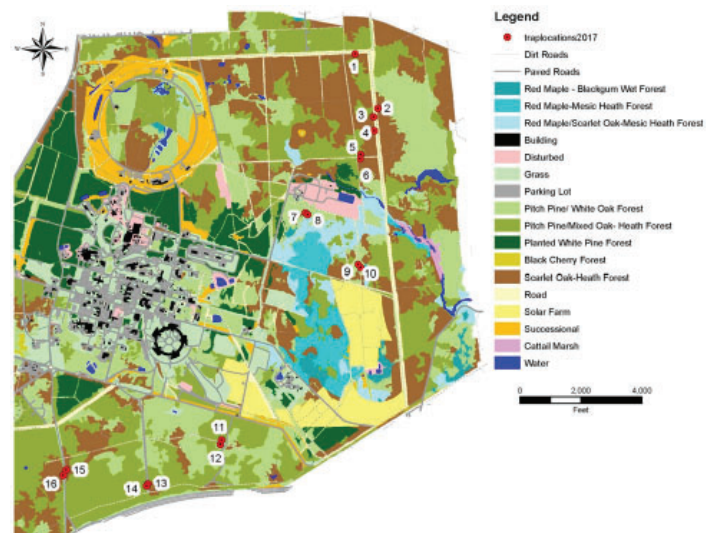


Figure 1. Map of Brookhaven National Laboratory with the sixteen sites surveyed.



# Modeling of superconducting magnet for ALPHA G experiment

Justin Tufaro

Mechanical Engineering, Stony Brook University, Stony Brook, NY 11720

Michael Anerella and Andrew Marone

Superconducting Magnet Division, Brookhaven National Laboratory, Upton, NY 11973

## Abstract

The ALPHA experiments conducted by Conseil Européen pour la Recherche Nucléaire (CERN) are an ongoing search to discover the secrets of antimatter, and how its properties differ from that of ordinary matter. When the experiments began in 2005, CERN trusted Brookhaven National Laboratory (BNL) with the task of constructing the superconducting magnets necessary to capture and contain antiparticles. CERN and BNL's Superconducting Magnet Division have been working closely ever since, and are currently working in tandem to create a containment device for the latest iteration of tests. The superconducting magnet produced for the ALPHA G experiment will be able to create and contain antihydrogen molecules for longer amounts of times, and most importantly be able to detect how the molecules react to the force of gravity between matter and antimatter. In order to accomplish this, the magnet must be able to create and maintain a .65 Tesla average internal field, and be able to withstand the axial and radial stresses due to intense magnetic forces. Moreover, the magnet will be subjected to extremely high thermal stress due to sections of the magnet being super cooled to 1.9 K. Over the course of the past ten weeks I aided in the design process of the ALPHA G magnet by creating 3D models and drawings for all parts using PTC Creo software. Additionally I learned how to use ANSYS software to get precise stress calculations by utilizing finite element analysis. The designs I have drawn and modeled have been approved by my mentor, Michael Anerella, and lead engineer of the project Andrew Marone, and will be soon sent out to vendors to be manufactured.

## I. Background

There have been many mysteries surrounding the properties of antimatter ever since it was first theorized by Paul Dirac in 1933, and the eventual discovery of antiparticles that came in the following decades. According to Dirac's theory the properties of antimatter should be symmetric but opposite to that of ordinary matter. (1) This principal of symmetric but opposite properties is essential in order for Einstein's theory of relativity to hold true. Experiments conducted by James Cronin and Val Fitch here at BNL provided evidence that contradicted these claims back in 1964, the tests they ran showed that a particle and its antiparticle can have differing lifetimes. Their Nobel Prize winning work have inspired researchers to dig deeper into whether or not antimatter and matter are symmetric. The ALPHA G experiment is pursuing the answer to this very same question by testing whether or not acceleration due to gravity between matter and antimatter is symmetric between the two.

Previous experiments have been conducted on the topic, but early experiments were very inaccurate due to their use of non-neutral particles. The disadvantage of using non-neutral par-

ticles is that electromagnetic forces are very strong relative to the force of gravity of particle which directly effects results. Previous ALPHA experiments have been able to set parameters on acceleration due to gravity on antimatter, but was not able to make precise measurements. (2)

## II. Methods Project Overview

The magnet being produced for the ALPHA G experiment will allow for research that has previously been unachievable due to electromagnetic forces between molecules being overwhelmingly stronger than the gravitational force. The advantage of being able to contain antihydrogen for an extended amount of time is that antihydrogen is a neutral molecule which allows researchers to mitigate the electromagnetic forces. The magnet works by first being able to capture and contain antiprotons and positrons (anti-electrons) and stores them separately, after these anti particles are trapped they are cooled so that they can bond and create antihydrogen. Once the antihydrogen is created it will be release from a vertical atom trap and the analysis coils found towards the center of the magnet will be able to record the position of the antihydrogen until it eventually hits one of the walls of the magnet and disintegrates. Designing the magnet as vertical fixture as opposed to a horizontal fixture, along with advancements in cooling technology, will allow for researchers to obtain measurements within 1%. (2) This will provide researchers with more accurate measurements of acceleration due to gravity. In order to achieve the goals of this research, several critical design requirements had to be met. The magnet must be able to be installed vertically, must be able to support the magnetic forces that vary by region throughout the magnet, and most importantly be able to precisely place the mirror and analysis coils in order to create the desired magnetic field and achieve the most accurate measurements possible.

### A. Modeling

The use of 3D modeling software is an essential part of the modern design process, and allows for changes to easily be made and assessed visually, as well as analyzed with tools of the software itself. I began my work this summer by making revisions to the rough model of the main support tube for the magnet using PTC Creo 3D modeling software. Key features had to be added to the support tube, and several adjustments had to be made to the length and diameter of certain sections of the magnet. The first step was to make grooves along the flanges of tube, as well as entering and exiting areas for both electrical and cryogenic leads. Size M5x.8 mm radial tapped holes were then added to the flanges on both sides of the tube so that the mirror coil bobbins can eventually be attached to it. The radial holes in the flanges were originally axial holes, but had to be changed so that the tube would have a means to resist rotation while being machined. Additionally a pilot hole will be drilled into the top end of the support tube,

this will act as a reference point for alignment when the magnet is being assembled.

Two mirror coil bobbins had to be designed and modeled for this project, one can be found on either end of the support tube. These bobbins are where the superconducting copper alloy coils that allow for the successful operation of this magnet will be wound, and are the two parts that will experience the highest levels of stress while the magnet is being used. The most critical design requirement of the bobbins is that they must be able to precisely position the coils set distances from each other in order to create the proper magnetic field. To do this I had to calculate the thickness of the flanges in between coils as well the spacing between each flange in the bobbins. Radial holes were made to line up with the aforementioned holes in the support tube. Additional holes were made for pressure relief in the event that the liquid helium that is used to supercool the magnet began to boil too rapidly and large bubble started to form and become trapped within the casing of the magnet. Another key feature that had to be added were small 3x1.5 grooves that must be milled into flanges where the superconducting coil will enter or exit from while being wrapped. Superconducting copper alloy has many advantageous properties, but one disadvantage that comes with its use is that it isn't very flexible. The rigid alloy can face high stresses if there are any twists in it or it is wound improperly, so it is important that the coil be able to access the bobbin on a proper angle tangent to the outer diameter of the bobbin so there is no twisting. The end of each mirror coil bobbin that will attached to the analysis coil support needed to tapered to fit a M95x1.5 mm thread. One of the bobbins was created with a left handed thread, and the other with a right handed thread so that the two bobbins can be screwed on simultaneously. This helps to ensure that each bobbin is tightened to the same amount of turns on each side which increases accuracy in regards to the positioning of the coils.

To complete the form structure of the main support tube and two mirror coil bobbins, we had to design and model what is called the analysis coil support. This part will attach to each bobbin and bridge the gap between the two as well position and support an analysis coil on each end. Because this part will not experience high level of stresses we were able to make four sets of large oval holes that are evenly spaced throughout the middle of the support in order to cut costs of production. Additionally each end of the support had M95x1.5 mm thread added to it to fit with the bobbins, one end having right handed thread and the other left handed thread. In addition to making models for these four main support structures I modeled several other minor parts that are required for the full assembly of the magnet



Figure 1 Assembly model created using PTC Creo.

## B. Drawings

Another advantage of using 3D modeling software is that the model can easily be transferred into a “.drw” which allows you to make 2D sketches of the design you already modeled. Sketches were made and dimensioned for every part that was modeled, cross-sections and detailed views were made to show important features, and tolerances were added to critical dimensions. Assembly drawings were also drafted to better explain to technicians how the magnet should be properly assembled. Completed drawings were sent to the lead engineer and supervisor of the project for approval.

## C. ANSYS

Due to the complexity of forces acting upon the magnet, especially within the mirror coil bobbins, it is necessary to use ANSYS Workbench to calculate stresses. There are 11 different tensile loads that act upon the bobbins while the magnet is being energized, some of these forces go up to 4900 pounds. These axial loads come from magnetic forces between each coil in the magnet, additionally each coil also adds its own compressive load in the radial direction with pressures going as high about 815 psi from a single coil.

To run finite element analysis simulations on ANSYS Workbench I first had to create test parts for each main form structure that would be better compatible with the ANSYS program. I then imported files from PTC Creo into ANSYS where I was able to place forces and call out supports in the desired locations. All four parts of the form structure were made of the same material, 316 LN stainless steel which has an elastic modulus of 29 1 10n psi, and also shared the same allowable stress of 20,000 psi. Some areas of high concern during the design process were the area of the main support tube where the main octupoles are located, and the areas on the mirror coil bobbins in between a set of two coils.

The area between the two coils are most likely to fail due to axial tension because this is the region where surface area is minimum due to the hole pattern bored into it.

Figures 3 and 4 show that the stresses caused by the axial loads in both the bobbins and the support tube are well below the allowable stress of the design. Figure 5 shows a simulation of the form assembly that includes all possible forces that can act upon the magnet, and as you can see stresses peak at about 17,000 psi which is still below the allowable stress for the design.

## III. Results and Conclusion

Drawings of both the mirror coil bobbins, the analysis coil support, and the main support tube were checked and approved by the lead engineer, as well as my mentor and supervisor for the project. Final designs for main support tube, analysis coils supports, and the two mirror coil bobbins have been sent out to vendors for production, and will be delivered back to BNL in mid-September. Afterwards parts will be sent out to receive a ce-

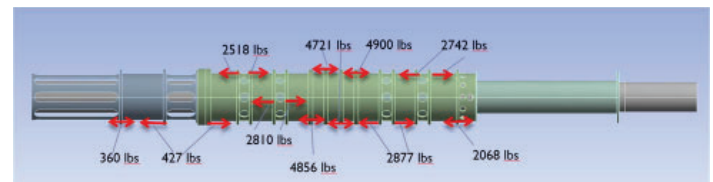


Figure 2 Axial load created by magnetic forces between coils.

ramic coating which will aid in thermal and electrical insulation before the winding of coils is to begin. After the winding of the coils is completed here at BNL, and the magnet is assembled it will be sent out to CERN for operation.

#### IV. References

1. The story of antimatter | CERN timelines. <https://timeline.web.cern.ch/timelines/The-story-of-antimatter>
2. P. Perez, M. Doser, and W. Bertsche, Does antimatter fall up?, CERN Courier, February 2017.

#### V. Acknowledgements

I would like to acknowledge and extend my thanks to my mentor for the summer Michael Anerella and engineer Andrew Marone. The knowledge I gained working underneath these two talented engineers, as well as all the engineers in the Superconducting Magnet Division, is invaluable and I am very thankful for the opportunities I was granted this summer. This project was supported in part by the U.S. Department of Energy, Office of Science, Office of Workforce Development for Teachers and Scientists (WDTS) under the Science Undergraduate Laboratory Internships Program (SULI).

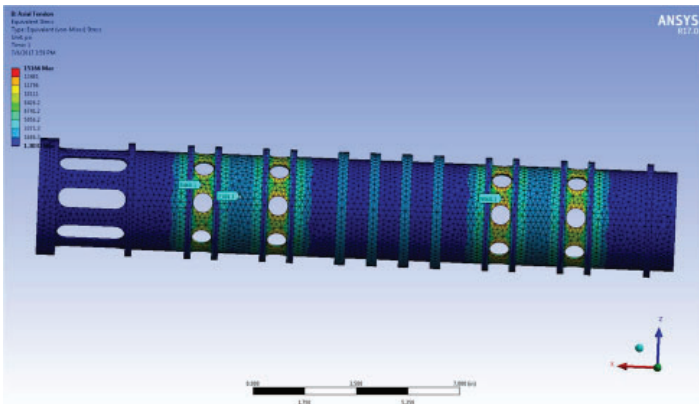


Figure 3 Mirror coil bobbin stresses due to axial forces.

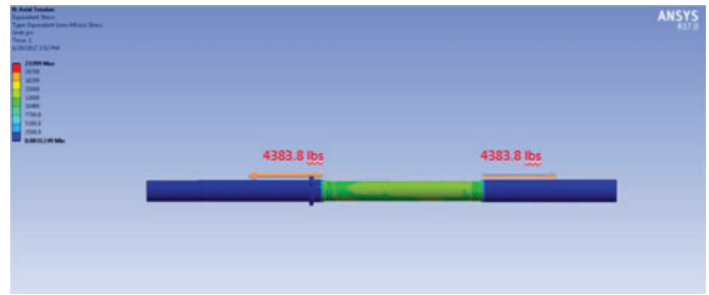
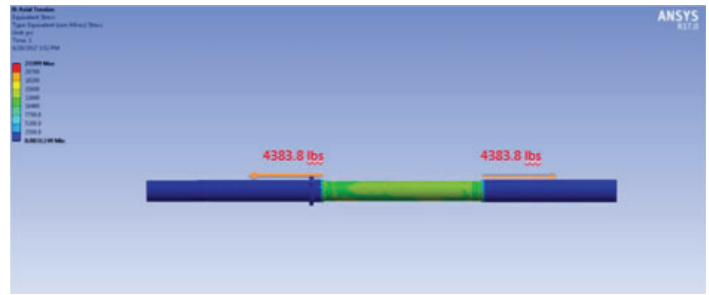


Figure 5 Stresses of full assembly of magnet with all loads acting upon it.



# Optimizing the Large Synoptic Survey Telescope camera's thermal mechanical performance

Julianna Volpe

Engineering Science, Suffolk County Community College, Selden, NY 11784

Steven Bellavia

Accelerator Department, Brookhaven National Laboratory, Upton, NY 11973

## Abstract

The Large Synoptic Survey Telescope (LSST) is being built by several organizations to take high resolution astronomical images of the entire sky. The LSST camera team at Brookhaven National Laboratory (BNL), funded by the Department of Energy, is responsible for the development of the 21 camera modules called Raft Tower Modules (RTM), which make up the LSST's focal plane. Each RTM is composed of 9 Charge Coupled Device (CCD) sensors. The tower holds the electronics for the detector which when running, will generate large amounts of heat. It is important to keep the detector cool because heat creates electronic noise which disrupts the image quality. Electro-optical testing of a single RTM indicated that the CCD sensors were reaching temperatures higher than originally anticipated. As this test was not instrumented for thermal-mechanical testing, a dedicated test setup was required to fully test the thermal impedance of all the mechanical components, from the CCD sensor to the source of cryogenic cooling. Actual camera components were used in the thermal mechanical test setup, including the thermal strap, a silicon carbide sensor support baseplate, and the copper raft electronics cage walls, which provide the thermal path to the cryogenically cooled cryoplate. The various tests performed included a baseline test, wrapping the baseplate and chamber walls in a gold-plated foil to reduce the radiant heat load, and applying indium between mating surfaces to reduce the thermal resistance. The results are then formatted, evaluated and uploaded to an LSST collaboration knowledge base for further evaluation by other LSST project members. Upon analysis of the results it seems the strap is performing as originally proposed although the baseplate was absorbing significantly more heat through radiation from the cage walls. Therefore, we are currently investigating adding heat shields

to the system and/or redesigning the straps to handle a higher heat load.

## I. Background

BNL engineers designed a thermal strap to act as the primary cooling device for removing heat from the raft sensor assemblies (RSAs) in the LSST. Testing of the LSST thermal strap's performance began due to results of tests performed in test stand 8 (TS8) on RTM#2 concluding the CCDs were running hotter than specifications allowed. Furthering testing performed in TS9 and comparing of theoretical vs experimental results will give a better understanding of the straps thermal performance and what can be done to make improvements.

## II. Theory

- The thermal conductance may be increased by:
  - Improving thermal contact between mating surfaces.
  - Improving thermal contact within swaged area of the strap.
- The RSA baseplate is made of silicon carbide (SiC) which has a high emissivity value. This could have a negative effect on cooling the system as it will easily absorb heat. Therefore, blocking the radiant heat can aid in reducing the total heat load, thus reducing the final CCD temperature.
- The design of the strap may be changed to improve its heat removal efficiency.

## III. Thermal Specifications

The strap is composed of two solid copper end pieces connected though swaging 4 copper wire braids (see figure 3). Each braid contains 4655 wires, each wire being 50.8 $\mu$ m in diameter

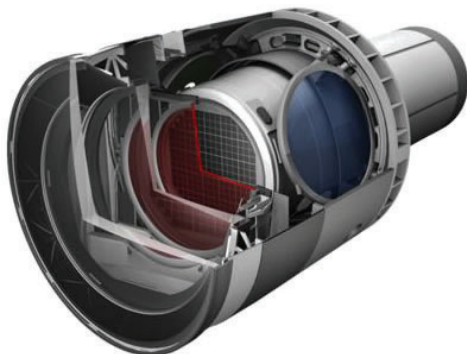


Figure 1: Sectional view of LSST camera

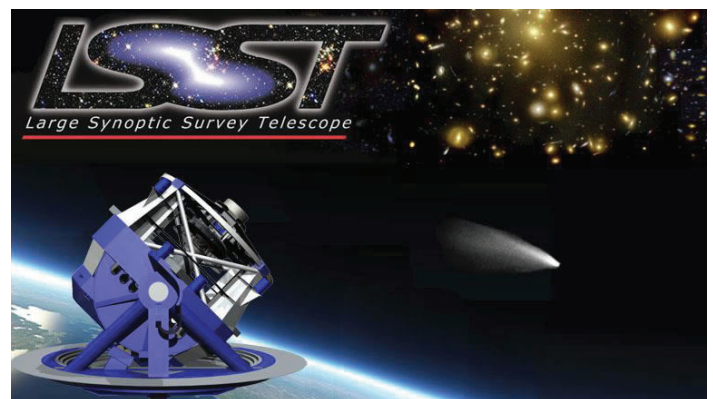


Figure 2: LSST and logo

and 62mm in length. Per hand calculations the strap is proposed to have a thermal resistance of 5.47K/W or thermal conductance of 0.183W/K.

Thermal requirements state the working temperature for the RSA plate will range between -110°C and -95°C, and for the REC wall between -130°C and -115°C. The temperature gradient across the thermal strap will be approximately 16° and the gradient from CCDs to the cryoplate will be about 30°C.

#### IV. Calculations

To calculate the thermal conductance across the strap the following equations were used:

$$G_{strap} = \frac{K \times A}{L} \quad (1)$$

Where  $G_{strap}$  is the conductance of the strap itself measured in  $\frac{Watt}{Kelvin}$ .  $K$  is the conductivity, which is a value dependent upon material type and temperature, measured in  $\frac{Watt}{meter \times Kelvin}$ . The  $K$  value used in these equations,  $400 \frac{Watt}{m \cdot K}$ , which is approximately a steady value from -100°C to room temperature.  $A$  is the total area of the strap (end blocks and braids) measured in meters<sup>2</sup>.  $L$  is the length of the object measured in meters.

$$G_{contact} = h \times A \quad (2)$$

Where  $G_{contact}$  is the thermal conductance through mating surfaces and  $h$  is the thermal contact conductance which is a function of material type and pressure, measured in  $\frac{Watt}{meter^2 \cdot Kelvin}$ .

$$G_{total} = \left( \frac{1}{G_{strap}} + \frac{1}{G_{RSA \rightarrow strap}} + \frac{1}{G_{strap \rightarrow REC}} \right)^{-1} \quad (3)$$

Where  $G_{total}$  is the total thermal conductance across the strap. This includes the conductance within the strap as well at the conductance at each mating surface. To find the thermal resistance use the equation below.

$$R = \frac{1}{G} \quad (4)$$

#### V. Testing performed in test stand 9

Tests in sections B-E were in vacuum pumped down to about  $3 \times 10^{-4}$  Torr, thermal strap screws were torqued to 52N-cm and a cryocooler was used to remove heat.

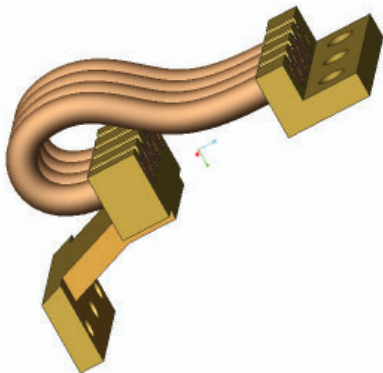


Figure 3: Image of thermal strap using Creo Parametric software

#### A. Baseline of RSA thermal strap

Using Creo™ Parametric, we designed a connector to be made of copper, for its good conductance, had it machined in the machine shop and attached it to the feedthrough which penetrates the cryostat. This connector provided a marriage between the feedthrough and the thermal strap, also consisting almost entirely of copper. Using dry ice and a Styrofoam container the outer side of the feedthrough was cooled resembling the Raft Electronics Crate to about 0°C. Then approximately 5W of heat was applied using a small electrical heater attached to the opposite end of the thermal strap (inside the cryostat), resembling the RSA for about 170 seconds, until the RSA side of the strap reached around 22°C.

Attached to each end of the thermal strap and to the outer end of the feedthrough are Resistance Temperature Diodes (or thermometers). These sensors were used to collect temperature readings over time, applying heat and cooling to obtain a temperature constant by analyzing the rate of cooling.

Results, seen in figure 5, comparing the finite element analysis (FEA) and the experimental data allows us to calculate the thermal contact resistance. It is very difficult to theoretically calculate thermal contact resistance, whereas conductance and capacitance are well known. This is the reason the experiment is so important as it provides us with the data necessary to determine the thermal contact resistance.

#### B. Baseline test

This test was setup to evaluate the thermal circuit using an REC wall, thermal strap, and baseplate (figure 8). The cryostat was pumped down and cooled until it reached steady state.

Results from this baseline test (figure 7) show a temperature gradient ( $\Delta T$ ) of about 15.0°C across the strap (end to end) and a  $\Delta T$  of about 1.0°C between mating surfaces of the RSA and strap end. The  $\Delta T$  between the REC wall and the strap end was less than 1.0°C.

Note: The uncertainty measured for each RTD is approximately  $\pm 0.25^\circ C$  for all tests.

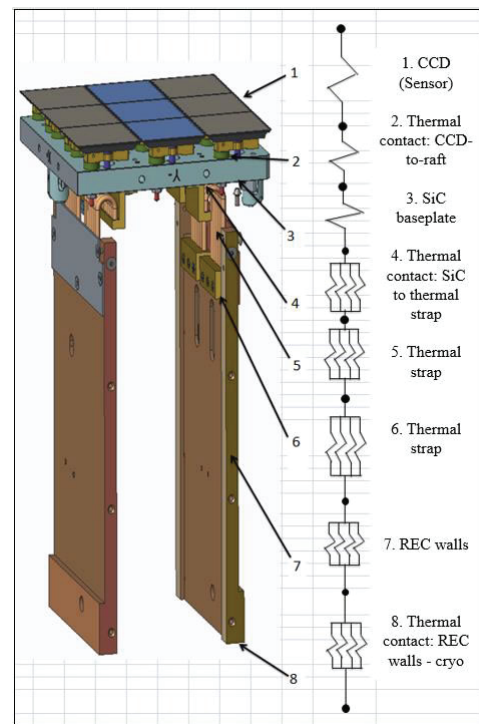


Figure 4: Sensor cooling circuit

### C. Gold foil test

This was a repeat of the baseline test except the RSA plate and chamber walls were now wrapped and/or lined with a reflective gold foil (figure 10). This foil was added to aid in blocking radiant heat from being absorbed by the SiC RSA.

Test results (figure 9) show about a 50% decrease in the  $\Delta T$  across the strap.

### D. Indium test foil

This was a repeat of the gold foil test except with a cut out of 0.01in indium foil added between mating surfaces of the REC wall and strap end (figure 12). This was performed to increase the thermal contact conductance.

Test results show about a 1°C decrease in the  $\Delta T$  between the REC wall and strap end.

### E. Stycast epoxy test

This was a repeat of the indium test except with Stycast epoxy applied around the ends of the braids and then swaged for optimal contact.

The test result show an increase in temperature gradient between the strap end and the REC wall.

## VI. Summary

After discussing the test results with an LSST thermal panel, it was decided to keep the design of the thermal strap. A new test will be performed in TS7 with a full RTM adding indium foil between the strap end block and REC wall. A radiation heat shield has been designed and proposed by another engineer on the project and it will be decided if this piece can and will be added to the next full RTM test in TS7.

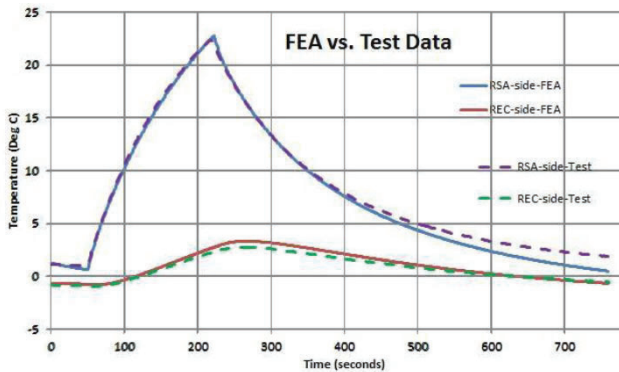


Figure 5: classic exponential rise and decay “sawtooth” response

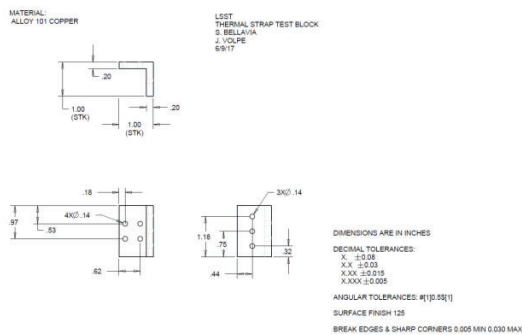


Figure 6: Drawing for copper connector used in test section A

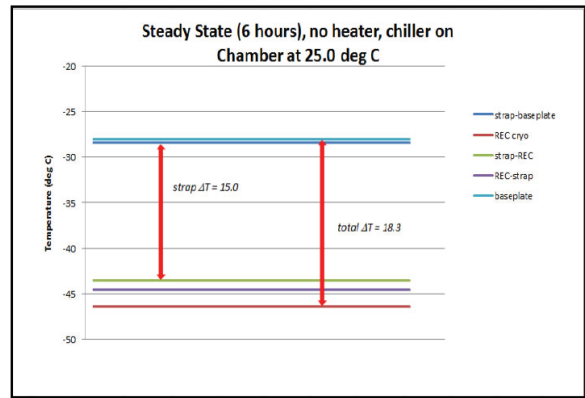


Figure 7: Baseline test results showing large  $\Delta T$

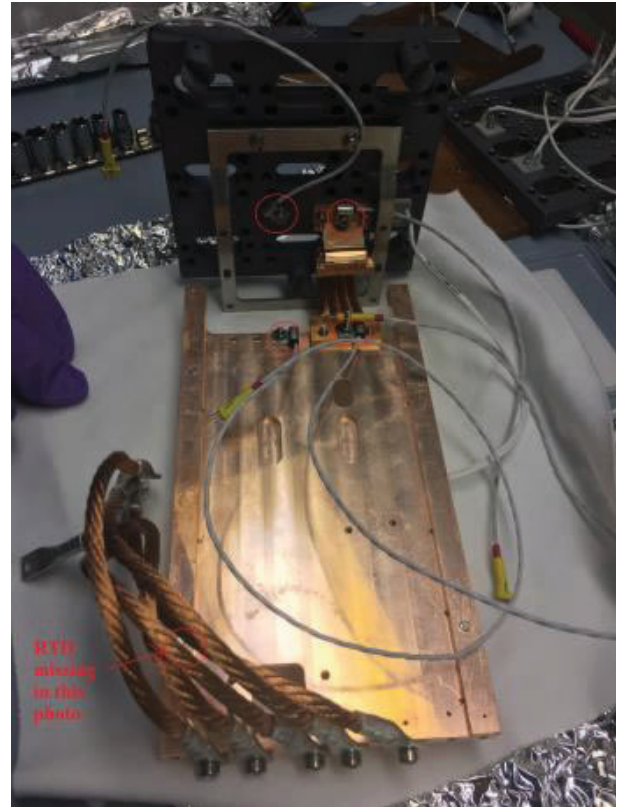


Figure 8. Baseline setup with RTDs showing (from bottom of photo up) RSA, Thermal strap, REC, cryocooler connectin braids within cryostat

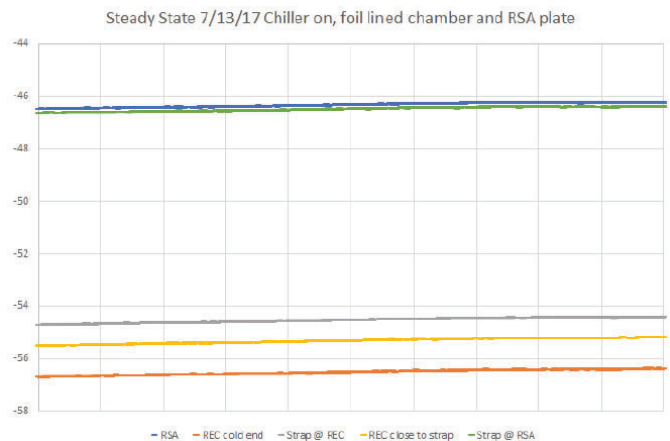


Figure 9: Foil test results showing decreased  $\Delta T$



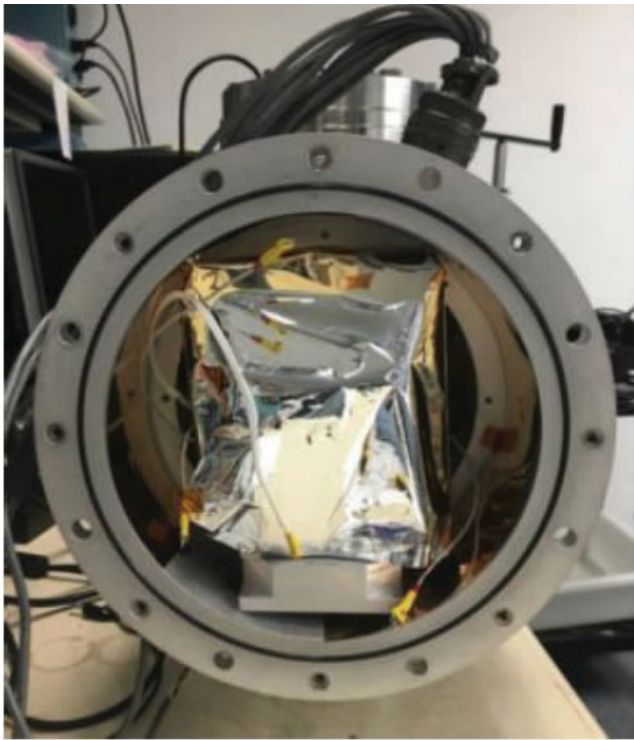


Figure 10: Image of foil lined chamber and wrapped RSA

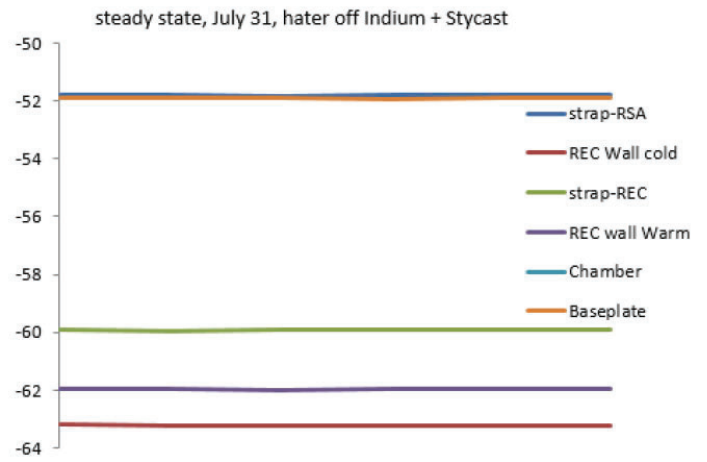


Figure 13: Stycast test showing an increase in the  $\Delta T$  from strap end to REC

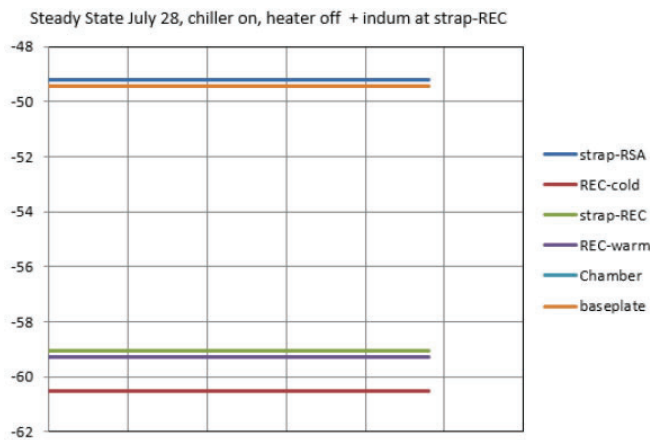


Figure 11: Indium test showing decreased  $\Delta T$  between mating surface (strap and REC)

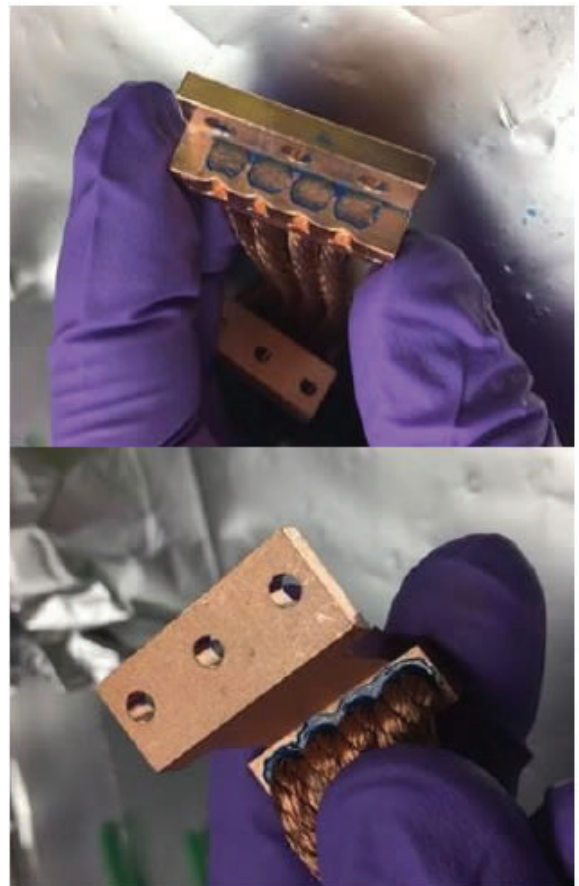


Figure 14: Thermal strap swaged with Stycast epoxy



Figure 12: 0.01” indium foil cut and applied to thermal strap end

# Using Fourier analysis of web server logs to defeat low observable cybersecurity threats

Janelle Walker, Department of Mathematics, CUNY Medgar Evers College, Brooklyn, New York 11225

Nicole Soder, Department of Mathematics, Stony Brook University, Stony Brook, New York 11794

David Biersach, Information Technology Department, Brookhaven National Laboratory, Upton, New York 11973

## ABSTRACT

Infrequent probing of internal web servers to uncover potential mistakes in document management permissions is often a precursor to successful industrial espionage. This research aims to develop algorithms to automatically identify and characterize non-standard browsing behavior of agents residing behind an organizational firewall. The research team will consider the practical application of Fourier analysis to develop statistic profiles of employees accessing an intranet web server, and to determine if these patterns can be leveraged to identify suspicious activity. Insider threats are often hiding in plain sight and effective cyber attackers smartly limit their attacks to such low frequency that their non-standard queries get lost in a sea of otherwise valid web traffic and are quickly buried in web server logs containing millions of records.

## I. INTRODUCTION

With our smart phones in hand and technology literally at our fingertips, our most valuable and confidential information has been made readily available to us and unfortunately, anybody else who manages to get into our phones. With the touch of the screen we can access back accounts, emails, transcripts and other sensitive personal information. But what if this information that we hold dear falls in the hands of the wrong person? In an instance, our entire life could take an unfortunate turn. Industrial espionage is a similar unfortunate situation on a scale times a million. Industrial Espionage is spying directed toward discovering the secrets of a rival manufacturer or other industrial company. Corporate companies and government organizations hold valuable information for customers, patients, clients and the country as a whole that could take a disastrous and devastating fall if even slightly compromised.

```
#Software: Microsoft Internet Information Services 8.5
#Version: 1.0
#Date: 2016-12-15 01:39:04
#Fields: date time s-ip cs-method cs-uri-stem cs-uri-query s-port cs-username c-ip cs(User-Agent) cs(Referer) cs-host sc-status sc-substatus sc-win32-status time-taken X-Forwarded-For
2017-01-26 00:02:29 130.199.70.170 GET / - 80 - 130.199.254.62 - - 200 0 64 15 -
2017-01-26 00:02:46 130.199.70.170 GET / - 80 - 130.199.254.62 Mozilla/4.0+(compatible);MSIE+8.0;+Windows+NT+5.1;+Trident/4.0 - ssp-webl.bn.gov 200 0 0 0 -
2017-01-26 00:02:46 130.199.70.170 GET / - 80 - 130.199.254.62 Mozilla/4.0+(compatible);MSIE+8.0;+Windows+NT+5.1;+Trident/4.0 - ssp-webl.bn.gov 200 0 64 0 -
2017-01-26 00:02:46 130.199.70.170 GET / - 80 - 130.199.254.62 Mozilla/4.0+(compatible);MSIE+8.0;+Windows+NT+5.1;+Trident/4.0 - 200 0 0 15 -
2017-01-26 00:02:55 130.199.70.170 GET / - 80 - 130.199.254.62 - ssp-webl.bn.gov 200 0 0 0 -
2017-01-26 00:03:50 130.199.70.170 GET / - 8080 - 130.199.72.250 Mozilla/5.0+(compatible);+PRG+Network+Monitor+(www.paessler.com);+Windows - ssp-webl.bn.gov:8080 200 0 0 0 -
2017-01-26 00:04:06 130.199.70.170 GET /nodehealth/health.php - 80 - 130.199.72.250 Mozilla/5.0+(compatible);+PRG+Network+Monitor+(www.paessler.com);+Windows - ssp-webl.bn.gov 200 0 0 0 -
2017-01-26 00:08:50 130.199.70.170 GET / - 8080 - 130.199.72.250 Mozilla/5.0+(compatible);+PRG+Network+Monitor+(www.paessler.com);+Windows - ssp-webl.bn.gov:8080 200 0 0 0 -
2017-01-26 00:08:58 130.199.70.170 GET / - 80 - 130.199.254.62 - - 200 0 0 31 -
2017-01-26 00:08:58 130.199.70.170 GET / - 443 - 130.199.254.62 - - 200 0 0 46 -
2017-01-26 00:08:58 130.199.70.170 GET / - 8080 - 130.199.254.62 - - 200 0 0 31 -
2017-01-26 00:09:06 130.199.70.170 GET /nodehealth/health.php - 80 - 130.199.254.62 Mozilla/5.0+(compatible);+PRG+Network+Monitor+(www.paessler.com);+Windows - ssp-webl.bn.gov 200 0 0 0 -
2017-01-26 00:09:07 130.199.70.170 GET / - 8080 - 130.199.254.62 Mozilla/4.0+(compatible);MSIE+8.0;+Windows+NT+5.1;+Trident/4.0 - ssp-webl.bn.gov:8080 200 0 0 0 -
2017-01-26 00:09:07 130.199.70.170 GET / - 8080 - 130.199.254.62 Mozilla/4.0+(compatible);MSIE+8.0;+Windows+NT+5.1;+Trident/4.0 - ssp-webl.bn.gov:8080 200 0 0 0 -
2017-01-26 00:09:07 130.199.70.170 GET / - 8080 - 130.199.254.62 Mozilla/4.0+(compatible);MSIE+8.0;+Windows+NT+5.1;+Trident/4.0 - ssp-webl.bn.gov:8080 200 0 0 0 -
2017-01-26 00:09:10 130.199.70.170 GET / - 80 - 130.199.254.62 Mozilla/4.0+(compatible);MSIE+8.0;+Windows+NT+5.1;+Trident/4.0 - ssp-webl.bn.gov 200 0 0 15 -
2017-01-26 00:09:10 130.199.70.170 GET / - 80 - 130.199.254.62 Mozilla/4.0+(compatible);MSIE+8.0;+Windows+NT+5.1;+Trident/4.0 - ssp-webl.bn.gov 200 0 0 0 -
2017-01-26 00:09:10 130.199.70.170 GET / - 80 - 130.199.254.62 Mozilla/4.0+(compatible);MSIE+8.0;+Windows+NT+5.1;+Trident/4.0 - ssp-webl.bn.gov 200 0 0 15 -
2017-01-26 00:09:16 130.199.70.170 GET / - 80 - 130.199.254.62 Mozilla/4.0+(compatible);MSIE+8.0;+Windows+NT+5.1;+Trident/4.0 - ssp-webl.bn.gov 200 0 0 0 -
2017-01-26 00:09:16 130.199.70.170 GET / - 80 - 130.199.254.62 Mozilla/4.0+(compatible);MSIE+8.0;+Windows+NT+5.1;+Trident/4.0 - ssp-webl.bn.gov 200 0 0 0 -
2017-01-26 00:09:16 130.199.70.170 GET /favicon.ico - 80 - 130.199.254.62 Mozilla/4.0+(compatible);MSIE+8.0;+Windows+NT+5.1;+Trident/4.0 - ssp-webl.bn.gov 404 0 2 0 -
2017-01-26 00:09:16 130.199.70.170 GET /favicon2.iso - 443 - 130.199.254.62 Mozilla/4.0+(compatible);MSIE+8.0;+Windows+NT+5.1;+Trident/4.0 - ssp-webl.bn.gov 404 0 2 15 -
2017-01-26 00:09:16 130.199.70.170 GET /favicon.ico - 443 - 130.199.254.62 Mozilla/4.0+(compatible);MSIE+8.0;+Windows+NT+5.1;+Trident/4.0 - ssp-webl.bn.gov 404 0 2 0 -
2017-01-26 00:09:16 130.199.70.170 GET /favicon2.iso - 8080 - 130.199.254.62 Mozilla/4.0+(compatible);MSIE+8.0;+Windows+NT+5.1;+Trident/4.0 - ssp-webl.bn.gov:8080 404 0 2 0 -
2017-01-26 00:09:16 130.199.70.170 GET /favicon.ico - 8080 - 130.199.254.62 Mozilla/4.0+(compatible);MSIE+8.0;+Windows+NT+5.1;+Trident/4.0 - ssp-webl.bn.gov:8080 404 0 2 0 -
2017-01-26 00:09:20 130.199.70.170 GET / - 443 - 130.199.254.62 Mozilla/4.0+(compatible);MSIE+8.0;+Windows+NT+5.1;+Trident/4.0 - ssp-webl.bn.gov 200 0 0 31 -
2017-01-26 00:09:20 130.199.70.170 GET / - 443 - 130.199.254.62 Mozilla/4.0+(compatible);MSIE+8.0;+Windows+NT+5.1;+Trident/4.0 - ssp-webl.bn.gov 200 0 0 0 -
2017-01-26 00:09:20 130.199.70.170 GET / - 443 - 130.199.254.62 Mozilla/4.0+(compatible);MSIE+8.0;+Windows+NT+5.1;+Trident/4.0 - ssp-webl.bn.gov 200 0 0 46 -
2017-01-26 00:09:20 130.199.70.170 GET / - 80 - 130.199.254.62 Mozilla/4.0+(compatible);MSIE+8.0;+Windows+NT+5.1;+Trident/4.0 - ssp-webl.bn.gov 200 0 64 31 -
2017-01-26 00:09:20 130.199.70.170 GET / - 443 - 130.199.254.62 Mozilla/4.0+(compatible);MSIE+8.0;+Windows+NT+5.1;+Trident/4.0 - ssp-webl.bn.gov 200 0 64 31 -
2017-01-26 00:09:20 130.199.70.170 GET / - 8080 - 130.199.254.62 Mozilla/4.0+(compatible);MSIE+8.0;+Windows+NT+5.1;+Trident/4.0 - ssp-webl.bn.gov:8080 200 0 0 46 -
```

FIGURE 1. Screenshot of a HTTP web server log data file for Brookhaven National Laboratory

## II. BACKGROUND INFORMATION

### A. Economic Espionage Act

The Economic Espionage Act of 1996, enacted October 11, 1996, was a 6 title Act of Congress that dealt with a wide range of issues, including not only industrial espionage, but also the United States Sentencing Commission reports regarding encryption or scrambling technology, and other technical and minor amendments. 18 U.S.C. §§ 1831-1839, defines the term “economic espionage” as the theft or misappropriation of a trade secret with the intent or knowledge that the offense will benefit any foreign government, foreign instrumentality, or foreign agent. The penalties for economic espionage can be stiff – those using stolen trade secrets to benefit a foreign government face a fine of up to \$500,000 and/or up to 15 years in federal prison, while those who steal trade secrets for their own gain may be fined or put in prison for up to ten years.

### B. W3C Extended Log File Format

The W3C Extended Log File Format permits control over the data recorded. It supports needs of proxies, clients and servers in a common format, provide robust handling of character escaping issues, allow exchange of demographic data and allow summary data to be expressed.

### C. Advanced Persistent Threats

An advanced persistent threat (APT) is a network attack in which an unauthorized person gains access to a network and stays there undetected for a long period of time. The intention of an APT attack is to steal data rather than to cause damage to the network or organization.



### III. METHODS AND MATERIALS

#### A. FourierAnalysis

Converting a complex wave into a series of simple waves, each with different amplitudes at integer frequencies, is called the Fourier Transform. The reverse process of reconstructing the original complex wave by summing all of the contributing simple wave forms is called the Inverse Fourier Transform. It is a transform because we are converting back and forth between representing a wave as a sample of amplitudes over time or a sample of amplitudes at given frequencies. It is two sides of the same mirror – both approaches equally describe the same wave– but the frequency “view” often reveals hidden patterns in the wave.

#### B. Discrete Fourier Transform

Converting a sampled complex wave into a series of sampled simple waves, each with different amplitudes at specific frequencies, is called the Discrete Fourier Transform (DFT). The reverse process of reconstructing the original complex wave by summing all of the contributing simple wave forms is called the Inverse Discrete Fourier Transform (IDFT). The sum of many discrete samples of a wave approximates its continuous integral if the spacing (time) between samples is sufficiently small.

#### C. K-means Clustering

*k*-means clustering aims to partition *n* observations into *k* clusters (where each cluster has its own  $\mu$  point). Each observation is assigned to the cluster whose  $\mu$  point is closest to that observation’s point. The problem is computationally difficult (NP-hard); however, there are efficient heuristic algorithms that are commonly employed and converge quickly to a local optimum. The term “*k*- means” was first used by James MacQueen in 1967, though the idea goes back to Hugo Steinhaus in 1957. A more efficient version was published Hartigan and Wong in 1979.

### IV. RESULTS

This research project was aimed at highlighting 4 key Advanced persistent threats (APT):

- Logon (Authentication request)- over a period of time.
- Search query submission – over time (misconfigured access control lists- ACLs) The total number of searches by a given user – over a period of time.
- Server-side generated HTTP error code responses – over a period of time(404).
  - Analysis Approach: Consider all users: DFT -> kMeans -> Outlier detection

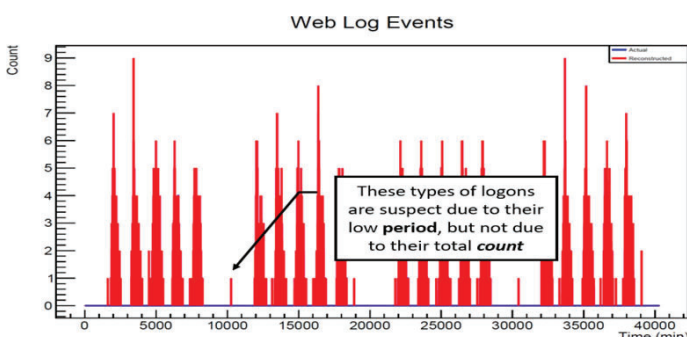


FIGURE 2. Shows the total number of weblog events against the sample period. Normal human behavior has a low frequency and a high period.

- Logon (Authentication request) – over space {from source/ client IPAddress}
  - Analysis Approach: Consider single users at a time: Simple “subnet” Histogram.

Intranet (insider threats) sites (intranet.bnl.gov) vs internet (outsider threats) sites ([www.bnl.gov](http://www.bnl.gov)) pose more of a threat to an organization because there are less efforts to keep people on the inside out. Over the years, this has proven to be one of the most dangerous form of industrial espionage. Normal behavior generally follows reproducible patterns; hackers do not. Hackers are patient in waiting for the good guys to make a mistake and they are usually hiding in plain sight; lost in the avalanche of valid traffic. This concept is intuitively “finding a needle in a haystack”, but it must be done very quickly (quasi real-time).

### V. FUTURE WORK

For future work, we will consider the spatial arrangements of Advanced Persistent Threats by using IP (Internet Protocol) addresses (Logon (Authentication request) – over space {from source/ client IP address}); Analysis Approach: Consider single users at a time: Simple “subnet” Histogram). Logons to the same site for the same search inquiry from the same login information but from a different location will spike suspicion. This suspicion is further intensified if there is a significant distance between geographical locations of IP addresses. An example of this would be a search of “Apollo” from New York, China and England in the search tool for Brookhaven or even just a logon from these locations using the same login information.

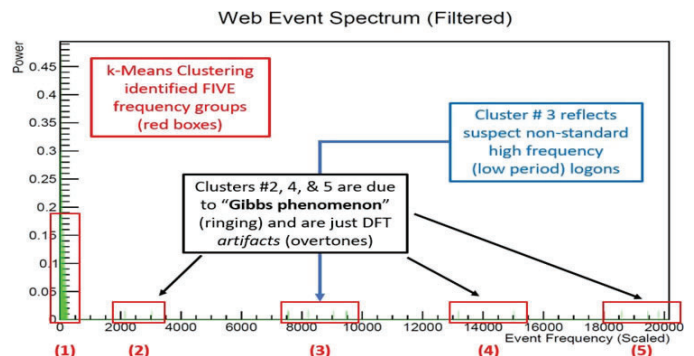


FIGURE 3. Demonstrates the 1<sup>st</sup> type of the 4 types of Advanced Persistent Threats under investigation for this research. Normal human behavior will fall into clusters. Our aim is to find the frequencies that fall outside these clusters.

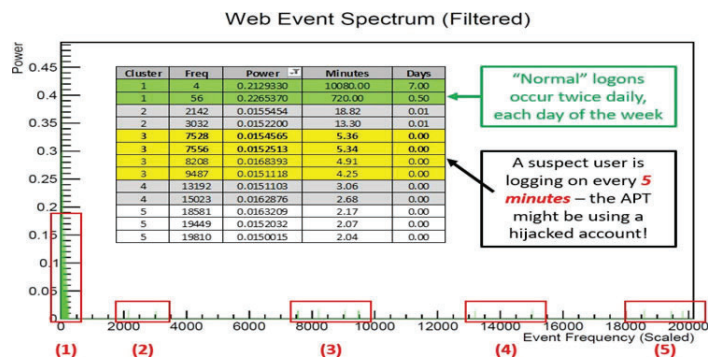


FIGURE 4. Explains the mapping of frequencies back to the original time domain. Abnormal behavior has a high frequency but a low period. The following table and graph analyses the frequency of logons and group them into clusters to identify outliers.



## VI. ACKNOWLEDGEMENTS

A special thanks to the following people for their guidance and leadership:

- Brookhaven National Laboratory
- Office of Educational Programs
- Noel Blackburn (Program Coordinator)
- David Biersach (Mentor)
- Mel Morris

This project was supported in part by the U.S. Department of Energy, Office of Science, Office of Workforce Development for Teachers and Scientists (WDTS) under the Science Undergraduate Laboratory Internships Program (SULI).

## VII. REFERENCES

Butz, Tilman. "Fourier Transformation for Pedestrians." *Tilman Butz | Springer*. Springer International Publishing. cern root 5.36/windows

Transnational College of Lex (Author). "Who Is Fourier? A Mathematical Adventure 2nd Edition (9780964350434): Transnational College of Lex: Books." *Amazon.com: Who Is Fourier? A Mathematical Adventure 2nd Edition (9780964350434): Transnational College of Lex: Books, Language Research Foundation, 1995, [www.amazon.com/Who-Fourier-Mathematical-Adventure-2nd/dp/0964350432](http://www.amazon.com/Who-Fourier-Mathematical-Adventure-2nd/dp/0964350432)*.

Weert, Peter Van, and Marc Gregoire. *C Standard Library Quick Reference*. Berkeley, CA: Apress, 2016. Print.

# Impact of Pine Barrens forest vegetation on population density of mice (small mammals) at Brookhaven National Laboratory

Tre' Wise

Department of Natural Sciences, Southern University at New Orleans, LA 70126

Russell Burke

Department of Biology, Hofstra University, Hempstead, NY 11549

Murty S. Kambhampati

Department of Natural Sciences, Southern, University at New Orleans, New Orleans, LA 70126

Jennifer Higbie and Timothy Green

Environmental Science, Brookhaven National Laboratory, Upton, NY 11973

## Abstract

The abundance of vegetation, and how it varies across a landscape, may be decisive to habitat use by mice (small mammal) populations. This study addressed the relative importance of vegetation types and their abundance/heights to mice population density. During summer, we collected data on mouse populations and vegetation structure at 16 experimental sampling plots. We hypothesized that mice density would be higher in areas where the vegetation is taller than 35 centimeters. We have placed ten plots on the East side and six plots on the South side of Pine Barren forest of Brookhaven National laboratory. At each plot we set up a 35x35m grid and placed 64 traps (12x3x3) with flags at every 5 m inside of the grid. Over a period of 8 weeks, we have studied mice population densities twice in 1,024 trap/nights. Prior to trapping mice, we established a linear transect down the middle of each grid. Along these transects we measured the heights of litter, slash (woody debris), dead standing shrubs, and live standing shrubs. At each location we trapped mice, marked them with ear tags, and identified the sex. At locations 1, 3, 4, 7, 9, and 16, vegetation was taller than 1 foot. Fifty percent of the locations had vegetation heights greater than 1 foot. We captured 45-59 mice at each of these locations. Two sites were burned prior to trap studies, and 0-5 mice were captured after a week of trapping. This project has helped me understand the scientific method and its application better in a field based ecological experiment. Being a part of small mammals (mice) team project at BNL, I appreciate science better.

## I. Introduction

The white-footed mouse (*Peromyscus leucopus*) is a habitat generalist and a permanent resident of shrub land, forest and grassland (Adler & Wilson, 1987). Observations show that it is found generally at higher densities in hardwood forests with a large volume of stumps and logs, and dense ground cover (Brannon, 2002). The spatial distribution of small mammal species is influenced by interaction of various factors including food availability, water and predators (Poulin et al., 2002). Climate change allows reservoir hosts and vectors to expand their range into new territories (Brownstein et al. 2005). In addition, fragmentation of forested landscapes due to human activities affects local biodiversity by favoring habitat generalists and species that experience high population densities and small home ranges. Although forest fragmentation generally reduces species diversity within remnant

patches (Allan et al. 2003), numerous studies found that *P. leucopus* population densities increased as patch size decreased, indicating that their abundance is actually enhanced by forest fragmentation (Yahner 1992).

White-footed mice play an important role in the ecosystem. White-footed mice help spread various kinds of fungi by eating the sporing bodies and excreting spores. Forest trees' ability to take up nutrients is enhanced by the mycorrhizal associations formed by these fungi. For many temperate forest trees, these fungi have been shown to be an essential element in order for trees to prosper. White-footed mice also help control populations of some harmful insect pests, such as gypsy moths. They are active primarily at night and are secretive and alert, thus avoiding many predators. Undesirably, White-footed mice carry deer ticks, which spread Lyme disease. They also may be a reservoir for Four-Corners disease, as their fecal matter can contain Hantavirus, the organism that causes this disease. White-footed mice may also act as seed predators of oaks and pines, hindering their growth and spread.

Our study objectives were: 1) to determine the relationship between mouse population density to vegetation height, (2) to increase the knowledge base of ecological studies of mice, (3) to provide information to National Resource Management at BNL for future management strategies on vegetation height and altering plant community characteristics and, (4) to identify the opti-

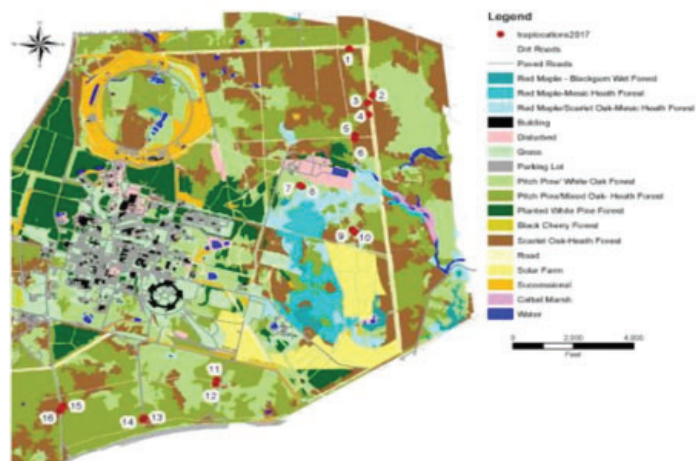


Fig 1. Map of BNL showing the 16 sites used in this study. GPS coordinates (Universal Transverse Mercator units) were used to locate the sites.

mum vegetation height for mice population in undisturbed Pine Barren forest at BNL

## II. Methods

Sixteen experimental sites were sampled over a four week period allowing each site to be studied twice over the eight week period. At each site, we established an 8x8 grid of Sherman traps spaced 5 meters apart, resulting in 64 traps per grid. Traps were baited with peanut butter/oat mixture. Cotton pads were placed under the bait to provide insulation overnight if the temperature plummeted.

To examine habitat preference in mice, 35 meter linear transects were conducted down the middle of each grid to estimate ground level vegetation heights (cm) within each plot. Litter, slash (woody debris), rooted dead standing, and rooted live standing heights (cm) were taken at every 5 meters of our linear transect. Each trap session was conducted over four consecutive nights. Traps were checked each morning; captured animals were weighed, sexed, and marked with individual ear tags. Recaptured individuals were noted. All attached ticks were removed and preserved. Program MARK Version 8.1, was used for a parameter estimate of mice abundance at each site. The design model considers the time interval between trapping sessions as “open” and the time interval during trapping as “closed”. Furthermore, Program DENSITY Version 5.0 was used to estimate the density of mice population using the spatially unambiguous capture-recapture data collected (Efford 2012).

## III. Results

Using program DENSITY for calculation, the basic linear regression in Figure 2A showed that there was a significant relationship between the density of mice to heights of vegetation at sites 1-8 (Fig2A;  $R^2= 0.13$ ,  $t(14) = 5.68$ ,  $p=0.05$ ,  $n=8$ ). Conversely, using the same program for Figure 2B, there was no significant correlation between density of mice and heights of vegetation at sites 9-16 (Fig2B;  $R^2= 0.28$ ,  $t(14) = 1.02$ ,  $p=0.13$ ,  $n=8$ )

## IV. Discussion

The white-footed mouse ranges in color from grayish-brown to reddish-brown on its dorsal side and face while its ventral side and legs are white. Its average mass is 0.81 oz but can range from 0.5 oz to 1 oz. Other members of the *Peromyscus* family all have similar looks or ranges but can be differentiated by either tail length or mass. *Peromyscus leucopus* is a plentiful disperser and colonizer, and a single mating pair may establish a successful population upon entering a new habitat. They have been

found to expand their range at an astonishing rate: approximately 15 km/year in the Great Lakes region and 10 km/year in southern Québec (V. Millien, pers. comm.) but their local movements may get hindered by various landscape barriers including agricultural fields, water, and roads. Other studies indicate, however, that *P. leucopus* shows high levels of dispersal regardless of their habitat. Since the white-footed mouse is primarily nocturnal, its main predators are those that are active between dusk and dawn. Snakes, owls, bobcats, weasels, and foxes are common predators of the white-footed mouse. The primary diet of the white-footed mouse is seeds, grains, small fruits, and small insects.

Our study indicates mice optimum habitat is dense shrubland. At sites with vegetation higher than 35cm, more mice were captured over the one week span of trapping at that site. As the vegetation height decreased to below 35cm, mouse populations plummeted. Low vegetation heights are subject to change overtime due to growth. Population size in areas of low vegetation will change subsequently to vegetation growth and mice reproduction. Contrarily, mouse populations may decrease in areas with vegetation higher than 35cm due to vegetation fragmentation. Predation affects low population of mice in areas lacking dense vegetation.

## V. Acknowledgments

We would like to give a special thanks to Jennifer Higbie for all of her guidance on this project. We would also like to thank the rest of the Environmental Protection Division interns for their help and insight. We would also like to thank National Science Foundation – LSAMP program for allowing me to participate in this summer research project at BNL. This project was supported in part by the U.S. Department of Energy, Office of Science, Office of Workforce Development for Teachers and Scientists (WDTS), and the NSF LSAMP program.

## VI. References

- Adler, G. H., & Wilson, M. L. (1987). Demography of a Habitat Generalist, the White-Footed Mouse, in a Heterogeneous Environment. *Ecology*, 68(6), 1785-1796.
- Borchert, M., & Borchert, S. M. (2013). Small mammal use of the burn perimeter following a chaparral wildfire in southern California. *Bulletin, Southern California Academy of Sciences*, 112(2), 63-73.
- Ford, S. D. (1977). Range, distribution and habitat of the western harvest mouse, *Reithrodontomys megalotis*, in Indiana. *American Midland Naturalist*, 422-432.
- Grelle, C. E. V. (2003). Forest structure and vertical stratification of small mammals in a secondary Atlantic forest,

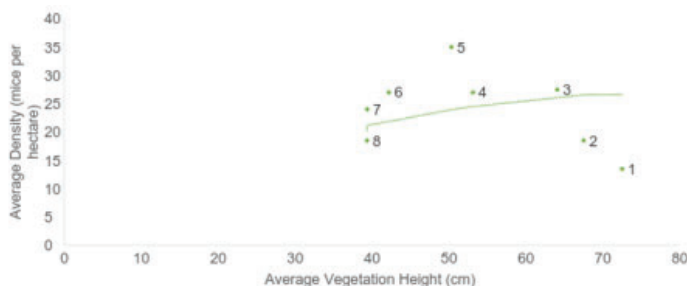


Fig2A. Density of mice in relation to vegetation heights greater than 35cm (1-8).

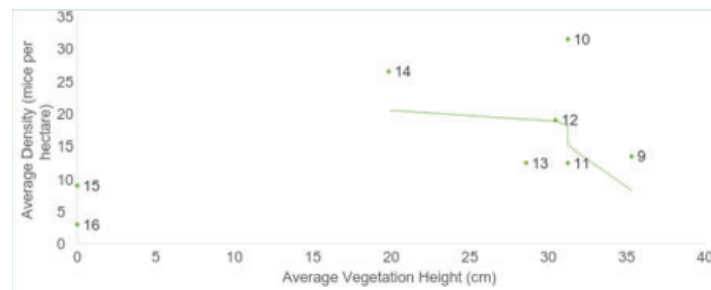


Fig2B. Density of mice in relation to vegetation heights less than 35cm (9-16).



- southeastern Brazil. *Studies on Neotropical Fauna and Environment*, 38(2), 81-85.
- Stevens, S. M., & Husband, T. P. (1998). The influence of edge on small mammals: evidence from Brazilian Atlantic forest fragments. *Biological Conservation*, 85(1-2), 1-8.
- Tattersall, F. H., Macdonald, D. W., Hart, B. J., Manley, W. J., & Feber, R. E. (2001). Habitat use by wood mice (*Apodemus sylvaticus*) in a changeable arable landscape. *Journal of Zoology*, 255(4), 487-494.

# The process of aligning the carbon dioxide laser final amplifier in the Accelerator Test Facility II

Rick Zirkel

Biomedical Engineering, SUNY University at Buffalo, Buffalo, NY 14261

Christian Cullen

C-AD, Brookhaven National Laboratory, Upton, NY 11973

## Abstract

The Accelerator Test Facility II (ATF-II) is currently undergoing construction to upgrade the original ATF in order to provide the best possible experimental resources to the community. The upgrade will include an increase in laser and electron beam energies, enabling an increase in power from 1 TW to ~100 TW in sub-picosecond pulses for the CO<sub>2</sub> laser. Such technology will be made possible by the addition of stages to the laser's amplification chain, and will open the first-time opportunity to explore strong-field physics in the mid-IR spectral domain. Our work consisted of the alignment of the final amplifier for the CO<sub>2</sub> laser. With the use of a 3D model of ATF-II and survey data, and performing several stress analysis calculations, we were able to develop a set of step-by-step instructions for riggers and surveyors to take in order to align the three units. Nine total components, each with six degrees of freedom, were aligned to complete the final amplifier assembly. The centerline of the pressure vessels were aligned with the beamline and were bolted together in order to ensure minimal strain on the vessels, greatly reducing the chance of damage or pressure release. To enable us to move the units together, I designed support and positioning fixtures that were used as points of leverage to be able to shift the units horizontally and lock into final position. Each unit also consisted of a water capacitor and marx generator, which were adjusted to align with the flanges of the other components, again ensuring minimal stress on the system. While working through such processes, I gained valuable 3D modelling skills with the use of Creo Parametric, as well as structural analysis simulation experience with the use of ANSYS. I also learned important planning skills with various skilled trades in my efforts to construct an alignment plan for the amplifier.

## I. Introduction

The Accelerator Test Facility II (ATF-II) is currently undergoing construction to upgrade the original ATF in order to provide the best possible experimental resources to the community. The upgrade will consist of an increase in experimental space, and laser and electron beam energies. The ATF-II will be in a larger building, with space to accommodate multiple experiment halls. The upgrade of the CO<sub>2</sub> laser will enable an increase in power from 1 TW to ~100 TW in sub-picosecond pulses.<sup>1</sup> This upgrade will be made possible by the addition of stages to the laser's amplification chain. With such a significant increase in laser power, the experimental capabilities offered will allow, most notably, ion generation at radiotherapy relevant energies and will also lead to further development of high luminosity laser wakefield accelerators.<sup>1</sup>

Our work dealt with the alignment of the final amplifier of the CO<sub>2</sub> laser that will be functional in ATF-II. The amplifier system

consisted of nine components, two of which are not yet available due to their current use in ATF-I (see Figure 1). Three pressure vessels, two water capacitors, and two marx generators were the focus of our project, in order to properly prepare the amplifier for use with the CO<sub>2</sub> laser upgrade.

## II. Alignment of Each Unit

At the beginning of the alignment process we measured the height of the carriages of each unit off of the ground, and the distance that we had to lower them. At this time, the vessels were well above the beam height, where we did not have enough distance in our adjustments to lower them to the proper height. These measurements were crucial in determining our approach to leveling the units.

We were then able to, with the help of survey, level the carriages using adjustments located on the wheels. During this leveling, we also needed to make the flanges located on the vessels vertical. The adjustment pads underneath the vessels, which had prior been bottomed out and prevented our use of them, now had enough room for us to use them for the purpose of aligning the vessels.

With the vessels in the correct position, the next step was to align the water capacitors with their respective pressure vessels. This was able to be done using the adjustment pads underneath the water capacitors. The connection between the two pieces of hardware, however, is a ceramic voltage feedthrough. Because this is such an extremely delicate connection, we planned to verify the alignment using other methods as to not risk damage to the ceramic piece. To do this, we designed a dummy flange to represent the connection the feedthrough would make with the vessel (see Figure 2). Using this and the collar that then mates up and attaches to the water capacitor, we were able to verify the alignment safely.

Finally, the marx generators of the north and south units were then aligned with their respective connections on the water capacitors. This was a much easier connection to make and verify, as it is much less rigid and requires a fraction of the delicacy that went into ensuring the precision of the ceramic connection of the water capacitor to the pressure vessel.

## III. Vessel Connection

With all pieces aligned, the next step would be to bolt together the pressure vessels, solidifying the functional state of the units and creating a pressure-tight seal inside the amplifier. The distance separating the vessels, however, was too great to overcome by bolting them together. The welds that attach the outer flanges of their vessels to each other might undergo deformation due to the stress of the bolts pulling the units together.

In order to determine a safe distance apart at which we could bolt the vessels together, an ANSYS simulation was performed on

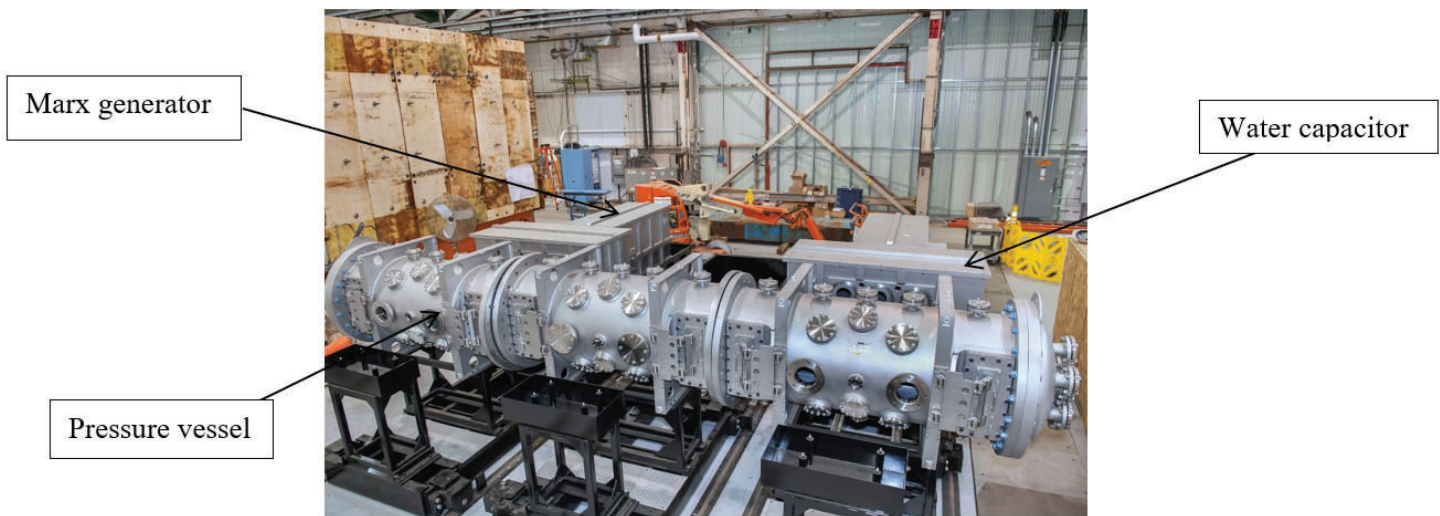


Figure 1. Final amplifier assembly with 7/9 components in place in ATF-II

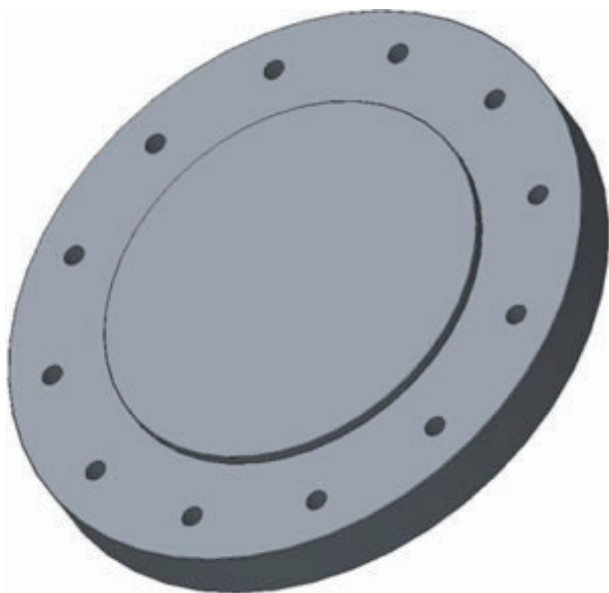


Figure 2. Dummy flange connection

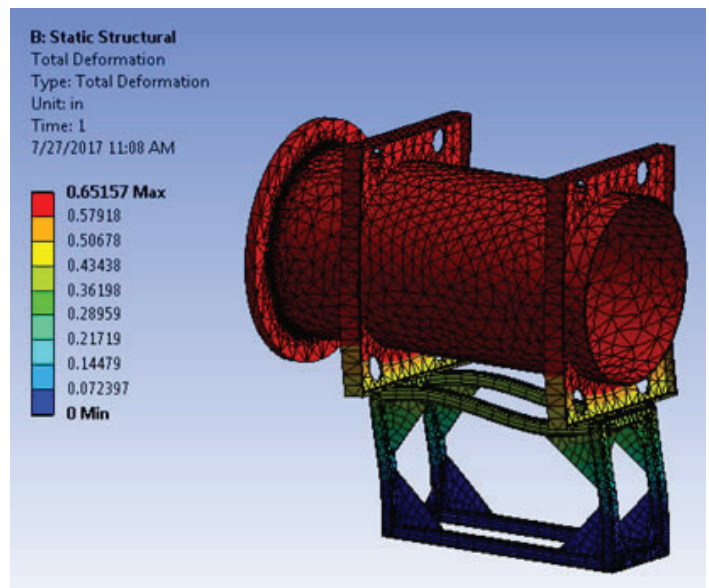


Figure 3. Total deformation of vessel due to deflection

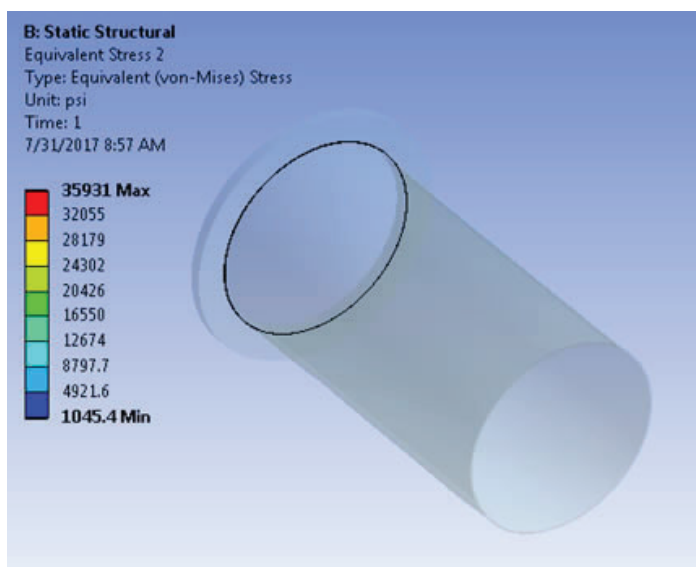


Figure 4. Equivalent stress of weld

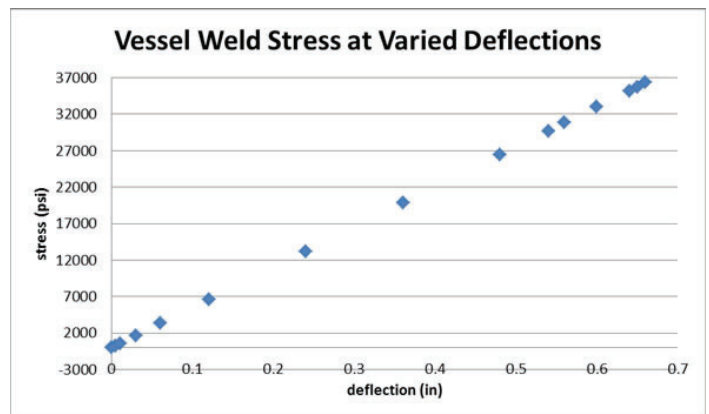


Figure 5. Table showing varied values and pattern of stress based on changed deflection (sample data shown for displacement of 0.65")



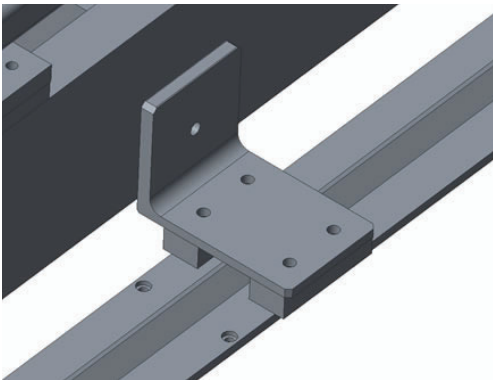


Figure 6. Angle fixture with blocks to raise it above the track

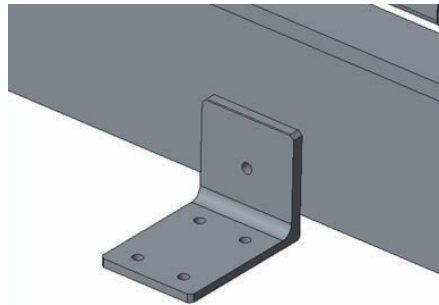


Figure 7. Angle fixture to keep the carriage from moving on track

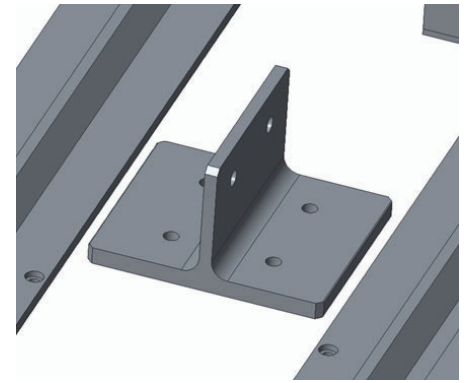


Figure 8. Tee fixture placed in between carriages

a modified version of the vessel assembly, with a focus on the integrity of the weld. A displacement of the flange was set at varied distances. The total deformation of the vessel, shown in Figure 3, shows how the displacement had an effect on the overall system. Figure 4 displays an equivalent stress analysis also added to the solution, which showed the amount of stress that was being put on the weld when the displacement took place. These data were organized into Figure 5: a chart comparing the deflection of the flange and the stress that was recorded at the weld. In order to avoid risking potential damage to the weld and compromising the

pressure-containing capability of the amplifier, a new method had to be drawn up.

After brainstorming various methods we could employ, we decided to examine positioning fixtures set up on the floor throughout the assembly as a possible option.

In determining the method we would use for horizontal displacement of the carriages, we had to take into account several factors. One of the main factors was the load that would need to be supported by such method. Determining whether or not positioning fixtures would be a viable option depended on the bending force that would be put on the pieces, and if that force could be withstood. Based on the measurements of the web thicknesses and flange dimensions of the I-beams in the steel yard, and several calculations regarding moments of inertia and loads, it seemed that the pieces would be able to provide the support necessary to move the carriages.

After deciding that the best method to use in our efforts to shift the units horizontally would be positioning fixtures, we made our way to the steel yard to pick out a proper I-beam. After recording 10 different I-beams, along with their distinguishing features, such as flange width, web thickness, and beam height, we needed to choose a beam that was best suited to our needs. For our purposes, a thick web was very important for a solid support to push off of. It was also crucial that we had a beam with a height tall enough for a rod to connect the fixture to the unit carriage. In finding the best beam, we had riggers remove it from the steel yard, and it was then machined to the dimensions of our fixtures. Two angles on both sides of each unit were placed on blocks as to have them sit above the track (see Figure 6). Two more angles were then placed on the front and back of each unit, as a support to hold the carriages in place (see Figure 7). Two tees were then also placed in each space in-between carriages (see Figure 8).

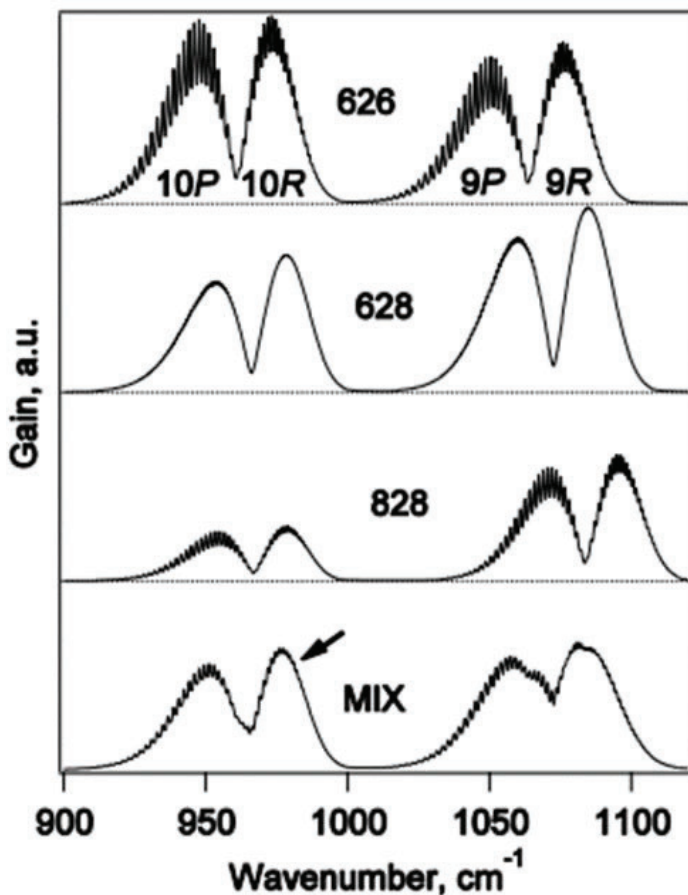


Figure 9. Gain spectra for three CO<sub>2</sub> isotopologues with different combinations of oxygen-16 and oxygen-18 atoms: 16O-12C-16O (626), 16O-12C-18O (628) and 18O-12C-18O (828) and a combined spectrum of their mixture in the statistically equilibrium proportion 1:2:1 (MIX). The arrow shows the 10R branch used in the laser in ATF-I.<sup>2</sup>

#### IV. Results

We were able to level and align the units of the final amplifier with the help of survey and our alignment methods. The amplifier units were bolted together carefully, with minimal stress applied to the vessel.

The alignment of the final amplifier is extremely important because it allows for the laser to be brought up to the ultimate operating power of 100 TW. As the beam enters the amplifier, it moves back and forth within the vessels using optical equipment. Collision with the excited isotopic gas mixture inside the pressurized vessels causes an emission of the same entering photon, thereby doubling the power of the pulse.<sup>2</sup>

A higher pressure means the molecules will become more active and collide with the beam more, decreasing the pulse duration. As power is determined by the energy divided by the time it spans, the decrease in pulse duration is essential to reaching the peak power of the laser.<sup>2</sup>

The isotopic mixture of gases allows for a smoother gain spectrum, due to an increase in the density of rotational lines (see Figure 9), which occur due to losses and gains in energy during changes in angular momentum. This makes it easier for more frequencies of the photon to collide with the gases, causing a shorter pulse duration.<sup>2</sup>

The amplifier, and CO<sub>2</sub> laser, will not operate at full power until the marx generator and water capacitor being used in ATF-I are moved to ATF-II and a clean room is built around the units.

## **V. Acknowledgments**

This project was supported in part by the U.S. Department of Energy, Office of Science, Office of Workforce Development for Teachers and Scientists (WDTS) under the Science Undergraduate Laboratory Internships Program (SULI)

## **VI. References**

<sup>1</sup>C. Swinson, “Facility Upgrade – ATF-II on the Horizon” Spring 2014.

<sup>2</sup>M. N. Polyanskiy, I. V. Pogorelsky, V. Yakimenko, “Picosecond pulse amplification in isotopic CO<sub>2</sub> active medium.” 6 Apr 2011.